NSF/CEE-83003

FINAL REPORT

PB83-195891

CLADDING–STRUCTURE INTERACTION IN HIGHRISE BUILDINGS

By

B. J. Goodno
J. I. Craig
M. Meyyappa
H. Palsson

Prepared for

NATIONAL SCIENCE FOUNDATION
CIVIL AND ENVIRONMENTAL ENGINEERING
EARTHQUAKE HAZARDS MITIGATION

Under

Grant CEE–7704269

January 1983

GEORGIA INSTITUTE OF TECHNOLOGY
A UNIT OF THE UNIVERSITY SYSTEM OF GEORGIA
SCHOOL OF CIVIL ENGINEERING AND
SCHOOL OF AEROSPACE ENGINEERING
ATLANTA, GEORGIA 30332

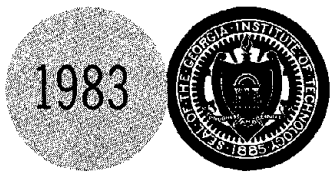

50272-101

REPORT DOCUMENTATION PAGE	1. REPORT NO. NSF/CEE-83003	2.	3. Recipient's Accession No. PB83 195891
4. Title and Subtitle: Cladding Structure Interaction in Highrise Buldings, 1983 Final Report			5. Report Date: January 1983 6.
7. Author(s): B.J. Goodno, J.I. Craig, M. Meyyappa, H. Palsson			8. Performing Organization Rept. No.
9. Performing Organization Name and Address: Georgia Institute of Technology School of Civil Engineering and School of Aerospace Engineering Atlanta, GA 30332			10. Project/Task/Work Unit No. 11. Contract(C) or Grant(G) No. (C) (G) CEE7704269
12. Sponsoring Organization Name and Address: Directorate for Engineering (ENG) National Science Foundation 1800 G Street, N.W. Washington, DC 20550			13. Type of Report & Period Covered: Final 1983 14.

15. Supplementary Notes: Submitted by: Communications Program (OPRM)
National Science Foundation
Washington, DC 20550

16. Abstract (Limit: 200 words)

The potential lateral stiffness contribution of heavy-weight claddings on buildings and the role of cladding in altering dynamic properties and linear seismic response were investigated. The prototype structure studied was a 24-story steel frame office building of core construction with a contoured precast panel facade. Results obtained from a sheer stiffness model were compared to those obtained from three-dimensional finite element models. Lateral stiffness was shown to be heavily dependent on details of the panel-frame attachment. The addition of cladding models to conventional frame models of highrise buildings was found to alter predicted overall structure frequencies and linear seismic response.

17. Document Analysis a. Descriptors

Buildings
Mathematical models
Computers
Earthquake resistant structures
Dynamic structural analysis
Cladding
Stiffness

b. Identifiers/Open-Ended Terms

Highrise buildings
B.J. Goodno, /PI

c. COSATI Field/Group

18. Availability Statement: NTIS

19. Security Class (This Report)
20. Security Class (This Page)
21. No. of Pages
22. Price

(See ANSI-Z39.18) See Instructions on Reverse OPTIONAL FORM 272 (4-77) (Formerly NTIS-35) Department of Commerce

CLADDING-STRUCTURE INTERACTION IN HIGHRISE BUILDINGS

B.J. Goodno
J.I. Craig
M. Meyyappa
H. Palsson

FINAL REPORT

NSF Grant CEE-7704269

Prepared for the

National Science Foundation
Civil and Environmental Engineering
Earthquake Hazards Mitigation

GEORGIA INSTITUTE OF TECHNOLOGY
Schools of Civil and Aerospace Engineering

January 1983

ACKNOWLEDGEMENTS

The authors would like to acknowledge Dr. John B. Scalzi, Program Manager, Earthquake Hazards Mitigation, NSF, for his continued support and guidance provided throughout the course of this research program.

Dr. Kenneth M. Will, Associate Professor, School of Civil Engineering, Georgia Tech, is recognized for his contributions to the analytical research effort, principally in the area of finite element modeling of cladding panels and their connections.

The following students were supported to varying degrees on the research project and made significant contributions leading to its successful completion: H. Palsson, M. Meyyappa, K. Gram, P. LeBoeuf, R. Roglin, G. Saurer, M. Ansley, D. Pless, J. Hopkins, and M. Keister.

Any opinions, findings, and conclusions or recommendations expressed in this report are those of the authors and do not necessarily reflect the views of the National Science Foundation.

TABLE OF CONTENTS

SUMMARY

Heavyweight cladding systems on modern highrise buildings are often regarded as nonstructural ornamentation by structural designers. Reported failures, however, suggest that cladding components are participating structural elements which can provide considerable additional lateral stiffness to aid in resistance to wind and moderate eathquake loadings. This research program has employed a combination of analytical and field-experimental studies of a medium highrise office building with precast concrete cladding to investigate the potential role of the building facade.

Analytical models were used to study cladding's influence on building frequencies and linear seismic response. Dynamic properties of the structure model were altered by 15-30% for translational modes and by up to 65% for torsional modes by the addition of cladding. However, finite element studies demonstrated that interstory shear stiffness is heavily dependent on cladding connection details and panel support conditions.

Experimental studies were carried out on two highrise buildings to quantify these effects and confirm analytical models. The first series of tests consisted of ambient vibration measurements on a 24 story steel frame structure throughout the course of construction from bare to fully clad. From modal response results, it was observed that cladding measurably stiffens the structure and raises natural frequencies, most pronouncedly for higher modes. Full

scale forced vibration tests were performed on a second completed 24 story building to determine twelve bending and torsion frequencies and mode shapes. The tests were carried out using a specially designed transient vibration generator, multichannel response measurement and time series methods for modal analysis. System identification methods were used to estimate stiffness parameters associated with the core, exterior frame and cladding stiffness. The results were generally within bounds established by analytical models.

Studies of overall building response to earthquake ground motion showed that structure response may be either increased or decreased by including cladding effects depending on the frequencies of the clad and unclad models and their relation to the frequency content of the ground motion. A simple panel failure model was proposed, and localized cladding failure was shown to result in a substantial increase in building torsional response. Studies of 'nonstructural' cladding and its interaction with the primary structure are expected to lead to a better understanding of curtain wall behavior and to improved procedures for its design.

PREFACE

1.0 INTRODUCTION

Claddings on highrise buildings form a first line of defense for the structure against environmental loadings such as wind or earthquake. However, building designers usually treat the curtain wall as nonstructural, and often leave the choice of cladding and its connections to the architect and cladding manufacturer. Aesthetic considerations usually play a major role in selection of a building's facade, but the potential structural stiffening effect of heavy weight claddings (e.g., precast concrete, brick, or granite) must be studied, as well, for lateral motions.

A number of previous studies of nonstructural components have suggested that cladding may be used as a participating structural element for control of wind and earthquake motions in modern highrise construction, resulting in substantial economies. However, the prevailing design philosophy at present in the United States, as expressed in the design recommendations of the Prestressed Concrete Institute, is to isolate precast panels from interstory drift motions. Slots and oversize holes in clip angle connections are suggested as ways to limit force transfer into panels, but sliding connections may be rendered ineffective by poor construction practice and lack of inspection, or connection deterioration with time.

The principal objective of the present study was to investigate the possible role which heavy claddings might play in the lateral response of a medium highrise building for moderate earthquake ground motions. The investigation involved a balanced combination of analytical and experimental studies of the effect of a precast concrete cladding system on the behavior of a 24-story steel frame office building. A number of different computer models of the cladding (both linear and nonlinear) were formulated and added to a three dimensional model of the building frame. The overall structure model was used in dynamic response studies of the building with and without cladding stiffening effects. In the experimental studies, the dynamic properties of the case study building were determined in a series of ambient and forced vibration tests conducted at the site using a rectilinear forced vibration generator built during the course of the research program. At the same time, vibration testing was performed on a second structure (steel frame, glass cladding) before, during and after installation of cladding, to determine if addition of cladding resulted in a measurable increase in lateral stiffness. System identification procedures were applied to obtain improved estimates of model properties on the basis of measured dynamic response data.

A brief overview of the analytical and experimental phases of the overall research effort is provided below in Sections 2

and 3, respectively. Then, in the full report which follows this preface, the analytical modeling effort as well as results of parameter studies obtained from a computer model of the structure-cladding system is described in Part I. An in-depth description of the experimental program is provided in Part II of this report.

2.0 ANALYTICAL STUDIES

The principal objective of the analytical studies was to investigate the potential lateral stiffness contribution of heavy-weight claddings on buildings and the role of cladding in altering dynamic properties and linear seismic response. A 24-story steel frame office building of core construction with a contoured pre-cast panel facade was selected as the prototype structure for the bulk of the analytical and experimental work. This structure and the three-dimensional computer model of its mass and stiffness properties are described in the references [1-6] and in Part I of this report.

A variety of cladding models were developed to represent the building's facade and to study linear and nonlinear response of cladding up to failure for moderate earthquake loadings. Initially, an interstory shear stiffness model, in the form of a tridiagonal stiffness matrix, was formulated for the cladding and its properties adjusted to bring analytical predictions of structure frequencies into agreement with test results [10-13].

X

Results obtained from the shear stiffness model were compared to three-dimensional finite element models [3] of both of the cladding panels and connection angles to establish a range of values for cladding lateral stiffness. Lateral stiffness was seen to be heavily dependent upon details of the panel-frame attachment. Later an incremental failure model [10] was formulated to study possible degradation of cladding stiffness with interstory drift level and the consequences of loss of cladding stiffness on overall torsional response of the building. Finally, a degrading stiffness model [12] of the cladding was postulated, in the absence of supporting laboratory data, to study the nonlinear response of panels and connections for actual earthquake ground motion loadings. Results of studies employing these different cladding models are contained in the references and in Part I of this report.

In Chapter 5 of Part I, results of studies of localized response of a typical portion of the facade are presented. Cladding panels were assumed completely rigid, connections were treated as linear or nonlinear spring elements, and supporting framing members were taken to be linearly elastic. Parameter studies were performed to investigate the influence of the use of oversize bolt holes, slotted connections, and connection initial friction on localized cladding response. Results include forces in connections and shears and moments induced in framing members as a result of specified interstory drift motions.

In general, the addition of cladding models to conventional frame models of highrise buildings was found to alter predicted overall structure frequencies and linear seismic response, substantially.

3.0 EXPERIMENTAL STUDIES

The experimental studies complement the analytical studies and were carried out in parallel using facilities and resources from the structures labs in the Schools of Civil and Aerospace Engineering. The experimental research was designed with several objectives in mind:

1. Acquire information from the full-scale buildings to answer questions raised in the course of formulating the various analytical models,

2. Determine the dynamic response characteristics of each of the buildings, one in the as-built condition, and the other during the course of construction as both mass and stiffness were added to the structure,

3. Using the dynamic response information, determine the most reasonable values of the various system parameters needed in the analytical models.

The overall objective in this work was, of course, to develop a quantitative measure of the influence of cladding stiffness, mass, and connection details on the dynamic response of the total building structure. These effects are complex at best and at the outset of this work were not clearly understood. Consequently, any attempts at laboratory simulation using either relatively costly full-scale cladding assemblies or simplified scale models

were ruled out. Rather, the approach was to develop a detailed analytical model that incorporated cladding-structure interaction mechanisms and use measured full-scale dynamic response information to identify the key interaction parameters. The main thrust of the experimental work was, then, to develop a measurement methodology for use in full-scale structures that would allow determination of the dynamic response and to apply it to two representative structures. While the ultimate aim was to accurately predict behavior under strong motion conditions, it was only possible for obvious reasons to carry out the present tests under low-level, essentially linear, nondestructive conditions.

At the outset, a survey was made of the various methods used previously for carrying out full-scale vibration surveys of tall buildings and other large and complex structures such as aerospace vehicles [18]. Based on these results and the developing capabilities in the area of time series analysis, it was decided to arrange the experimental program around a combination of full-scale tests using both ambient excitation (wind, occupant motion) and forced transient excitation. The use of transient forcing coupled with digital time series measurement and analysis techniques was felt to offer the most powerful and flexible approach to vibration measurement. The use of ambient excitation was felt to be most suitable for the measurements in the building under construction where access would be severely limited,

security for on-site excitation and measurement equipment would be uncertain, and test logistics would be difficult.

Two key aspects of the experimental work were the development of an efficient method for field measurement of the vibration response [16,18] and the design and construction of a powerful transient forced vibration excitor for use in these tests. A novel rectilinear force generator capable of producing either controlled periodic or transient horizontal forces of up to 5,000 pounds at frequencies up to about 20 Hz was designed and built [8,18]. A chirp type of excitation (rapidly swept sinusoidal forcing) was generated in a desktop computer and used to drive the excitor. Vibration response at different locations throughout the structure was measured using low level accelerometers and acquired and processed with analog tape recorders and multichannel digital time series analyzers. A two channel analyzer was used in the field and a more powerful multichannel analyzer was used for off-line analysis of recorded forcing and response data. In the case of the ambient tests, only the measurement portion of the equipment was used and tests were carried out over periods of up to twelve hours at a time (record length) in order to acquire enough data for precise definition of the structural response functions during subsequent analysis [9].

The final stage of the experimental program involved development of several methods for estimating the various parameters in

the analytical model by using the acquired dynamic response data [15,18]. First the modal parameters for the structure were determined using established techniques for the forced vibration tests and new techniques for the ambient tests. These results were then used along with the a priori finite element model of the building to estimate key cladding-structure interaction stiffness parameters. In this approach, the stiffness matrix was decomposed into components representing core, exterior framing, and cladding stiffnesses multiplied by unknown correction parameters. These parameters were estimated from the measured response data using (i) ordinary least squares, (ii) weighted least squares, (iii) maximum likelihood, and (iv) Bayesian techniques. Method (ii) was found to yield the most reasonable values for the parameters (best consistency with other more detailed analytical studies of the particular cladding and cladding connection details for these buildings).

4.0 CONCLUSIONS

The analytical and experimental studies, described in Parts I and II of this report, confirmed results presented in the literature which suggest that the exterior facade is a participating structural element, in spite of design assumptions to the contrary. Computed building frequencies and dynamic responses were found to be appreciably affected by cladding panel effects for

the prototype structure. It was shown that translational frequencies were increased by as much as 33% and torsional frequencies by as much as 65% for the overall structure model. In addition, results showed that it may not always be conservative to neglect the additional stiffening contribution of heavyweight cladding-connection systems. Neglecting cladding effects may be unconservative because dynamic characteristics of the overall structure model can be altered to such a degree by the added stiffness that the sensitivity of the overall structure to certain earthquake loadings may be increased substantially. When results for cases employing the nonlinear cladding models were compared to results for the linear clad and unclad cases, the linear models were generally found to bracket the nonlinear cases. However, several instances of increased nonlinear response as compared to linear response values were observed. For example, rotational response was found to be amplified more than twenty-fold, for the symmetric structure with initial partial cladding failure, in studies employing the incremental failure model. Either poor construction or prior motion of the building were taken as the reasons for the initial failure. The increase in rotational response was obtained even in the absence of enforced accidental mass eccentricity in the model. These results demonstrated clearly the potential effects of cladding on overall structure response.

In addition to the overall structure response studies, localized panel response studies were performed to examine panel connection force levels and the influence of connection stiffnesses on cladding lateral stiffness. Connection forces and interstory shear stiffness values for the local cladding model were found to be affected significantly by the presence of oversized bolt holes, slots in connection angles and initial friction in cladding connection attachments. However, the load bearing bottom connections were observed to exceed their ultimate vertical shear capacity at relatively low interstory displacement levels in all cases except when both top panel connections were slotted horizontally.

In the experimental program, described in Part II of this report, two highrise buildings were studied in an effort to investigate the effects of the exterior cladding on the dynamic behavior of the main structure. The role of cladding was studied experimentally by conducting vibration tests and employing parameter estimation techniques to determine the dynamic properties from test data. Parameter estimation techniques were also employed to evaluate certain parameters in the structural stiffness matrix which included the effects of cladding as an added interstory shear stiffness.

The first building was studied during its construction as the cladding was installed in order to directly assess its

effects on the dynamic response. Ambient tests were carried out over a period of several months at different stages of construction, starting after the erection of the steel frame and the commencement of the installation of cladding and continuing at regular intervals until the building was completely clad. It was found that the frequencies (a) show an initial decreasing trend and, except for the fundamental frequencies in braced frame bending and torsion (b) show a subsequent increasing trend throughout the construction phase. A detailed evaluation of the test data indicated that at least part of the increase in the frequencies could be ascribed to the exterior curtain wall. It should be noted that some of this increase could also be due to other effects or elements such as the interior partitions which were not explicitly considered in either the analytical or experimental studies of the structures.

The second building was employed to evaluate the cladding performance from an analytical viewpoint, making use of dynamic test results. Full scale forced vibration tests were carried out with the aid of an electrohydraulic shaker. Transfer functions were computed and fitted to determine the modal parameter estimates for the building.

The forced vibration test results were used to modify an *a priori* stiffness matrix model of the building so that the match between the analytical and the experimental modal parameters was

improved and also a measure of the cladding stiffness was obtained. A weighted least squares method was employed to estimate the stiffness parameters associated with the stiffness matrices for the core, the exterior frame and the cladding in each of the three directions, namely bending in the braced and rigid frame directions and torsion. The parameters were also determined using the ordinary least square, maximum likelihood and maximum posterior density (Bayesian) estimation procedures and the results from the various methods were compared.

With only the frequencies taken into account in estimation, all the methods yielded reasonable parameter values that were close to unity. But when the mode shapes were also included, it was found that if the initial mode shapes were not sufficiently close to the experimental values, large and unacceptable changes in the parameters were necessary to significantly improve the mode shapes predicted by the analytical model. The final parameter values were chosen as those that gave an acceptable match for the frequencies alone. The interstory shear stiffness parameter utilized in constructing the cladding stiffness matrix was found to be somewhat higher in torsion than in either of the two bending directions. This could imply that, for the highrise building considered, the stiffness effects of the curtain wall are slightly more evident in torsion.

REFERENCES

1. Goodno, B.J., "Cladding-Structure Interaction in Highrise Buildings," Proceedings, Fifth National Meeting of the Universities Council for Earthquake Engineering Research, Massachusetts Institute of Technology, Cambridge, Massachusetts, June 23-24, 1978, pp. 190-192.

2. Goodno, B.J., and Will, K.M., "Dynamic Analysis of a Highrise Building Including Cladding-Structure Interaction Effects," Proceedings, ASCE/ICES/CEPA Specialty Conference on Computing in Civil Engineering, Atlanta, Georgia, June 27-29, 1978, pp. 623-638.

3. Will, K.M., Goodno, B.J., and Saurer, G., "Dynamic Analysis of Buildings with Precast Cladding," Proceedings, ASCE Seventh Conference on Electronic Computation, held at Washington University, St. Louis, Missouri, August 6-8, 1979, pp. 251-264.

4. Goodno, B.J., Will, K.M., and Craig, J.I., "Analysis of Cladding on Tall Buildings," Invited Paper, presented at the ASCE National Convention and Exposition, Session on Developments in Methods of Structural Analysis, held in Atlanta, Georgia, October, 1979 (Meeting Preprint No. 3744).

5. Goodno, B.J., Craig, J.I., and Will, K.M., "Analytical and Experimental Studies of Cladding - Structure Interaction in Highrise Buildings," Proceedings, Sixth National Meeting of the Universities Council for Earthquake Engineering Research, University of Illinois, Urbana, Illinois, May 1-2, 1980, pp. 221-223.

6. Goodno, B.J., Will, K.M., and Palsson, H., "Effect of Cladding on Building Response to Moderate Ground Motion," Proceedings, Seventh World Conference on Earthquake Engineering, Istanbul, Turkey, September 8-13, 1980, Vol. 7, pp. 449-456.

7. Palsson, H., "Cladding - Structure Interaction Case Study for a Highrise Office Tower," selected for presentation in the Student Paper Competition, AIAA/ASCE/ASME/AHS Symposium, Dayton, Ohio, USA, October 3, 1980.

8. Craig, J.I. and Lewis, F.D., "A rectilinear Force Generator for Full Scale Vibration Testing," Proceedings, ASCE/EMD Specialty Conference on Dynamic Response of Structures, Atlanta, Georgia, January 1981, pp. 102-110.

9. Meyyappa, M., Palsson, H. and Craig, J.I., "Modal Parameter Estimation for a Highrise Building Using Ambient Response Data Taken During Construction," Proceedings, ASCE/EMD Specialty Conference on Dynamic Response of Structures, Atlanta, Georgia, January 1981, pp. 141-151.

10. Goodno, B.J., and Palsson, H., "Torsional Response of Partially-Clad Structures," Proceedings, Conference on Earthquakes and Earthquake Engineering: The Eastern U.S., September 14-16, 1981, Knoxville, Tennessee, Vol. 2, pp. 859-877.

11. Goodno, B.J., and Palsson, H., "Earthquake Performance of Building Cladding," Proceedings, Sino-American Symposium on Bridge and Structural Engineering, Beijing, China, September 13-19, 1982.

12. Palsson, H., and Goodno, B.J., "A Degrading Stiffness Model for Precast Concrete Cladding," Proceedings, Seventh European Conference on Earthquake Engineering, Athens, Greece, September 20-25, 1982, Vol. 5, pp. 135-142.

13. Goodno, B.J., "Analysis of Precast Concrete Cladding on Tall Buildings," to appear in The Tall Buildings Monograph Update Volume: Structural Design of Tall Steel Buildings, Vol. SB, 1983.

14. Goodno, B.J., "Analytical Studies of Precast Concrete Cladding/Structure Interaction," Invited Presentation, Prestressed Concrete Institute Annual Convention, October 31 - November 3, 1982, Chicago, Illinois.

15. Meyyappa, M. and Craig, J.I., "Identification of Cladding-Structure Interaction Using Parameter Estimation Methods," in preparation for submittal to the Journal of the Structural Division, ASCE.

16. Meyyappa, M. and Craig, J.I., "Full-Scale Modal Measurements of a Highrise Building Using Transient Forced Vibration Testing," in preparation for submittal as a journal paper.

17. Palsson, H., "Influence of Nonstructural Cladding on Dynamic Properties and Performance of Highrise Buildings," Ph.D. Dissertation, School of Civil Engineering, Georgia Institute of Technology, December, 1982, 427 pages.

18. Meyyappa, M., "Identification of Cladding-Structure Interaction in Highrise Buildings Using Parameter Estimation Methods," Ph.D. Dissertation, School of Aerospace Engineering, Georgia Institute of Technology, Atlanta, Georgia, March, 1982, 194 pages.

19. Gram, K.G., "The Shear Effects of Precast Cladding Panels on Multistory Buildings," M.S. Special Problem Report, School of Civil Engineering, Georgia Institute of Technology, Atlanta, Georgia, June, 1976, 84 pages.

20. LeBoeuf, P.M.S., "Dynamic Cladding-Structure Interaction in Highrise Buildings," M.S.C.E. Thesis, School of Civil Engineering, Georgia Institute of Technology, Atlanta, Georgia, September, 1980, 129 pages.

21. Roglin, R., "A Dynamic Model of the West Tower of the Georgia Twin Office Towers," M.S.C.E. Special Problem Report, School of Civil Engineering, Georgia Institute of Technology, Atlanta, Georgia, May, 1980, 74 pages.

22. Ansley, M., "Modal Analysis Experiments on a Plane Frame Model," M.S.C.E. Special Problem Report, School of Civil Engineering, Georgia Institute of Technology, Atlanta, Georgia, April, 1981, 125 pages.

23. Pless, D.G., "Static and Dynamic Response of Precast Cladding to Interstory Drift," M.S.C.E. Special Problem Report, School of Civil Engineering, Georgia Institute of Technology, Atlanta, Georgia, March, 1982, 259 pages.

24. Keister, J.J., "Testing and Evaluation of Wedge-type Precast Concrete Inserts Subjected to Pullout," M.S.C.E. Special Problem Report, School of Civil Engineering, Georgia Institute of Technology, Atlanta, Georgia, February, 1983.

Part I

INFLUENCE OF NONSTRUCTURAL CLADDING ON DYNAMIC PROPERTIES AND PERFORMANCE OF HIGHRISE BUILDINGS

Part I

TABLE OF CONTENTS

SUMMARY

Precast concrete panels provide an attractive facade and lend an aesthetic appeal to a building, and are becoming increasingly popular for steel frame buildings. Precast concrete panels have been found to transfer forces back to the primary structure and to add lateral stiffness until their capacity or that of their connections is exceeded. However, structural engineers generally regard the panels as nonstructural and are currently interested only in their weight when designing the main structure. Results of recent research have shown that cladding-structure interaction effects can change the dynamic properties of the overall structural system significantly. As a result, the computed dynamic response based on a model of the structural framing alone may be quite different from that experienced by the actual structure, and may not be conservative as originally assumed during design. In addition, if partial cladding failure occurs, overall torsional response effects may be considerably amplified.

As a case study, the influence of heavily-contoured precast concrete panels on the lateral and torsional stiffness of a 25-story, doubly-symmetric, steel frame office building of core construction was investigated. The effect of the cladding on the dynamic properties and the linear seismic response of the structure was explored by varying the panel stiffness. In these studies, the centers of mass and rigidity were assumed to coincide and cladding stiffness was added to the bare

frame model until analytical frequency values agreed with measured frequencies from ambient-level field tests. Then, using the cladding stiffness values for the symmetric model, an accidental eccentricity between centers of mass and rigidity was imposed, as required by building codes, and linear seismic response computed for the fully clad and unclad structures. Torsional response effects were increased substantially.

In the absence of experimental data on cladding failure, several simplified nonlinear models for precast cladding and its connections were assumed. The influence of the different nonlinear curtain wall models on overall structure response was determined for different ground motion inputs. Results are presented in the form of tables containing peak roof responses and peak interstory drift values. Selected plots of displacement response time histories due to earthquake ground motion are also presented.

Finally, a study of localized panel response was performed to obtain information on connection forces and the effects of cladding panels and connections on lateral force resistance of the overall system. Sources of nonlinearity in this model included oversized holes, initial friction in connections and slotted connections. Parameter study results demonstrated that connection forces and lateral stiffness were highly dependent upon the above factors for the cladding models and loadings considered in this study.

1. INTRODUCTION

1.1 Statement of Problem

Heavyweight curtain wall systems such as those of precast concrete, brick and granite provide an attractive facade and lend an aesthetic appeal to a building. They have long been used to clad modern highrise buildings and as of late their popularity has been increasing [23]. Cladding is an expensive part of a building and has been estimated to cost as much as 10-20% of the initial cost of a building [11]. Given the initial expense, the popular heavyweight architectural enclosure system is expected to be nearly maintenance free during the life span of the building. Recent reports of facade failures [9, 11, 45] indicate otherwise. One report [11] blames the failures on a lack of proper preventive maintenance, and another [45] attributes most curtain wall failures to the inability of architects and engineers to recognize the incompatibility between specifications for the structural system and the exterior wall. It has been reported [45] that insurance claims for facade failures have increased from 15% of all claims in 1960 to 33% in 1980 against architects alone.

Current design practice usually follows the recommendations of the Prestressed Concrete Institute [35]. According to PCI, cladding panels are to be designed and detailed to transfer external loads such as wind loads, thermal loads and seismic loads to the supporting frame. The panel connections are to be designed to resist the external loads

together with the gravity loads of the panels and the use of sliding or flexible connections is recommended to remove any interaction with the supporting frame in order to protect the expensive, brittle exterior panels. Compliance with the above recommendations is assumed to permit interstory displacements and thermal movements to take place, within limits, without causing any damage to the panels. Based on the above recommendations, structural engineers generally regard the panels as nonstructural elements and are currently interested only in their weight when designing the main structure.

In spite of the design assumption that cladding panel interaction with the supporting frame has been removed, panels have been found to transfer forces back to the primary structure and to add lateral stiffness until their capacity or that of their connections is exceeded. In many instances, connections deteriorate with time and seize up so that the intended isolating role of the connection is defeated. In addition, connections are often installed improperly as in the case when slots are used for alignment only. Once the panel is in place, connection bolts are tack-welded to the connection angle. Finally, the design may not be sound since panel interaction with the supporting frame may not be removed when PCI recommended connection details are used. Several studies [15, 25, 26, 41, 52, 53], both analytical and experimental, suggest that in addition to transferring external loads back to the supporting frame, the cladding panels add to the lateral stiffness of the primary structure as well. Experimental studies [26] have shown that even lightweight cladding can affect the dynamic properties of a structure. Cladding-structure interaction effects in the case of heavyweight cladding can

then change the dynamic properties of the overall structural system significantly. As a result, the computed dynamic response based on a model of the structural framing alone may be quite different from that experienced by the actual fully-clad structure, and may not be conservative as originally assumed during design. In addition, a partially clad structure (either during construction or after partial cladding failure) can cause rotational response to be greatly amplified due to the eccentricity introduced by the absence of several panels.

The increasing costs of building construction and materials has added to the interest in utilizing the lateral stiffness and energy absorbing capacity available in the exterior heavyweight cladding. Lightweight cladding has much different performance characteristics than heavyweight cladding and has to be regarded as a system of passive elements which do not contribute significantly to overall structure lateral stiffness. Several investigators [8, 13, 21, 25, 41, 53] claim that integrating the cladding panels as participating structural elements would result in better economy, and according to some, in better safety of the overall structural system as well. The need for improved understanding of cladding behavior is evident based on the reports of failures above. However, a knowledge of actual force levels experienced by both panels and their connections is required before design modifications can be made.

1.2 Previous Studies

1.2.1 Introduction

The analysis and understanding of the behavior of clad structures and cladding-structure interaction is a subject of considerable interest in the literature. Although this interest is mainly analytical, several

experimental studies have been performed. A number of studies of relevance to the present investigation are discussed below.

1.2.2 Analytical Studies

Several investigators examined the contribution of cladding to structure lateral stiffness. Gram [17], continuing the work of Sherwood [42], reported on studies of a 25-story steel frame structure which incidentally is the prototype structure for the current study. The contribution of cladding to structure lateral stiffness was determined by matching ambient-level measured frequencies and computed frequencies. Based on this approach, the cladding was found to contribute 30% or more to the lateral stiffness of the primary structure. Oppenheim [29] and Dubas [8] also considered cladding effects in their studies of tall structures. Again, the overall stiffness was increased 30% or more with the addition of cladding. Weidlinger [52] studied shear field panels which could be used as wind bracing in highrise buildings. The principal conclusion was that panel capacity to resist wind shear was effectively diminished if vertical (gravity) forces were transmitted to the panels. The use of shear field panels was also concluded to be economical. Henry [18] studied the behavior of cladding frame interaction for reinforced concrete structures. The study revealed that it may not be conservative to ignore cladding effects during design and that design of connectors was critical.

Other researches have studied the effects of connections on cladding-structure interaction. LeBoeuf [22] continued studies reported by Will et al. [53] where finite elements were used to model a precast concrete panel and its clip-angle connections (same prototype structures as in present study). The effects of connection details on the interstory shear

stiffness of the curtain wall was analyzed. A wide range of stiffness values (0-741 kips/inch (0-1.3 x 10^5 kN/m)) was obtained depending on panel support conditions and connections details. Further studies involving laboratory tests of an actual panel and connections were suggested to determine the contribution of cladding to structure lateral stiffness. Sack et al. [39] also investigated the interaction between structural framing and precast concrete curtain walls. Panels were found to provide additional lateral stiffness if connected by bar inserts, or bolted and/or welded structural angles to the exterior frame. However, the stiffness contribution was found to be negligible if the structural angles were slotted or the connections were loaded into the post-yield range. Gjelsvik [13] was also interested in the interaction between frames and precast panels. Elastic-plastic analysis was applied to determine collapse loads and deformations. The panels were assumed to be rigid, weightless and connected by four bolts to the beams of the frame with no panel-to-panel contact. Two collapse mechanisms were considered: a weak bolt design in which the mechanism was unaffected by the presence of the panels and a strong bolt design in which the panels governed the collapse. A short bolt design (little ductility required) was found to be most suitable to reduce horizontal deflections when the panels were used for wind bracing.

A number of investigators have discussed design and behavior of nonstructural elements. Sharpe [41] discussed seismic design of nonstructural elements and stated that if damage was to be minimized then building elements extending from floor to floor had to be designed to accommodate interstory displacements. Sharpe reported that recorded building response during the 1971 San Fernando, California earthquake

showed evidence of cladding-structure interaction. The primary conclusions were that nonstructural elements could be designed to resist structure motions due to wind and moderate earthquakes with little or no damage. Special attention would have to be given to connections to prevent failures and subsequent falling of panels to the ground. McCue et al. [25] discussed the behavior of nonstructural curtain walls during seismic action. Recent earthquakes had demonstrated that precast cladding panels were particularly dangerous. Panel-to-structure connections were considered of critical importance in situations in which failure resulted in collapse of panels into the street. The presence of cladding and finish systems was expected to increase the structure stiffness resulting in a shift of vibration frequencies. This shift could push the structure into a more critical earthquake ground motion frequency range, which could result in higher seismic response than if the stiffening effects had not been accounted for in the analysis. Glogau [14] advocated damage control in buildings through separation of nonstructural components such as exterior precast panels. Separation was justified by the high degree of life hazard expected in case of nonstructural damage and that nonstructural damage had resulted in the failure of the primary system by inducing accidental torsion. The principal conclusion was that by separating nonstructural components from the main structure, an unfavorable change in the intended performance of the overall structure could be prevented. An opposing view was presented by Kulka et al. [21] which described the design and construction of multistory buildings using precast elements. Integration of exterior wall panels into the load resisting walls was advocated to carry both vertical loads and horizontal loads such as those

due to earthquake and wind. One claim was that to disregard exterior concrete wall panels as load-carrying elements, particularly for horizontal loads, was an illusion in the case of steel buildings, and an impossibility in the case of concrete buildings. While a designer might disregard the stiff panels in his calculations, nature would not disregard them in the event of an earthquake. The action of exterior panels should be included from the beginning of design resulting in great benefit to the overall structure behavior.

Several studies involving large panel structures have been reported. Spencer [43] investigated the effect of nonstructural interfloor elements on the nonlinear dynamic response of a 20-story prestressed concrete frame structure. The force-deformation behavior of the interfloor elements was idealized to have either yielding or essentially linear hysteretic behavior. A Ramberg-Osgood function with an appropriate hysteresis law was used to define the hysteresis loops on which the element loops were based. The first eight seconds of the N-S component of the 1940 El Centro earthquake were used as excitation. The conclusions were that the elements could be useful in reducing interstory drift and that non-yielding elements with low energy dissipation tended to be more effective than yielding elements which dissipated more energy. Powell and Schricker [38] examined ductility demands on joints in large panel structures. A large panel shear wall is not a monolithic structure but contains planes of weakness at the joints at which both sliding and tilting could occur. The joints were considered as structural "fuses," which limited the amount of shear force and overturning moment that could be transferred between panels, thereby limiting the stresses developed in the panels. The primary

conclusion of the study was that the design of joints which could accommodate sliding could dramatically reduce earthquake-induced stresses without placing undue demands on the deformability of the joints. In addition, it is preferable to consider ductility demand in terms of actual deformations rather than in terms of some less meaningful ratio for this type of structures (and perhaps all structures). Becker et al. [4] reported on research into the seismic behavior of a simple precast concrete wall which in this case was a vertical stack of panels having only horizontal connections. The model assumed that all nonlinear, inelastic behavior was concentrated in the connection regions and that the precast panels remained linearly-elastic. The nonlinear-inelastic seismic analysis was capable of handling both rocking type motions throughout the height of the structure and slippage due to shear in the plane of the connections. The results showed seismic response to be governed mainly by a nonlinear-elastic rocking phenomenon associated with a period elongation with a consequent increase or decrease in the seismic response depending on the nature of the ground motion. Shear slip occurred only when friction coefficients were extremely low or when the normal forces across the connections were low as in the case of low buildings or in the upper floors of tall buildings. Mueller and Becker [28] explored the potential of an aseismic design concept that used the vertical connections in large panel precast concrete walls as primary energy dissipating elements. It was considered easier to provide vertical connections with sufficient ductility than more complex, gravity load bearing horizontal connections. The relationship betwen the vertical connection characteristics and overall response was investigated, and a rule of thumb for the optimum strength

of the primary energy dissipating elements established. The design concept was thought to be viable provided that the vertical connections exhibited full and stable hysteresis loops.

1.2.3 Experimental Studies

Fewer experimental studies on cladding have been reported in the literature compared to the number of analytical studies discussed above. Anicic et al. [3] performed experimental studies on two reinforced concrete facade panels measuring 277 inches (704 cm) by 96.5 inches (245 cm) by 7.5 inches (19 cm) deep with two webs that were 4.7 inches (12 cm) thick and 8.3 inches (21 cm) deep. One of the panels had a window opening that measured 39.4 inches (100 cm) by 70.9 inches (180 cm). In the tests, only cyclic loads perpendicular to the plane of the panels were applied. The studies showed that the load-deformation relationship is linear in the range of possible loads and that no difference in behavior was observed between the panel with an opening and the one without one. The panels were found to withstand much higher loads than computed and failed by plastic buckling of the main web reinforcement. Uchida et al. [48] performed vibration tests on a two-story, two-bay steel frame with precast concrete panels to obtain data on the effects of cladding on the dynamic properties of the structure. Both free vibration and forced vibration tests were conducted on the clad frame and dynamic load tests during dismantling of cladding. The studies showed that the presence of precast cladding increased the stiffness and the damping of the test frame. Meyyappa et al. [26] measured the ambient response of a 24-story steel frame office building to determine the effects of lightweight cladding on frequencies and damping of different modes. Response measurements

were collected at different stages of construction and frequencies and damping were found to change as additional cladding was placed on the building. The frequencies of the second and third modes increased, while the fundamental frequencies were not affected during construction. It was also found that cladding had an increasing effect on damping values in general, with the increase for torsional modes being more substantial.

Experimental studies of panel connections have also been undertaken. Sack et al. [39] studied the stiffness characteristics of connection devices and the capacity to withstand low-cycle fatigue tests. Analytical studies of the same connections were also performed and differences were within 30%. Yield tests on connection angles showed that the stiffness was negligible in the post-yield range. The low-cycle fatigue tests revealed that, for the angles tested, the original stiffness was maintained after 2000 cycles and there were no signs of damage. Sack et al. also conducted experimental studies on a one-story, one-bay frame clad with two 6 feet (183 cm) by 12 feet (366 cm) flat precast concrete panels. Each panel was connected to the steel frame with two rods at the top and two clip angles at the bottom. Several earthquake floor motion records were used to excite the test structure. Top connectors (rods) were found to be highly stressed in horizontal bending during earthquake loading and the rods were also highly susceptible to low-cycle fatigue. Pall and Marsh [31] investigated the use of limited-slip, friction-bolted joints in precast concrete large panel construction. The proposed connection consisted of steel plates, with slotted holes, connected by high strength steel bolts to steel inserts anchored in the concrete panels. Both static and dynamic cyclic tests were conducted

on the connection. When heavy duty brake lining pads were inserted between the sliding steel plates, the joint exhibited a constant, repeatable slip load and simulated near "elasto-plastic" behavior with negligible degradation. Nonlinear time-history dynamic analysis was performed to study the influence of connection behavior on seismic response. The influence of horizontal joints was neglected and the nonlinear behavior of the wall limited to the proposed joint located in vertical joint lines only. The limited-slip, bolted connection was found to act as both a safety valve and a structural damper and it was capable of improving overall seismic response of large panel structures. Several connectors used in large panel construction were also tested experimentally by Osborn et al. [30]. Both bolted and welded connections were tested and results showed welded connections to be more suitable in seismic environments.

1.2.4 Additional Comments

Several papers [15, 16, 33, 34] have been generated during the course of the work presented in this report. Several of these papers were presented at technical meetings to stimulate discussion on the research findings as they became available. Results of both research and discussions will be presented in following chapters.

Several of the above studies showed that cladding contributed to the lateral stiffness of structures and hence affected dynamic properties and response. Other studies demonstrated the influence of panel connections and panel support conditions on the contribution of cladding to overall structure lateral stiffness. Further analytical and experimental studies were also indicated to improve understanding of the influence of nonstructural cladding on dynamic properties and performance of highrise buildings.

1.3 Objectives and Outline

1.3.1 Objectives

Currently, designers assume cladding panels to be nonstructural. However, the discussions above clearly demonstrated that interaction exists between the panels and the supporting structure. This study investigated the influence of heavily-contoured precast concrete panels on the lateral and torsional stiffness of a 25-story, doubly-symmetric, steel frame office building of core construction. In addition, localized panel response studies were performed to obtain information about connection force levels and interstory shear stiffness values.

A better knowledge of basic properties influencing panel-frame behavior is needed for a more economical and safer design of modern structures employing heavyweight cladding systems. The principal objectives of the present study are:

1. To develop three-dimensional analytical models for dynamic analysis of the prototype structure described in Chapter 2.

2. To calibrate the analytical models by adjusting the amount of lateral stiffness provided by cladding until model frequencies matched ambient experimental values.

3. To perform linear dynamic response studies to compare models which assumed composite action of floor beams to noncomposite ones, and to compare models which accounted for the contribution of lateral stiffness by cladding to models that did not.

4. To perform nonlinear dynamic response studies to compare the influence of different force-deformation relationships for cladding and its connections on overall structure response; the core and the exterior frame were assumed to remain linear.

5. To perform linear and nonlinear static response studies on a one-story, one-bay frame model with attached cladding panels to obtain force levels in connections and contribution of cladding to lateral stiffness.

A description of how the above objectives were met is contained in the following section.

1.3.2 Outline

Descriptive data for the prototype structure including joint coordinates, member incidences, member sizes, support conditions and the distributed mass of the structure were partially prepared by earlier investigators [17, 42]. The current study was divided into six major parts. The first part was concerned with the development of the analytical models for the prototype structure described in Section 2.1. Two models were developed. One assumed composite action of floor beams and the other assumed noncomposite action as discussed in Section 2.2.

In the second part of the study, the structure frequencies were determined experimentally. The ambient response of the structure was measured simultaneously at different locations and then analyzed to obtain the lowest three frequencies in each of the three structure directions (rigid frame direction, braced frame direction, and rotation). This procedure is described in Section 2.3.

Calibration of the analytical models comprised the third part of the study. Analytical and experimental frequencies were matched by adjusting the amount of interstory shear stiffness contributed by the exterior cladding. The interstory shear stiffness values obtained were then compared to values obtained from finite element studies of panels and connections for comparison. This work is presented in Section 2.4.

The fourth part of the study was devoted to linear dynamic response studies of the analytical models for base excitation input. Symmetric structure response with and without cladding stiffening effects was computed for several different earthquake ground motion loadings and results presented in time-history plots and tables containing peak responses. In addition, structure response with enforced mass eccentricity for the composite case was computed for two different loadings as discussed in Chapter 3.

In the fifth part of the study a number of nonlinear dynamic response studies were performed. These studies involved the composite model only and the nonlinearity was confined to the interstory shear stiffness contribution of cladding. Several different force-deformation relationships were employed to describe the behavior of cladding and its connections in the absence of experimental data. Results were developed in the form of peak interstory drifts, peak roof responses and time-history plots as shown in Chapter 4.

Localized panel response studies were undertaken in the sixth and final part of this investigation. A linear static analysis computer program written by another investigator [37] was used to analyze a one-story, one-bay plane frame with two cladding panels to obtain information about connection force levels and the contribution of cladding panels and connections to lateral force resistance. The computer program was modified in this study to include nonlinear static analysis capabilities in which the nonlinearity was limited to the cladding panel-to-frame connections only. The nonlinearity was assumed to be caused by initial friction in connections, as well as the effects of oversized holes and

slotted connections. This analysis is described in Chapter 5.

Finally, all conclusions drawn from these studies and recommendations for further study are contained in Chapter 6. The need to complement analytical research with experimental testing is always present. Design of cladding, in general, is complicated by the fact that a wide variety of different designs for panels and attachments exists. This thesis presents a general analysis methodology rather than a resolution of questions pertaining to use of cladding as a participating structural element. This study has focused attention on one structure only and has only considered the influence of one type of panel and connection scheme employed in the case study building; hence it may be premature at this point to use the analytical procedures and results as the basis of a recommended design approach.

With identification of and improved understanding of key parameters which influence performance of more common types of cladding, more rational engineering design procedures for cladding are expected to follow.

2. DESCRIPTION OF STRUCTURE AND ANALYTICAL MODELS

2.1 Prototype Structure

2.1.1 Physical Description

A 25-story office building completed in 1970 and shown in Fig. 2.1-1 was selected for the cladding-structure interaction studies. The office tower is a steel frame structure supported by a pier foundation drilled to bedrock. It is built around a steel core intended to provide all of the lateral force resistance (Fig. 2.1-2). The core is made up of braced framing in one direction and rigid framing in the other as shown in Fig. 2.1-3. The core extends down to the lowest basement level even though it is not shown on the figure. Typically, the columns in the core are 14 inches (3.56 cm) deep with f_y ranging from 36 to 50 ksi (248 to 345 MPa). Girders are 14 inches (35.6 cm) deep with f_y = 36 ksi (248 MPa) in the braced direction of the core and range from 24 to 36 inches (61.0 to 91.4 cm) with f_y = 36 ksi (248 MPa) in the core rigid direction. The flooring is a concrete slab (f'_c = 5000 psi (34.5 MPa)) on light gage metal decking supported by beams spanning from the core to the exterior frame (Fig. 2.1-1). The majority of the floor beams are 21 inches (53.3 cm) deep with f_y = 50 ksi (345 MPa).

The building has a heavy precast concrete panel facade (Fig. 2.1-4) supported by a lightweight exterior steel frame which in turn is supported around the perimeter of the structure by a massive reinforced concrete, rigid frame pedestal (Fig. 2.1-3). The exterior frame typically consists

of 10 inch (25.4 cm) deep columns with f_y = 36 ksi (248 MPa) above the 15th floor and 12 inch (30.5 cm) deep columns with f_y = 50 ksi (345 MPa) at the 15th floor and below. The girders of the exterior frame are in general 18 inches (45.7 cm) deep below the 17th floor and 16 inches (40.6 cm) deep at the 17th floor and above with f_y = 36 ksi (248 MPa). All four faces of the structure have 12 bays and two panels per bay.

The structure was designed for actual dead loads, live loads were 50 lbs/foot^2 (2.4 kN/m^2) and partitions 25 lbs/foot^2 (1.2 kN/m^2). The Atlanta City Code was used for determination of wind loads and all cladding was assumed to be nonstructural.

2.1.2 Cladding Panels and Connections

The cladding panels are highly contoured precast concrete with light reinforcing steel and wire mesh imbedded to prevent cracking. The majority of the panels are 12 feet (3.66 m) high, five feet (1.52 m) wide and 18 inches (0.46 m) deep with a window cutout measuring 6 feet 8 inches x 2 feet 8 inches (2.03 m x 0.81 m) which covered about 30% of the projected panel face area. Each panel weighs about 3.7 kips (16.6 kN) and the cladding alone contributes approximately 30% of the total dead load on a typical floor [42].

Each panel is connected in four places to the exterior frame spandrel beams (Fig. 2.1-5). A typical top connection consists of a 3/4 inch (1.9 cm) adjustable loop insert bolted to a 4 inch x 4 inch x 3/8 inch x 4 inch (10.2 cm x 10.2 cm x 1.0 cm x 10.2 cm) long clip angle which in turn is welded to the frame spandrel beam (Fig. 2.1-6). The loop insert has a safe working load of 3000 lbs (13.34 kN) [1]. Inspection of accessible top clip angles on the mechanical floor and the parapet

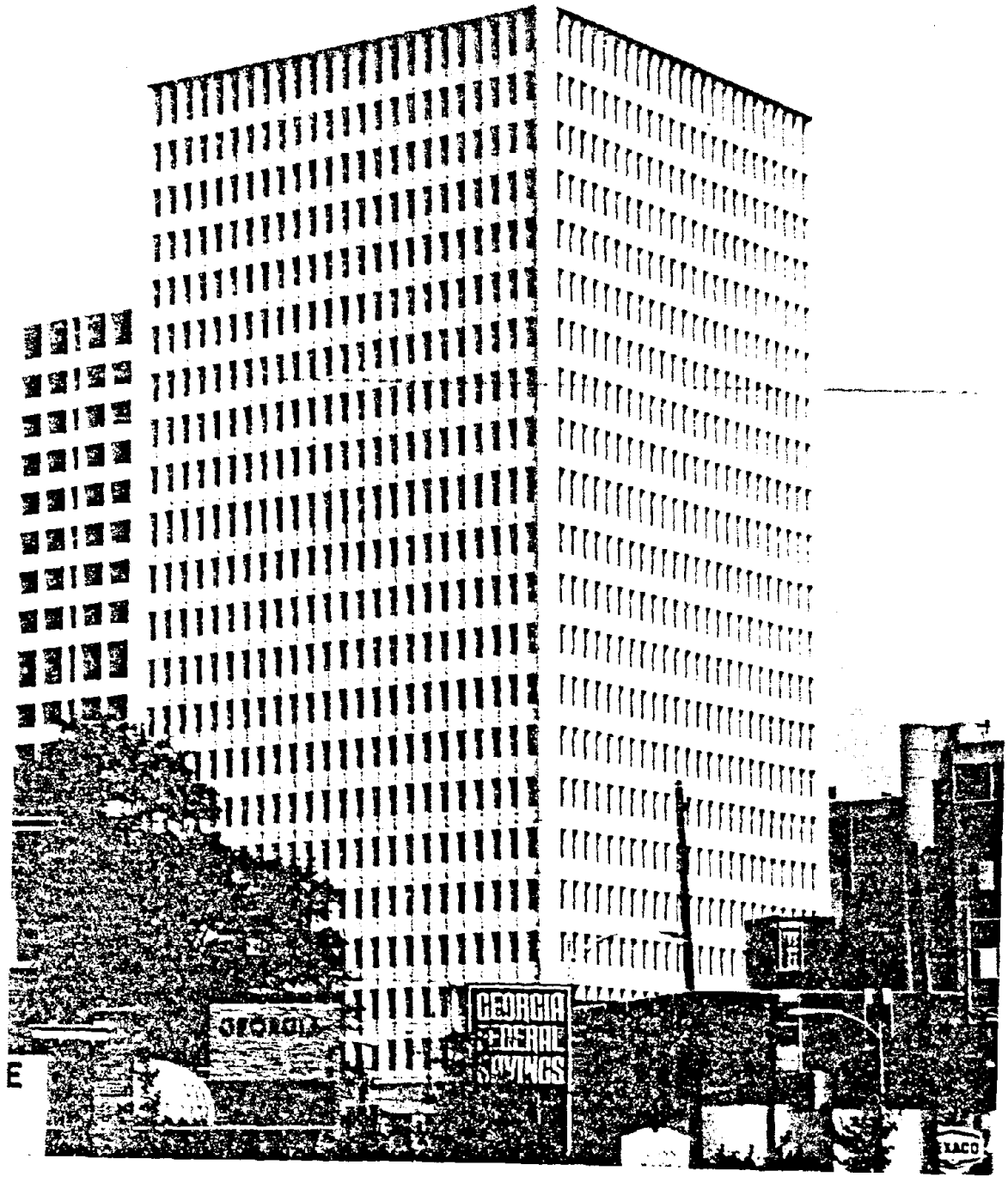

Figure 2.1-1. Photograph of Prototype Structure.

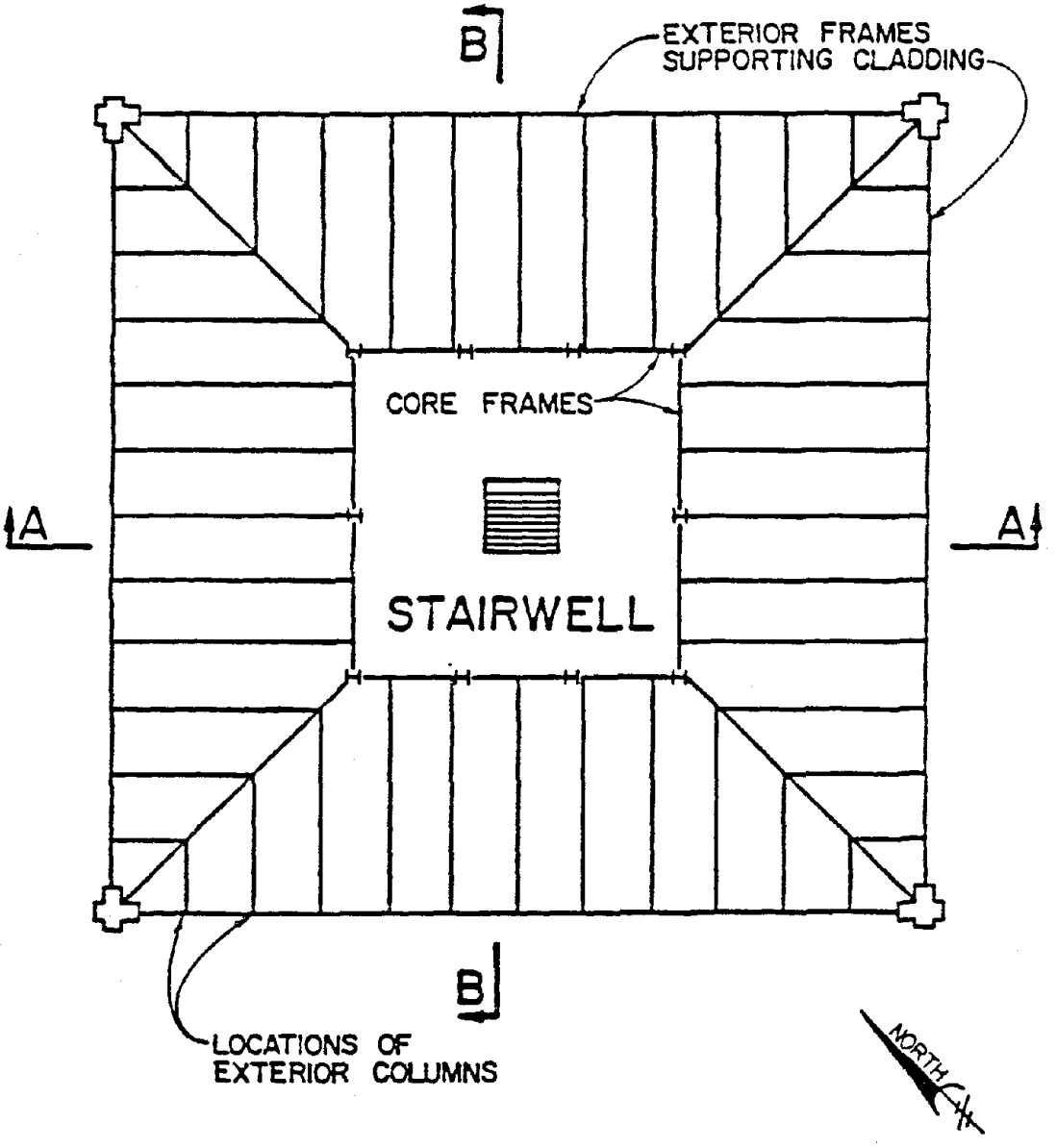

Figure 2.1-2. Typical Floor Plan.

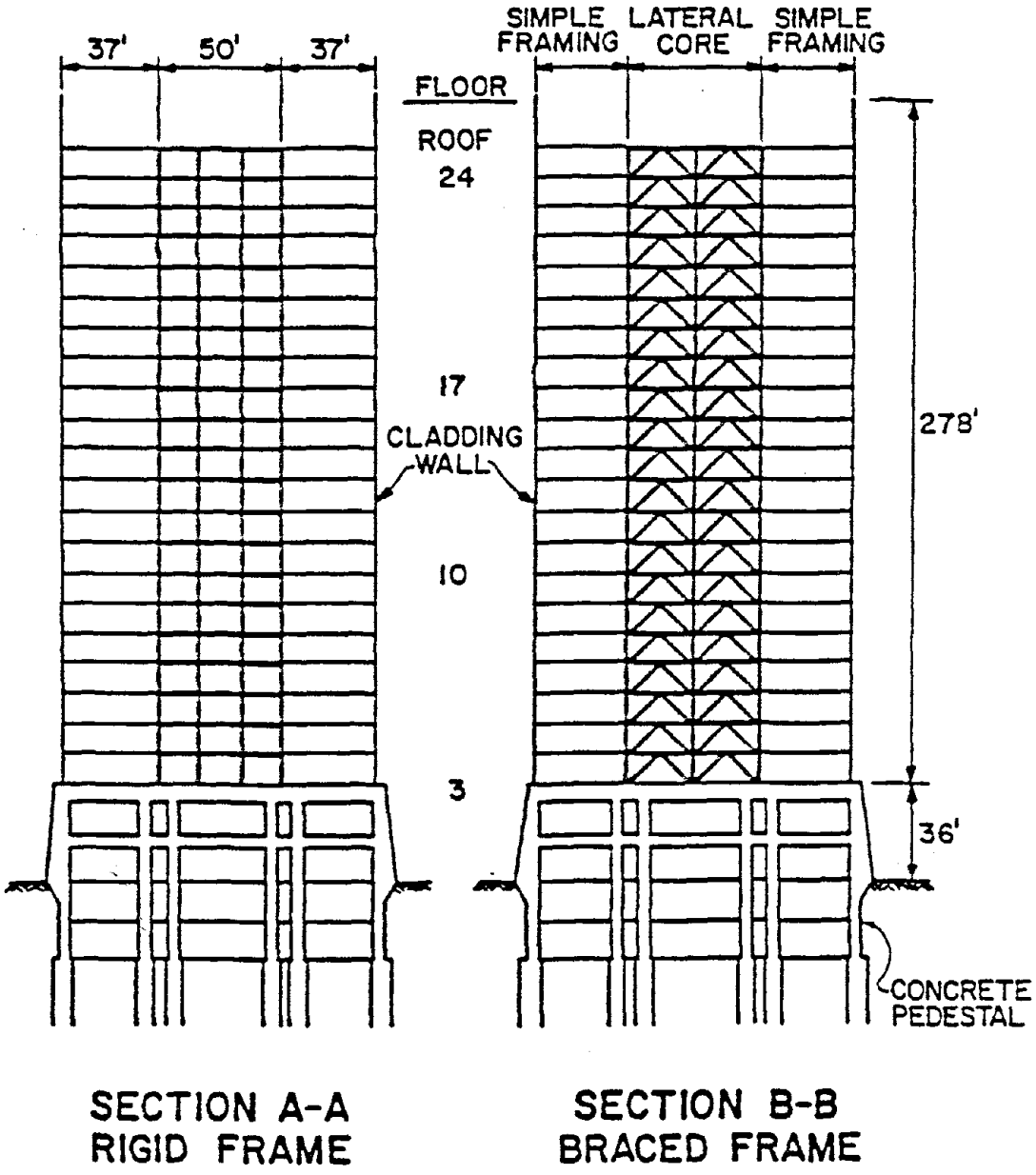

Figure 2.1-3. Structural Elevations.

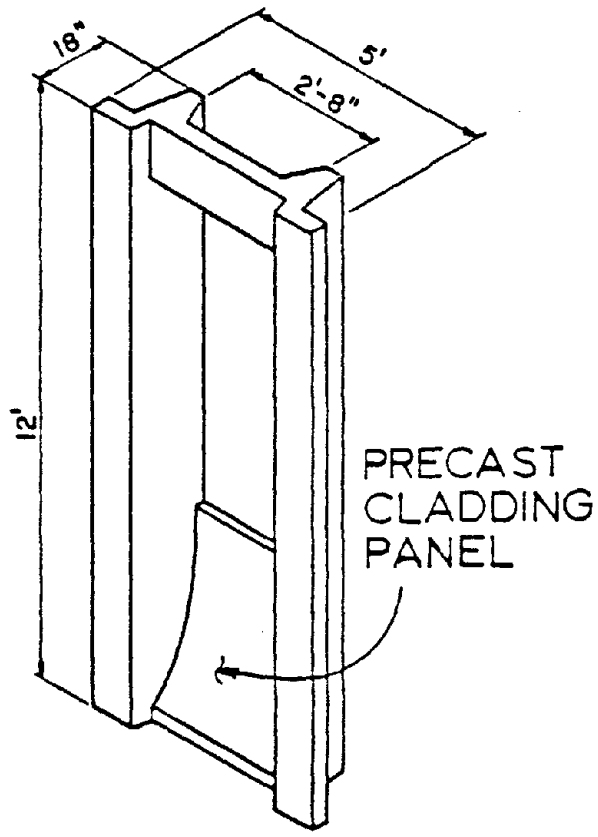

Figure 2.1-4. Precast Cladding Panel.

revealed that all angles had 1.5 inch (3.8 cm) horizontally slotted bolt holes. These slots are for easier installation and to permit movement (thermal, drift) to take place without resulting in high force levels in the panels and their connections. A typical bottom connection, which is designed to support the weight of the panel, consists of a shelf angle insert bolted to a 5 inch x 3.5 inch x 3/8 inch x 6 inch (12.7 cm x 8.9 cm x 1.0 cm x 15.2 cm) long clip angle. The clip angle is welded to the frame spandrel beam as shown in Fig. 2.1-7. The insert is made of ductile iron (ASTM A 536-67) with a wedge shaped track to allow for vertical adjustment and prevent slippage. The safe working load of the insert is 4000 lbs (17.79 kN) [1].

2.2 Analytical Models

2.2.1 Stiffness

A tier building model [50] was developed to represent the primary core structure. A key assumption for use of this model was that floor slabs were rigid in their own planes. An additional requirement was that the floors had to be connected by a structural space frame arranged in a rectangular pattern. Three degrees of freedom (two translational and one rotational) were retained at the center of the core of the doubly-symmetric structure in developing a stiffness model for use in subsequent dynamic response analysis.

The effects of eccentric connection of bracing members in the braced frame direction and finite size of framing joints were included in the model, which was developed using GTSTRUDL [10]. Although the floor slab framing members were not designed for composite action, it was assumed that composite action was likely to occur for low-level

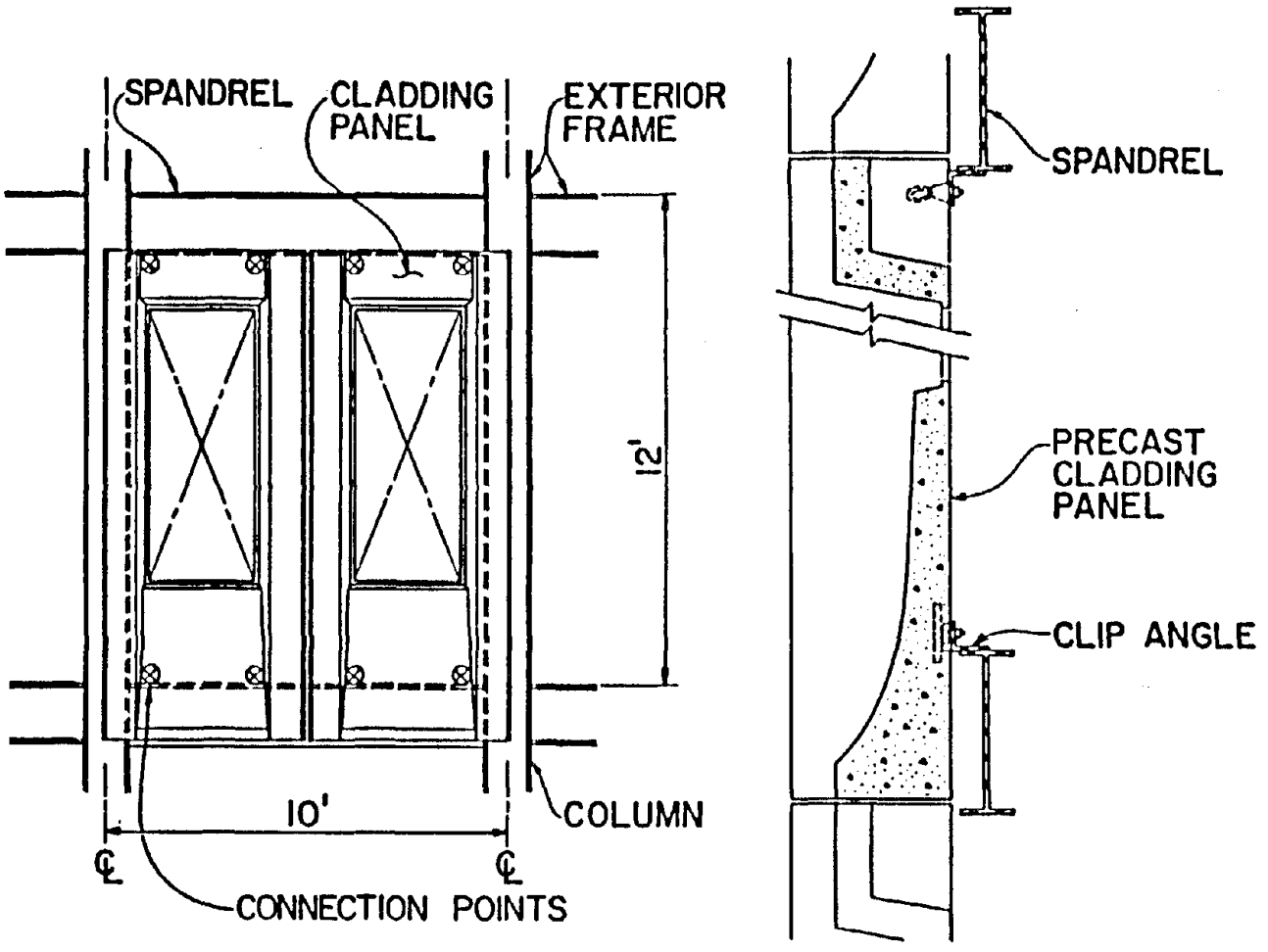

Figure 2.1-5. Typical Exterior Bay of Curtain Wall and Connection Details.

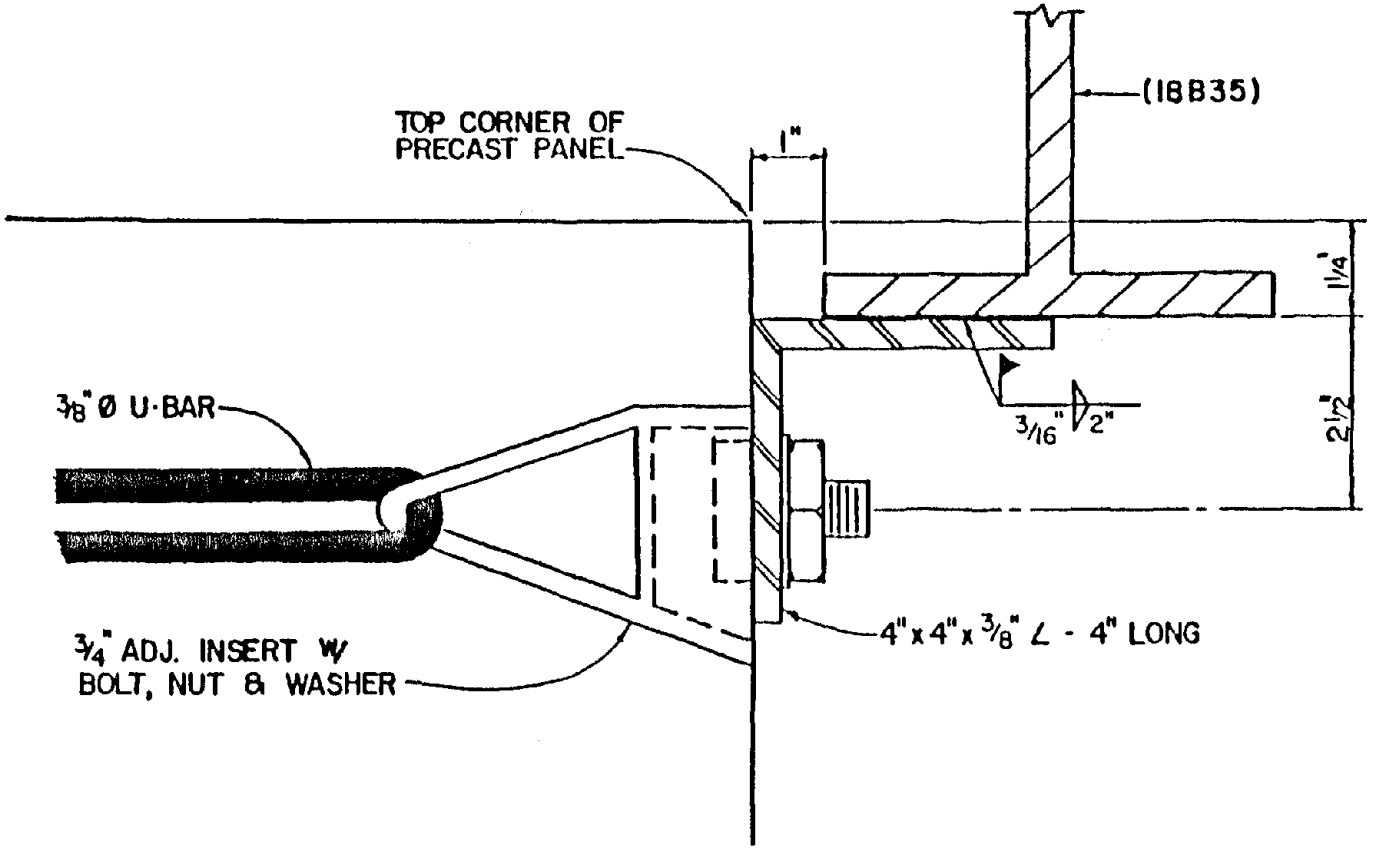

Figure 2.1-6. Typical Top Connection Detail [37].

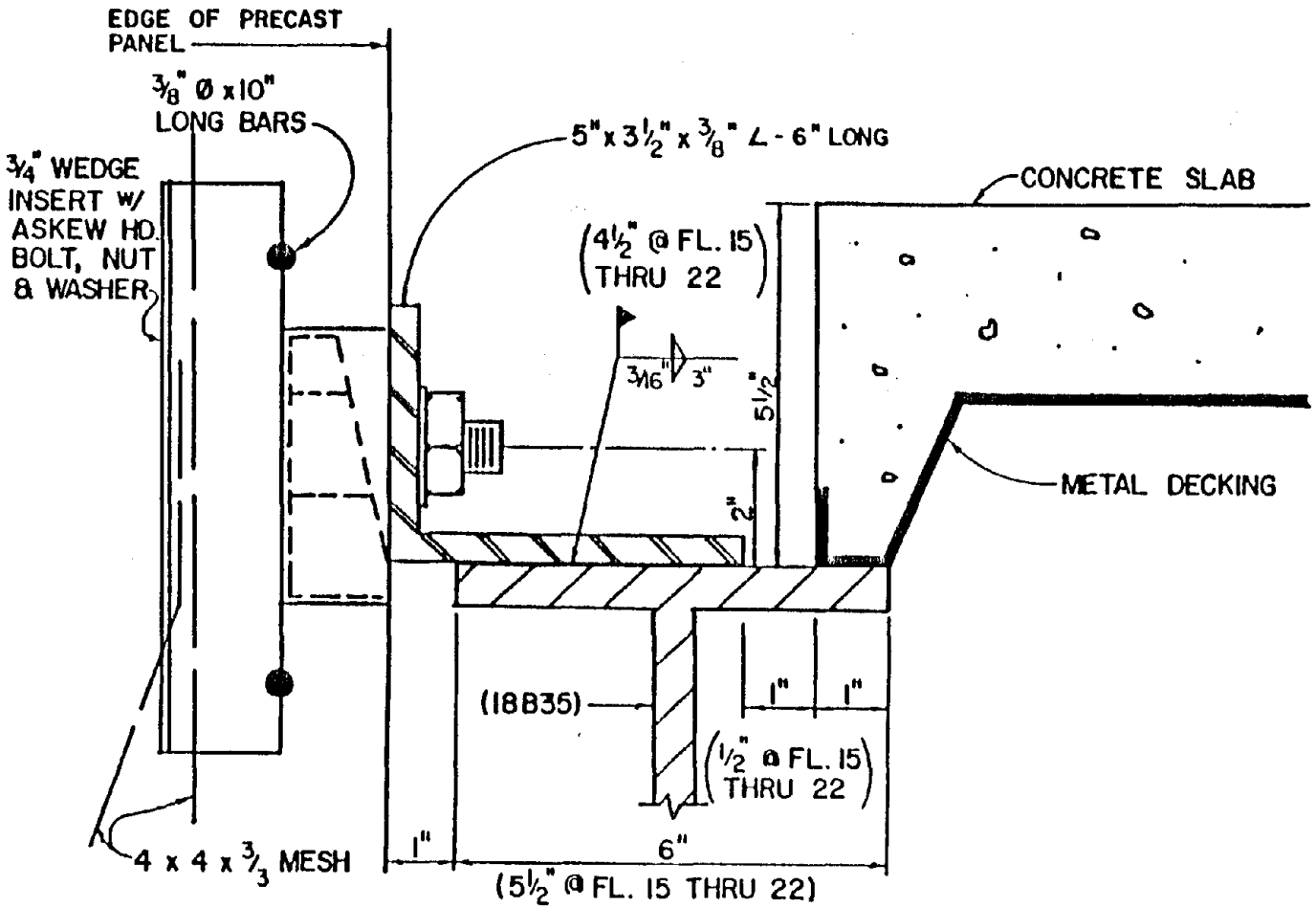

Figure 2.1-7. Typical Bottom Connection Detail [37].

excitations (wind, small earthquakes) provided that the structure had not experienced any large motions in its history. Both composite and noncomposite member properties were computed for floor framing members and the influence of each on structure frequencies and dynamic response compared. Unit translational and rotational displacements were applied at each floor level in turn and reactions obtained to construct a 63 x 63 stiffness matrix for the core.

The lateral stiffnesses of the exterior frames which support the cladding panels were developed independently then transformed to the center of the core and added to the stiffness matrix for the primary (core) structure. For translational degrees of freedom, this was accomplished with the following equation:

$$\underset{\sim}{K}_{TOT} = \underset{\sim}{K}_{C} + 2\underset{\sim}{K}_{EF} + 2\underset{\sim}{K}_{CP} \qquad (2.2\text{-}1)$$

where $\underset{\sim}{K}_{TOT}$ was overall structure stiffness, $\underset{\sim}{K}_{C}$ core stiffness, $\underset{\sim}{K}_{EF}$ exterior frame stiffness, and $\underset{\sim}{K}_{CP}$ cladding panel stiffness (see below and Fig. 2.2-1). For rotational degrees of freedom, the equation used was:

$$\underset{\sim}{K}_{TOT} = \underset{\sim}{K}_{C} + 4D\,(\underset{\sim}{K}_{EF} + \underset{\sim}{K}_{CP})\,\theta D \qquad (2.2\text{-}2)$$

where D was half the side length of the square structure and θ a unit rotation (Fig. 2.2-1). The exterior frame stiffness model was reduced to a single degree of freedom per floor by assuming that each floor acted as a rigid body. This was accomplished by using a plane frame program

written by Gram [17]. The program included frame elements which can accommodate shear deformation and arbitrary elastic rotational stiffnesses at either end. Typical spandrel-column connection stiffnesses range from 2 x 10^3 to 1.5 x 10^5 kips-inch/radian (226 to 1.69 x 10^4 kNm/radian) [12]. In this study, an intermediate rotational connection stiffness of 8 x 10^4 kips-inch/radian (9.04 x 10^4 kNm/radian) was used to model the stiffness of the exterior frame joints.

The lateral stiffness contribution of the row of cladding panels and connection angles between story levels on each building face was defined by an assumed shear stiffness constant V_i. Parameter V_i was used to form a tridiagonal stiffness matrix

$$\underset{\sim}{K}_{CP} = \begin{bmatrix} V_1 & -V_1 & & & & & \\ -V_1 & V_1 + V_2 & -V_2 & & & & \\ & -V_2 & \ddots & \ddots & & & \\ & & \ddots & V_i + V_{i-1} & -V_{i-1} & & \\ & & & \ddots & \ddots & \ddots & -V_{20} \\ & & & & -V_{20} & V_{21} + V_{20} & \end{bmatrix} \qquad (2.2\text{-}3)$$

where i denoted the story number, starting at the top, representing the lateral stiffness of each face of the structure. The tridiagonal stiffness array was transformed to the center of the core and added to other stiffness contribution according to Eqs. (2.2-1) and (2.2-2) (Fig. 2.2-1). Parameter V_i was used to calibrate the overall computer model of both the structure and cladding on the basis of ambient vibration data for

K_C = Core Stiffness
K_{EF} = Exterior Frame Stiffness
K_{CP} = Cladding Panel Stiffness

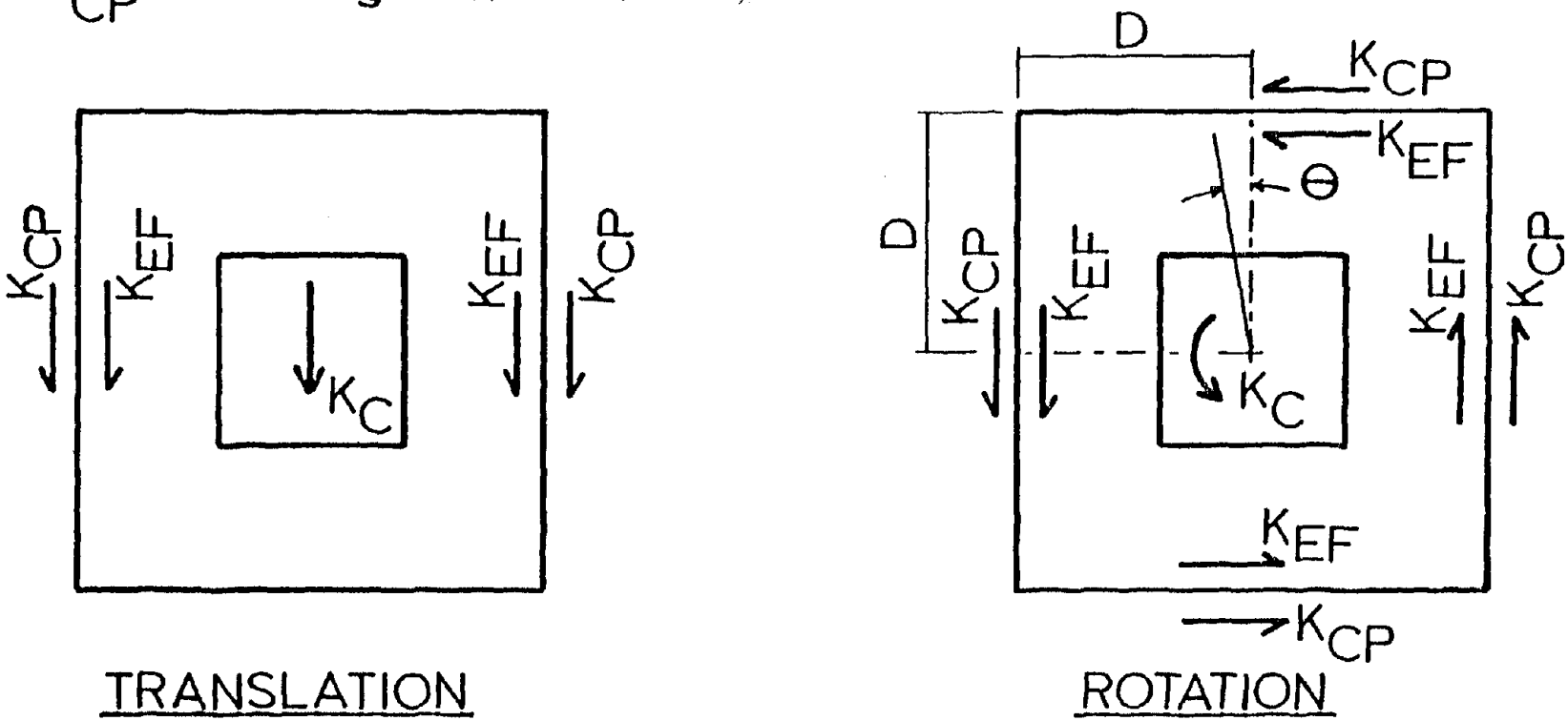

Figure 2.2-1. Geometric Transformation of Exterior Frame Stiffness and Cladding and Connections Stiffness to Core.

the prototype structure. This was accomplished by adjusting the value of V_i in steps until a match was obtained as discussed in Section 2.4.

2.2.2 Mass

The mass matrix for the prototype structure was prepared by an earlier investigator [42]. Each mass in the model was assumed to be concentrated at floor level in the center of the core which implies the assumption of symmetry. The mass of structural framing, curtain walls, floor slabs and building partitions was evaluated directly from the structure drawings and lumped in standard fashion. The actual live load distribution of the building was not determined and since using code values would have overestimated the live loads, an alternative approach was chosen. The National Bureau of Standards conducted a study on the distribution of live loads in office buildings which showed the mean uniform live load to be 10.63 lbs/ft^2 (509 N/m^2) with a standard deviation of 4.8 lbs/ft^2 (230 N/m^2) [5]. Based on the above study a live load of 10.63 lbs/ft^2 (509 N/m^2) was used in addition to dead load mass computations for the prototype structure.

2.3 Measurement of Structure Frequencies

The structure frequencies were measured to determine the contribution of the cladding panels and their connections to the overall lateral stiffness of the structure. The stiffness properties of the core and exterior framing can be determined rather accurately using analytical modeling procedures while knowledge is lacking as to properly account for the presence of the exterior wall panels in the overall system. The contribution of cladding was determined by matching analytical and experimental frequencies of the clad and unclad building models as detailed in the next section.

The normal daily activities at the prototype structure precluded having any permanent fixtures and necessitated transportation of the measuring equipment to the building every time a set of measurements was taken. Several low level force-balance accelerometers (Kinemetrics FBA-1) were used to measure the ambient response simultaneously at different locations. The accelerometer signals were amplified, filtered and then recorded on magnetic tape using an HP-3968 eight channel tape recorder (Fig. 2.3-1).

Three measurements were made, each lasting up to six hours. The first two tests employed three accelerometers all located on the roof. Given previous knowledge of structure frequencies, two were positioned at opposite edges of the roof to determine rigid frame translational frequencies and torsional frequencies. Meanwhile, the third accelerometer was located in the core of the structure to determine braced frame translational frequencies. The third measurement was directed only at translational frequencies. Five accelerometers were positioned on different floors (2, 9, 17, 21, roof) in the core of the structure. During the first half of the data acquisition, all the accelerometers were oriented in the rigid frame direction while they were rotated to measure movements in the braced frame direction during the second half of the measurement. Data reduction was performed using an HP 5420A digital signal analyzer [27]. Typically, the number of averages employed ranged between 800 and 1400 depending on the amount of data available. The first three frequencies in each direction are shown in columns 3 to 5 in Table 2.3-1. Later, in a related study [27], forced vibration tests were performed using a rectilinear force generator on the same structure. Frequencies

Table 2.3-1. Experimental Frequencies for the Prototype Structure.

		Vibration Frequencies, in Hertz			
		Ambient, 1979			Forced Vibration
Direction (1)	Mode (2)	6/21 (3)	9/5 (4)	9/13 (5)	Test Results, 1981 (6)
Braced frame	1	0.41	0.40	0.40	0.41
	2	1.32	1.30	1.29	1.30
	3	2.38	2.38	2.38	2.35
Rigid frame	1	0.32	0.30	0.30	0.32
	2	0.98	0.95	0.93	0.96
	3	1.69	1.65	1.66	1.66
Torsion	1	0.43	0.40	--	0.41
	2	1.26	1.22	--	1.23
	3	2.16	2.12	--	2.09

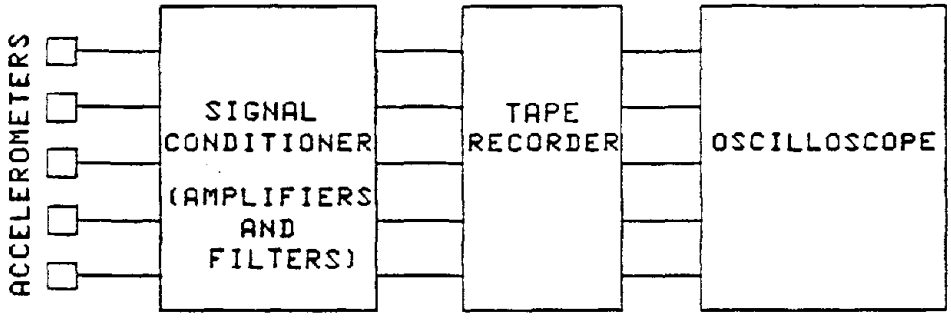

Figure 2.3-1. Ambient Response Measurement Instrumentation.

obtained were in good agreement with ambient level results and are shown in column 6 of Table 2.3-1.

2.4 Calibration of Analytical Models

Currently, knowledge is lacking on how to estimate the contribution of cladding panels and their connections to overall structure lateral stiffness. The contribution of cladding was identified in this study by matching ambient experimental frequencies and computed frequencies for the lowest three modes for both translational and torsional modes. This was accomplished by adjusting the shear stiffness parameters, V_i, in the analytical model discussed above in Section 2.2 in steps until computed and measured frequencies were nearly equal for lower modes. Cladding stiffness parameter V_i was assumed to be constant over the height of the structure.

The least-squares criterion with percent differences was used in the process of correlating measured and computed frequencies. The use of percent differences was chosen as a logical way of assigning a higher level of importance to matching lower frequency values. A value of V = 625 kips/inch (1.1×10^5 kN/m) produced the best match of experimental and analytical values for the composite floor slab model. The best match for the noncomposite model was obtained with V = 800 kips/inch (1.4×10^5 kN/m). The frequencies for the above analytical models are summarized in Table 2.4-1 for both the clad and the unclad models. These shear stiffness values were verified by a finite element study of one cladding panel and its connection angles by earlier investigators [53].

As the percent increase in frequency values in columns 5 and 8 of Table 2.4-1 demonstrates, the addition of cladding stiffness effects

results in a substantial increase in lower mode (especially torsional) frequencies when compared to the frequency values for the unclad (V = 0) structure. The increase in structure frequencies due to cladding effects is higher for the noncomposite model than for the composite model. Increases are up to 25% in the braced direction, 52% in the rigid direction, and 95% in torsion. Apparently, the dynamic properties of the model are altered significantly by consideration of cladding lateral stiffness effects for low level motions. Recall that the mass of the cladding was included in all frequency computations, but that, in the so-called unclad state, the contributory effect of cladding to overall structure lateral stiffness is neglected.

Table 2.4-1. Analytical Frequencies.

Direction (1)	Mode (2)	Vibration Frequencies, in Hertz: Noncomposite Model: Without Cladding[a] (3)	Noncomposite Model: With Cladding[b] (4)	Noncomposite Model: Percent Increase (5)	Composite Model: Without Cladding (6)	Composite Model: With Cladding[c] (7)	Composite Model: Percent Increase (8)
Braced frame	1	0.32	0.40	25	0.34	0.40	18
	2	1.02	1.24	22	1.10	1.26	15
	3	1.95	2.26	16	2.12	2.35	11
Rigid Frame	1	0.23	0.33	43	0.26	0.34	31
	2	0.63	0.96	52	0.75	1.00	33
	3	1.14	1.67	46	1.39	1.78	28
Torsion	1	0.23	0.42	83	0.26	0.41	58
	2	0.63	1.23	95	0.71	1.17	65
	3	1.14	2.08	82	1.28	2.00	56

[a]Interstory shear stiffness V = 0.

[b]Interstory shear stiffness V = 800 kips/inch (1.4 x 10^5 kN/m).

[c]Interstory shear stiffness V = 625 kips/inch (1.1 x 10^5 kN/m).

3. LINEAR DYNAMIC RESPONSE STUDIES

3.1 Introduction

The increasing costs of building construction and materials has added to the interest in utilizing the lateral stiffness and energy absorbing capacity available in the exterior cladding. However, an understanding of cladding behavior is lacking. What is known is qualitative in nature and not enough quantitative information is available, although continuing studies are providing additional information. Increase in height of structures and use of high strength materials has generated more flexible structures which are more responsive to wind or moderate earthquakes. Lateral deflections are often the governing factor during design rather than vertical load resistance due to the added responsiveness of modern tall buildings.

Analytical models describing the elastic and inertial properties of the prototype structure in the form of condensed stiffness and mass matrices for the selected degrees of freedom were developed above in Chapter 2. These models were used in the dynamic response studies of the prototype structure to evaluate the influence of cladding lateral stiffness on overall structure response. Both the composite and non-composite models were considered. In addition, the structure dynamic response with enforced mass eccentricity was computed as required by 1982 UBC [49] for combined translational and torsional response studies. Again, the influence of cladding was evaluated but in this case for

the composite model only to reduce the amount of computation and limit the number of cases for consideration. Linear elastic, small displacement response behavior was assumed throughout the studies in this chapter. The internal damping present in the structure was represented by using a simple modal formulation. In simple modal damping, a damping ratio γ_i is defined for each of i modes and the damping matrix defined as

$$\underset{\sim}{C} = (\underset{\sim}{X}_N^{-1})^T \begin{bmatrix} 2\gamma_1 P_1 & & & \\ & \ddots & & \\ & & 2\gamma_i P_i & \\ & & & \ddots \\ & & & & 2\gamma_n P_n \end{bmatrix} \underset{\sim}{X}_N^{-1} \qquad (3.1\text{-}1)$$

where P_i is the natural circular frequency for mode i, n is the number of modes considered, and $\underset{\sim}{X}_N$ is the modal matrix normalized with respect to the mass matrix. A damping ratio of five percent was specified for all modes in these studies. Later experimental measurements [27] conducted on the prototype structure revealed damping ratios in the range of two to five percent for the first several modes for forced vibration excitation of the prototype structure.

In this chapter, the computational procedures used to determine structure response to moderate earthquake ground motion are described first. Then, structure displacement time-histories for the variety of ground motion loadings are presented and structure response with and without cladding stiffening effects compared. Finally, the structure

dynamic response with enforced mass eccentricity was computed for both the clad and unclad structure models.

3.2 Integration Method

The dynamic response of a structure may be obtained by a step-by-step integration procedure. In this approach, the response is evaluated for a series of short time increments, Δt, generally taken of equal length for computational convenience. The condition of dynamic equilibrium is established at the beginning and at the end of each interval, and the motion of the system during the time increment is evaluated approximately on the basis of an assumed linear distribution of displacement and velocity. The evaluation ignores the lack of equilibrium which may develop during the interval unless equilibrium iterations are included. The complete response is obtained by using the velocity and displacement computed at the end of one interval as the initial conditions for the next interval; the process may be continued step by step from the initiation of loading to any desired time. A FORTRAN computer program was written to do the step-by-step computations in this study [32].

A number of numerical integration procedures are available for the solution of the equations of motion.

$$\underset{\sim}{M}\,\ddot{\underset{\sim}{D}} + \underset{\sim}{C}\,\dot{\underset{\sim}{D}} + \underset{\sim}{S}\,\underset{\sim}{D} = \underset{\sim}{A} \qquad (3.2\text{-}1)$$

where $\underset{\sim}{M}$, $\underset{\sim}{C}$ and $\underset{\sim}{S}$ are the mass, damping and stiffness matrices respectively for the assembled structure. Vectors $\underset{\sim}{D}$, $\dot{\underset{\sim}{D}}$, $\ddot{\underset{\sim}{D}}$ and $\underset{\sim}{A}$ represent displacements, velocities, accelerations and actions at the degrees of freedom, respectively.

The direct linear extrapolation technique with the trapezoidal rule was used to solve for total displacements of the structure at each time step. In this technique, uniform time steps are used and total response evaluated at the end of each step. Velocities are approximated at the end of the step from the trapezoidal rule as:

$$\dot{\underset{\sim}{D}}_i = \dot{\underset{\sim}{D}}_{i-1} + (\ddot{\underset{\sim}{D}}_{i-1} + \ddot{\underset{\sim}{D}}_i) \frac{\Delta t}{2} \tag{3.2-2}$$

and displacements are assumed to be

$$\underset{\sim}{D}_i = \underset{\sim}{D}_{i-1} + (\dot{\underset{\sim}{D}}_{i-1} + \dot{\underset{\sim}{D}}_i) \frac{\Delta t}{2} \tag{3.2-3}$$

where subscripts indicate current response time point i and prior time point i-1. Substituting Eq. (3.2-2) into Eq. (3.2-3) results in:

$$\underset{\sim}{D}_i = \underset{\sim}{D}_{i-1} + \dot{\underset{\sim}{D}}_{i-1} \Delta t + (\ddot{\underset{\sim}{D}}_{i-1} + \ddot{\underset{\sim}{D}}_i) \frac{(\Delta t)^2}{4} \tag{3.2-4}$$

The linear damped equations of motion (see Eq. (3.2-1)) can be written for the i-th time point as:

$$\underset{\sim}{M}\, \ddot{\underset{\sim}{D}}_i + \underset{\sim}{C}\, \dot{\underset{\sim}{D}}_i + \underset{\sim}{S}\, \underset{\sim}{D}_i = \underset{\sim}{A}_i \tag{3.2-5}$$

Solving for $\dot{\underset{\sim}{D}}_i$ in Eq. (3.2-3) leads to

$$\dot{\underset{\sim}{D}}_i = (\underset{\sim}{D}_i - \underset{\sim}{D}_{i-1} - \dot{\underset{\sim}{D}}_{i-1} \frac{\Delta t}{2}) \frac{2}{\Delta t} \tag{3.2-6}$$

and solving for $\ddot{D}_i$ in Eq. (3.2-4) gives

$$\ddot{\underset{\sim}{D}}_i = (\underset{\sim}{D}_i - \underset{\sim}{D}_{i-1} - \dot{\underset{\sim}{D}}_{i-1}\,\Delta t - \ddot{\underset{\sim}{D}}_{i-1}\,\frac{(\Delta t)^2}{4})\,\frac{4}{(\Delta t)^2} \tag{3.2-7}$$

Substituting Eqs. (3.2-6) and 3.2-7) into Eq. (3.2-5) and collecting terms results in

$$\underset{\sim}{S}^* \underset{\sim}{D}_i = \underset{\sim}{A}_i^* \tag{3.2-8}$$

where

$$\underset{\sim}{S}^* = \underset{\sim}{S} + \underset{\sim}{M}\,\frac{4}{(\Delta t)^2} + \underset{\sim}{C}\,\frac{2}{\Delta t} \tag{3.2-9}$$

and

$$\underset{\sim}{A}_i^* = \underset{\sim}{A}_i + \underset{\sim}{M}\,(\underset{\sim}{D}_{i-1} + \dot{\underset{\sim}{D}}_{i-1}\,\Delta t + \ddot{\underset{\sim}{D}}_{i-1}\,\frac{(\Delta t)^2}{4})\,\frac{4}{(\Delta t)^2} + \underset{\sim}{C}\,(\underset{\sim}{D}_{i-1} + \dot{\underset{\sim}{D}}_{i-1}\,\frac{\Delta t}{2})\,\frac{2}{\Delta t} \tag{3.2-10}$$

By letting

$$\underset{\sim}{Q}_{i-1} = (\underset{\sim}{D}_{i-1} + \dot{\underset{\sim}{D}}_{i-1}\,\Delta t + \ddot{\underset{\sim}{D}}_{i-1}\,\frac{(\Delta t)^2}{4})\,\frac{4}{(\Delta t)^2} \tag{3.2-11}$$

and

$$\underset{\sim}{P}_{i-1} = (\underset{\sim}{D}_{i-1} + \dot{\underset{\sim}{D}}_{i-1}\,\frac{\Delta t}{2})\,\frac{2}{\Delta t} \tag{3.2-12}$$

Equation (3.2-10) can be written as

$$\underset{\sim}{A}_i^* = \underset{\sim}{A}_i + \underset{\sim}{C}\ \underset{\sim}{P}_{i-1} + \underset{\sim}{M}\ \underset{\sim}{Q}_{i-1} \tag{3.2-13}$$

Equation (3.2-6) as

$$\dot{\underset{\sim}{D}}_i = \underset{\sim}{D}_i \frac{2}{\Delta t} - \underset{\sim}{P}_{i-1} \tag{3.2-14}$$

and Eq. (3.2-7) as

$$\ddot{\underset{\sim}{D}}_i = \underset{\sim}{D}_i \frac{4}{(\Delta t)^2} - \underset{\sim}{Q}_{i-1} \tag{3.2-15}$$

The solution algorithm can be summarized as follows:

(a) Initialize $\underset{\sim}{D}_i$ and $\dot{\underset{\sim}{D}}_i$ which are the displacements D_o, and the velocities $\dot{D}_o$ at i = 0. Compute $\ddot{\underset{\sim}{D}}_o$ ($\ddot{\underset{\sim}{D}}_i$ at i = 0) from the equation of motion where D_o and $\dot{D}_o$ are specified

$$\underset{\sim}{M}\ \ddot{\underset{\sim}{D}}_o = \underset{\sim}{A}_o - \underset{\sim}{C}\ \dot{\underset{\sim}{D}}_o - \underset{\sim}{S}\ \underset{\sim}{D}_o \tag{3.2-16}$$

The Cholesky method is used to obtain the accelerations $\ddot{\underset{\sim}{D}}_o$.

(b) Compute $\underset{\sim}{S}^*$ and decompose. $\underset{\sim}{S}^* = \underset{\sim}{U}'\ \underset{\sim}{U}$ using the Cholesky method, where $\underset{\sim}{U}$ is an upper triangular matrix.

(c) Perform the following sequence of calculations for time step i ($\geq$ 1)

(1) Compute $\underset{\sim}{P}_{i-1}$

(2) Compute $\underset{\sim}{Q}_{i-1}$

(3) Compute $\underset{\sim}{A}_i^*$

(4) Solve for $\underset{\sim}{D}_i$ in two steps

$$\underset{\sim}{U}' \underset{\sim}{D}_i^* = \underset{\sim}{A}_i^* \qquad \text{(forward solution)}$$

$$\underset{\sim}{U} \underset{\sim}{D}_i = \underset{\sim}{D}_i^* \qquad \text{(backward solution)}$$

(5) Compute $\dot{\underset{\sim}{D}}_i$

(6) Compute $\ddot{\underset{\sim}{D}}_i$

(7) Go to (1) and continue

Time step Δt must be selected by considering the characteristics of the structure, in particular the natural periods of vibration. The usual recommendation is to choose Δt less than or approximately equal to $\tau/10$, where τ is the period of the highest significant mode. In addition to the above, the nature of the forcing function must be considered; a Δt which is less than or equal to the time interval at which the forcing function has been interpolated should be chosen.

The load-time history matrix A for the degrees of freedom was evaluated using linear interpolation of independent time functions

F_x, F_y and F_z to produce Q_x, Q_y and Q_z. Then matrix $\underset{\sim}{A}$ at time station i was formed as

$$\underset{\sim}{A}_i = -\underset{\sim}{M}\ \underset{\sim}{R}\ \underset{\sim}{Q}_i \tag{3.2-17}$$

where $\underset{\sim}{R}$ is a matrix of influence coefficients and

$$\underset{\sim}{Q}_i = \begin{Bmatrix} \underset{\sim}{Q}_{ix} \\ \underset{\sim}{Q}_{iy} \\ \underset{\sim}{Q}_{iz} \end{Bmatrix} \tag{3.2-18}$$

The entries in $\underset{\sim}{Q}_i$ were evaluated at the center of the time interval under consideration $(t_{i-1} + \frac{\Delta t}{2})$. They were evaluated at the center of the interval to reduce interpolation error in the representation of the forcing function [47]. Direct linear extrapolation was an unconditionally stable integration procedure and was found to be reliable for obtaining response-time history of the prototype structure. This procedure is restricted to linear analysis only but can be modified to handle nonlinear cases also as will be discussed in Chapter 4.

3.3 Symmetric Structure Response

The response of the structure models with cladding effects V = 625 kips/inch (1.1×10^5 kN/m) for composite and V = 800 kips/inch (1.4×10^5 kN/m) for noncomposite and without cladding effects (V = 0) was determined for several different earthquake ground motions. The loading cases used are summarized in Table 3.3-1. Five percent modal damping was assumed and the equations of motion were integrated directly

using the procedure described in Section 3.2. Displacement response results are shown in Tables 3.3-2 and 3.3-3 for the cases considered. Maximum displacement responses at the roof and the square-root-of-the-sum-of-the-square (SRSS) of the maximum responses at the degrees of freedom are listed for both the composite and the noncomposite models.

In the braced frame direction of the prototype structure, peak and SRSS values were reduced when cladding was added for both models in all cases except Cases 3, 5, and 4 + 3. However, in the rigid direction the values were only reduced for Cases 2, 4 and 4 + 3. The drastic change in dynamic characteristics of the prototype structure when the stiffening effects of cladding and its connections were added, as discussed in Section 2.4, was recognized as the reason for this response behavior. The effects of the addition of cladding panel lateral stiffness on dynamic response for loading Case 1 are displayed in Figs. 3.3-1 to 3.3-4. These figures illustrate the change in structure frequencies with the shorter distance between response peaks for the stiffer clad cases. When the dynamic responses for the clad composite model (Figs. 3.3-1 and 3.3-2) and the clad noncomposite model (Figs. 3.3-3 and 3.3-4) were compared, good agreement was observed. It may not alwyas be conservative to neglect cladding-structure interaction effects for buildings with heavyweight cladding systems since the change in linear dynamic properties and response of the structure is considerable as shown by response data presented above.

3.4 Structure Response with Mass Eccentricity

3.4.1 Mass Eccentricity Model

In the actual model of the prototype structure, the centers of mass and rigidity were almost coincident and very small torsional response

Table 3.3-1. Ground Motion Input Cases.

Case (1)	Earthquake (2)	Date (3)	Component (4)	Duration[a] (5)	Peak[b] Accel. (6)	RMS[b] Accel. (7)
1	Western Washington	13 April, 1949	N86E	89.15	28	3.0
2	Kern County, CA	21 July, 1952	S69E	54.38	18	2.7
3	San Francisco, CA	22 March, 1957	S80E	39.86	10	1.0
4	San Francisco, CA	22 March, 1957	N10E	39.86	8	0.7
5	San Fernando, CA	9 February, 1971	N00E	10.41	3	0.6

[a] In seconds.

[b] In percent g.

Table 3.3-2. Earthquake Response Summary for Composite Model.

	Displacement Response (inches)[b]							
	Braced Frame Direction				Rigid Frame Direction			
	V = 0		V = 625[c]		V = 0		V = 625[c]	
Case[a]	Peak[d]	SRSS[e]	Peak	SRSS	Peak	SRSS	Peak	SRSS
1	13.6	37.2	10.0	27.9	12.4	30.9	12.5	35.2
2	6.0	16.7	5.4	14.7	7.6	18.3	5.7	16.5
3	0.4	1.1	0.4	1.1	0.3	1.0	0.4	1.2
4	1.4	3.9	1.1	3.2	1.8	4.4	1.3	3.8
5	0.6	1.6	0.6	1.8	0.4	1.0	0.6	1.6
3 + 4[f]	1.4	4.0	1.1	3.4	0.3	4.0	0.4	3.4
4 + 3[g]	0.4	4.5	0.5	4.0	1.8	4.5	1.3	4.0

[a]See Table 3.3-1.

[b]1 inch = 25.4 mm

[c]Kips per inch (1 k/inch = 175 kN/m).

[d]At roof.

[e]Square root of sum-of-squares of maximum response at degrees of freedom.

[f]Loading 3 in Rigid Direction and loading 4 in Braced Direction.

[g]Loading 4 in Rigid Direction and loading 3 in Braced Direction.

Table 3.3-3. Earthquake Response Summary for Noncomposite Model.

	Displacement Response (inches)[b]							
	Braced Frame Direction				Rigid Frame Direction			
	V = 0		V = 800[c]		V = 0		V = 800[c]	
Case[a]	Peak[d]	SRSS[e]	Peak	SRSS	Peak	SRSS	Peak	SRSS
1	14.4	39.7	9.9	28.2	8.6	23.9	13.1	38.7
2	6.2	16.7	5.3	14.8	7.8	21.8	5.7	17.2
3	0.4	1.1	0.5	1.1	0.4	1.1	0.4	1.1
4	1.5	4.0	1.1	3.3	1.9	4.7	1.3	3.9
5	0.5	1.4	0.6	1.8	0.5	1.3	0.5	1.6
3 + 4[f]	1.5	4.2	1.1	3.5	0.4	4.2	0.4	3.5
4 + 3[g]	0.4	4.8	0.5	4.1	1.9	4.8	1.3	4.1

[a]See Table 3.3-1.

[b]1 inch = 25.4 mm

[c]Kips per inch (1 k/inch = 175 kN/m)

[d]At roof.

[e]Square root of sum-of-squares of maximum response at degrees of freedom.

[f]Loading 3 in Rigid Direction and loading 4 in Braced Direction.

[g]Loading 4 in Rigid Direction and loading 3 in Braced Direction.

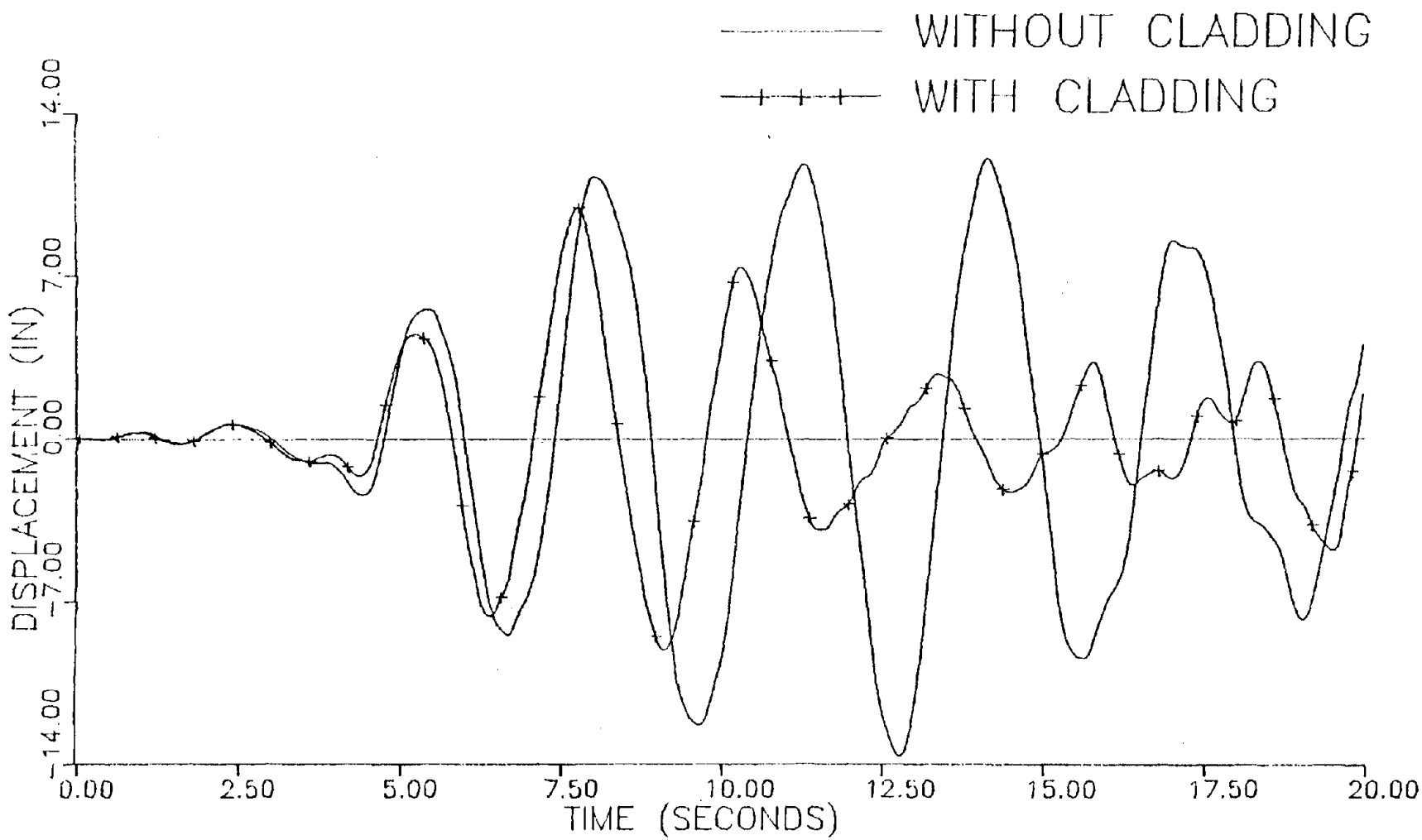

Figure 3.3-1. Roof Displacement-Time Histories for the Composite Model in the Braced Direction for April 13, 1949, Western Washington Earthquake, N86E Component.

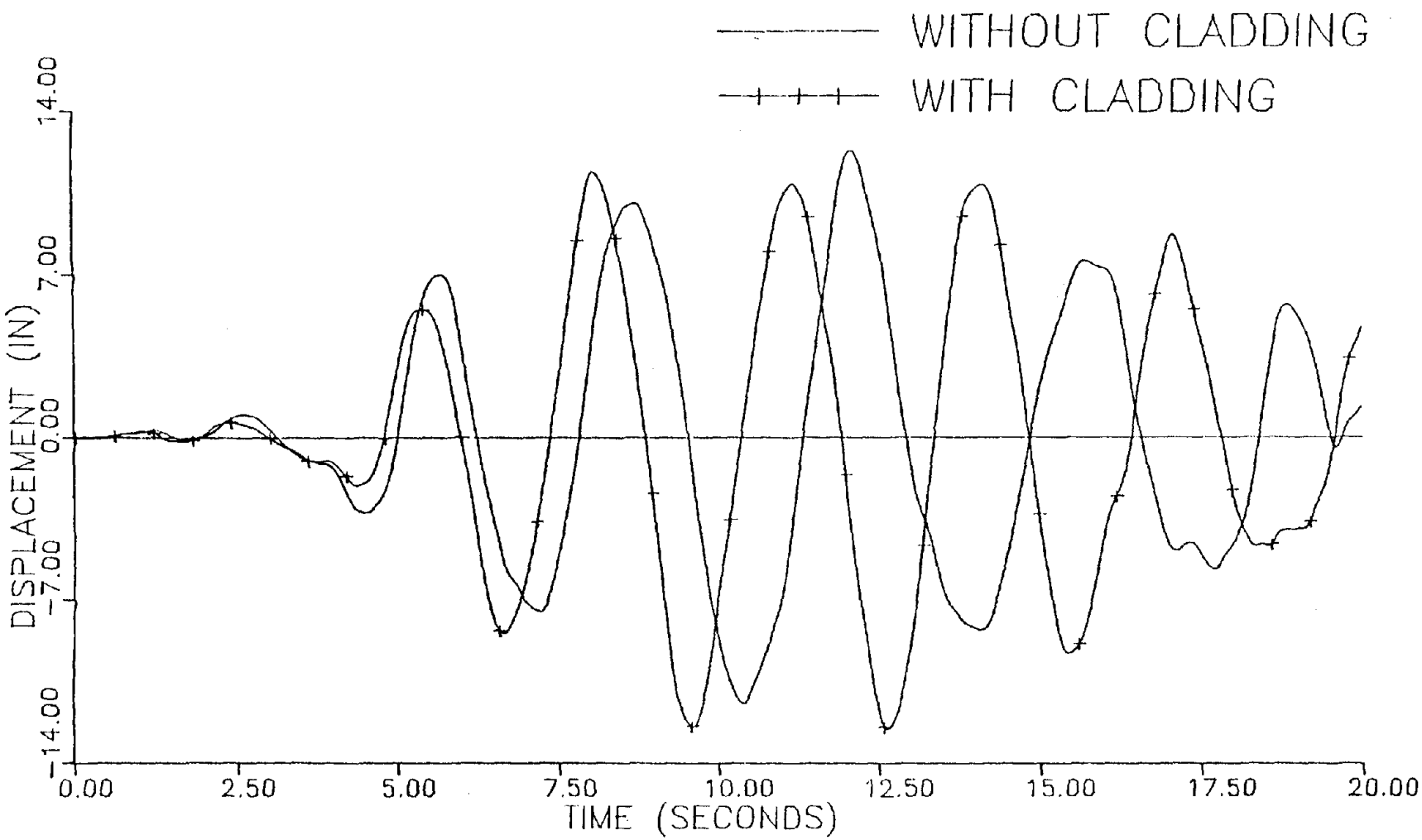

Figure 3.3-2. Roof Displacement-Time Histories for the Composite Model in the Rigid Direction for April 13, 1949, Western Washington Earthquake, N86E Component.

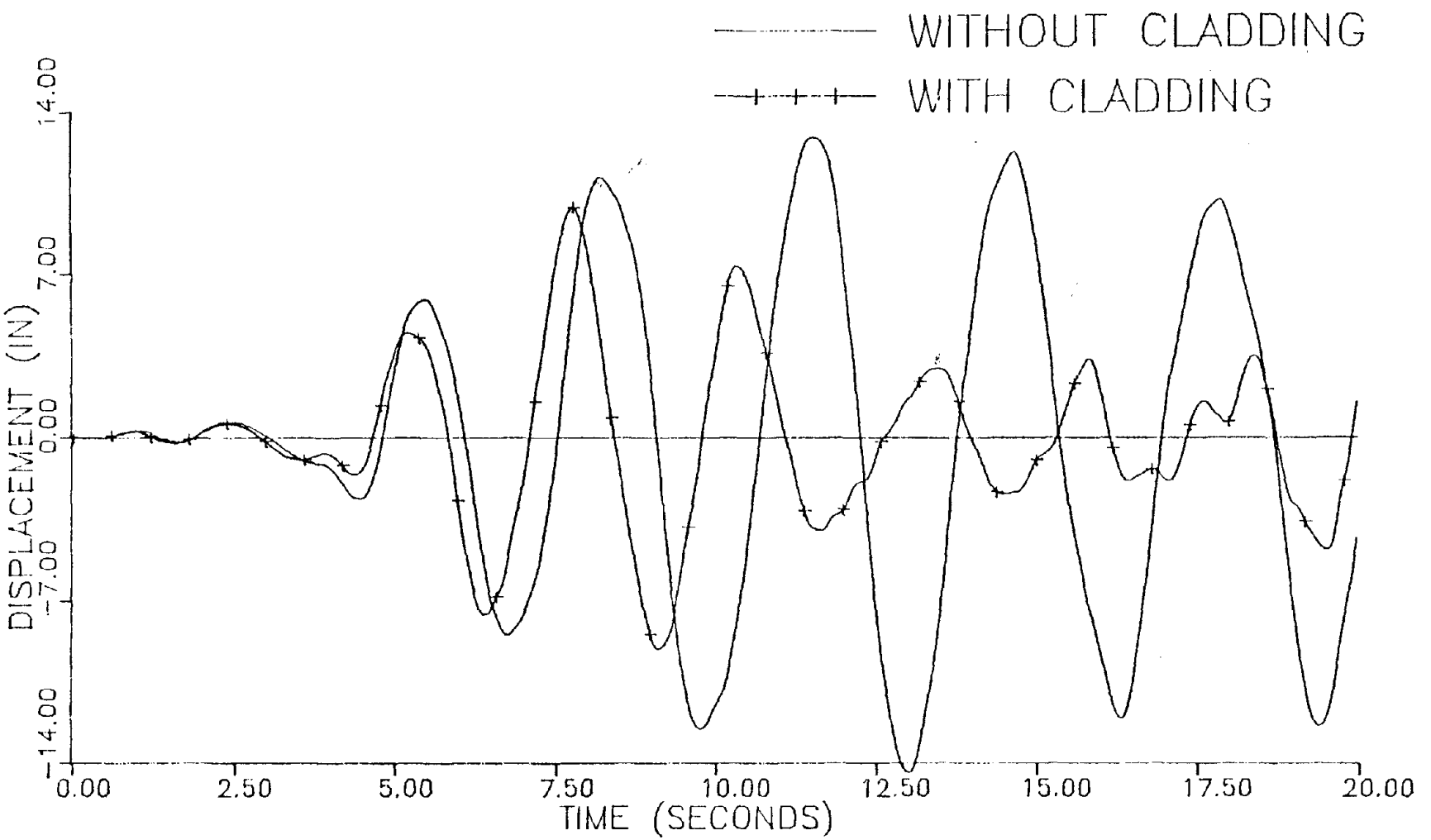

Figure 3.3-3. Roof Displacement-Time Histories for the Noncomposite Model in the Braced Direction for April 13, 1949, Western Washington Earthquake, N86E Component.

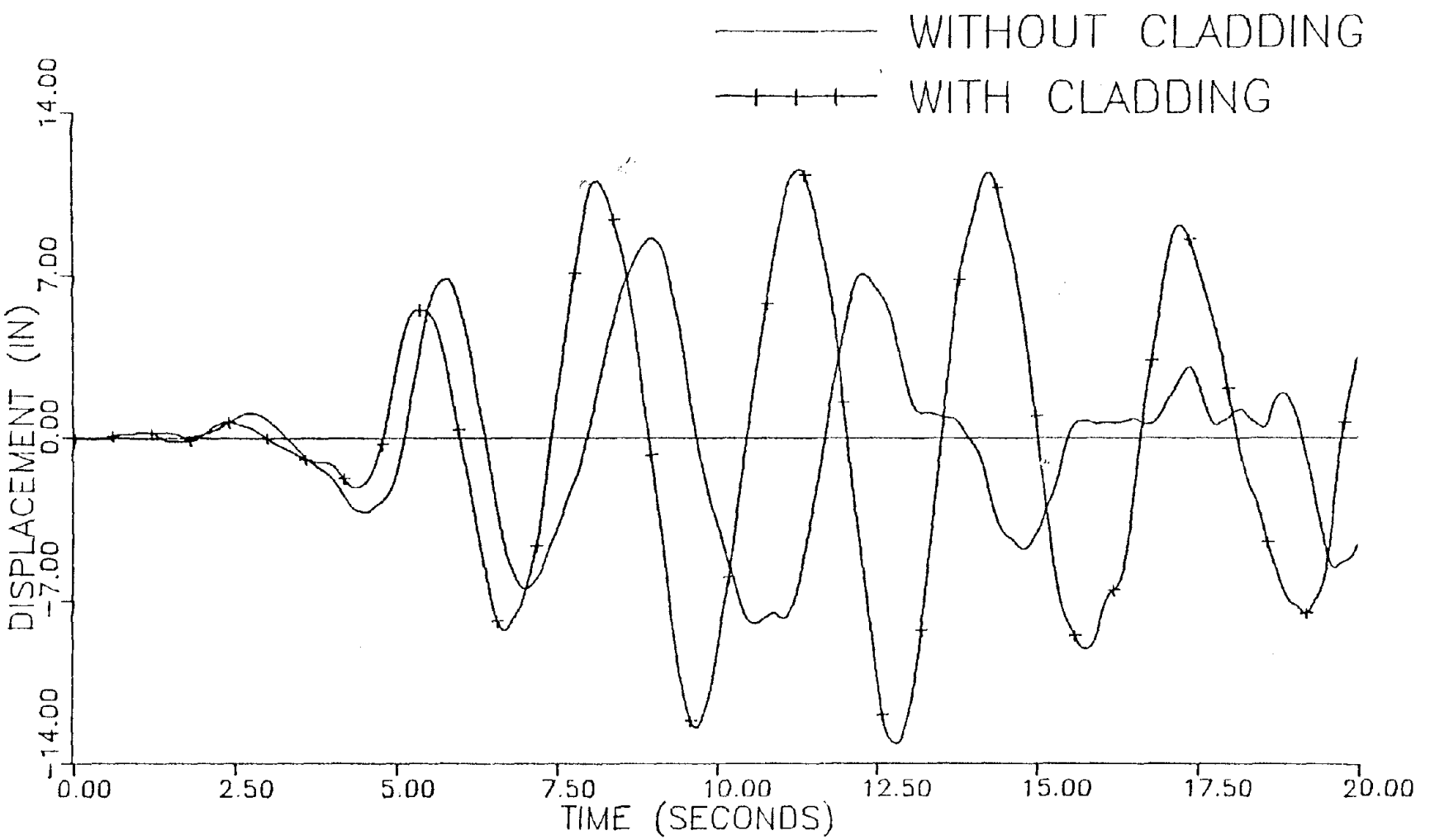

Figure 3.3-4. Roof Displacement-Time Histories for the Noncomposite Model in the Rigid Direction for April 13, 1949, Western Washington Earthquake, N86E Component.

resulted from applied ground motion input in either the rigid or braced frame directions. However, a minimum 5% eccentricity between center of mass and center of rigidity in each structure direction is required by 1982 UBC [49] for combined translational and torsional response studies. The equations of motion were written with respect to the center of rigidity at each floor level in the model. The transformation of the mass matrix from the center of mass, set at the required minimum eccentricity of 5% (Fig. 3.4-1), to the center of rigidity was accomplished by following procedures described by Weaver et al. [51] in developing the overall tier building representation of the prototype structure.

The frequencies and mode shapes for the prototype structure were computed. The first twelve modes with corresponding frequencies for unclad eccentric model are shown in Fig. 3.4-2 and the first ten for the clad model in Fig. 3.4-3. The reason for showing the first twelve and ten mode shapes was to include at least the first three modes in each direction (braced frame direciton, rigid frame direction and rotation). Similarly, the first twelve and ten mode shapes with corresponding frequencies for the unclad and clad symmetric models, respectively, are shown in Figs. 3.4-4 and 3.4-5 for comparison. Inspection of the figures showed that the mode shapes differed significantly for the symmetric and eccentric models. Torsion was greatly amplified in the mode shapes for the eccentric model as expected. Frequencies were also seen to change moderately (extreme case 6%). Calculation of modal participation factors [3] which are listed in Tables 3.4-1 and 3.4-2 confirmed the introduction of additional torsion for eccentric models. A strong translational-torsional coupling was observed for the unclad eccentric model with rigid

direction input and for the clad eccentric model with braced direction input.

3.4.2 Loadings

The response of the structure model was computed for two earthquake records listed in Table 3.4-3 and displayed in Figs. 3.4-6 and 3.4-7. The El Centro record was chosen because of its widespread use in the literature, and the Parkfield record because of its simplicity, representing the application of a single displacement pulse to the structure. To save computer time in the time history response analysis, it was of interest to determine if approximately the same response spectra could be obtained for only the first 10 seconds of each of the two earthquake records as for the full durations of each of the records. Damping was set at five percent of critical in these calculations. In the case of the Parkfield record the first 10 seconds yielded a perfect match for the frequency range of interest as shown in Figs. 3.4-8 to 3.4-10 displaying the displacement, velocity and acceleration response spectra, respectively. The El Centro record required more than the 10 seconds used initially and 14 seconds were needed to obtain a match with the full duration spectra in the frequency range of interest. The displacement, velocity and acceleration response spectra for the El Centro record are displayed in Figs. 3.4-11 to 3.4-13, respectively. A perfect match was obtained in all cases for the range shown in the figures. Given the above results, only the first 10 seconds of the Parkfield record and the first 14 seconds of the El Centro record were used in the dynamic response computations below resulting in substantial (74% and more) computational savings.

3.4.3 Response Studies

All dynamic response computations were performed using direct integration of the equations of motion by linear extrapolation and the trapezoidal rule as described in Section 3.2. Only the composite model was considered to reduce the number of cases to be included, and five percent modal damping was assumed in these studies as discussed in Section 3.1.

Symmetric Model. For reference purposes, the dynamic response of the symmetric model, both with (V = 625 kips/inch (1.1×10^5 kN/m)) and without (V = 0) cladding effects, to the ground motion records in Table 3.4-3 was computed prior to considering the enforced eccentricity case as required by 1982 UBC [49]. Peak roof displacement response values for the symmetric case to the El Centro record are listed in Table 3.4-4 and roof translational and torsional responses are displayed in Figs. 3.4-14 to 3.4-17. Translational response was increased by 34% in the rigid direction (Fig. 3.4-14) and by 7% in the braced direction (Fig. 3.4-16) at the roof when cladding stiffness effects were included. The response in the direction of the ground motion input displayed mostly first mode response but the presence of higher modes was observed in the rigid response of the unclad model (Fig. 3.4-14). Torsional response levels were relatively low, as will be shown below by interstory drift values and showed considerable higher mode action (Figs. 3.4-15 and 3.4-17). Peak relative interstory drift values were computed for the different faces of the structure and are listed in Table 3.4-5. In addition, the peak interstory drift values of each story are plotted in Figs. 3.4-18 to 3.4-21. The peak interstory drift values for the different faces

were the same for the clad and unclad models in the case of rigid frame direction input. When the input was in the braced frame direction, the drift values were lower for the clad model but not by a significant amount. It was observed that drift was low for faces which were not in the direction of input ground motion which was to be expected given the symmetrical configuration of the structure. The figures of interstory drift for input in rigid direction (Figs. 3.4-18 and 3.4-19) showed that while maximum values for each face were not affected by consideration of cladding effects, the peak values at each story were substantially increased for all stories except the top two. When the input was in the braced direction, the influence of cladding lead to a reduction in peak values for about the top third of the structure (Figs. 3.4-20 and 3.4-21). Finally, peak face drift values for the clad model occurred at a lower story number than for the unclad model.

When the Parkfield record was applied to the symmetric case, the peak roof displacement values listed in Table 3.4-6 were obtained. Roof translational and torsional time-historeis are plotted in Figs. 3.4-22 to 3.4-25. The effect of including cladding stiffness was that translational response was reduced by 12% in the rigid direction (Fig. 3.4-22) and 14% in the braced direction (Fig. 3.4-24) at the roof. The presence of higher modes was observed in the torsional time-history responses (Figs. 3.4-23 and 3.4-25) but was not seen to affect translational response to a significant degree. Peak relative interstory drift values for the four structure faces listed in Table 3.4-7 were lowered considerably when cladding effects were added. Peak drift for rigid direction input was reduced by 42% and for braced direction input by 12%. Drift for

faces which were not in the direction of input motion was low as was to be expected based on the symmetry of the structure. Plots of peak drift values at each story (Figs. 3.4-26 go 3.4-29) showed that cladding effects reduced drift in the top third of the structure significantly when input was in the rigid direction. While drift was also reduced when input was in the braced direction, the level of reduction was lower but spread over about the top two thirds of the structure. Again, the clad model had the peak drift values occur at lower stories as compared to the unclad model.

Comparison of response values for the El Centro and Parkfield records showed that while cladding effects reduced response levels for the Parkfield record, response levels were generally increased for the El Centro record. However, overall response levels remained higher for the Parkfield record than for the El Centro input. The changes in response levels indicated that consideration of cladding stiffness in the overall structure model, which resulted in a model with substantially different dynamic properties, altered the sensitivity of the model to the earthquake records. Inspection of the displacement response spectrum for the El Centro record with fundamental periods in the different structure directions shown for the clad and unclad models (Figs. 3.4-30 to 3.4-32) showed response levels for the clad model to be considerably higher in the rigid frame direction (43%) and in torsion (46%) than for the unclad model while being only slightly higher in the braced frame direction (6%). A similar inspection of the displacement response spectrum for the Parkfield record (Figs. 3.4-33 to 3.4-35) showed the response level for the clad model to be 2% higher in the rigid direction but lower in

both braced direction (5%) and torsion (3%) than for the unclad model. The modal participation factors listed in Tables 3.4-1 and 3.4-2 were found to be lower for the clad model as compared to the unclad model in the direction of input motion (3-6% for the first mode and less than or equal for higher modes). When these findings were combined, the conclusion was that El Centro displacement response values were expected to increase and Parkfield displacement response values to decrease with the consideration of lateral stiffening effects of cladding. Finally, relative interstory drift levels were observed to be rather high and to indicate possible nonlinear response levels. However, the model was assumed to govern for linear response levels only (see Section 3.1), so actual response values may be different from those reported.

Eccentric Model. In addition to the studies reported above for the symmetric model, the dynamic response was computed for the structure with eccentric mass with V = 625 kips/inch (1.1×10^5 kN/m) and without (V = 0) cladding stiffness effects. Peak displacement response values at the roof for the El Centro record are listed in Table 3.4-8 and roof translational and torsional time-histories are shown in Figs. 3.4-36 to 3.4-39. Inspection of these data revealed that peak roof response values increased in all cases with the addition of cladding lateral stiffening effects. For example, when the El Centro record was applied in the rigid direction, rigid frame response increased by 27% (Fig. 3.4-36) and rotational response by 41% (Fig. 3.4-37) at the roof. Braced frame response was increased by 3% (Fig. 3.4-38) and rotational response by 39% (Fig. 3.4-39) at the roof when the input motion was in the braced frame direction. The response of the structure was observed to be dominated

by first mode action except for the unclad model as input was applied in the rigid direction (Figs. 3.4-36 and 3.4-37). Peak interstory drift values for each face, along with the story at which the drift occurred, are listed in Table 3.4-9. In addition, the peak interstory drift values for every story are displayed in Figs. 3.4-40 to 3.4-43 for the four faces of the building. While peak drift was only increased on Face 4 for the clad state as compared to the unclad state when ground motion was applied in rigid direction, it was only lowered on Face 3 as the braced direction was the direction of input motion. Comparison of peak story drift values when input was applied in the rigid direction revealed that drift was lowered in the top portion of the structure on Faces 1 to 3 as cladding effects were considered while drift on Face 4 substantially increased on all floors except the top one. A similar comparison of drift values with input in braced direction showed drift to be reduced on Face 3 for all floors and by the largest amount at the top, while drift was generally increased on the other three faces with the exception of the top two to four floors. Peak drift values were observed to shift downwards in the structure for the clad model when clad and unclad models were compared.

Peak roof displacement values for the Parkfield record applied to the eccentric case are tabulated in Table 3.4-10 and roof displacement time-histories displayed in Figs. 3.4-44 to 3.4-47. Rigid frame response was reduced 13% (Fig. 3.4-44) and rotational response by 35% (Fig. 3.4-45) when cladding stiffness was accounted for and the Parkfield ground motion applied in the rigid direction. When the ground motion was applied in the braced direction, braced frame response was lowered 13% (Fig. 3.4-46)

but torsional response was increased by 9% (Fig. 3.4-47). Some evidence of higher mode action was observed with the rotational response due to rigid direction input being the most obvious case. The peak interstory drift values for the different faces listed in Table 3.4-11 were lower for the clad model than the unclad model. The reduction was substantial for input in the rigid frame direction (47% on Face 2 and 64% on Face 1). Figures of peak drift values at different stories (Figs. 3.4-48 and 3.4-49) further demonstrate this reduction and display the change in response character as peak values move from the top to about midheight of the structure. The changes were less significant due to braced direction input motion, but comparison of Figs. 3.4-50 and 3.4-51 again showed the shift in peak values towards lower stories in the structure when clad values were compared to unclad values.

When response values for the eccentric case were compared for the two earthquake loadings, Parkfield response values were observed to be higher than El Centro values. On the other hand, the contribution of lateral stiffening effects of cladding caused El Centro values to increase while Parkfield values were reduced. Displacement response spectrum values for the El Centro ground motion showed the clad model to be more sensitive to the earthquake record than the unclad model (Figs. 3.4-52 to 3.4-54). Rigid direction values were increased 23%, braced direction values 2% and torsion values 42%. Parkfield values, however, were only increased in the rigid direction (1%) but reduced in both braced direction (3%) and torsion (4%) as displayed in Figs. 3.4-55 to 3.4-57. When modal participation factors for the eccentric models were computed (see Tables 3.4-1 and 3.4-2), a strong translational-torsional coupling was observed to exist for the unclad model for input

in the rigid direction, and for the clad model for input in the braced direction. This coupling resulted in a complicated motion of the structure and made all comparisons between clad and unclad models difficult. Again, as for the symmetric case interstory drift levels were found to be high and possibly into the nonlinear range which would violate the initial assumption of linearity of the model. Hence, actual response values may be different from those reported here.

Comparison of response data for the symmetric and eccentric cases demonstrated that a dramatic increase in torsional response occurred with the introduction of eccentric mass as expected. The response data for the eccentric case will serve as reference cases for studies in Chapter 4 in which nonlinear force-deformation relationships for cladding and its connections will be introduced and their influence on structure response investigated.

Table 3.4-1. Modal Participation Factors for Different Structure Models with Input in Rigid Frame Direction

Mode (1)	Modal Participation Factors			
	Clad Eccentric Model (2)	Unclad Eccentric Model (3)	Clad Symmetric Model (4)	Unclad Symmetric Model (5)
1 in Braced Direction	0.23(2)[a]	0.07(3)	0.02(2)	0.02(3)
2 in Braced Direction	0.03(6)	0.01(6)	4.10^{-3}(6)	4.10^{-3}(6)
3 in Braced Direction	0.05(10)	0.01(11)	9.10^{-3}(9)	2.10^{-3}(11)
1 in Rigid Direction	1.24(1)	0.89(2)	1.38(1)	1.47(2)
2 in Rigid Direction	0.50(4)	0.52(5)	0.55(4)	0.66(5)
3 in Rigid Direction	0.28(7)	0.29(8)	0.32(7)	0.35(8)
1 in Torsion	0.15(3)	0.57(1)	9.10^{-6}(3)	2.10^{-4}(1)
2 in Torsion	0.06(5)	0.14(4)	3.10^{-6}(5)	4.10^{-6}(4)
3 in Torsion	0.05(8)	0.06(7)	3.10^{-7}(8)	9.10^{-7}(7)

[a]Actual mode number shown in parentheses.

Table 3.4-2. Modal Participation Factors for Different Structure Models with Input in Braced Frame Direction.

Mode (1)	Modal Participation Factors			
	Clad Eccentric Model (2)	Unclad Eccentric Model (3)	Clad Symmetric Model (4)	Unclad Symmetric Model (5)
1 in Braced Direction	0.83(2)[a]	1.36(3)	1.40(2)	1.44(3)
2 in Braced Direction	0.42(6)	0.59(6)	0.56(6)	0.60(6)
3 in Braced Direction	0.31(10)	0.36(11)	0.36(9)	0.36(11)
1 in Rigid Direction	0.12(1)	0.27(2)	0.02(1)	0.02(2)
2 in Rigid Direction	0.04(4)	0.07(5)	4.10^{-3}(4)	5.10^{-3}(5)
3 in Rigid Direction	0.03(7)	0.03(8)	9.10^{-3}(7)	1.10^{-4}(8)
1 in Torsion	0.56(3)	0.15(1)	1.10^{-3}(3)	6.10^{-5}(1)
2 in Torsion	0.13(5)	0.04(4)	2.10^{-4}(5)	4.10^{-5}(4)
3 in Torsion	0.06(8)	0.01(7)	2.10^{-5}(8)	2.10^{-5}(7)

[a]Actual mode number shown in parentheses.

Table 3.4-3. Ground Motion Input Cases.

Case (1)	Earthquake (2)	Date (3)	Component (4)	Duration[a] (5)	Peak[b] Accel. (6)	RMS[b] Accel. (7)
1	Imperial Valley, CA (El Centro)	May 18, 1940	S00E	53.73 (14.0)[c]	35	4.9
2	Parkfield, CA	June 27, 1966	N65E	43.64 (10.0)[c]	49	5.2

[a] In seconds.

[b] In percent g.

[c] Duration used in response calculations.

Table 3.4-4. Peak Roof Displacements, Symmetric Case, for the First 14 Seconds of the 1940 Imperial Valley Earthquake Recorded at El Centro in the S00E Direction.

Ground Motion Input Direction (1)	Case (2)	Peak Roof Displacement Response		
		Rigid Direction (inches) (3)	Braced Direction (inches) (4)	Rotation (radians) (5)
Braced	Clad	0.2	16.4	8.8×10^{-5}
	Unclad	0.2	15.3	8.3×10^{-5}
Rigid	Clad	15.8	0.2	3.0×10^{-6}
	Unclad	11.8	0.2	4.1×10^{-6}

Table 3.4-5. Peak Interstory Drift, Symmetric Case for the First 14 Seconds of the 1940 Imperial Valley Earthqauke Recorded at El Centro in the SOOE Direction.

Ground Motion Input Direction (1)	Case (2)	Peak Relative Interstory Drift (inches)			
		Face 1[a] (3)	Face 2 (4)	Face 3 (5)	Face 4 (6)
Braced	Clad	1.1(16)	0.02(16)	1.1(16)	0.02(17)
	Unclad	1.2(20)	0.03(24)	1.2(20)	0.03(17)
Rigid	Clad	0.01(11)	1.3(19)	0.01(11)	1.3(19)
	Unclad	0.01(20)	1.3(24)	0.01(20)	1.3(24)

[a]Story at which peak drift occurred is shown in parentheses. (See Fig. 3.4-1 for numbered faces.)

Table 3.4-6. Peak Roof Displacements, Symmetric Case, for the First 10 Seconds of the 1966 Parkfield Earthquake Recorded in the N65E Direction.

Ground Motion Input Direction (1)	Case (2)	Peak Roof Displacement Response		
		Rigid Direction (inches) (3)	Braced Direction (inches) (4)	Rotation (radians) (5)
Braced	Clad	0.3	20.7	1.3×10^{-4}
	Unclad	0.4	24.1	1.8×10^{-4}
Rigid	Clad	22.3	0.3	3.5×10^{-6}
	Unclad	25.3	0.4	1.3×10^{-5}

Table 3.4-7. Peak Interstory Drift, Symmetric Case, for the First 10 Seconds of the 1966 Parkfield Earthquake Recorded in the N65E Direction.

Ground Motion Input Direction (1)	Case (2)	Peak Relative Interstory Drift (inches) Face 1[a] (3)	Face 2 (4)	Face 3 (5)	Face 4 (6)
Braced	Clad	1.4(8)	0.02(19)	1.4(8)	0.02(17)
	Unclad	1.6(20)	0.05(24)	1.6(11)	0.03(17)
Rigid	Clad	0.02(11)	1.8(12)	0.02(11)	1.8(12)
	Unclad	0.03(20)	3.1(22)	0.02(21)	3.1(22)

[a]Story at which peak drift occurred is shown in parentheses. (See Fig. 3.4-1 for numbered faces).

Table 3.4-8. Peak Roof Displacements, Eccentric Case, for the First 14 Seconds of the 1940 Imperial Valley Earthquake Recorded at El Centro in the S00E Direction.

Ground Motion Input Direction (1)	Case (2)	Peak Roof Displacement Response		
		Rigid Direction (inches) (3)	Braced Direction (inches) (4)	Rotation (radians) (5)
Braced	Clad	2.7	15.2	7.8×10^{-3}
	Unclad	1.7	14.8	5.6×10^{-3}
Rigid	Clad	15.0	1.9	5.2×10^{-3}
	Unclad	11.8	1.0	3.7×10^{-3}

Table 3.4-9. Peak Interstory Drift, Eccentric Case, for the First 14 Seconds of the 1940 Imperial Valley Earthquake Recorded at El Centro in the S00E Direction.

Ground Motion Input Direction (1)	Case (2)	Peak Relative Interstory Drift (inches) Face 1[a] (3)	Face 2 (4)	Face 3 (5)	Face 4 (6)
Braced	Clad	1.1(16)	0.5(5)	1.0(16)	0.4(4)
	Unclad	1.0(21)	0.4(19)	1.3(18)	0.2(22)
Rigid	Clad	0.3(4)	1.0(19)	0.3(11)	1.3(19)
	Unclad	0.5(24)	1.3(24)	0.4(24)	1.2(24)

[a]Story at which peak drift occurred is shown in parentheses. (See Fig. 3.4-1 for numbered faces.)

Table 3.4-10. Peak Roof Displacements, Eccentric Case, for the First 10 Seconds of the 1966 Parkfield Earthquake Recorded in the N65E Direction.

Ground Motion Input Direction (1)	Case (2)	Peak Roof Displacement Response		
		Rigid Direction (inches) (3)	Braced Direction (inches) (4)	Rotation (radians) (5)
Braced	Clad	3.1	20.7	1.2×10^{-2}
	Unclad	2.8	23.9	1.1×10^{-2}
Rigid	Clad	21.9	2.3	7.8×10^{-3}
	Unclad	25.2	1.6	1.2×10^{-2}

Table 3.4-11. Peak Interstory Drift, Eccentric Case, for the First 10 Seconds of the 1966 Parkfield Earthquake Recorded in the N65E Direction.

Ground Motion Input Direction (1)	Case (2)	Peak Relative Interstory Drift (inches) Face 1[a] (3)	Face 2 (4)	Face 3 (5)	Face 4 (6)
Braced	Clad	1.5(11)	0.7(7)	1.4(7)	0.4(4)
	Unclad	1.6(18)	0.7(22)	1.6(20)	0.5(22)
Rigid	Clad	0.4(16)	1.6(12)	0.4(4)	1.9(12)
	Unclad	1.1(22)	3.0(22)	1.0(22)	3.1(24)

[a]Story at which peak drift occurred is shown in parentheses.

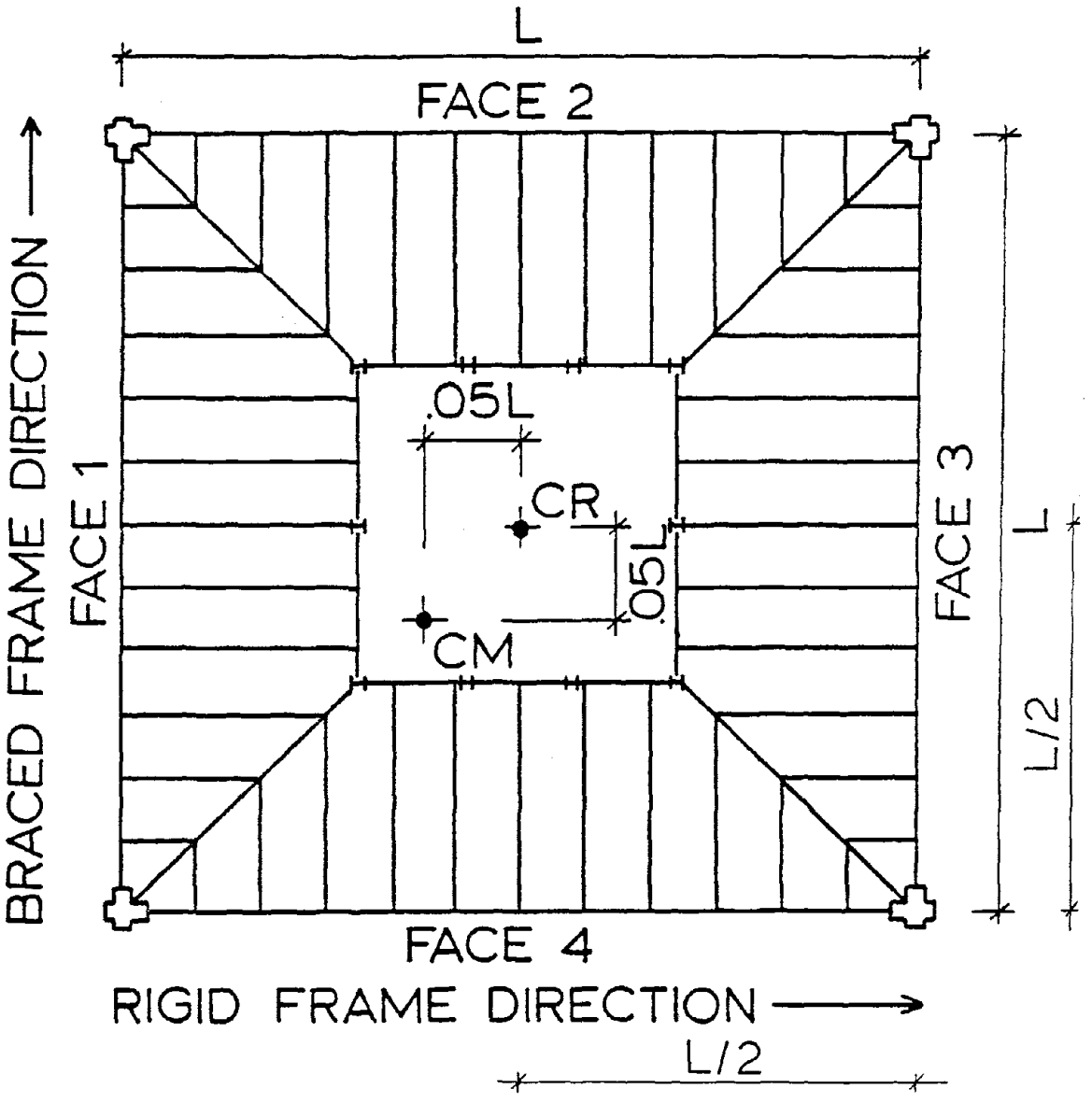

Figure 3.4-1. Floor Plan and Face Numbering for the Eccentric Model.

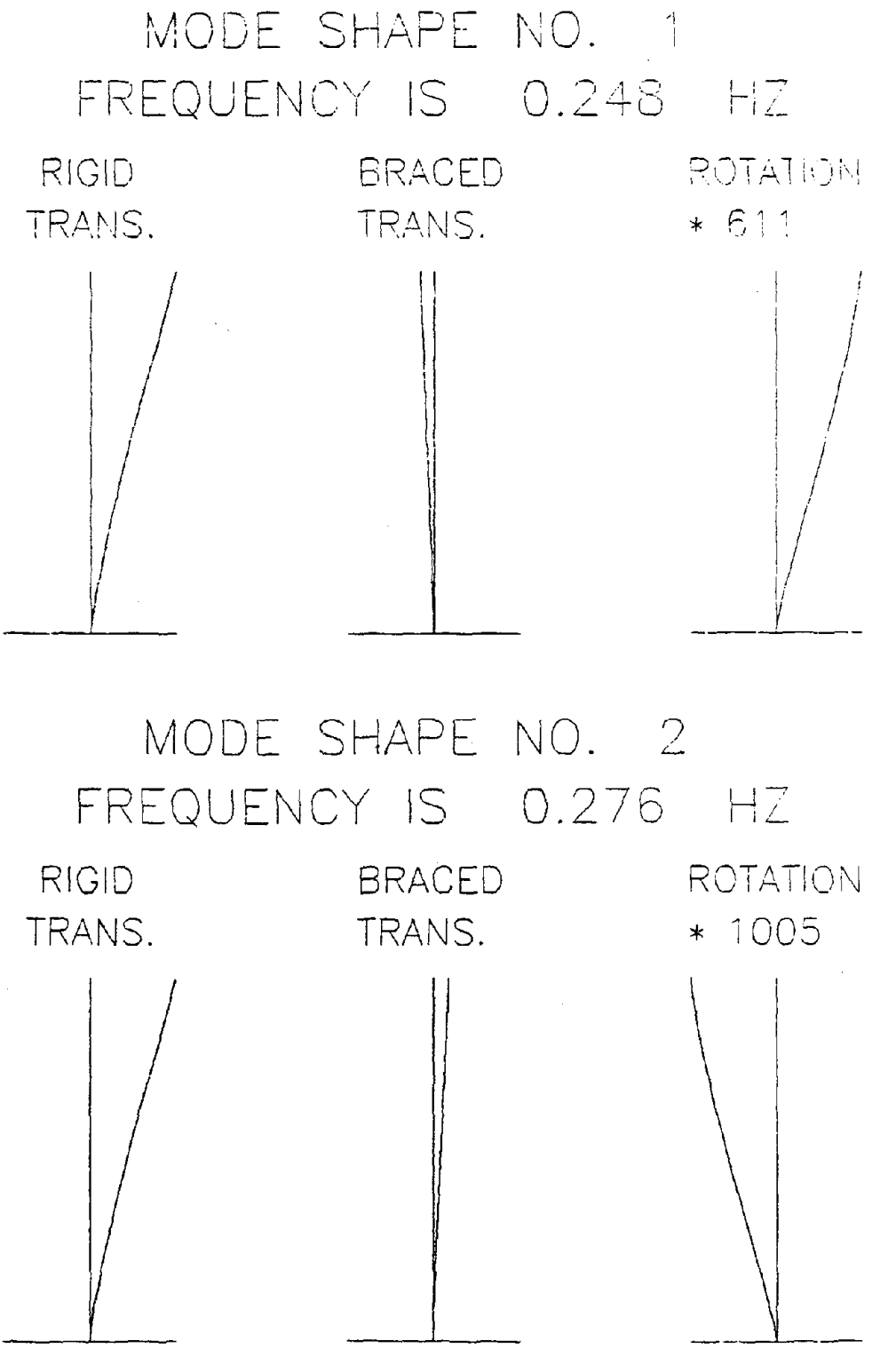

Figure 3.4-2. The First Twelve Mode Shapes with Corresponding Frequencies for the Unclad Eccentric Model.

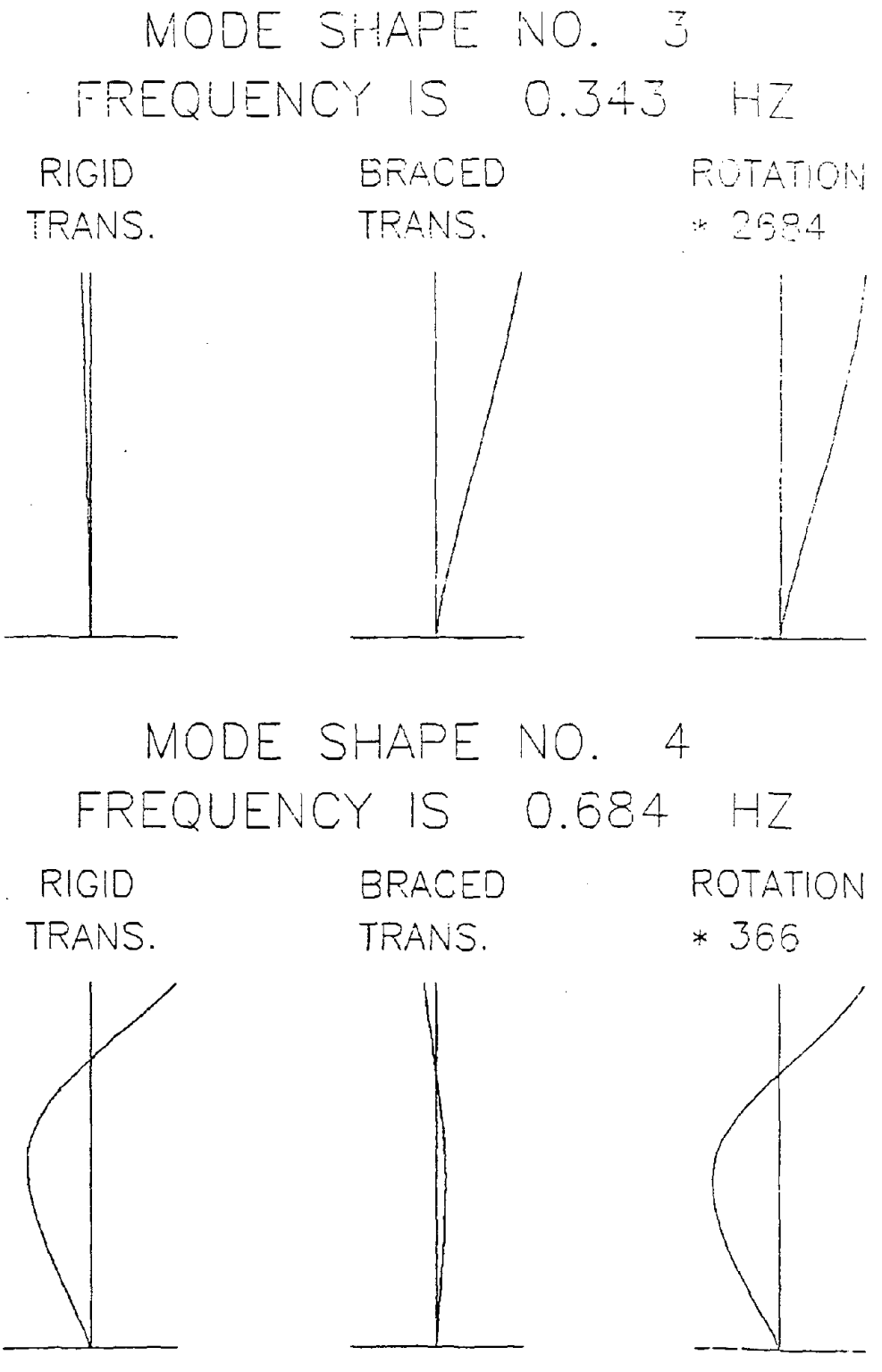

Figure 3.4-2. (continued)

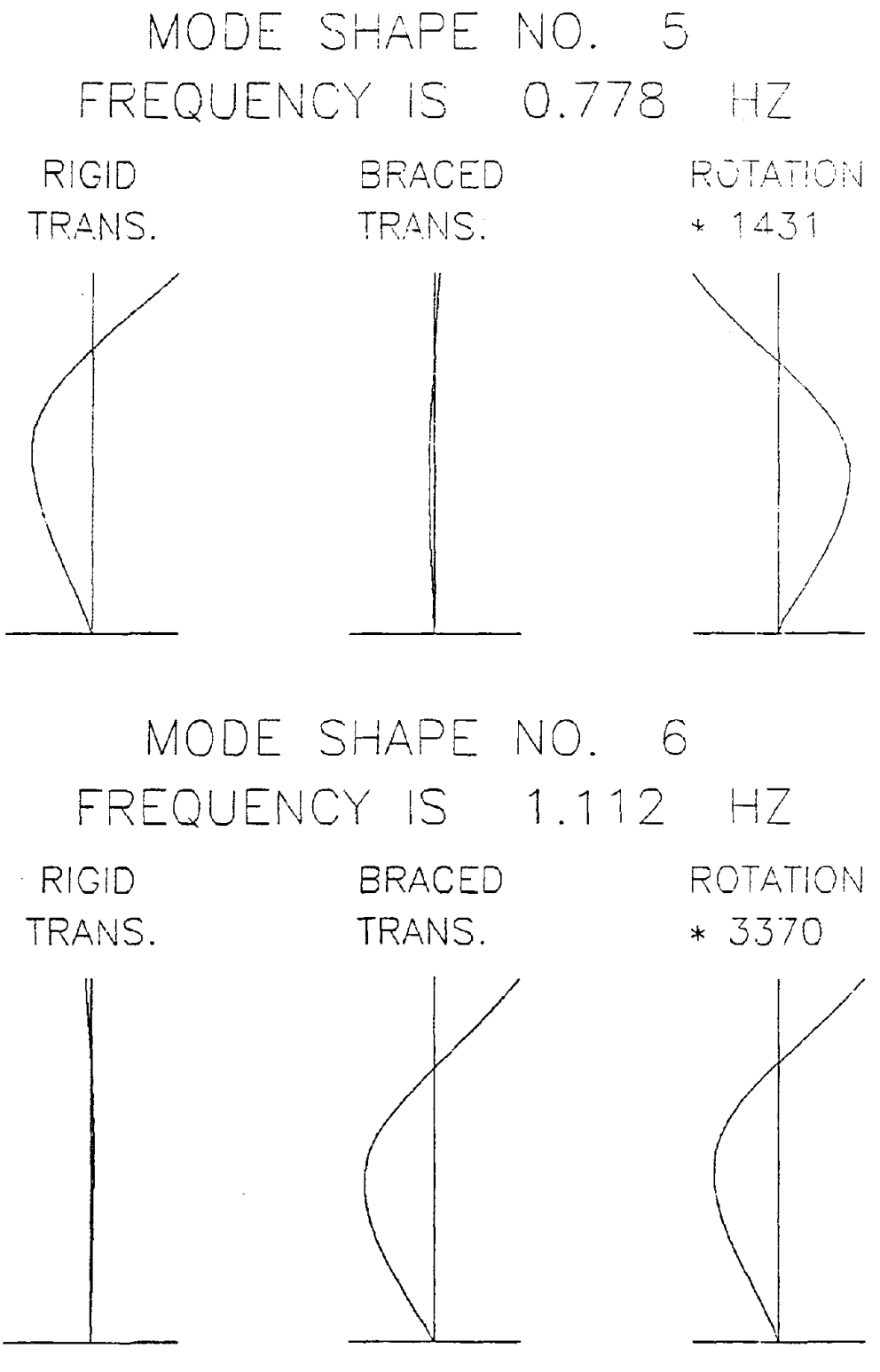

Figure 3.4-2. (continued)

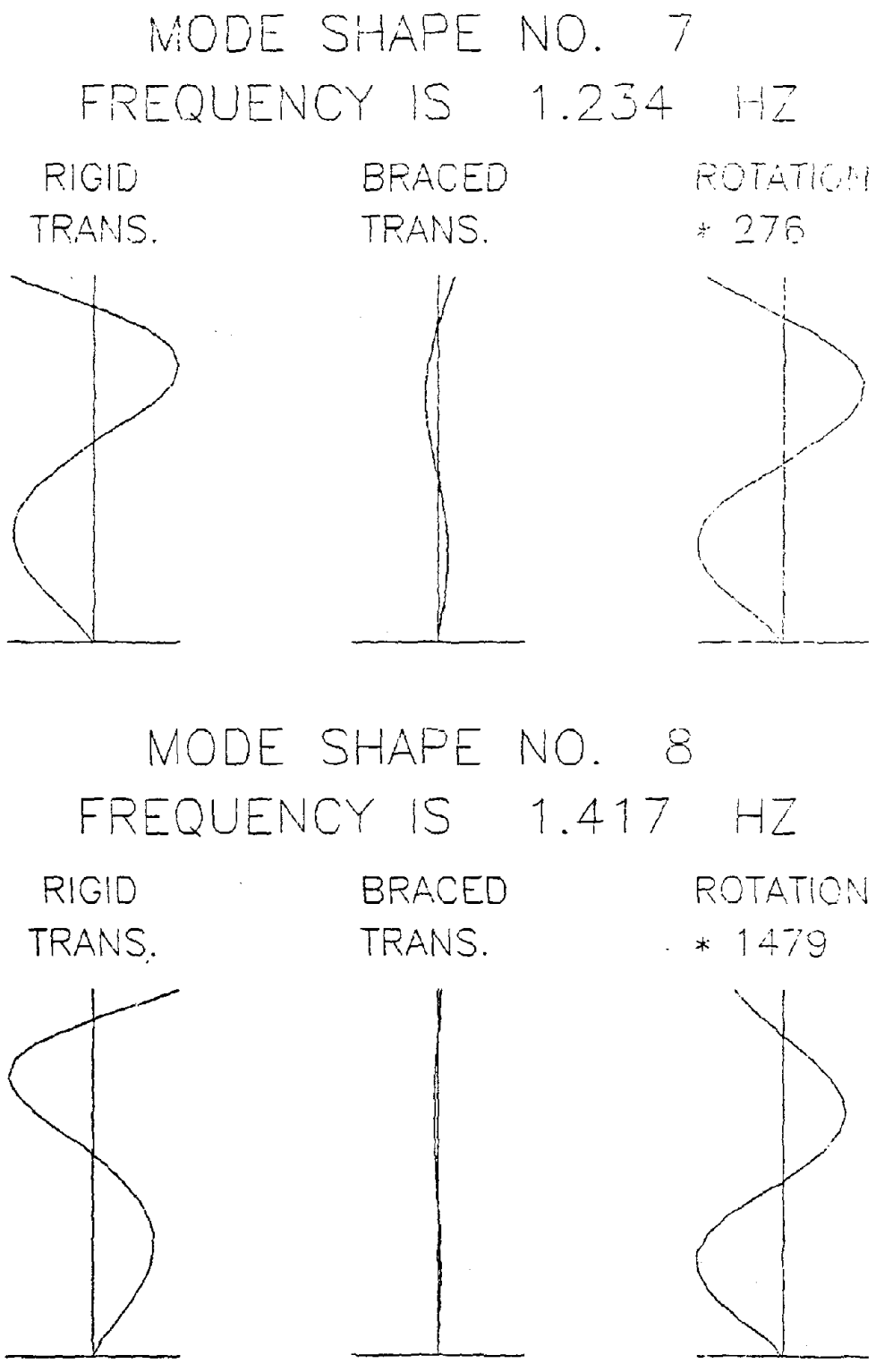

Figure 3.4-2. (continued)

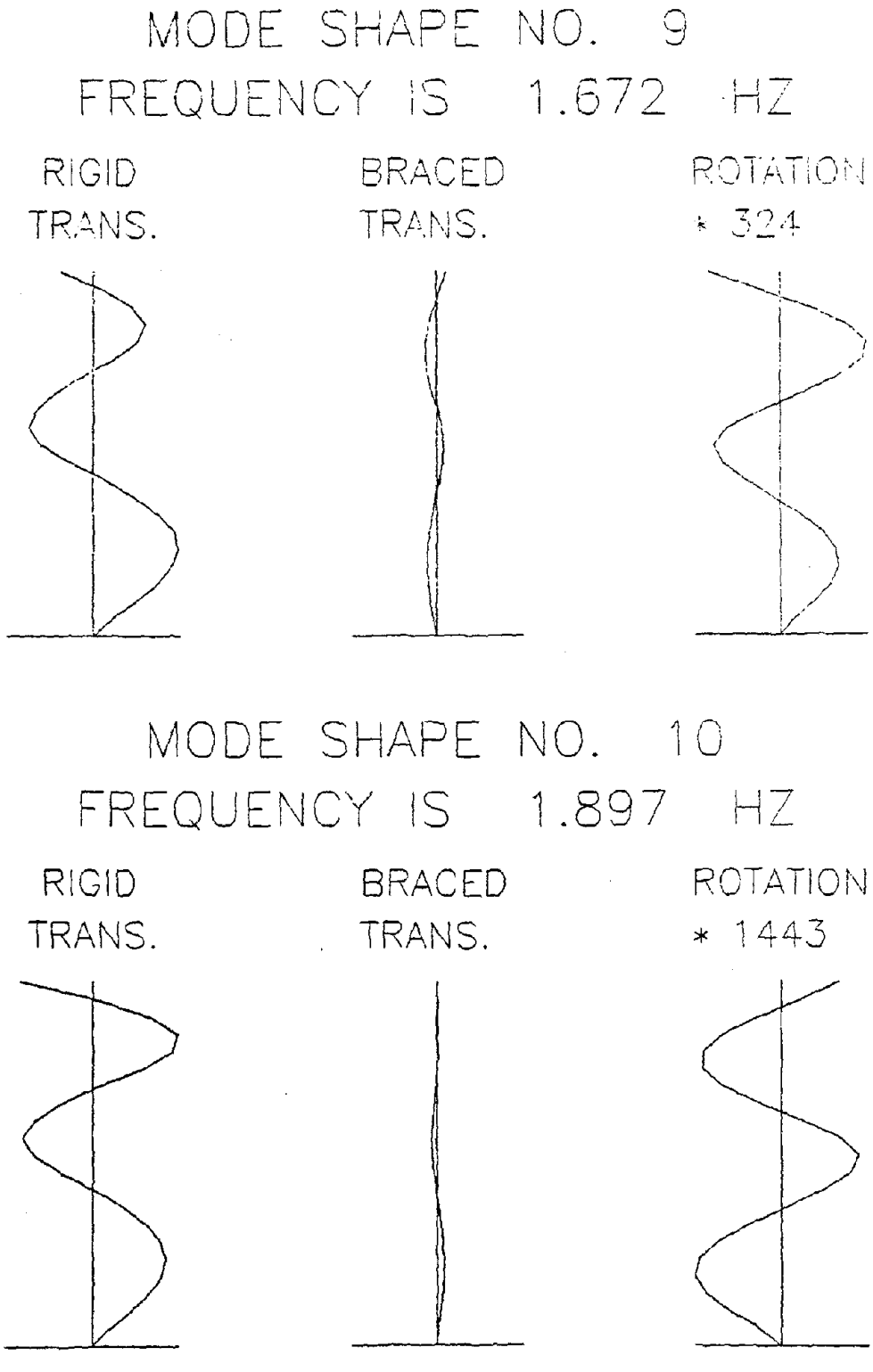

Figure 3.4-2. (continued)

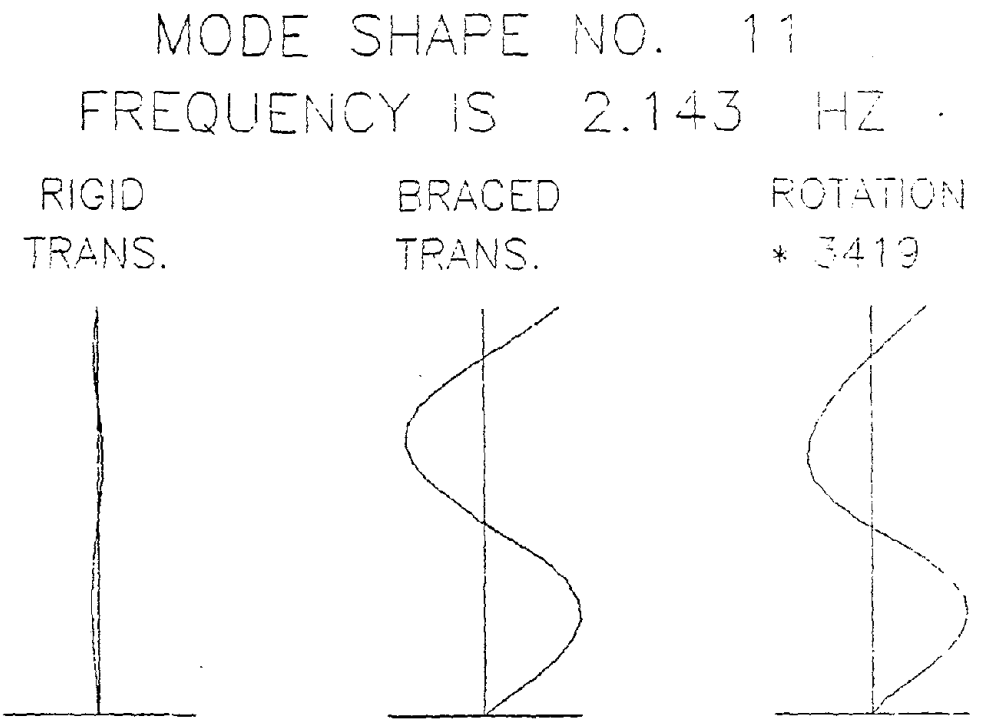

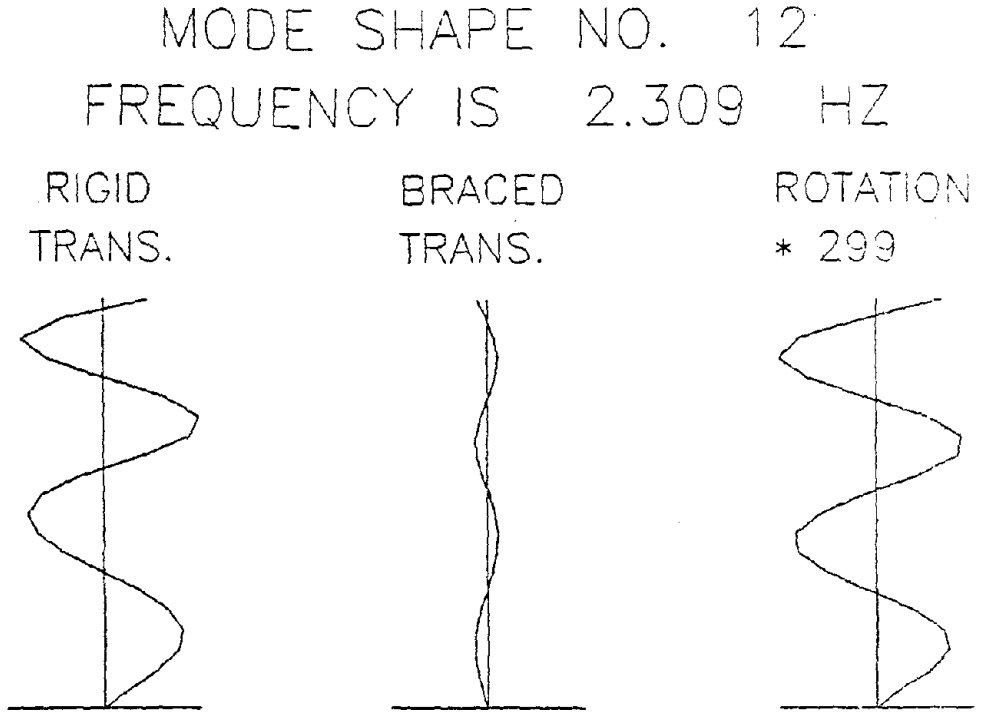

Figure 3.4-2. (continued)

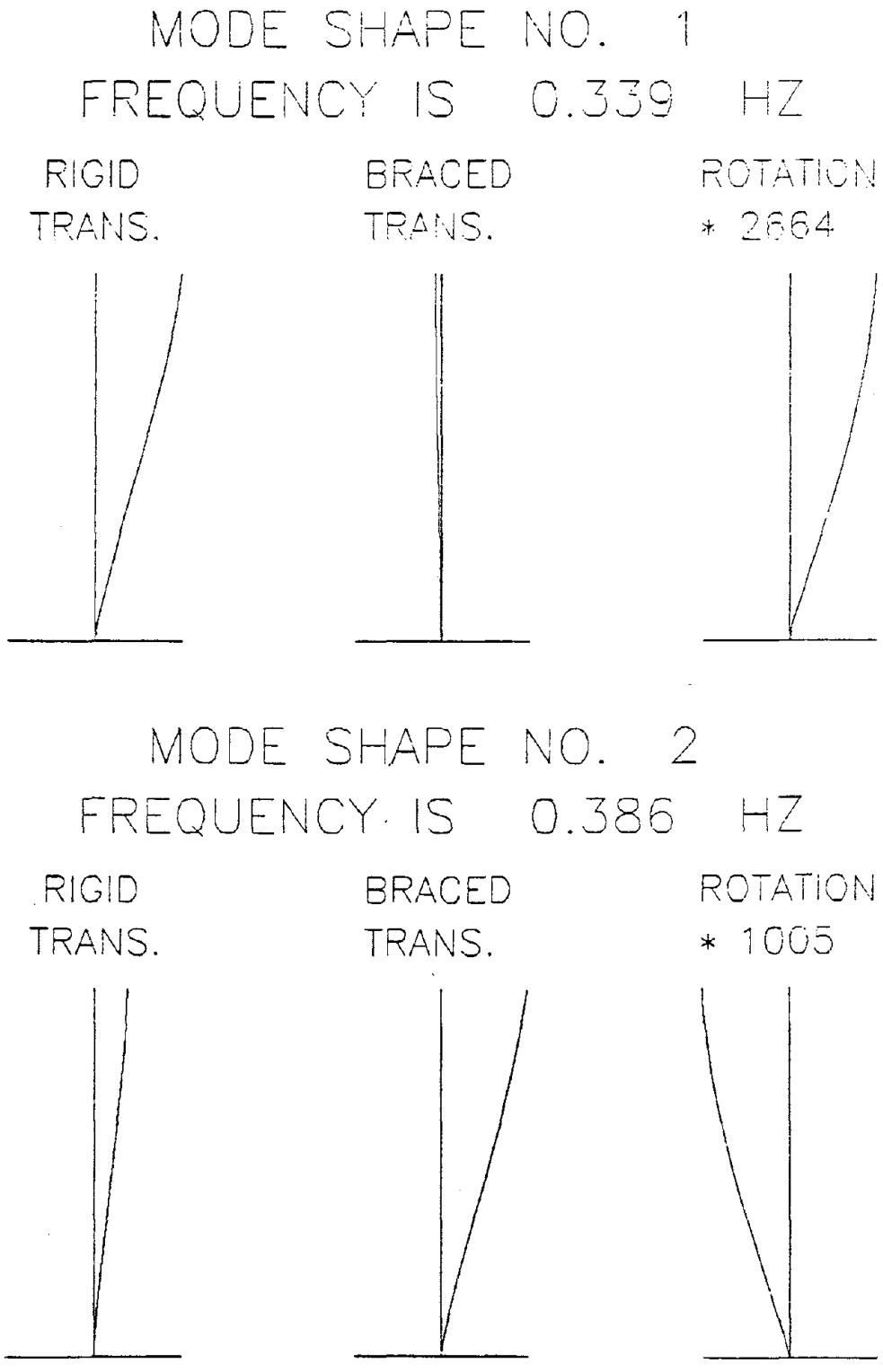

Figure 3.4-3. The First Ten Mode Shapes with Corresponding Frequencies for the Clad Eccentric Model.

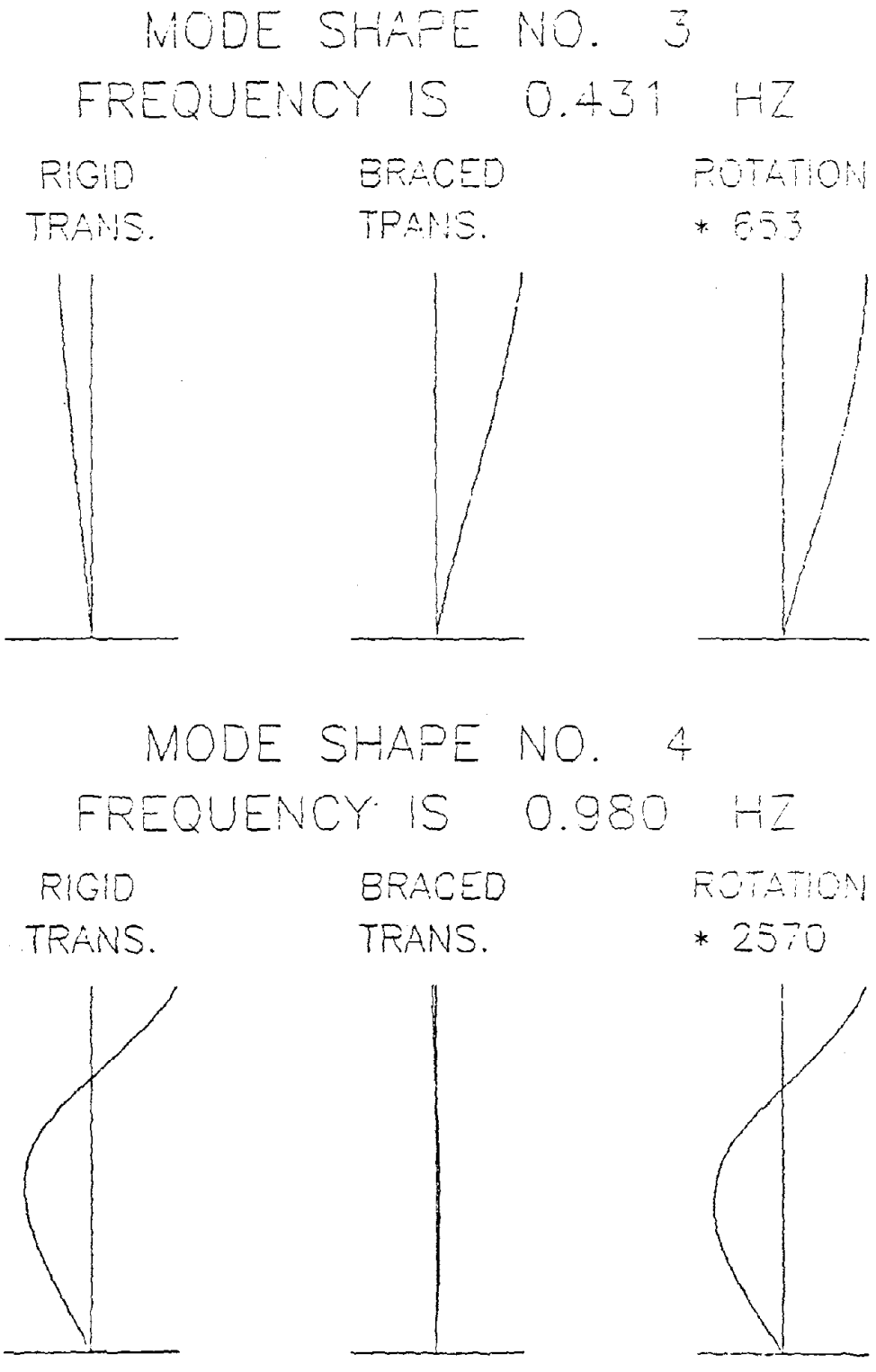

Figure 3.4-3. (continued)

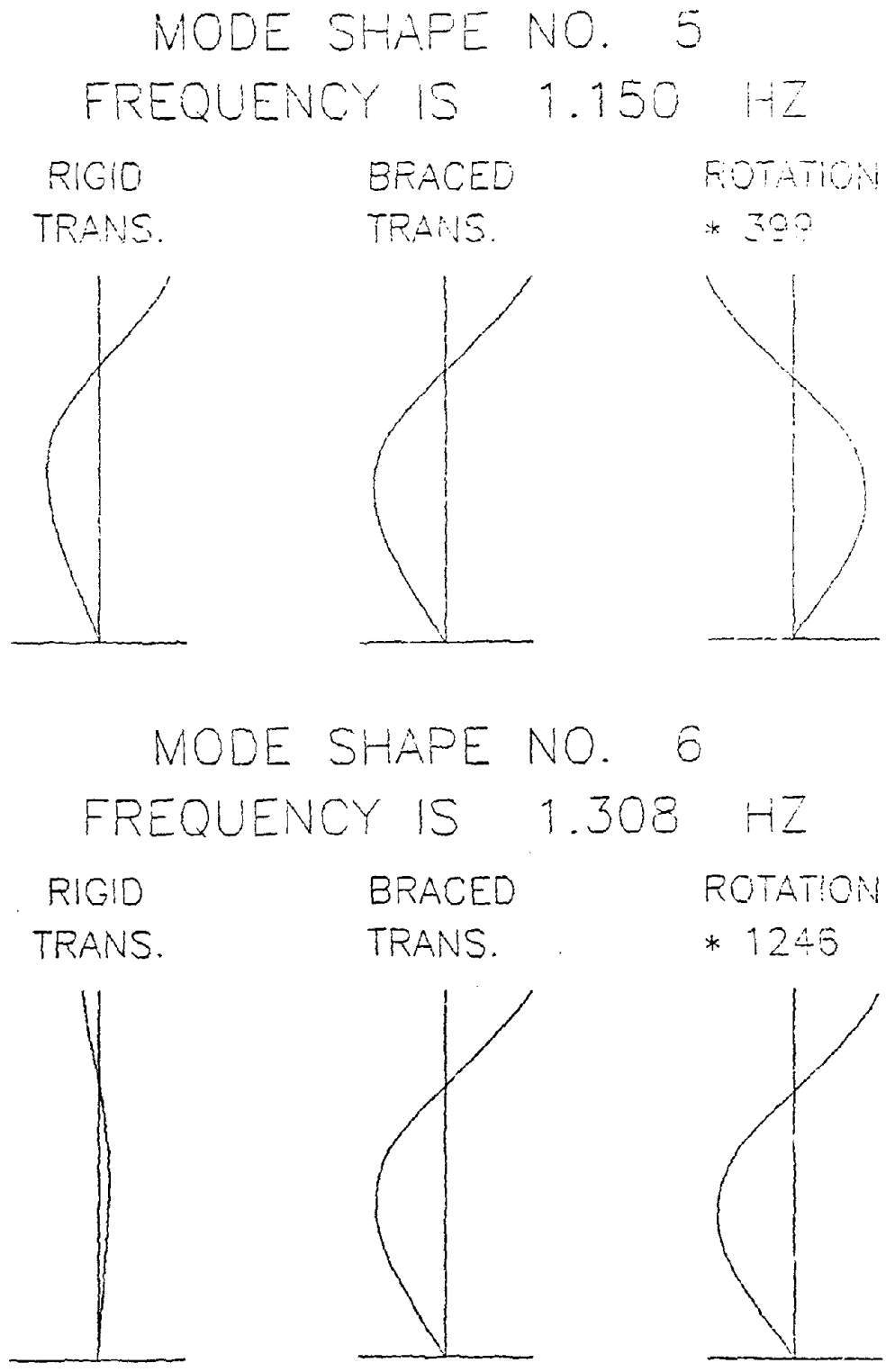

Figure 3.4-3. (continued)

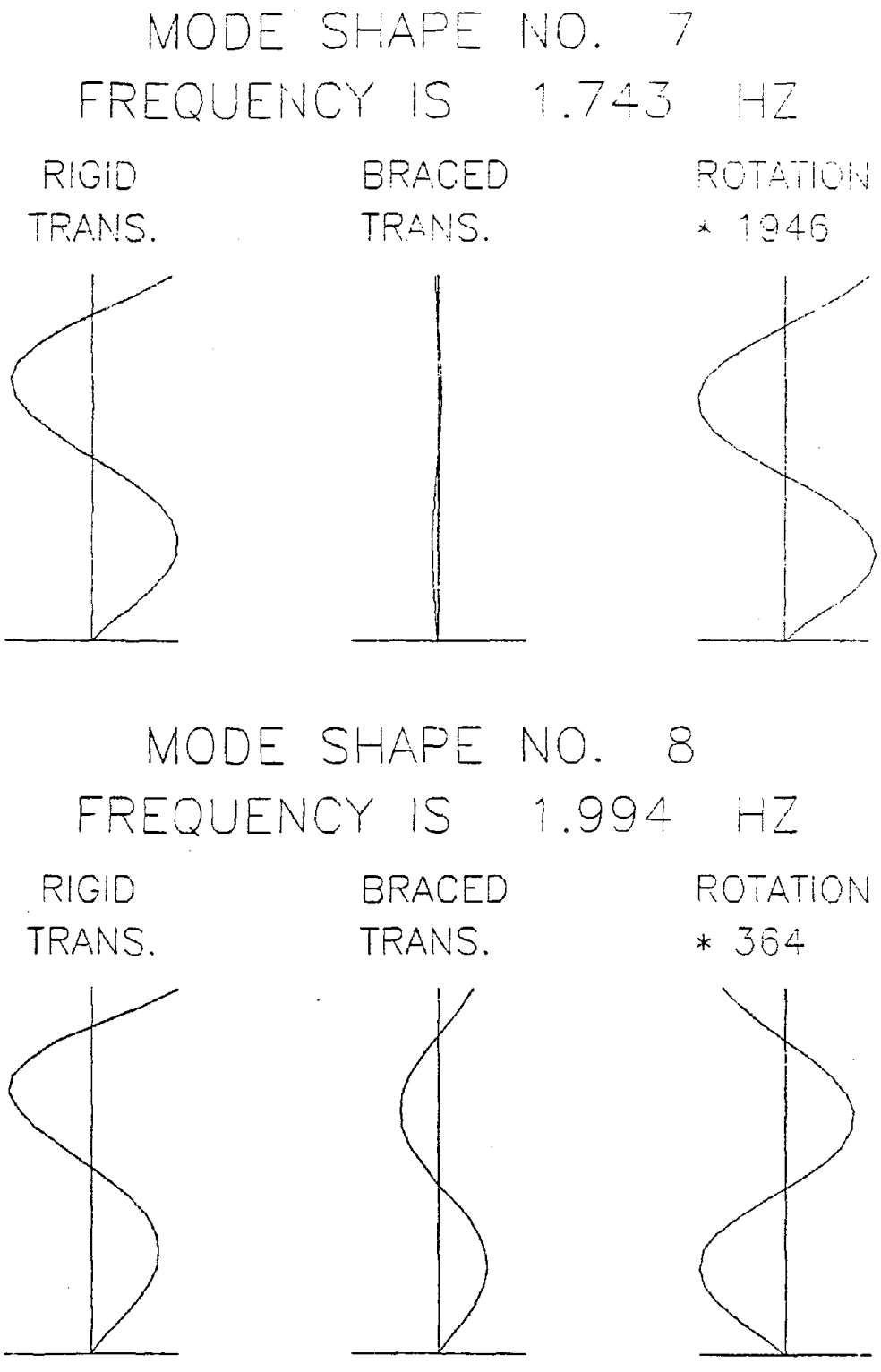

Figure 3.4-3. (continued)

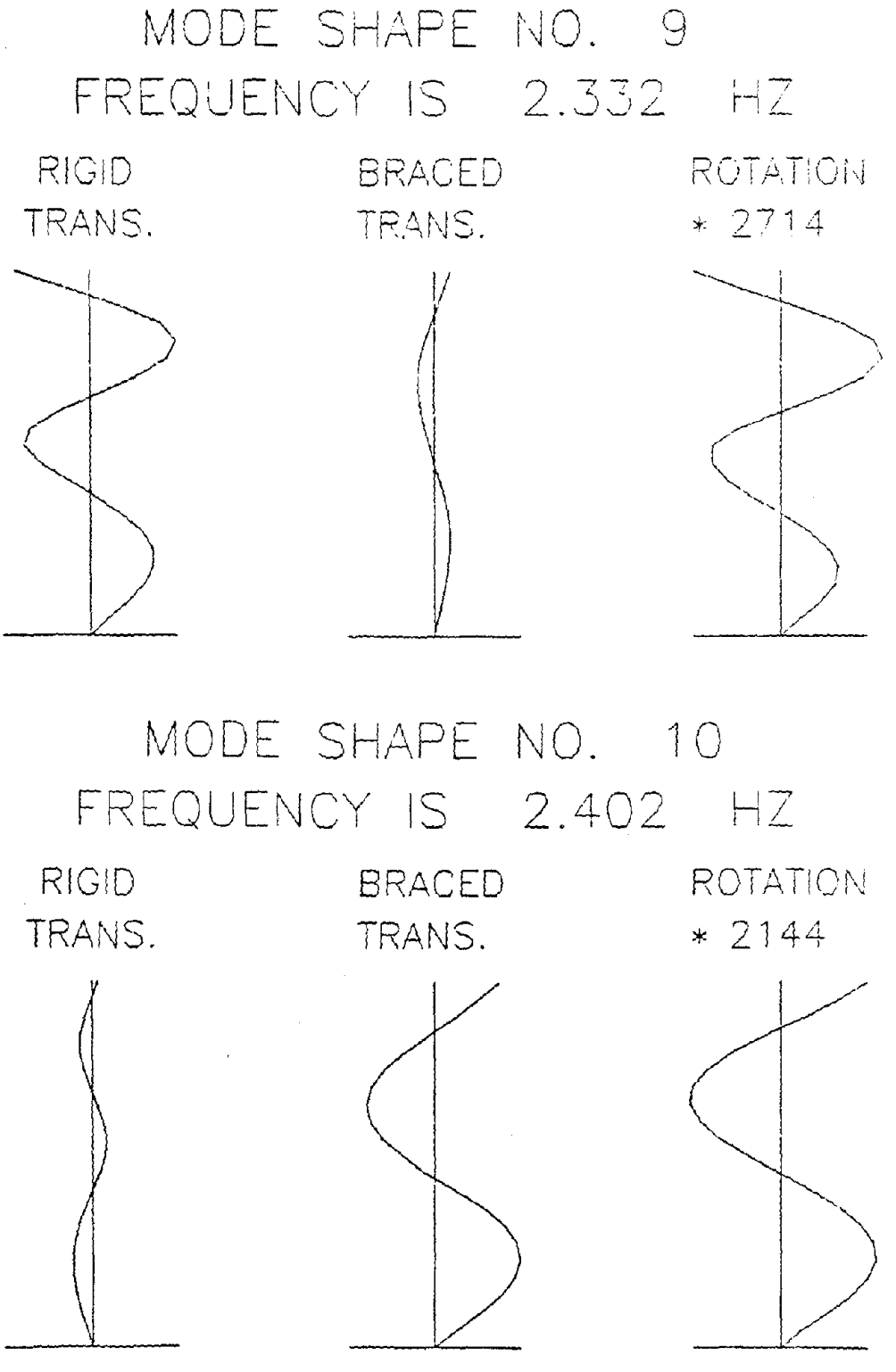

Figure 3.4-3. (continued)

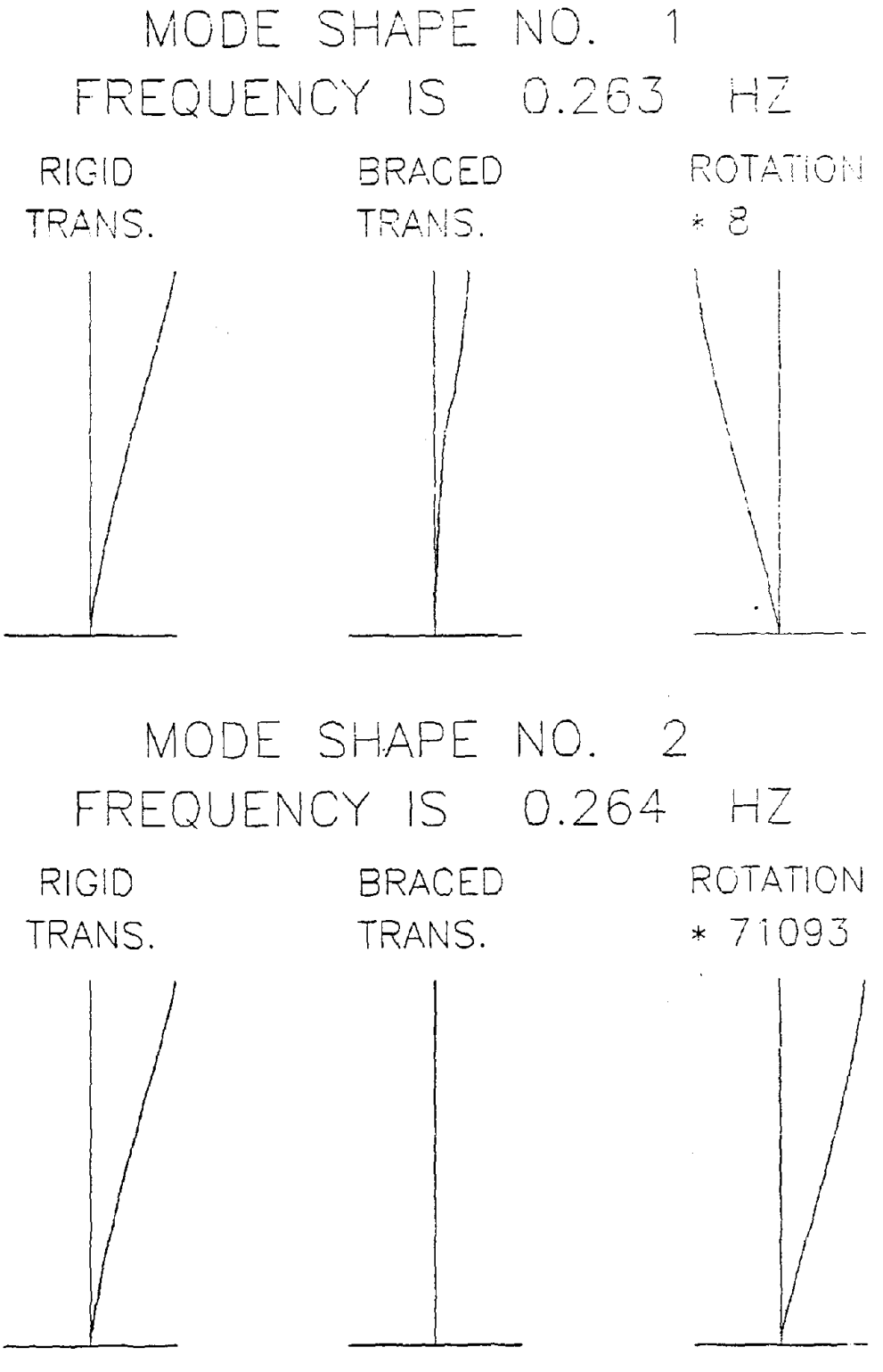

Figure 3.4-4. The First Twelve Mode Shapes with Corresponding Frequencies for the Unclad Symmetric Model.

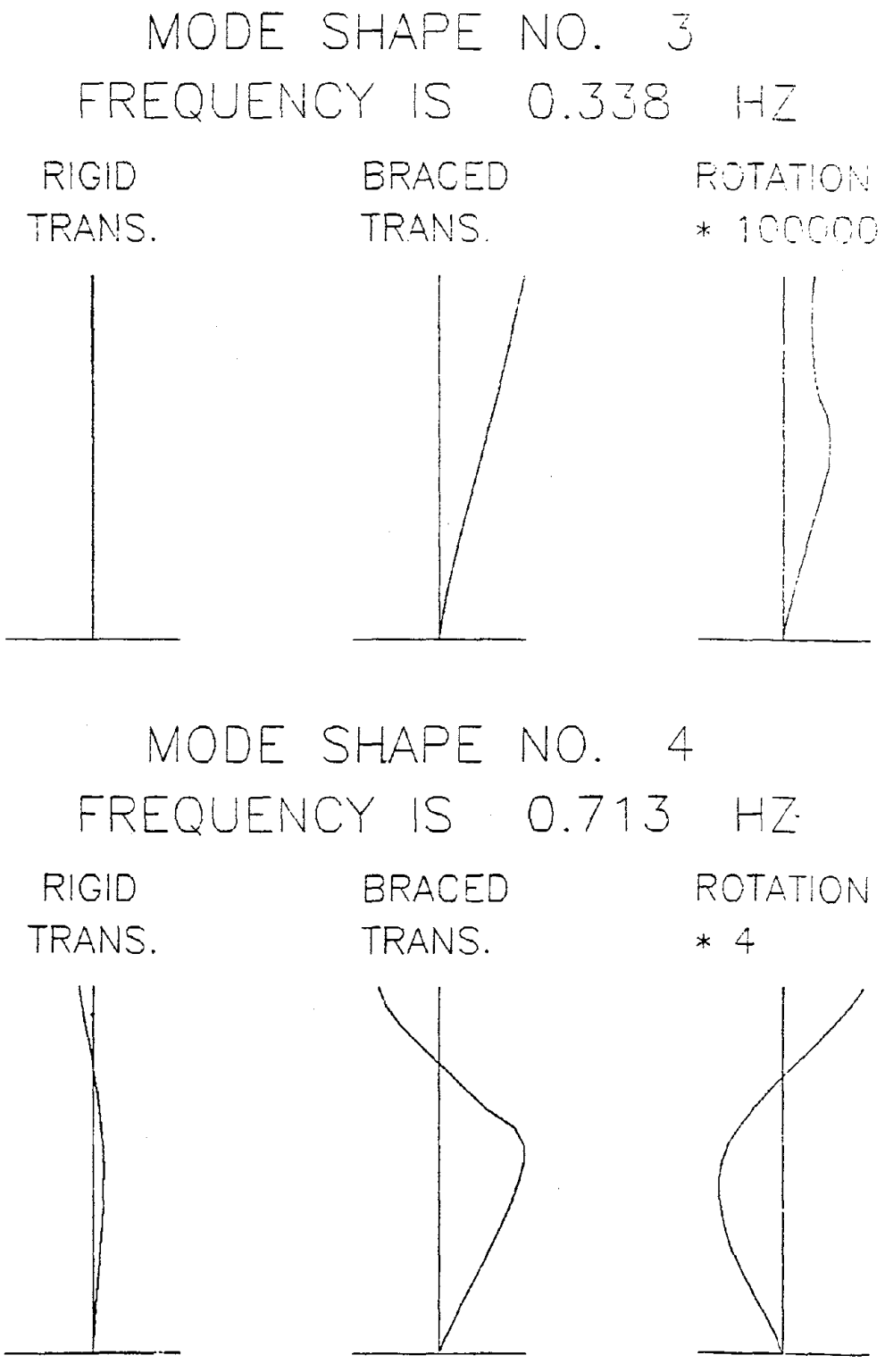

Figure 3.4-4. (continued)

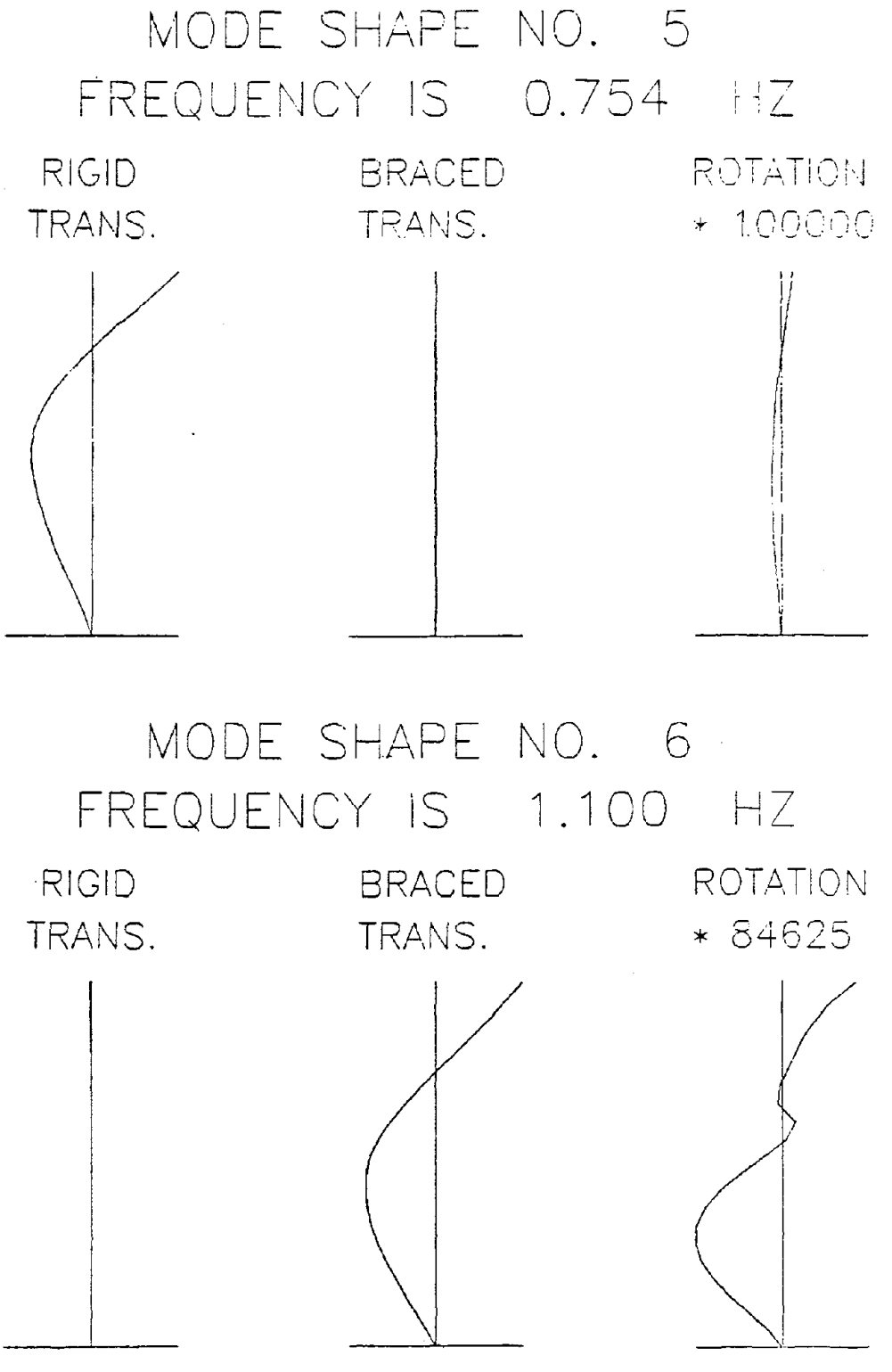

Figure 3.4-4. (continued)

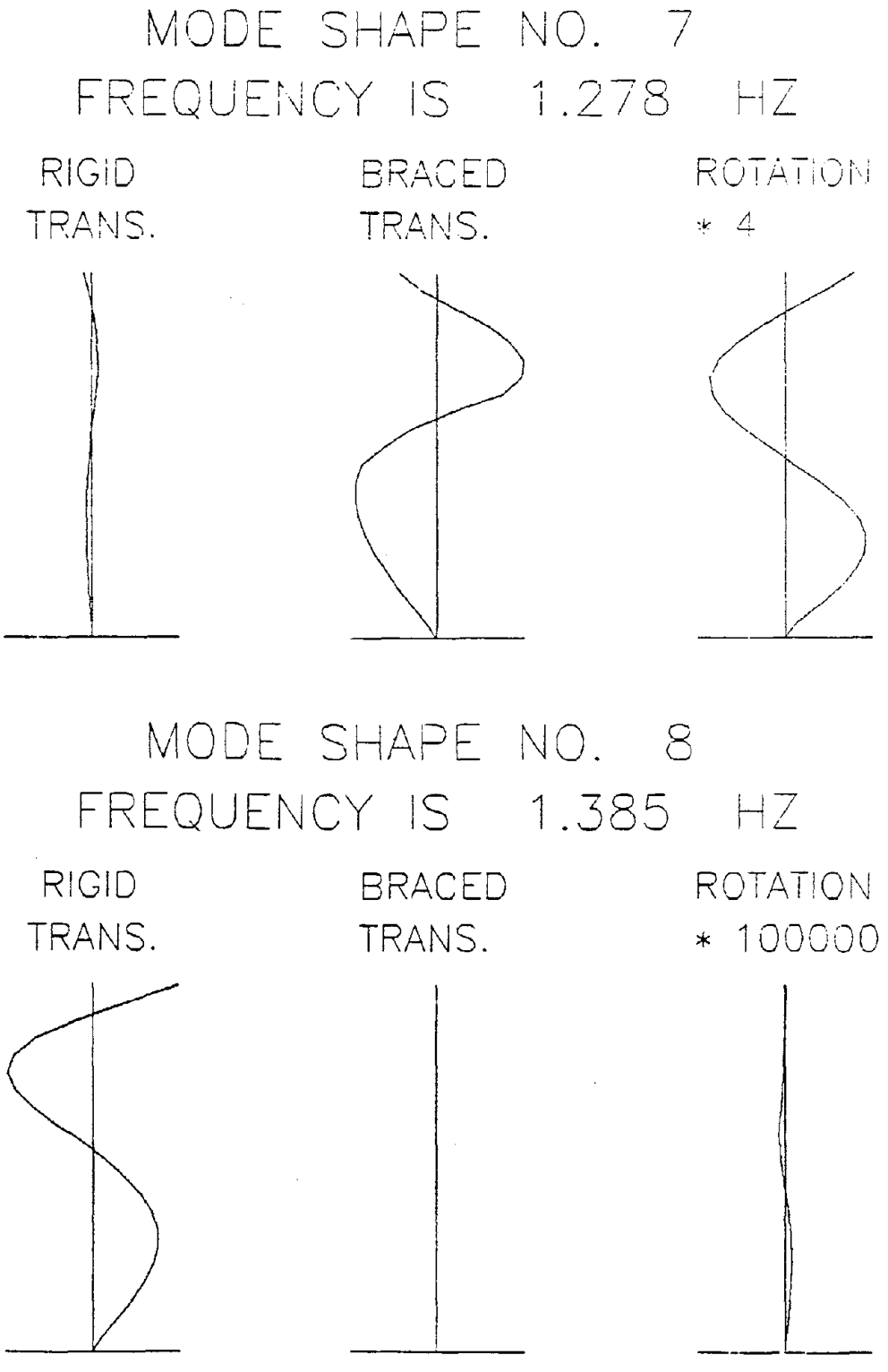

Figure 3.4-4. (continued)

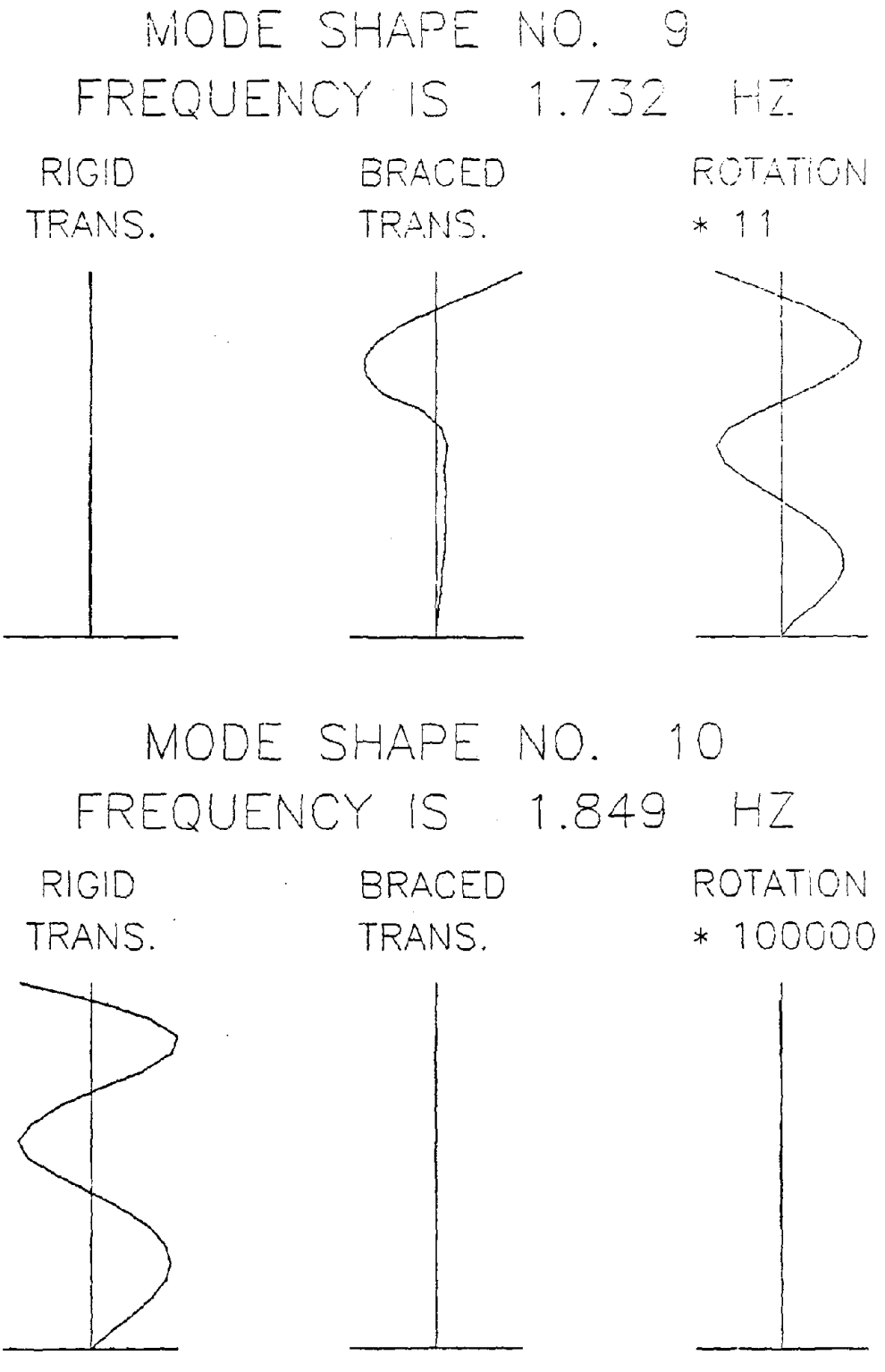

Figure 3.4-4. (continued)

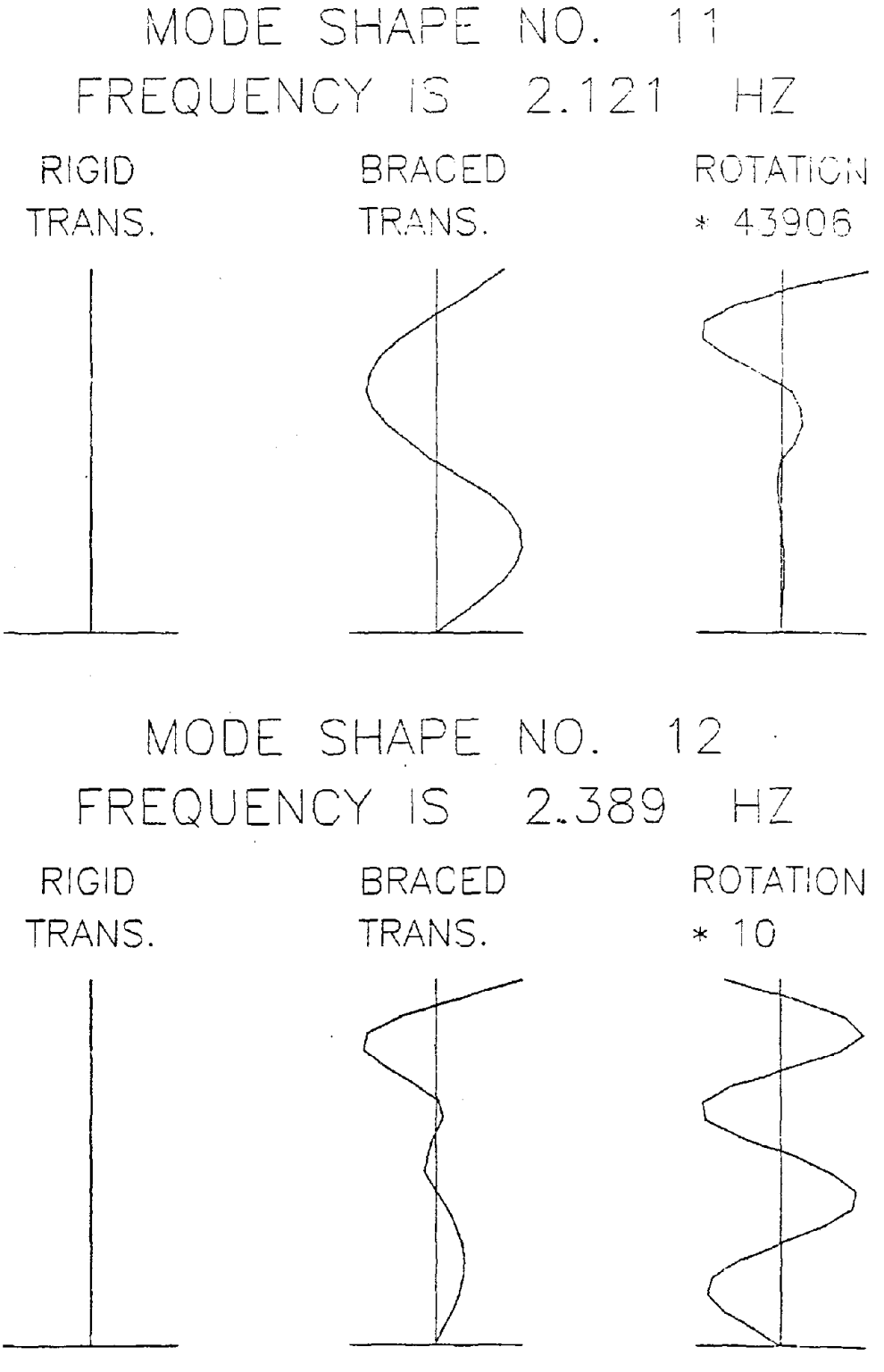

Figure 3.4-4. (continued)

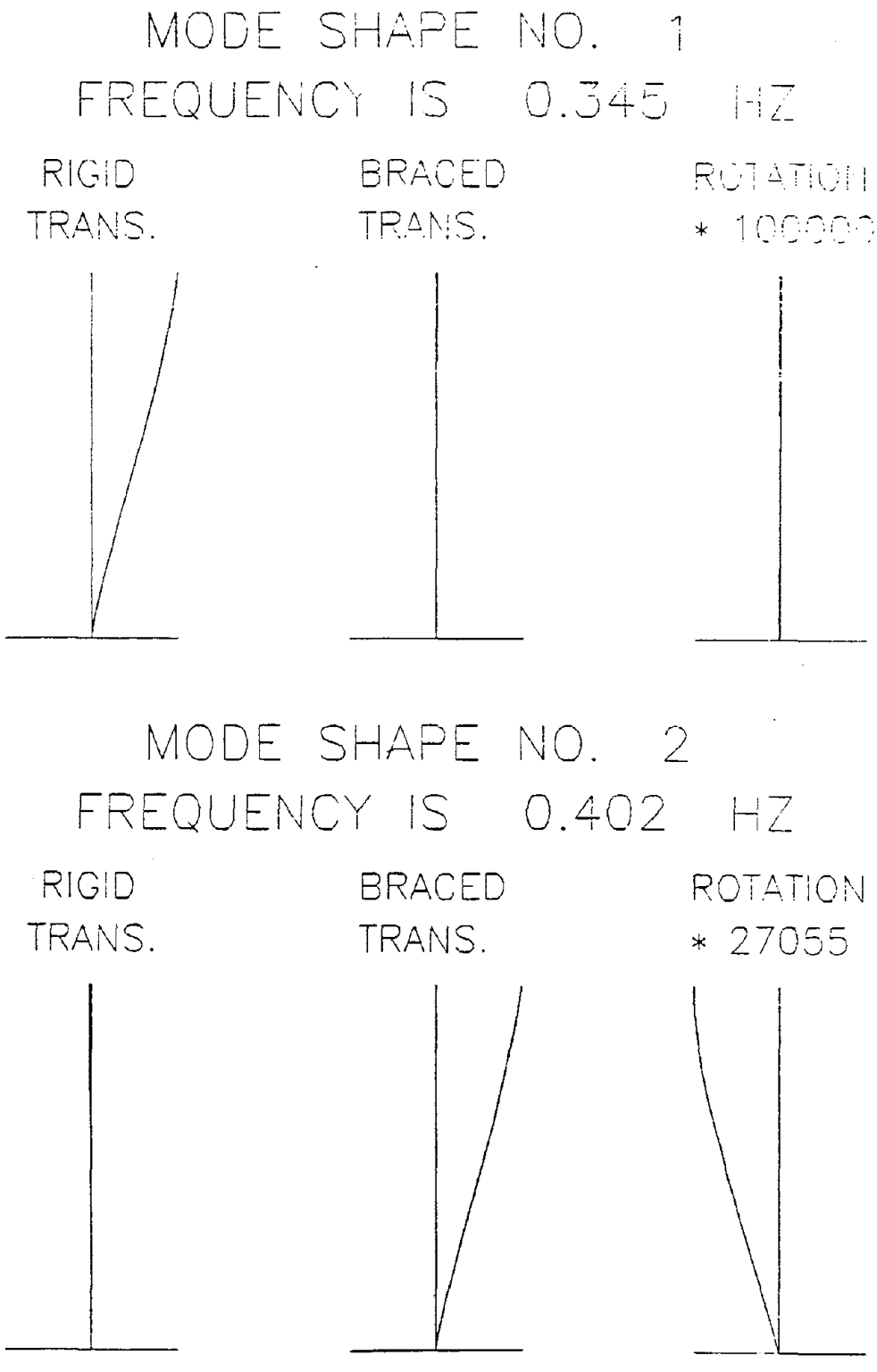

Figure 3.4-5. The First Ten Mode Shapes with Corresponding Frequencies for the Clad Symmetric Model.

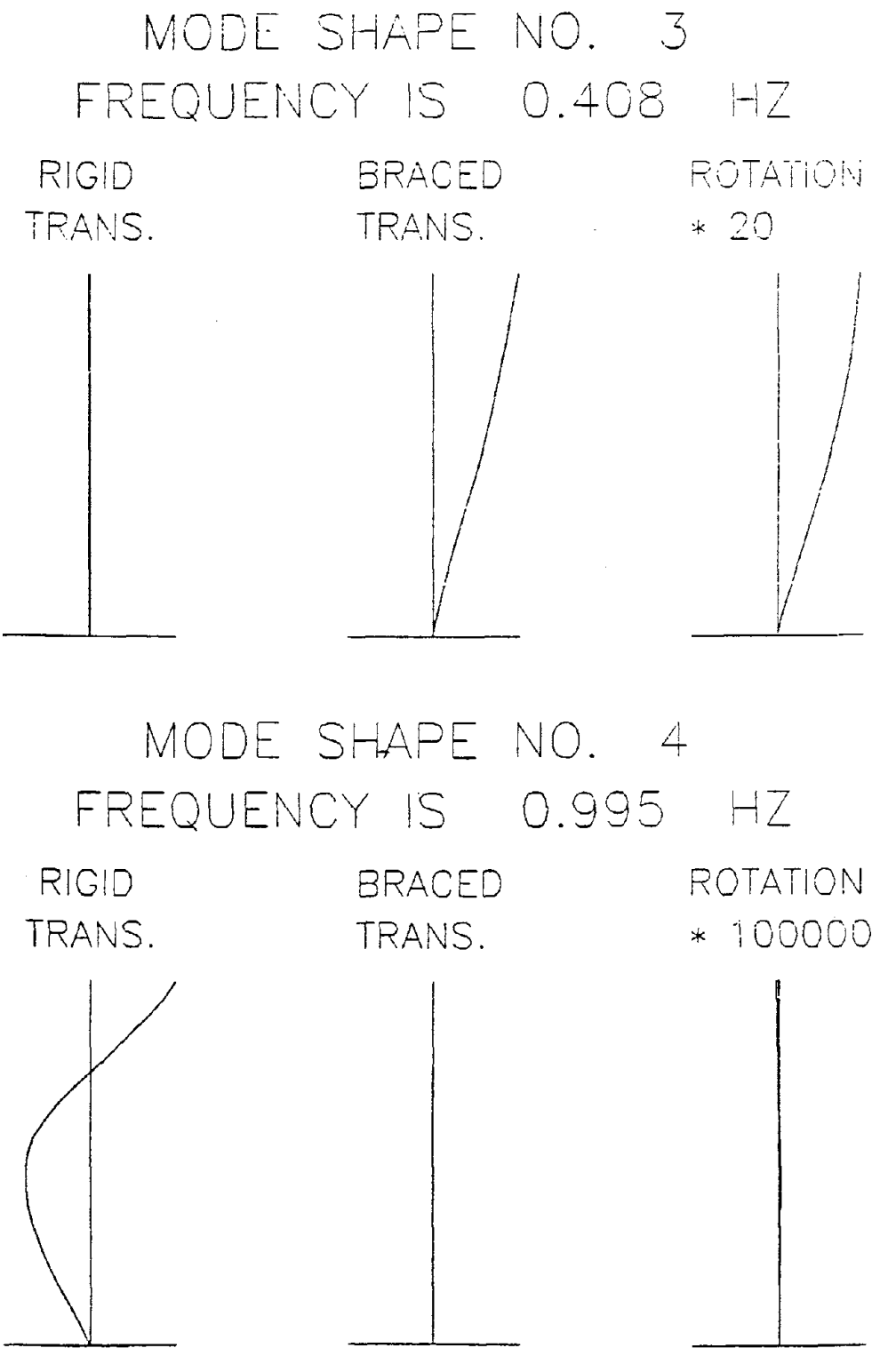

Figure 3.4-5. (continued)

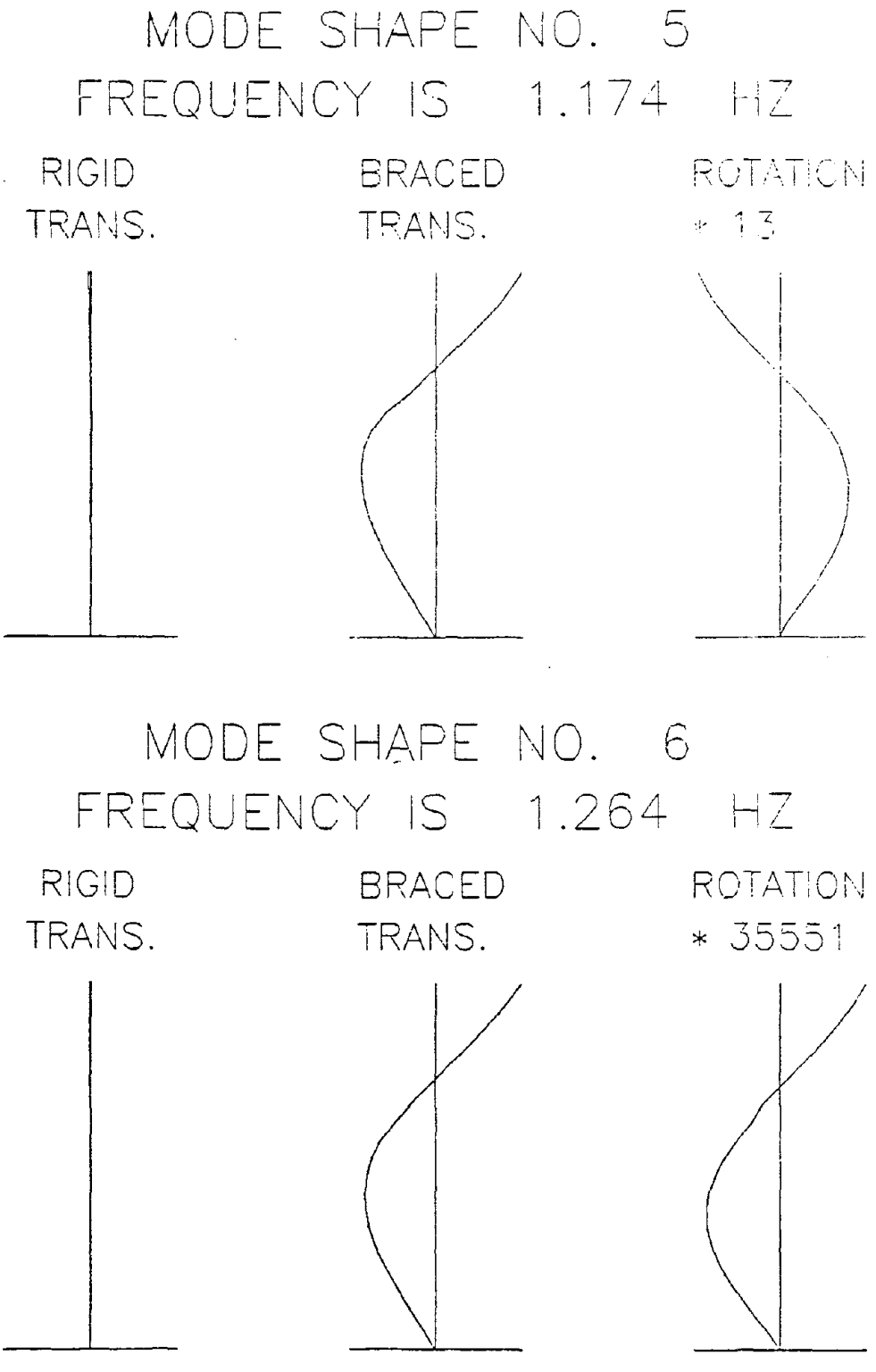

Figure 3.4-5. (continued)

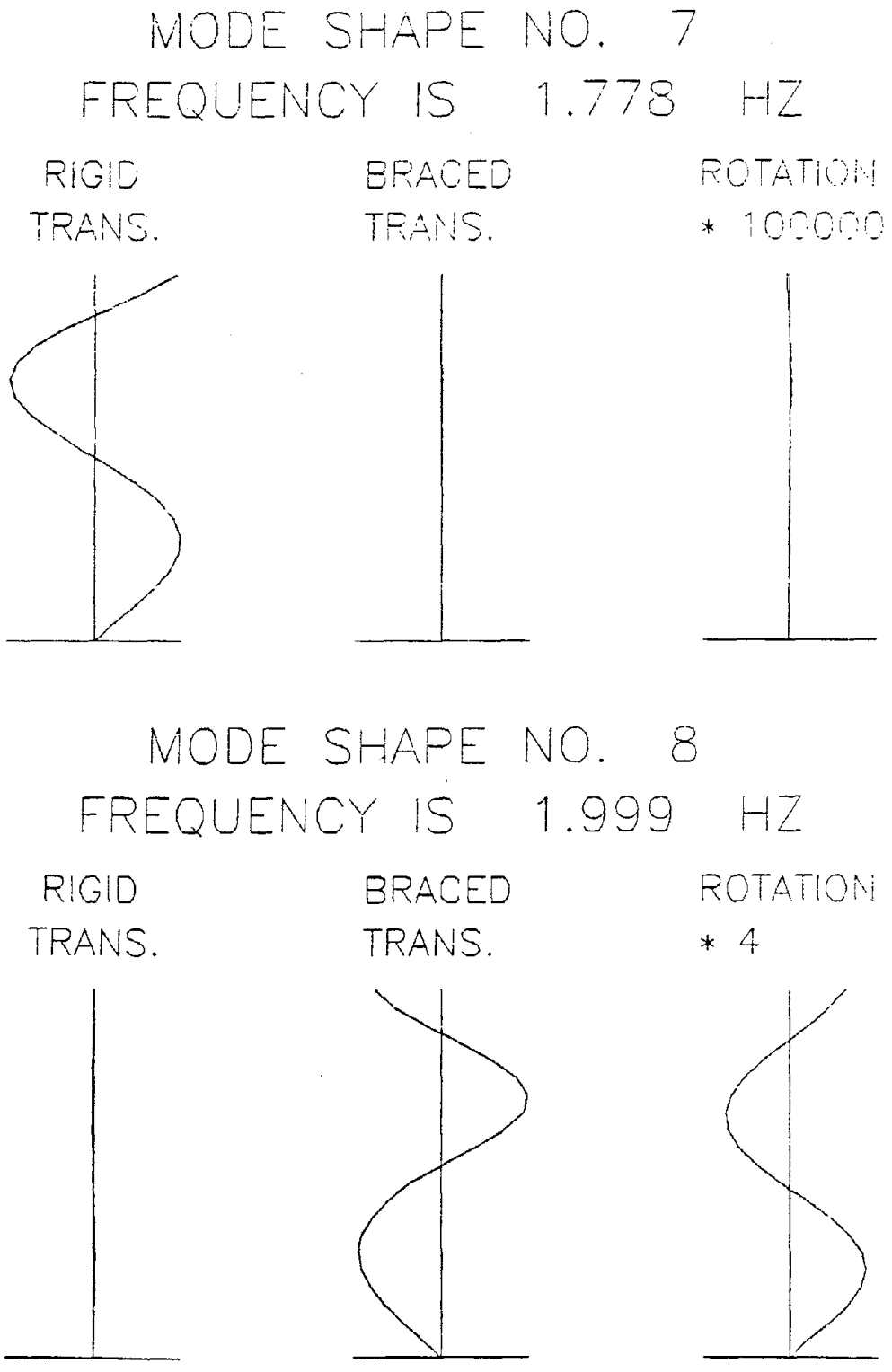

Figure 3.4-5. (continued)

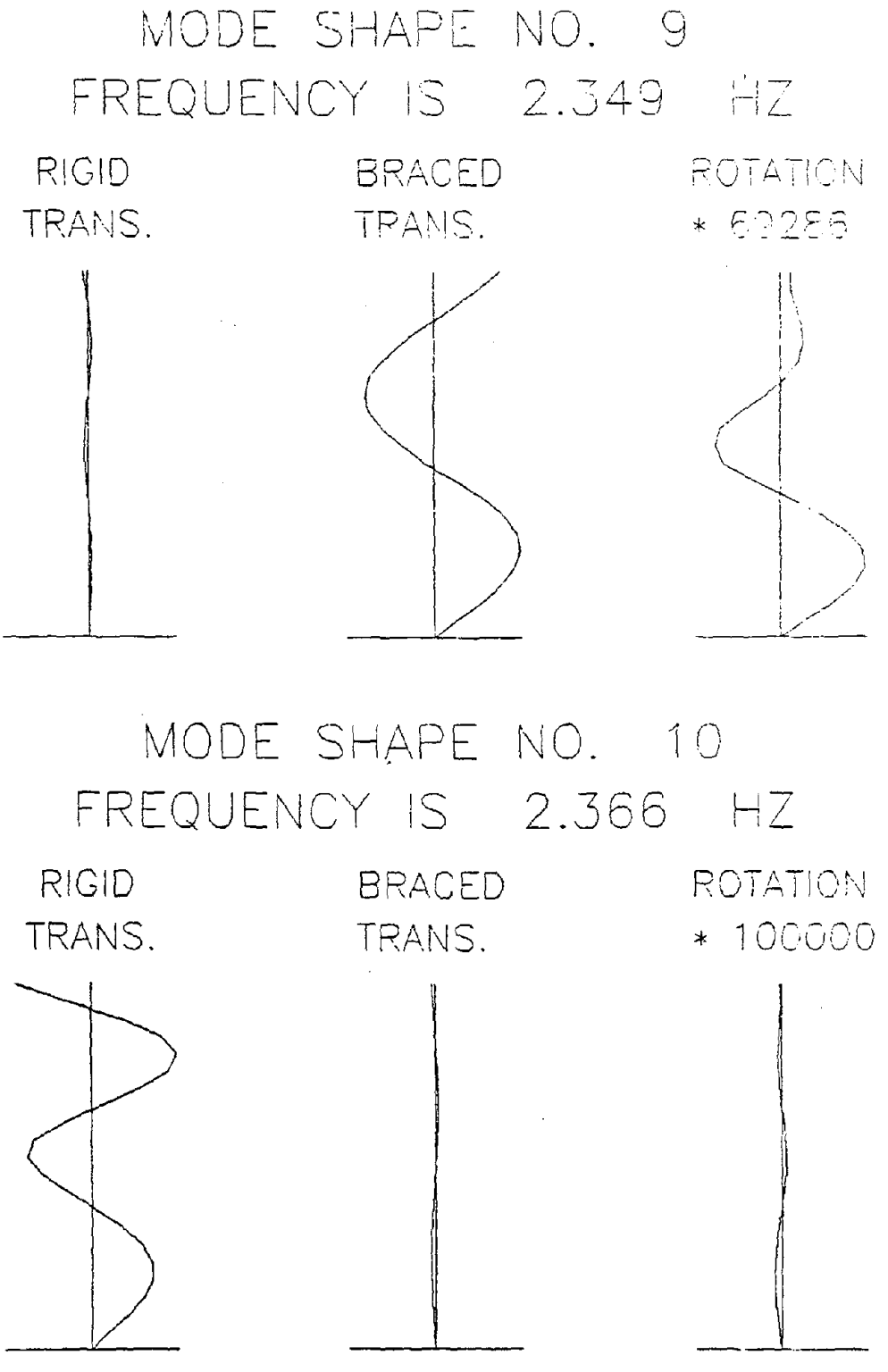

Figure 3.4-5. (continued)

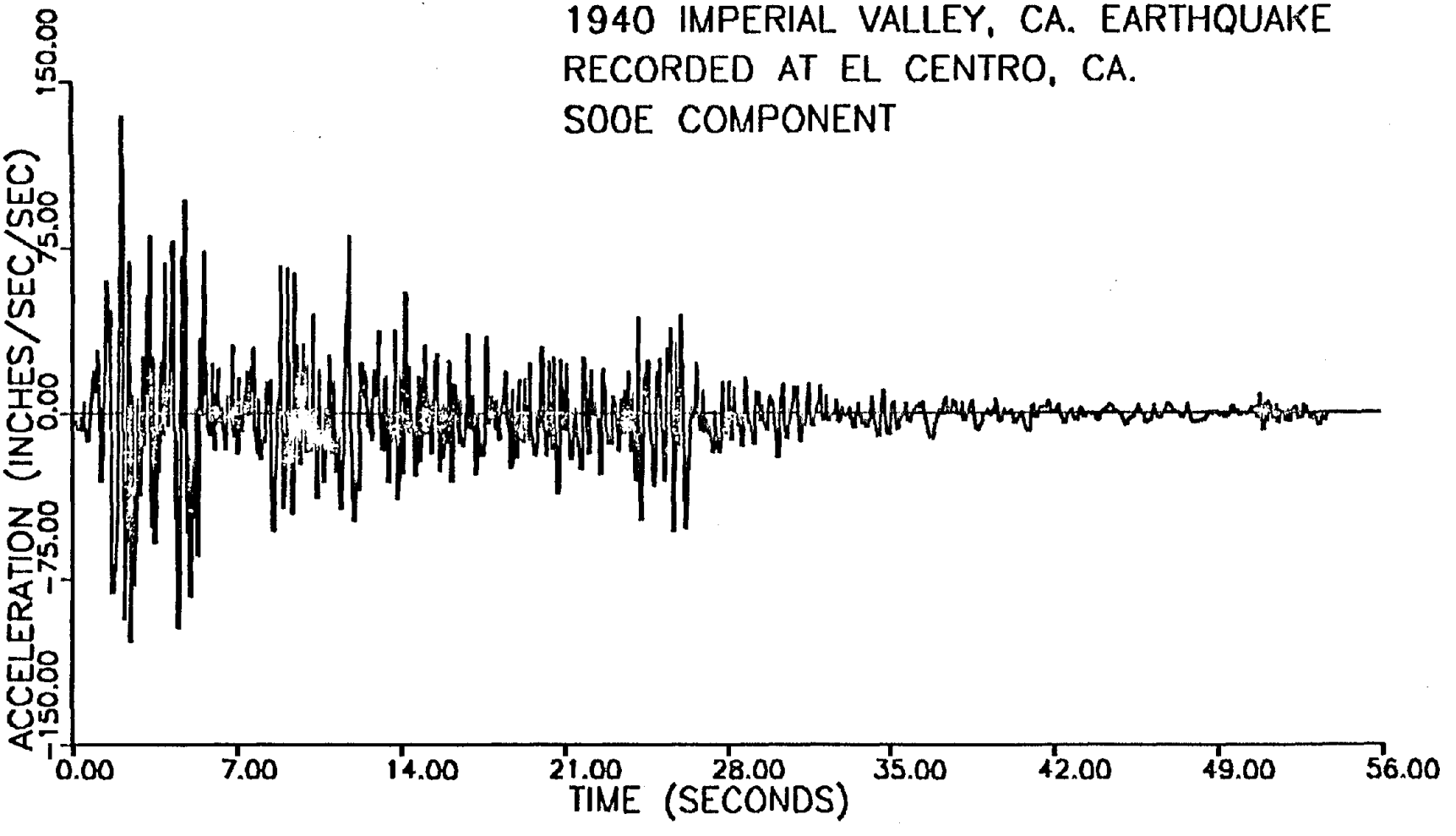

Figure 3.4-6. The S00E Component of the May 18, 1940, Imperial Valley, California Earthquake Recorded at El Centro, California.

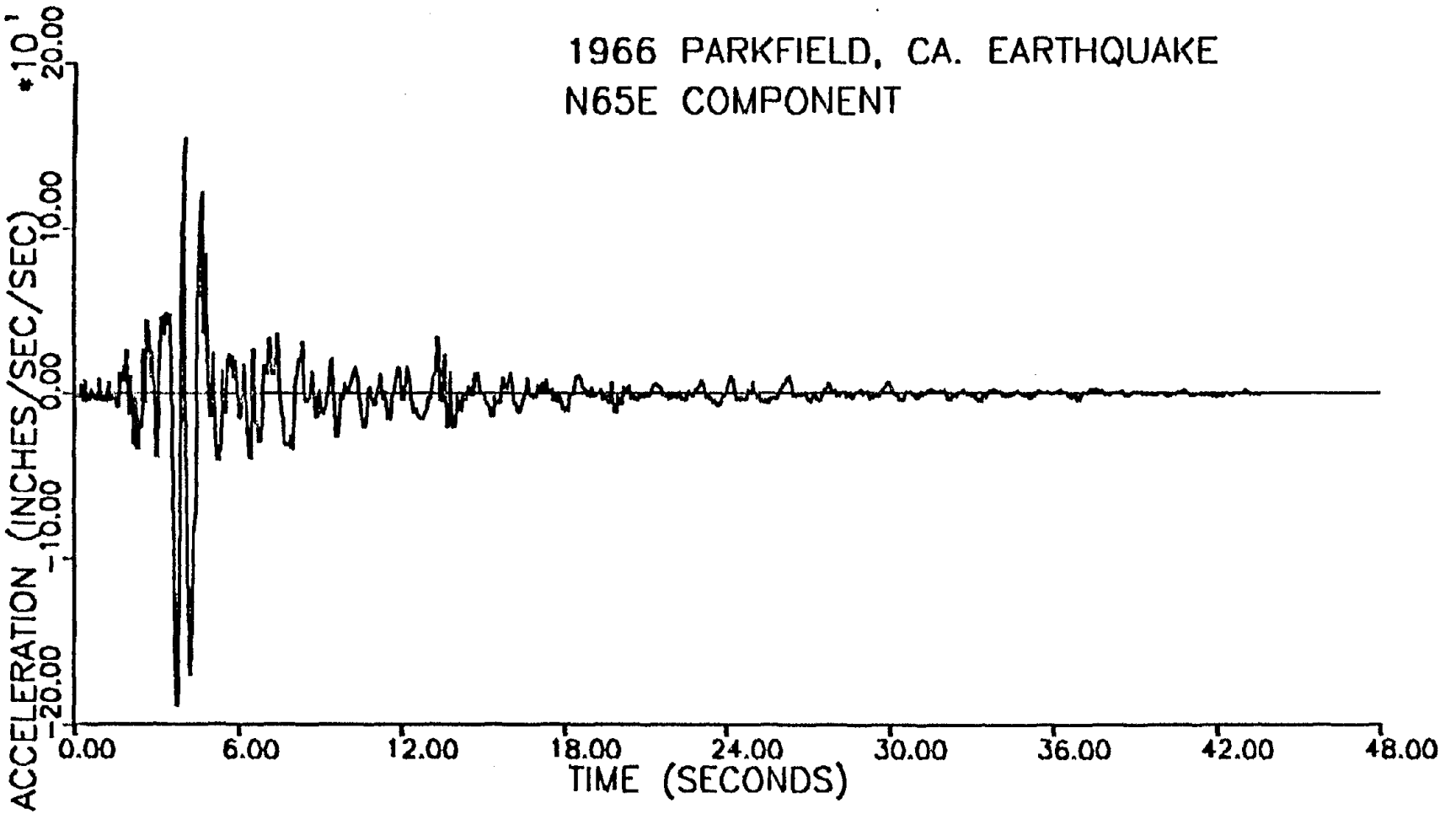

Figure 3.4-7. The N65E Component of the June 27, 1966, Parkfield, California Earthquake.

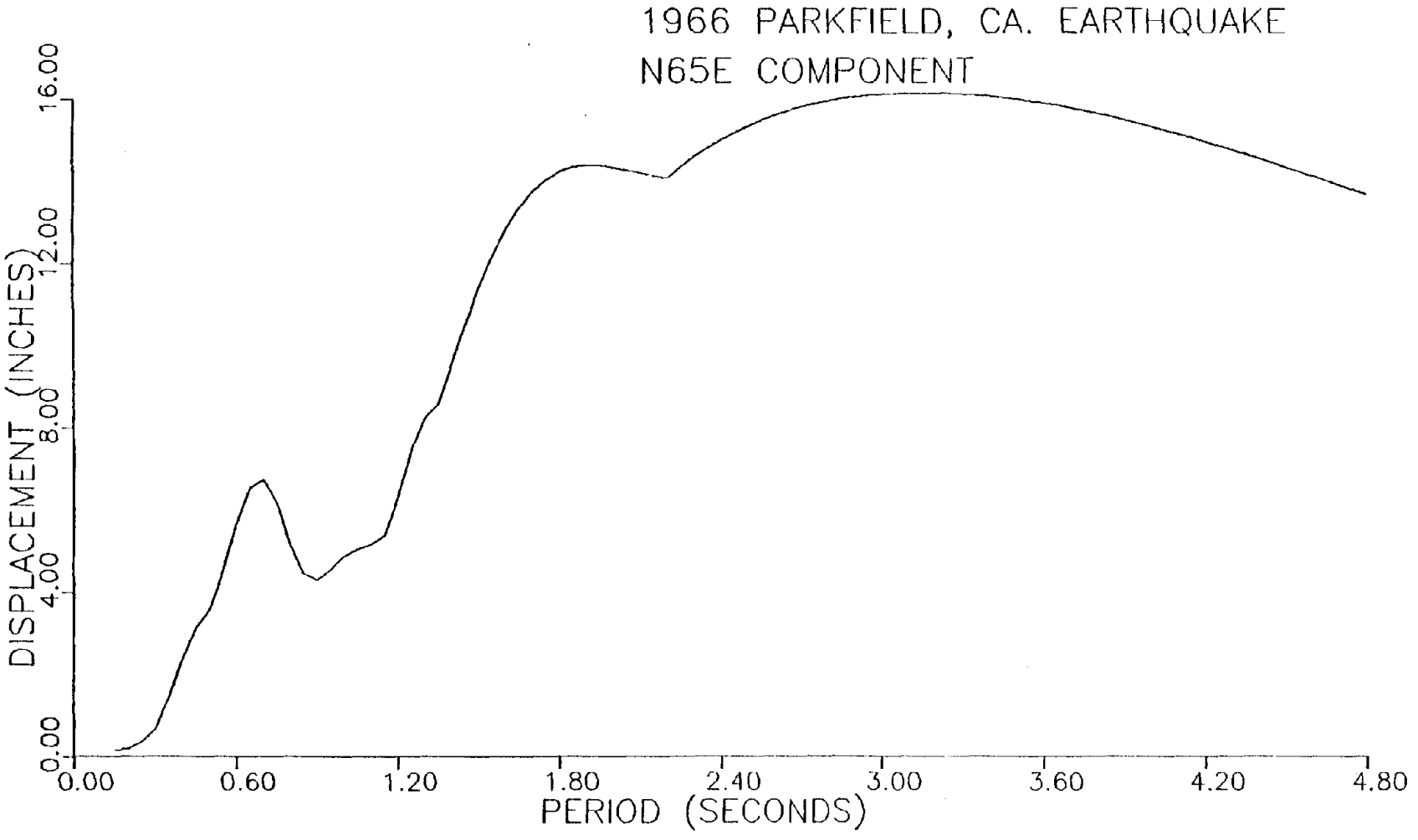

Figure 3.4-8. Relative Displacement Response Spectrum for N65E Component of June 27, 1966, Parkfield, California Earthquake.

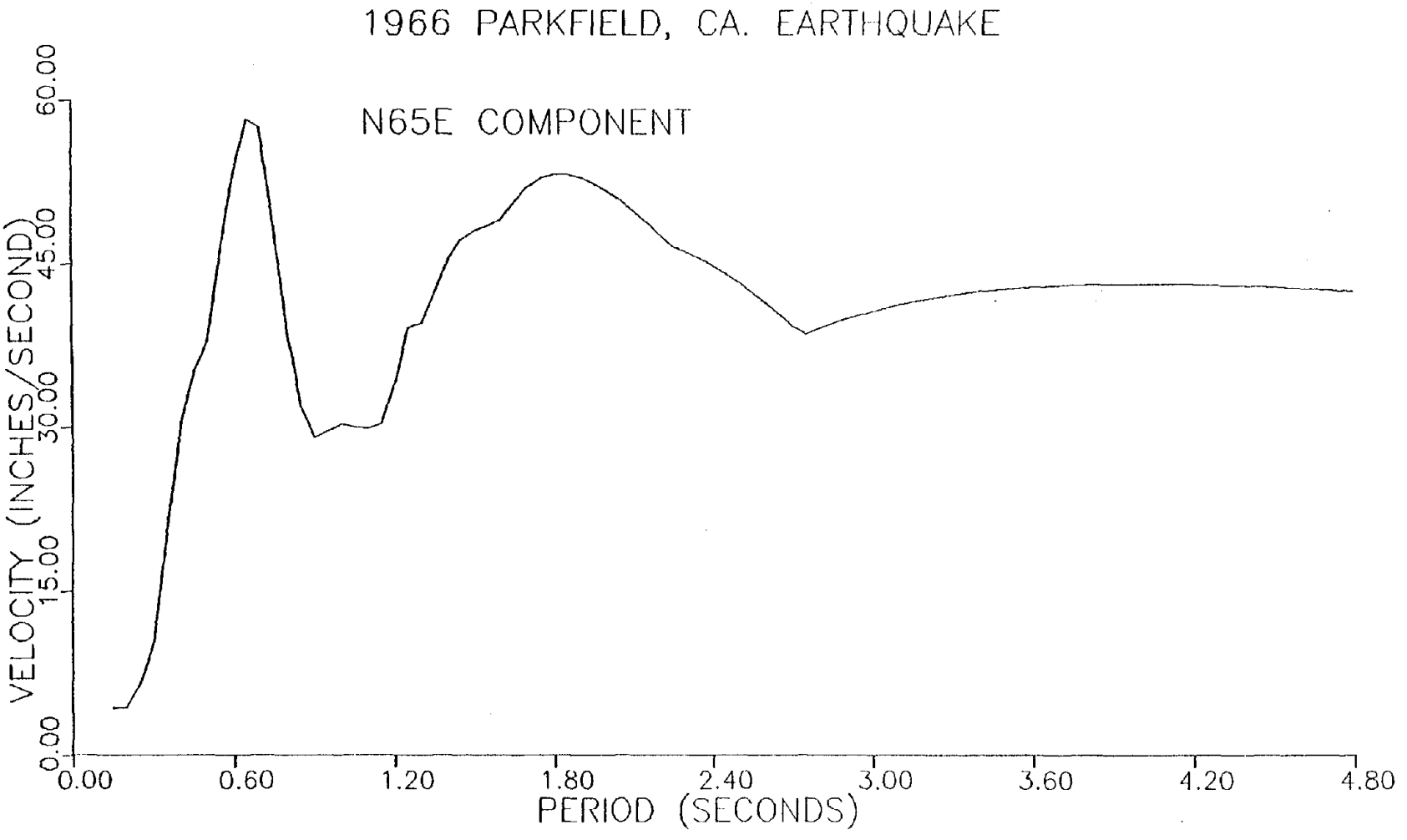

Figure 3.4-9. Relative Velocity Response Spectrum for N65E Component of June 27, 1966, Parkfield, California Earthquake.

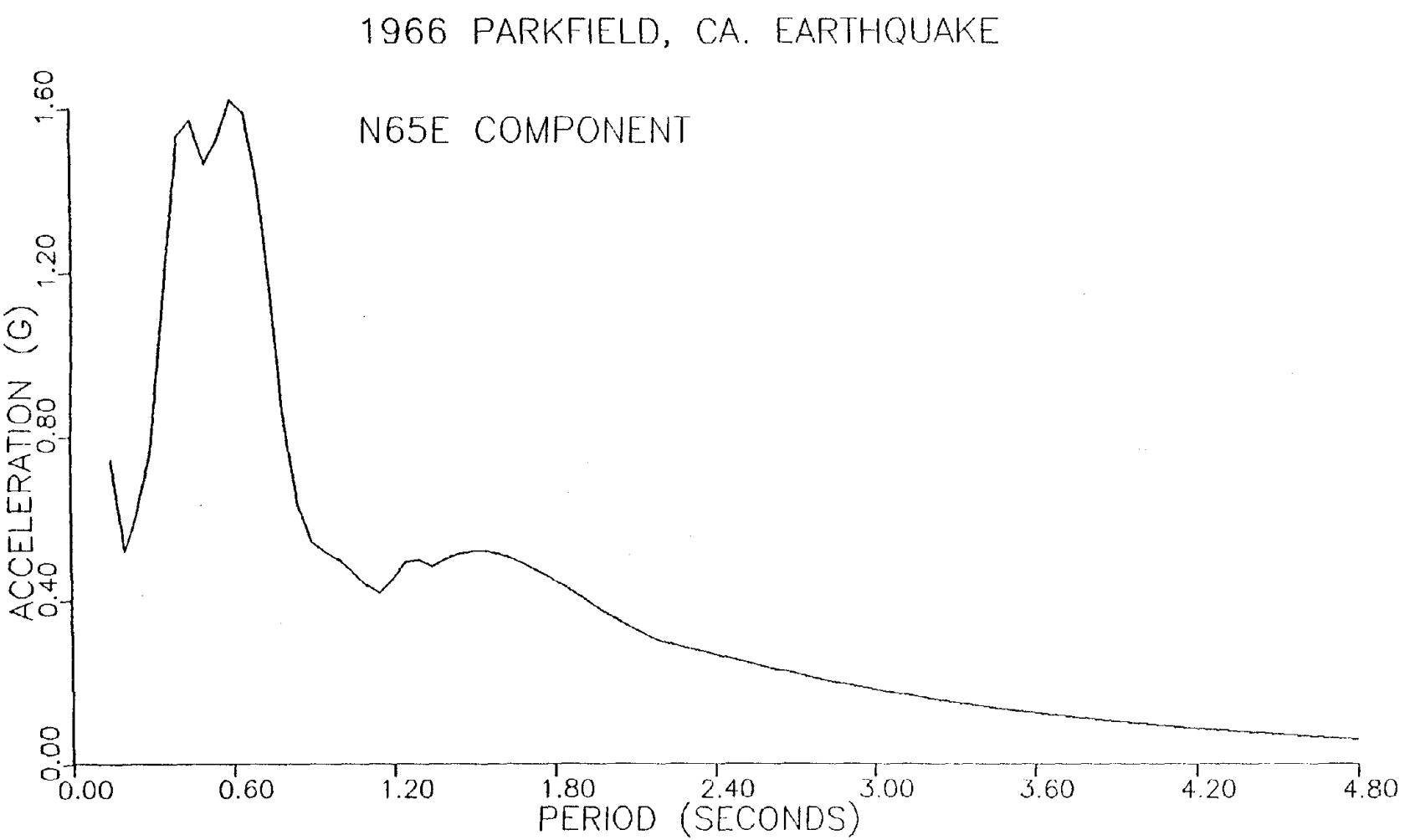

Figure 3.4-10. Absolute Acceleration Response Spectrum for N65E Component of June 27, 1966, Parkfield, California Earthquake.

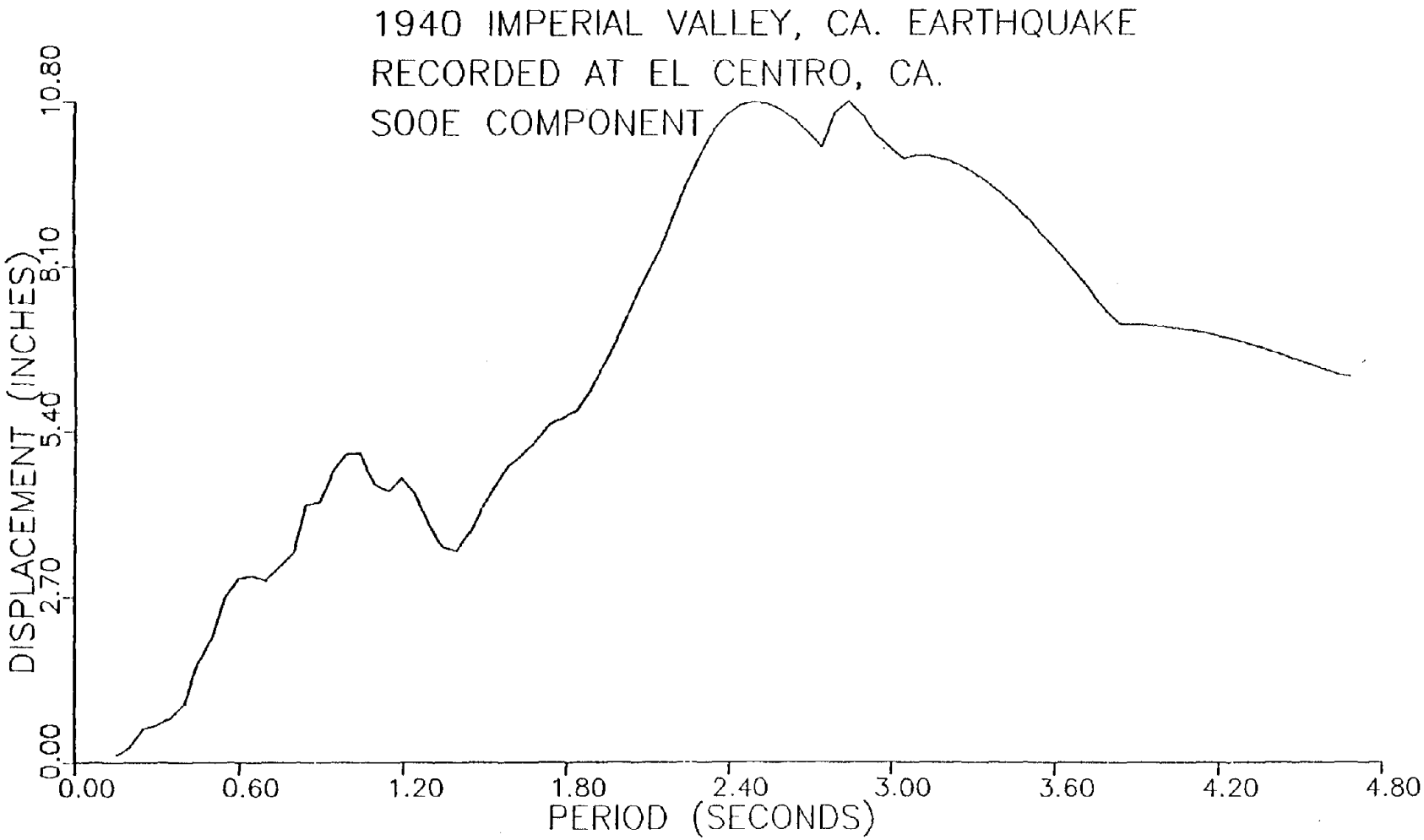

Figure 3.4-11. Relative Displacement Response Spectrum for S00E Component of May 18, 1940, Imperial Valley, California Earthquake Recorded at El Centro, California.

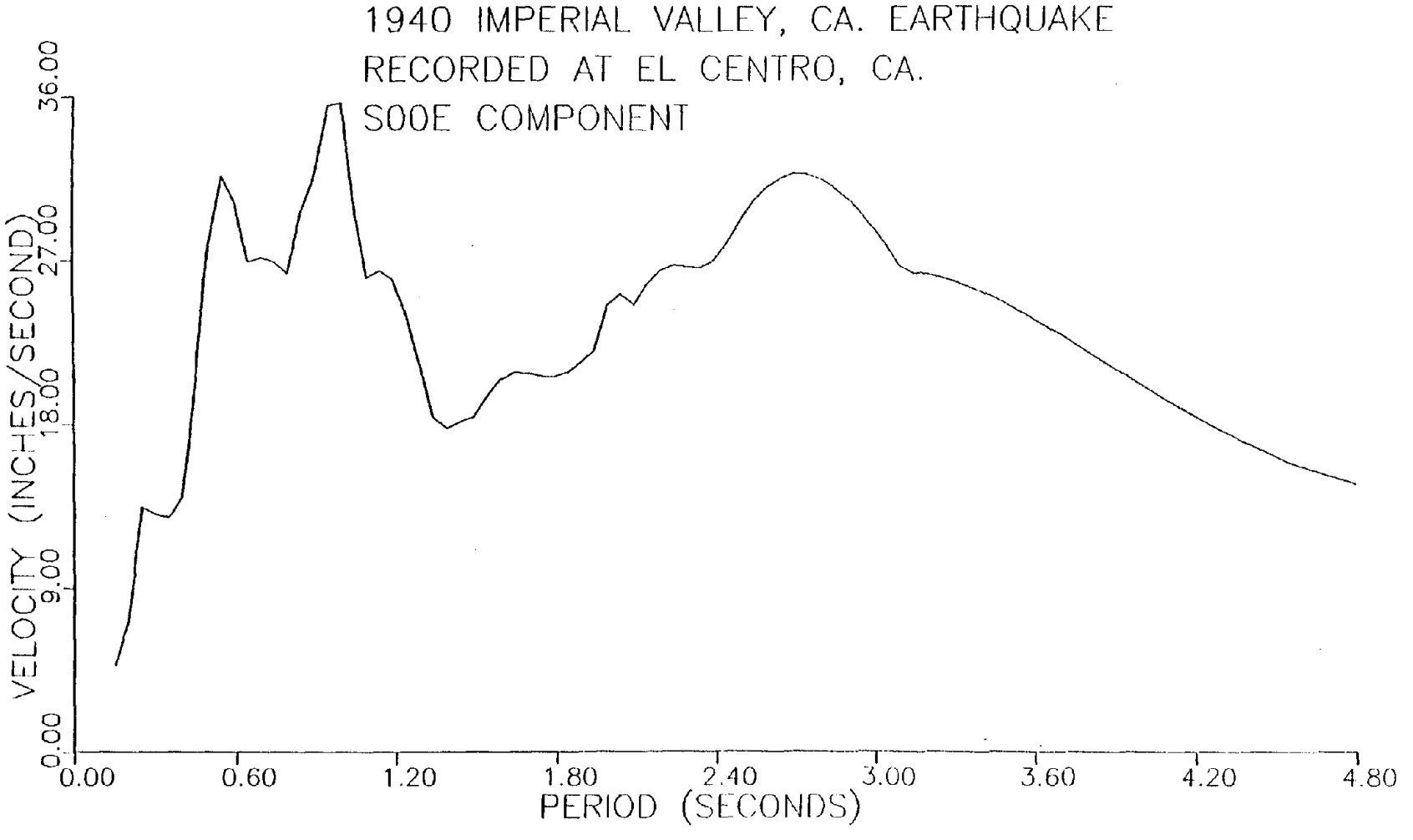

Figure 3.4-12. Relative Velocity Response Spectrum for S00E Component of May 18, 1940, Imperial Valley, California Earthquake Recorded at El Centro, California.

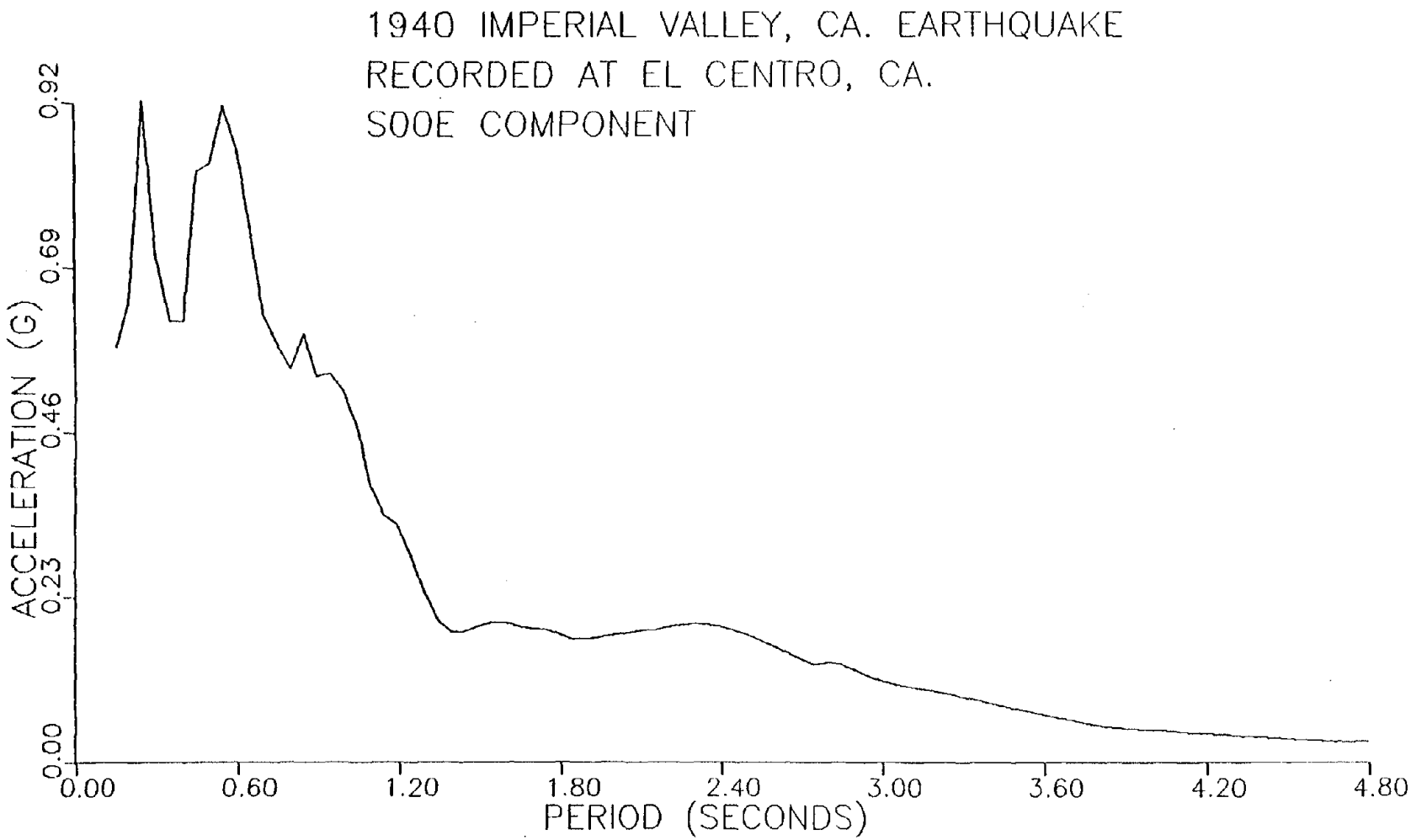

Figure 3.4-13. Absolute Acceleration Response Spectrum for S00E Component of May 18, 1940, Imperial Valley, California Earthquake Recorded at El Centro, California.

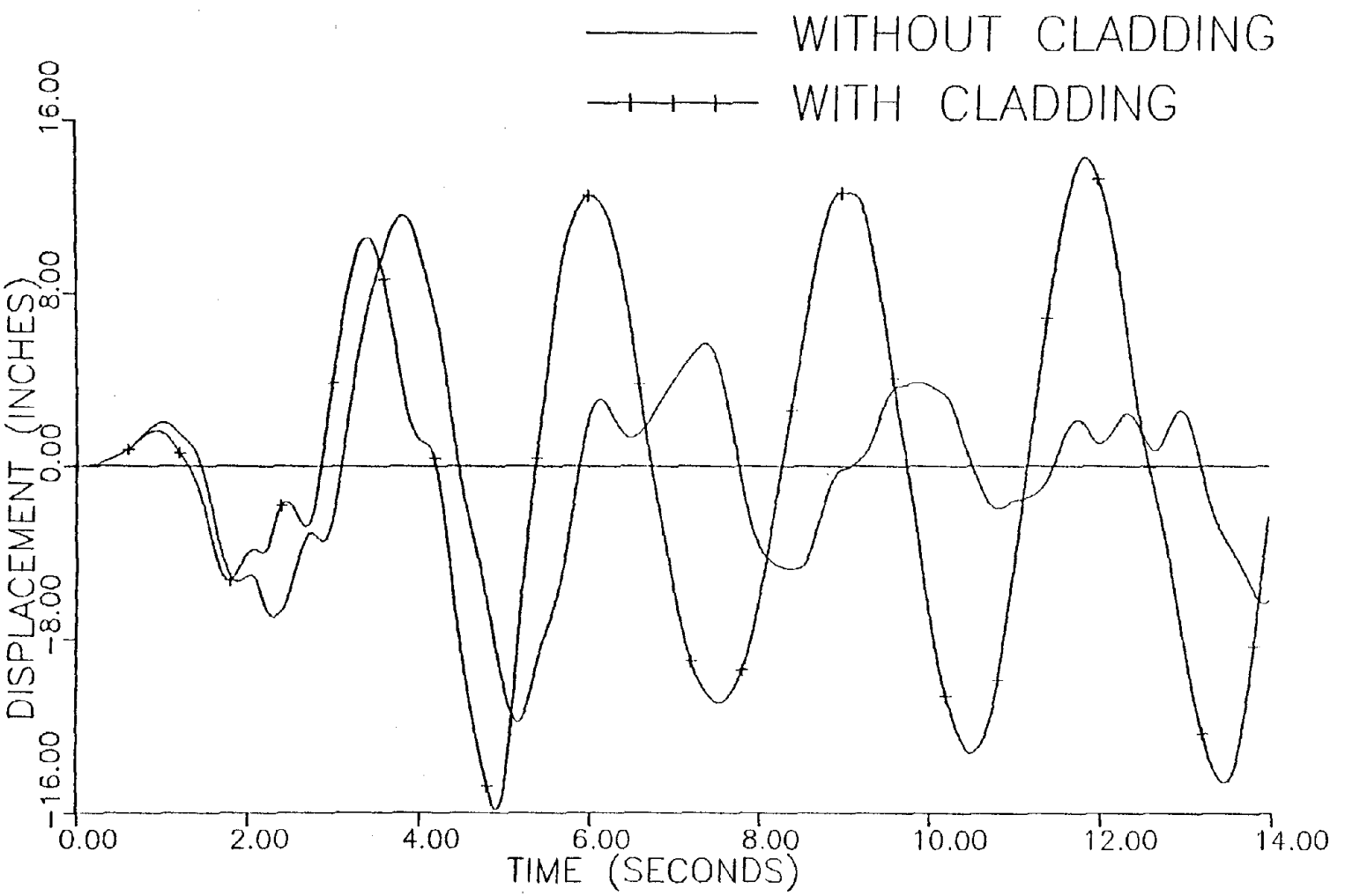

Figure 3.4-14. Roof Translational Response in Rigid Direction, Symmetric Case, for the First 14 Seconds of 1940 El Centro Record Acting in Rigid Direction.

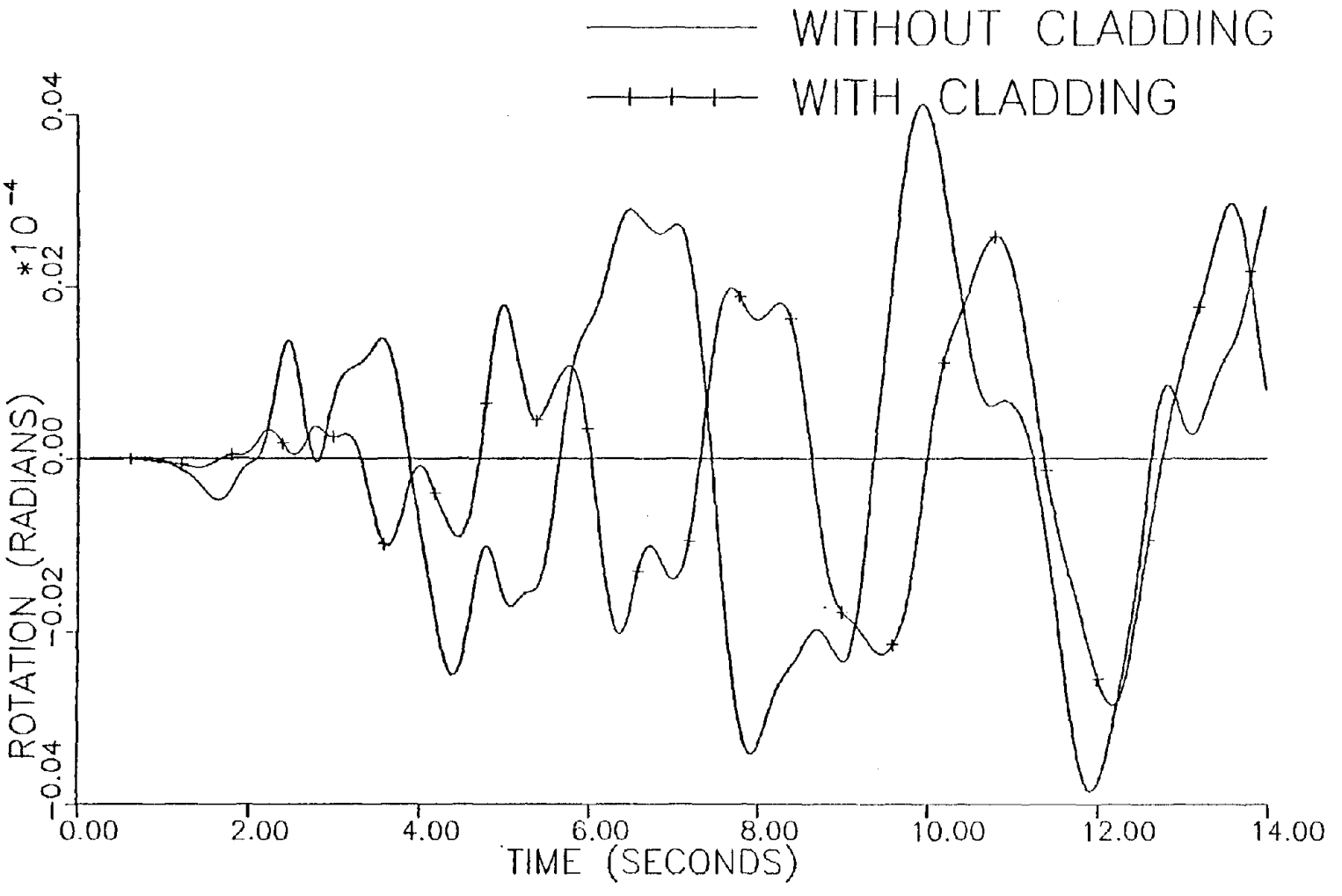

Figure 3.4-15. Roof Rotational Response, Symmetric Case, for the First 14 Seconds of 1940 El Centro Record Acting in Rigid Direction.

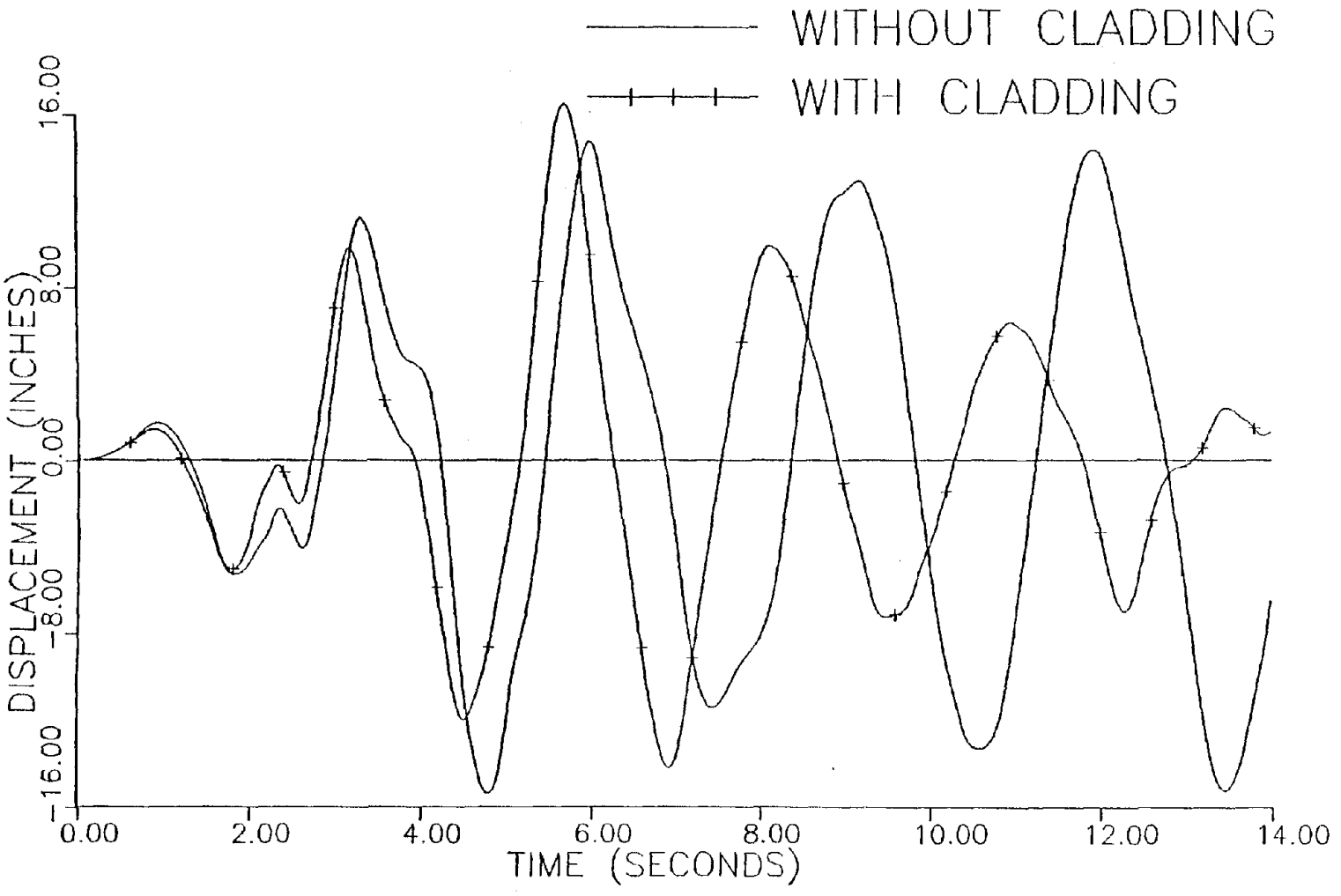

Figure 3.4-16. Roof Translational Response in Braced Direction, Symmetric Case, for the First 14 Seconds of 1940 El Centro Record Acting in Braced Direction.

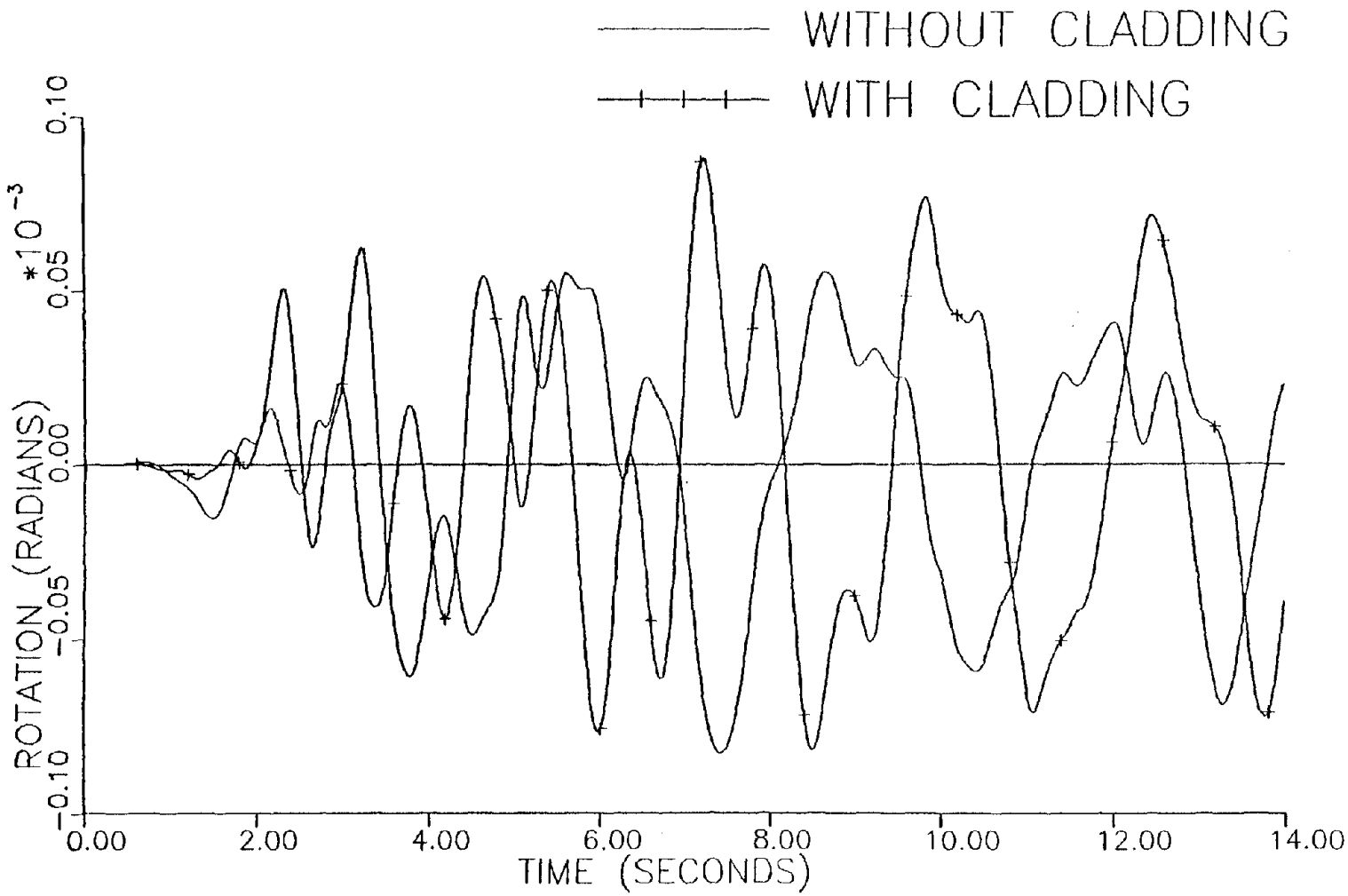

Figure 3.4-17. Roof Rotational Response, Symmetric Case, for the First 14 Seconds of 1940 El Centro Record Acting in Braced Direction.

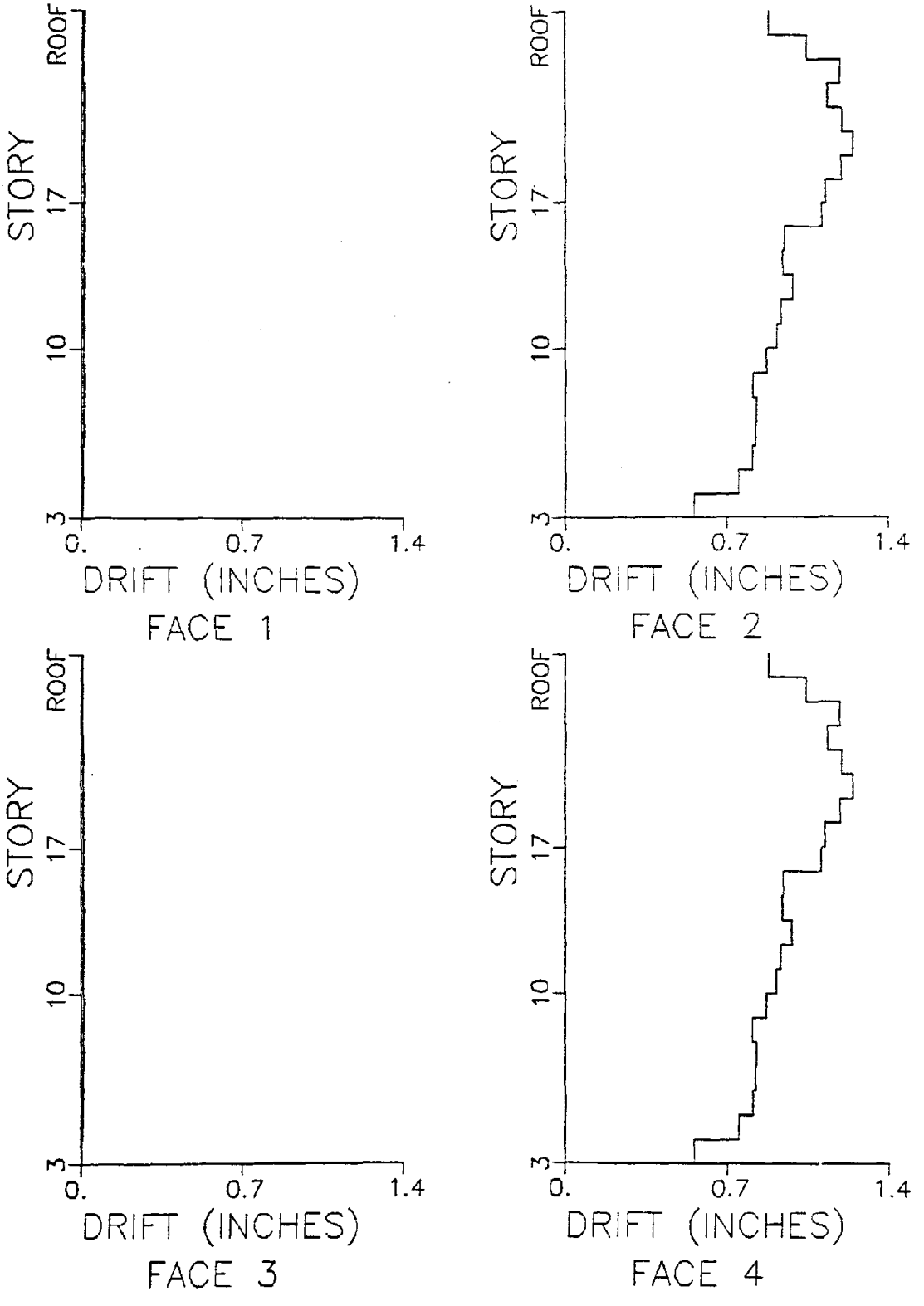

Figure 3.4-18. Peak Drift Values, Symmetric Case with Cladding, for 1940 El Centro Record Acting in Rigid Direction.

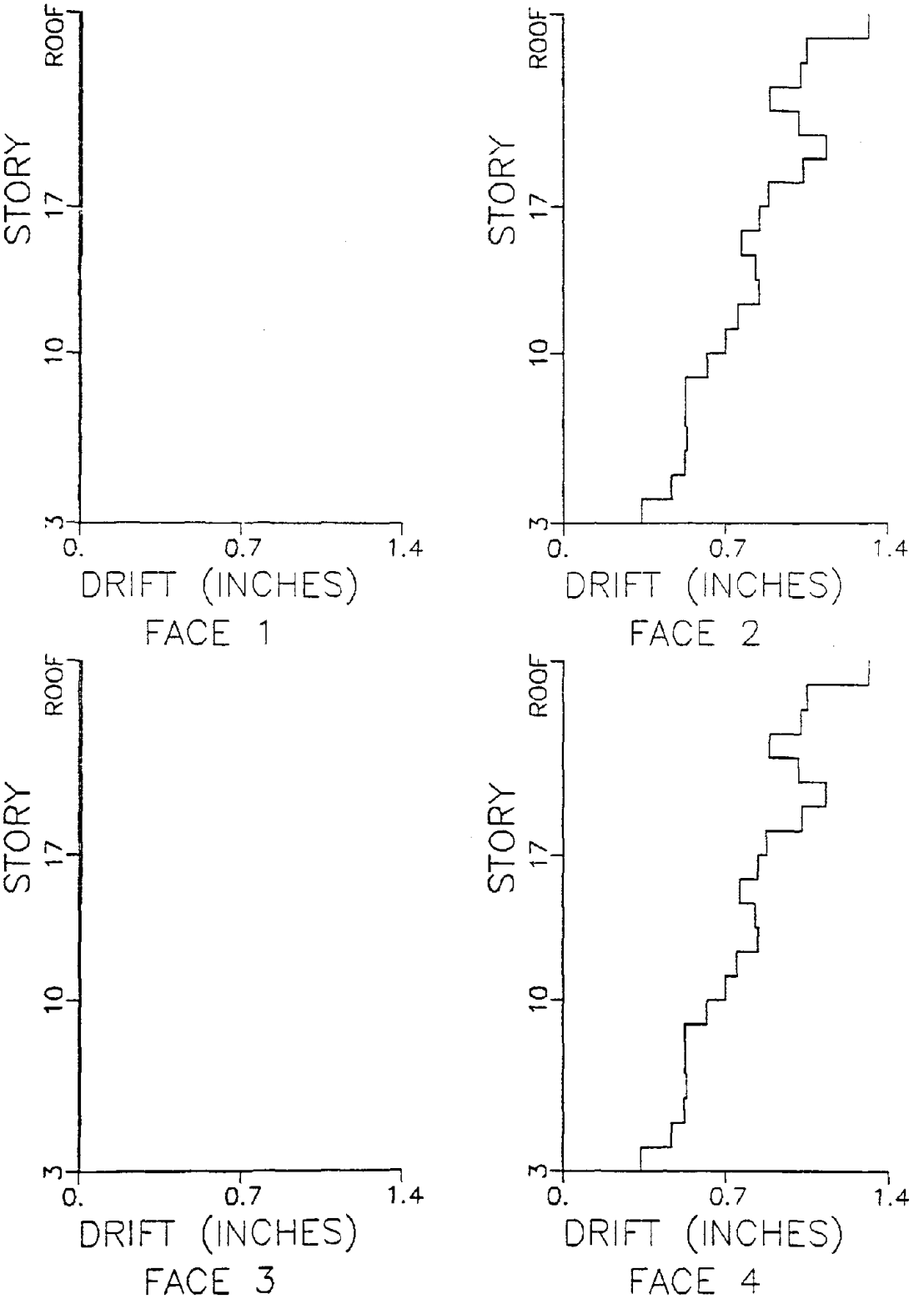

Figure 3.4-19. Peak Drift Values, Symmetric Case without Cladding, for 1940 El Centro Record Acting in Rigid Direction.

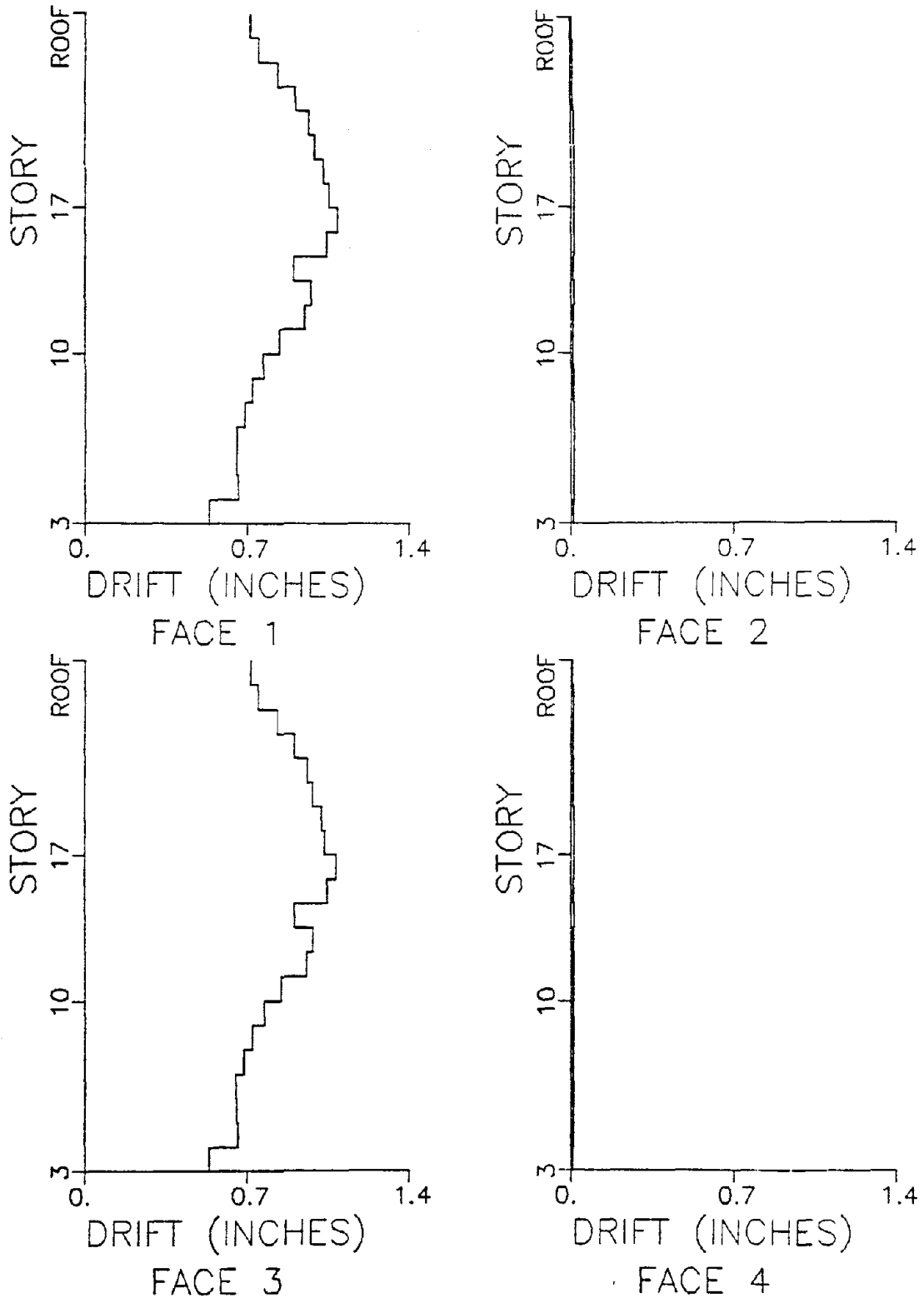

Figure 3.4-20. Peak Drift Values, Symmetric Case with Cladding, for 1940 El Centro Record Acting in Braced Direction.

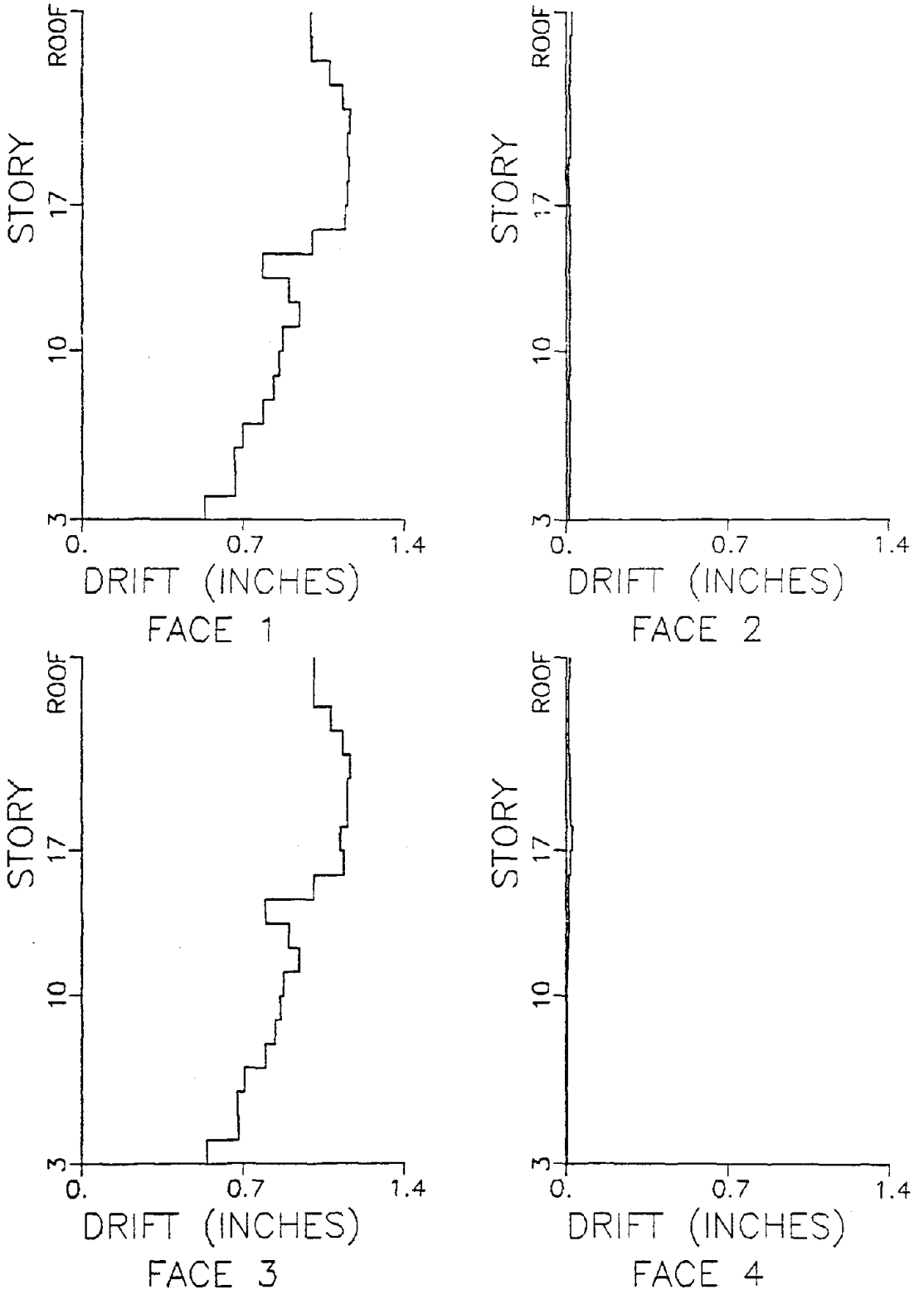

Figure 3.4-21. Peak Drift Values, Symmetric Case without Cladding, for 1940 El Centro Record Acting in Braced Direction.

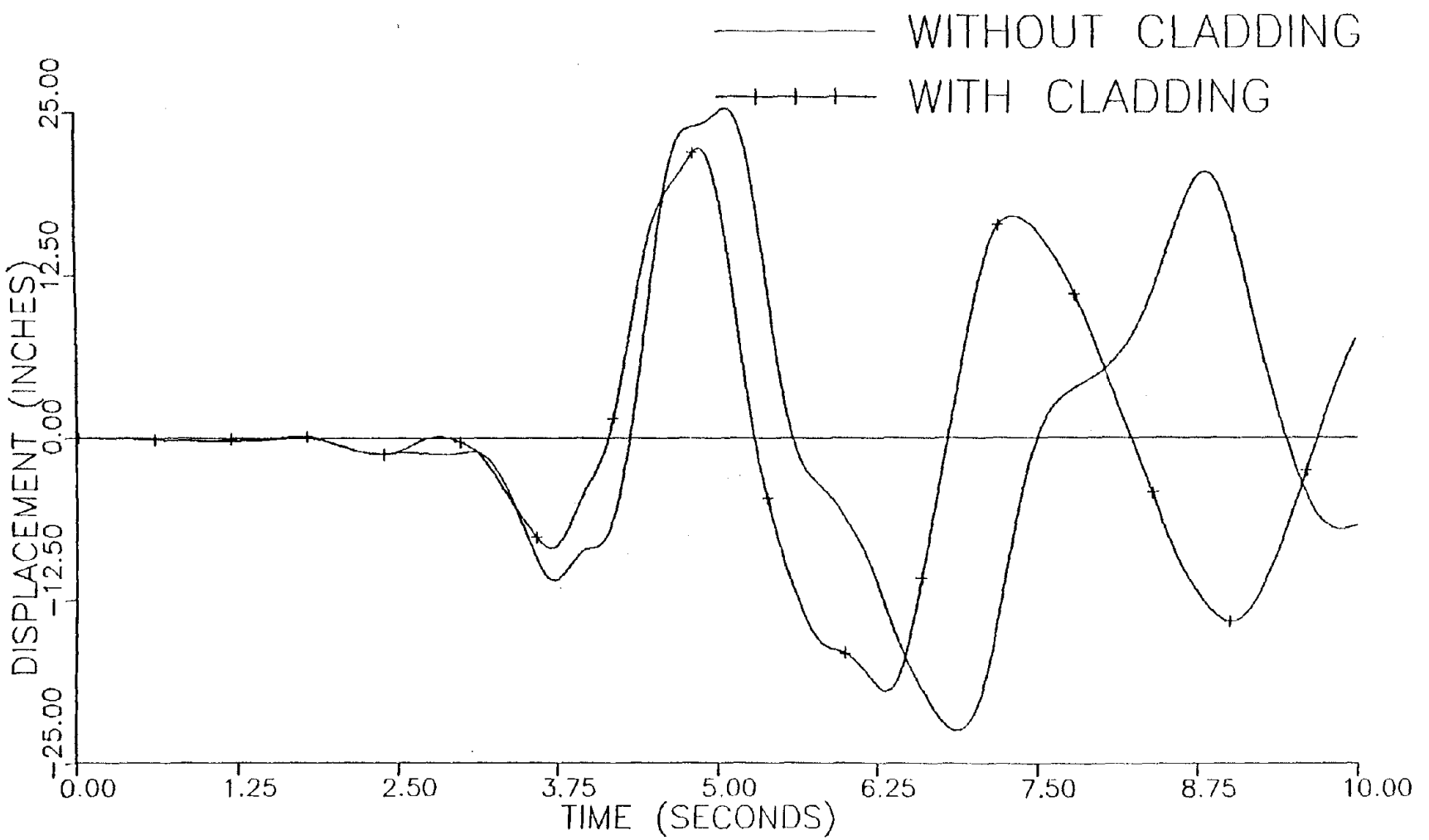

Figure 3.4-22. Roof Translational Response in Rigid Direction, Symmetric Case, for the First 10 Seconds of 1966 Parkfield Record Acting in Rigid Direction.

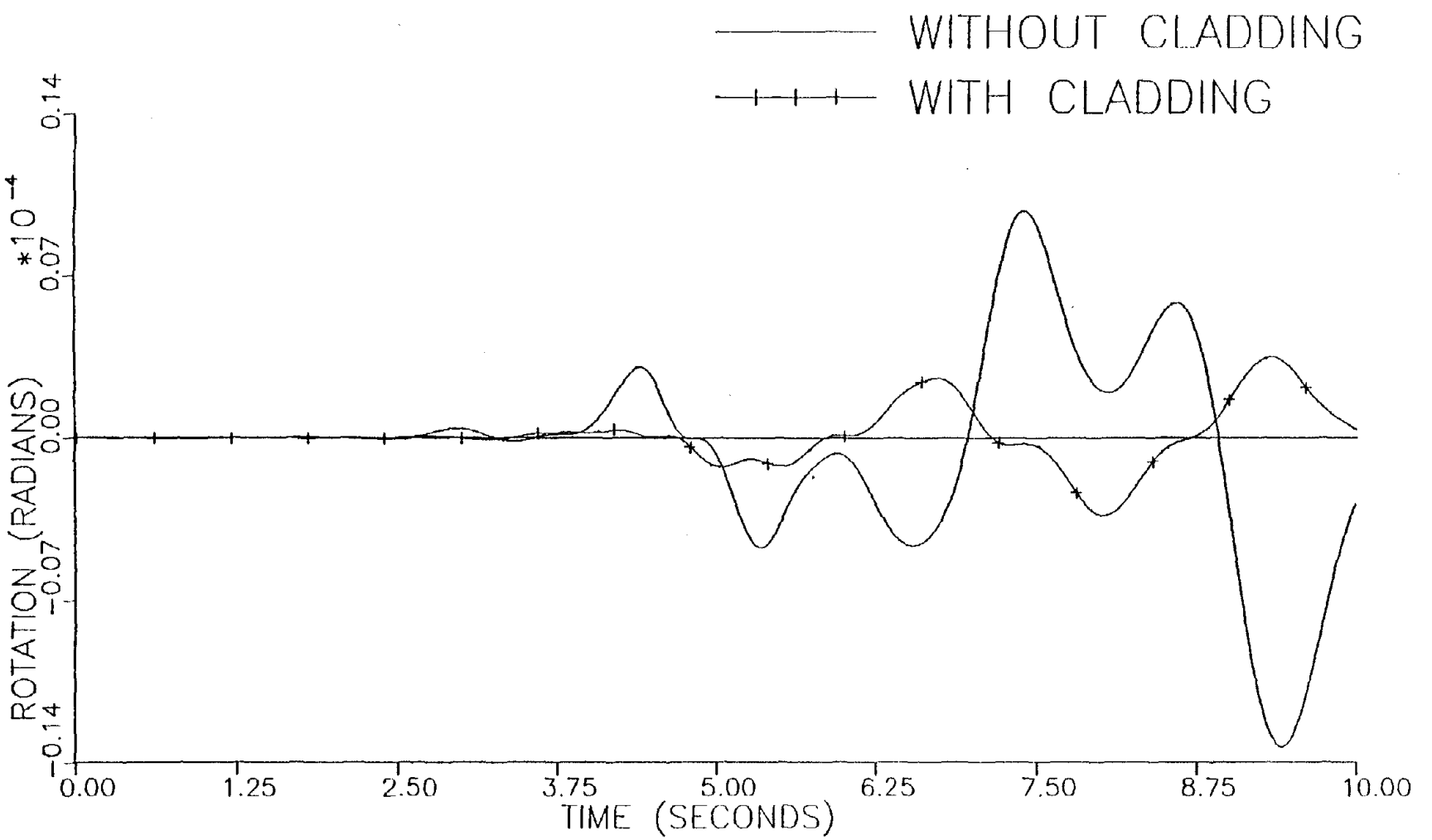

Figure 3.4-23. Roof Rotational Response, Symmetric Case, for the First 10 Seconds of 1966 Parkfield Record Acting in Rigid Direction.

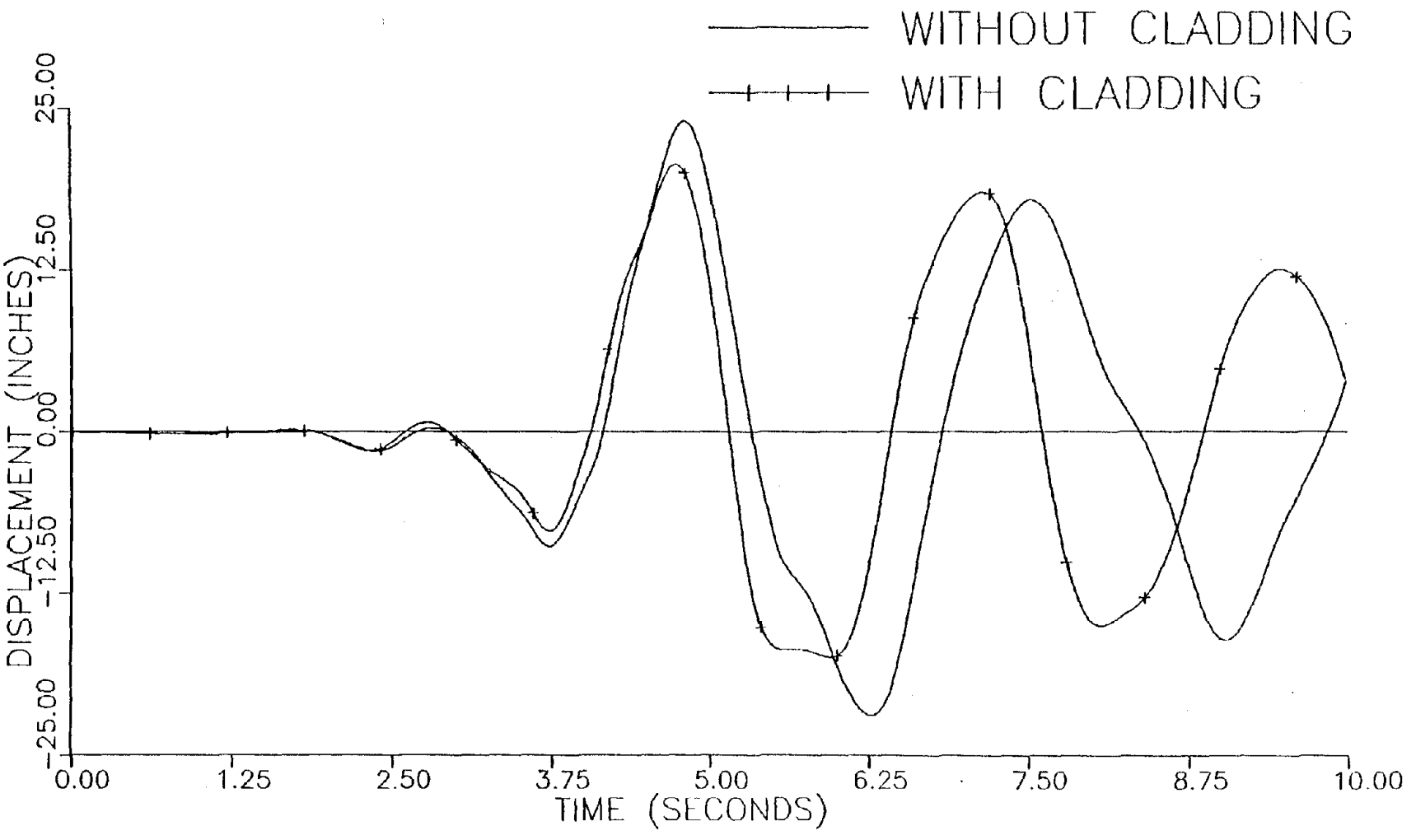

Figure 3.4-24. Roof Translational Response in Braced Direction, Symmetric Case, for the First 10 Seconds of 1966 Parkfield Record Acting in Braced Direction.

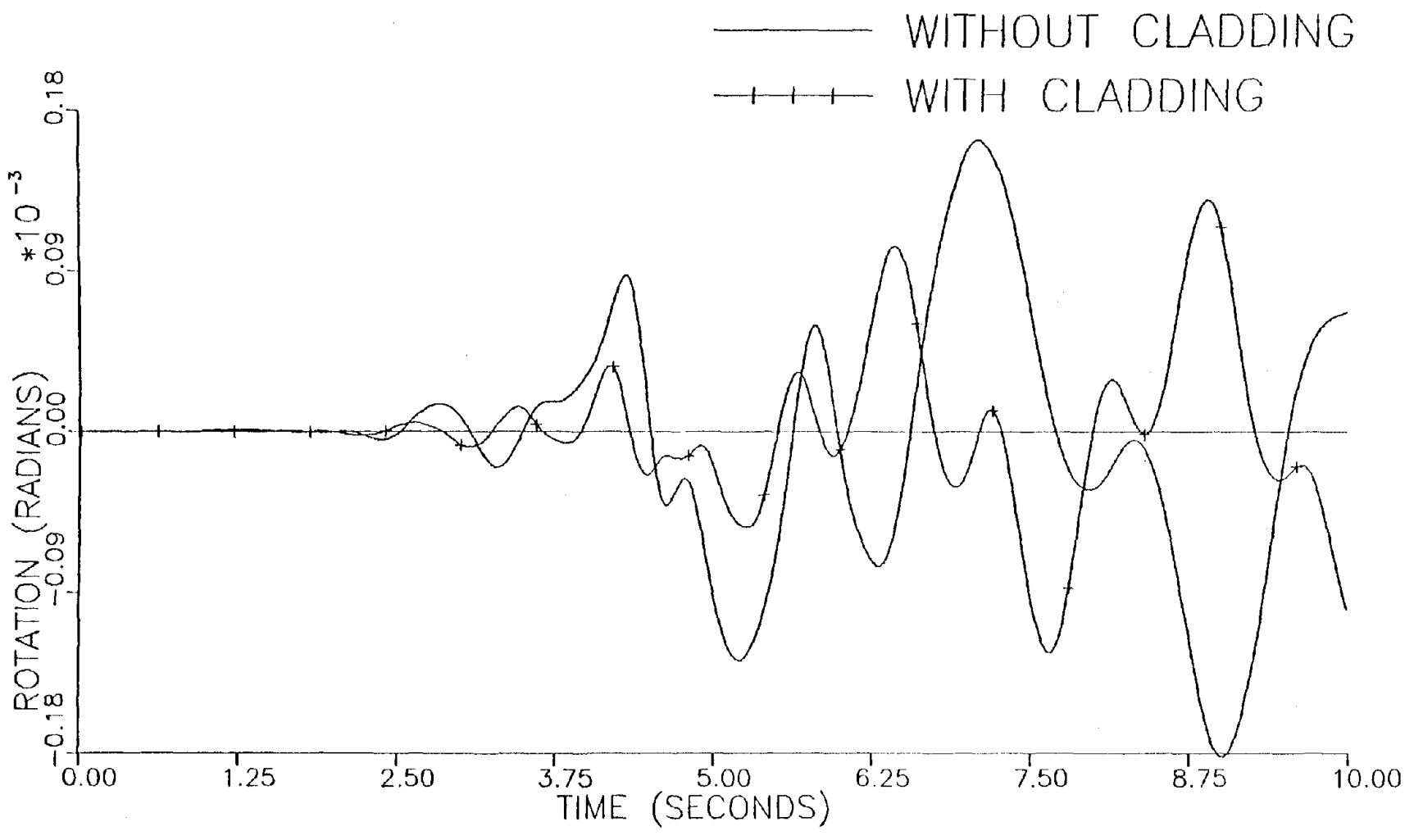

Figure 3.4-25. Roof Rotational Response, Symmetric Case, for the First 10 Seconds of 1966 Parkfield Record Acting in Braced Direction.

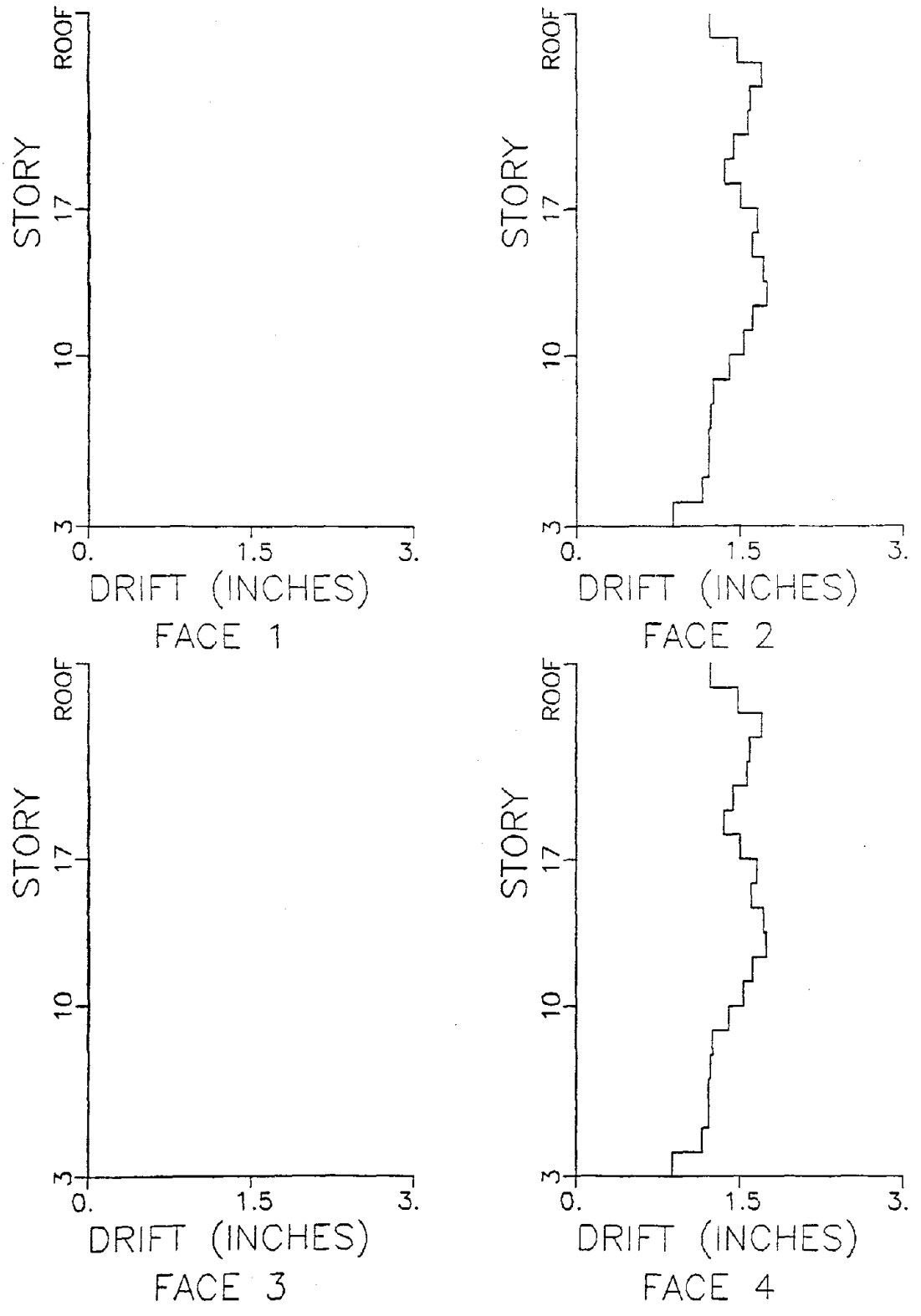

Figure 3.4-26. Peak Drift Values, Symmetric Case with Cladding, for 1966 Parkfield Record Acting in Rigid Direction.

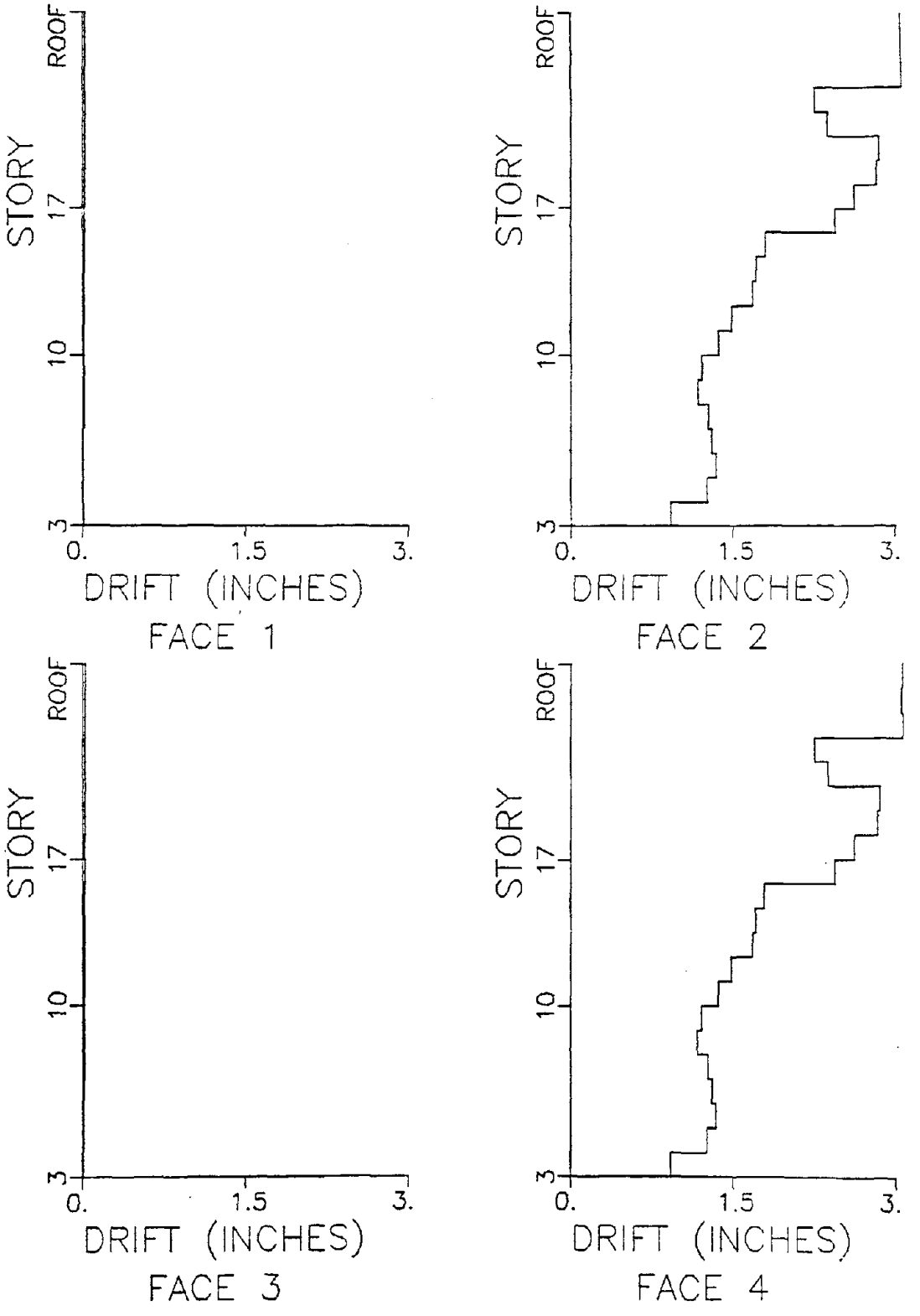

Figure 3.4-27. Peak Drift Values, Symmetric Case without Cladding, for 1966 Parkfield Record Acting in Rigid Direction.

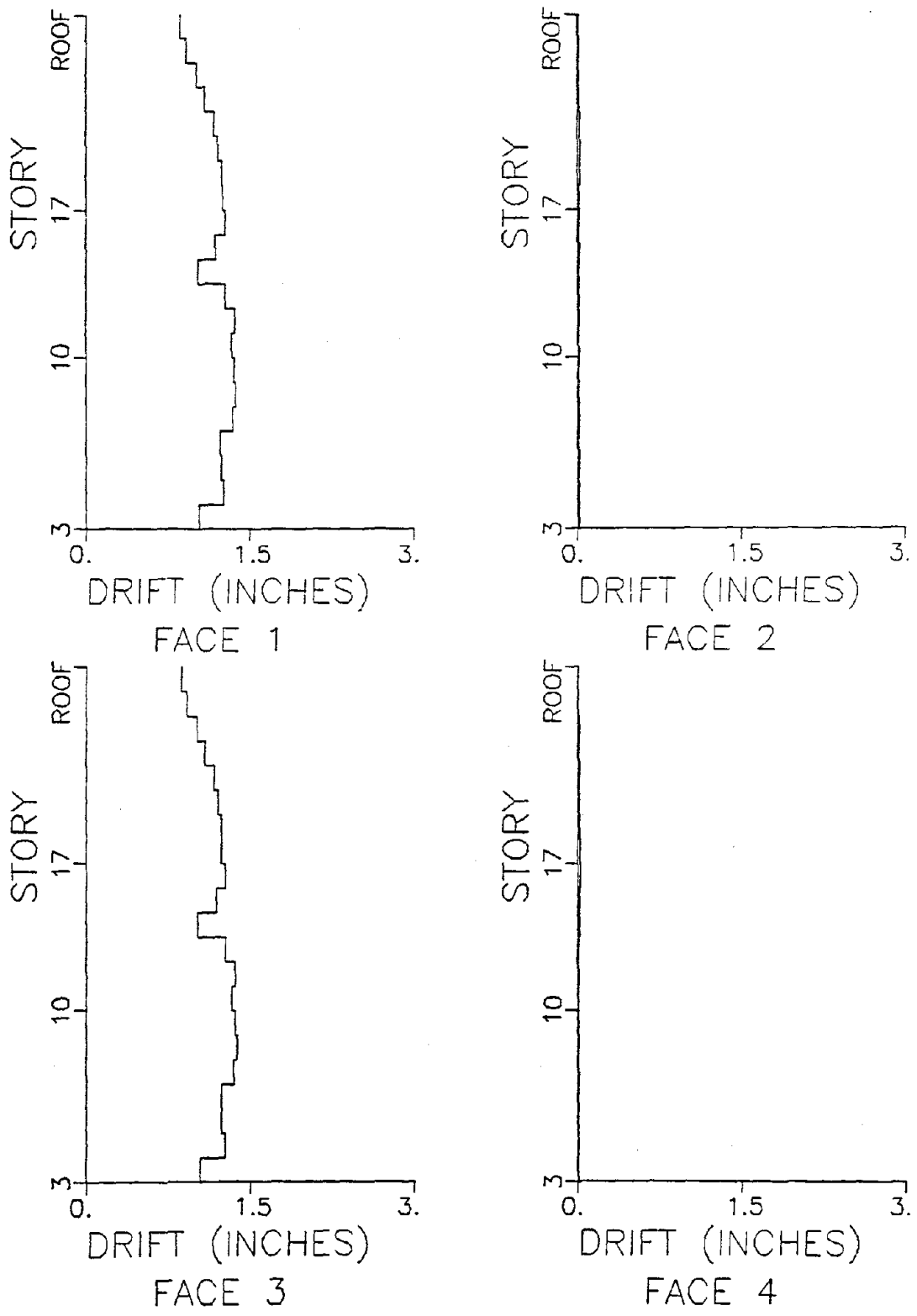

Figure 3.4-28. Peak Drift Values, Symmetric Case with Cladding, for 1966 Parkfield Record Acting in Braced Direction.

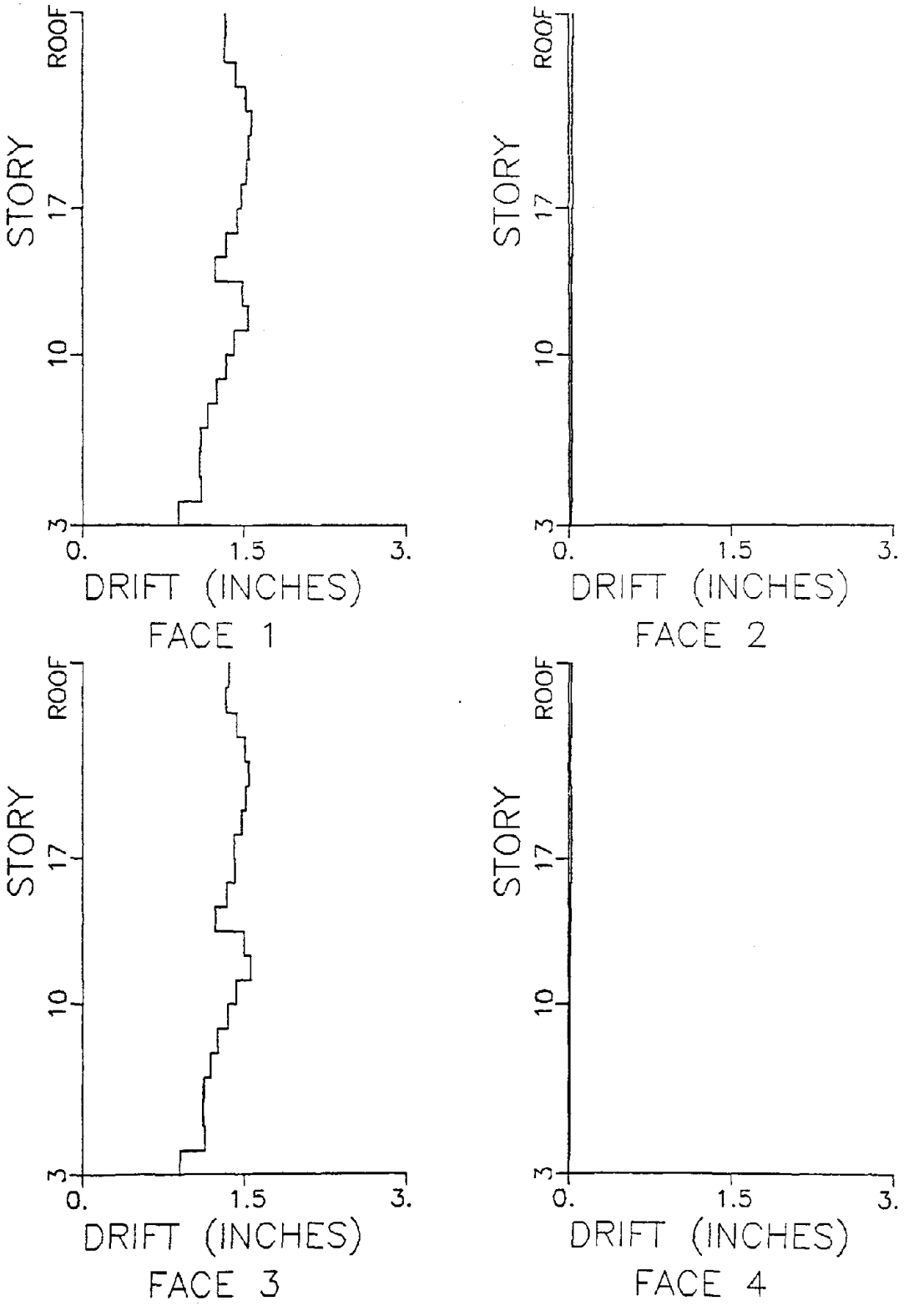

Figure 3.4-29. Peak Drift Values, Symmetric Case without Cladding, for 1966 Parkfield Record Acting in Braced Direction.

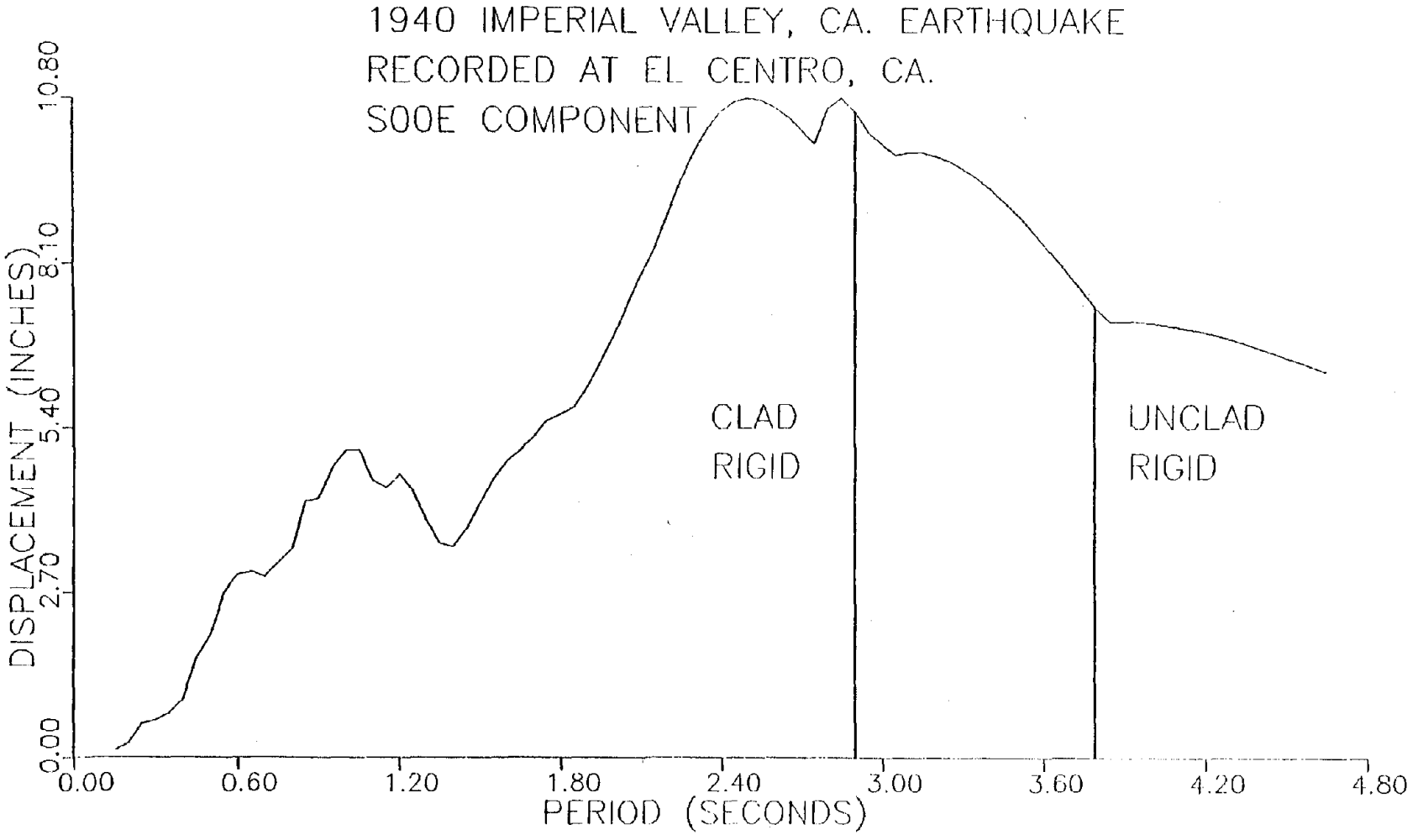

Figure 3.4-30. Relative Displacement Response Spectrum for S00E Component of the 1940 El Centro Record with Fundamental Periods in Rigid Direction Shown for the Clad and Unclad Symmetric Models.

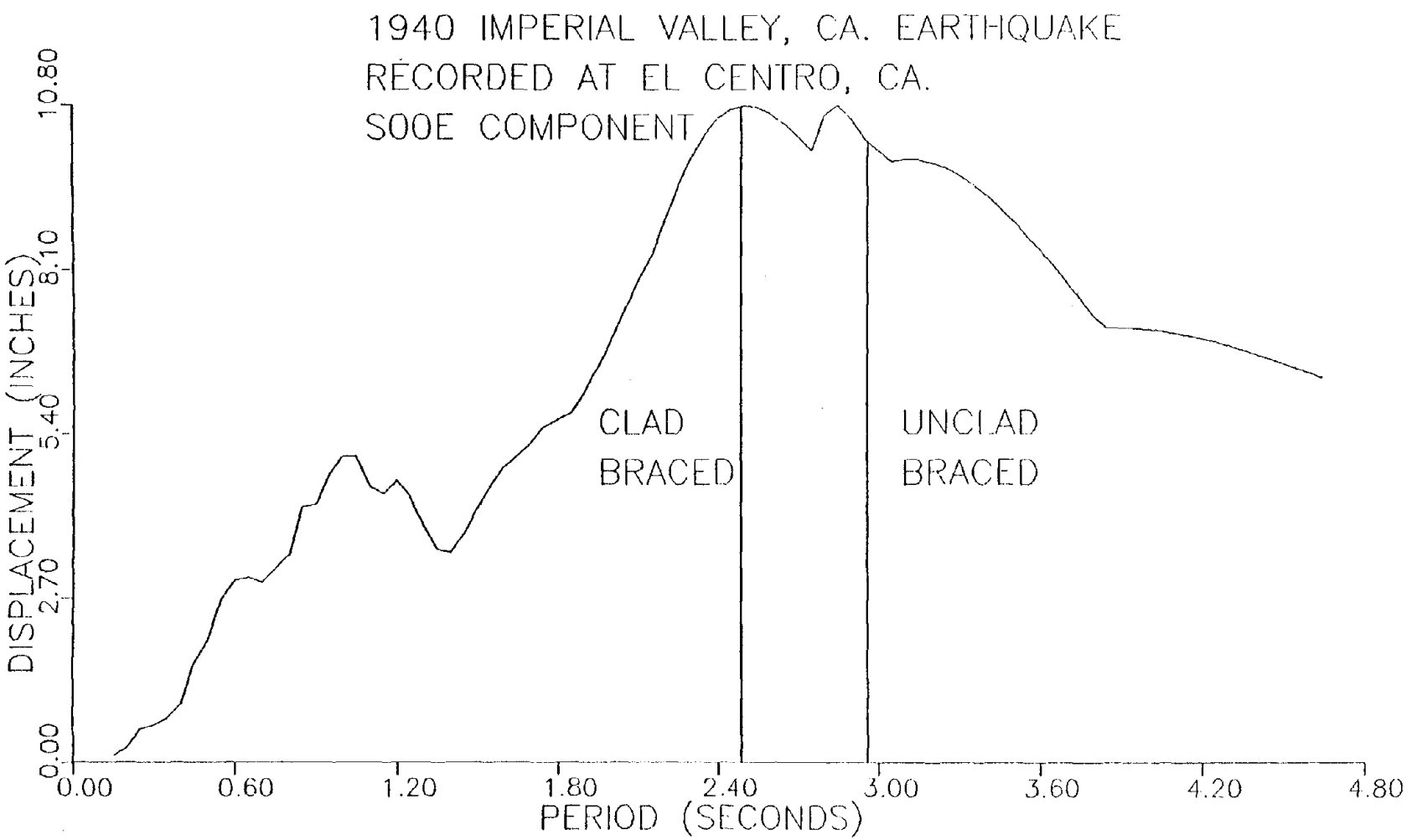

Figure 3.4-31. Relative Displacement Response Spectrum for S00E Component of the 1940 El Centro Record with Fundamental Periods in Braced Direction Shown for the Clad and Unclad Symmetric Models.

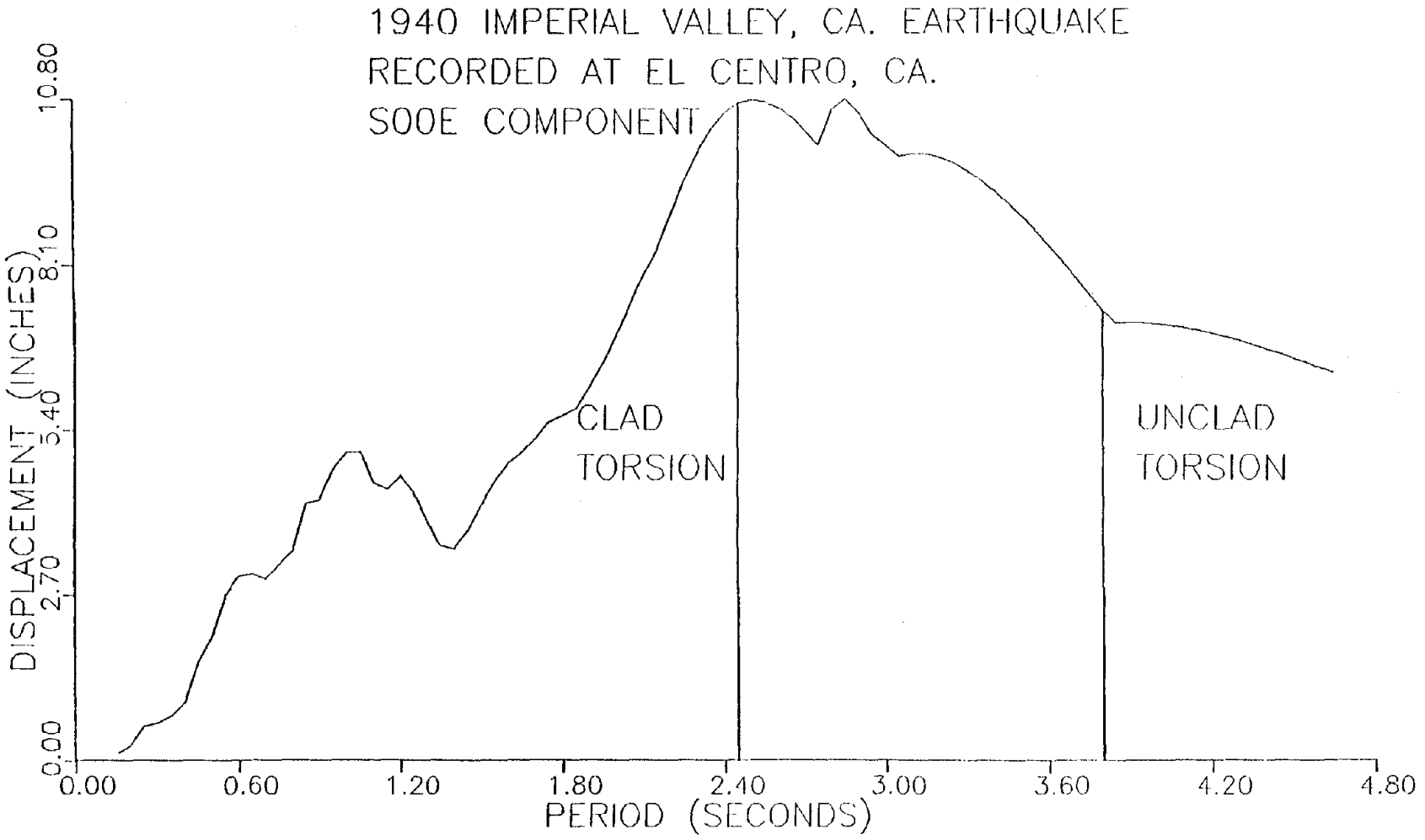

Figure 3.4-32. Relative Displacement Response Spectrum for S00E Component of the 1940 El Centro Record with Fundamental Periods in Torsion Shown for the Clad and Unclad Symmetric Models.

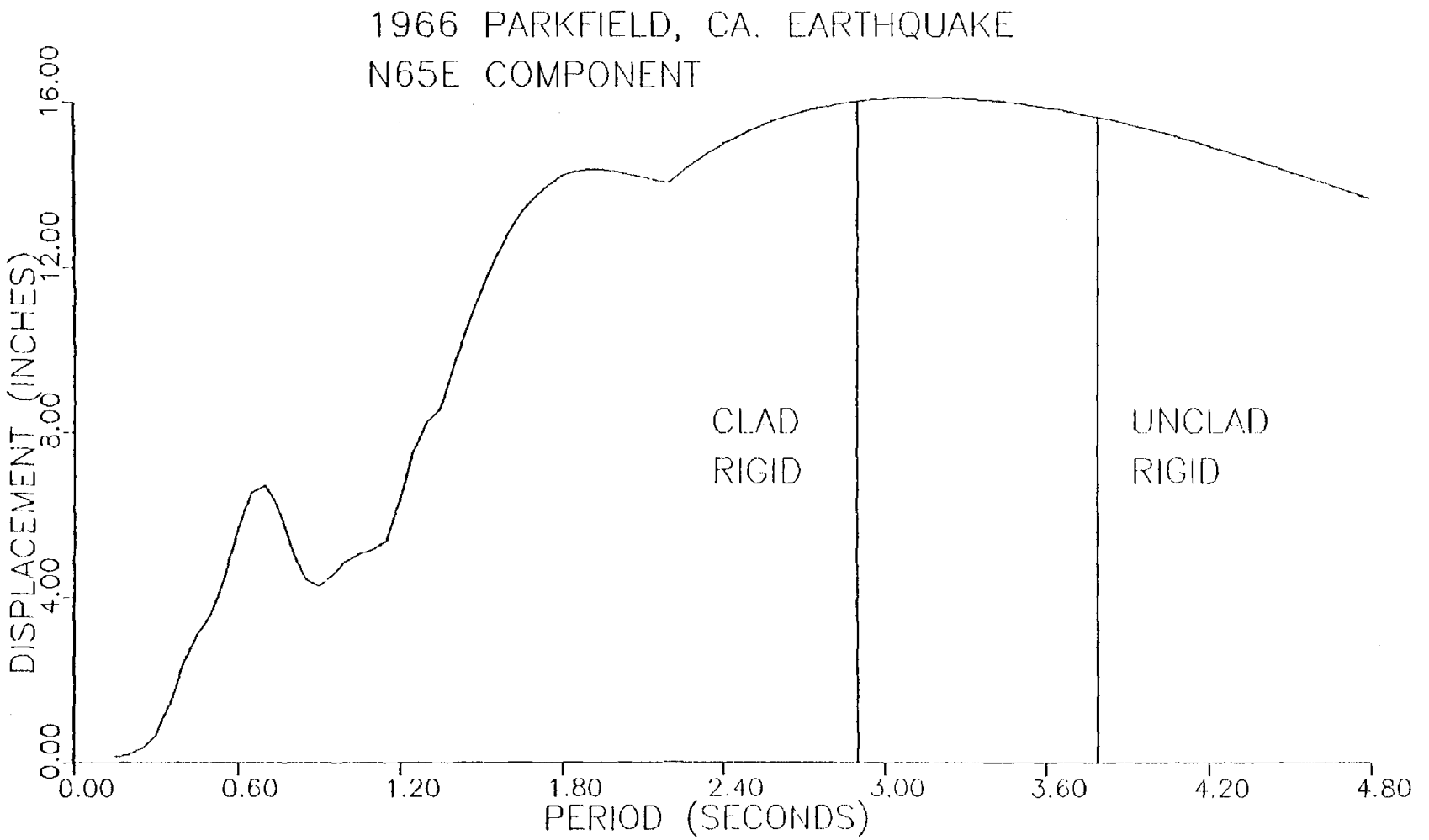

Figure 3.4-33. Relative Displacement Response Spectrum for N65E Component of the 1966 Parkfield Record with Fundamental Periods in Rigid Direction Shown for the Clad and Unclad Symmetric Models.

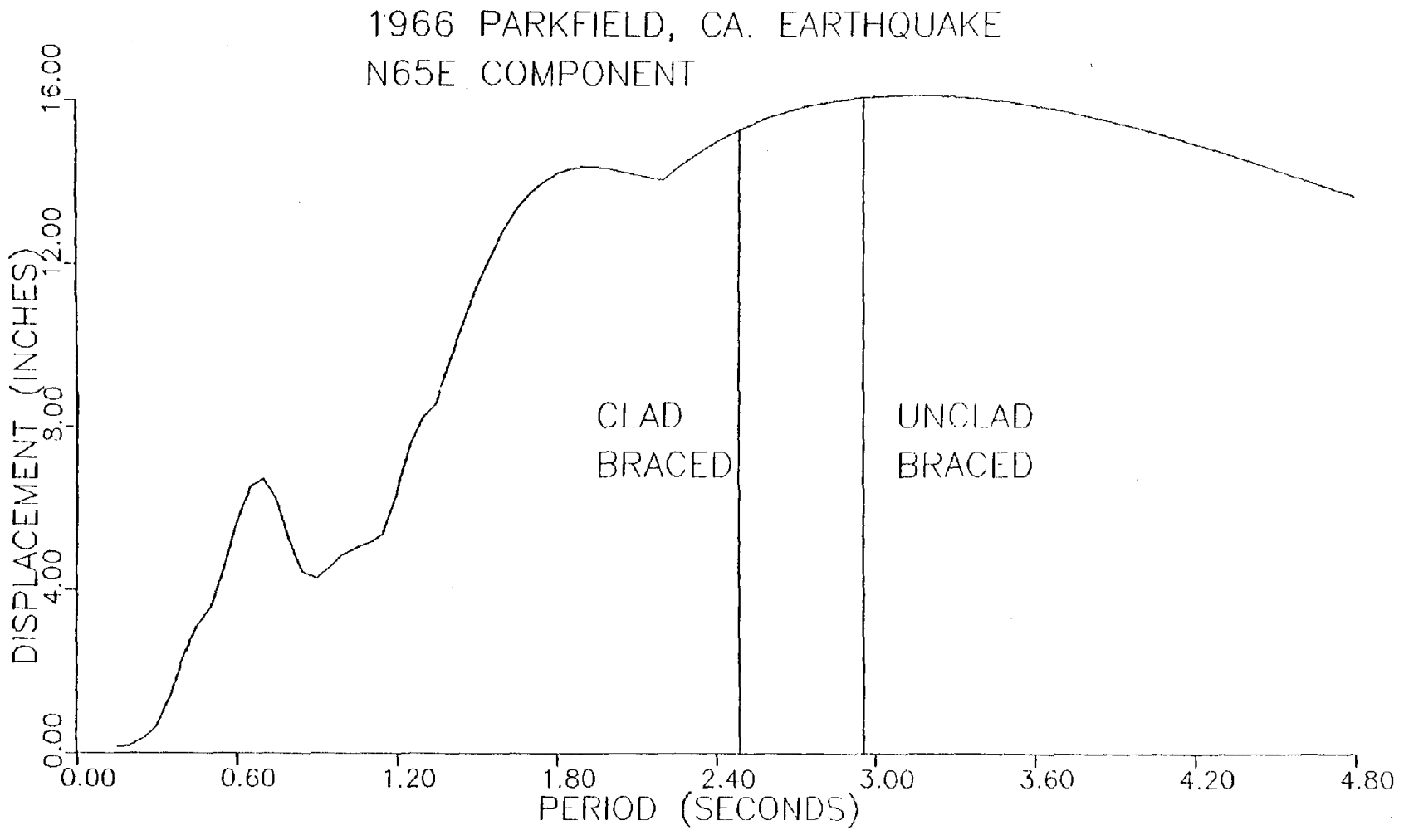

Figure 3.4-34. Relative Displacement Response Spectrum for N65E Component of the 1966 Parkfield Record with Fundamental Periods in Braced Direction Shown for the Clad and Unclad Symmetric Models.

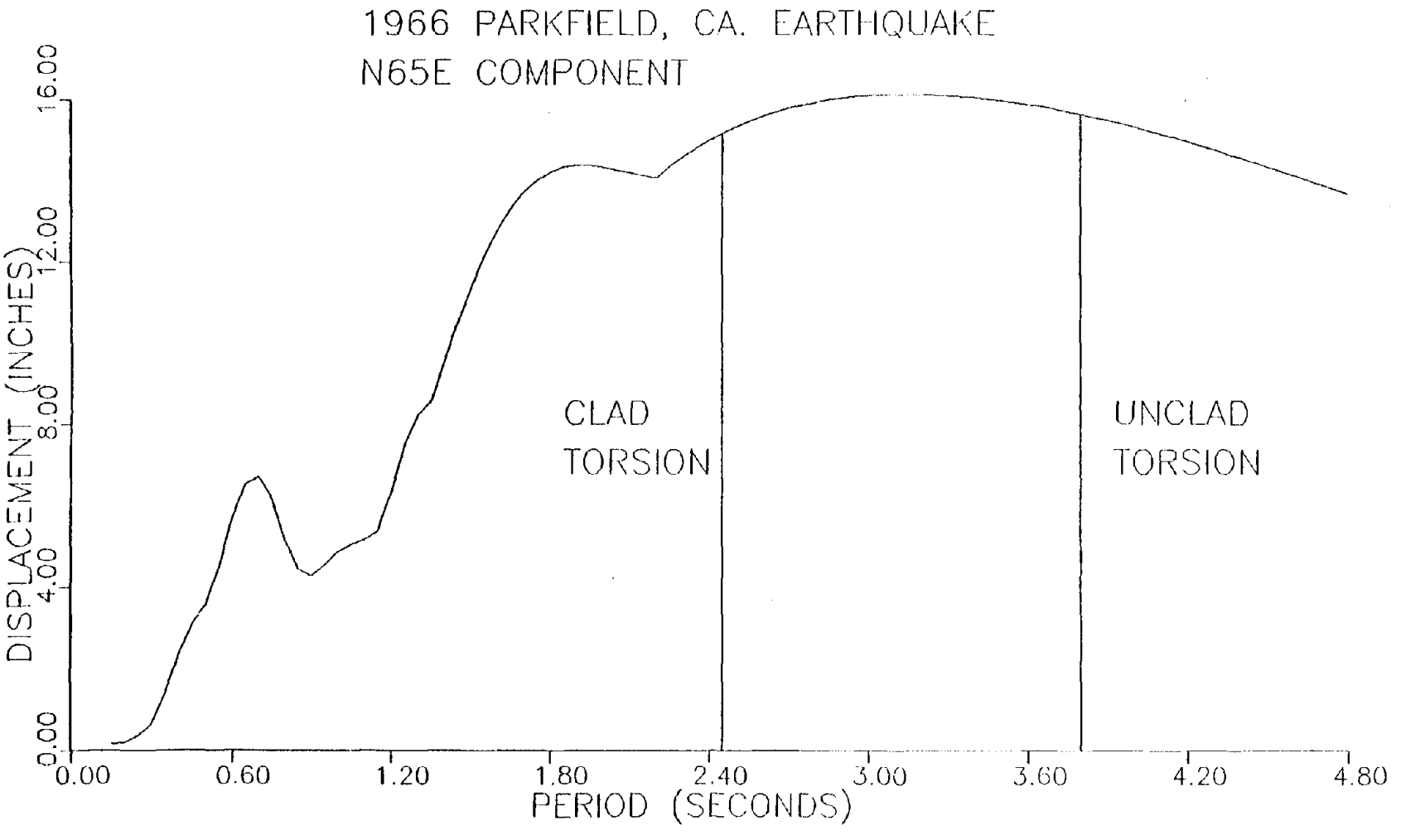

Figure 3.4-35. Relative Displacement Response Spectrum for N65E Component of the 1966 Parkfield Record with Fundamental Periods in Torsion Shown for the Clad and Unclad Symmetric Models.

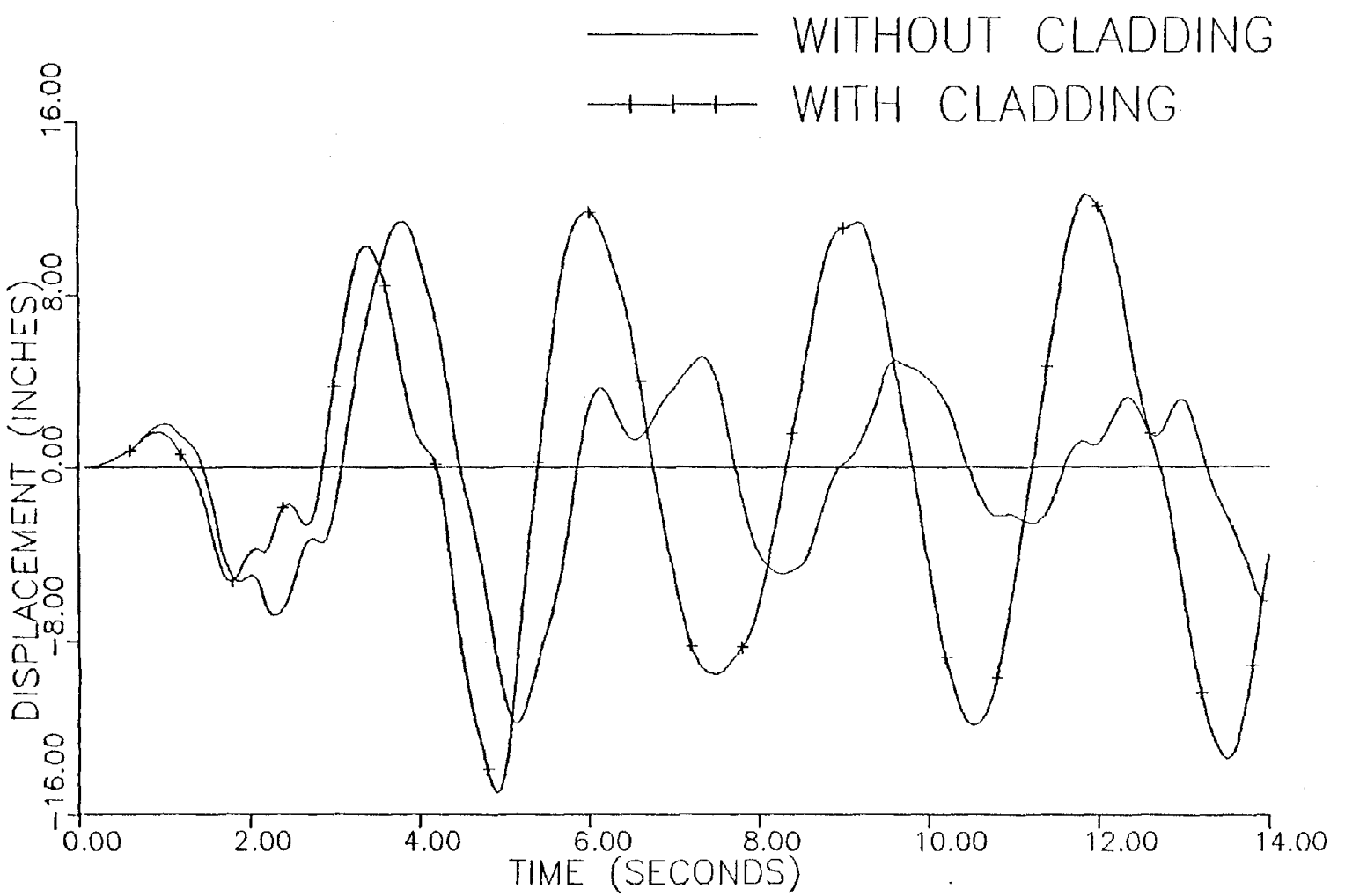

Figure 3.4-36. Roof Translational Response in Rigid Direction, Eccentric Case, for the First 14 Seconds of 1940 El Centro Record Acting in Rigid Direction.

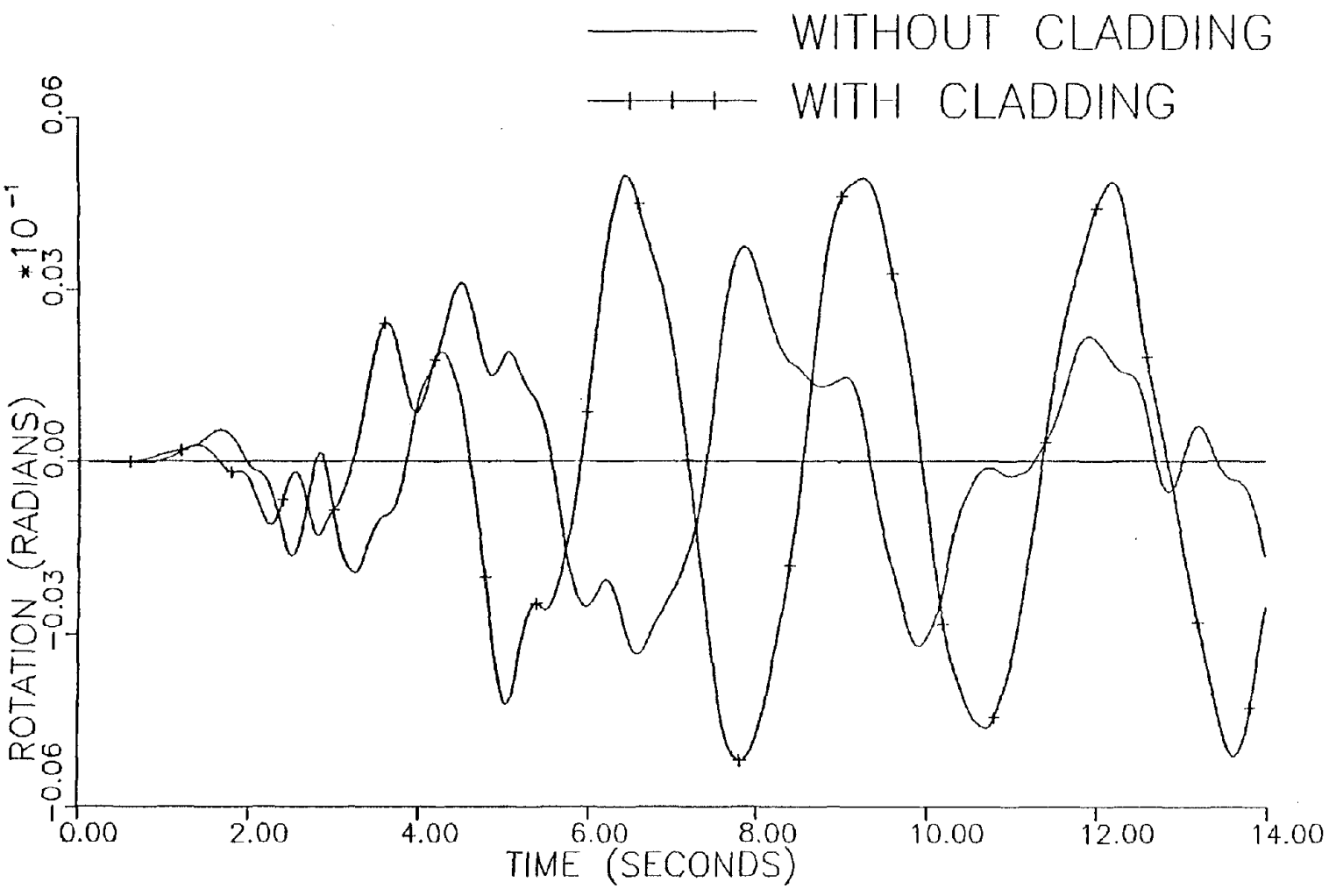

Figure 3.4-37. Roof Rotational Response, Eccentric Case, for the First 14 Seconds of 1940 El Centro Record Acting in Rigid Direction.

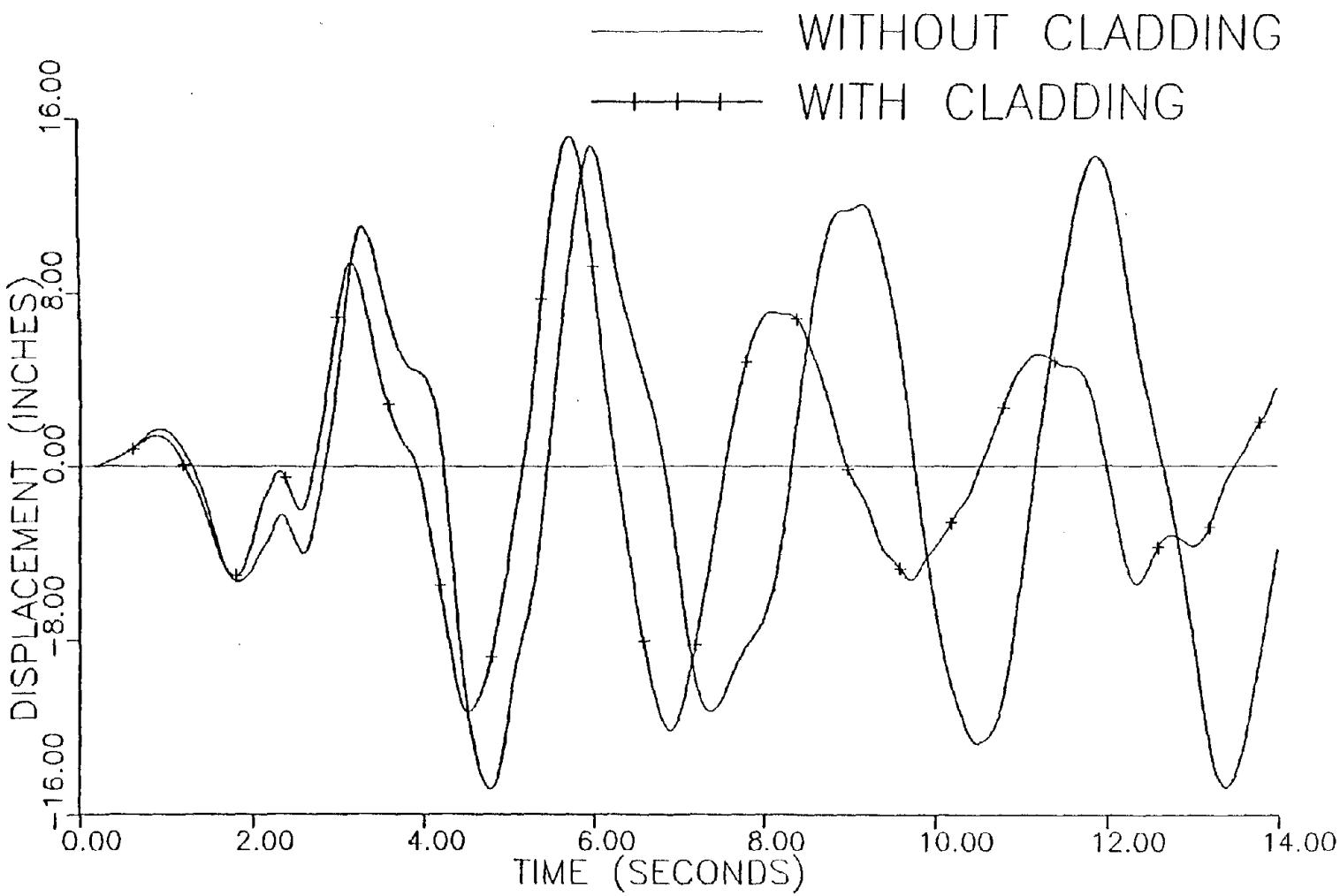

Figure 3.4-38. Roof Translational Response in Braced Direction, Eccentric Case, for the First 14 Seconds of 1940 El Centro Record Acting in Braced Direction.

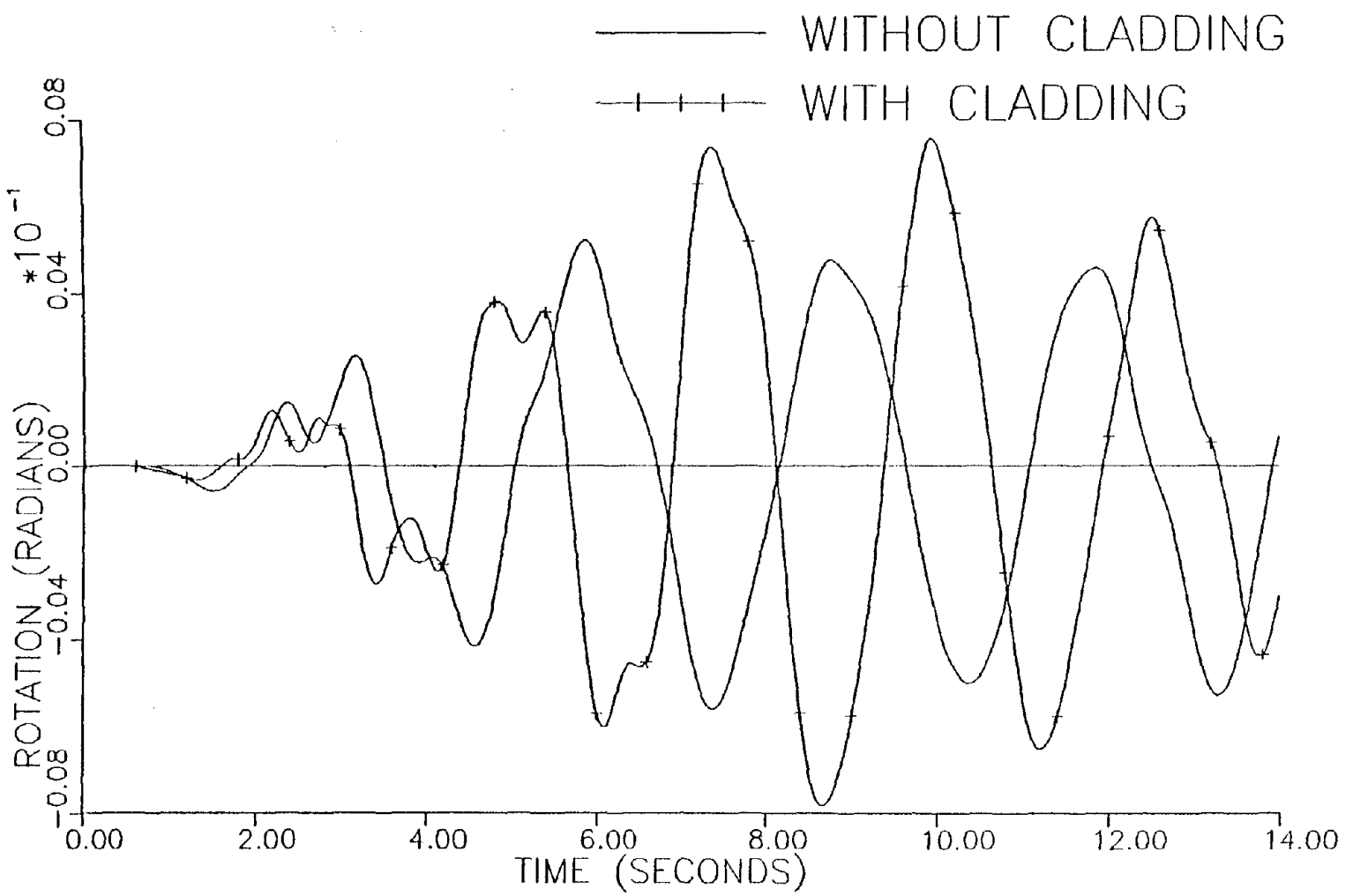

Figure 3.4-39. Roof Rotational Response, Eccentric Case, for the First 14 Seconds of 1940 El Centro Record Acting in Braced Direction.

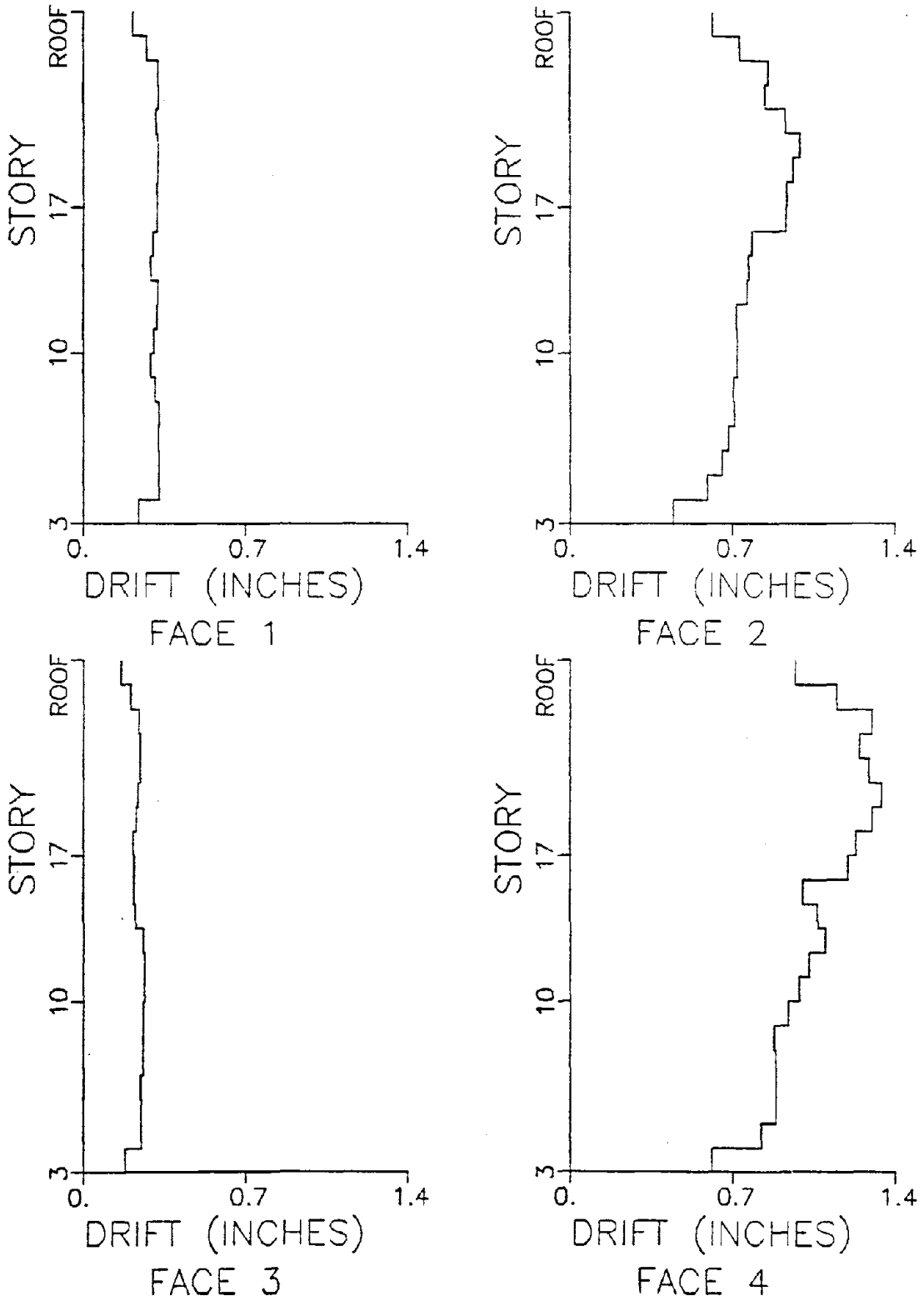

Figure 3.4-40. Peak Drift Values, Eccentric Case with Cladding, for 1940 El Centro Record Acting in Rigid Direction (See Fig. 3.4-18 for Symmetric Case).

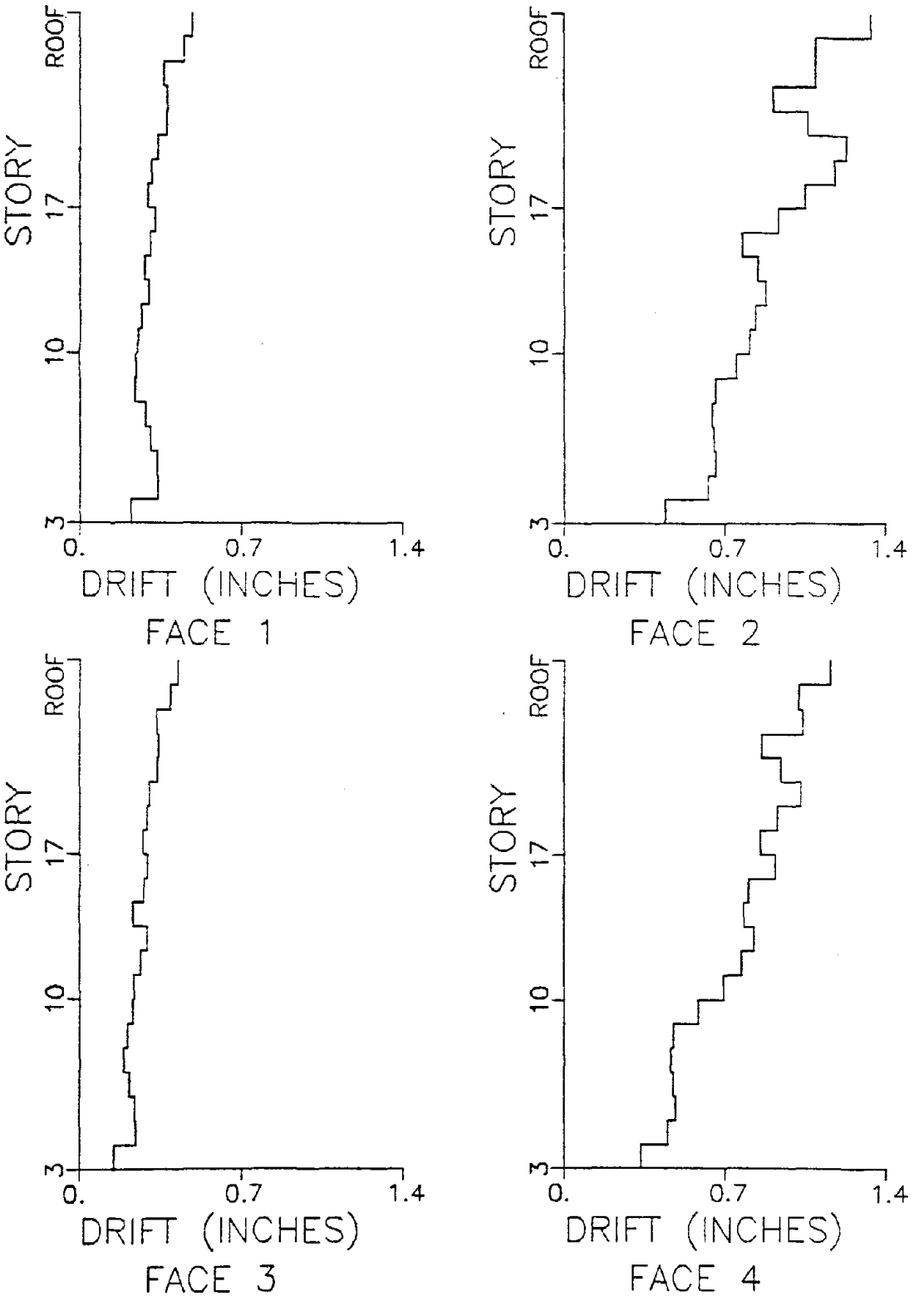

Figure 3.4-41. Peak Drift Values, Eccentric Case without Cladding, for 1940 El Centro Record Acting in Rigid Direction (See Fig. 3.4-19 for Symmetric Case).

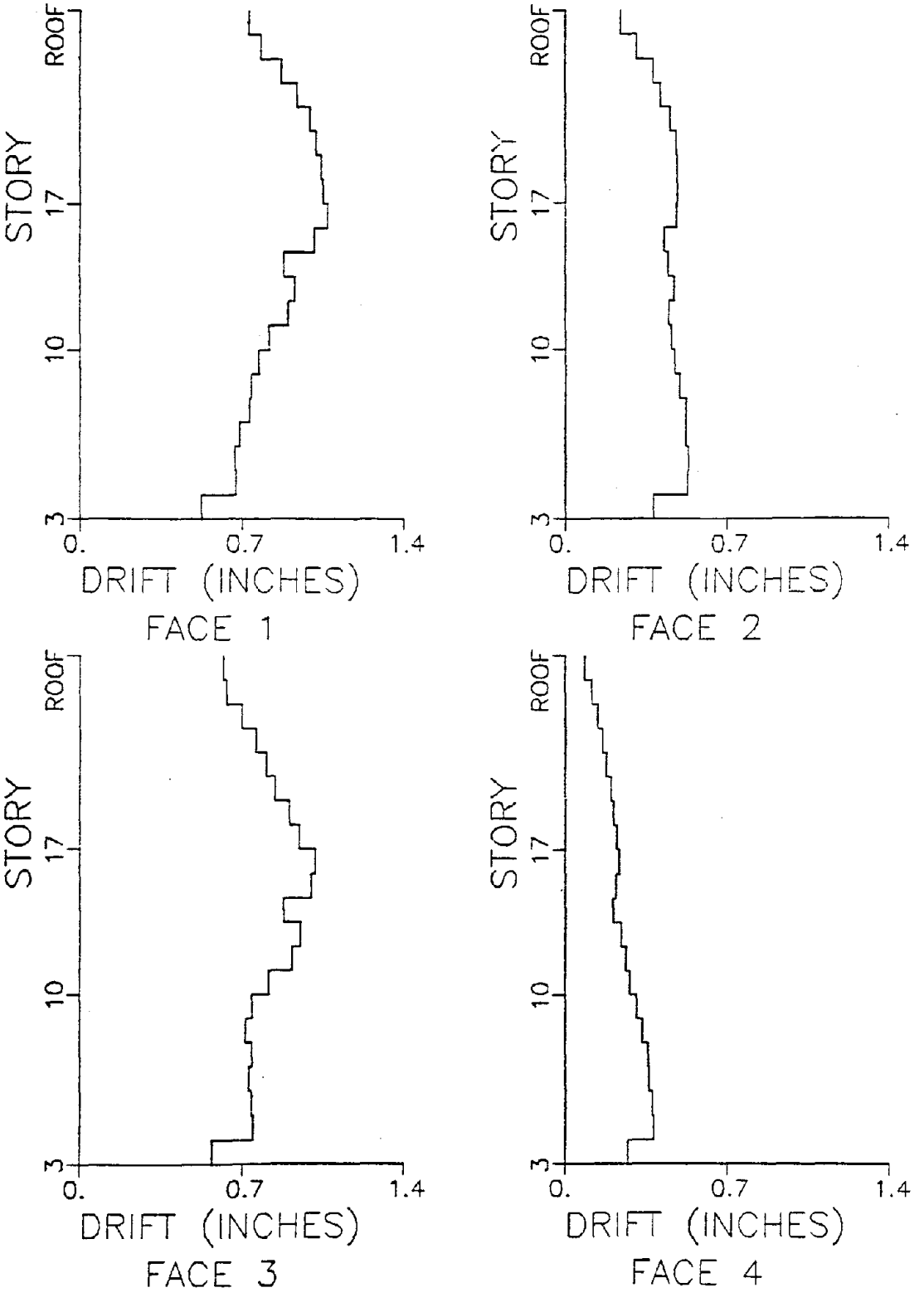

Figure 3.4-42. Peak Drift Values, Eccentric Case with Cladding, for 1940 El Centro Record Acting in Braced Direction (See Fig. 3.4-20 for Symmetric Case).

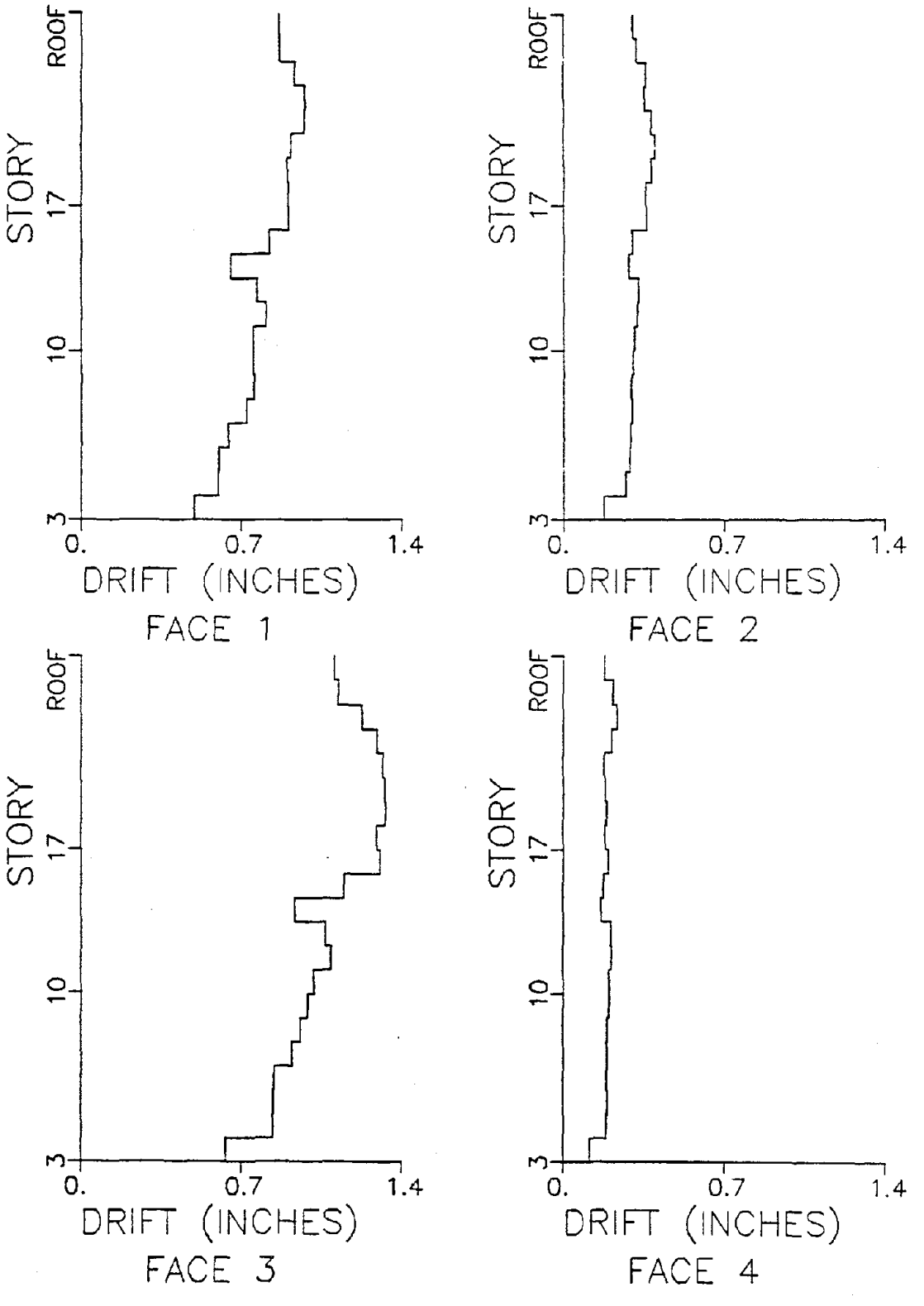

Figure 3.4-43. Peak Drift Values, Eccentric Case without Cladding, for 1940 El Centro Record Acting in Braced Direction (See Fig. 3.4-21 for Symmetric Case).

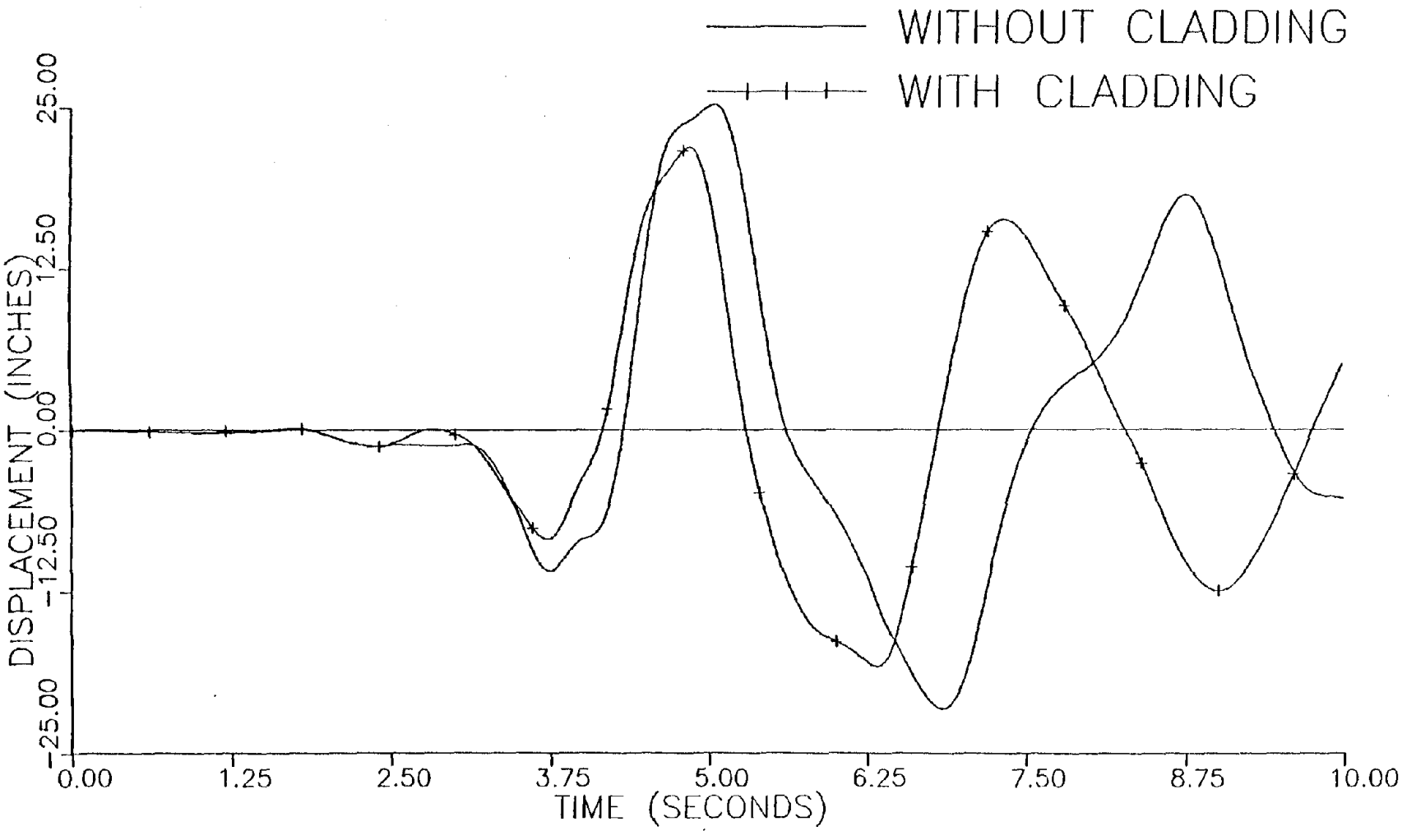

Figure 3.4-44. Roof Translational Response in Rigid Direction, Eccentric Case, for the First 10 Seconds of 1966 Parkfield Record Acting in Rigid Direction.

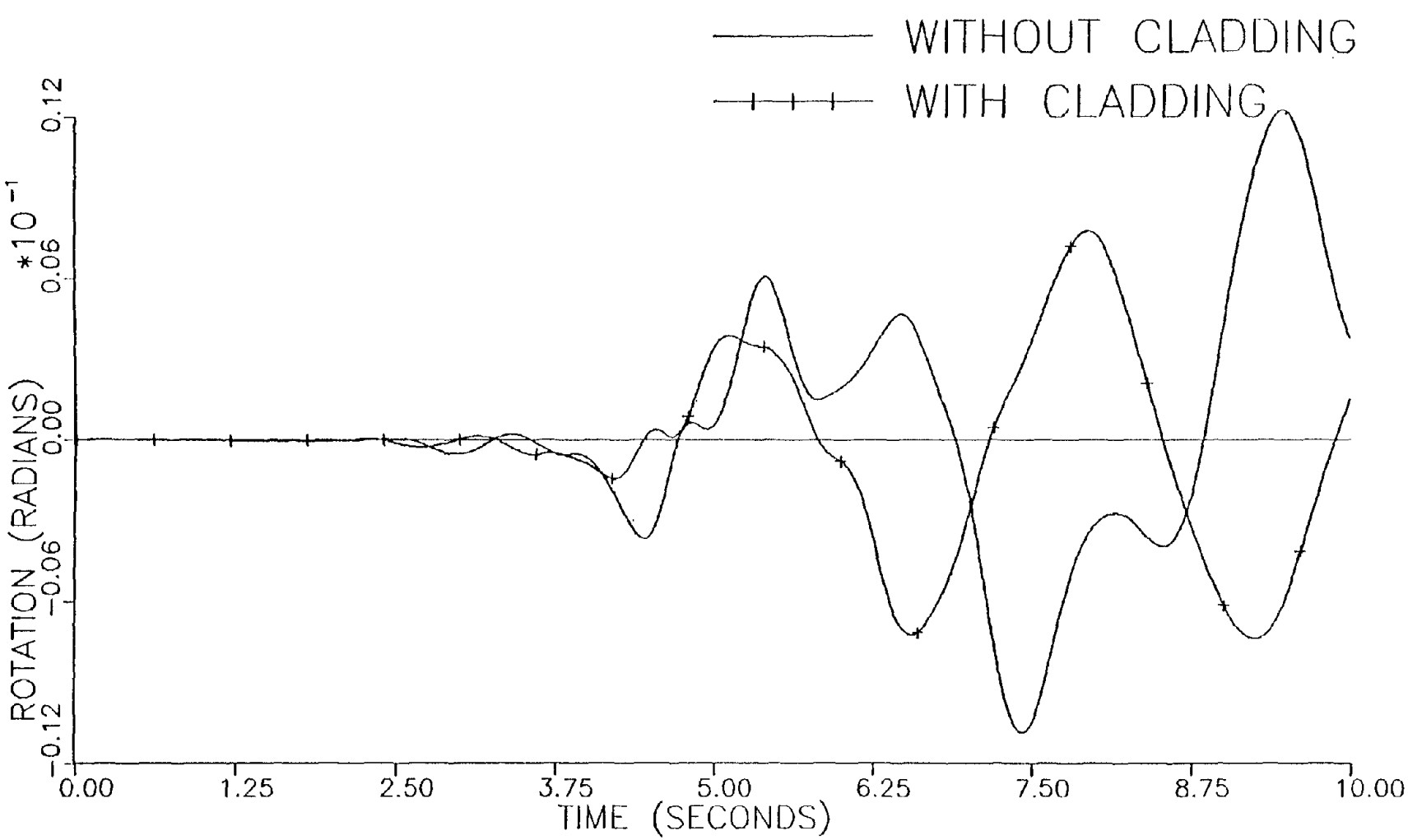

Figure 3.4-45. Roof Rotational Response, Eccentric Case, for the First 10 Seconds of 1966 Parkfield Record Acting in Rigid Direction.

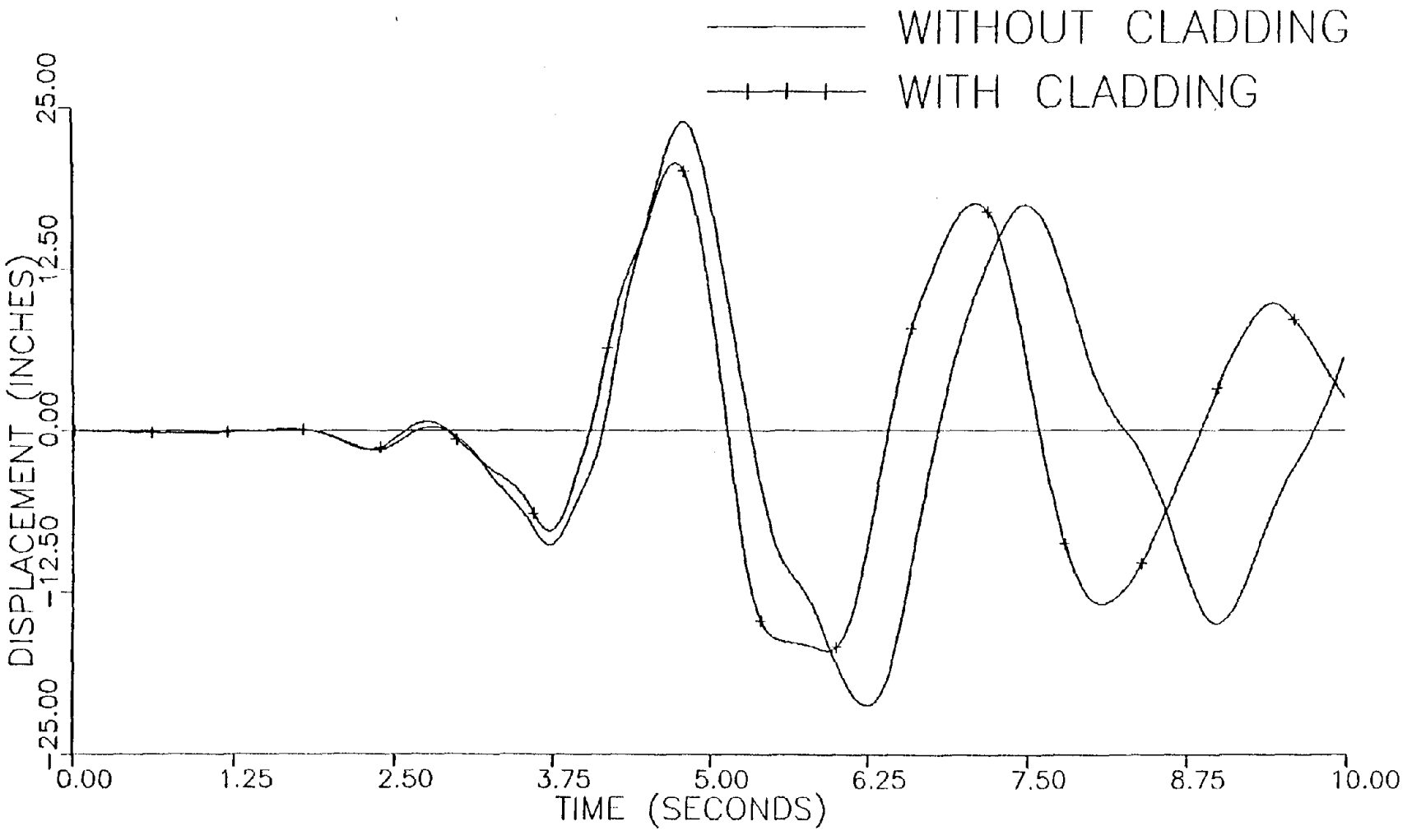

Figure 3.4-46. Roof Translational Response in Braced Direction, Eccentric Case, for the First 10 Seconds of 1966 Parkfield Record Acting in Braced Direction.

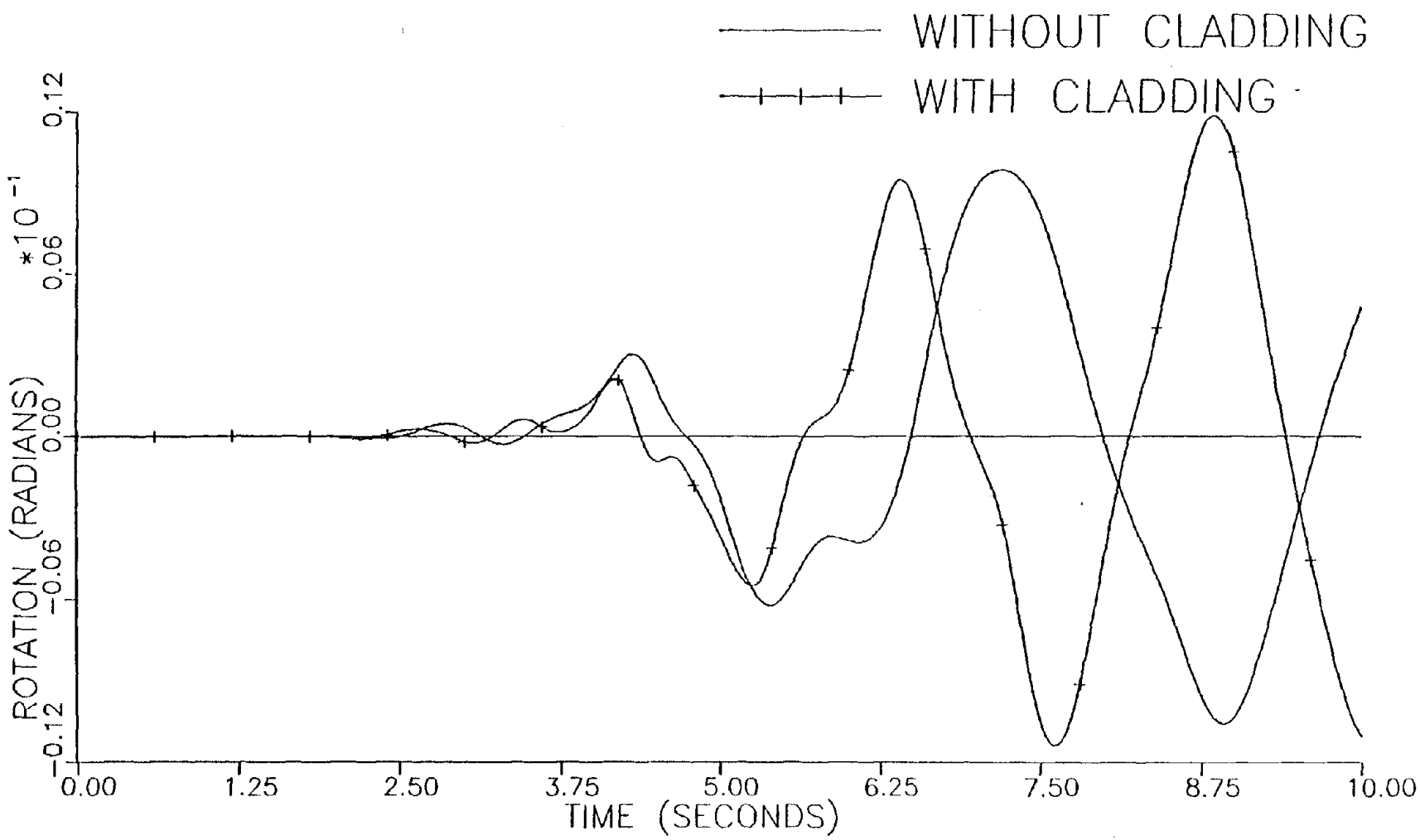

Figure 3.4-47. Roof Rotational Response, Eccentric Case, for the First 10 Seconds of 1966 Parkfield Record Acting in Braced Direction.

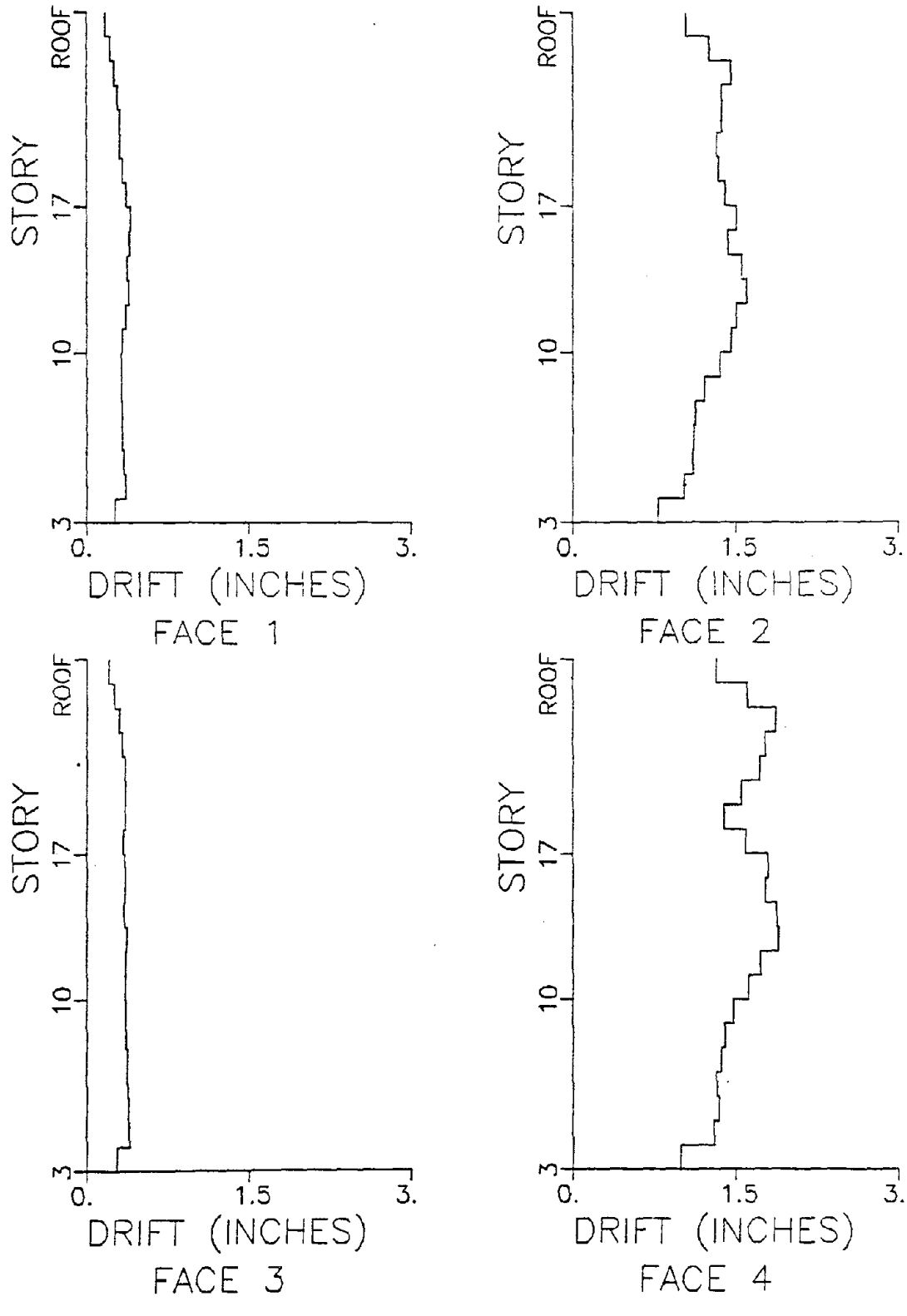

Figure 3.4-48. Peak Drift Values, Eccentric Case with Cladding, for 1966 Parkfield Record Acting in Rigid Direction (See Fig. 3.4-26 for Symmetric Case).

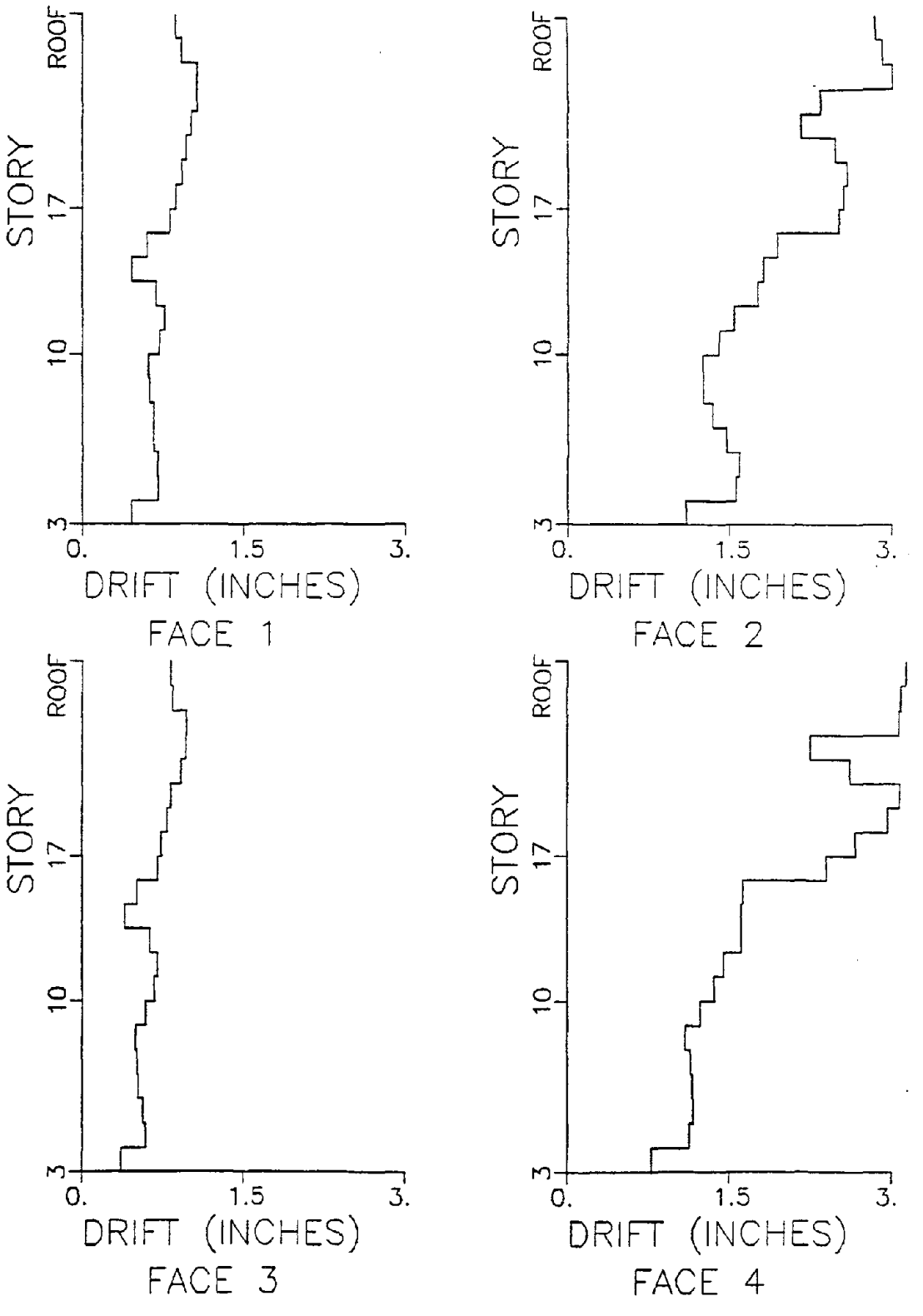

Figure 3.4-49. Peak Drift Values, Eccentric Case without Cladding, for 1966 Parkfield Record Acting in Rigid Direction (See Fig. 3.4-27 for Symmetric Case).

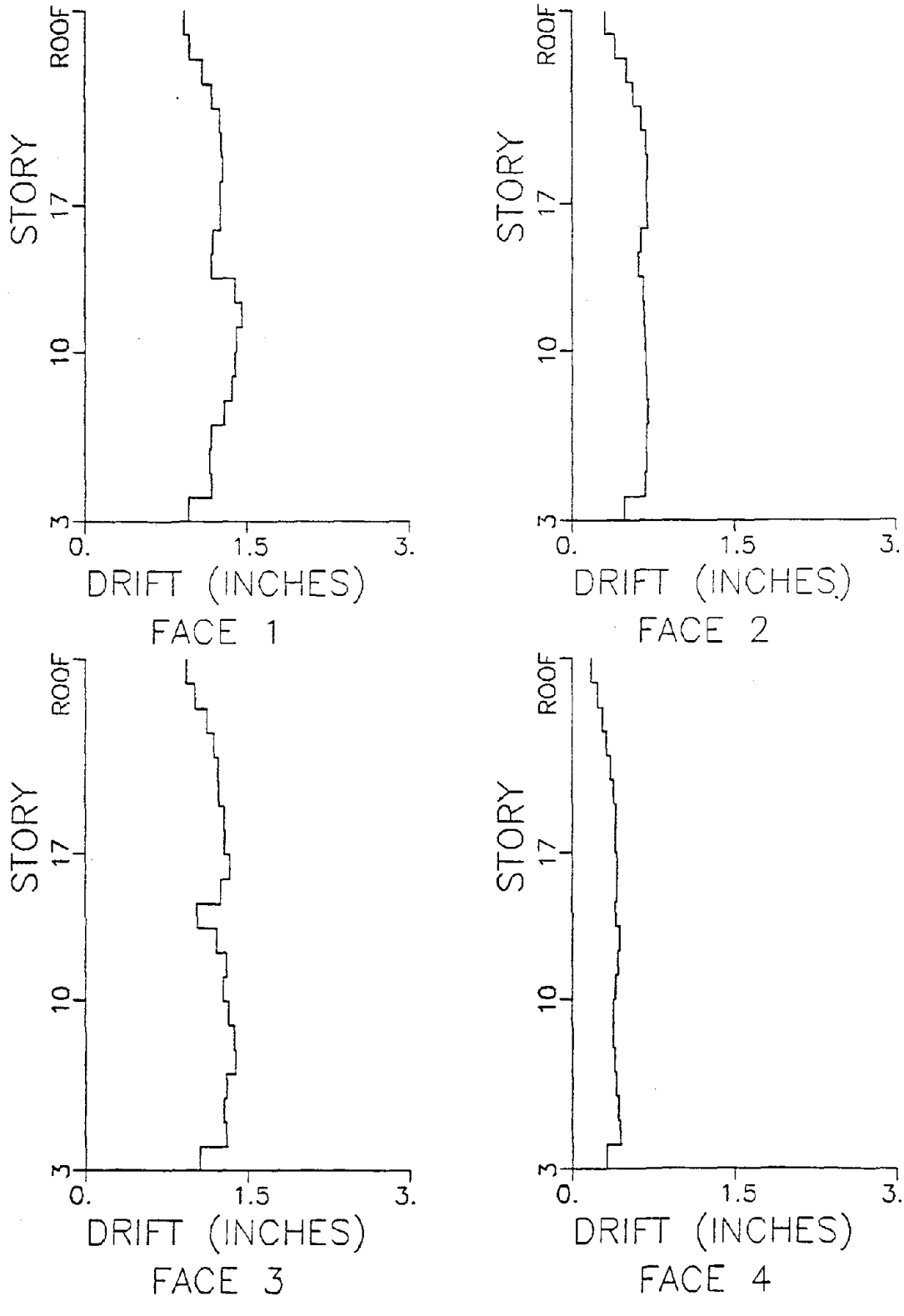

Figure 3.4-50. Peak Drift Values, Eccentric Case with Cladding, for 1966 Parkfield Record Acting in Braced Direction (See Fig. 3.4-28 for Symmetric Case).

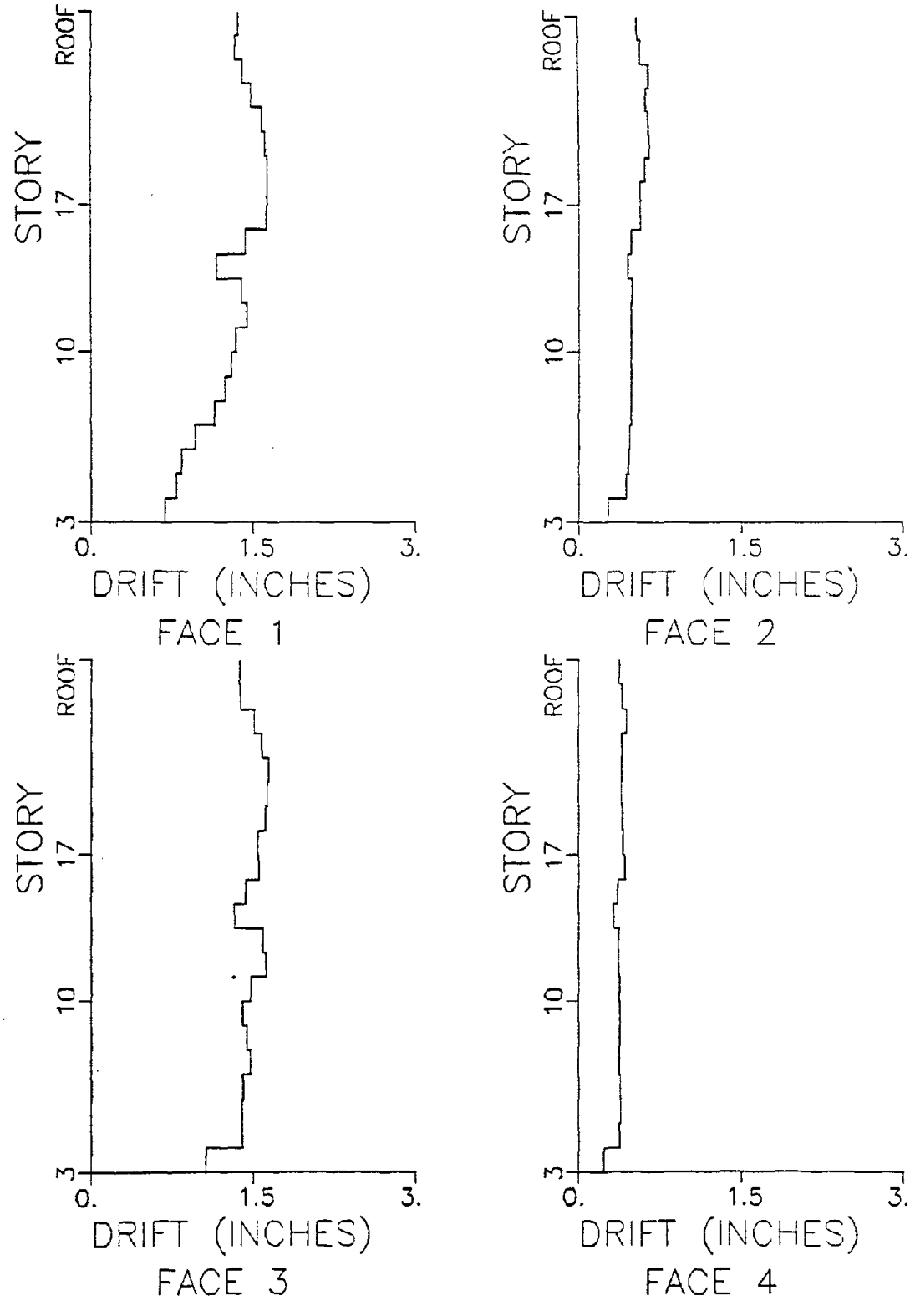

Figure 3.4-51. Peak Drift Values, Eccentric Case without Cladding, for 1966 Parkfield Record Acting in Braced Direction (see Fig. 3.4-29 for Symmetric Case).

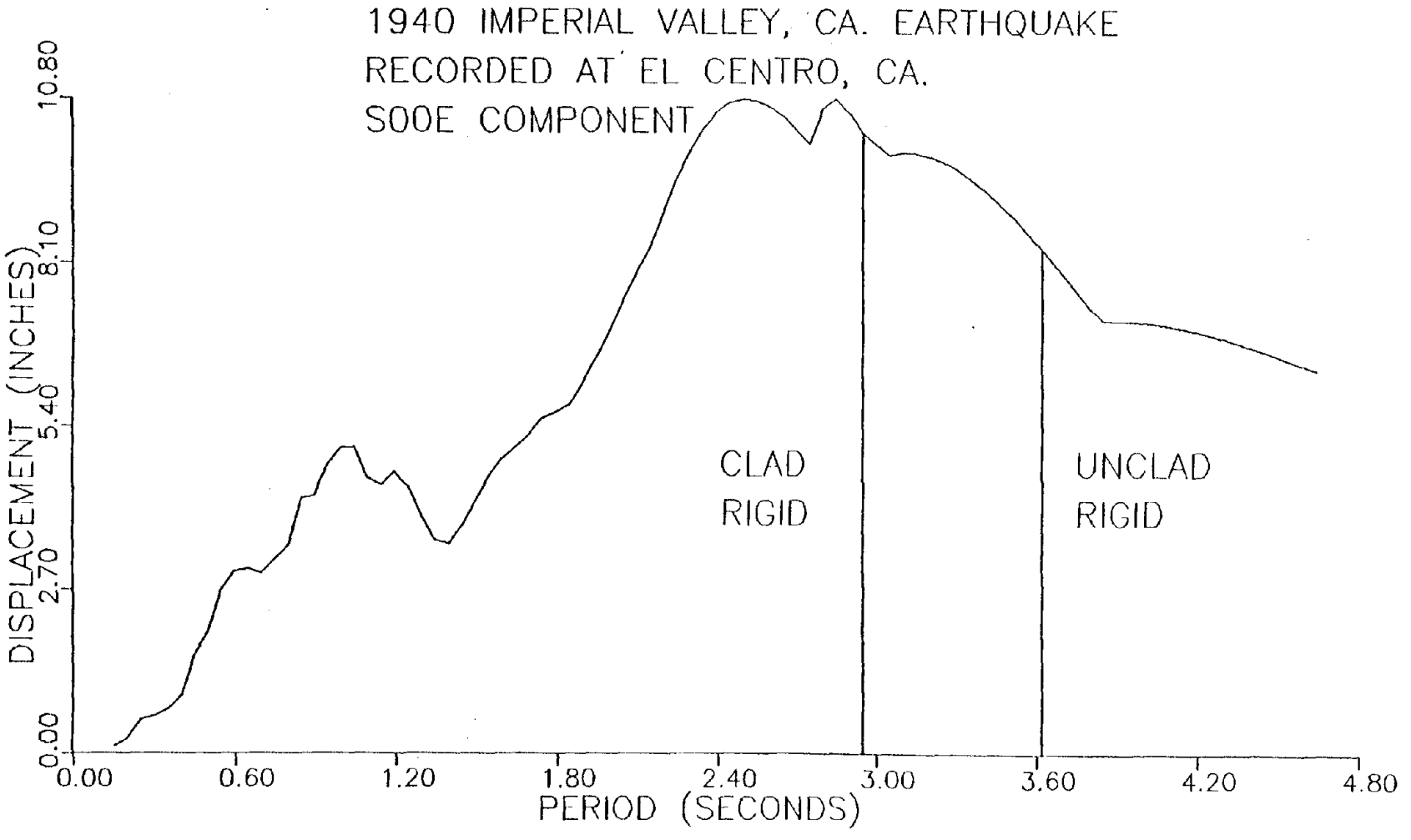

Figure 3.4-52. Relative Displacement Response Spectrum for S00E Component of the 1940 El Centro Record with Fundamental Periods in Rigid Direction Shown for the Clad and Unclad Eccentric Models.

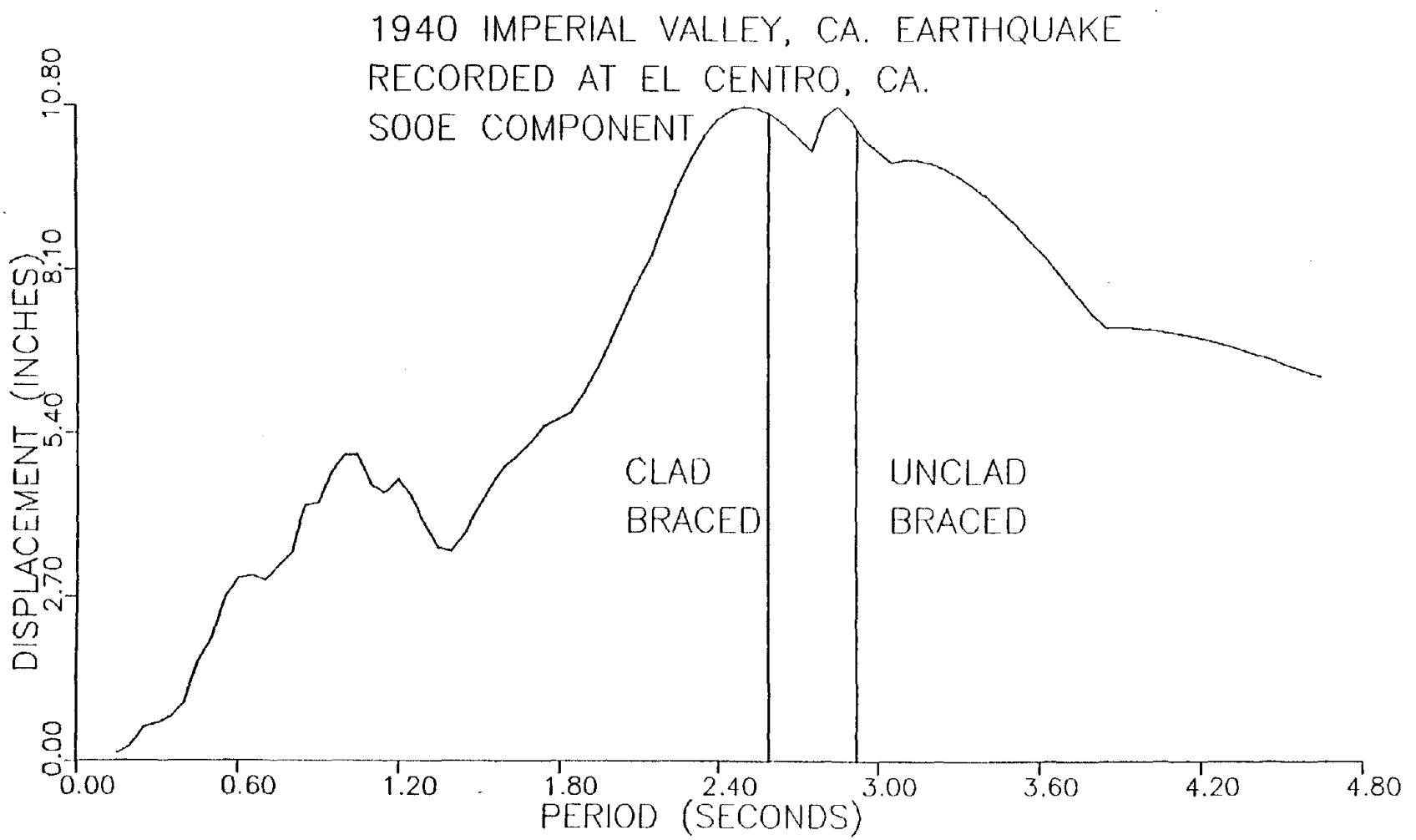

Figure 3.4-53. Relative Displacement Response Spectrum for S00E Component of the 1940 El Centro Record with Fundamental Periods in Braced Direction Shown for the Clad and Unclad Eccentric Models.

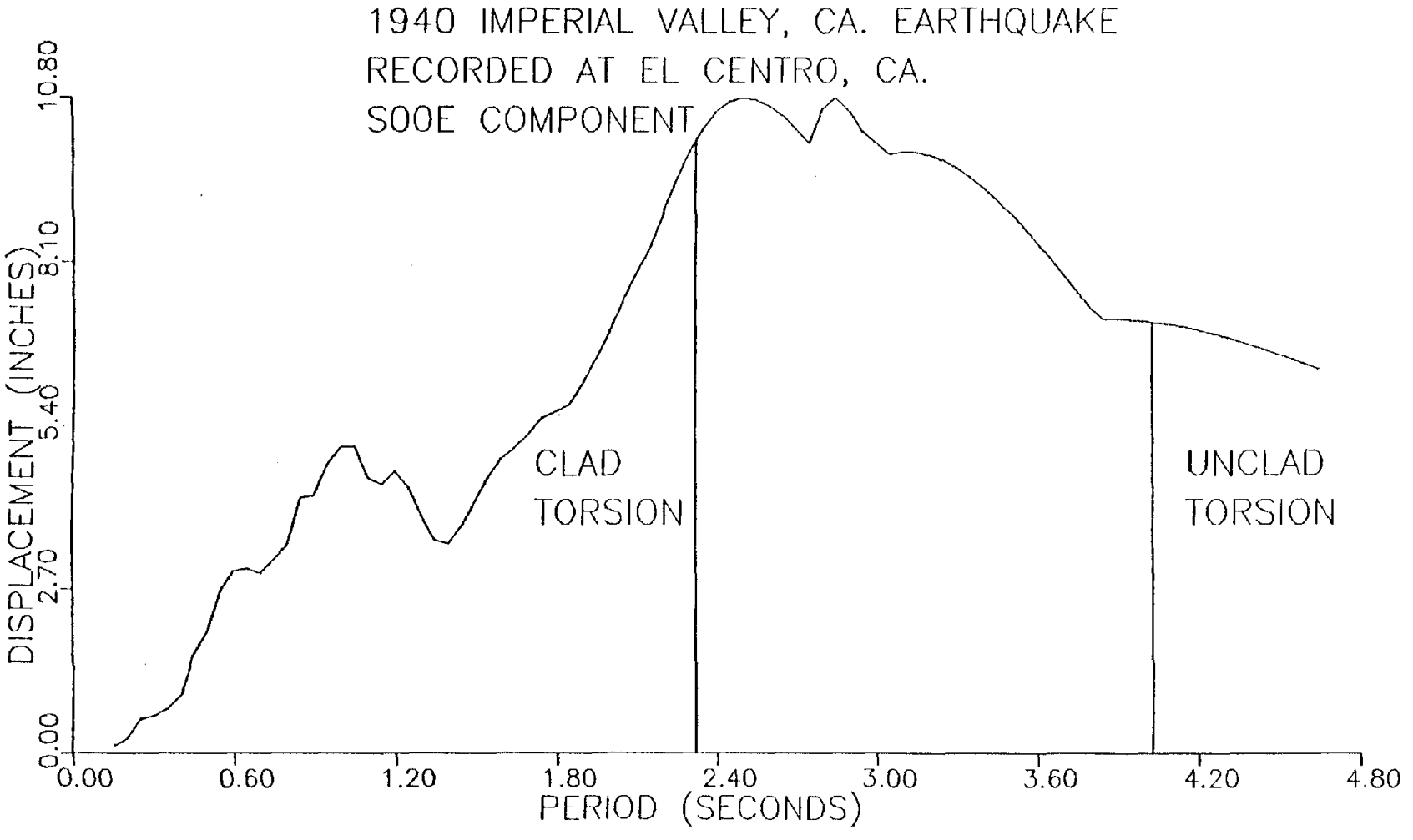

Figure 3.4-54. Relative Displacement Response Spectrum for S00E Component of the 1940 El Centro Record with Fundamental Periods in Torsion Shown for the Clad and Unclad Eccentric Models.

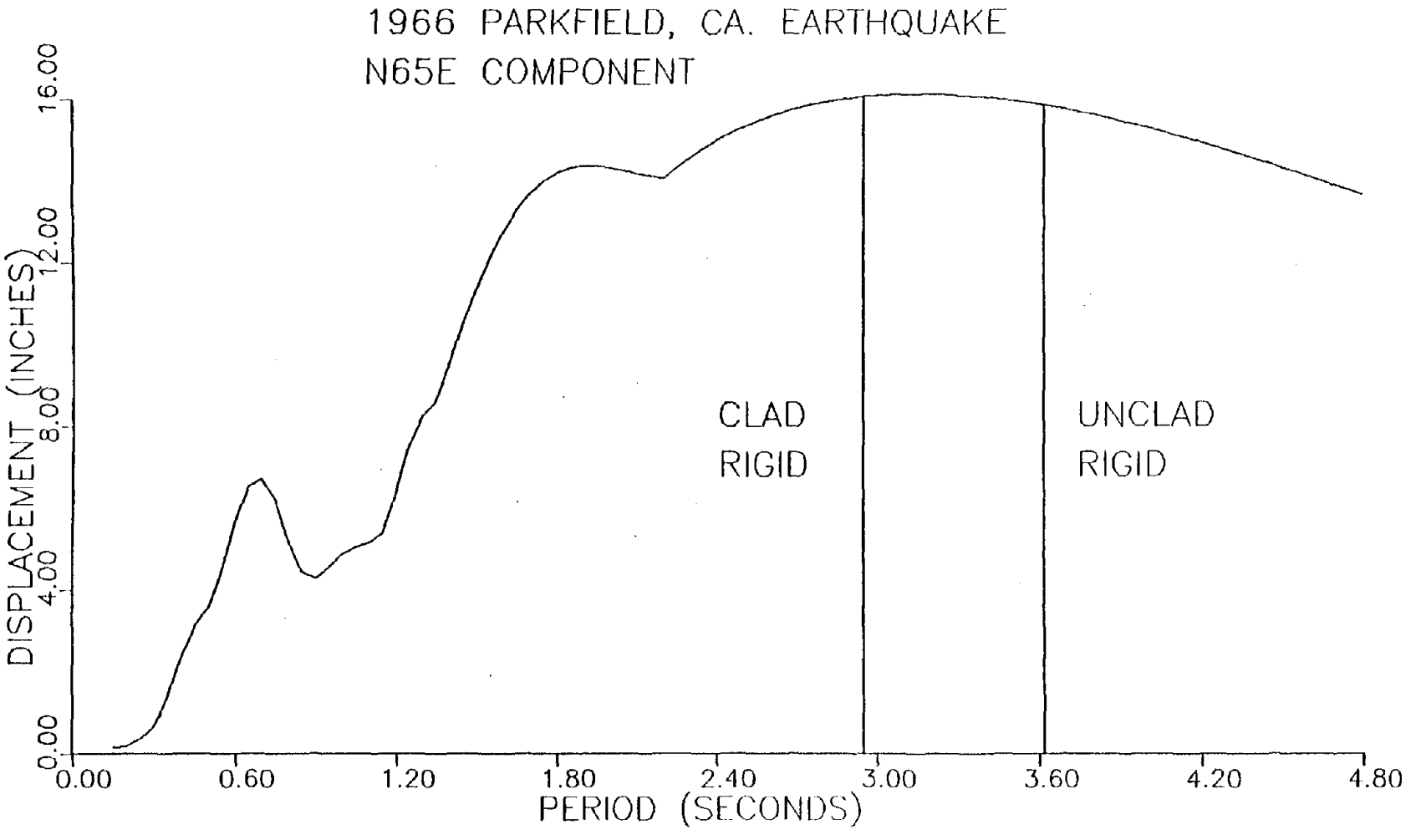

Figure 3.4-55. Relative Displacement Response Spectrum for N65E Component of the 1966 Parkfield Record with Fundamental Periods in Rigid Direction Shown for the Clad and Unclad Eccentric Models.

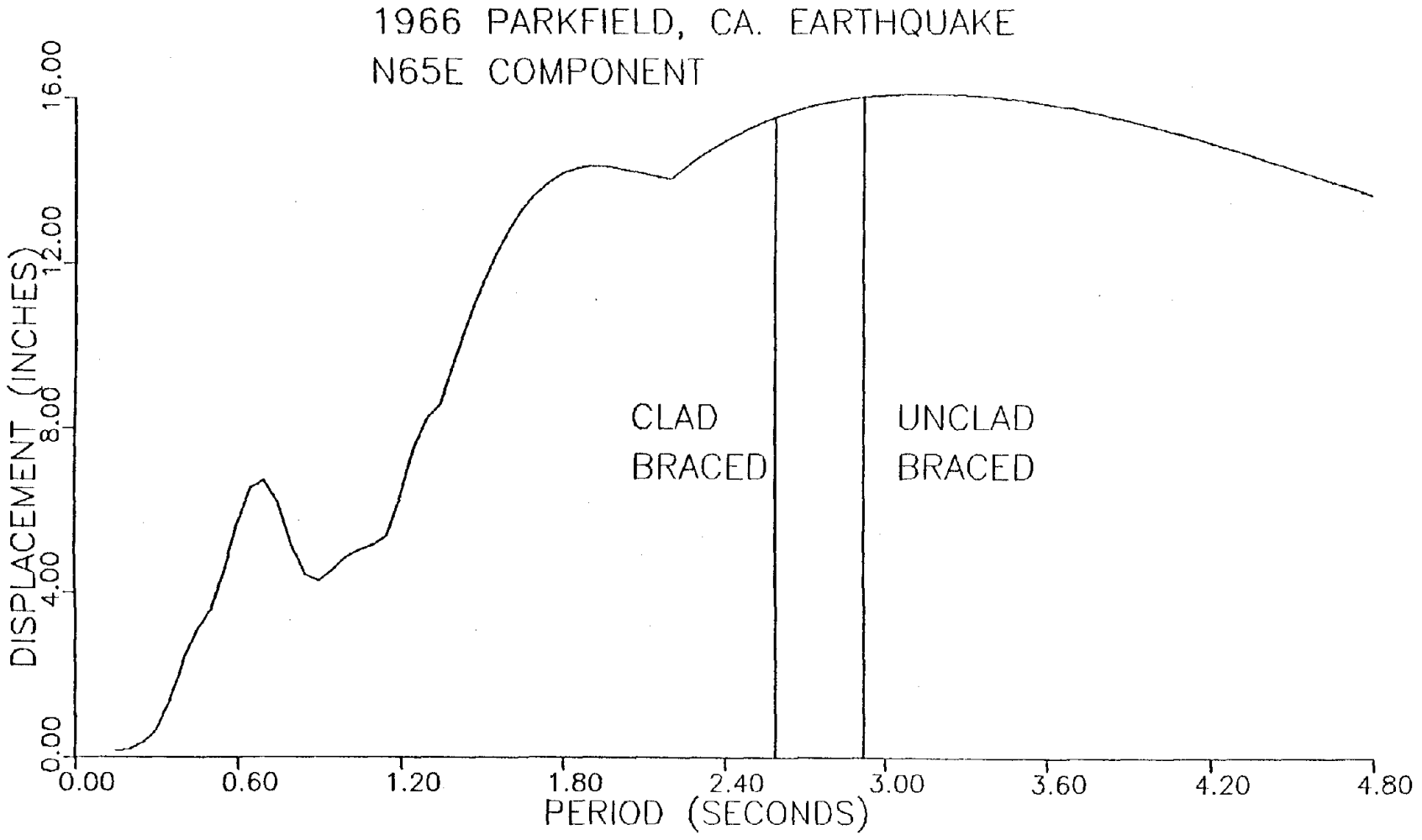

Figure 3.4-56. Relative Displacement Response Spectrum for N65E Component of the 1966 Parkfield Record with Fundamental Periods in Braced Direction Shown for the Clad and Unclad Eccentric Models.

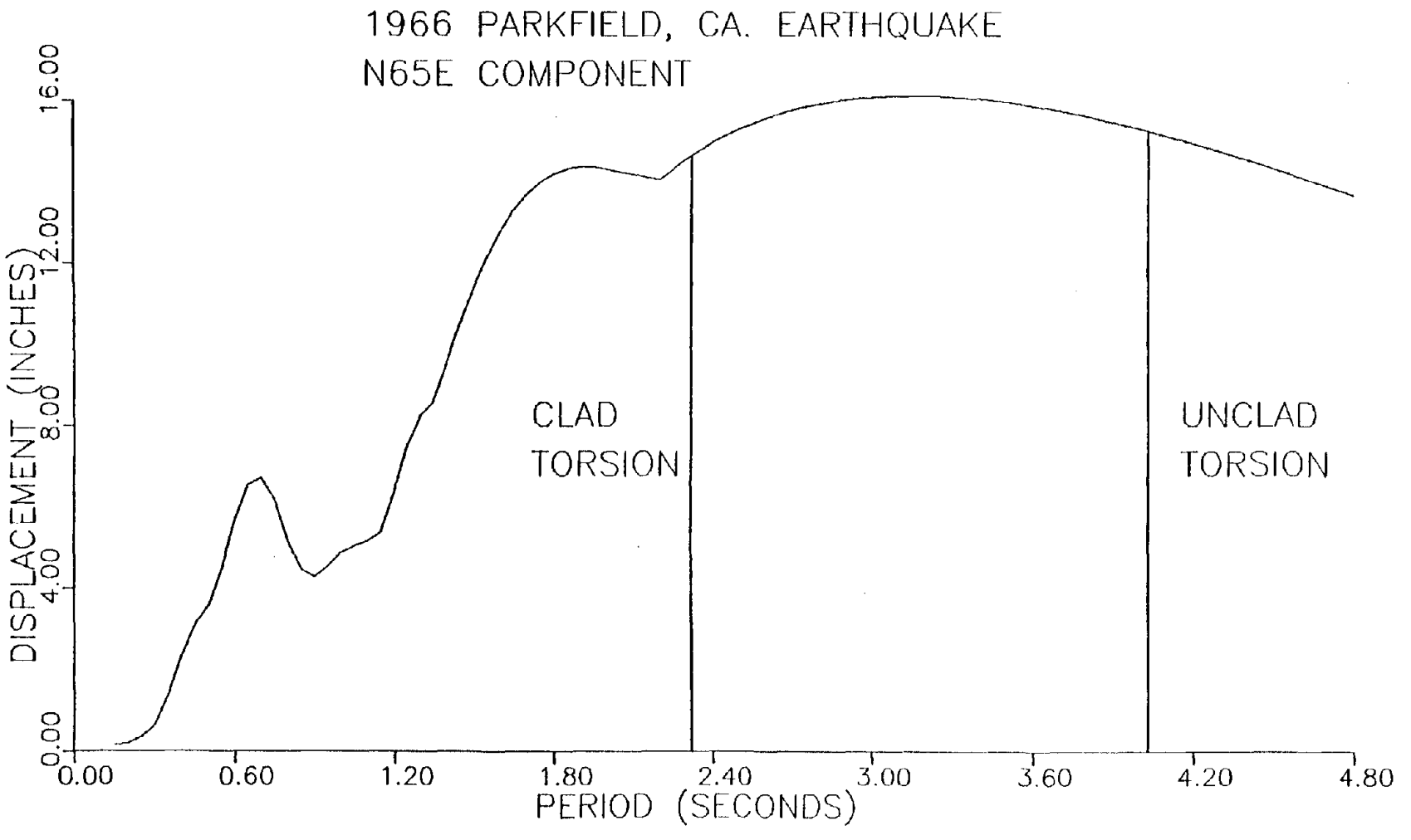

Figure 3.4-57. Relative Displacement Response Spectrum for N65E Component of the 1966 Parkfield Record with Fundamental Periods in Torsion Shown for the Clad and Unclad Eccentric Models.

4. NONLINEAR DYNAMIC RESPONSE STUDIES

4.1 Introduction

A number of recent studies [17, 22, 42, 53] of curtain wall behavior have shown that heavyweight cladding systems might alter building frequencies and dynamic response to a substantial degree depending upon the panel configuration and attachment details. The potential influence of the curtain wall was usually neglected by designers despite the fact that the added lateral stiffness of the cladding might result in increased lateral-torsional response for certain moderate ground motion inputs as discussed in Chapter 3. It appeared likely that strong ground motion would result in partial cladding failure and/or cladding connection slip once allowable interstory drift limits, based on cladding and connection properties, were exceeded. Nonlinear structural response, a general reduction in building lateral stiffness, and increased torsional response were expected to occur as a result of the cladding stiffness degradation.

In the absence of experimental data for the cladding, four different nonlinear force-deformation relationships for the cladding and its connections were studied. Several different hysteresis models for reinforced concrete have been used in the literature [40]. Their existence was acknowledged but they were not expected to represent a good approximation of cladding behavior. The various cladding models considered in this chapter were added to the linear elastic model of the unclad building structure and their influence on structure response investigated. Allowable

drift values were varied based on code recommendations [49] and design practice [19], since actual measured cladding properties were not available, and structure dynamic response to the ground motion loadings listed in Table 3.4-3 computed. Interstory drift was monitored on each face and at each story level of the structure, and when allowable values were exceeded structure stiffness was adjusted and response calculations continued. Results are presented below in the form of peak interstory drift values for the different structure faces, peak roof displacement responses, plots of peak interstory drift at each story level for the four faces, and figures of roof displacement time-histories.

4.2 Incremental Failure Model

4.2.1 Description of Model

In the absence of experimental data describing the behavior of a typical cladding panel, the simplified panel response model depicted in Fig. 4.2-1 was developed for initial studies of the influence of cladding failure on overall structure response. Loading and unloading and reversed cycle curves were idealized to be straight lines with decreasing slope (stiffness) for panels at story levels which exceeded code-specified allowable drift levels, Δ. Initial stiffness was taken to be 625 kips/inch (1.1×10^5 kN/m) based on parameter studies for the composite model discussed earlier. For drift values greater than Δ and up to 2Δ, one half of the cladding panels at that story level were assumed to fail resulting in an effective shear stiffness from that point on over the entire 0 to 2Δ range of V = 312.5 kips/inch (5.5×10^4 kN/m). When interstory drift exceeded 2Δ, an additional one half of the remaining panels at that story level were assumed to fail giving V = 156.25 kips/inch

(2.7×10^4 kN/m); and beyond 3Δ, V was taken to be 0. Reverse cycle deflections followed the curve of constant slope which described the current state of the cladding lateral stiffness.

The simple cladding model described above was assumed to be an adequate initial assumption of gross failure states of cladding which permitted the analyst to monitor the state of the cladding at each story level on each face of the building.

Overall structure dynamic response was computed step by step using the procedure discussed in Section 3.2 and the state of the cladding determined on the basis of a check of story drift values on each face at the end of each time step. When the state of the cladding changed, the overall stiffness properties were adjusted based on the force-displacement relationship for the cladding model, and the step-by-step analysis was then continued. Five percent modal damping based on initial stiffness was assumed throughout the time-history analysis as in Chapter 3 and no adjustment was made in damping level as cladding failure progressed. It was realized that this might not represent actual damping levels during cladding failure but given the knowledge about damping or the lack thereof, this was felt to serve as an adequate approximation.

4.2.2 Response Studies Using the Eccentric Mass Model

The minimum 5% eccentricity between center of mass and center of rigidity in each structure direction was used, as required by UBC and described above in Chapter 3, as the basis for combined translational and torsional response studies using the incremental failure model for cladding. Given the lack of experimental data, allowable drift levels were varied based on Code recommendations [49] and design practice [19],

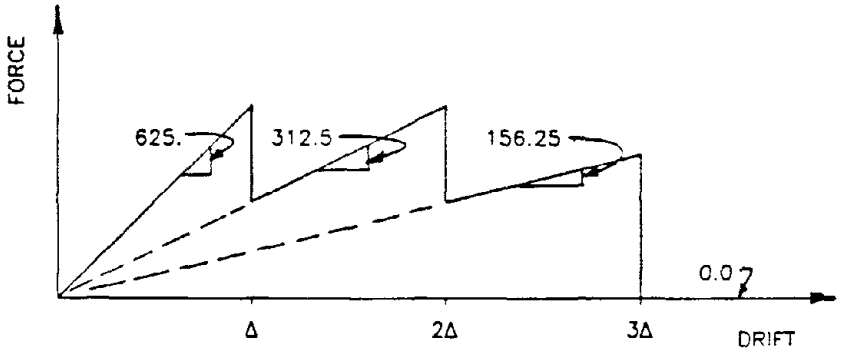

Figure 4.2-1. Cladding Failure Model.

and the influence of different cladding behavior on overall structure response investigated. Four allowable interstory drift (Δ) conditions were considered:

(1) Δ = 0 (i.e., all cladding fails immediately resulting in interstory shear stiffness V = 0).

(2) Δ = 0.0025 times an average story height of 12 feet (i.e., Δ = 0.36 inches or 0.9 cm). This condition corresponds to current design practice in the New York City area in which maximum allowable drift is limited to 0.0025 times story height for highrise curtain wall office buildings [19].

(3) Δ = 0.005 times an average story height of 12 feet (i.e., Δ = 0.72 inches or 1.8 cm). Code recommendations specify that drift of a story relative to its adjacent stories should not exceed 0.005 times story height unless toleration of increased values is demonstrated.

(4) Δ = infinity (i.e., no cladding failure regardless of drift level, V = 625 kips/inch or 1.1×10^5 kN/m).

Conditions (1) and (4) represent the unclad and fully clad states, respectively, for the eccentric structure model (see Section 3.4.3) and may be considered as limiting cases for conditions (2) and (3). In conditions (2) and (3), the piecewise-linear cladding stiffness model was employed to track the progressive failure of cladding panels on different faces and at different story levels in the structure.

First, the structure response to the 1940 El Centro earthquake record was computed. Only the first 14 seconds of the record were used as discussed in Section 3.4.2. Peak roof displacement response values are listed in Table 4.2-1 for the braced and rigid frame directions and

translational and rotational displacement time-histories of roof response are presented in Figs. 4.2-2 to 4.2-5. While peak response values increased in the direction of applied ground motion with increasing allowable drift (Δ) values (i.e., conditions (1) to (4) above), that was not the case in three instances out of four for the other directions (see Table 4.2-1). For example, for ground motion applied in the braced direction, the rigid direction roof response for condition (2) was lower than for any of the other three conditions while the rigid response for condition (3) was the highest. Also, for braced direction input, roof rotational response for conditions (2) and (3) was higher than for both condition (1) and (4) with condition (2) response being the larger of the two. In addition, peak relative interstory drift values for the different structure faces were computed and are listed in Table 4.2-2 and plots of peak interstory drift for each story and each face are depicted in Figs. 4.2-6 to 4.2-9. Peak drift for conditions (2) and (3) was observed to be bracketed by conditions (1) and (4) in all cases but one. However, several instances of increased maximum drift for the fully clad structure (condition (4)), compared to the unclad or partially-clad structures were found in Table 4.2-2. When the drift plots in Figs. 4.2-6 to 4.2-9 were compared to those for the clad and unclad cases (Figs. 3.4-40 to 3.4-43) no drastic changes were noticed in the overall character of drift behavior. Finally, the successive states of cladding failure for different building faces are shown in Figs. 4.2-10 to 4.2-18. When no cladding failure occurred (i.e., interstory drift never exceeded allowable values) on a given face of the structure, no figure is presented

for that face. For example, peak drift did not exceed the allowable drift of 0.36 inches (0.9 cm) on Faces 1 and 3 when the El Centro record was applied in the rigid direction as shown in Fig. 4.2-6.

It is of interest to note that no cladding failure took place in the braced direction (Faces 1 and 3) when applied motion was in the rigid direction, while failure was observed on Face 2 (rigid direction) for braced direction input and allowable drift set at 0.36 inches (0.9 cm). When modal participation factors for the clad eccentric model (Tables 3.4-1 and 3.4-2) were inspected, a strong torsional-translational coupling was observed for braced direction input but not for rigid direction input. Inspection of the failure plots revealed that in most instances, failure started in the mid-third of the structure reducing the interstory shear stiffness to 312.5 kips/inch (5.5×10^4 kN/m) and progressed upwards and downwards from there until most of the face had uniform cladding stiffness. This process then was repeated for the next stiffness reduction and even beyond when Δ was 0.36 inches (0.9 cm) but stopped for $\Delta = 0.72$ inches (1.8 cm). Comparison of peak drift plots and progressive failure plots showed that the final state of cladding could be obtained based on peak interstory drift values as expected.

When the 1966 Parkfield ground motion record was used as loading, only the first 10 seconds were used in structural response calculations as discussed in Section 3.4.2. Peak roof displacement response values

are tabulated in Table 4.2-3 and roof translational and torsional time-histories contained in Figs. 4.2-19 to 4.2-22. Inspection of these data showed that response values decreased in the direction of ground motion input with increasing allowable drift, Δ (see conditions (1) to (4)). On the other hand, for ground motion applied in the rigid direction, braced direction and rotational response was lower for both condition (2) and (3) than for either the clad or unclad models. In a similar fashion, rigid response and rotational response for condition (2) were lower than for any of the other conditions, while response for condition (3) was bracketed by the clad and unclad cases when input was applied in the braced frame direction. When peak interstory drift values were computed, peak face values were listed in Table 4.2-4 and peak story values for the different faces plotted in Figs. 4.2-23 to 4.2-26. The clad and unclad drift values were seen to bracket the partially-clad cases (conditions (2) and (3)) in all instances and drift values were reduced with increasing allowable drift, Δ. Comparison of drift plots for conditions (2) and (3) with those for the clad and unclad models (Figs. 3.4-48 and 3.4-51) showed condition (2) resemble the unclad case (condition (1)) while condition (3) followed the clad case (condition (4)) more closely on Faces 2 and 4 with rigid direction input while other cases did not display much change in drift behavior. Again, as for the El Centro record, the progressive failure of cladding was plotted and is depicted in Figs. 4.2-27 to 4.2-36 for the different cases with no figures included for faces with no cladding failure. It was observed that cladding failure occurred only on faces which were in the direction of input motion,

except when input was applied in the braced direction and allowable drift, Δ, was set at 0.36 inches (0.9 cm). In this case, all four faces had cladding failing and as discussed above, for the El Centro record the strong torsional-translational coupling for braced direction input displayed by modal participation factors was thought to be an explanation of this response behavior. No overall pattern in failure sequence was observed when all the failure plots were compared.

While results were presented for the El Centro and Parkfield ground motion records only, it was evident that it might be unconservative to use the unclad model as the basis for design. The several instances of increased response when the contribution of cladding stiffening effects were included support this conclusion. As discussed above in Section 3.4, the addition of cladding lateral stiffness effects can alter the dynamic characteristics of the structure to such a degree that the clad rather than the unclad system is more sensitive to the design ground motion, at least during the early part of the ground motion. However, the above results suggest that the effects of partial cladding failure on structure translational response can be bracketed by study of the clad and unclad models, while torsional response may be more difficult to predict.

4.2.3 Response Studies of Symmetric Mass Model with Partial Cladding Failure

As a final case for the incremental failure model, partial cladding failure was imposed upon the symmetric model containing no eccentricity between centers of mass and rigidity. Prior motion of the structure or poor construction practice in selected locations randomly distributed throughout the structure face was assumed to be the reason for the initial failure state. Allowable drift, Δ, was set at 0.36 inches (0.9 cm) in

this part of the study and response compared to that of the clad and unclad structure models. In other words, initial failure was only imposed upon the case with Δ = 0.36 inches (0.9 cm). Peak roof displacements and peak interstory drift values are tabulated in Table 4.2-5 to 4.2-8. Translational and rotational roof response time-histories are displayed in Figs. 4.2-37 to 4.2-44 and peak drift at a story is plotted for the four building faces in Figs. 4.2-45 to 4.2-48. Finally, progressive cladding failure is shown, for all faces experiencing failure, in Figs. 4.2-49 to 4.2-56.

When response values and plots were compared, rotational response was seen to be substantially increased by partial cladding failure even in the absence of imposed accidental eccentricity. Rotational response was amplified more than twenty-fold over that for the symmetric model for the El Centro record input in the rigid direction as shown in Table 4.2-5 and Fig. 4.2-38. However, translational displacement and drift responses remained comparable to and, in most instances, were bracketed by the clad and unclad symmetric model values.

A piecewise linear failure model was formulated for the cladding in the absence of experimental data and the performance of the curtain wall under combined bending and torsional motions of the prototype structure was explored. In general, peak translational response values for the partially-clad models were found to be bracketed by the fully clad and unclad cases for the earthquake loadings considered, while torsional response was observed as being more unpredictable.

Table 4.2-1. Peak Roof Displacements, Incremental Failure Case, for the Eccentric Model for the First 14 Seconds of the 1940 Imperial Valley Earthquake Recorded at El Centro in the SOOE Direction.

Ground Motion Input Direction (1)	Allowable Drift, Δ (inches) (2)	Peak Roof Displacement Response		
		Rigid Direction (inches) (3)	Braced Direction (inches) (4)	Rotation (radians) (5)
Braced	0.0[a]	1.7	14.8	5.6×10^{-3}
	0.36	1.6	15.1	9.4×10^{-3}
	0.72	3.2	15.1	8.1×10^{-3}
	∞[b]	2.7	15.2	7.8×10^{-3}
Rigid	0.0	11.8	1.0	3.7×10^{-3}
	0.36	14.4	1.1	4.6×10^{-3}
	0.72	14.9	1.9	6.0×10^{-3}
	∞	15.0	1.9	5.2×10^{-3}

[a]Unclad case.

[b]Clad case.

Table 4.2-2. Peak Interstory Drift, Incremental Failure Case, for the Eccentric Model for the First 14 Seconds of the 1940 Imperial Valley Earthquake Recorded at El Centro in the S00E Direction.

Ground Motion Input Direction (1)	Allowable Drift, Δ (inches) (2)	Peak Relative Interstory Drift (inches) Face 1[a] (3)	Face 2 (4)	Face 3 (5)	Face 4 (6)
Braced	0.0[b]	1.0(21)	0.4(19)	1.3(18)	0.2(22)
	0.36	1.0(18)	0.5(18)	1.2(17)	0.4(11)
	0.72	1.1(16)	0.5(11)	1.1(16)	0.3(4)
	∞[c]	1.1(16)	0.5(5)	1.0(16)	0.4(4)
Rigid	0.0	0.5(24)	1.3(24)	0.4(24)	1.2(24)
	0.36	0.3(17)	1.0(22)	0.3(17)	1.4(18)
	0.72	0.4(8)	1.0(19)	0.3(7)	1.3(19)
	∞	0.3(4)	1.0(19)	0.3(11)	1.3(19)

[a]Story at which peak drift occurred is shown in parentheses.

[b]Unclad case.

[c]Clad case.

Table 4.2-3. Peak Roof Displacements, Incremental Failure Case, for Eccentric Model for the First 10 Seconds of the 1966 Parkfield Earthquake Recorded in the N65E Direction.

Ground Motion Input Direction (1)	Allowable Drift, Δ (inches) (2)	Peak Roof Displacement Response		
		Rigid Direction (inches) (3)	Braced Direction (inches) (4)	Rotation (radians) (5)
Braced	0.0[a]	2.8	23.9	1.1×10^{-2}
	0.36	2.2	22.6	9.5×10^{-3}
	0.72	2.9	21.4	1.2×10^{-2}
	∞[b]	3.1	20.7	1.2×10^{-2}
Rigid	0.0	25.2	1.6	1.2×10^{-2}
	0.36	24.3	1.0	7.0×10^{-3}
	0.72	22.8	1.5	7.7×10^{-3}
	∞	21.9	2.3	7.8×10^{-3}

[a]Unclad case.

[b]Clad case.

Table 4.2-4. Peak Interstory Drift, Incremental Failure Case for the Eccentric Model, for the First 10 Seconds of the 1966 Parkfield Earthquake Recorded in the N65E Direction.

Ground Motion Input Direction (1)	Allowable Drift, Δ (inches) (2)	Peak Relative Interstory Drift (inches)			
		Face 1[a] (3)	Face 2 (4)	Face 3 (5)	Face 4 (6)
Braced	0.0[b]	1.6(18)	0.7(22)	1.6(20)	0.5(22)
	0.36	1.6(11)	0.7(19)	1.5(11)	0.5(18)
	0.72	1.6(11)	0.7(18)	1.4(9)	0.5(4)
	∞[c]	1.5(11)	0.7(7)	1.4(7)	0.4(4)
Rigid	0.0	1.1(22)	3.0(22)	1.0(22)	3.1(24)
	0.36	0.4(19)	2.5(24)	0.4(23)	3.1(24)
	0.72	0.4(21)	1.9(22)	0.5(22)	2.6(22)
	∞	0.4(16)	1.6(12)	0.4(4)	1.9(12)

[a]Story at which peak drift occurred is shown in parentheses.

[b]Unclad case.

[c]Clad case.

Table 4.2-5. Peak Roof Displacements, Incremental Failure Case for the Symmetric Model, for the First 14 Seconds of the 1940 El Centro Record.

Ground Motion Input Direction (1)	Allowable Drift, Δ (inches) (2)	Peak Roof Displacement Response		
		Rigid Direction (inches) (3)	Braced Direction (inches) (4)	Rotation (radians) (5)
Braced	0.0[a]	0.2	15.3	8.3×10^{-5}
	0.36	0.4	16.5	2.5×10^{-4}
	∞[b]	0.2	16.4	8.8×10^{-5}
Rigid	0.0	11.8	0.2	4.1×10^{-6}
	0.36	15.4	0.1	8.9×10^{-5}
	∞	15.8	0.2	3.0×10^{-6}

[a]Unclad case.

[b]Clad case.

Table 4.2-6. Peak Roof Displacements, Incremental Failure Case for the Symmetric Model, for the First 10 Seconds of the 1966 Parkfield Record.

Ground Motion Input Direction (1)	Allowable Drift, Δ (inches) (2)	Peak Roof Displacement Response		
		Rigid Direction (inches) (3)	Braced Direction (inches) (4)	Rotation (radians) (5)
Braced	0.0[a]	0.4	24.1	1.8×10^{-4}
	0.36[b]	0.4	22.8	1.4×10^{-4}
	∞	0.3	20.7	1.3×10^{-4}
Rigid	0.0	25.3	0.4	1.3×10^{-5}
	0.36	25.0	0.2	9.0×10^{-5}
	∞	22.3	0.3	3.5×10^{-6}

[a]Unclad case.

[b]Clad case.

Table 4.2-7. Peak Interstory Drift, Incremental Failure Case for the Symmetric Model, for the First 14 Seconds of the 1940 El Centro Record.

Ground Motion Input Direction (1)	Allowable Drift, Δ (inches) (2)	Peak Relative Interstory Drift (inches) Face 1[a] (3)	Face 2 (4)	Face 3 (5)	Face 4 (6)
Braced	0.0[b]	1.2(20)	0.03(24)	1.2(20)	0.03(17)
	0.36	1.2(18)	0.08(18)	1.2(16)	0.09(18)
	∞[c]	1.1(16)	0.02(16)	1.1(16)	0.02(17)
Rigid	0.0	0.01(20)	1.3(24)	0.01(20)	1.3(24)
	0.36	0.03(22)	1.4(22)	0.04(22)	1.4(24)
	∞	0.01(11)	1.3(19)	0.01(11)	1.3(19)

[a]Story at which peak drift occurred is shown in parentheses.

[b]Unclad case.

[c]Clad case.

Table 4.2-8. Peak Interstory Drift, Incremental Failure Case for the Symmetric Model, for the First 10 Seconds of the 1966 Parkfield Record.

Ground Motion Input Direction (1)	Allowable Drift, Δ (inches) (2)	Peak Relative Interstory Drift (inches)			
		Face 1[a] (3)	Face 2 (4)	Face 3 (5)	Face 4 (6)
Braced	0.0[b]	1.6(20)	0.05(24)	1.6(11)	0.03(17)
	0.36	1.6(11)	0.06(24)	1.6(11)	0.06(24)
	∞[c]	1.4(8)	0.02(19)	1.4(8)	0.02(17)
Rigid	0.0	0.03(20)	3.1(22)	0.02(21)	3.1(22)
	0.36	0.04(6)	2.9(24)	0.03(6)	2.9(24)
	∞	0.02(11)	1.8(12)	0.02(11)	1.8(12)

[a]Story at which peak drift occurred is shown in parentheses.

[b]Unclad case.

[c]Clad case.

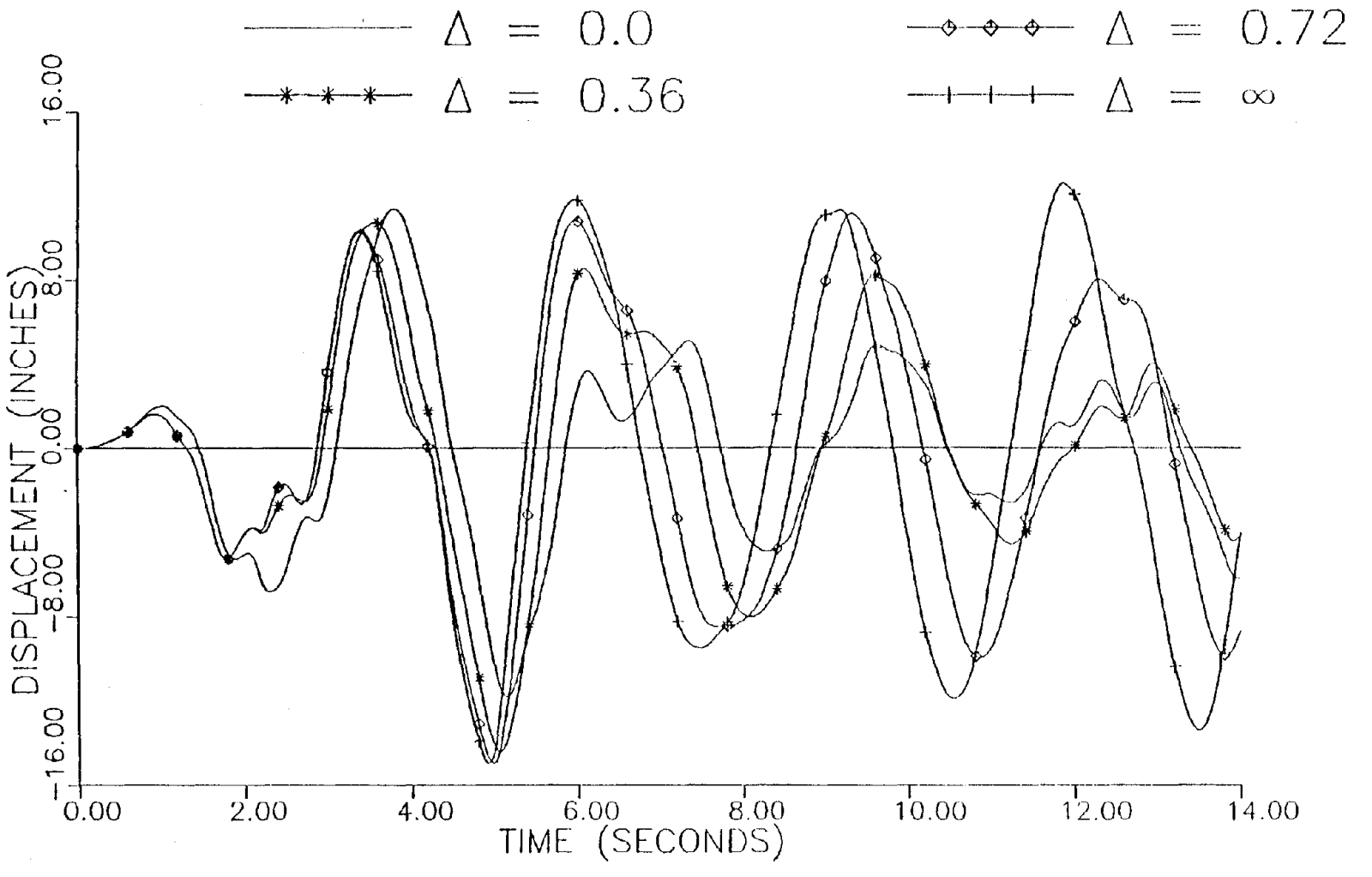

Figure 4.2-2. Roof Translational Response in Rigid Direction, Incremental Failure Case for Eccentric Model, for 1940 El Centro Record Acting In Rigid Direction.

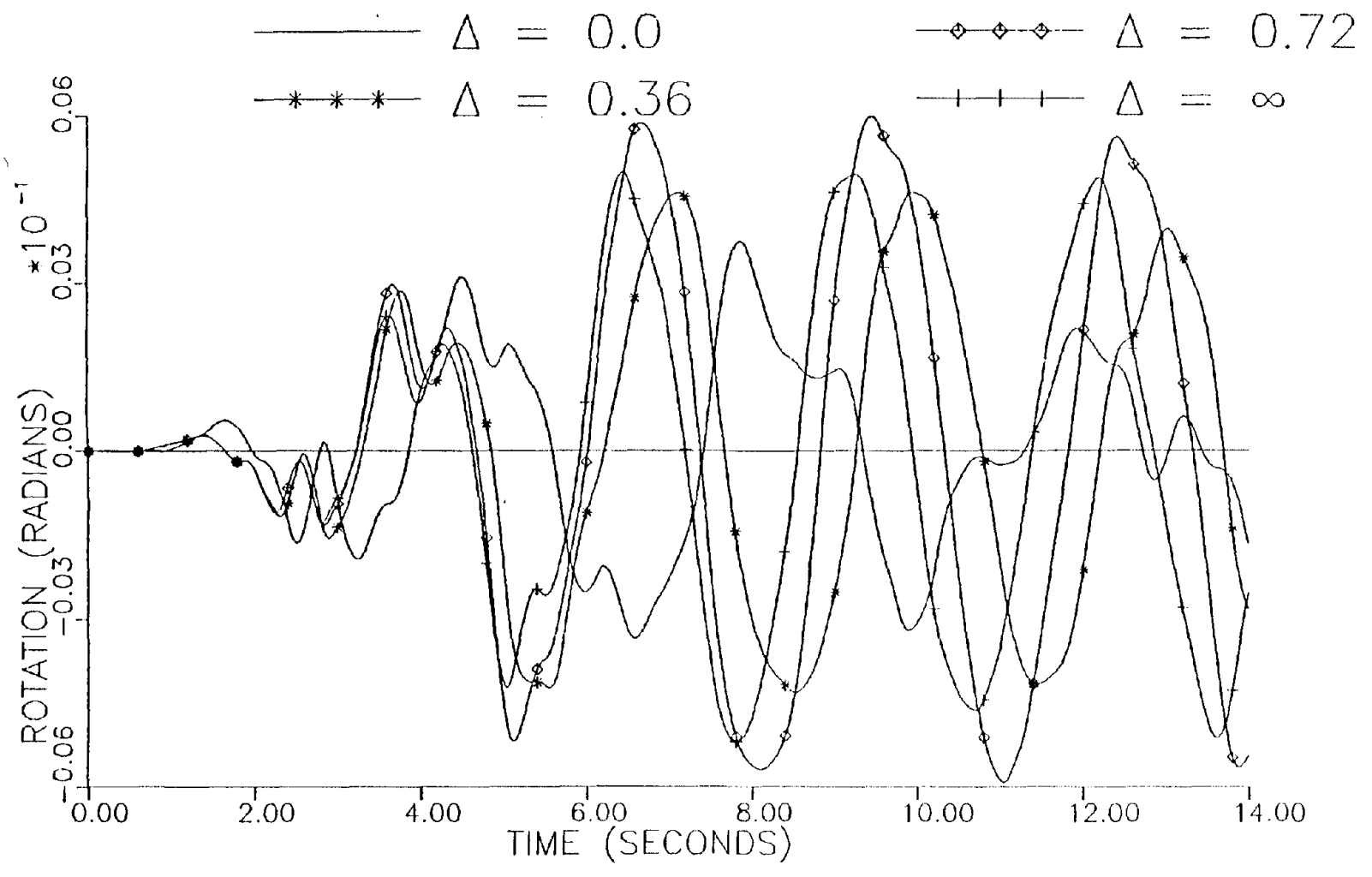

Figure 4.2-3. Roof Rotational Response, Incremental Failure Case for Eccentric Model, for 1940 El Centro Record Acting in Rigid Direction.

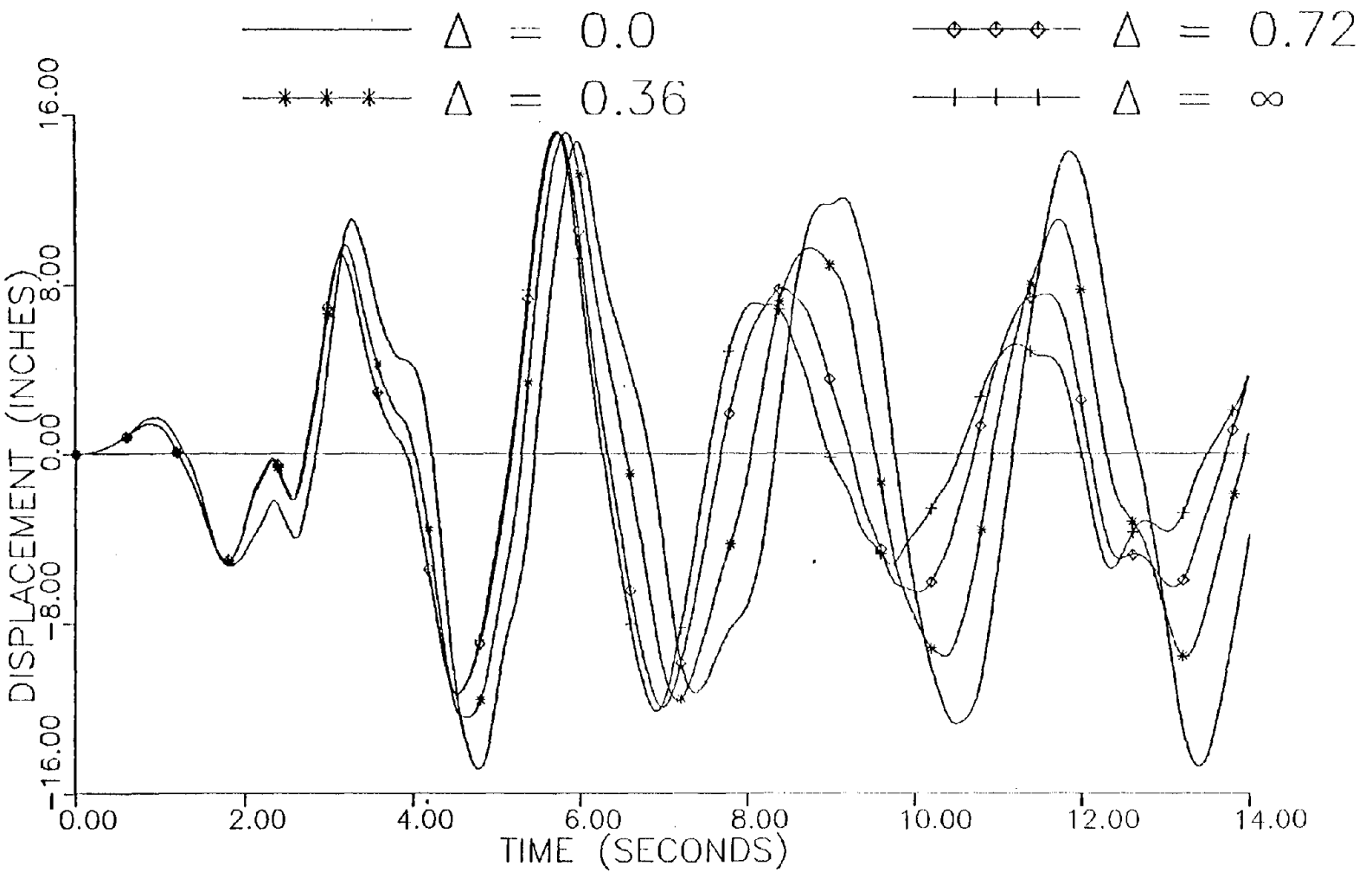

Figure 4.2-4. Roof Translational Response in Braced Direction, Incremental Failure Case for Eccentric Model, for 1940 El Centro Record Acting in Braced Direction.

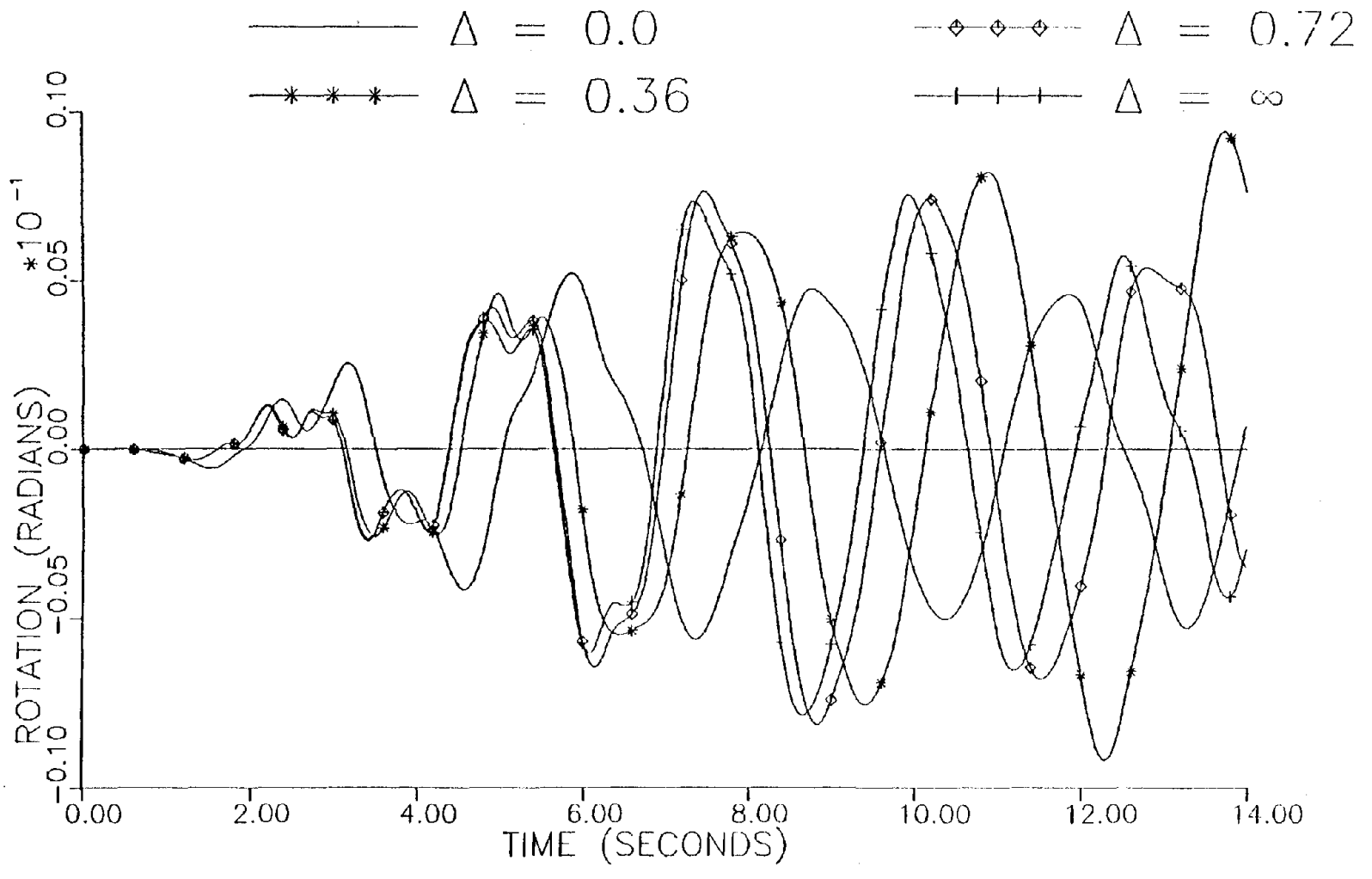

Figure 4.2-5. Roof Rotational Response, Incremental Failure Case for Eccentric Model, for 1940 El Centro Record Acting in Braced Direction.

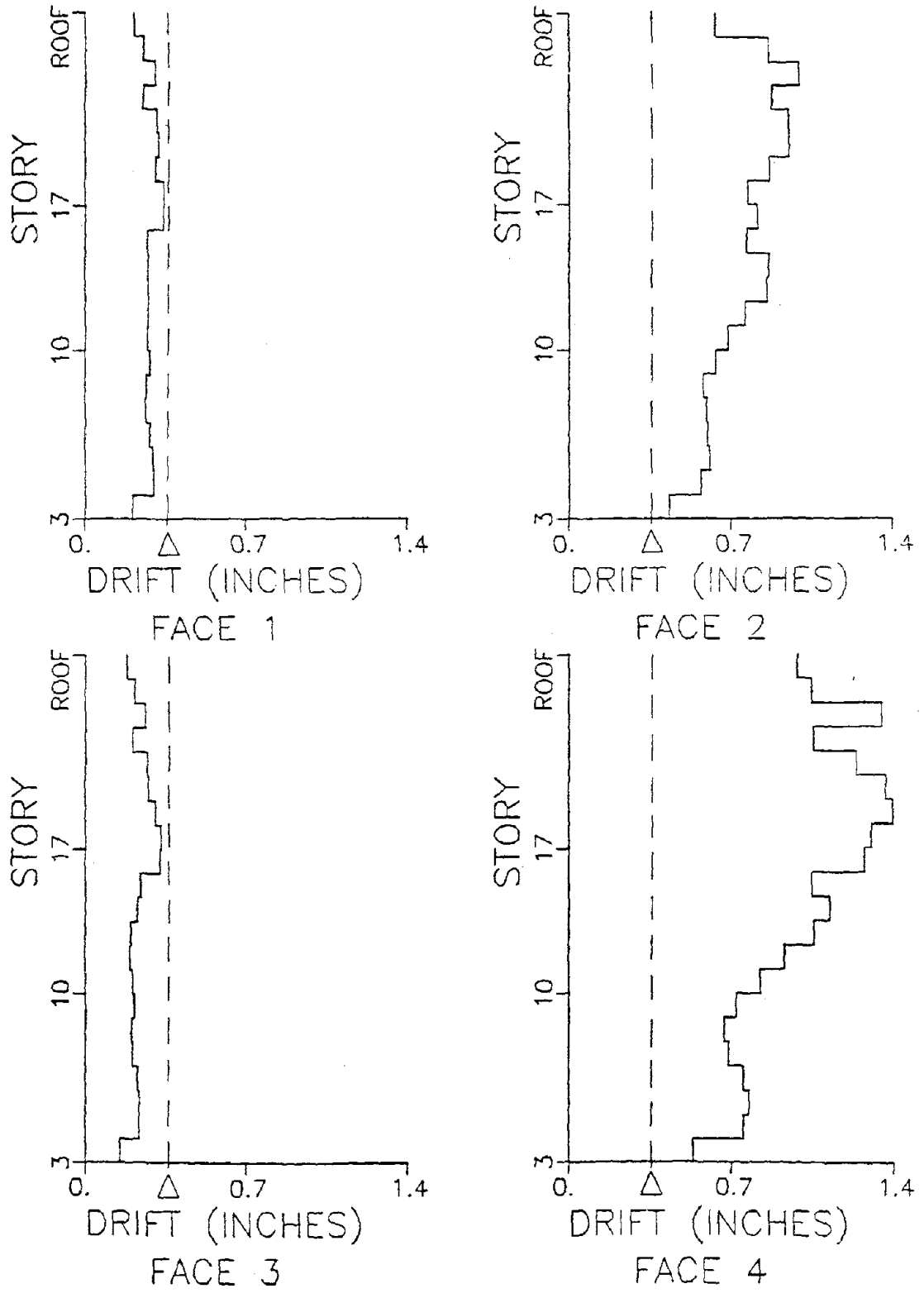

Figure 4.2-6. Peak Drift Values, Incremental Failure Case with Allowable Drift, Δ, set at 0.36 inches (0.9 cm), for 1940 El Centro Record Acting in Rigid Direction, Eccentric Model.

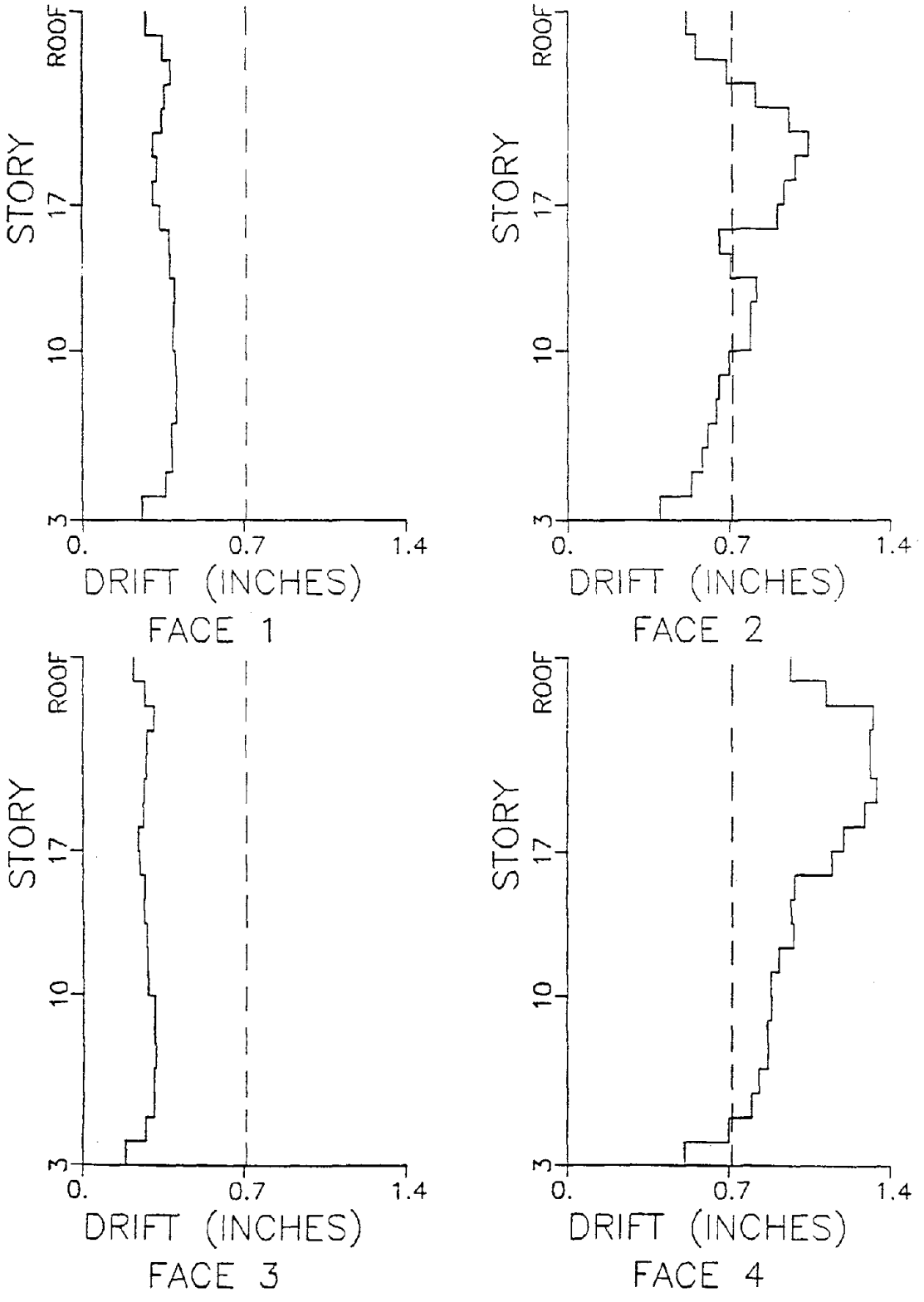

Figure 4.2-7. Peak Drift Values, Incremental Failure Case with Allowable Drift, Δ, set at 0.72 inches (1.8 cm), for 1940 El Centro Record Acting in Rigid Direction, Eccentric Model.

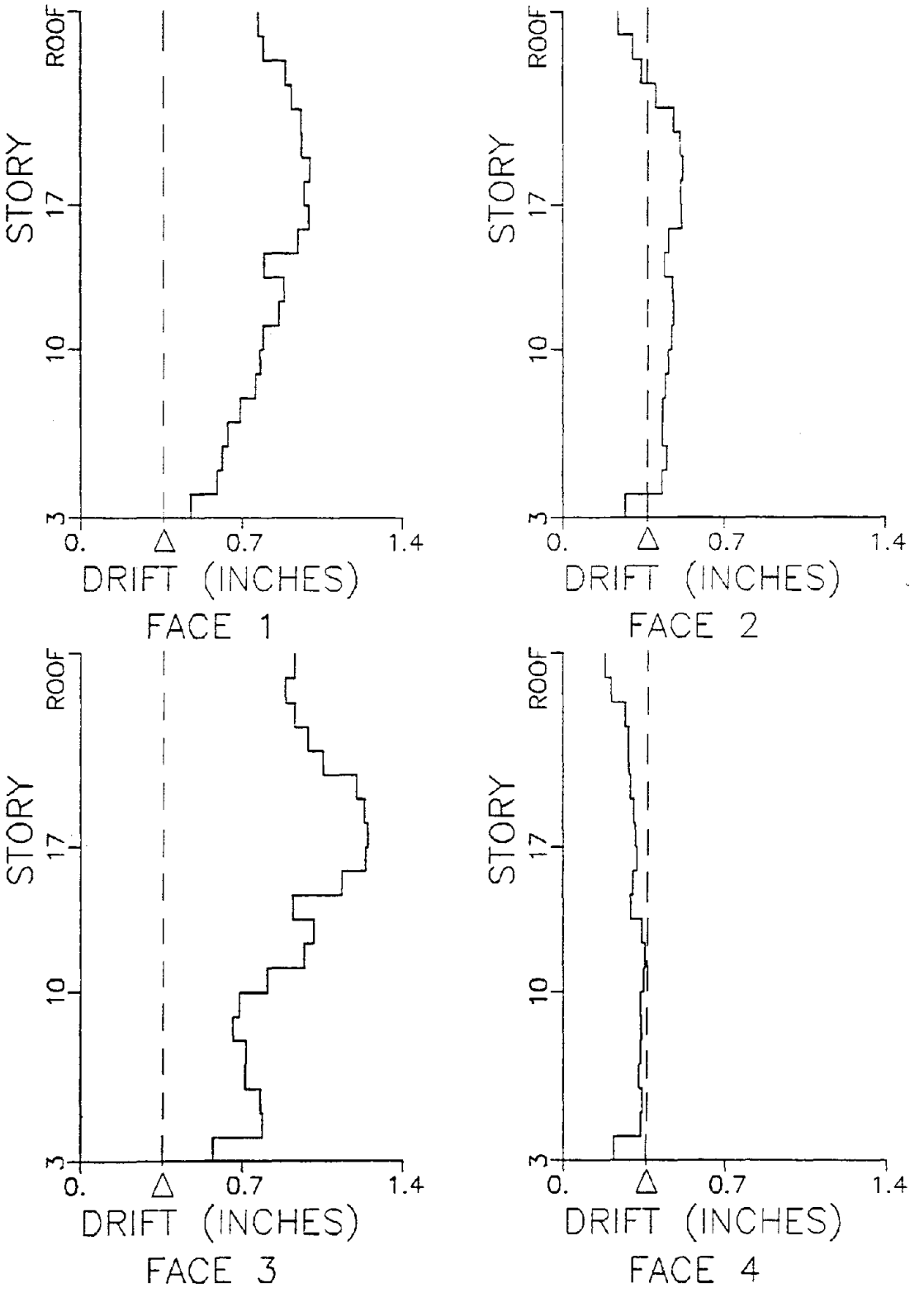

Figure 4.2-8. Peak Drift Values, Incremental Failure Case with Allowable Drift, Δ, set at 0.36 inches (0.9 cm), for 1940 El Centro Record Acting in Braced Direction, Eccentric Model.

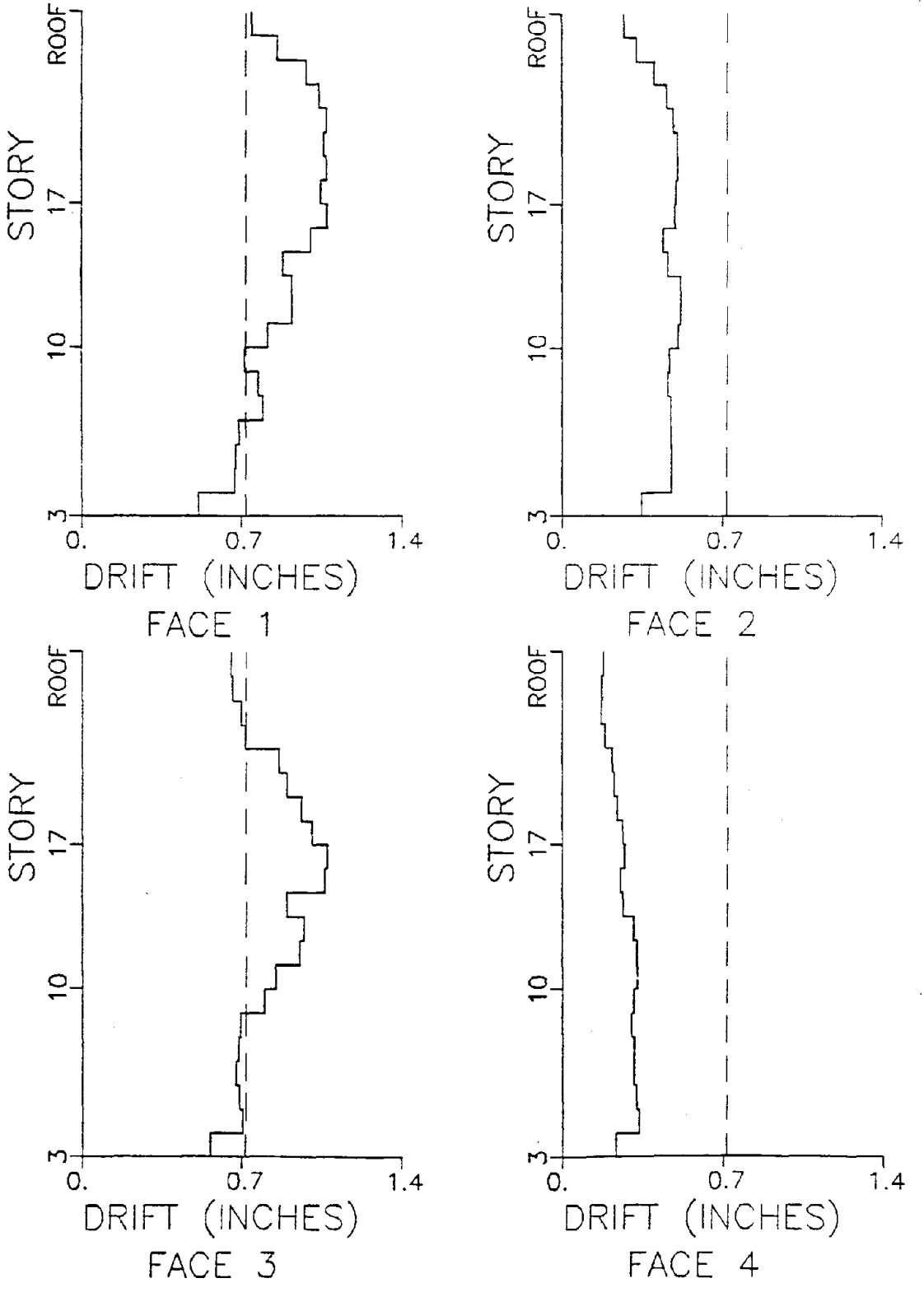

Figure 4.2-9. Peak Drift Values, Incremental Failure Case with Allowable Drift, Δ, set at 0.72 inches (1.8 cm) for 1940 El Centro Record Acting in Braced Direction, Eccentric Model.

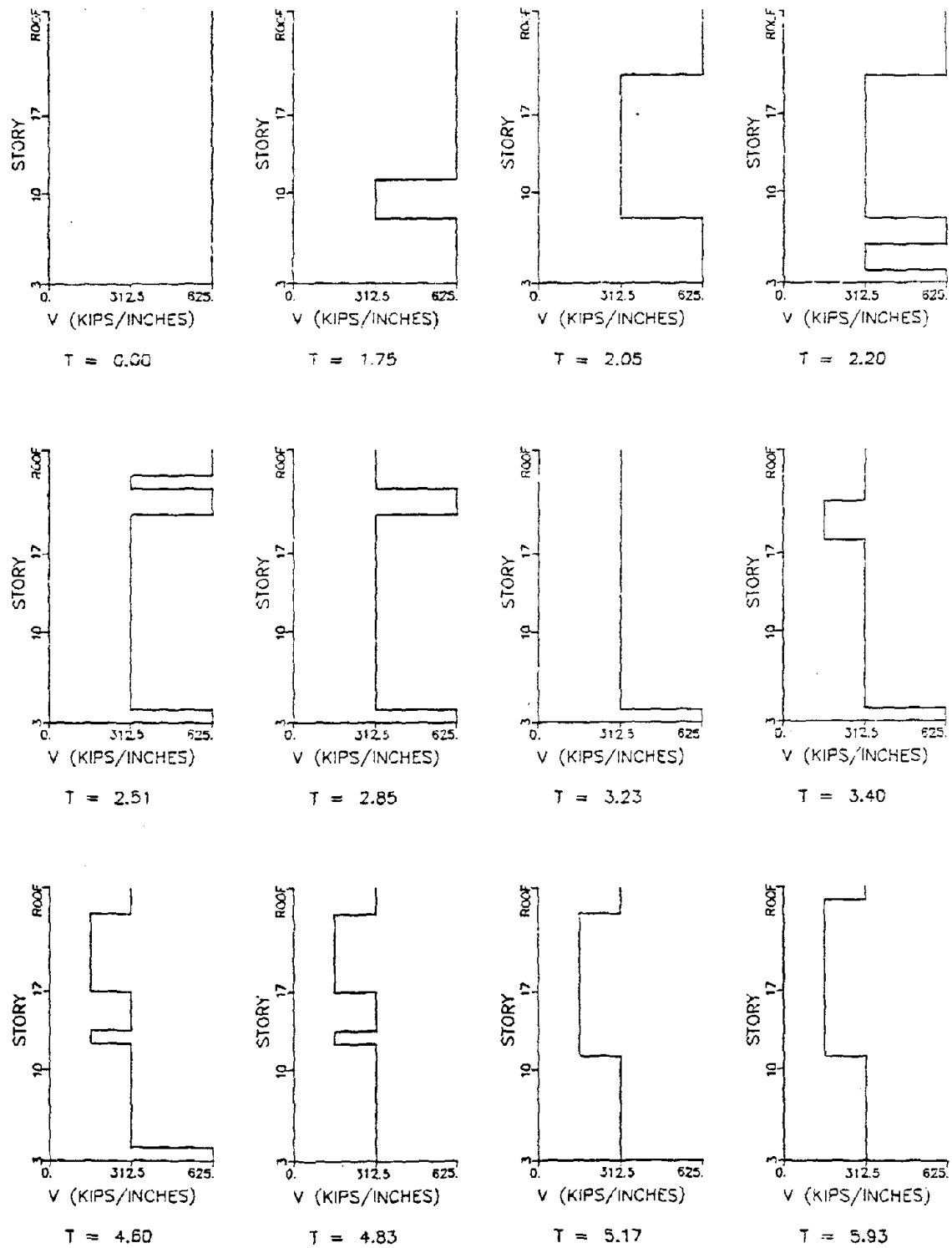

Figure 4.2-10. Progressive Failure of Cladding on Face 2 for 1940 El Centro Record Acting in Rigid Direction with Allowable Drift, Δ, set at 0.36 inches (0.9 cm), Eccentric Model (Time T in seconds).

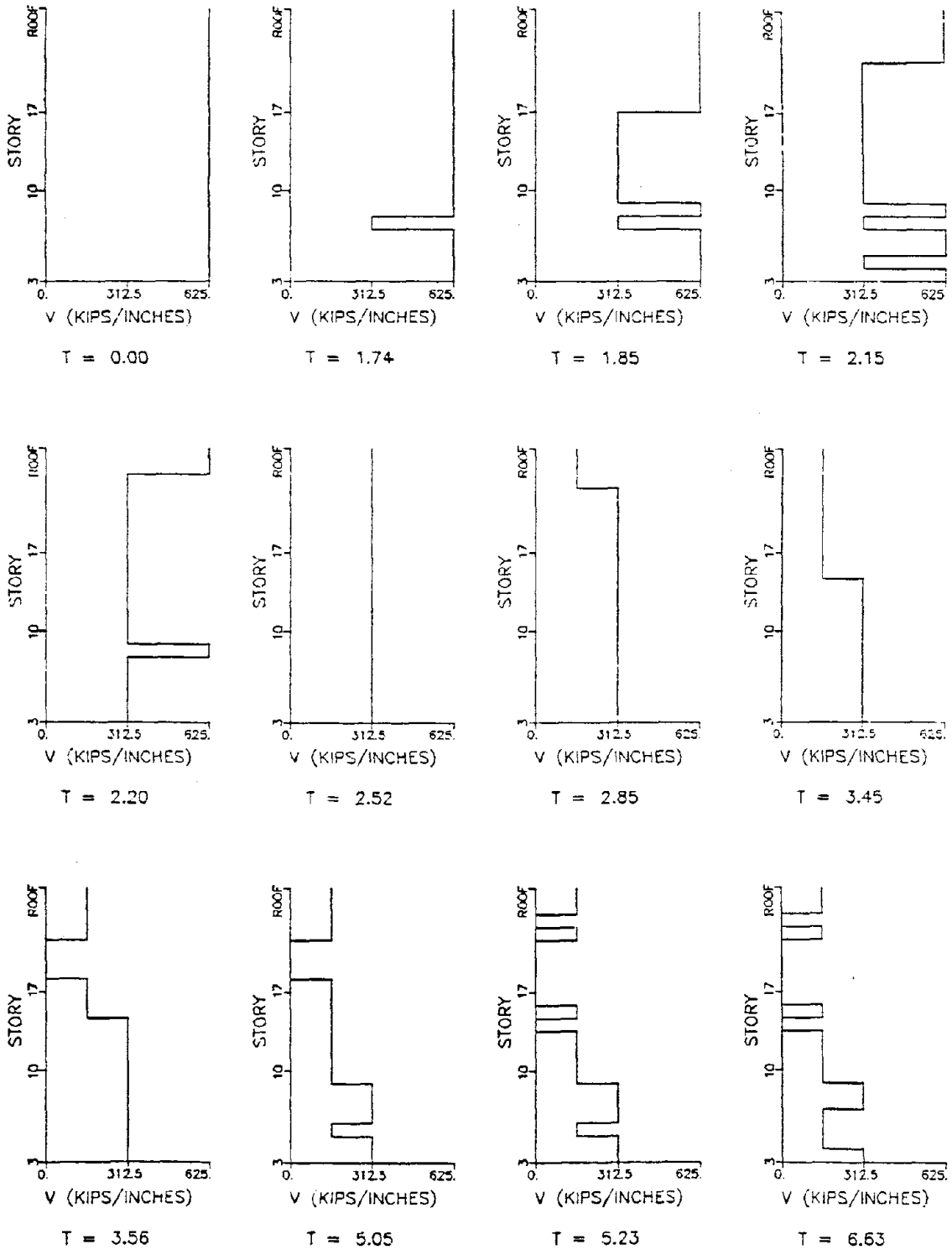

Figure 4.2-11. Progressive Failure of Cladding on Face 4 for 1940 El Centro Record Acting in Rigid Direction with Allowable Drift, Δ, set at 0.36 inches (0.9 cm), Eccentric Model (Time T in seconds).

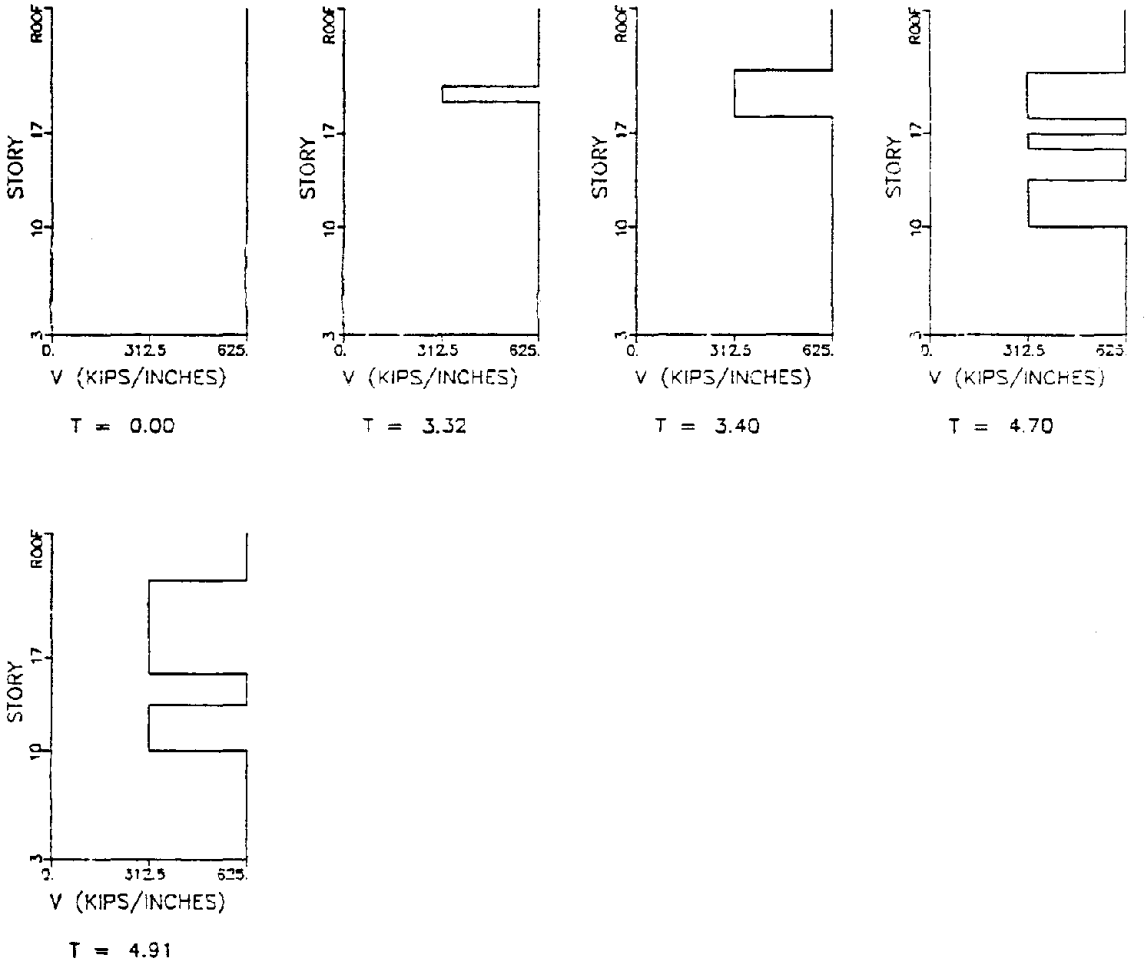

Figure 4.2-12. Progressive Failure of Cladding on Face 2 for 1940 El Centro Record Acting in Rigid Direction with Allowable Drift, Δ, set at 0.72 inches (1.8 cm), Eccentric Model (Time T in seconds).

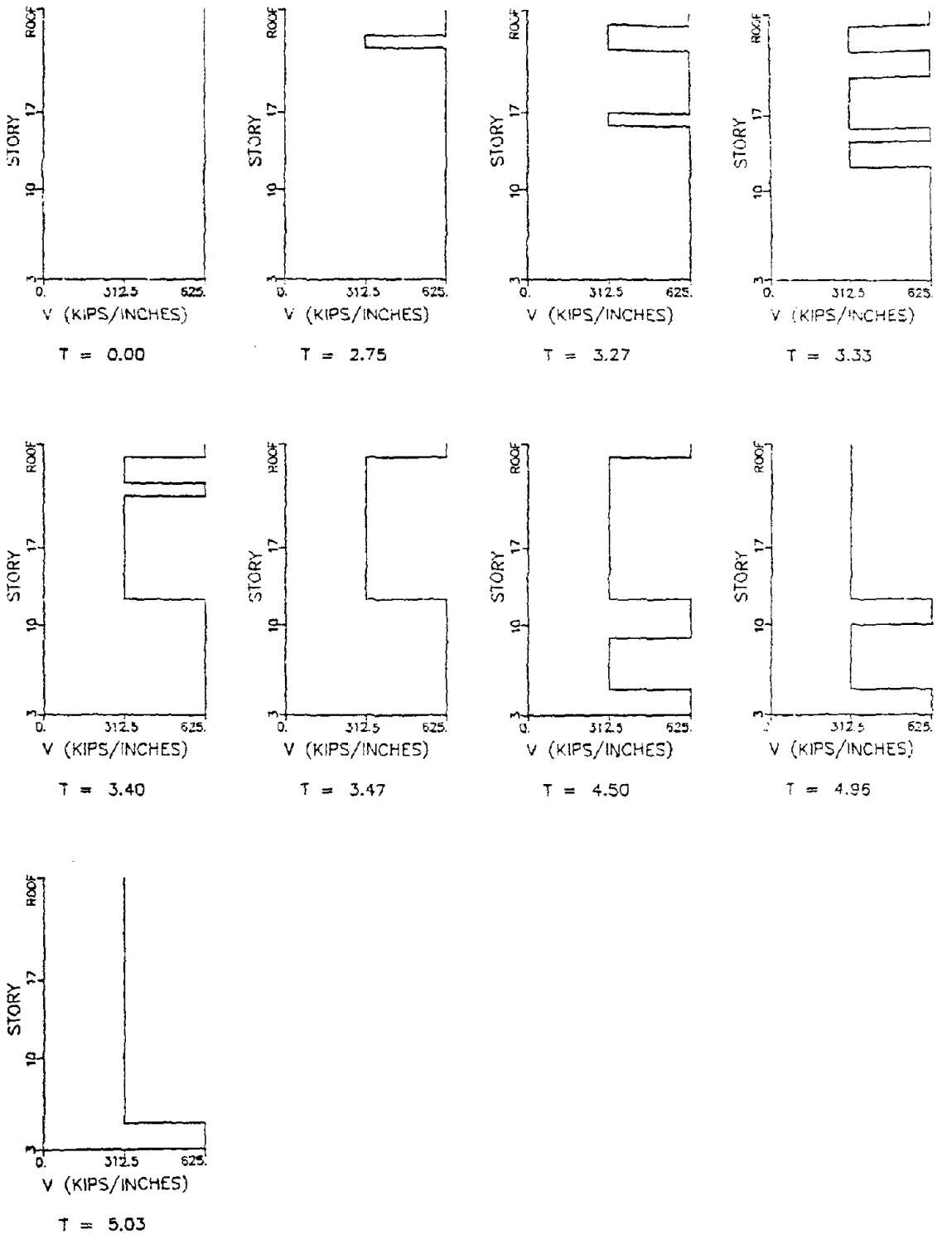

Figure 4.2-13. Progressive Failure of Cladding on Face 4 for 1940 El Centro Record Acting in Rigid Direction with Allowable Drift, Δ, set at 0.72 inches (1.8 cm), Eccentric Model (Time T in seconds).

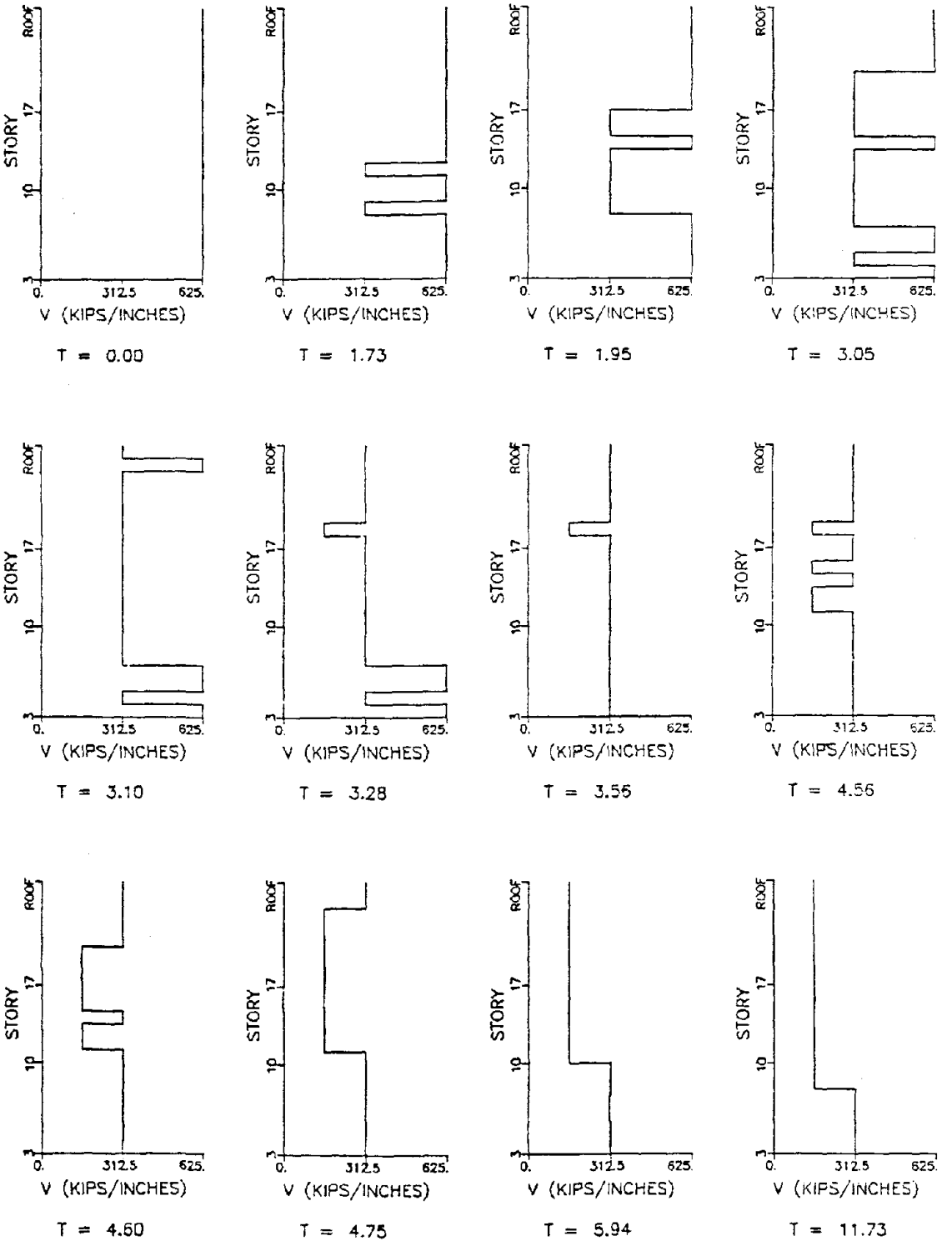

Figure 4.2-14. Progressive Failure of Cladding on Face 1 for 1940 El Centro Record Acting in Braced Direction with Allowable Drift, Δ, set at 0.36 inches (0.9 cm), Eccentric Model (Time T in seconds).

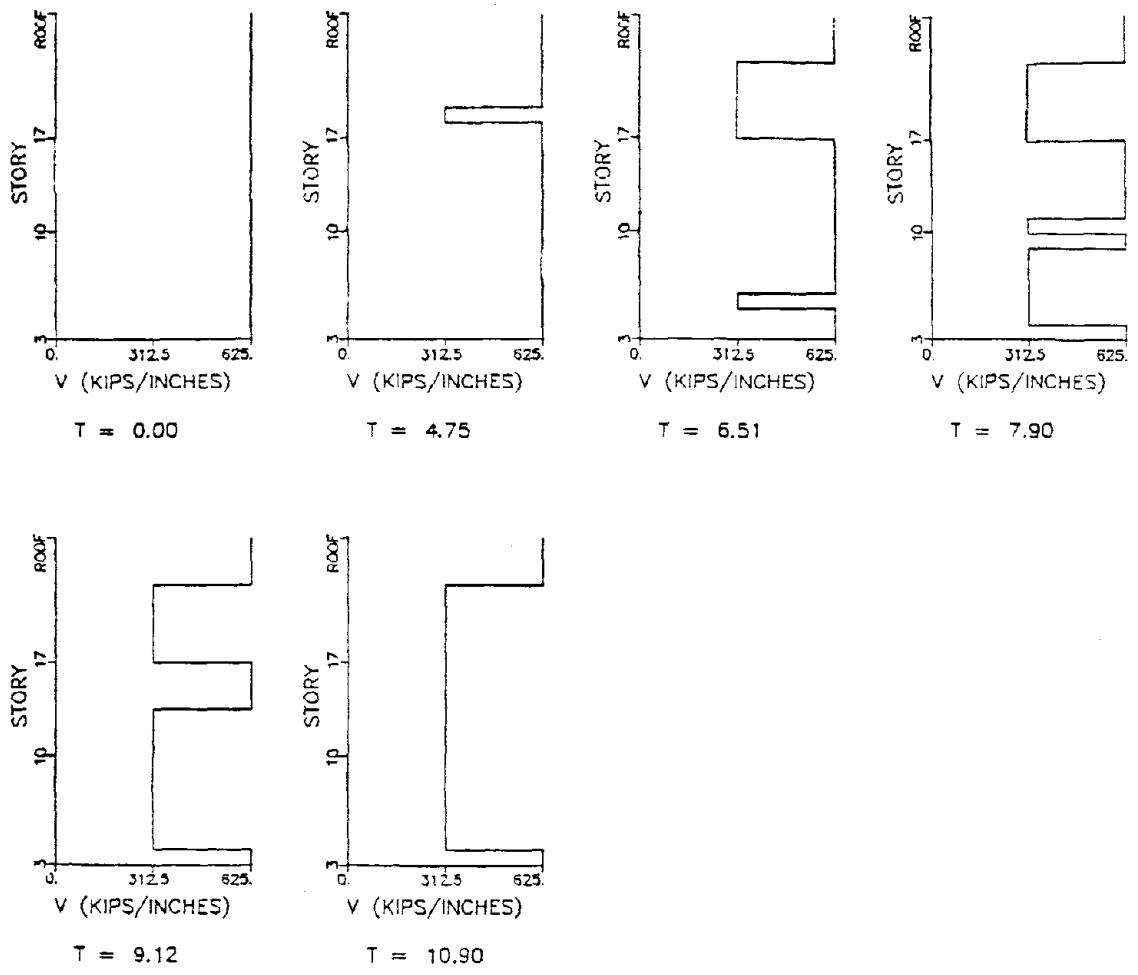

Figure 4.2-15. Progressive Failure of Cladding on Face 2 for 1940 El Centro Record Acting in Braced Direction with Allowable Drift, Δ, set at 0.36 inches (0.9 cm), Eccentric Model (Time T in seconds).

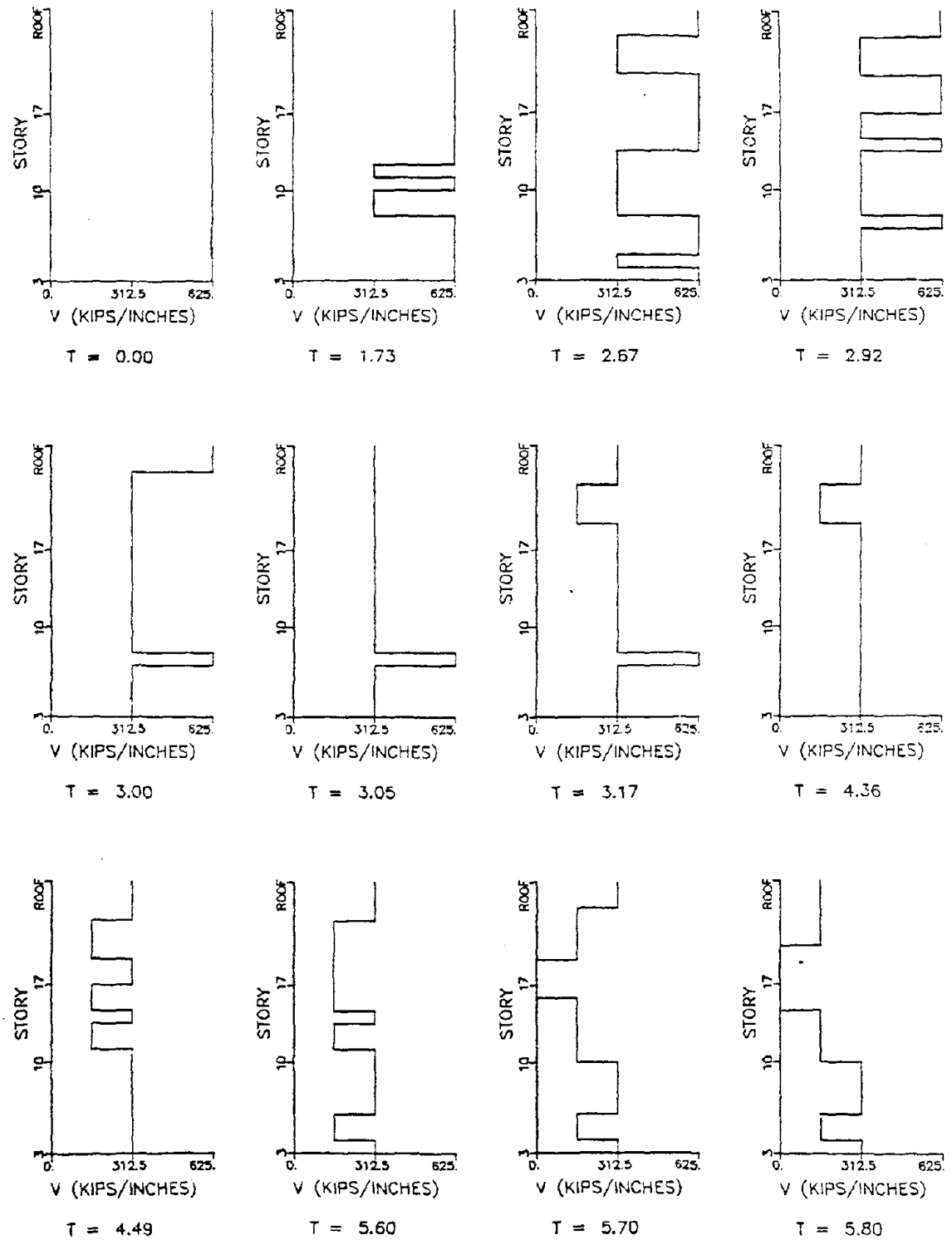

Figure 4.2-16. Progressive Failure of Cladding on Face 3 for 1940 El Centro Record Acting in Braced Direction with Allowable Drift, Δ, set at 0.36 inches (0.9 cm), Eccentric Model (Time T in seconds).

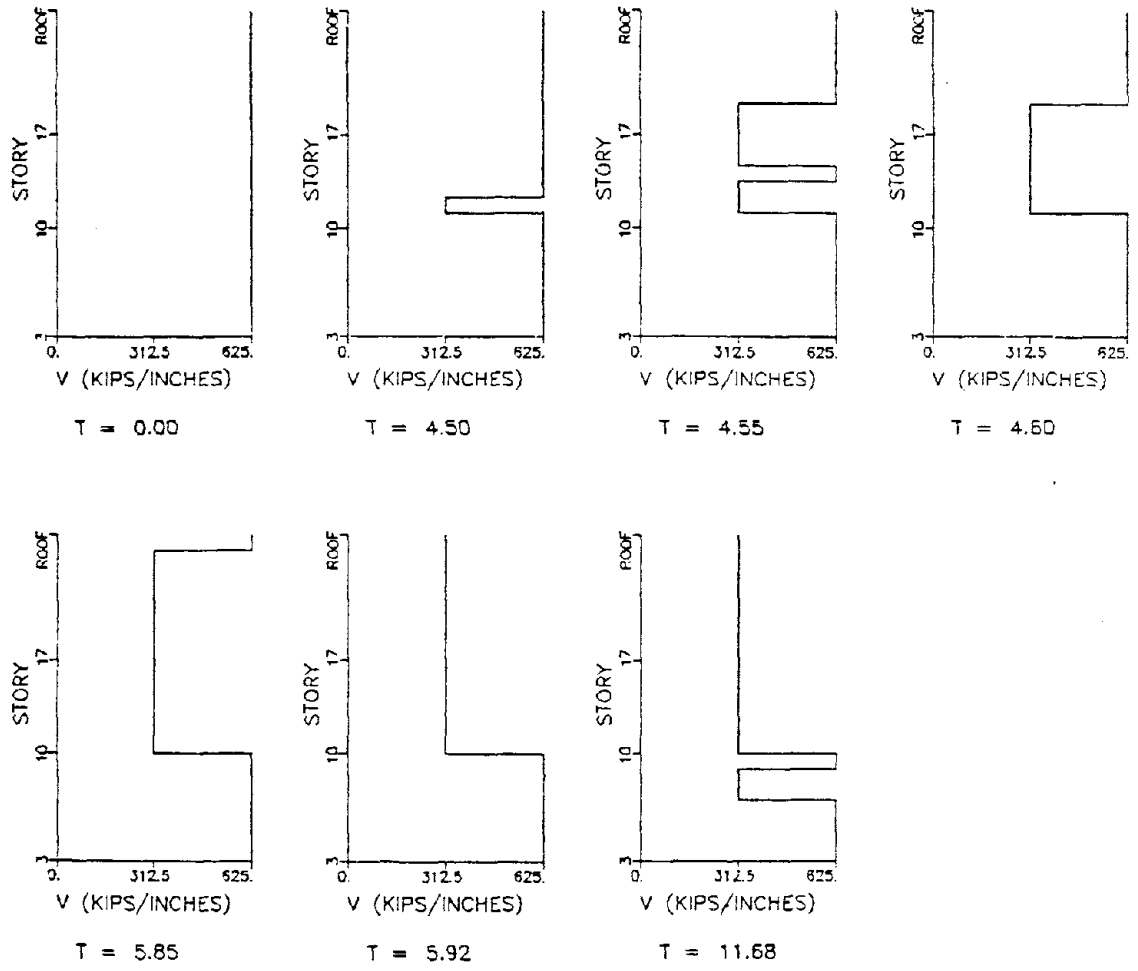

Figure 4.2-17. Progressive Failure of Cladding on Face 1 for 1940 El Centro Record Acting in Braced Direction with Allowable Drift, Δ, set at 0.72 inches (1.8 cm), Eccentric Model (Time T in seconds).

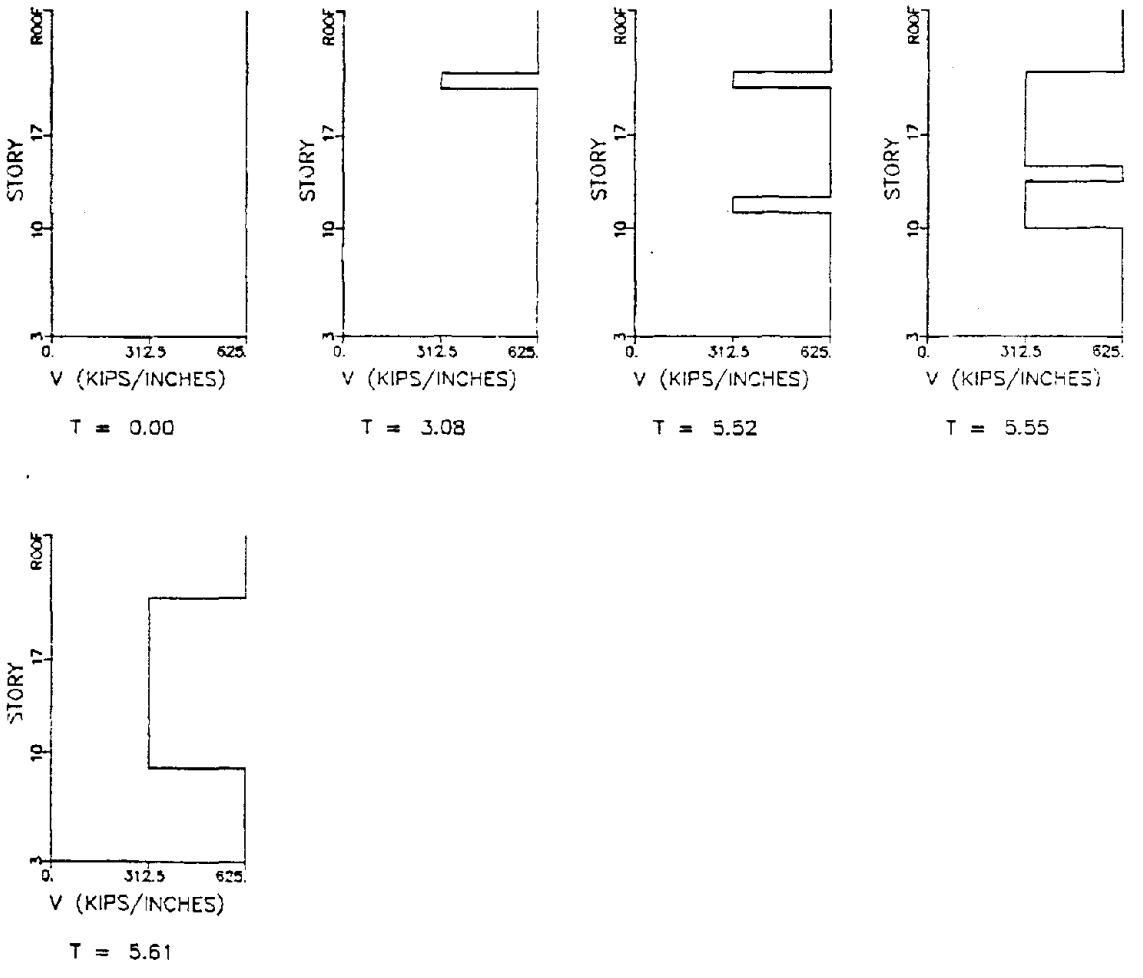

Figure 4.2-18. Progressive Failure of Cladding on Face 3 for 1940 El Centro Record Acting in Braced Frame Direction with Allowable Drift, Δ, set at 0.72 inches (1.8 cm), Eccentric Model (Time T in seconds).

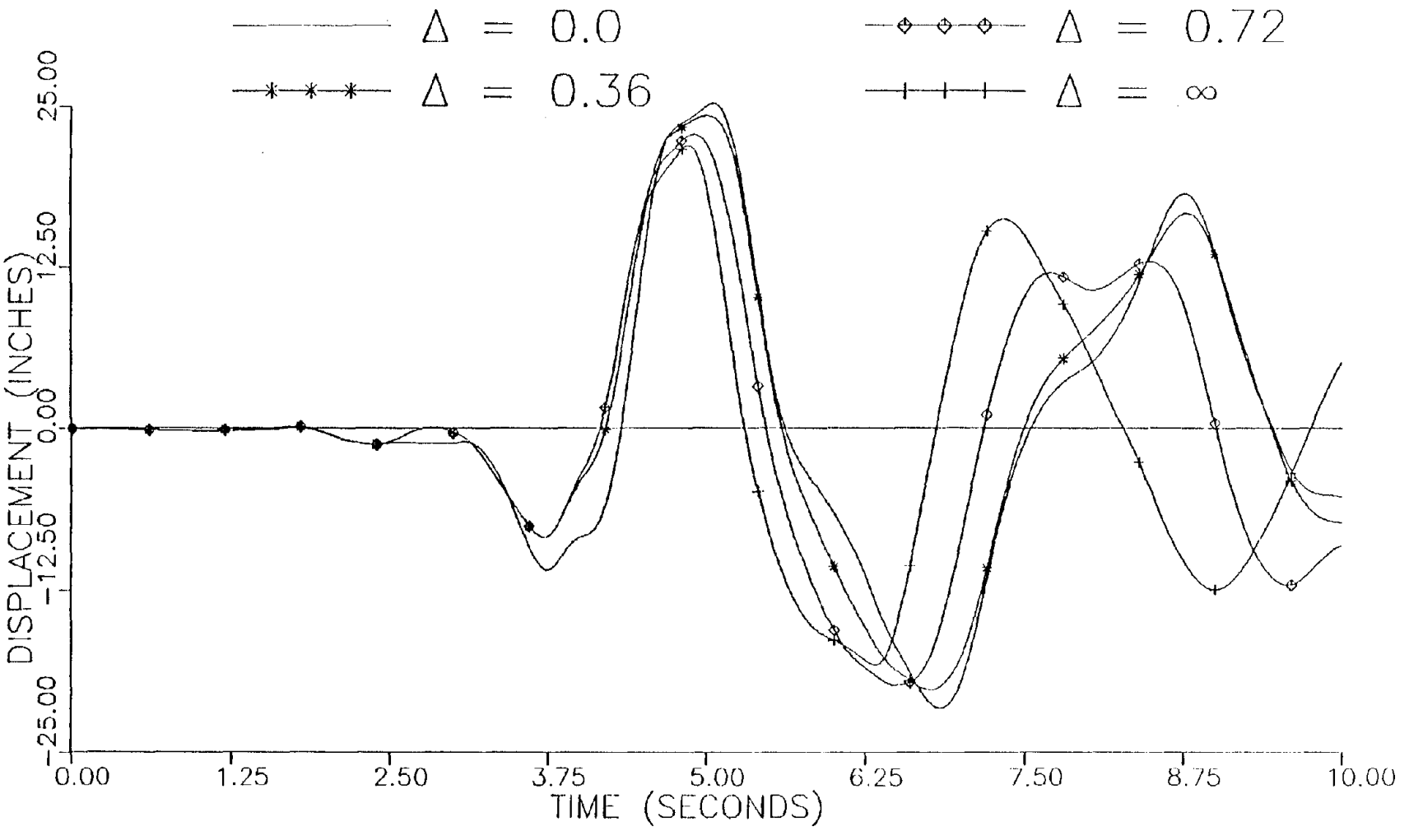

Figure 4.2-19. Roof Translational Response in Rigid Direction, Incremental Failure Case for Eccentric Model, for 1966 Parkfield Record Acting in Rigid Direction.

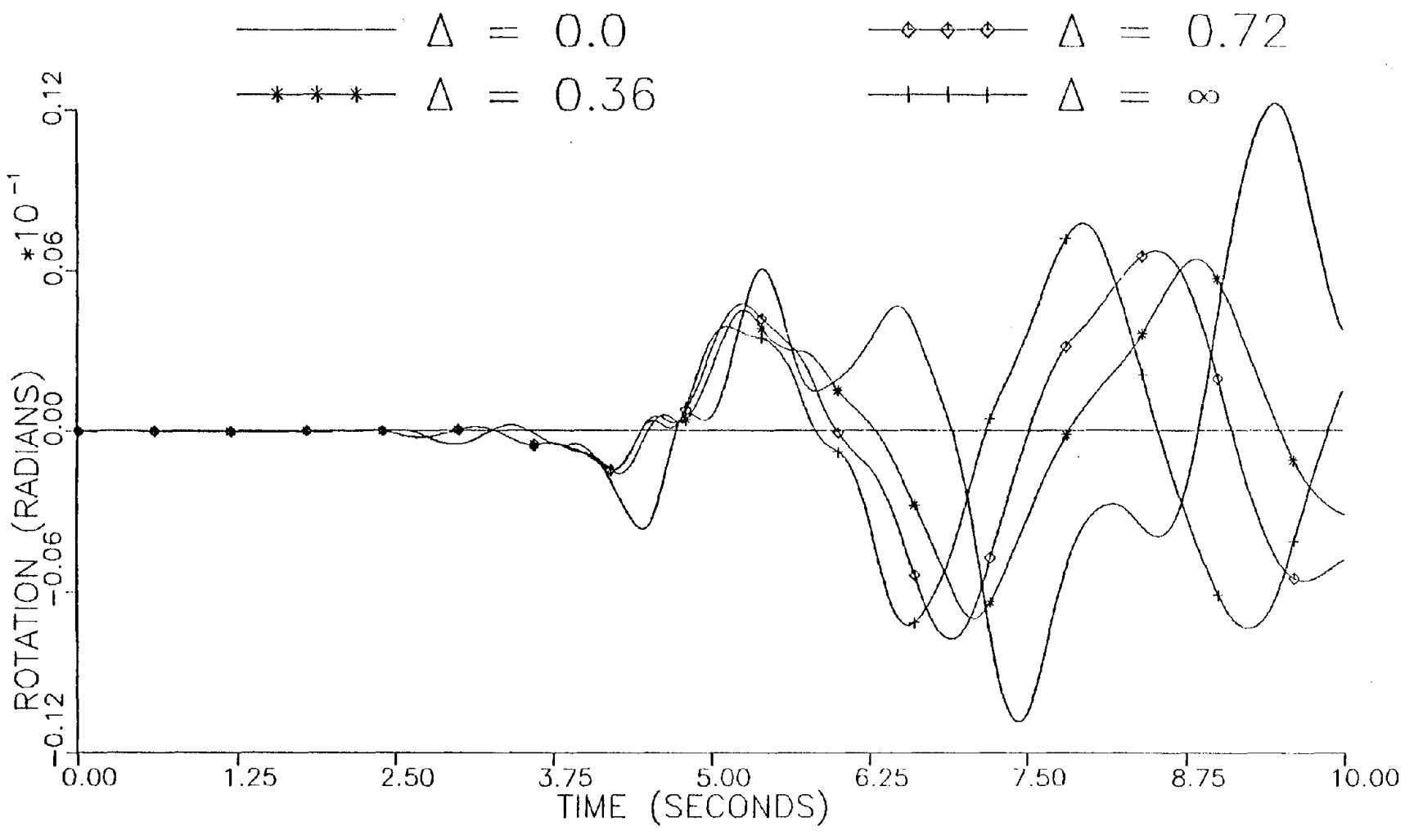

Figure 4.2-20. Roof Rotational Response, Incremental Failure Case for Eccentric Model, for 1966 Parkfield Record Acting in Rigid Direction.

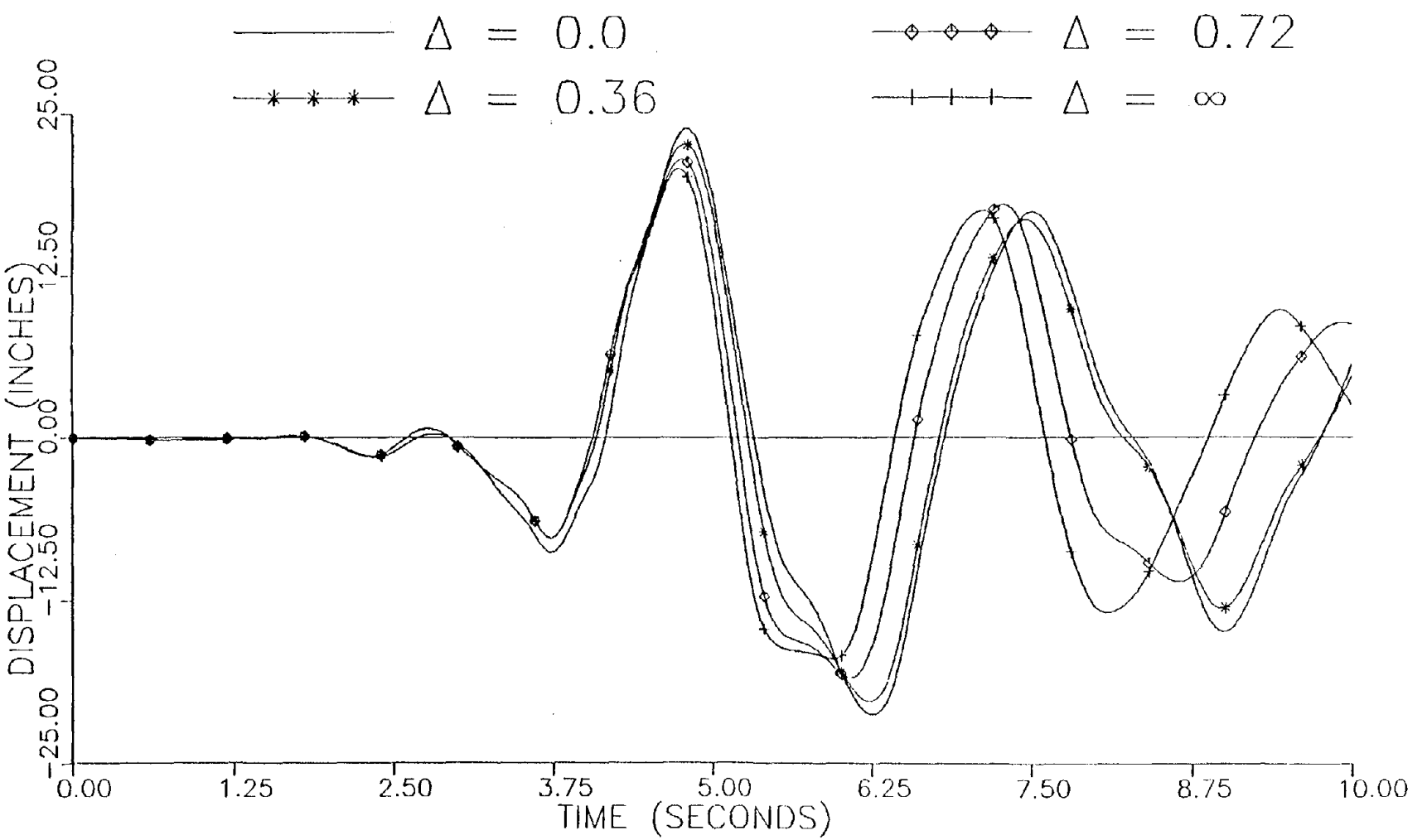

Figure 4.2-21. Roof Translational Response in Braced Direction, Incremental Failure Case for Eccentric Model, for 1966 Parkfield Record Acting in Braced Direction.

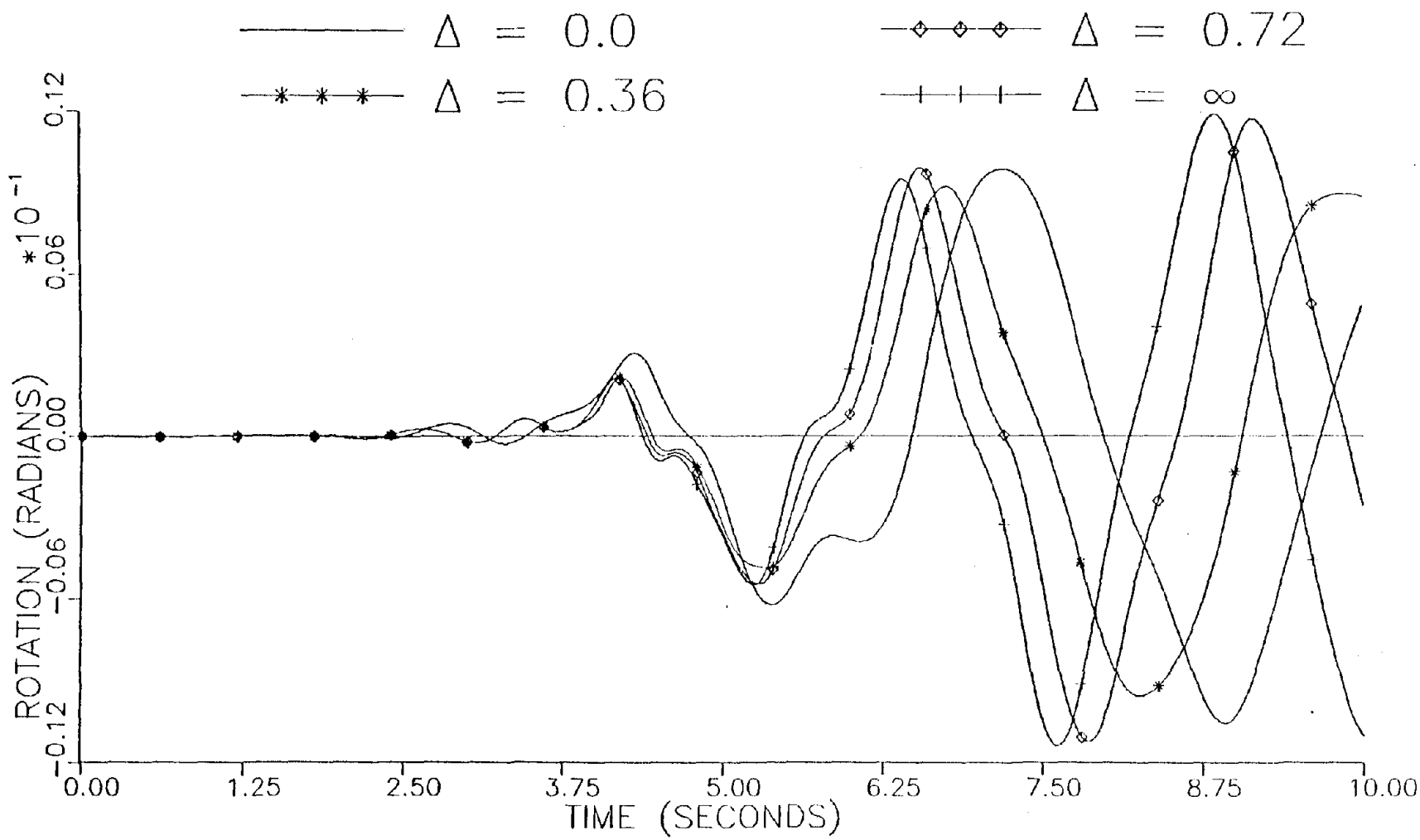

Figure 4.2-22. Roof Rotational Response, Incremental Failure Case for Eccentric Model, for 1966 Parkfield Record Acting in Braced Direction.

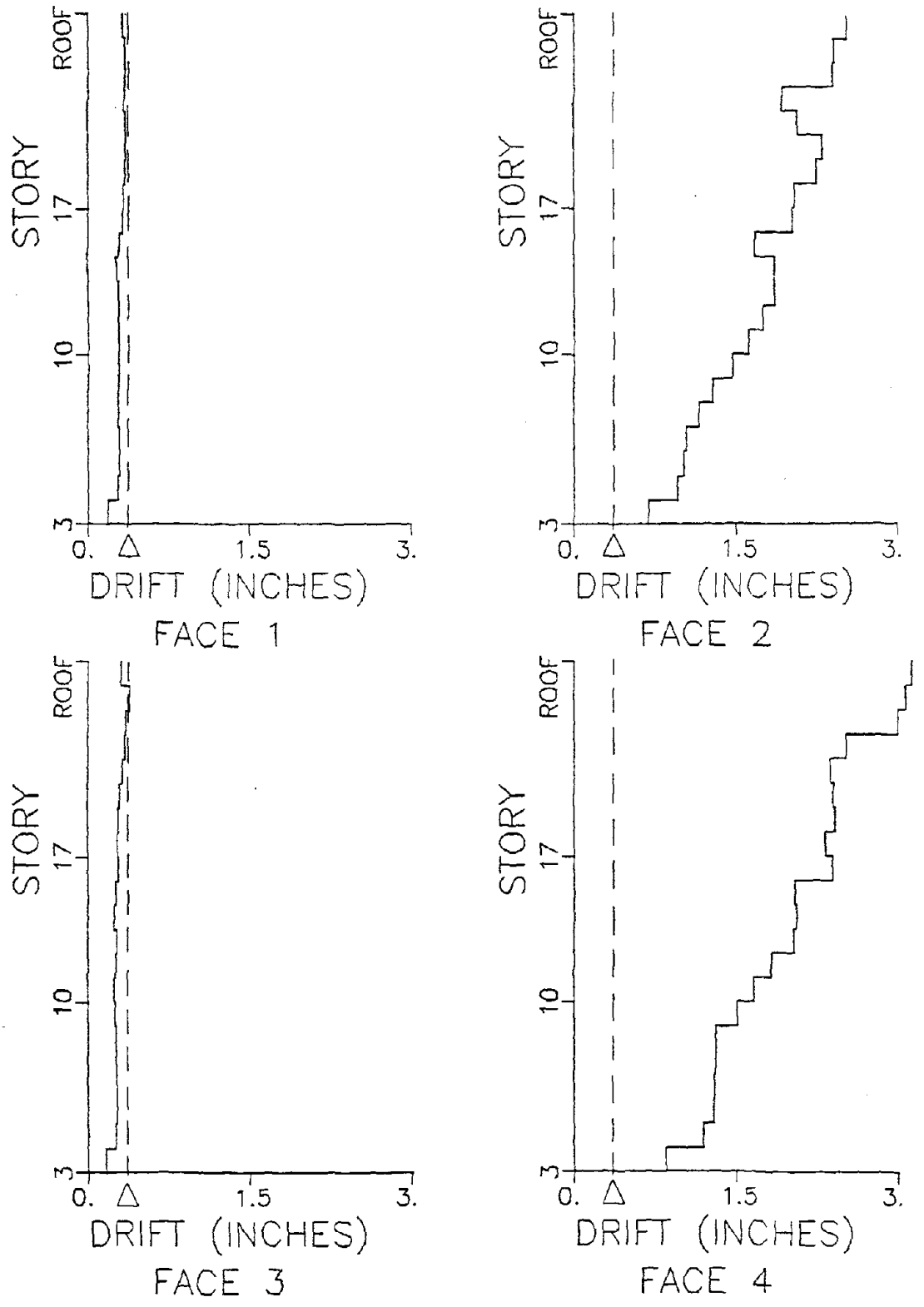

Figure 4.2-23. Peak Drift Values, Incremental Failure Case with Allowable Drift, Δ, set at 0.36 inches (0.9 cm), for 1966 Parkfield Record Acting in Rigid Direction, Eccentric Model.

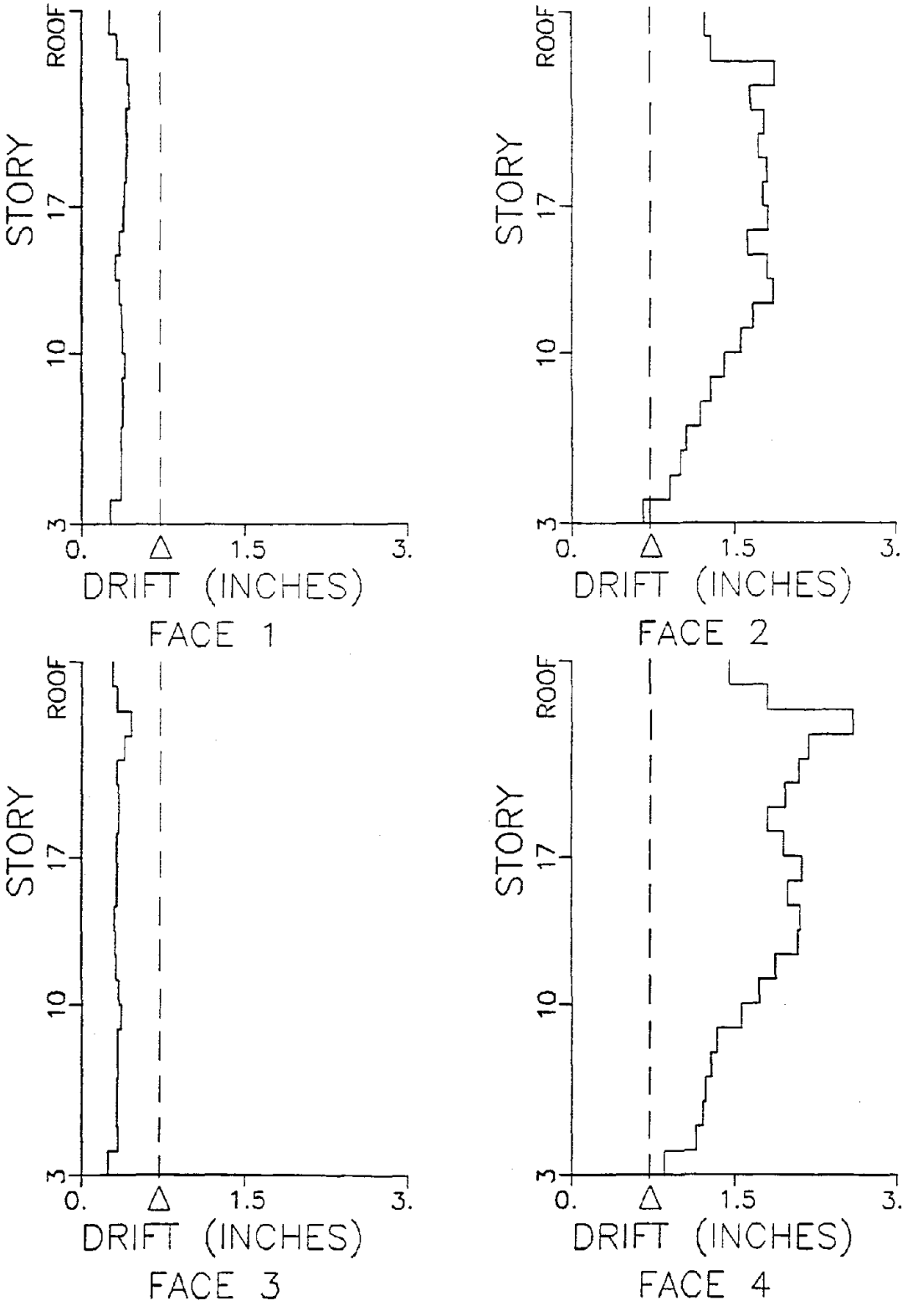

Figure 4.2-24. Peak Drift Values, Incremental Failure Case with Allowable Drift, Δ, set at 0.72 inches (1.8 cm), for 1966 Parkfield Record Acting in Rigid Direction, Eccentric Model.

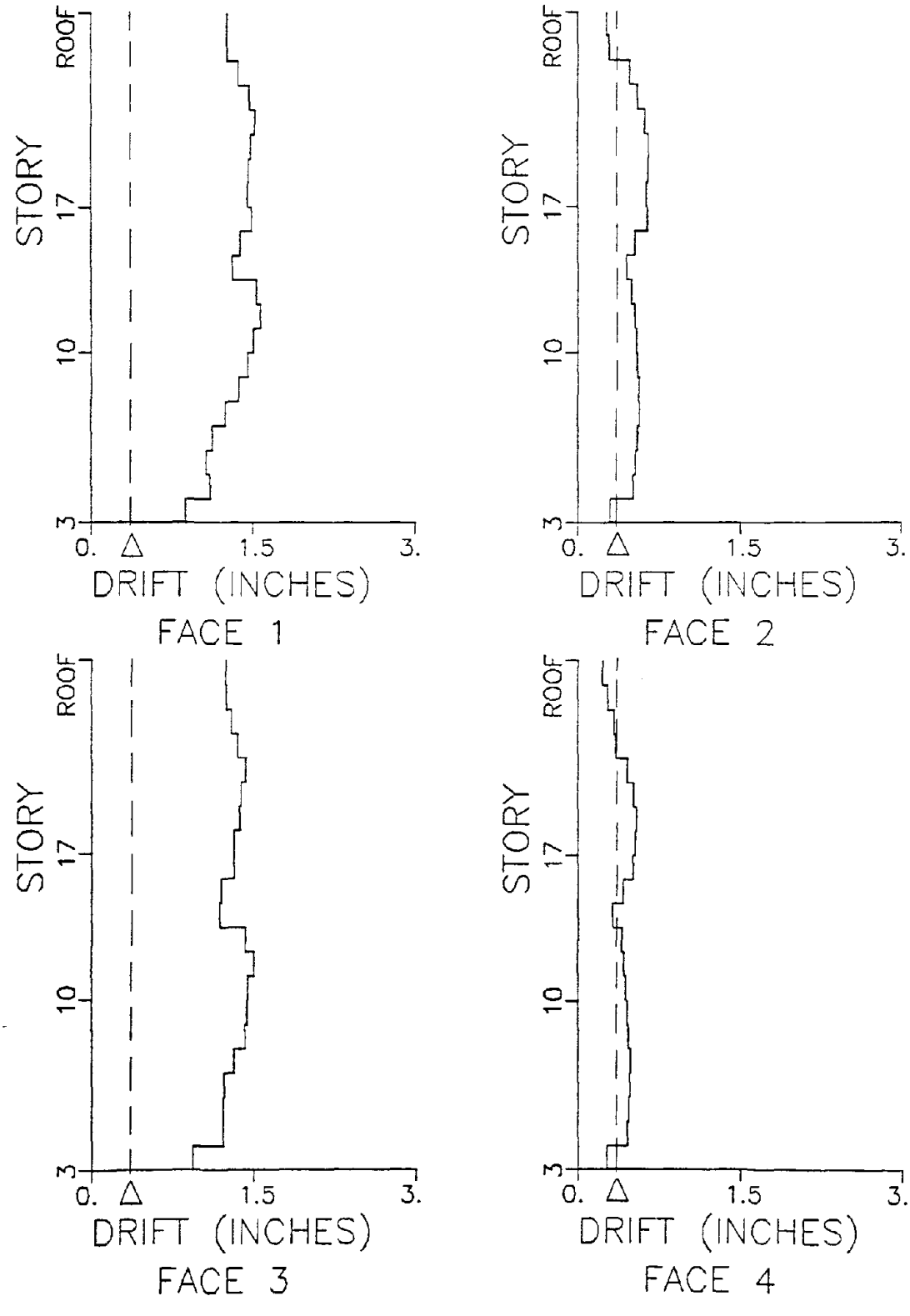

Figure 4.2-25. Peak Drift Values, Incremental Failure Case with Allowable Drift, Δ, set at 0.36 inches (0.9 cm), for 1966 Parkfield Record Acting in Braced Direction, Eccentric Model.

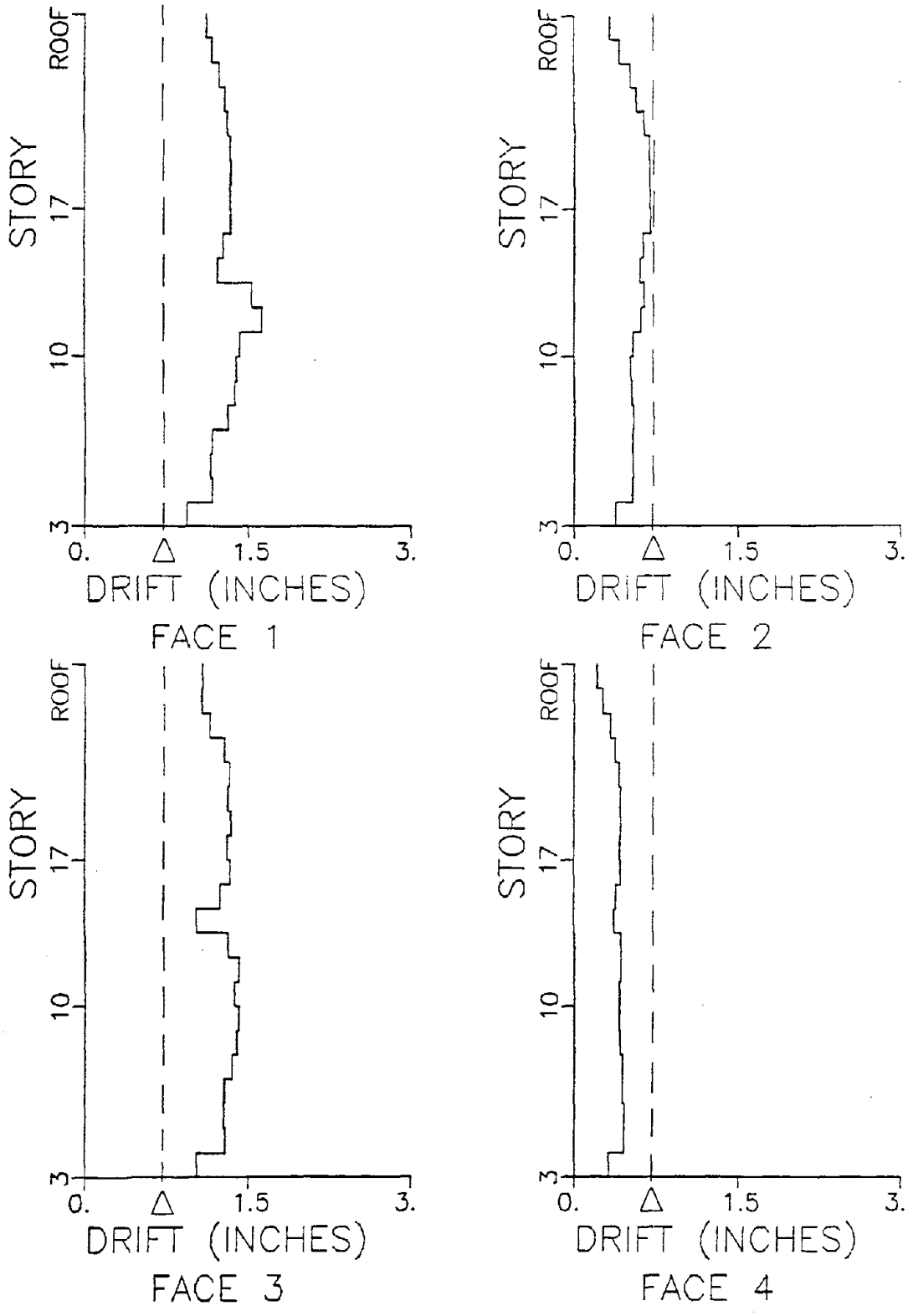

Figure 4.2-26. Peak Drift Values, Incremental Failure Case with Allowable Drift, Δ, set at 0.72 inches (1.8 cm), for 1966 Parkfield Record Acting in Braced Direction, Eccentric Model.

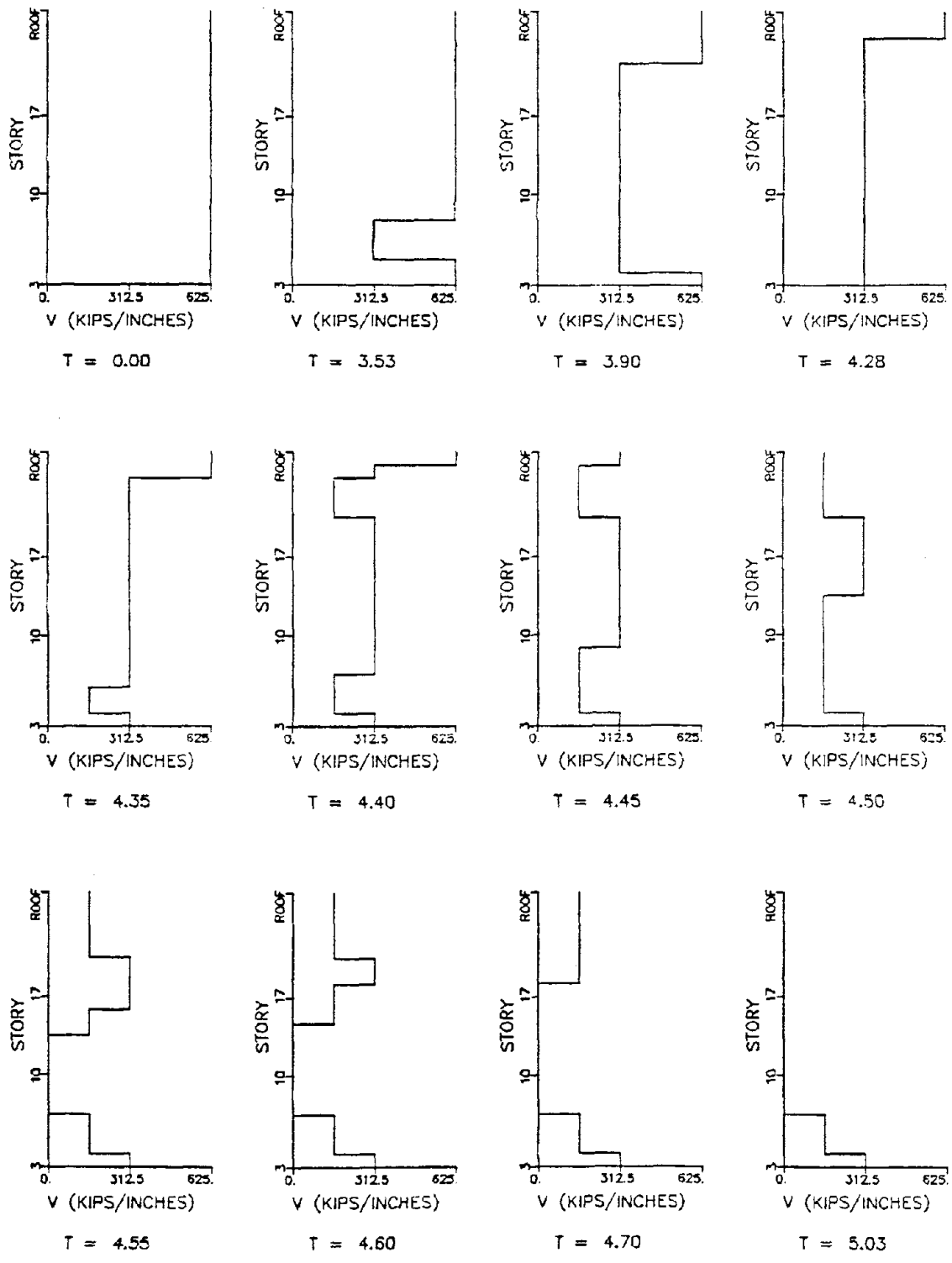

Figure 4.2-27. Progressive Failure of Cladding on Face 2 for 1966 Parkfield Record Acting in Rigid Direction with Allowable Drift, Δ, set at 0.36 inches (0.9 cm), Eccentric Model (Time T in Seconds.

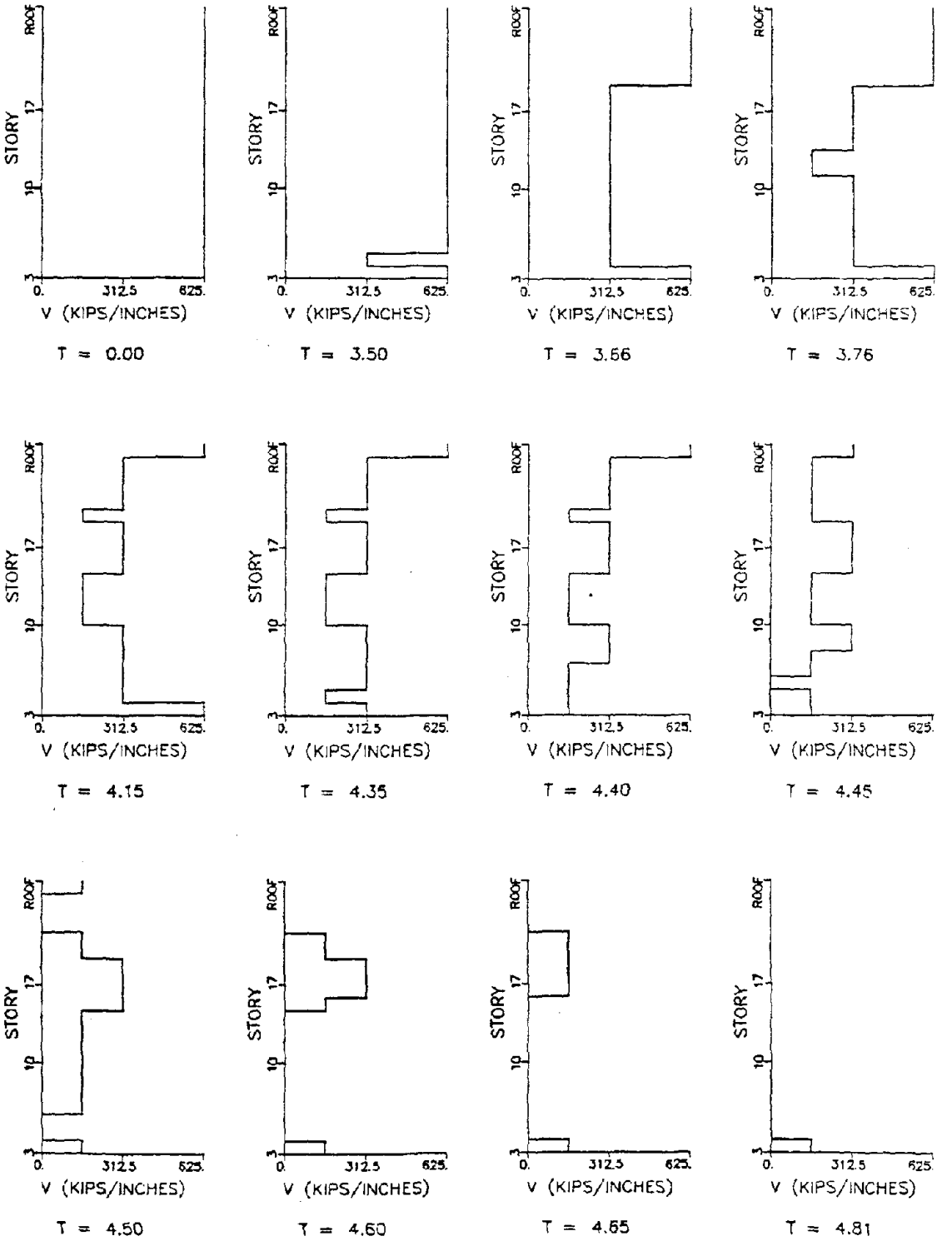

Figure 4.2-28. Progressive Failure of Cladding on Face 4 for 1966 Parkfield Record Acting in Rigid Direction with Allowable Drift, Δ, set at 0.36 inches (0.9 cm), Eccentric Model (Time T in seconds).

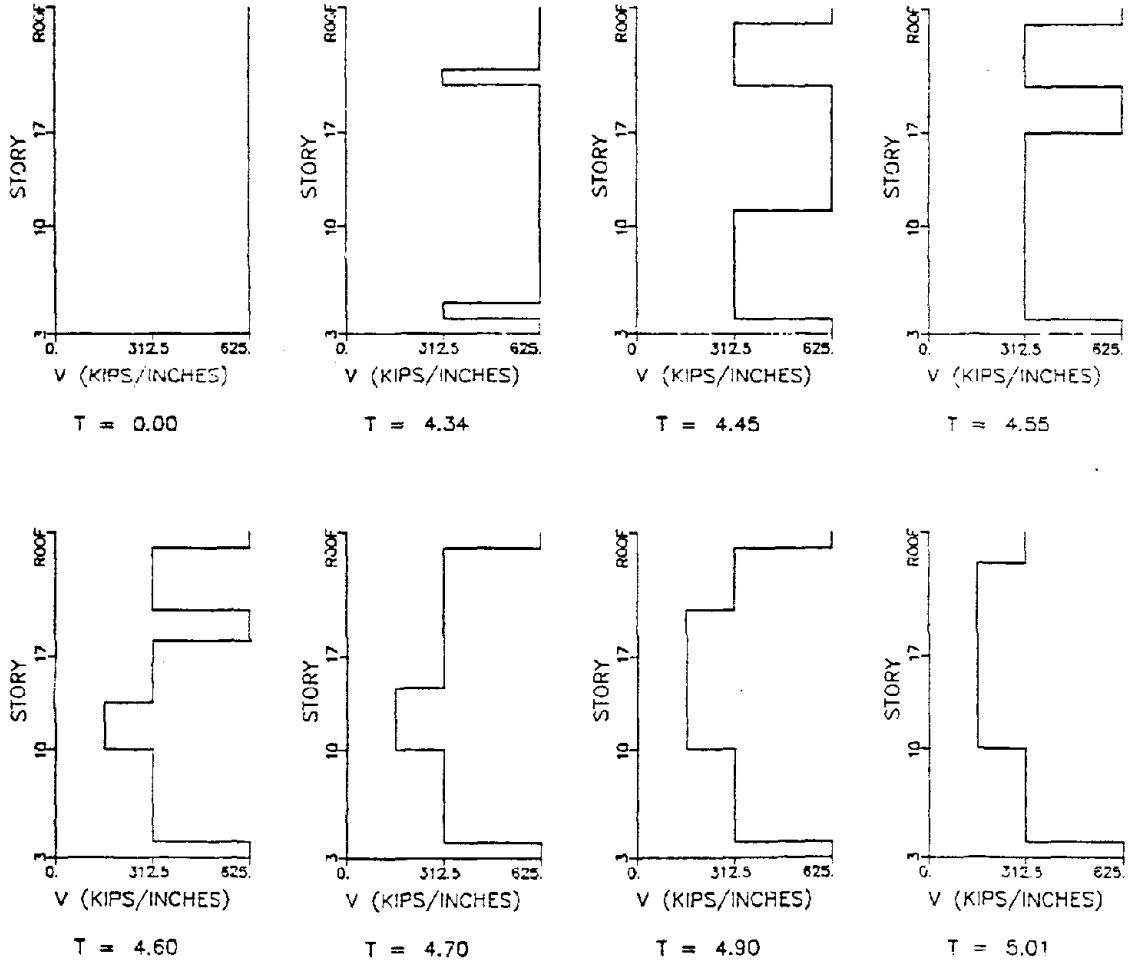

Figure 4.2-29. Progressive Failure of Cladding on Face 2 for 1966 Parkfield Record Acting in Rigid Direction with Allowable Drift, Δ, set at 0.72 inches (1.8 cm), Eccentric Model (Time T in seconds).

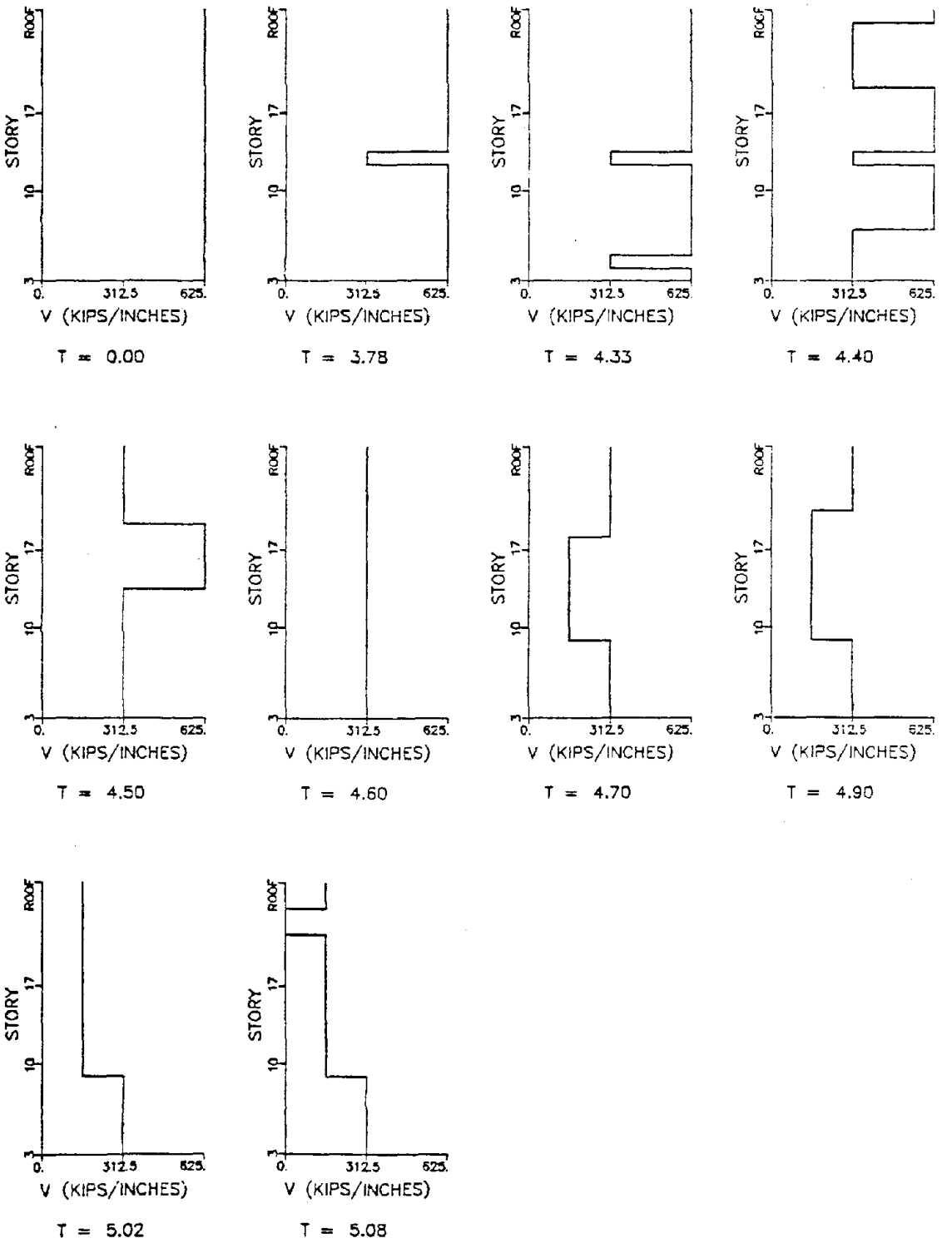

Figure 4.2-30. Progressive Failure of Cladding on Face 4 for 1966 Parkfield Record Acting in Rigid Direction with Allowable Drift, Δ, set at 0.72 inches (1.8 cm), Eccentric Model (Time T in seconds).

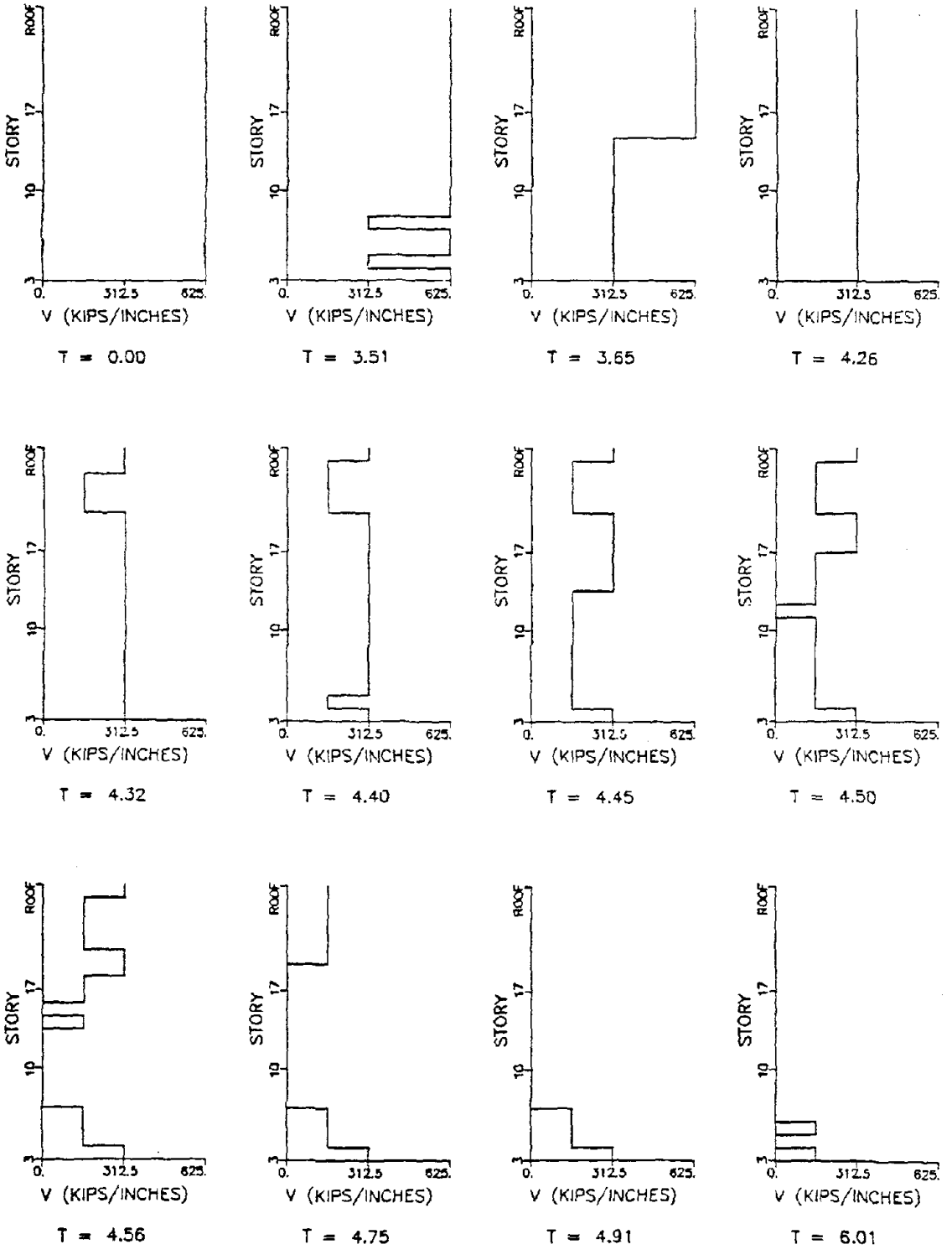

Figure 4.2-31. Progressive Failure of Cladding on Face 1 for 1966 Parkfield Record Acting in Braced Direction with Allowable Drift, Δ, set at 0.36 inches (0.9 cm), Eccentric Model (Time T in seconds).

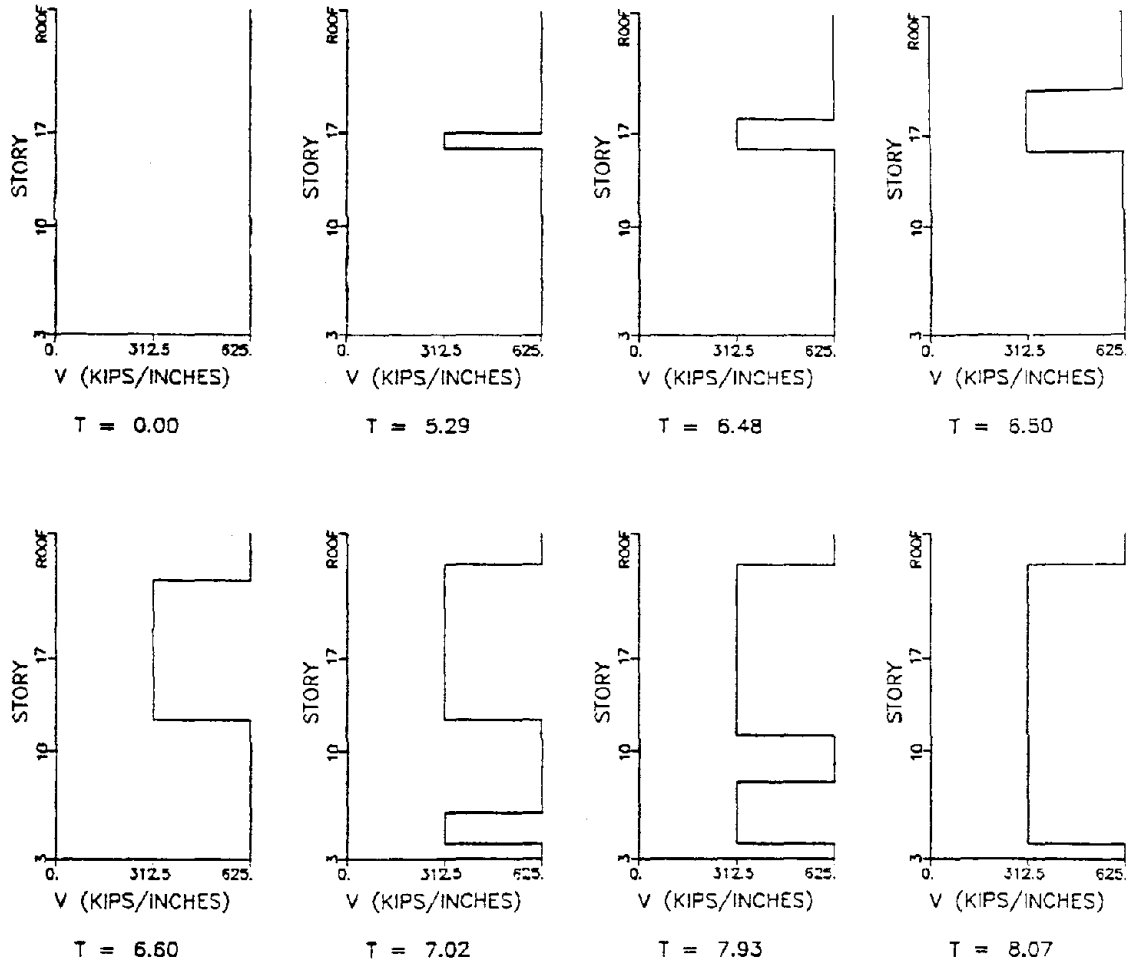

Figure 4.2-32. Progressive Failure of Cladding on Face 2 for 1966 Parkfield Record Acting in Braced Direction with Allowable Drift, Δ, set at 0.36 inches (0.9 cm), Eccentric Model (Time T in seconds).

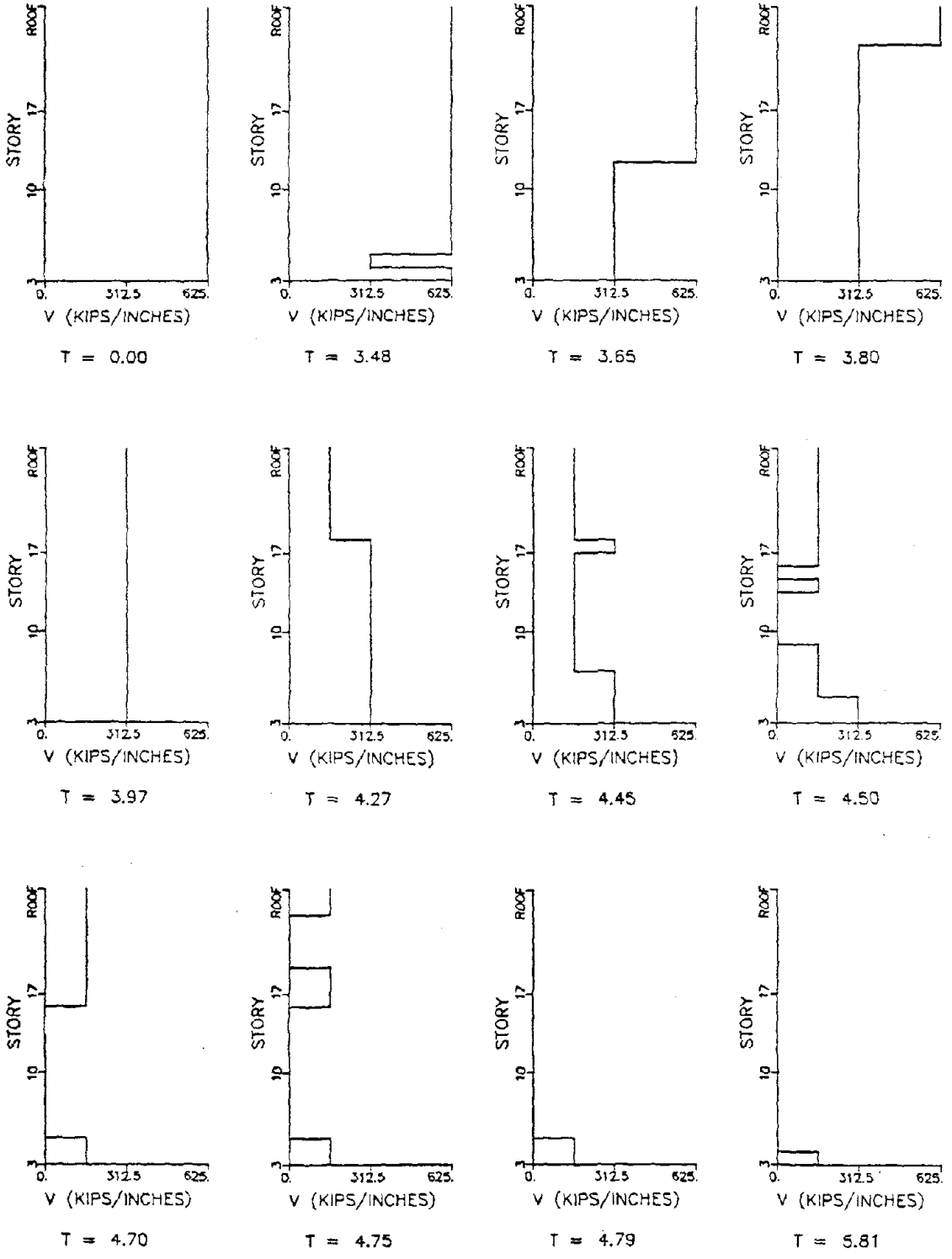

Figure 4.2-33. Progressive Failure of Cladding on Face 3 for 1966 Parkfield Record Acting in Braced Direction with Allowable Drift, Δ, set at 0.36 inches (0.9 cm), Eccentric Model (Time T in seconds).

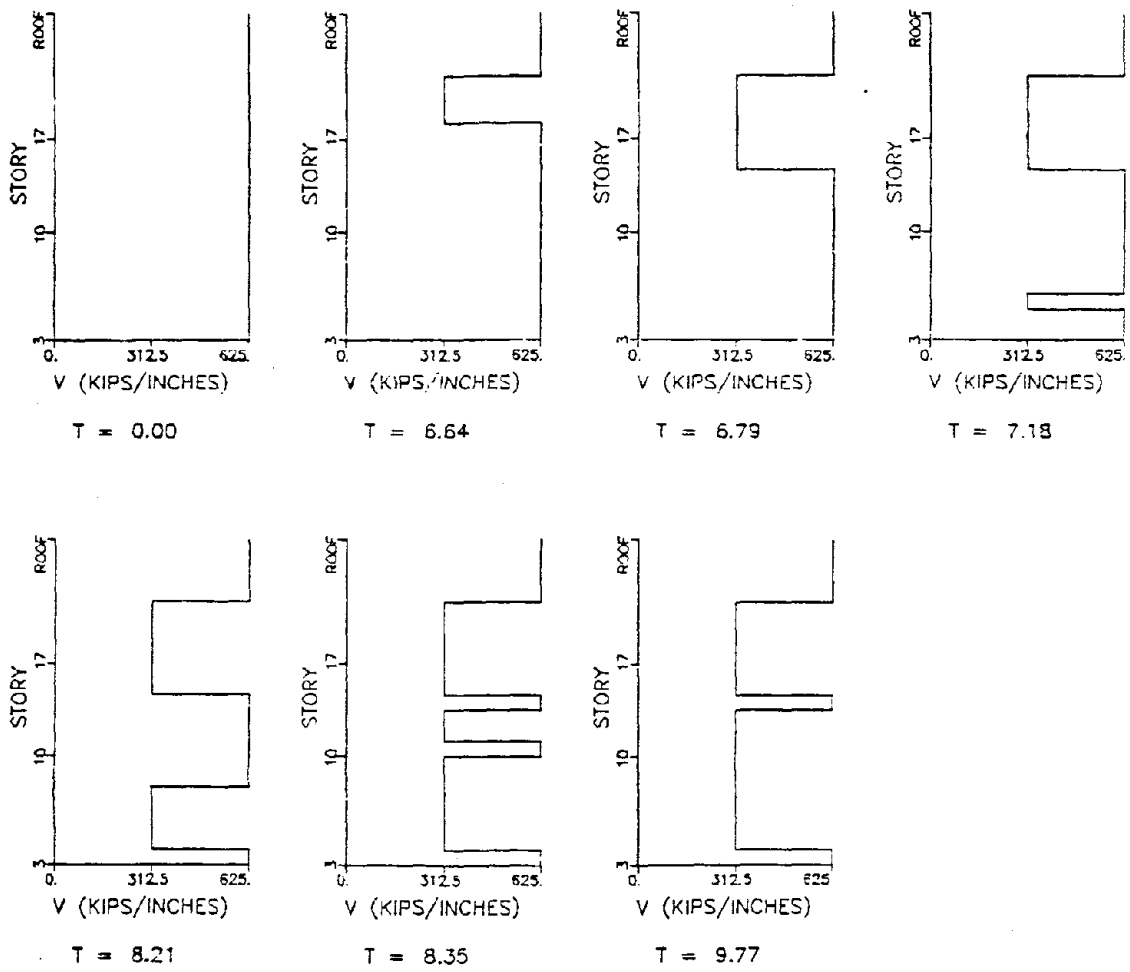

Figure 4.2-34. Progressive Failure of Cladding on Face 4 for 1966 Parkfield Record Acting in Braced Direction with Allowable Drift, Δ, set at 0.36 inches (0.9 cm), Eccentric Model (Time T in seconds).

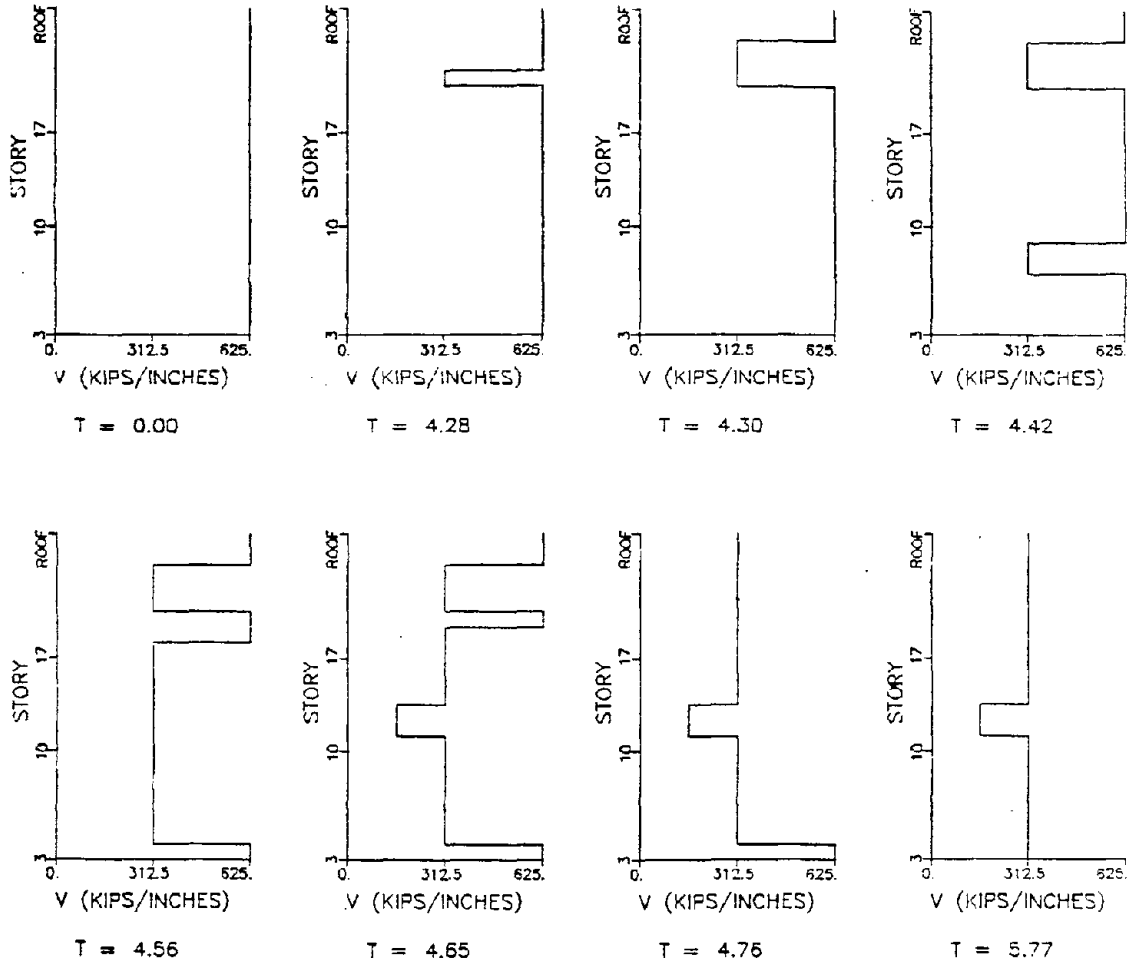

Figure 4.2-35. Progressive Failure of Cladding on Face 1 for 1966 Parkfield Record Acting in Braced Direction with Allowable Drift, Δ, set at 0.72 inches (1.8 cm), Eccentric Model (Time T in seconds).

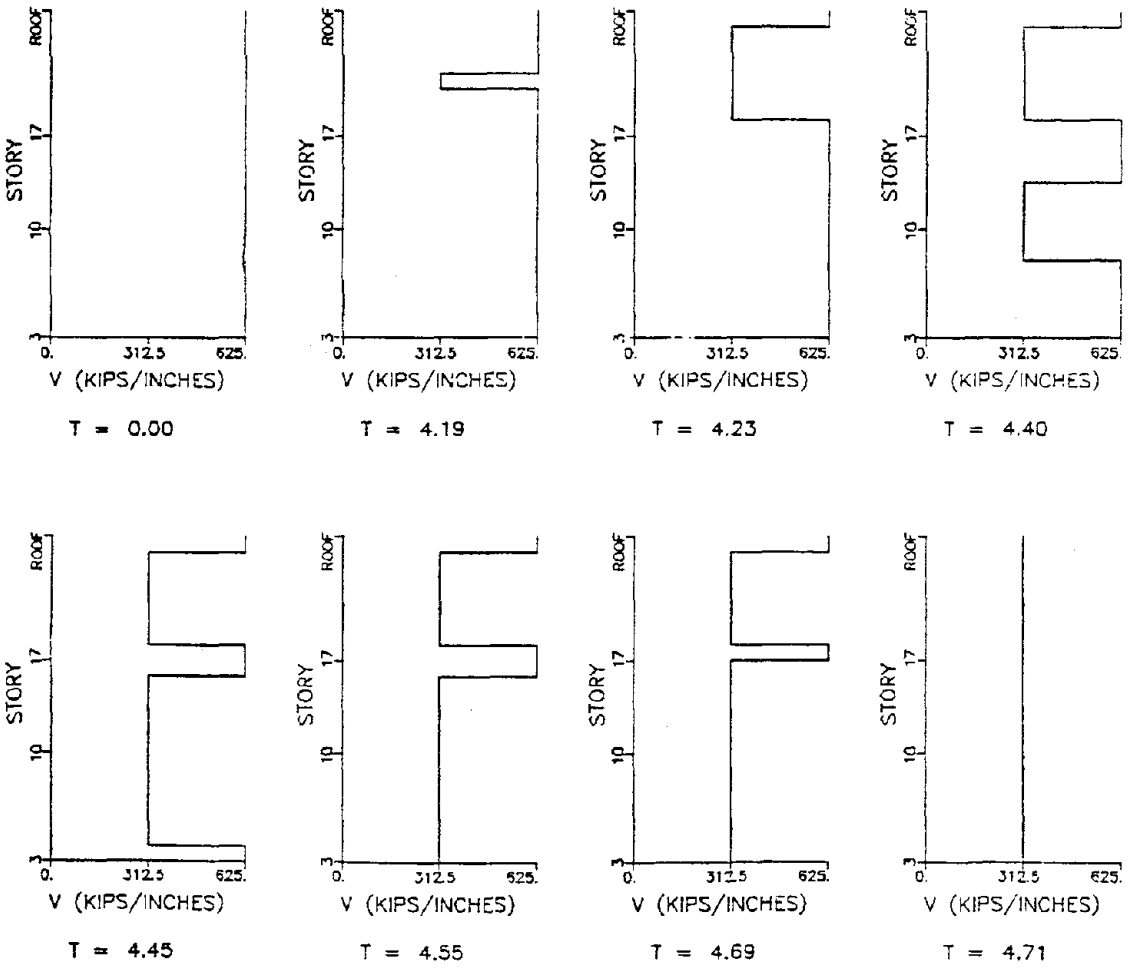

Figure 4.2- 36 Progressive Failure of Cladding on Face 3 for 1966 Parkfield Record Acting in Braced Direction with Allowable Drift, Δ, set at 0.72 inches (1.8 cm), Eccentric Model (Time T in seconds).

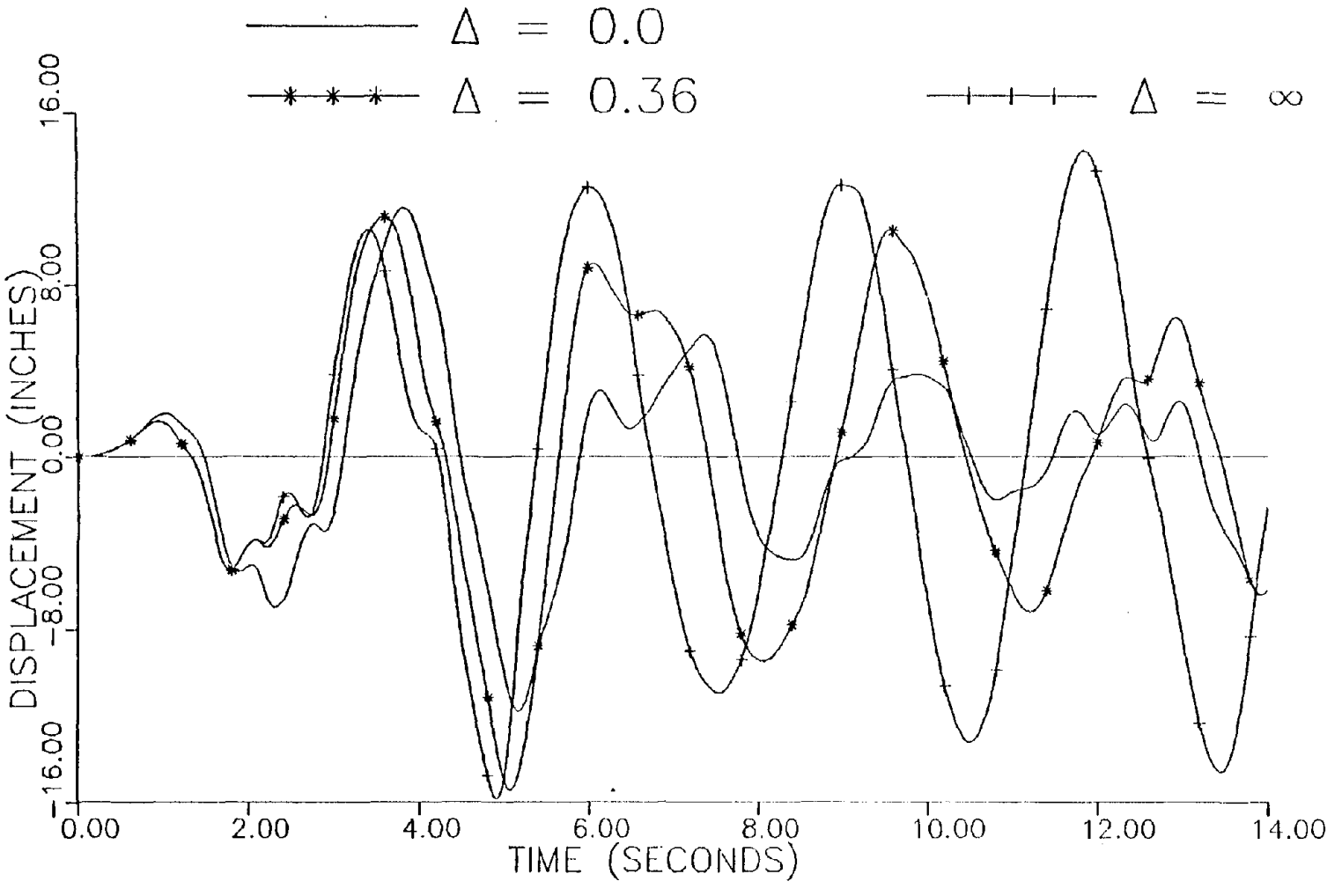

Figure 4.2-37. Roof Translational Response in Rigid Direction, Incremental Failure Case for Symmetric Model, for 1940 El Centro Record Acting in Rigid Direction.

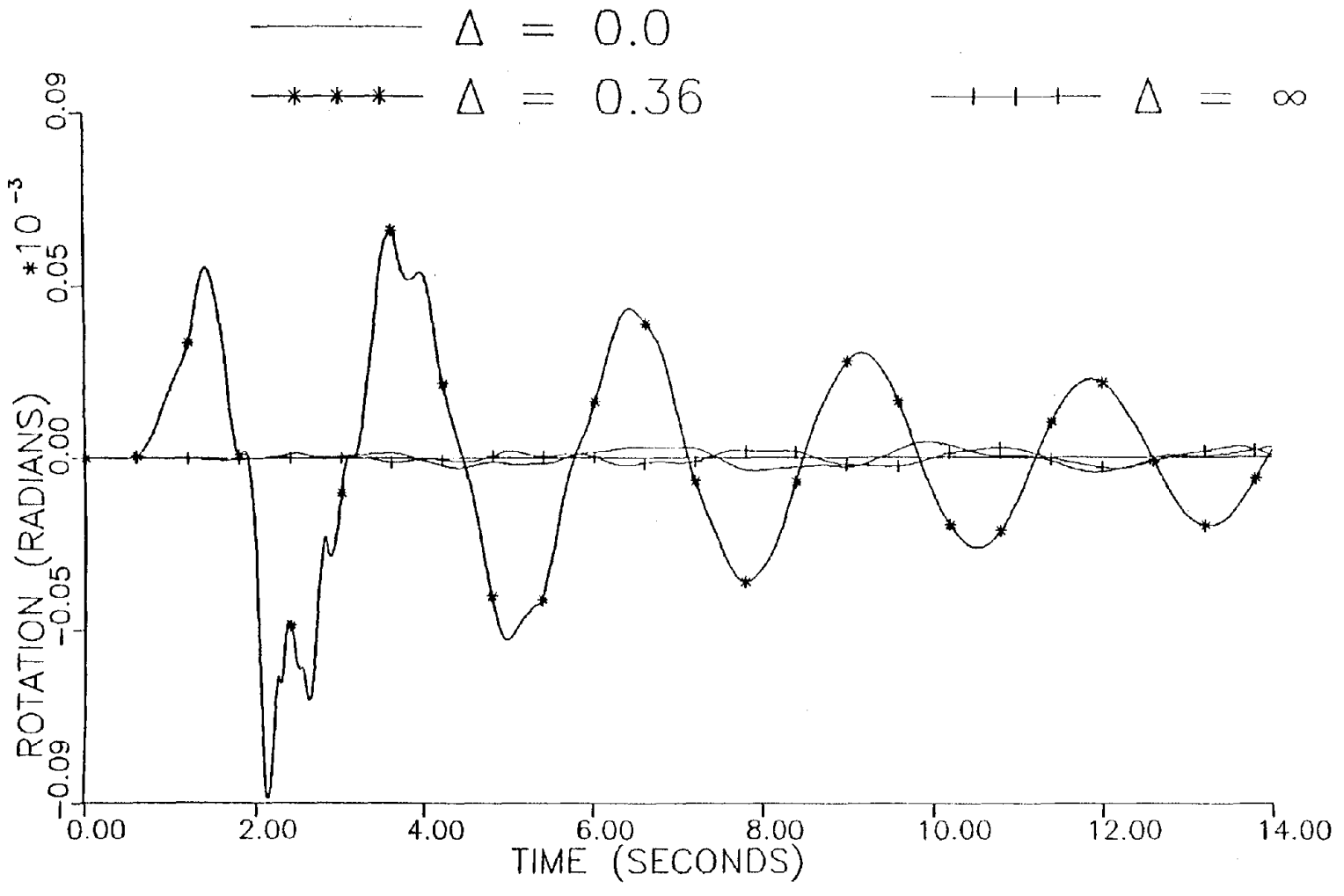

Figure 4.2-38. Roof Rotational Response, Incremental Failure Case for Symmetric Model, for 1940 El Centro Record Acting in Rigid Direction.

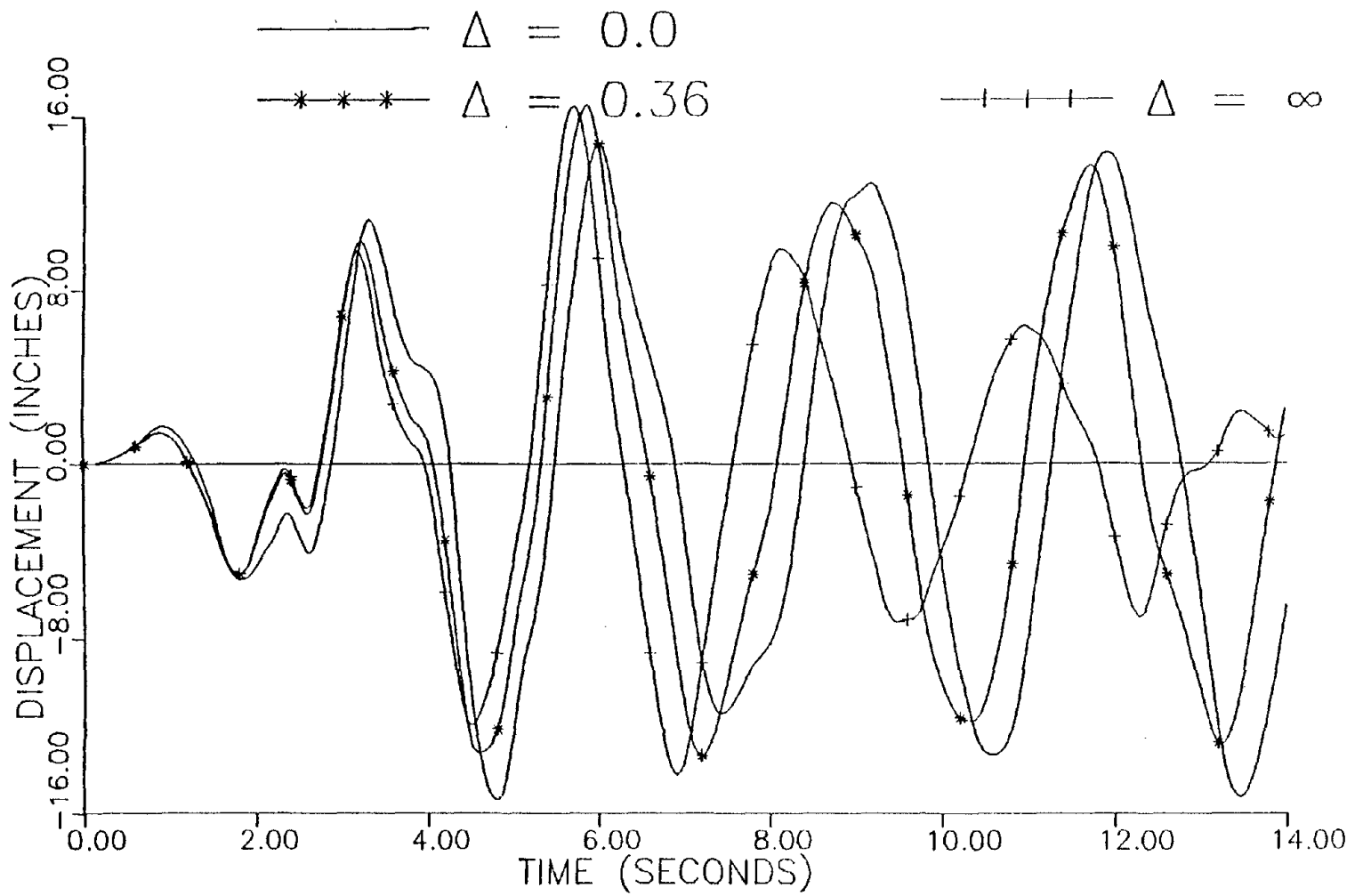

Figure 4.2-39. Roof Translational Response in Braced Direction, Incremental Failure Case for Symmetric Model, for 1940 El Centro Record Acting in Braced Direction.

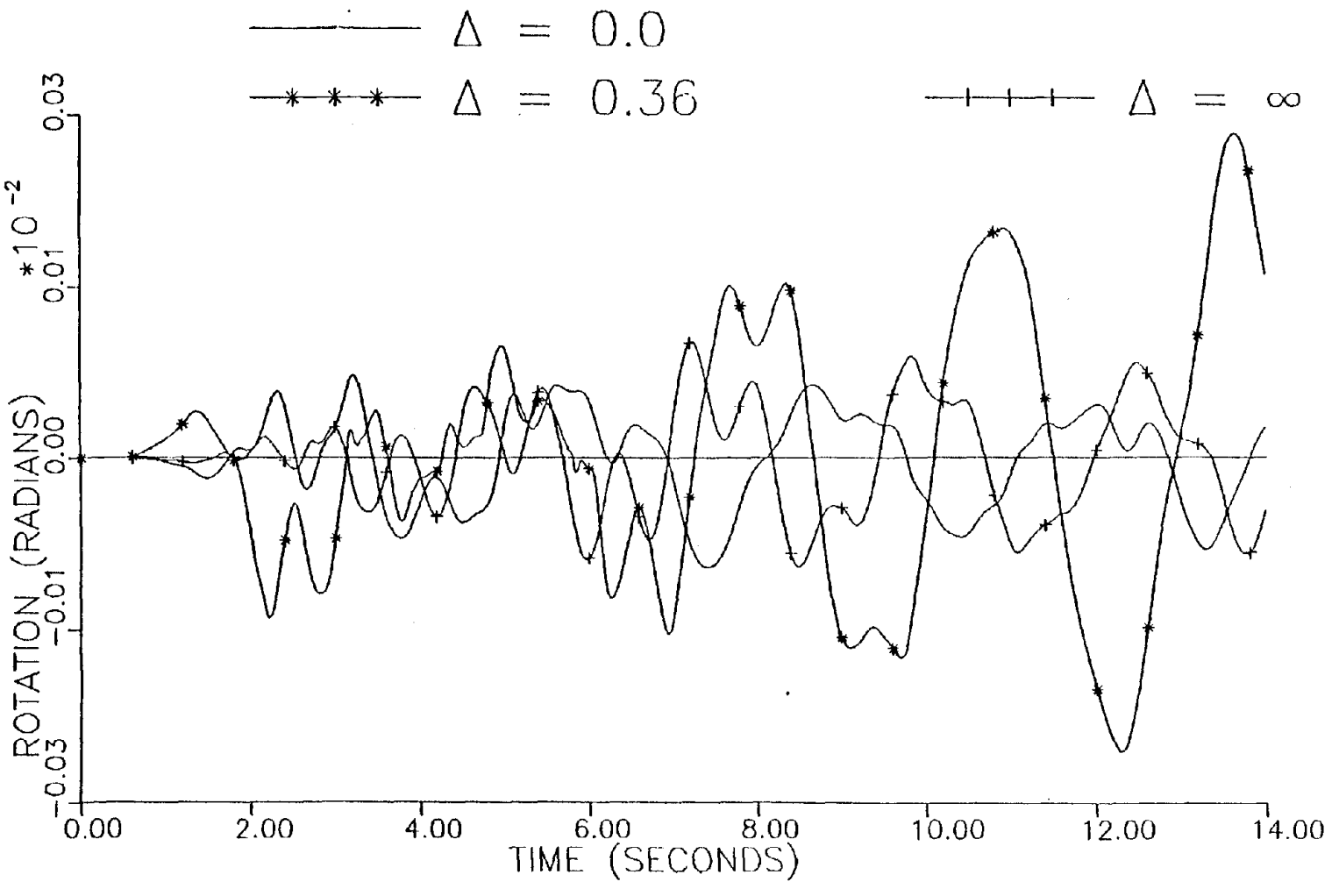

Figure 4.2-40. Roof Rotational Response, Incremental Failure Case for Symmetric Model, for 1940 El Centro Record Acting in Braced Direction.

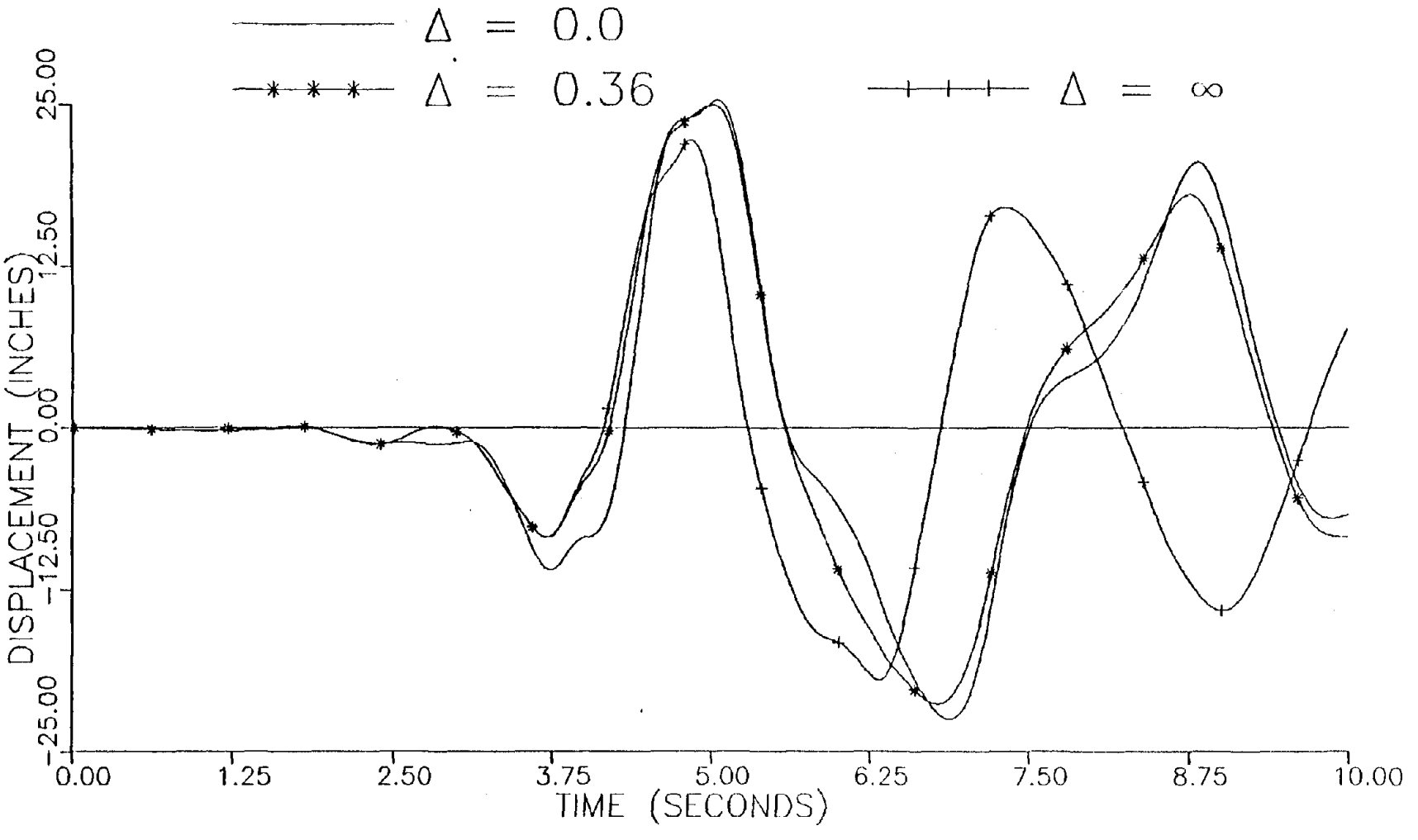

Figure 4.2-41. Roof Translational Response in Rigid Direction, Incremental Failure Case for Symmetric Model, for 1966 Parkfield Record Acting in Rigid Direction.

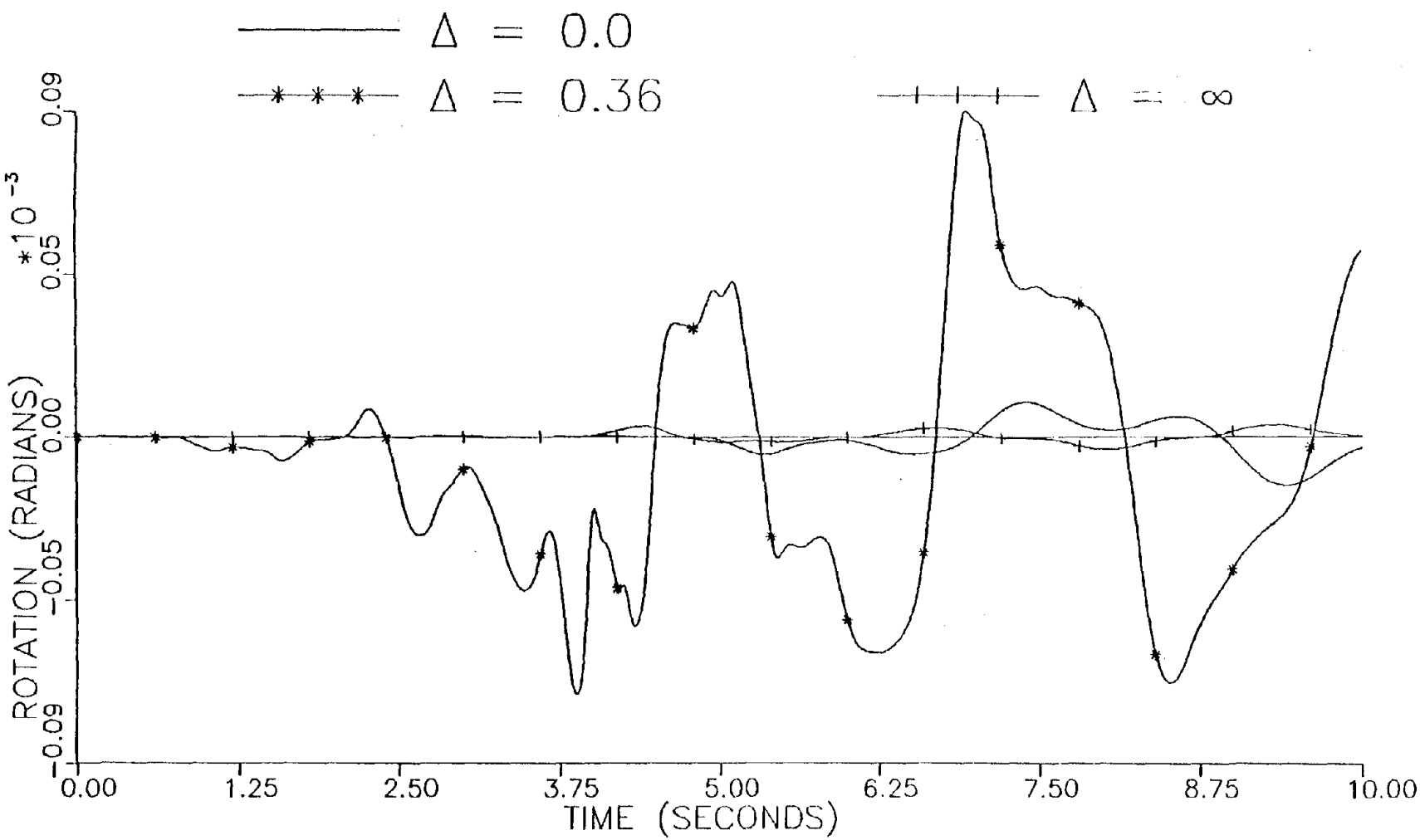

Figure 4.2-42. Roof Rotational Response, Incremental Failure Case for Symmetric Model, for 1966 Parkfield Record Acting in Rigid Direction.

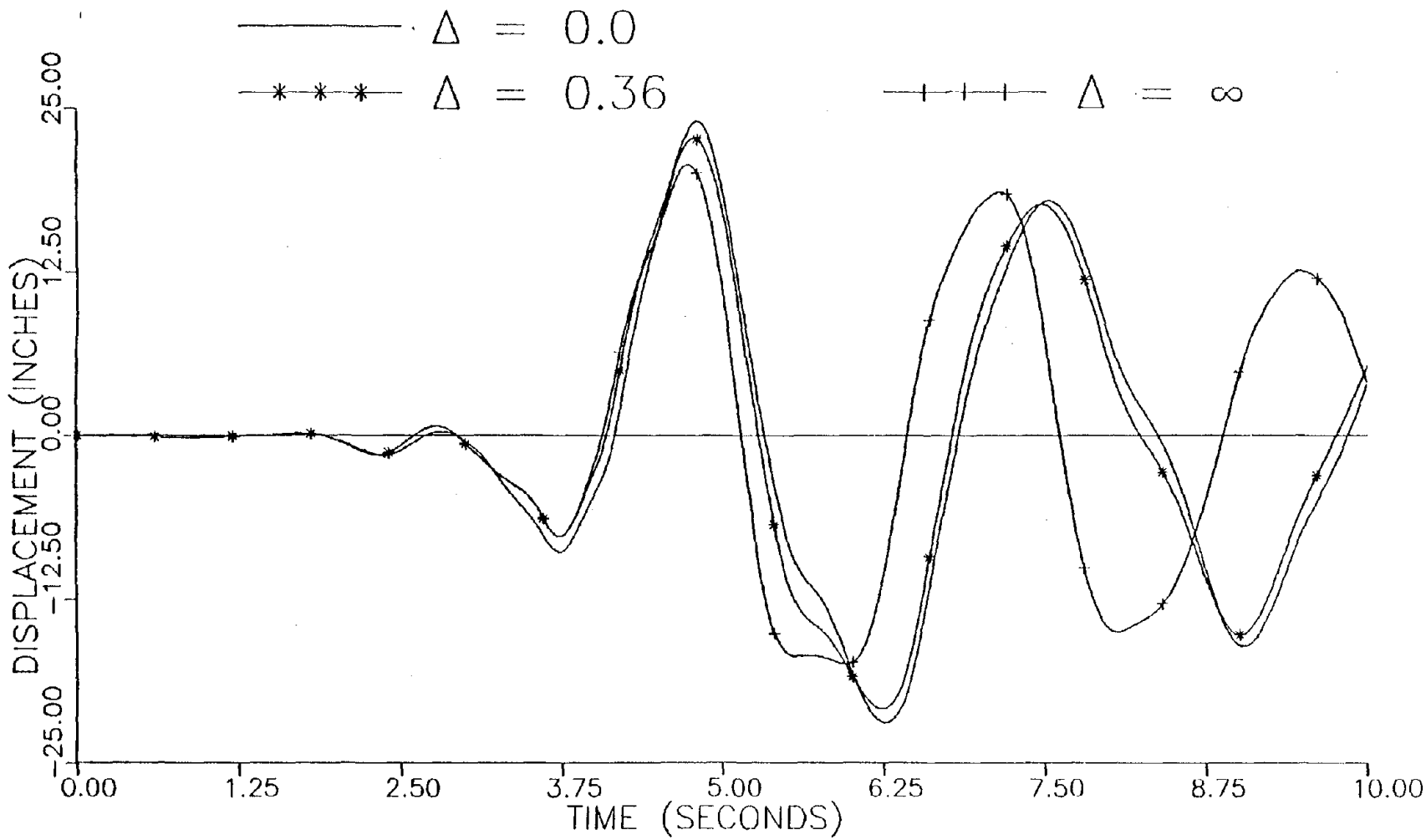

Figure 4.2-43. Roof Translational Response in Braced Direction, Incremental Failure Case for Symmetric Model, for 1966 Parkfield Record Acting in Braced Direction.

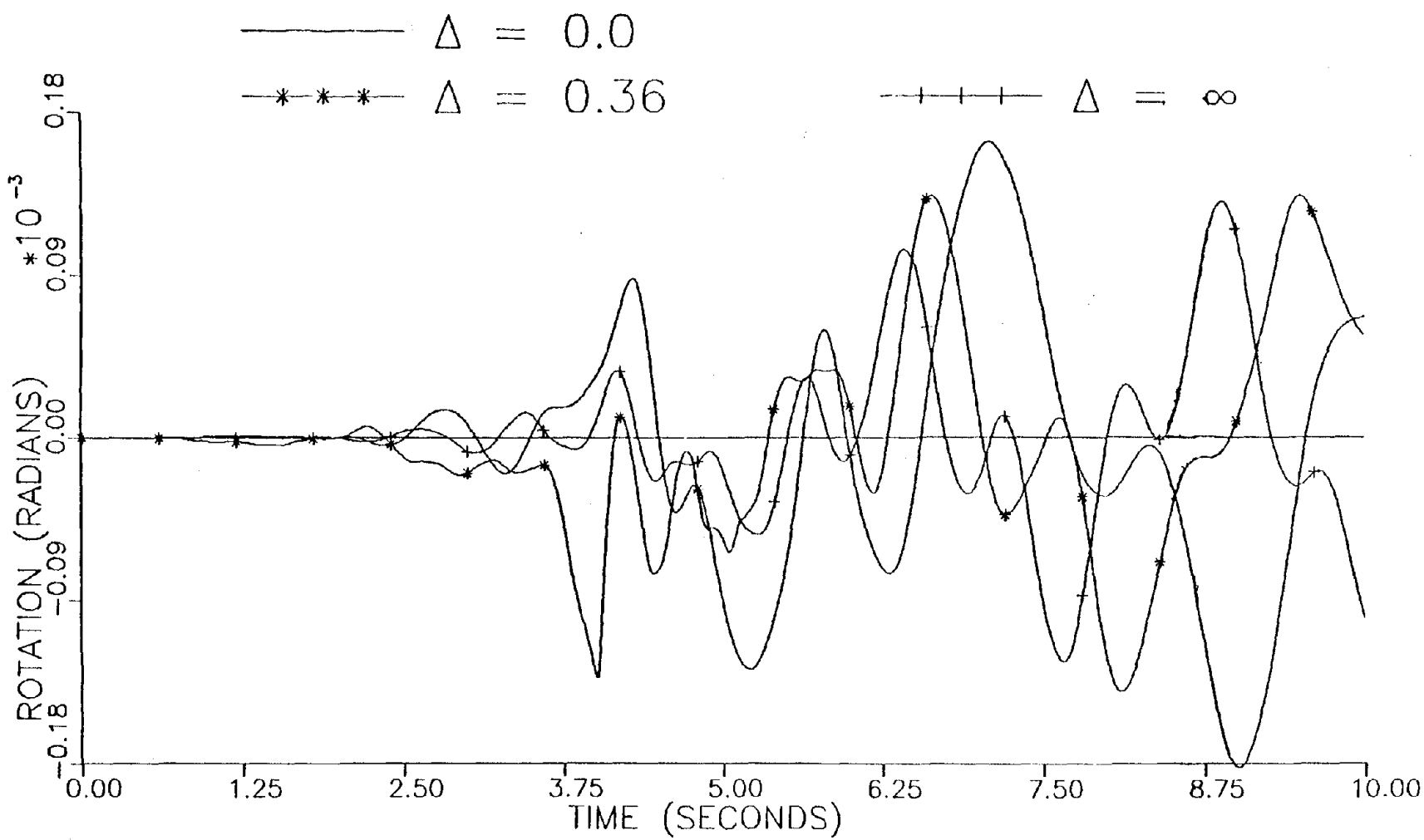

Figure 4.2-44. Roof Rotational Response, Incremental Failure Case for Symmetric Model, for 1966 Parkfield Record Acting in Braced Direction.

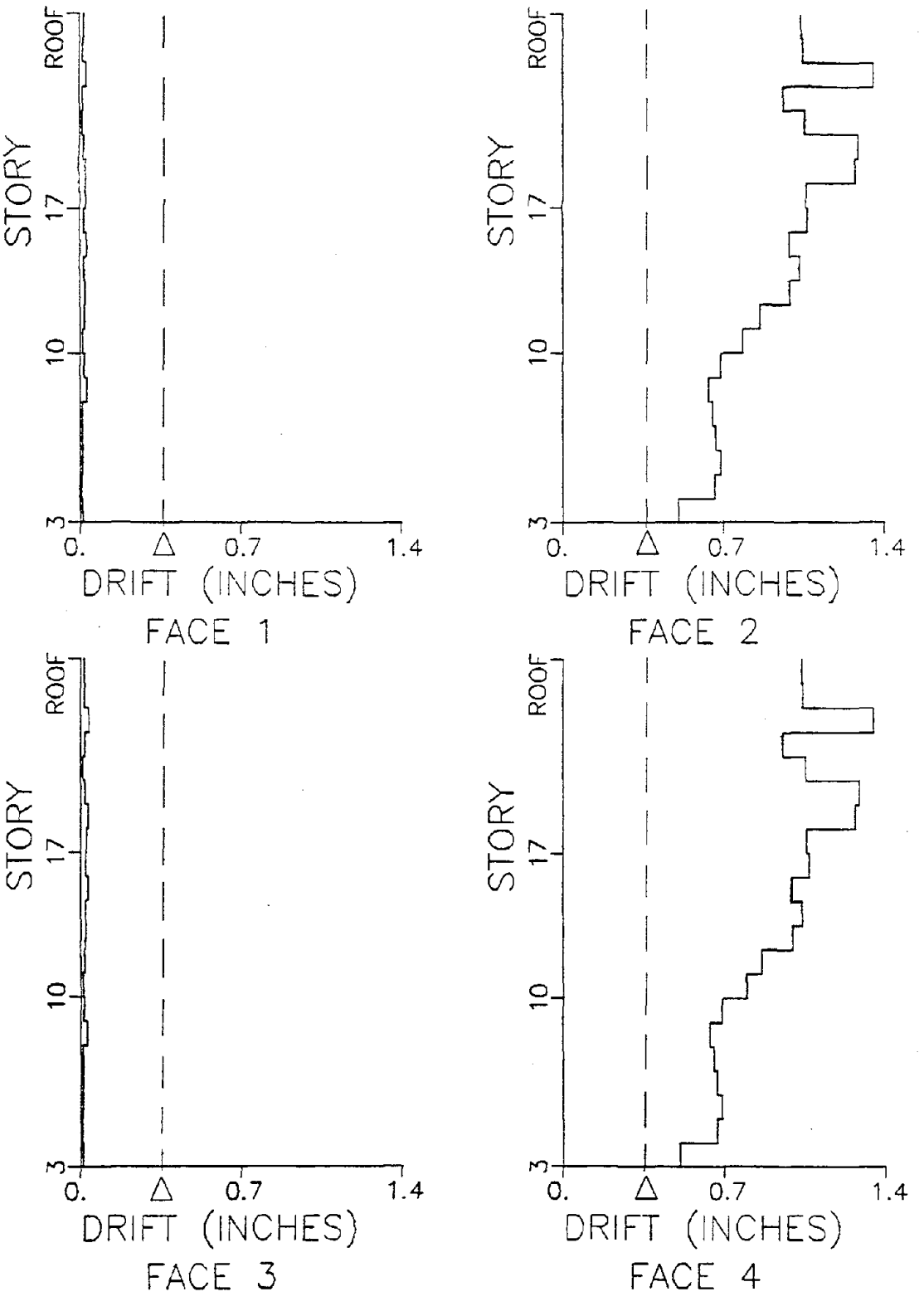

Figure 4.2-45. Peak Drift Values, Incremental Failure Case with Allowable Drift, Δ, set at 0.36 inches (0.9 cm), for 1940 El Centro Record Acting in Rigid Direction, Symmetric Model.

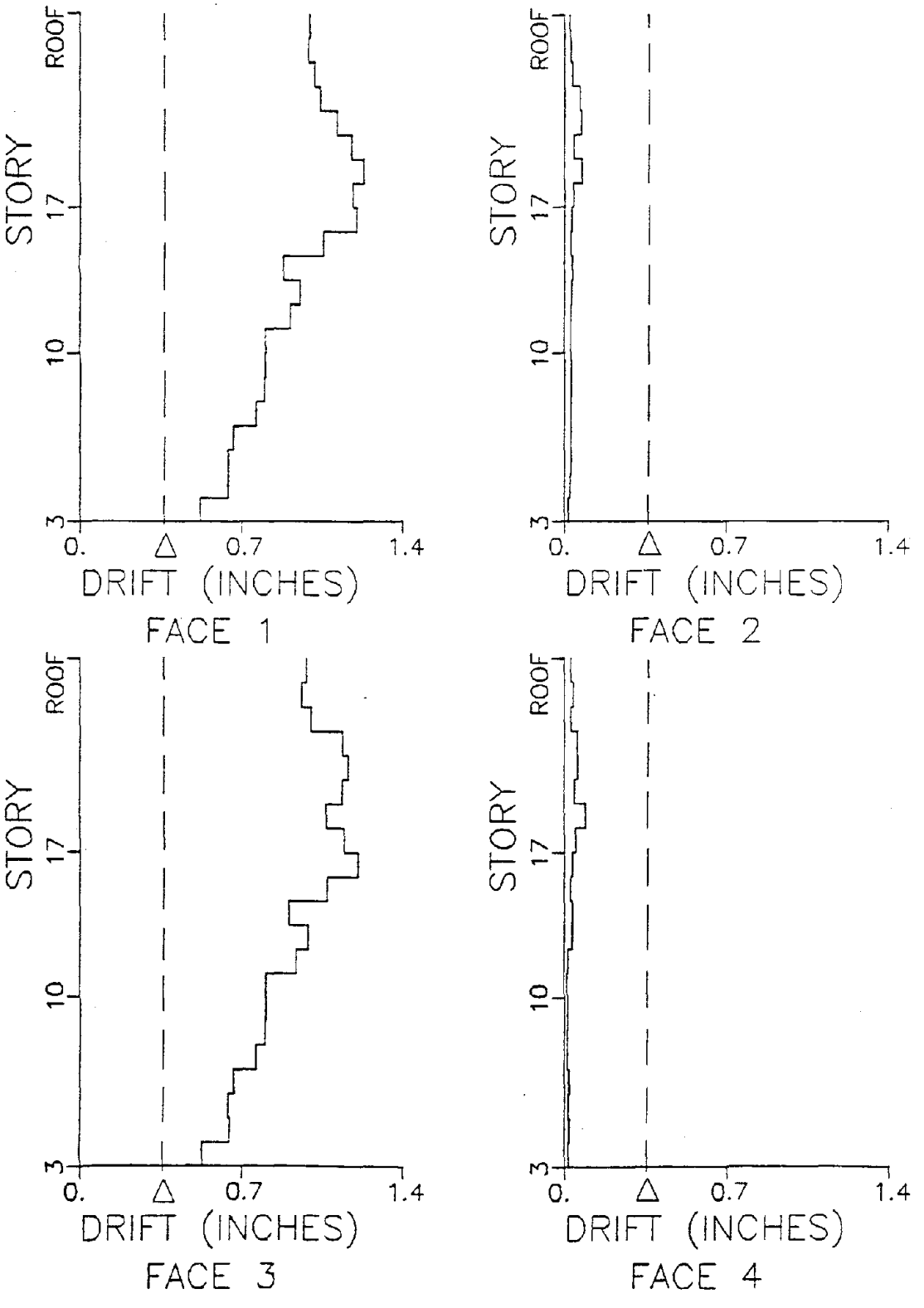

Figure 4.2-46. Peak Drift Values, Incremental Failure Case with Allowable Drift, Δ, set at 0.36 inches (0.9 cm), for 1940 El Centro Record Acting in Braced Direction, Symmetric Model.

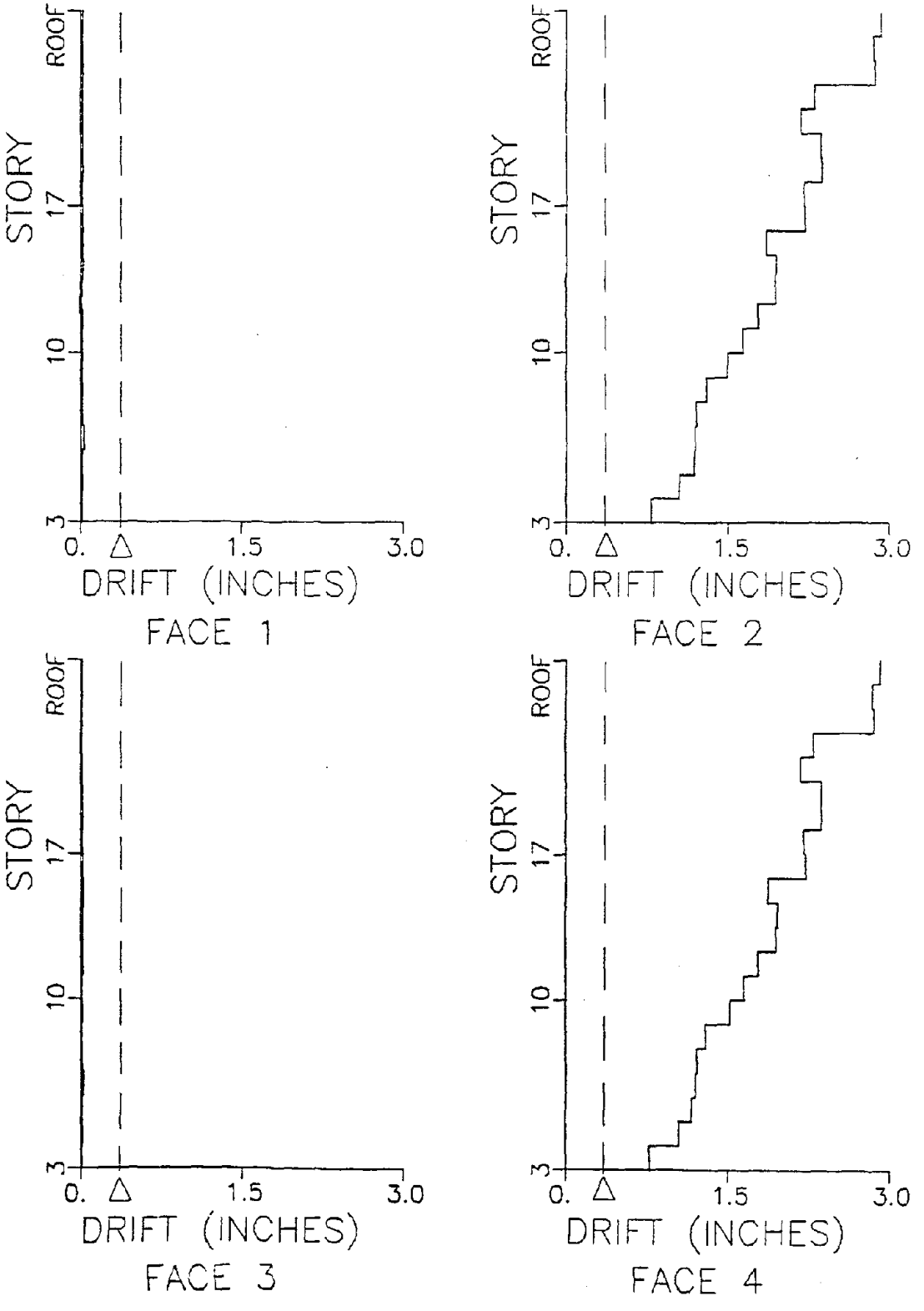

Figure 4.2-47. Peak Drift Values, Incremental Failure Case with Allowable Drift, Δ, set at 0.36 inches (0.9 cm), for 1966 Parkfield Record Acting in Rigid Direction, Symmetric Case.

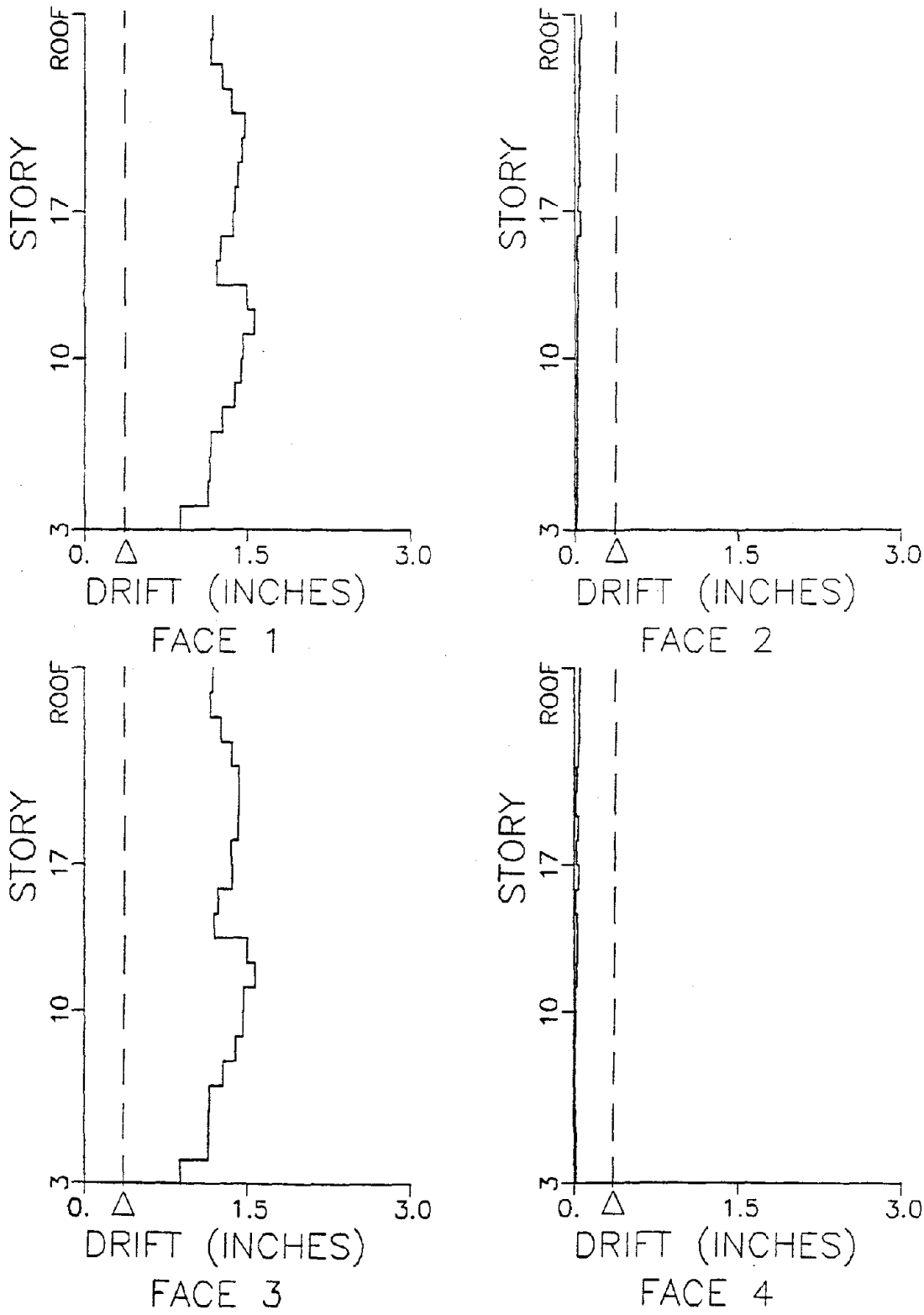

Figure 4.2-48. Peak Drift Values, Incremental Failure Case with Allowable Drift, Δ, set at 0.36 inches (0.9 cm), for 1966 Parkfield Record Acting in Braced Direction, Symmetric Model.

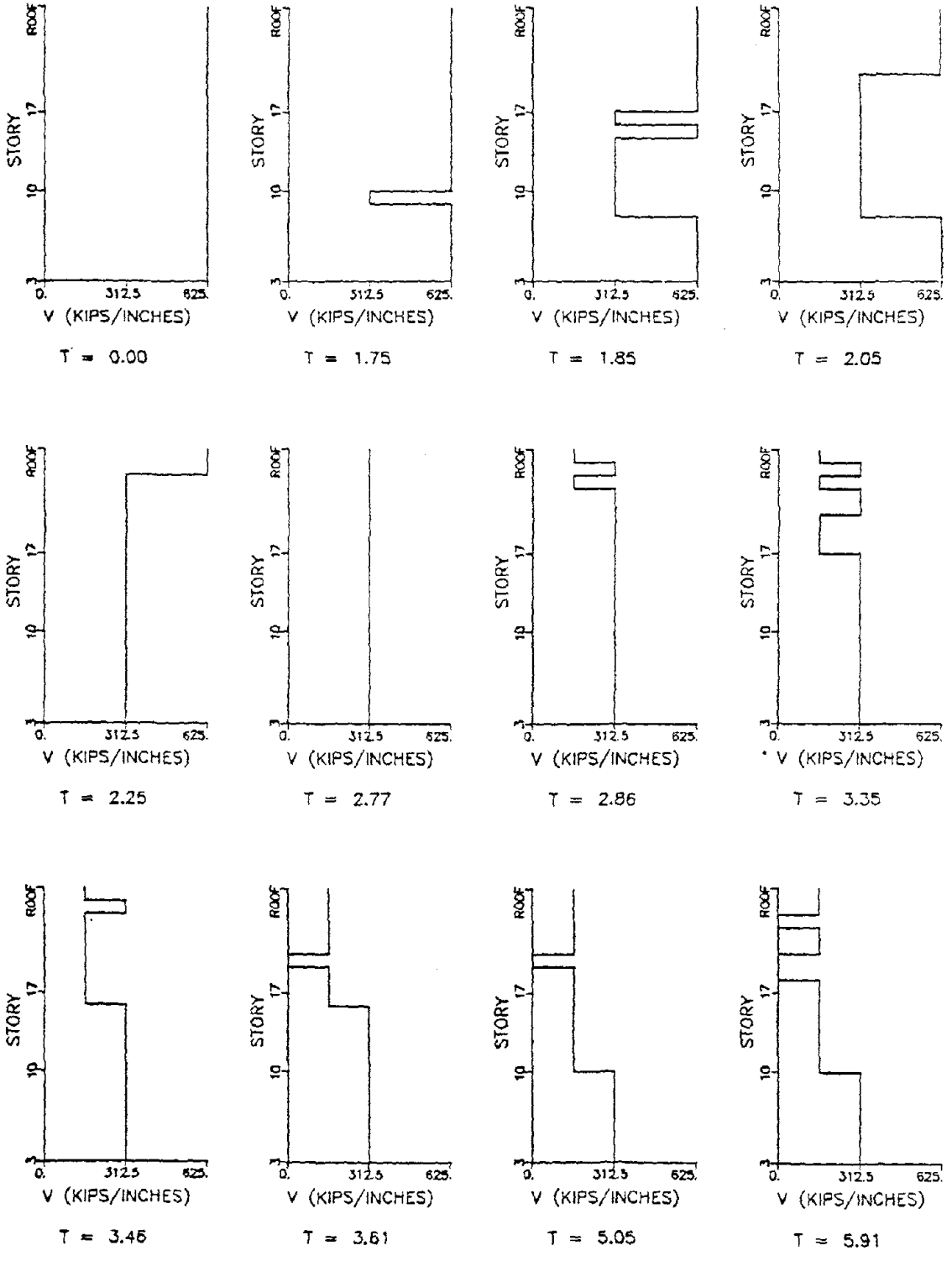

Figure 4.2-49. Progressive Failure of Cladding on Face 2 for 1940 El Centro Record Acting in Rigid Direction with Allowable Drift, Δ, set at 0.36 inches (0.9 cm), Symmetric Model (Time T in seconds).

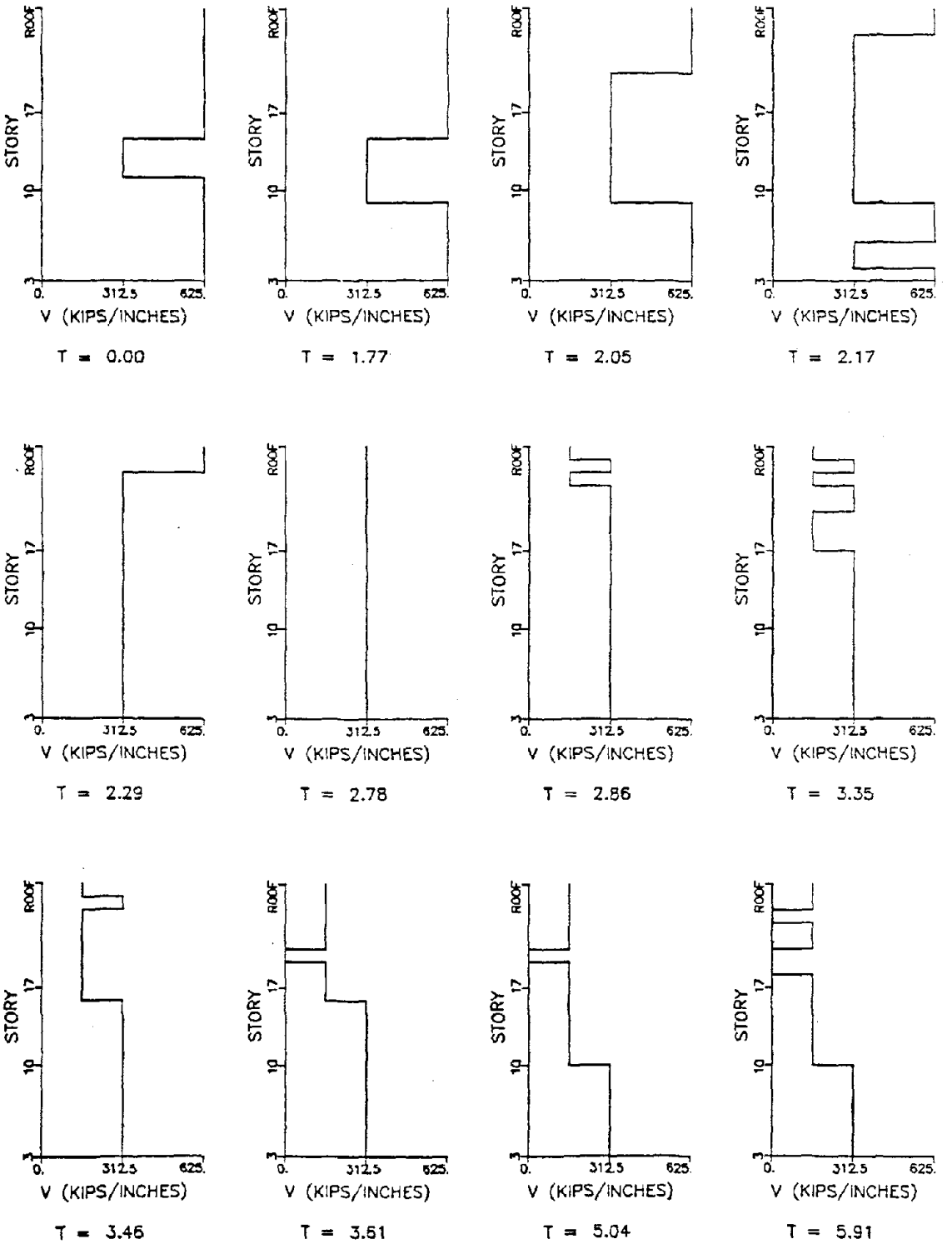

Figure 4.2-50. Progressive Failure of Cladding on Face 4 for 1940 El Centro Record Acting in Rigid Direction with Allowable Drift, Δ, set at 0.36 inches (0.9 cm), Symmetric Model (Time T in seconds).

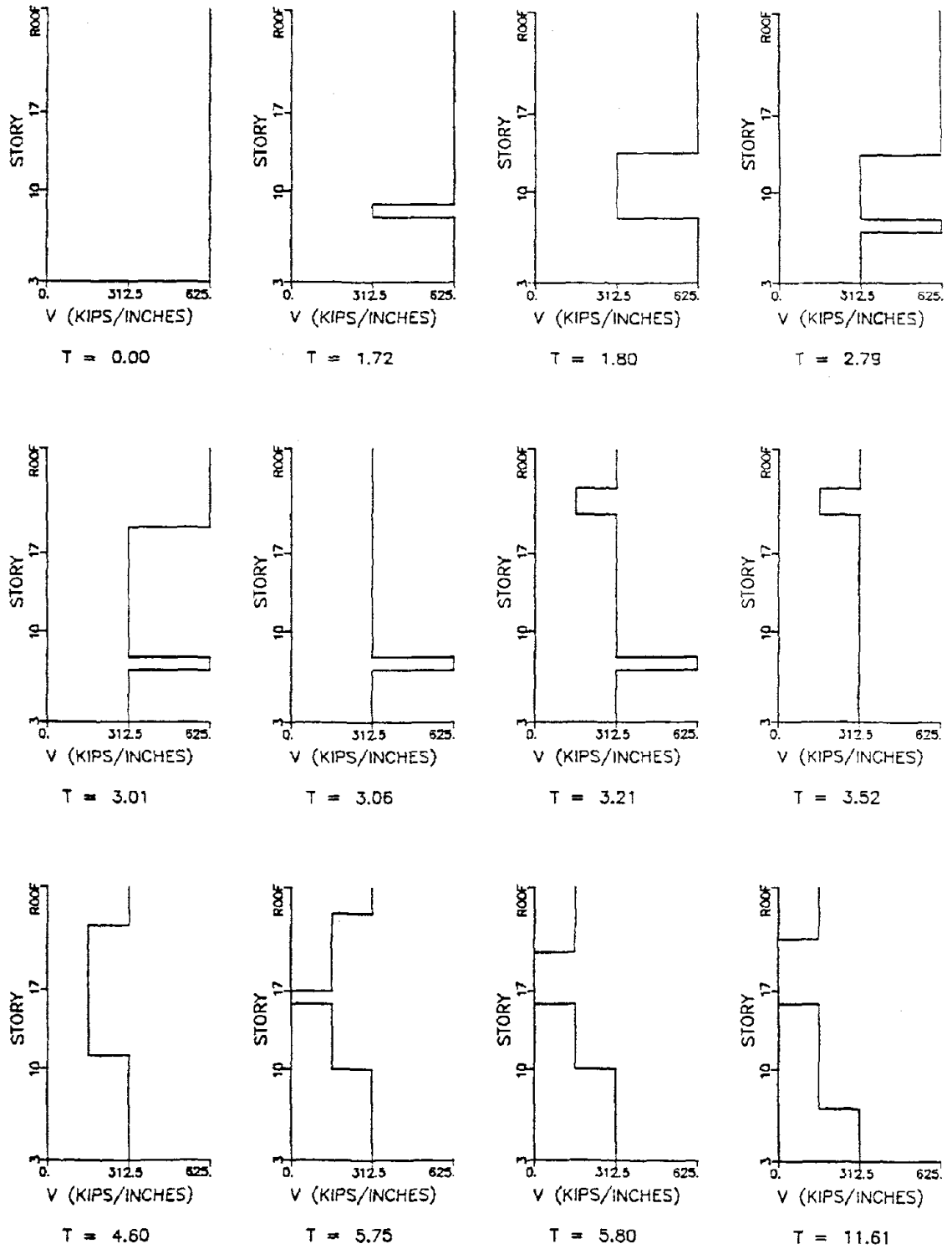

Figure 4.2-51. Progressive Failure of Cladding on Face 1 for 1940 El Centro Record Acting in Braced Direction with Allowable Drift, Δ, set at 0.36 inches (0.9 cm), Symmetric Model (Time T in seconds).

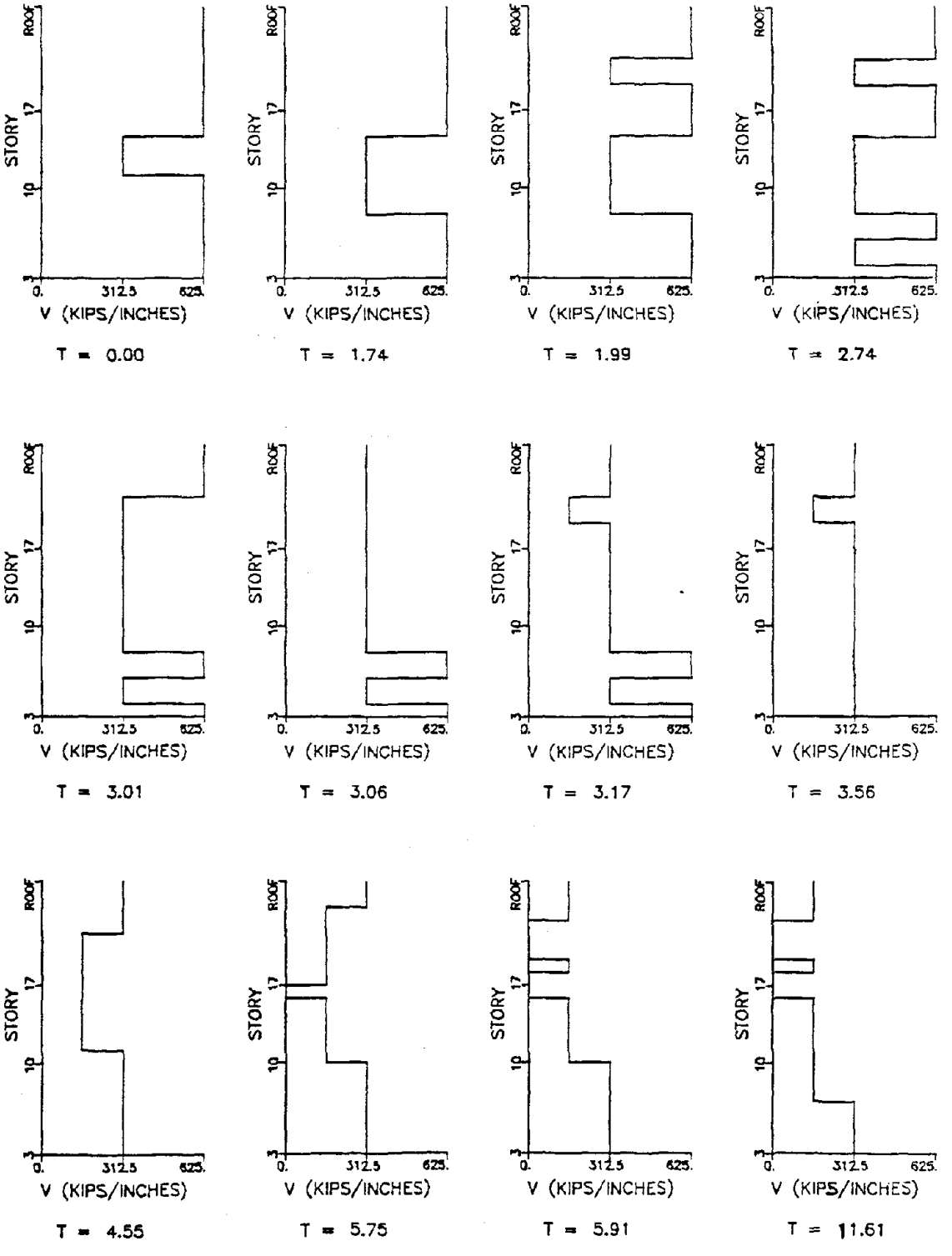

Figure 4.2-52. Progressive Failure of Cladding on Face 3 for 1940 El Centro Record Acting in Braced Direction with Allowable Drift, Δ, set at 0.36 inches (0.9 cm), Symmetric Model (Time T in seconds).

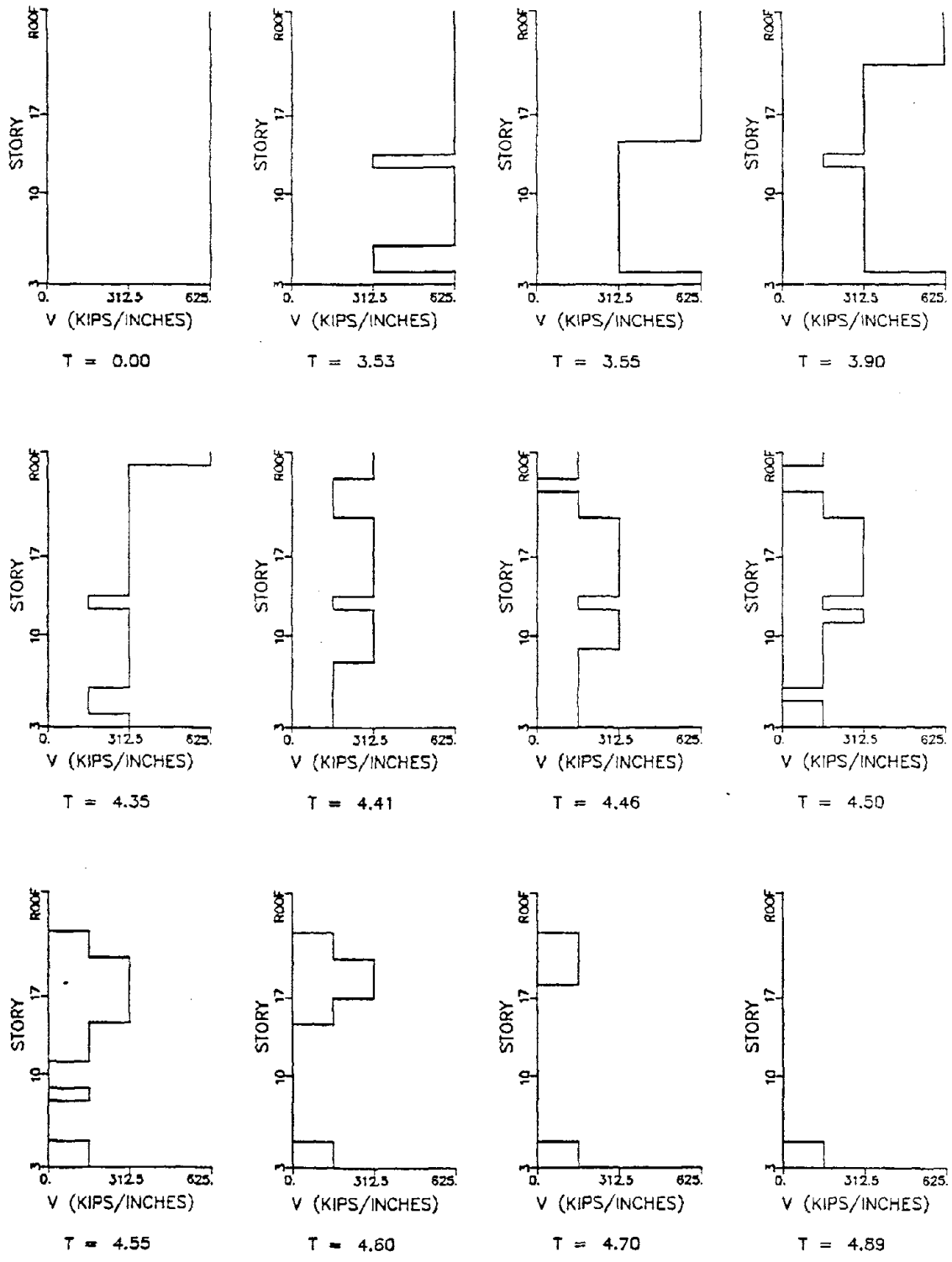

Figure 4.2-53. Progressive Failure of Cladding on Face 2 for 1966 Parkfield Record Acting in Rigid Direction with Allowable Drift, Δ, set at 0.36 inches (0.9 cm), Symmetric Model (Time T in seconds).

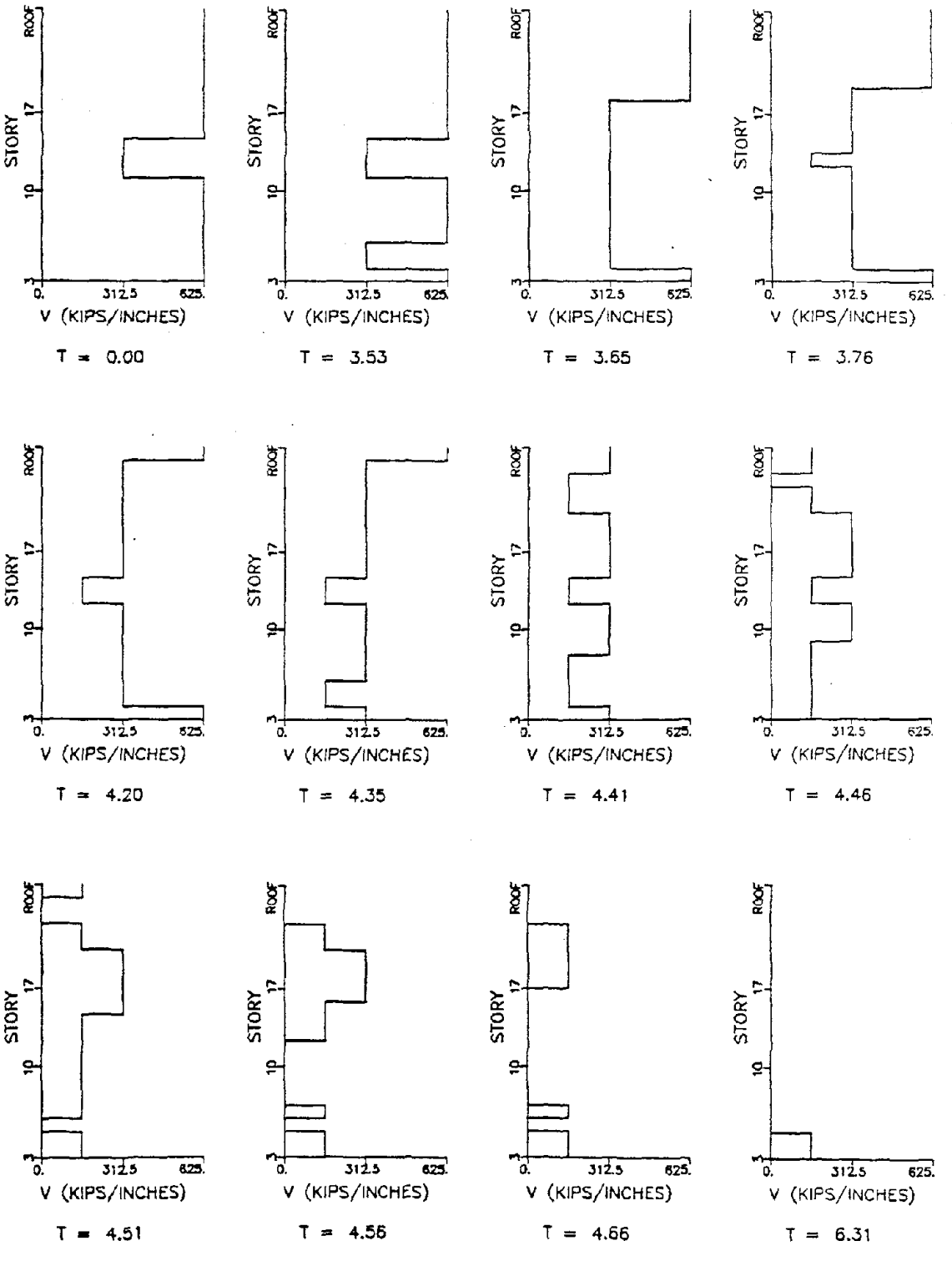

Figure 4.2-54. Progressive Failure of Cladding on Face 4 for 1966 Parkfield Record Acting in Rigid Direction with Allowable Drift, Δ, set at 0.36 inches (0.9 cm), Symmetric Model (Time T in seconds).

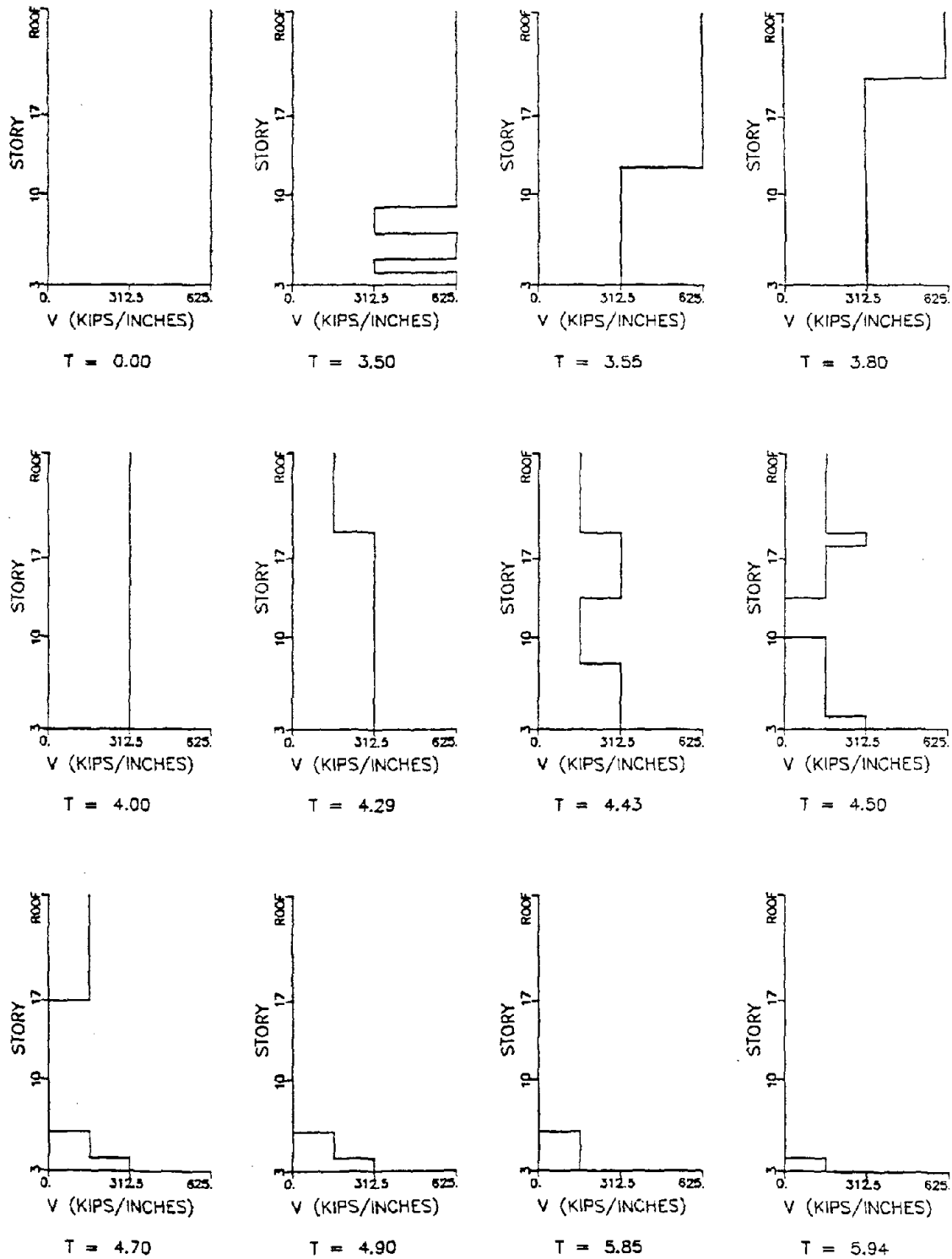

Figure 4.2-55. Progressive Failure of Cladding on Face 1 for 1966 Parkfield Record Acting in Braced Direction with Allowable Drift, Δ, set at 0.36 inches (0.9 cm), Symmetric Model (Time T in seconds).

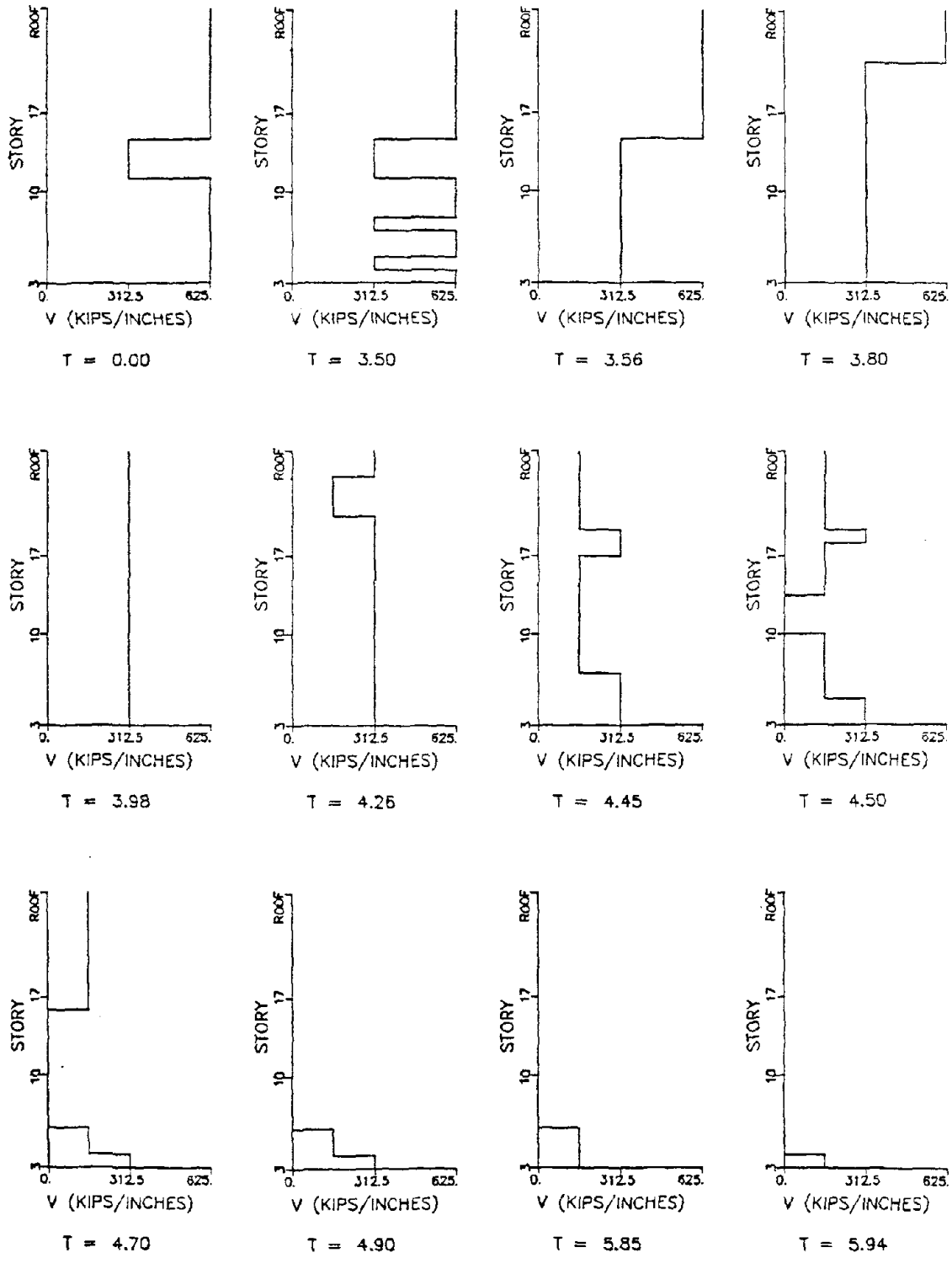

Figure 4.2-56. Progressive Failure of Cladding on Face 3 for 1966 Parkfield Record Acting in Braced Direction with Allowable Drift, Δ, set at 0.36 inches (0.9 cm), Symmetric Model (Time T in seconds).

4.3 Slotted Connection Model

4.3.1 Description of Model

The incremental failure model was introduced in the preceding section. In this section a different model which does not include any cladding failure will be considered. The force-deformation model shown in Fig. 4.3-1 was derived by modifying the PCI recommended support conditions [35] such that both top connections were free to slide horizontally and vertically as shown in Fig. 4.3-2. The free sliding was accomplished by providing slots in the corresponding connection directions and due to the presence of the slots the model was labeled as the slotted connection model. The support conditions depicted in Fig. 4.3-2 were felt to match PCI assumed behavior more closely than the PCI recommended support conditions, since force transfer into panels can be drastically reduced at low interstory displacement levels ($\leq\Delta$). When relative interstory drift was less than the allowable drift, Δ, a small stiffness, arbitrarily set at one-tenth of the full interstory shear stiffness (V = 625 kips/inch = 1.1×10^5 kN/m) of an entire row of panels at a story, or V = 62.5 kips/inch (1.1×10^4 kN/m), was provided. This small stiffness was assumed to result from friction in the panel connections. The full interstory shear stiffness of V = 625 kips/inch (1.1×10^5 kN/m) was employed when the interstory drift exceeded Δ (see Fig. 4.3-1). No failure of panels or connections was assumed in this model and piecewise-linear elastic cladding behavior was also assumed throughout.

The equations of motion were integrated step by step using the integration procedure described in Section 3.2 and the force-deformation relationship for the cladding was updated at each story and on each face

of the prototype structure at the end of each time step on the basis of story drift values on each face. Both the stiffness matrix, $\underset{\sim}{S}$, and the load vector, $\underset{\sim}{A}_i$ (see Section 3.2), were adjusted when allowable drift, Δ, was exceeded. While the nonlinearity of the model could have been accounted for by adjusting only the load vector [7], the correction was found to be constant for a given allowable drift value, Δ, provided that the stiffness matrix was also changed as shown in Fig. 4.3-3. The inter-story shear stiffness at story I and face J is 62.5 kips/inch (1.1×10^4 kN/m) before Δ is exceeded but changes to 625 kips/inch (1.1×10^5 kN/m) at that point. However, by changing the stiffness matrix, the force-deformation relationship follows the line going through the origin with a slope of 625 kips/inch (1.1×10^5 kN/m) if no correction is applied to the force. The correction in the force (CF) at story I and face J is

$$CF(I,J) = \Delta*(625 - 62.5) \qquad (4.3\text{-}1)$$

and the correction was the negative of the above when $-\Delta$ was exceeded for response in the negative direction. The correction in the load vector (CA) was then computed making use of assumptions used to construct the stiffness matrix in Section 2.2.1, and by summing forces and moments based on Fig. 4.3-4 resulting in:

$$CA(1) = CF(1,2) + CF(1,4)$$

$$CA(2) = CF(1,1) + CF(1,3)$$

$$CA(3) = (-CF(1,1) - CF(1,2) + CF(1,3) + CF(1,4))*R$$

For $I \geq 2$, where I is the floor number starting at the roof,

$$CA(3I-2) = CF(I,2) + CF(I,4) - CF(I-1,2) - CF(I-1,4) \quad (4.3\text{-}2a)$$

$$CA(3I-1) = CF(I,1) + CF(I,3) - CF(I-1,1) - CF(I-1,3) \quad (4.3\text{-}2b)$$

$$\begin{aligned} CA(3I) = (&-CF(I,1) - CF(I,2) + CF(I,3) + CF(I,4) \\ &+ CF(I-1,1) + CF(I-1,2) - CF(I-1,3) \\ &- CF(I-1,4))*R \end{aligned} \quad (4.3\text{-}2c)$$

where degrees of freedom 3I-2, 3I-1 and 3I were in rigid direction, braced direction and rotation, respectively. This correction was added to Eq. (3.2-10) and displacements solved for using Eq. (3.2-8). Response studies employing the slotted connection model and associated computational procedures will be discussed in the following section.

4.3.2 Response Studies

The eccentric model, in which a 5% eccentricity between centers of mass and rigidity was specified, was employed as the basis for combined translational and torsional response studies using the slotted connection model for cladding. Five allowable interstory drift (Δ) conditions were studied:

(1) $\Delta = 0$ (i.e., allowable drift equal to zero to preserve the fully clad case, V = 625 kips/inch (1.1×10^5 kN/m))

(2) Δ = 0.00125 times an average story height of 12 feet (i.e., Δ = 0.18 inches or 0.5 cm)

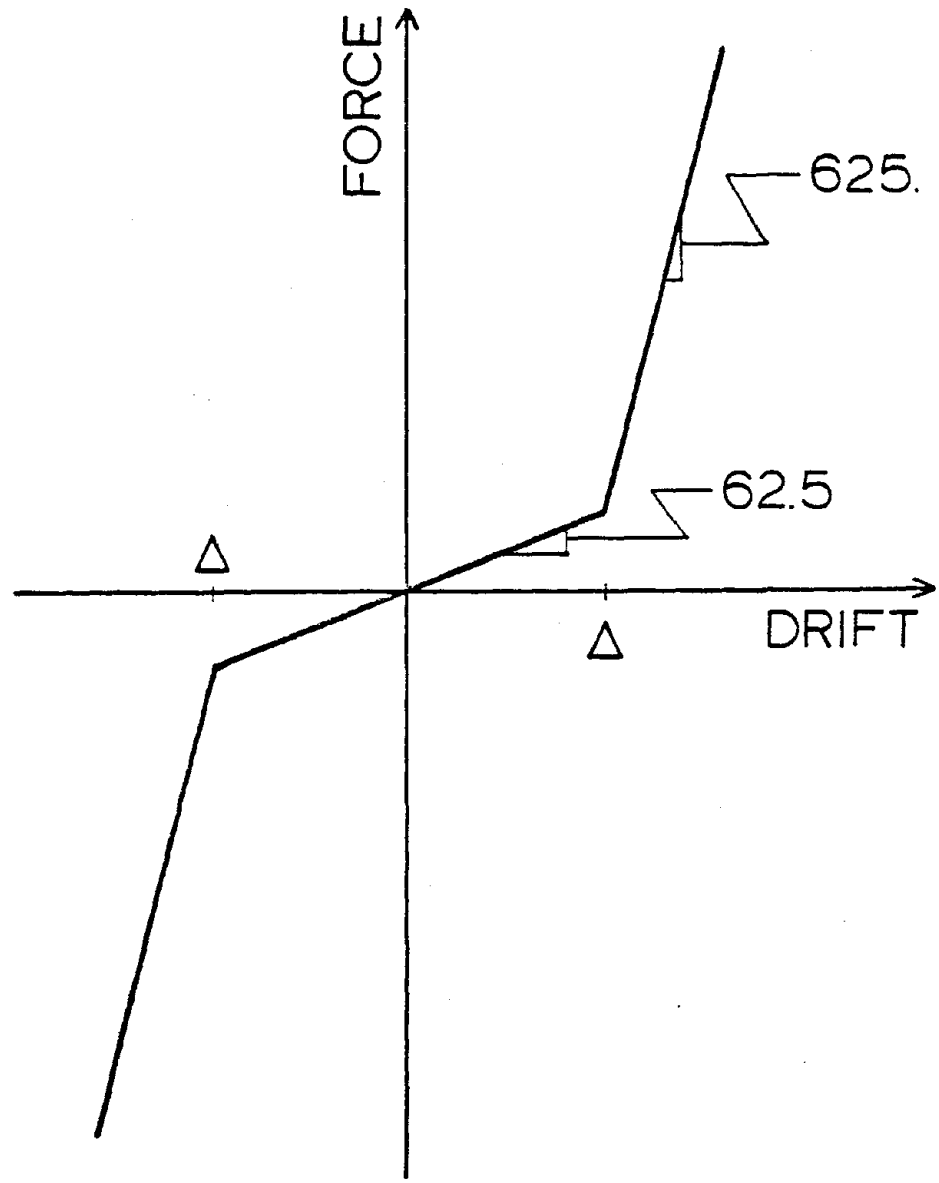

Figure 4.3-1. Force Deformation Relationship for the Slotted Connection Model (units are in kips and inches).

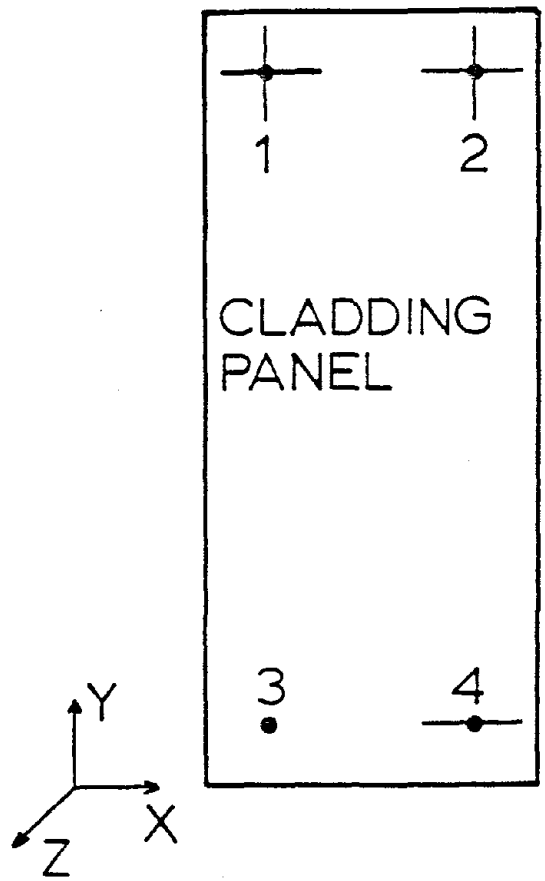

——— Connection free to slide in X-direction.

| Connection free to slide in Y-Direction.

● Panel connection.

Figure 4.3-2. Support Conditions for Slotted Connection Model.

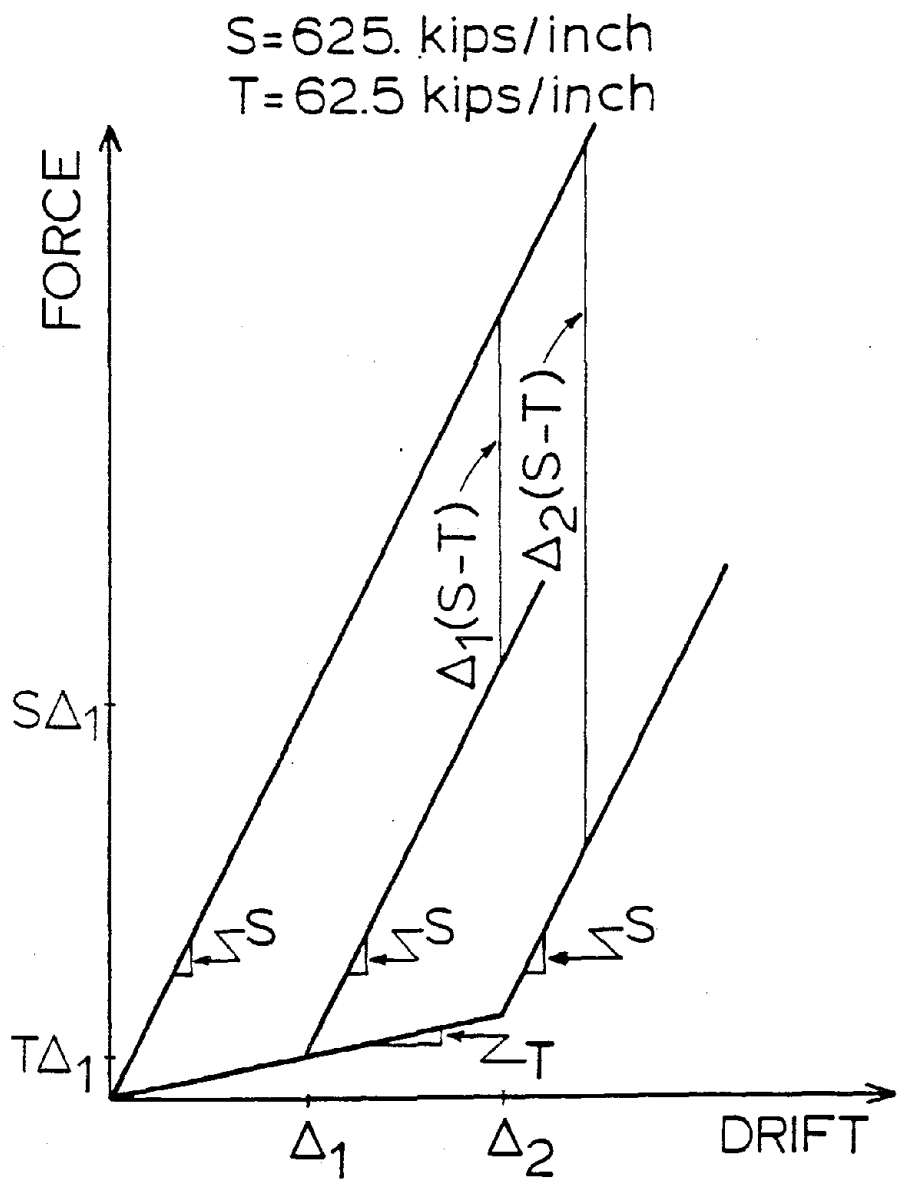

Figure 4.3-3. Correction Force for the Slotted Connection Model When Interstory Drift Exceeds Allowable Drift, Δ.

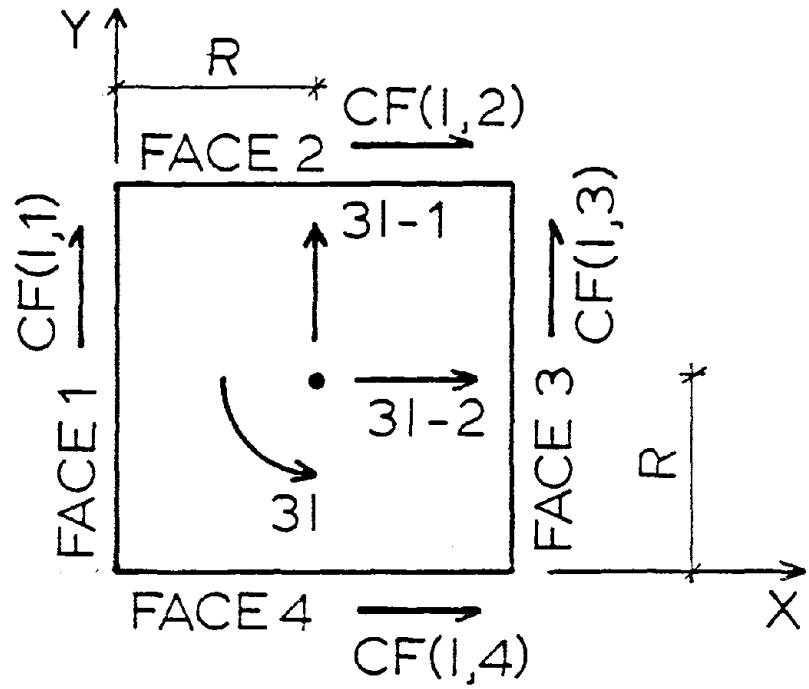

Figure 4.3-4. Correction in Load Vector for the Slotted Connection Model when Interstory Drift Exceeds Allowable Drift, Δ.

(3) Δ = 0.0025 times an average story height of 12 feet (i.e., Δ = 0.36 inches or 0.9 cm)

(4) Δ = 0.005 times an average story height of 12 feet (i.e., Δ = 0.72 inches or 1.8 cm)

(5) $\Delta = \infty$ (i.e., cladding removed to produce the unclad case, V = 0)

Conditions (1) and (5) above correspond to the clad and unclad cases, respectively, for the eccentric structure model. The resulting peak roof displacements are listed in Table 4.3-1 for El Centro ground motion input in both the rigid and braced frame directions. Time-history plots are displayed in Figs. 4.3-5 to 4.3-8. Inspection of these results showed most peak response values for conditions (2) to (4) were bracketed by the clad and unclad cases (conditions (1) and (5), respectively) but several exceptions were found as for example rotational response for conditions (2) and (3). Peak interstory drift values for each face are tabulated in Table 4.3-2 and maximum story drift values are plotted in Figs. 4.3-9 to 4.3-14 for the four building faces. Drift values were generally bracketed by the clad and unclad cases with only one occurrence of increased peak interstory drift observed. Comparison of the story drift plots revealed no major changes in response behavior as allowable drift was varied (see Figs. 3.4-40 to 3.4-43 for cases with and without cladding).

The structure response was also computed for the 1966 Parkfield earthquake record. Peak roof displacement response values are listed in Table 4.3-3 and roof translational and torsional time-histories are displayed in Figs. 4.3-15 to 4.3-18. While peak response values in the

direction of input motion were increasing with increasing allowable drift (conditions (1) to (5)), the response in the other directions behaved in that way in only one instance out of four. Only three instances of increased response for conditions (2) to (4) as compared to conditions (1) and (5) were observed, two in the rigid direction for braced direction input and one in the braced direction when input was applied in the rigid direction. Peak relative interstory drift values listed in Table 4.3-4 showed values for braced frame direction input to be similar, while conditions (2) to (4) compared well with the clad case (condition (1)) but differed from the unclad case when the rigid direction was the input direction. This observation was supported by inspection of story peak drift plots shown in Figs. 4.3-19 to 4.3-24 (see Figs. 3.4-48 to 3.4-51 for the clad and unclad cases). Note that current design practice does not assume any contribution from cladding to lateral stiffness and consequently corresponds to the unclad case.

When results for the slotted connection cladding model are compared to results for the incremental failure model, the obvious differences in the two models need to be kept in mind. While peak roof response in the direction of applied ground motion was always bracketed by the clad and unclad cases when the incremental failure model was employed, the use of the slotted connection model resulted in peak roof response values which were on two occasions outside the interval formed by the linear clad and unclad cases. Rotational response was in several instances, as for the incremental failure model, higher than for either of the linear cases with and without cladding.

In view of the above results, it was obvious that use of slots for isolation of panels is only successful as long as slot lengths exceed

Table 4.3-1. Peak Roof Displacements, Slotted Connection Case for the Eccentric Model, for the First 14 Seconds of the 1940 El Centro Record.

Ground Motion Input Direction (1)	Allowable Drift, Δ (inches) (2)	Peak Roof Displacement Response		
		Rigid Direction (inches) (3)	Braced Direction (inches) (4)	Rotation (radians) (5)
Braced	0.0[a]	2.7	15.2	7.8×10^{-3}
	0.18	4.2	15.5	8.6×10^{-3}
	0.36	2.6	15.0	8.5×10^{-3}
	0.72	1.8	14.5	6.4×10^{-3}
	∞[b]	1.7	14.8	5.6×10^{-3}
Rigid	0.0	15.0	1.9	5.2×10^{-3}
	0.18	14.4	2.4	5.9×10^{-3}
	0.36	13.3	1.8	5.7×10^{-3}
	0.72	12.2	1.1	4.3×10^{-3}
	∞	11.8	1.0	3.7×10^{-3}

[a]Clad case (V = 625 kips/inch).

[b]Unclad case (V = 0).

Note: one inch = 25.4 mm.

Table 4.3-2. Peak Interstory Drift, Slotted Connection Case for the Eccentric Model, for the First 14 Seconds of the 1940 El Centro Record.

Ground Motion Input Direction (1)	Allowable Drift, Δ (inches) (2)	Peak Relative Interstory Drift (inches) Face 1[a] (3)	Face 2 (4)	Face 3 (5)	Face 4 (6)
Braced	0.0[b]	1.1(16)	0.5(5)	1.0(16)	0.4(4)
	0.18	0.9(16)	0.5(16)	1.3(16)	0.3(4)
	0.36	0.9(20)	0.6(5)	1.3(19)	0.3(4)
	0.72	1.0(21)	0.4(19)	1.2(20)	0.2(12)
	∞[c]	1.0(21)	0.4(19)	1.3(18)	0.2(22)
Rigid	0.0	0.3(4)	1.0(19)	0.3(11)	1.3(19)
	0.18	0.4(21)	1.2(22)	0.3(4)	1.1(16)
	0.36	0.5(24)	1.0(23)	0.3(10)	1.0(18)
	0.72	0.4(23)	1.0(18)	0.3(22)	1.0(24)
	∞	0.5(24)	1.3(24)	0.4(24)	1.2(24)

[a]Story at which peak drift occurred is shown in parentheses.

[b]Clad case (V = 625 kips/inch).

[c]Unclad case (V = 0).

Note: 1 inch = 25.4 mm.

Table 4.3-3. Peak Roof Displacements, Slotted Connection Case for the Eccentric Model, for the First 10 Seconds of the 1966 Parkfield Record.

Ground Motion Input Direction (1)	Allowable Drift, Δ (inches) (2)	Peak Roof Displacement Response		
		Rigid Direction (inches) (3)	Braced Direction (inches) (4)	Rotation (radians) (5)
Braced	0.0[a]	3.1	20.7	1.2×10^{-2}
	0.18	3.8	21.6	1.2×10^{-2}
	0.36	3.3	21.9	1.2×10^{-2}
	0.72	2.4	22.7	1.1×10^{-2}
	∞[b]	2.8	23.9	1.1×10^{-2}
Rigid	0.0	21.9	2.3	7.8×10^{-3}
	0.18	22.2	2.4	8.4×10^{-3}
	0.36	22.5	2.2	8.6×10^{-3}
	0.72	22.9	1.6	7.8×10^{-3}
	∞	25.2	1.6	1.2×10^{-2}

[a]Clad case (V = 625 kips/inch).

[b]Unclad case (V = 0).

Note: one inch = 25.4 mm.

Table 4.3-4. Peak Interstory Drift, Slotted Connection Case for the Eccentric Model, for the First 10 Seconds of the 1966 Parkfield Record.

Ground Motion Input Direction (1)	Allowable Drift, Δ (inches) (2)	Peak Relative Interstory Drift (inches)			
		Face 1[a] (3)	Face 2 (4)	Face 3 (5)	Face 4 (6)
Braced	0.0[b]	1.5(11)	0.7(7)	1.4(7)	0.4(4)
	0.18	1.4(16)	0.7(16)	1.4(11)	0.5(4)
	0.36	1.5(16)	0.7(5)	1.4(11)	0.5(4)
	0.72	1.5(16)	0.6(7)	1.5(11)	0.5(5)
	∞[c]	1.6(18)	0.7(22)	1.6(20)	0.5(22)
Rigid	0.0	0.4(16)	1.6(12)	0.4(4)	1.9(12)
	0.18	0.5(4)	1.7(12)	0.4(11)	1.9(22)
	0.36	0.5(4)	1.9(22)	0.4(4)	2.0(22)
	0.72	0.5(4)	2.1(22)	0.5(20)	2.2(22)
	∞	1.1(22)	3.0(22)	1.0(22)	3.1(24)

[a]Story at which peak drift occurred is shown in parentheses.

[b]Clad case (V = 625 kips/inch).

[c]Unclad case (V = 0).

Note: 1 inch = 25.4 mm.

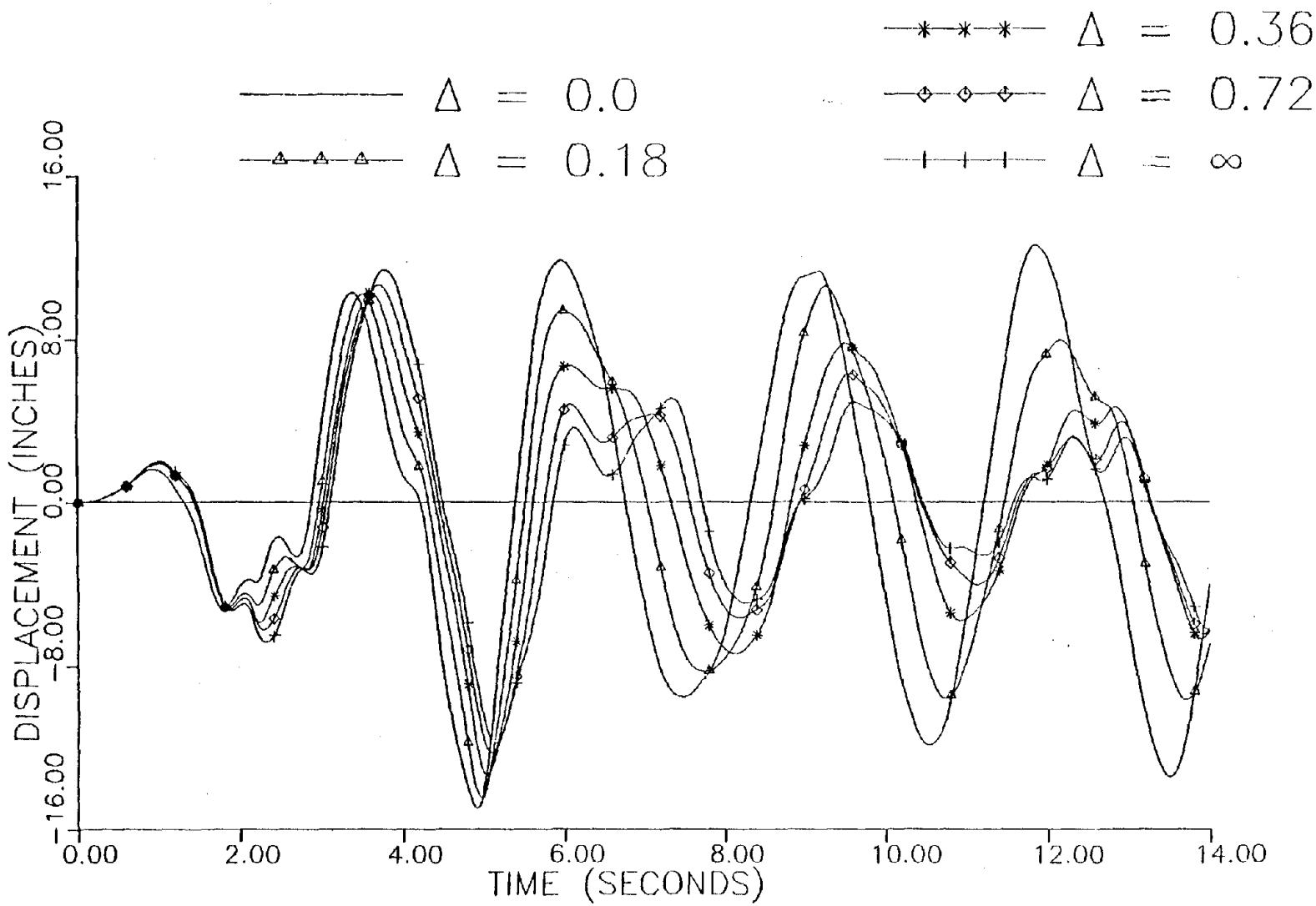

Figure 4.3-5. Roof Translational Response in Rigid Direction, Slotted Connection Case for Eccentric Model, for 1940 El Centro Record Acting in Rigid Direction.

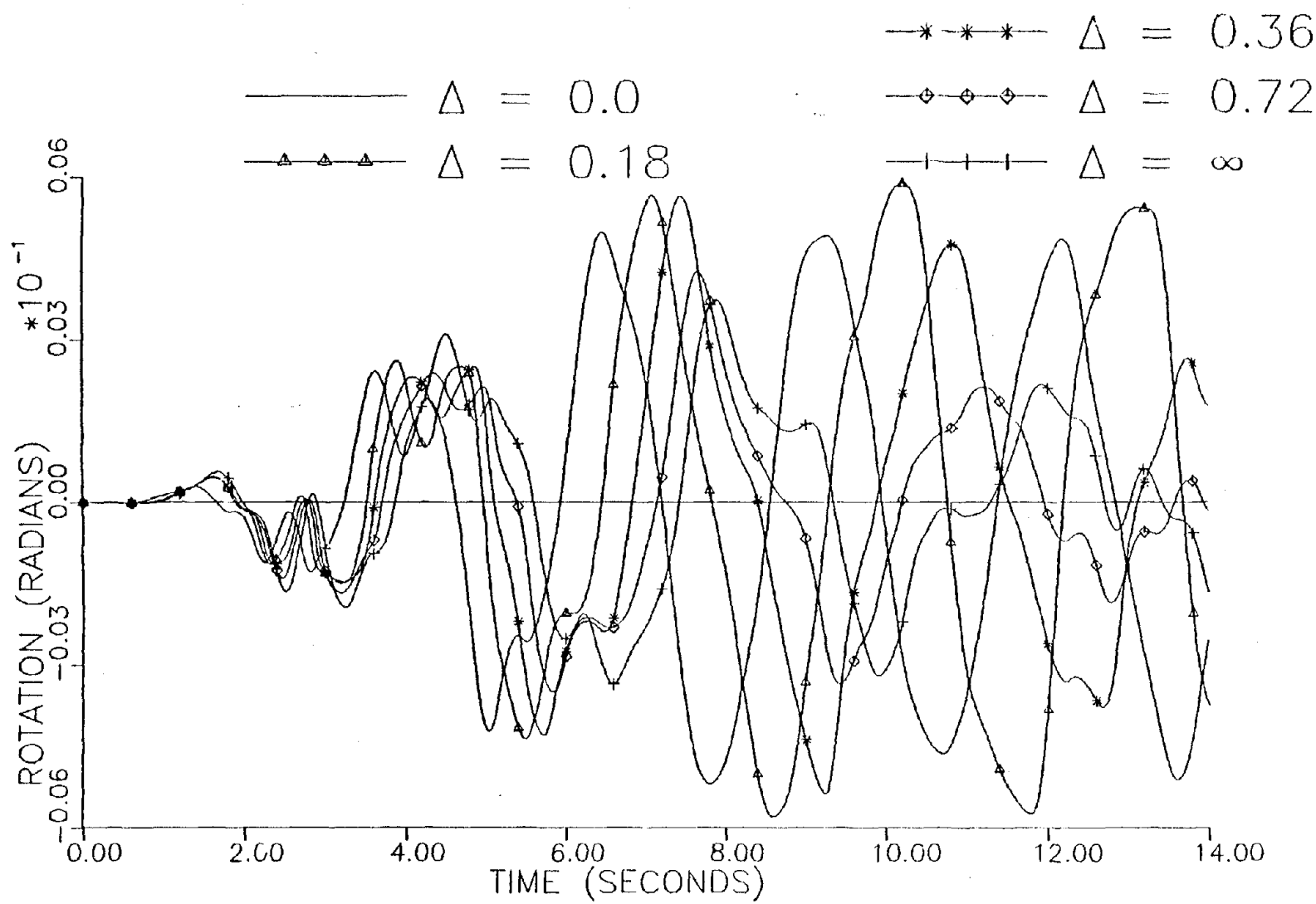

Figure 4.3-6. Roof Rotational Response, Slotted Connection Case for Eccentric Model, for 1940 El Centro Record Acting in Rigid Direction.

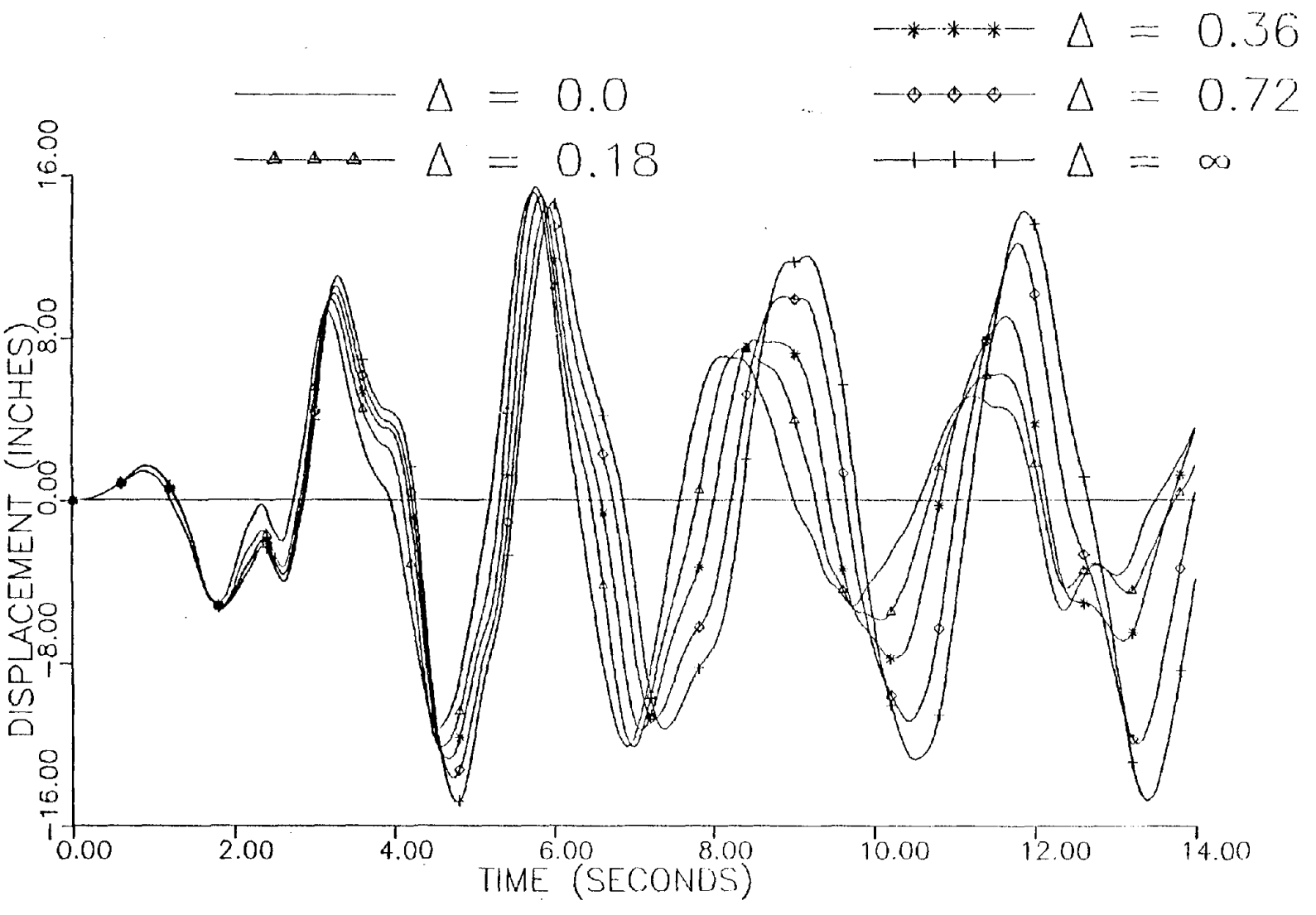

Figure 4.3-7. Roof Translational Response in Braced Direction, Slotted Connection Case for Eccentric Model, for 1940 El Centro Record Acting in Braced Direction.

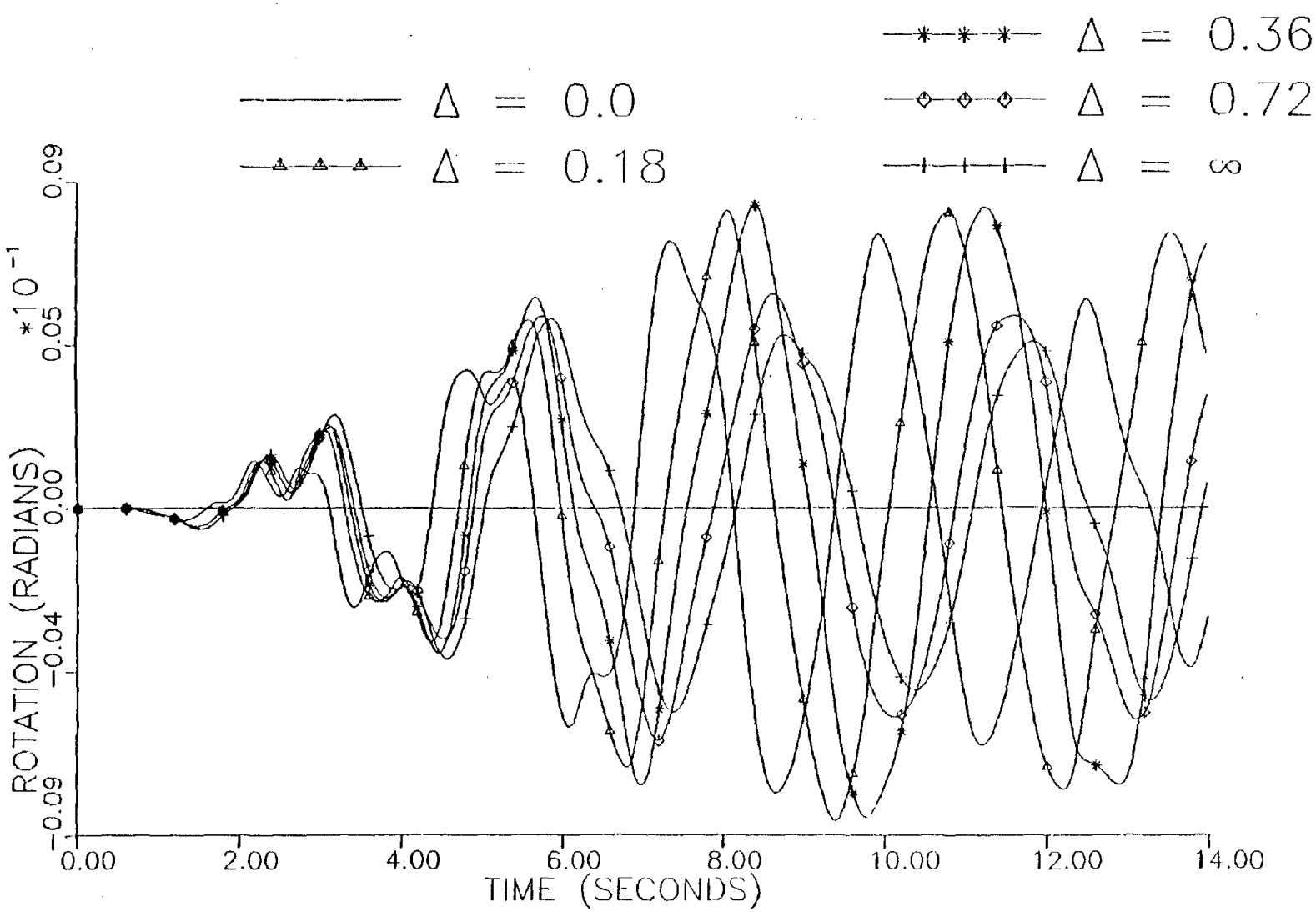

Figure 4.3-8. Roof Rotational Response, Slotted Connection Case for Eccentric Model, for 1940 El Centro Record Acting in Braced Direction.

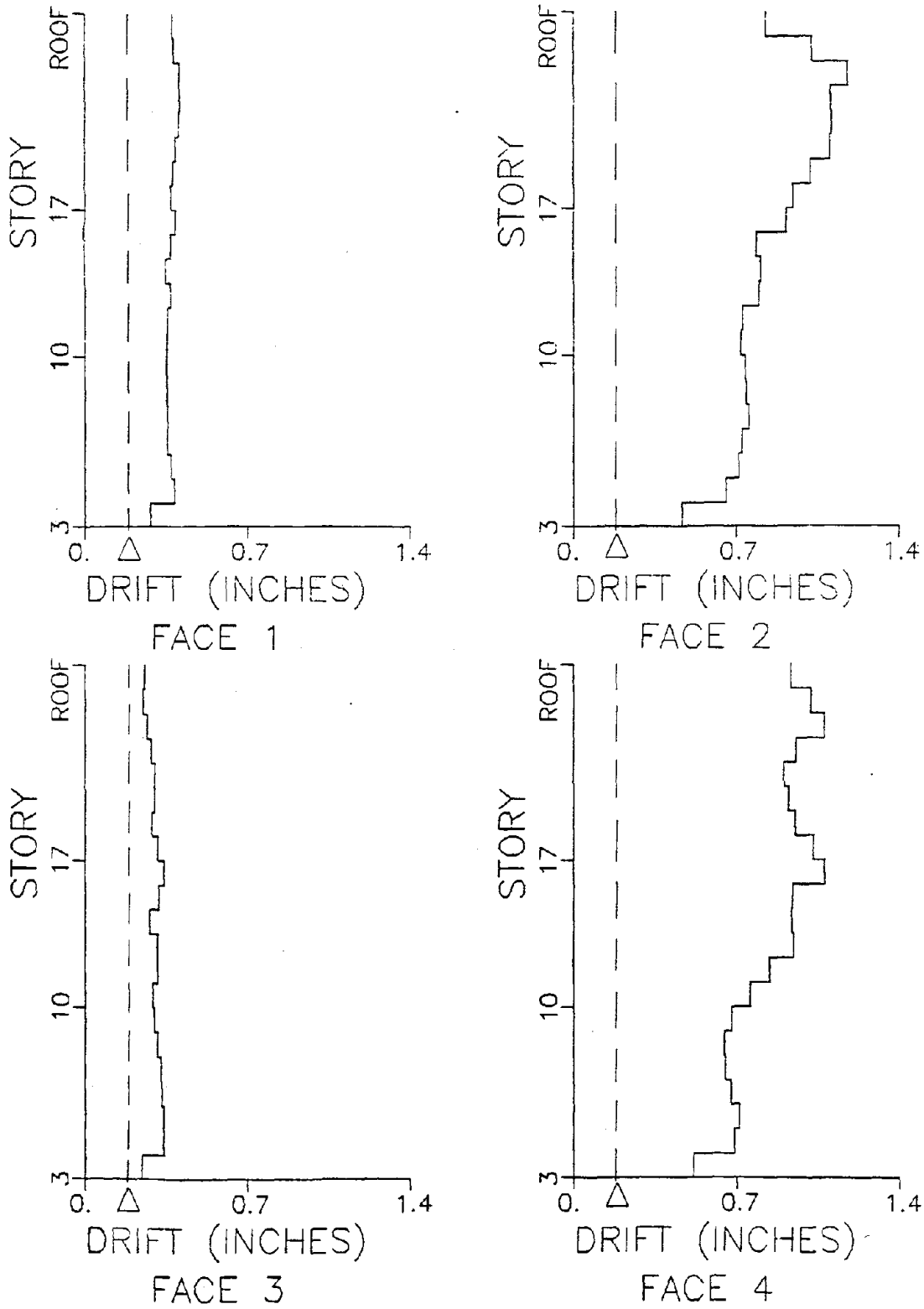

Figure 4.3-9. Peak Drift Values, Slotted Connection Case with Allowable Drift, Δ, set at 0.18 inches (0.5 cm), for 1940 El Centro Record Acting in Rigid Direction, Eccentric Model.

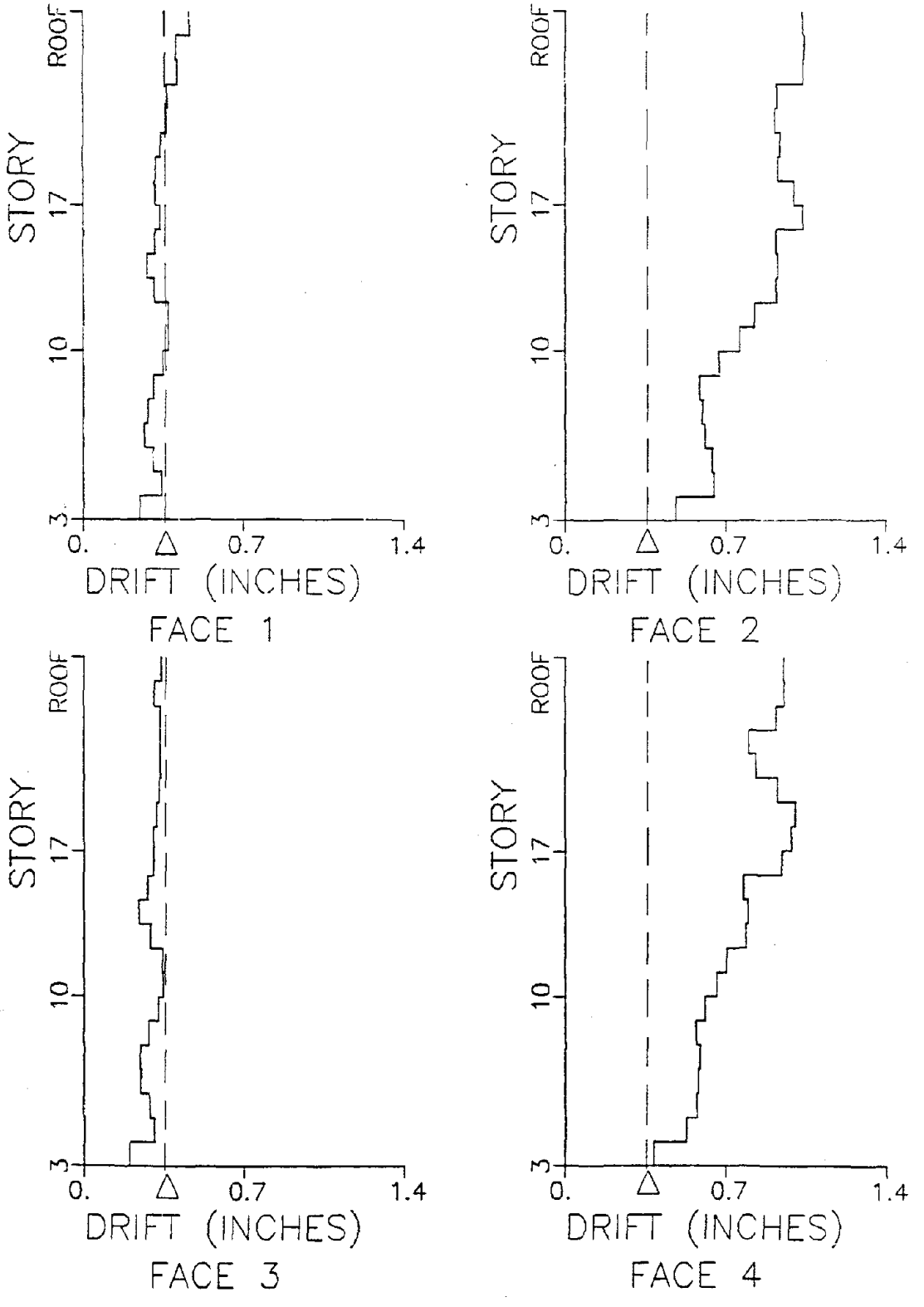

Figure 4.3-10. Peak Drift Values, Slotted Connection Case with Allowable Drift, Δ, set at 0.36 inches (0.9 cm), for 1940 El Centro Record Acting in Rigid Direction, Eccentric Model.

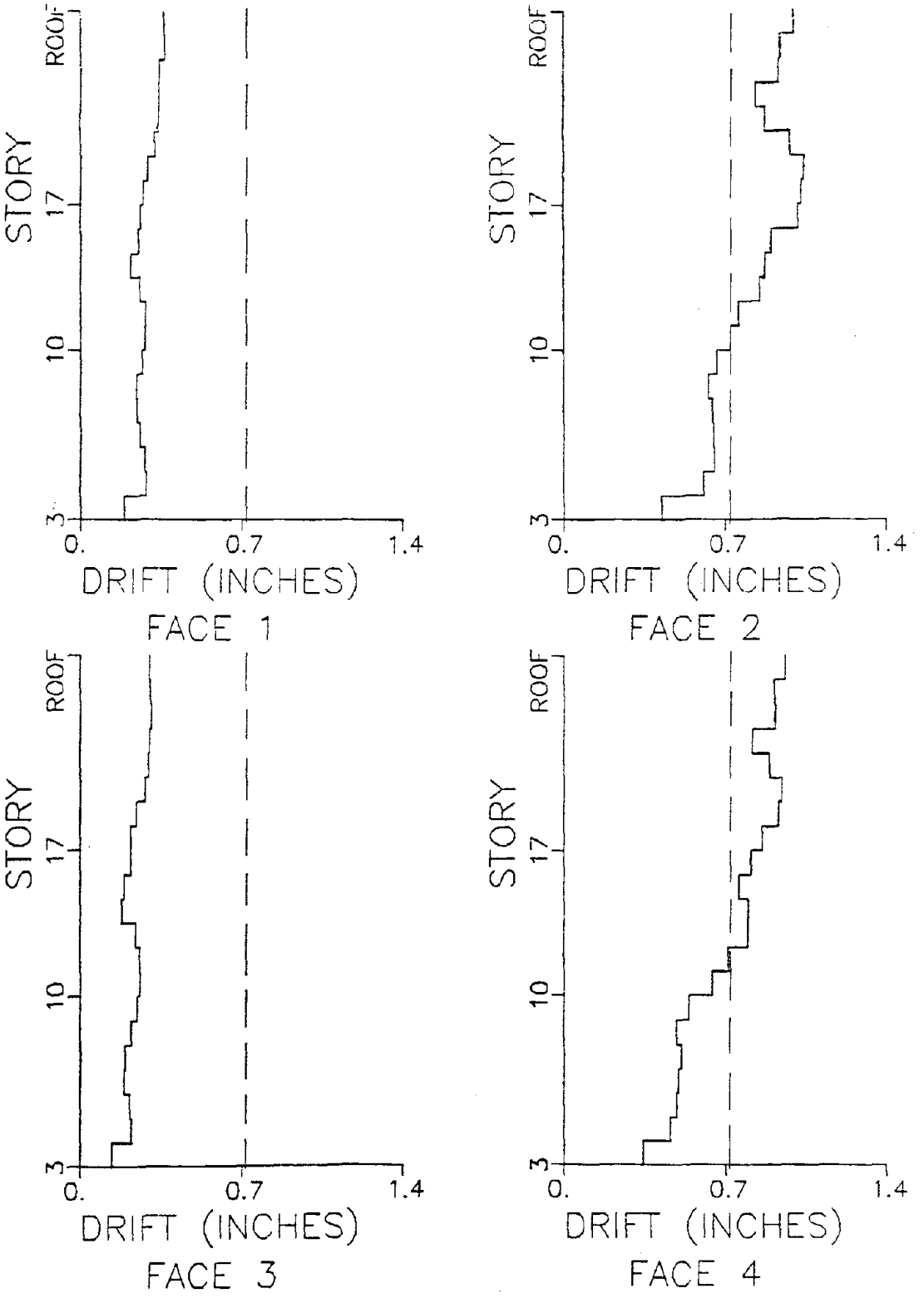

Figure 4.3-11. Peak Drift Values, Slotted Connection Case with Allowable Drift, Δ, set at 0.72 inches (1.8 cm), for 1940 El Centro Record Acting in Rigid Direction, Eccentric Model.

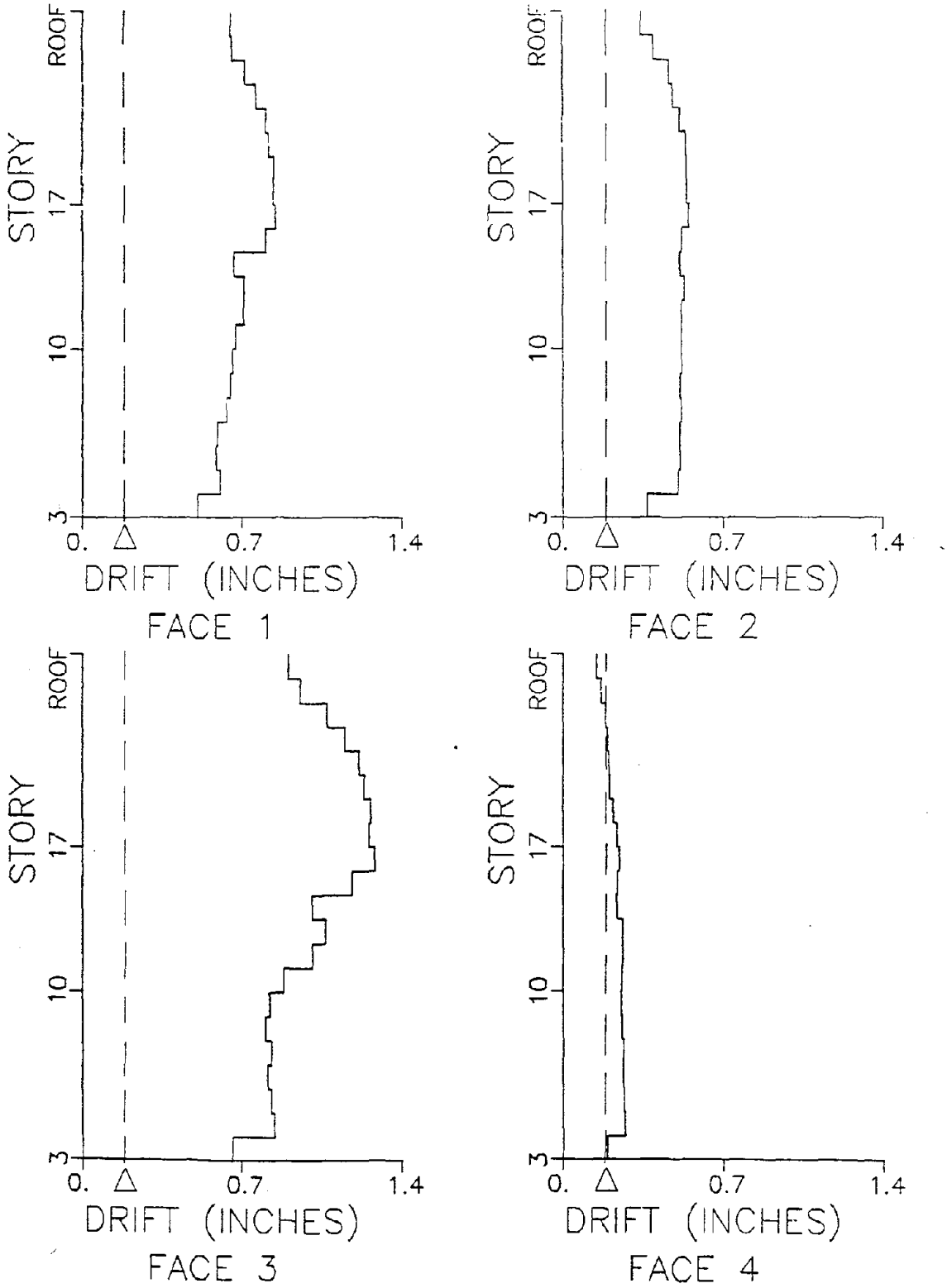

Figure 4.3-12. Peak Drift Values, Slotted Connection Case with Allowable Drift, Δ, set at 0.18 inches (0.5 cm), for 1940 El Centro Record Acting in Braced Direction, Eccentric Model.

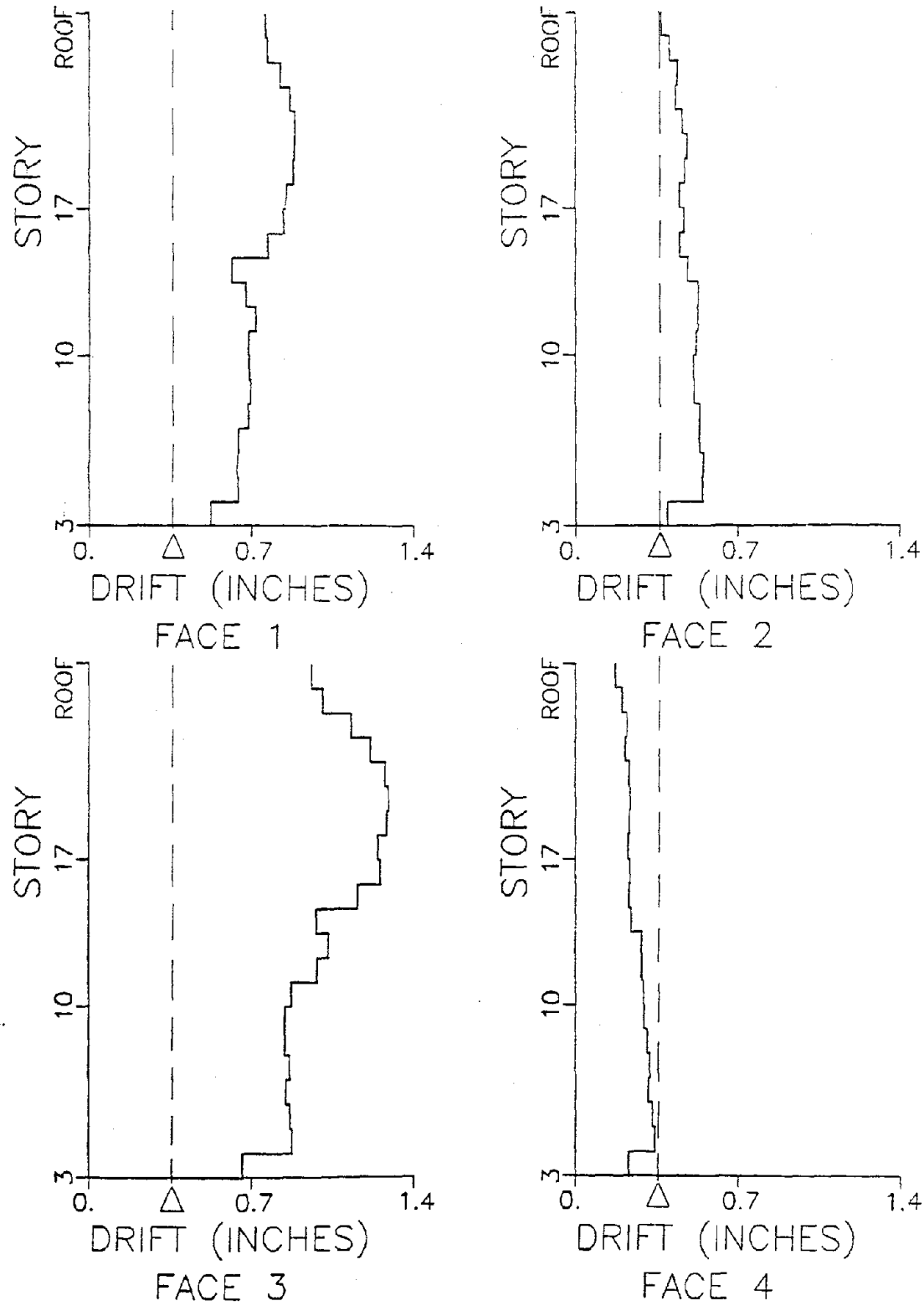

Figure 4.3-13. Peak Drift Values, Slotted Connection Case with Allowable Drift, Δ, set at 0.36 inches (0.9 cm), for 1940 El Centro Record Acting in Braced Direction, Eccentric Model.

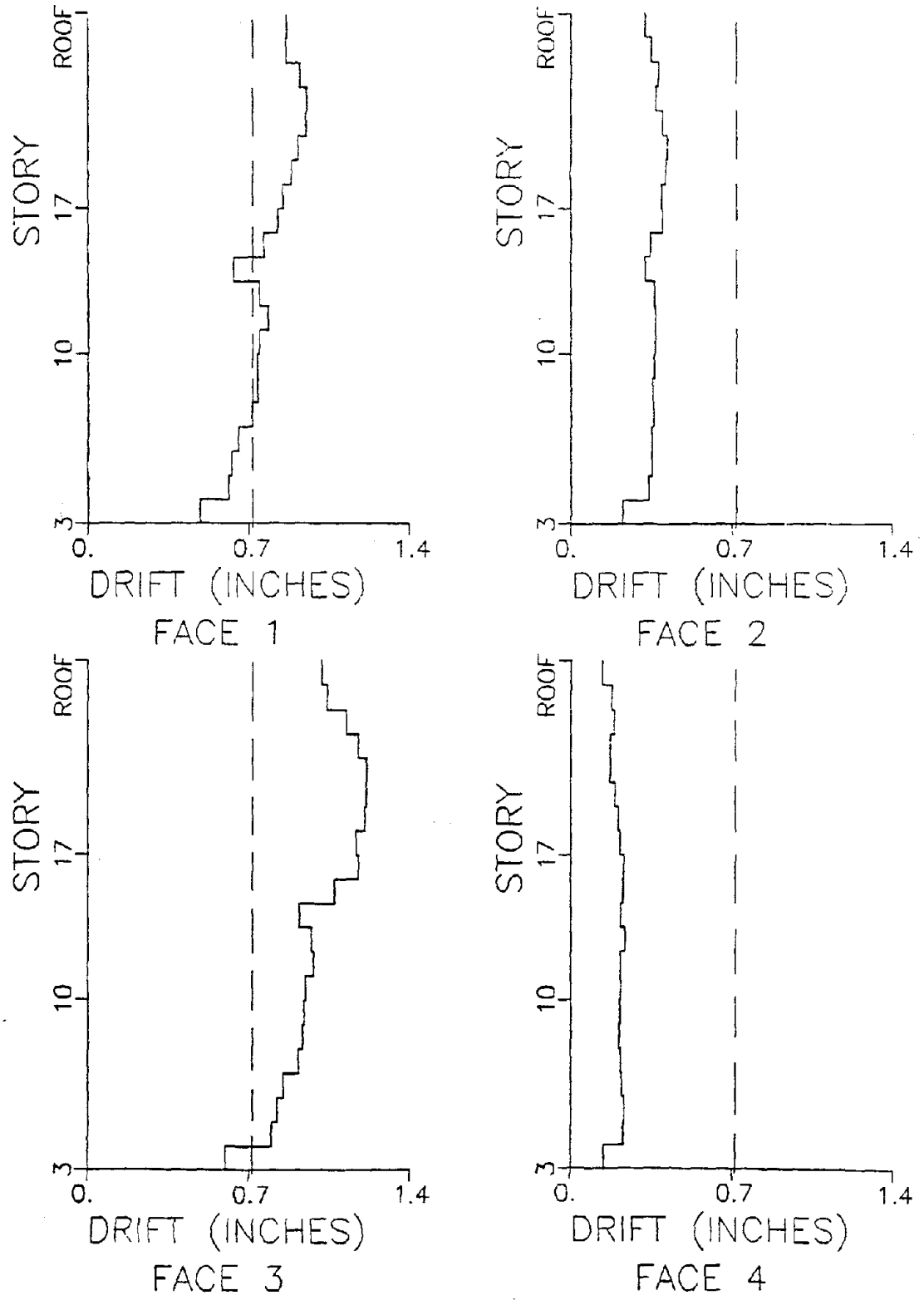

Figure 4.3-14. Peak Drift Values, Slotted Connection Case with Allowable Drift, Δ, set at 0.72 inches (1.8 cm), for 1940 El Centro Record Acting in Braced Direction, Eccentric Model.

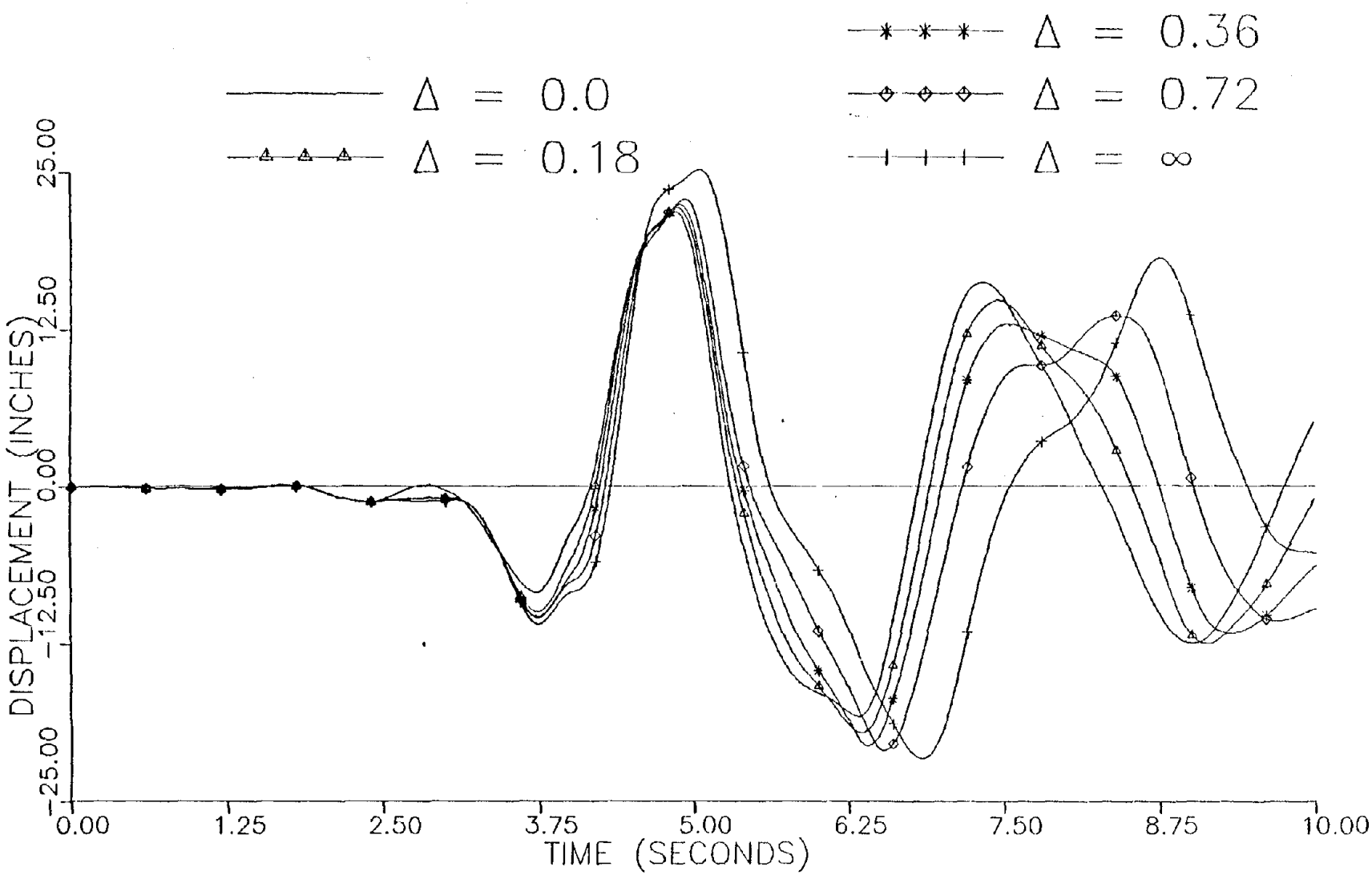

Figure 4.3-15. Roof Translational Response in Rigid Direction, Slotted Connection Case for Eccentric Model, for 1966 Parkfield Record Acting in Rigid Direction.

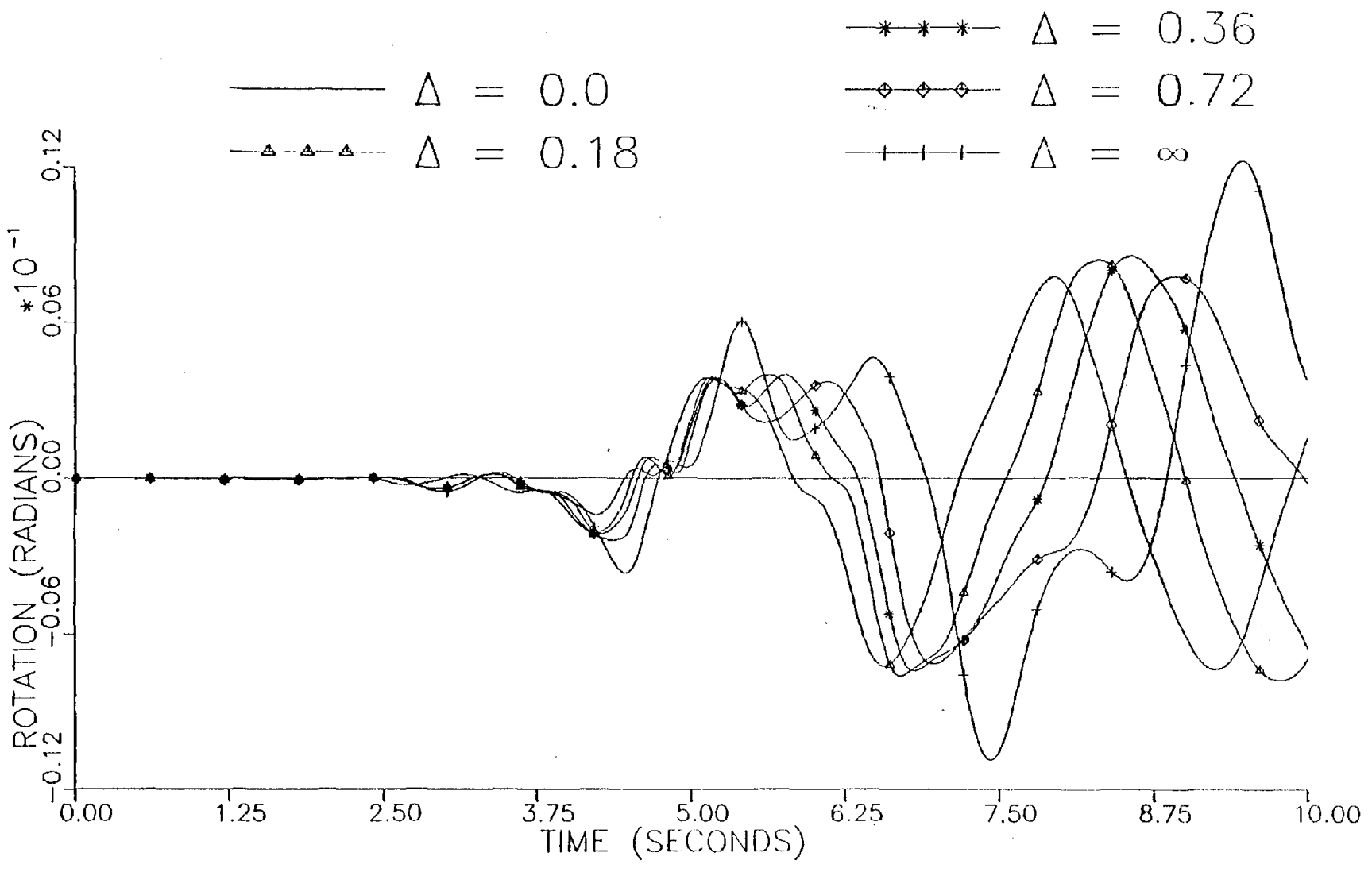

Figure 4.3-16. Roof Rotational Response, Slotted Connection Case for Eccentric Model, for 1966 Parkfield Record Acting in Rigid Direction.

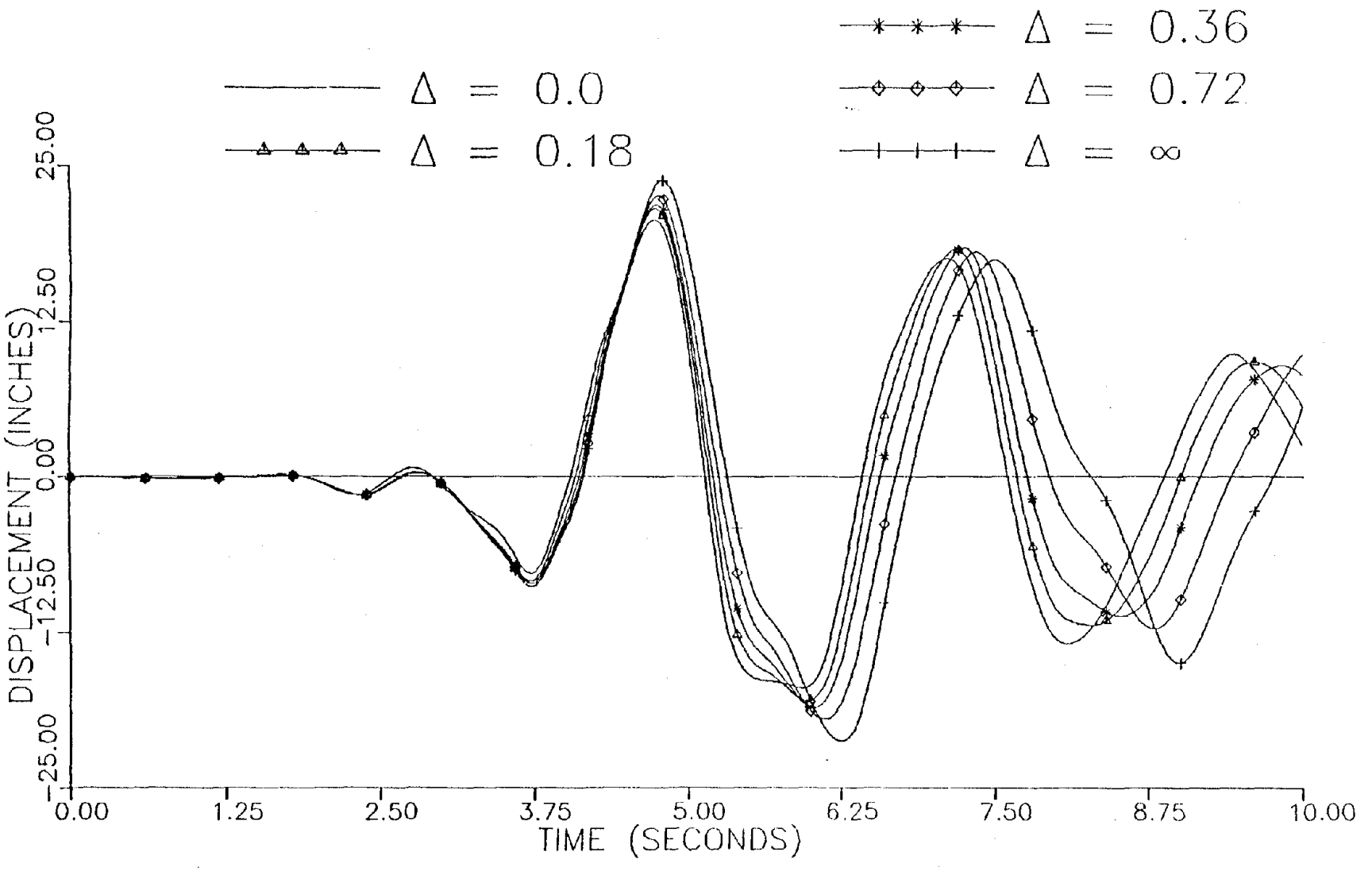

Figure 4.3-17. Roof Translational Response in Braced Direction, Slotted Connection Case for Eccentric Model, for 1966 Parkfield Record Acting in Braced Direction.

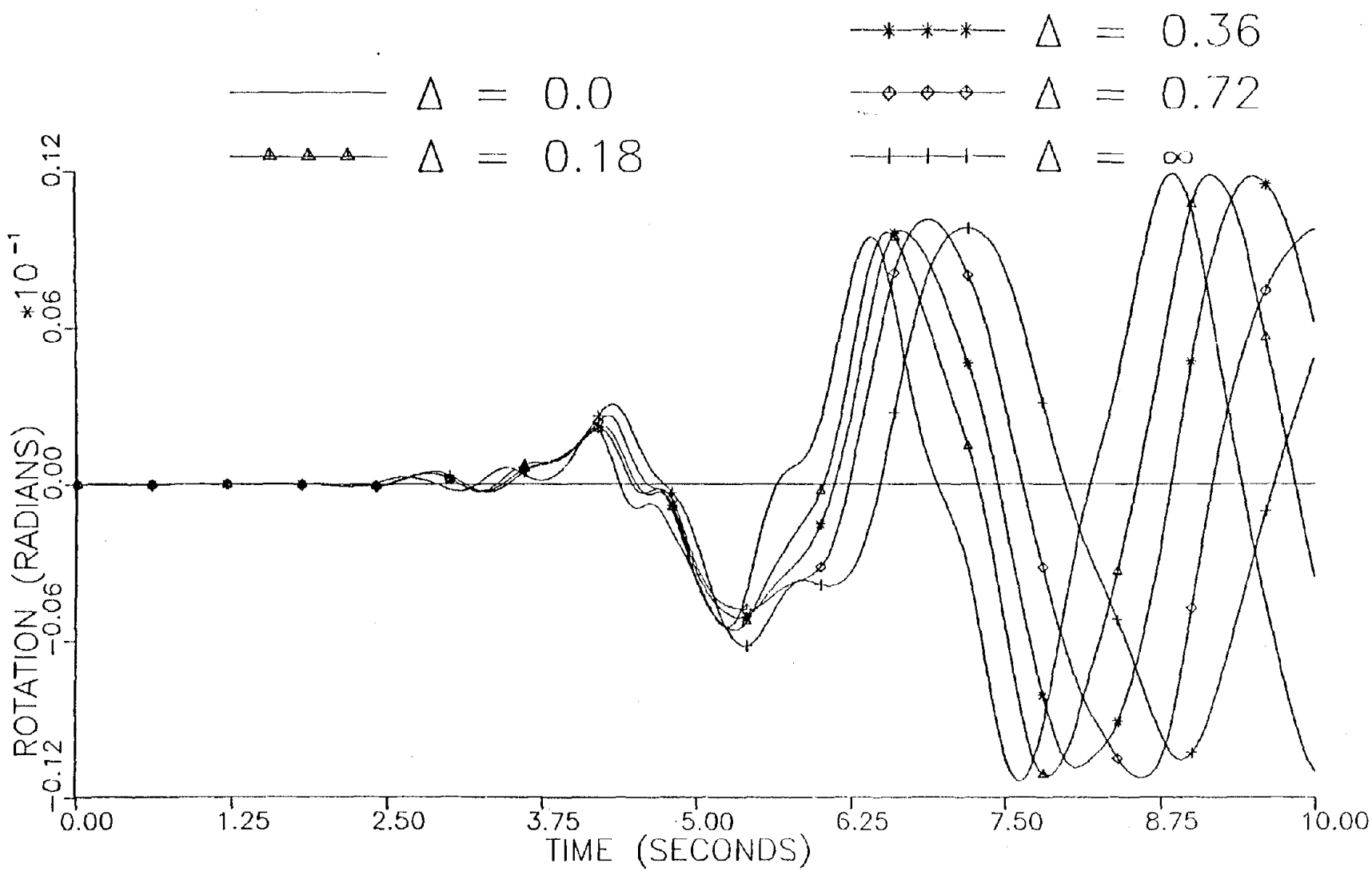

Figure 4.3-18. Roof Rotational Response, Slotted Connection Case for Eccentric Model, for 1966 Parkfield Record Acting in Braced Direction.

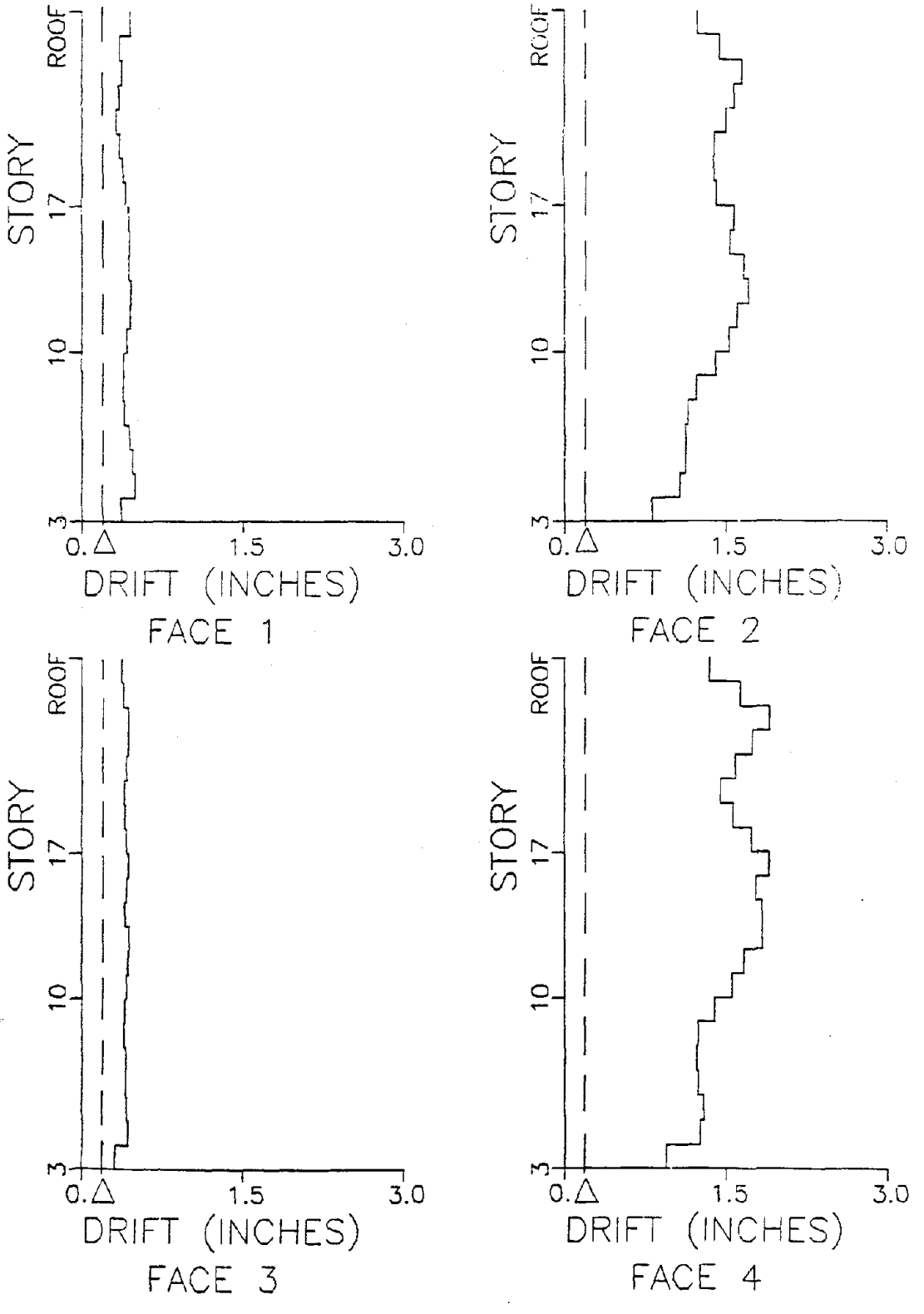

Figure 4.3-19. Peak Drift Values, Slotted Connection Case with Allowable Drift, Δ, set at 0.18 inches (0.5 cm), for 1966 Parkfield Record Acting in Rigid Direction, Eccentric Model.

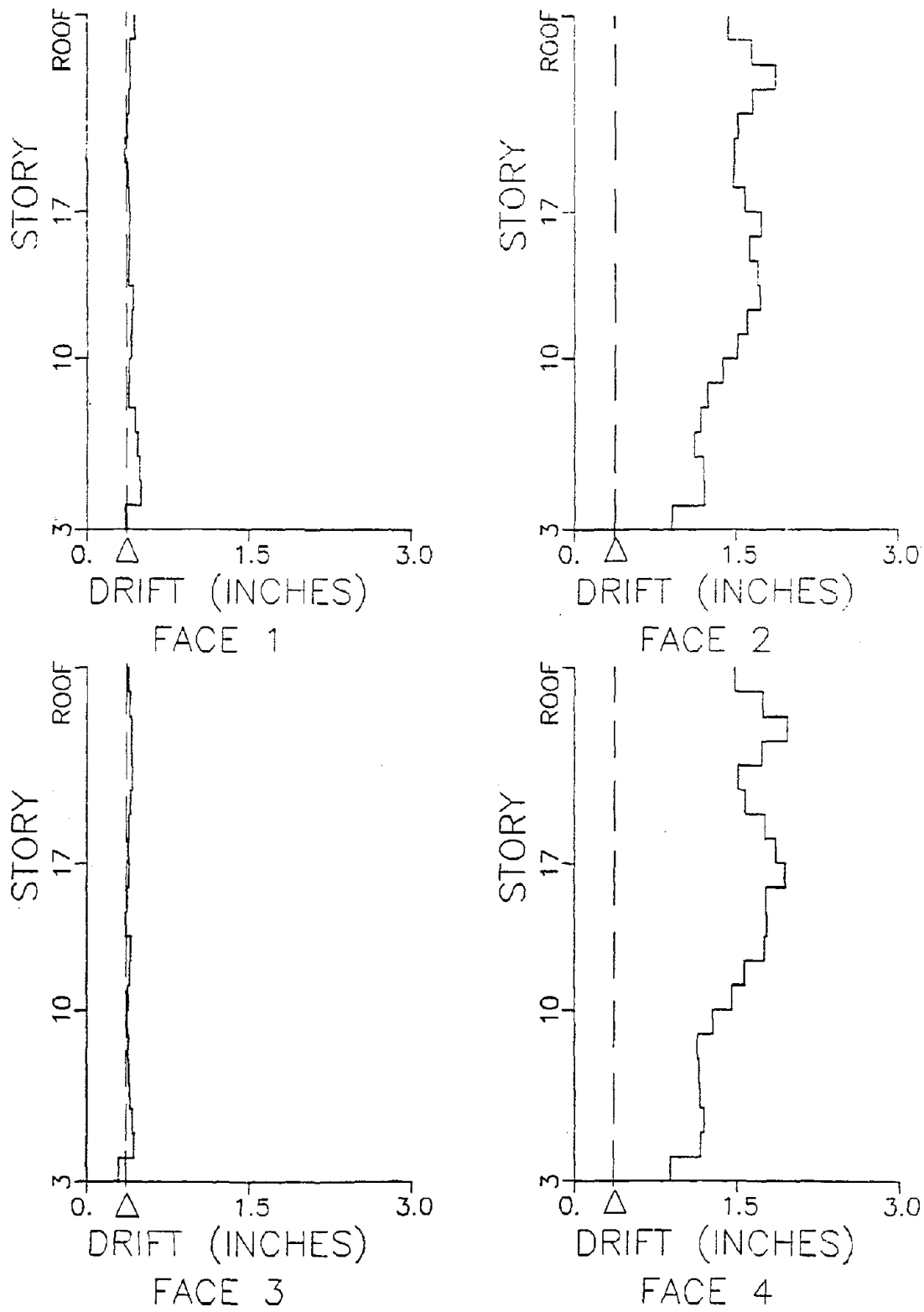

Figure 4.3-20. Peak Drift Values, Slotted Connection Case with Allowable Drift, Δ, set at 0.36 inches (0.9 cm), for 1966 Parkfield Record Acting in Rigid Direction, Eccentric Model.

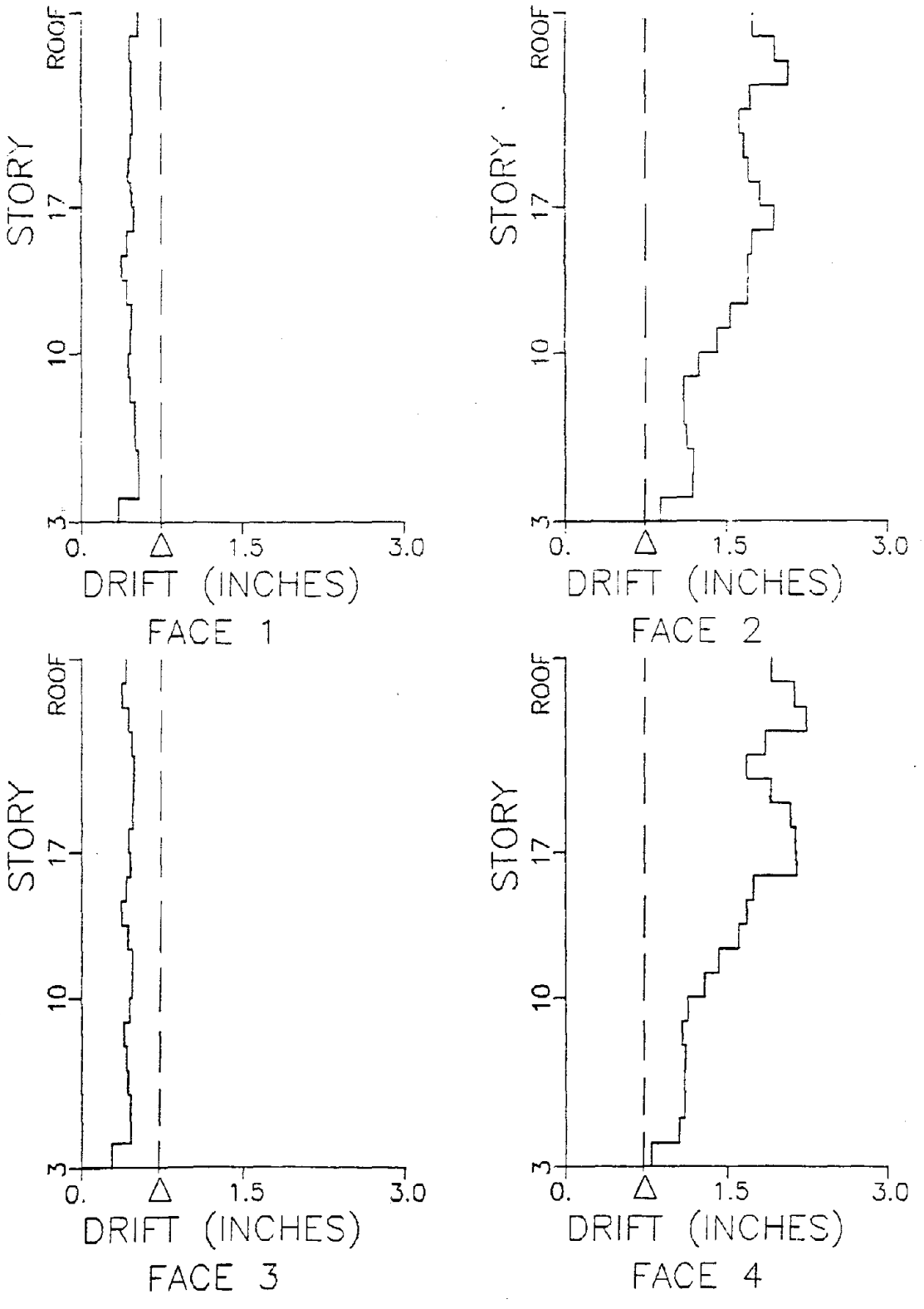

Figure 4.3-21. Peak Drift Values, Slotted Connection Case with Allowable Drift, Δ, set at 0.72 inches (1.8 cm) for 1966 Parkfield Record Acting in Rigid Direction, Eccentric Model.

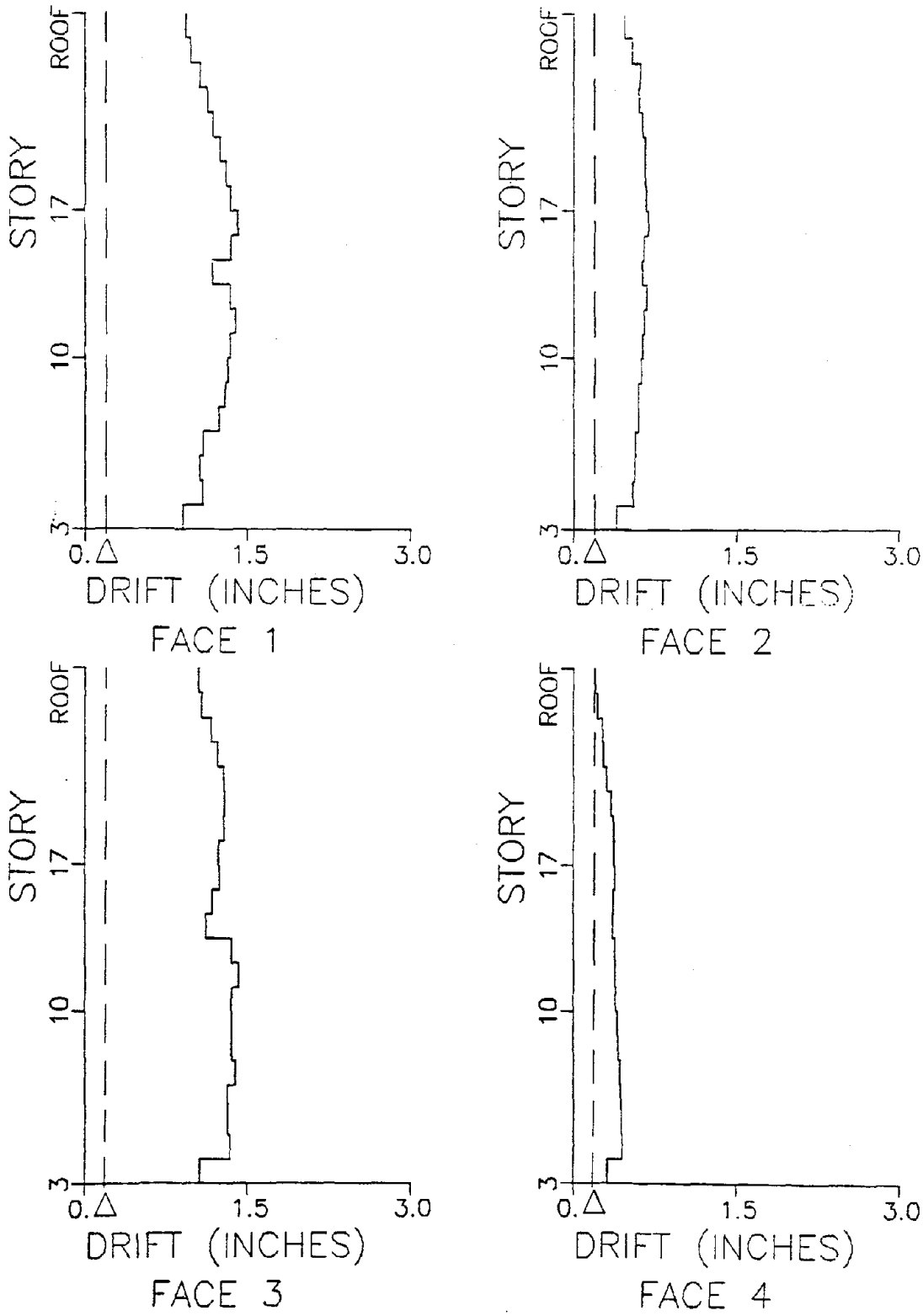

Figure 4.3-22. Peak Drift Values, Slotted Connection Case with Allowable Drift, Δ, set at 0.18 inches (0.5 cm) for 1966 Parkfield Record Acting in Braced Direction, Eccentric Model.

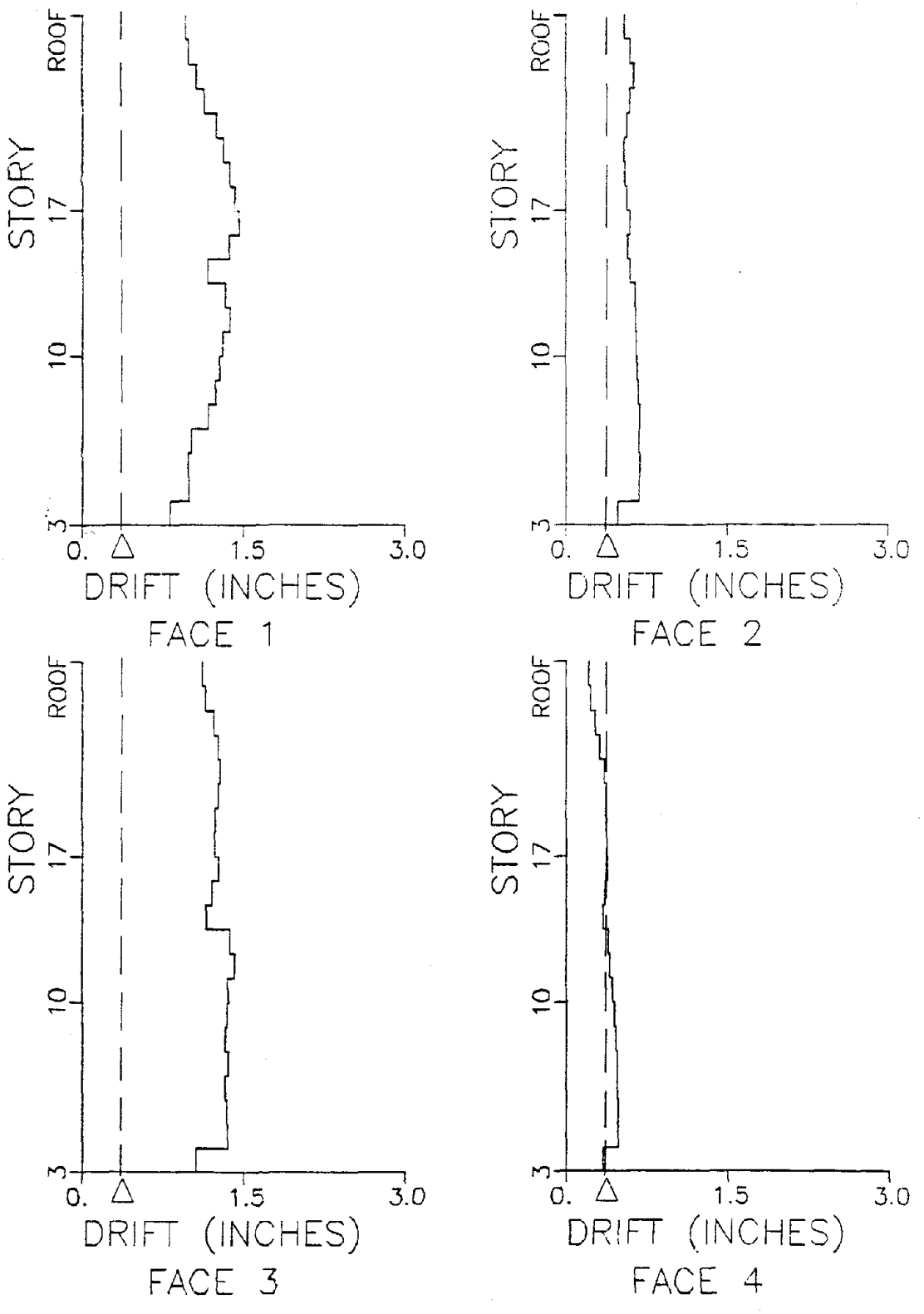

Figure 4.3-23. Peak Drift Values, Slotted Connection Case with Allowable Drift, Δ, set at 0.36 inches (0.9 cm) for 1966 Parkfield Record Acting in Braced Direction, Eccentric Model.

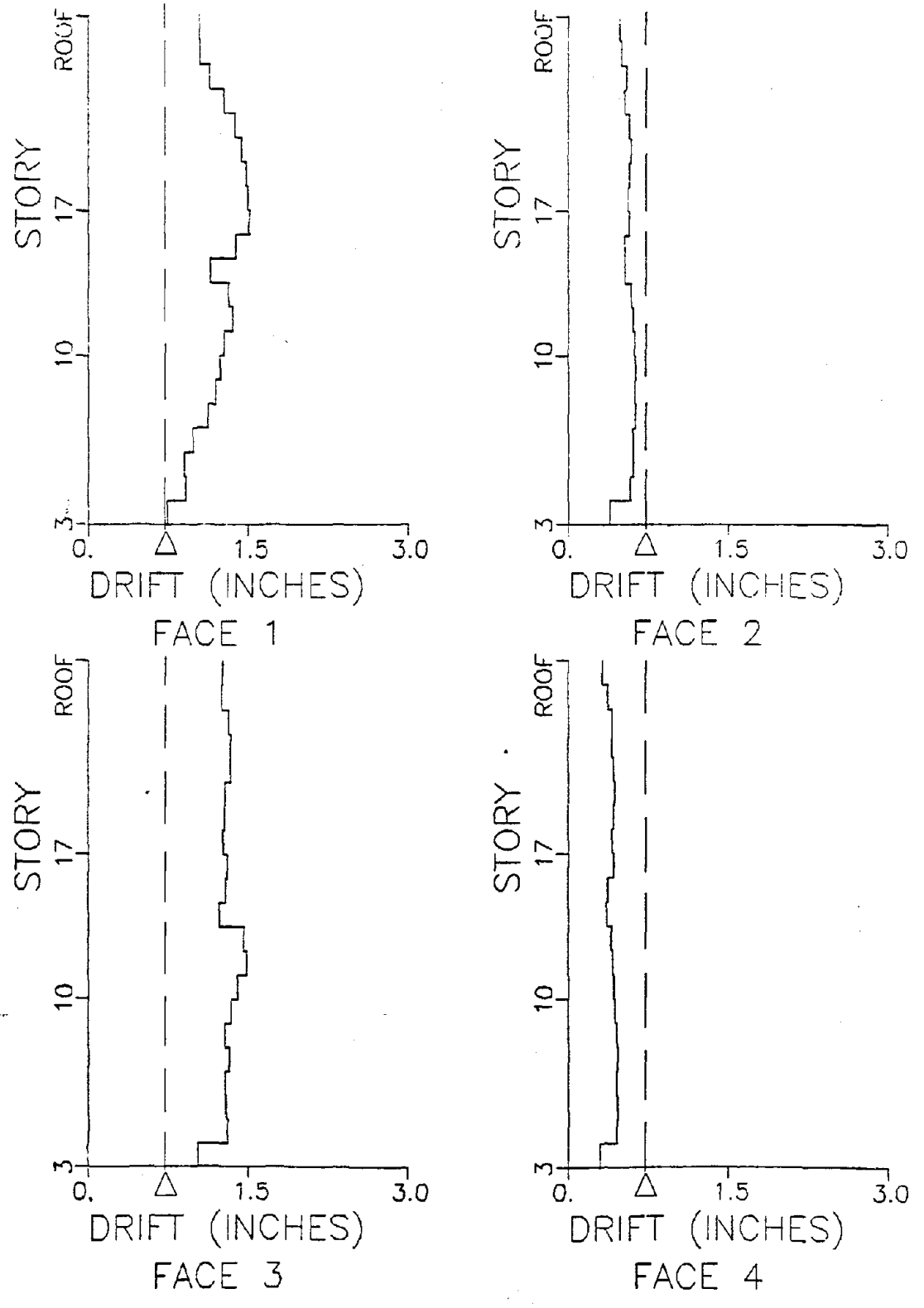

Figure 4.3-24. Peak Drift Values, Slotted Connection Case with Allowable Drift, Δ, set at 0.72 inches (1.8 cm) for 1966 Parkfield Record Acting in Braced Direction, Eccentric Model.

interstory drift levels. The slots would have had to be considerably longer than those used in the prototype structure to isolate the cladding elements when the two earthquake loadings considered in this study were applied.

4.4 Degrading Hysteresis Model

4.4.1 Description of Model

Two different force-deformation relationships for cladding were introduced in the two preceding sections. Neither included any hysteretic behavior in the case of cyclic loading. In the absence of experimental data describing the cyclic hysteretic behavior of a typical cladding panel, the simple hysteresis model shown in Fig. 4.4-1 was developed. The model combines both elasto-plastic and shear-slip behavior. This model approximates load-deflection behavior of frames with infilled panels as determined by laboratory studies of other investigators [20]. While cladding response to interstory motions may differ somewhat from the behavior of frames with infilled panels, the simple hysteresis model was considered to be a reasonable initial assumption for cladding cyclic behavior in the absence of definitive laboratory test data. It was recognized that neither partial cladding failure nor the presence of slotted connections could be accounted for using this model. Load-degradation at large displacements was not included in this model in order to maintain its simplicity.

The following rules were used to define the hysteresis model in the present study:

(1) Loading and unloading occurs along line 0-1 (see Fig. 4.4-1) prior to exceeding the allowable drift Δ. Here Δ was taken to be 0.005

times the story height (0.72 inches = 1.83 cm for the prototype structure) as specified by 1982 UBC [49]. The slope of line 0-1 was taken to be 625 kips/inch (1.1×10^5 kN/m) on the basis of the parameter study results noted earlier in Section 2.4.

(2) Maximum forces and yielding forces are the same in both tension and compression and occur along lines such as 1-2 and 11-12 in Fig. 4.4-1.

(3) For interstory displacements exceeding yield levels and followed by unloading, the unloading line is taken to be parallel to the loading line (see lines 2-3 and 12-13 in Fig. 4.4-1, for example).

(4) After yielding has first taken place in both tension and compression, the reversal loading has a maximum force of 10% of the yield force (this value was assumed for the present study) and the corresponding slope is zero (see lines 5-6 and 9-10 in Fig. 4.4-1). Lines 5-6 and 9-10 are referred to as slip lines. This behavior accounts for the assumed shear-slip response in the model and for deterioration of both maximum load at a given displacement level and energy dissipation capacity with successive cycles.

(5) When the reversal loading intersects the last unloading line in a quadrant (e.g., point 6), the slope of the loading line (e.g., line 6-7) again becomes parallel to the initial elastic loading line (line 0-1).

(6) Unloading from a slip line (see rule 4 above) follows a line parallel to the initial elastic loading line as illustrated by line 14-15 in Fig. 4.4-1.

The integration procedure for the overall structural system with the above cladding model included is described in the following section.

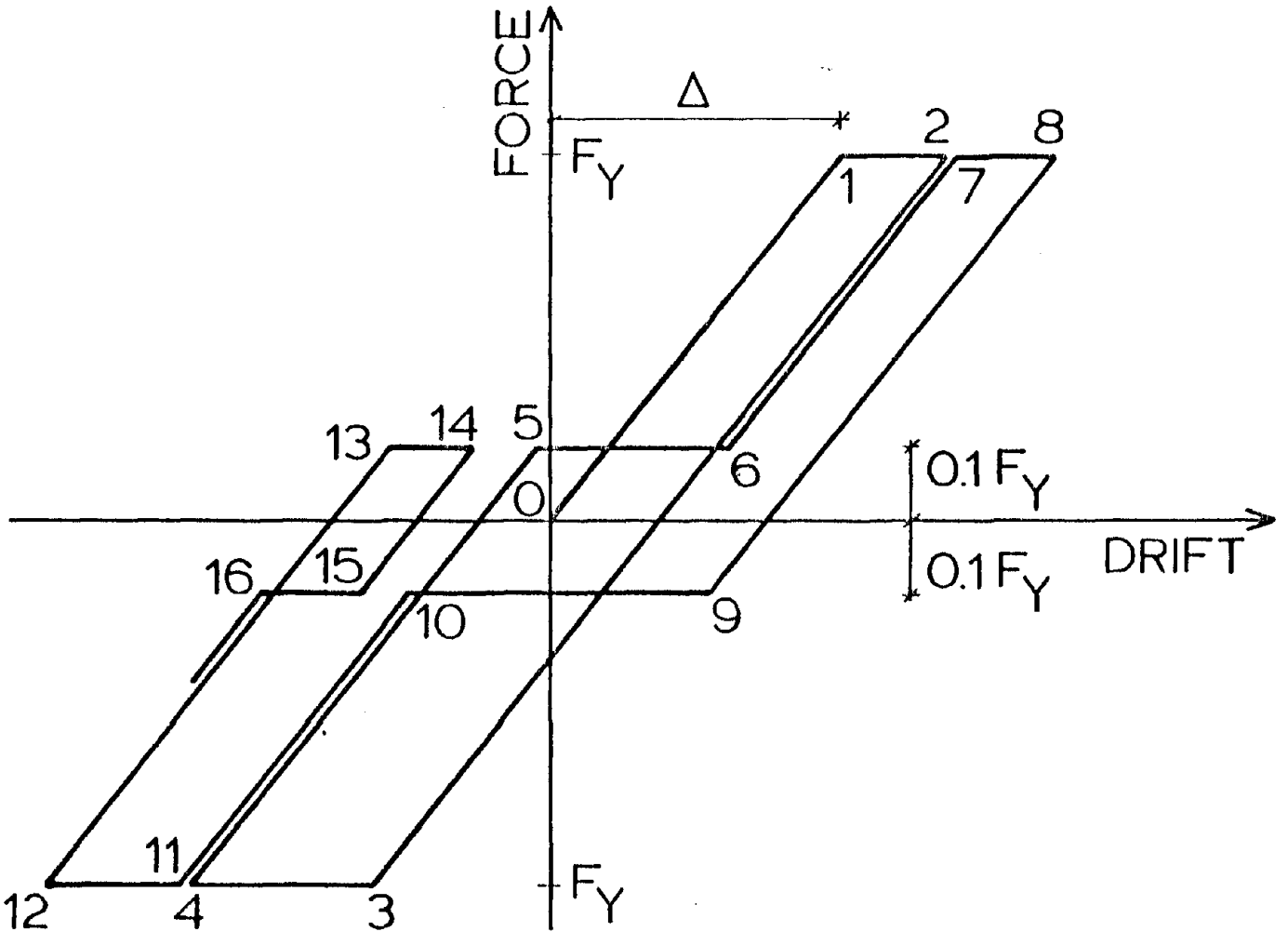

Figure 4.4-1. Degrading Hysteresis Model.

4.4.2 Integration Method

Several numerical integration procedures are available to solve the equations of motion

$$\underset{\sim}{M}\ddot{\underset{\sim}{D}} + \underset{\sim}{C}\dot{\underset{\sim}{D}} + \underset{\sim}{S}\underset{\sim}{D} = \underset{\sim}{A} \tag{4.4-1}$$

The direct linear extrapolation technique with the trapezoidal rule (discussed in Section 3.2) was chosen for the present study since the algorithm was available from the above studies. However, due to the assumed nonlinearity depicted in Fig. 4.4-1, several modifications in the computational procedures were needed. The choice was made to handle all the nonlinearity by adjusting the load vector rather than by adjusting the stiffness matrix, as discussed by Desai [7], when the system properties changed. Consequently, the stiffness matrix had only to be decomposed once at the start of the procedure.

The computational algorithm used here may be summarized as follows:

1. Use the trapezoidal rule and condense the equation of motion to

$$\underset{\sim}{S}^{*}\underset{\sim i}{D} = \underset{\sim i}{A}^{*} \tag{4.4-2}$$

where i indicates the time step under consideration, $\underset{\sim}{S}^{*}$ is defined by Eq. (3.2-9) and $\underset{\sim i}{A}^{*}$ by Eq. (3.2-10).

2. Solve for displacements $\underset{\sim i}{D}$ using the Cholesky method and compute velocities $\dot{\underset{\sim i}{D}}$ and accelerations $\ddot{\underset{\sim i}{D}}$ (see Eqs. (3.2-14) and (3.2-15)).

3. Set j = 0 (j is the number of iterations within a time step) and continue.

4. Start the jth iteration: j becomes j + 1.

5. Compute the vector of residual (or unbalanced) loads [2] as

$$\underset{\sim}{U}_i^j = \underset{\sim}{A}_i - \underset{\sim\sim}{M}\underset{\sim}{D}_i^{j-1} - \underset{\sim\sim}{C}\underset{\sim}{D}_i^{j-1} - \underset{\sim}{F}_i^{j-1} \tag{4.4-3}$$

where the vector of internal loads is

$$\underset{\sim}{F}_i^{j-1} = \underset{\sim u}{S}\underset{\sim}{D}_i^{j-1} + \underset{\sim}{B}_i^{j-1} \tag{4.4-4}$$

and where $\underset{\sim u}{S}$ is the stiffness matrix for the unclad structure. The vector $\underset{\sim}{B}_i^{j-1}$ is obtained in the following way:

a) Interstory displacements $\Delta\underset{\sim}{D}_i^{j-1}$ are computed at each story and each face as:

$$\begin{aligned}
\Delta D(I,1) &= D(3I-1) - D(3I+2) - R(D(3I) - D(3I+3)) \\
\Delta D(I,2) &= D(3I-2) - D(3I+1) - R(D(3I) - D(3I+3)) \\
\Delta D(I,3) &= D(3I-1) - D(3I+2) + R(D(3I) - D(3I+3)) \\
\Delta D(I,4) &= D(3I-2) - D(3I+1) + R(D(3I) - D(3I+3))
\end{aligned} \tag{4.4-5}$$

where I indicates the floor number starting at the roof and the second subscript for $\Delta\underset{\sim}{D}$ is the face number (see Fig. 4.4-2). When the interstory displacements are computed for the lowest floor level, the substracting terms become zero or

$$\begin{aligned} \Delta D(21,1) &= D(62) - R(D(63)) \\ \Delta D(21,2) &= D(61) - R(D(63)) \\ \Delta D(21,3) &= D(62) + R(D(63)) \\ \Delta D(21,4) &= D(61) + R(D(63)) \end{aligned} \qquad (4.4\text{-}6)$$

b) Current internal forces CIF_i^{j-1} in cladding are determined based on the interstory displacements, the force-deformation relationship (hysteresis loop in Fig. 4.4-1) and prior displacement history. For example:

(1) If interstory drift has never exceeded the allowable drift Δ (line 0-1 in Fig. 4.4-1), then

$$CIF(I,J) = 625 * \Delta D(I,J) \qquad (4.4\text{-}7)$$

(2) If interstory drift exceeds Δ for the first time (line 1-2 in Fig. 4.4-1), then

$$CIF(I,J) = 625 * 0.72 = 450 \text{ kips} \qquad (4.4\text{-}8)$$

(3) If interstory drift has exceeded Δ and unloading is taking place (line 2-3 in Fig. 4.4-1), then

$$CIF(I,J) = 450 - 625\ (\Delta D2 - \Delta D) \qquad (4.4\text{-}9)$$

where $\Delta D2$ is the drift at point 2 in Fig. 4.4-1. If CIF(I,J) is less than -450 kips, then

$$CIF(I,J) = -450 \text{ kips} \tag{4.4-10}$$

which corresponds to line 3-4 in Fig. 4.4-1.

(4) If loading starts to take place in the positive direction (line 4-5), then

$$CIF(I,J) = -450 + 625 * (\Delta D - \Delta D4) \tag{4.4-11}$$

where $\Delta D4$ is the drift at point 4 in Fig. 4.4-1. In case CIF(I,J) exceeds 45 kips, then

$$CIF(I,J) = 45 \text{ kips} \tag{4.4-12}$$

which follows line 5-6.

(5) When further loading takes place and the drift exceeds $\Delta D6$ (line 6-7), the drift at point 6 which is computed based on $\Delta D2$, the internal force is computed as

$$CIF(I,J) = 45 + 625 * (\Delta D - \Delta D6) \tag{4.4-13}$$

and if CIF(I,J) becomes greater than 450 kips, then

$$CIF(I,J) = 450 \text{ kips} \tag{4.4-14}$$

which corresponds to line 7-8.

(6) If unloading had started to take place before the drift equaled $\Delta D6$, then lines 13-14 and 14-15 describe the situation and the internal force is

$$CIF(I,J) = 45 - 625 * (\Delta D14 - \Delta D) \qquad (4.4\text{-}15)$$

where $\Delta D14$ is the drift at point 14. However, if CIF(I,J) is less than -45 kips, then

$$CIF(I,J) = -45 \text{ kips} \qquad (4.4\text{-}16)$$

c) The vector of internal loads due to cladding and its connections $\underset{\sim}{B}_i^{j-1}$ is computed as (see Fig. 4.4-2)

$$\begin{aligned}
&B(1) = CIF(1,2) + CIF(1,4)\\
&B(2) = CIF(1,1) + CIF(1,3)\\
&B(3) = (-CIF(1,1) - CIF(1,2) + CIF(1,3) + CIF(1,4)) * R\\
&\text{For } I \geq 2 \text{ (I is floor number starting at the roof)} \qquad (4.4\text{-}17)\\
&B(3I-2) = CIF(I,2) + CIF(I,4) - CIF(I-1,2) - CIF(I-1,4)\\
&B(3I-1) = CIF(I,1) + CIF(I,3) - CIF(I-1,1) - CIF(I-1,3)\\
&B(3I) = (-CIF(I,1) - CIF(I,2) + CIF(I,3) + CIF(I,4)\\
&\qquad + CIF(I-1,1) + CIF(I-1,2) - CIF(I-1,3) - CIF(I-1,4)) * R
\end{aligned}$$

6. Check iteration convergence: If RMS $(\underset{\sim}{U}_i^j)$ < tolerance, (set at 1.0 in this study), go to the next time step (step 1). Otherwise, if j is less than the maximum number of iterations (set at 15 in the present study and never exceeded), go to step 7.

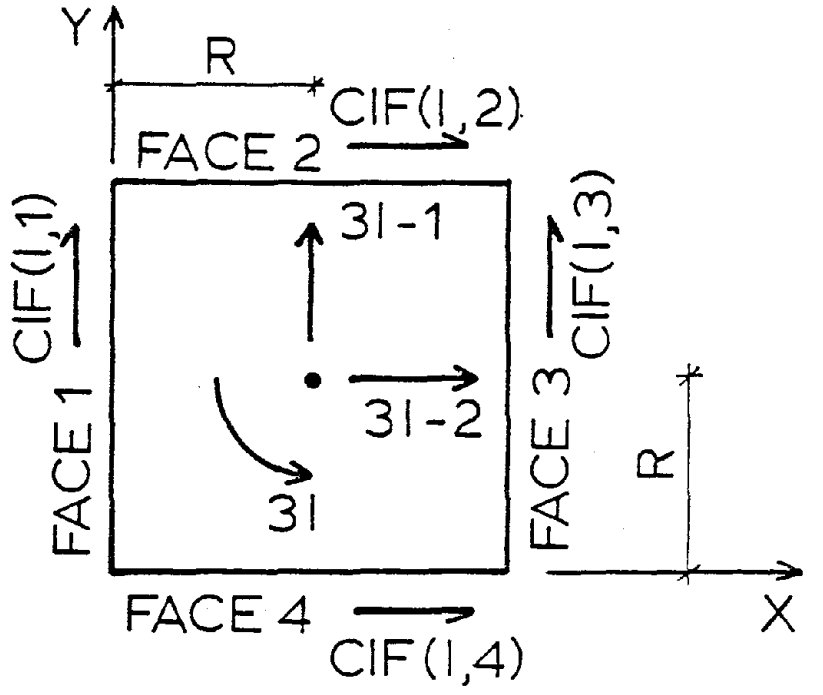

Figure 4.4-2. Internal Forces Due to Cladding and Its Connections for the Degrading Hysteresis Model.

7. Compute the new load vector.

$$\underset{\sim}{A}_i^{*j} = \underset{\sim}{A}_i^{*j-1} + \underset{\sim}{U}_i^{j} \qquad (4.4\text{-}18)$$

8. Solve for $\underset{\sim}{D}_i^{j}$ and compute $\dot{\underset{\sim}{D}}_i^{j}$ and $\ddot{\underset{\sim}{D}}_i^{j}$ in the same manner as in step 2.

9. Go to step 4 and continue.

The above algorithm was found to be stable for the cases considered and convergence was reached in five steps or less for the tolerance specified. This could be due to the relatively mild nonlinearity of the problem.

A listing of the computer program written for the response studies in this section is contained in Appendix A.

The following section presents the results of response studies using the above computational procedure for the degrading hysteresis model.

4.4.3 Response Studies

In the present study, response computations were performed only for the eccentric mass model as defined in Section 3.4. Simple modal damping was set at five percent of critical and the damping matrix was not adjusted as cladding stiffness changed. Only one allowable drift value, Δ, chosen as 0.005 times an average story height of 12 feet (i.e., Δ = 0.72 inches or 1.8 cm) was considered. Linear clad and unclad case responses for the eccentric model of Section 3.4 are repeated here in tables and time-history plots for comparison.

First, the dynamic response to the El Centro earthqauke record was considered. Peak roof displacements are tabulated in Table 4.4-1

and translational and torsional time-history plots are presented in Figs. 4.4-3 to 4.4-6. These results showed that peak response in the direction of input ground motion was in between the corresponding values for the clad and unclad cases. Rigid direction response for braced direction input and rotational response for rigid direction input were both greater than corresponding values for the clad and unclad cases. However, braced direction response for rigid direction input and rotational response for braced direction input were in between clad and unclad model responses. In spite of the differences observed in peak response values, inspection of the time-history plots showed that the hysteretic case response followed the clad case closely. When peak relative interstory drift values for the different faces were computed (see Table 4.4-2), the hysteretic values were bracketed by the linear clad and unclad responses in all cases except on face 4 for rigid direction input. The peak story drift values are plotted in Figs. 4.4-7 and 4.4-8. When these figures are compared to Figs. 3.4-40 to 3.4-43, showing peak story drift values for the clad and unclad cases, a good agreement was observed between the hysteretic model and the linear clad model.

When response to the Parkfield record was computed, peak roof displacement response values were as listed in Table 4.4-3 and translational and torsional roof time-histories are displayed in Figs. 4.4-9 to 4.4-12. Hysteretic peak response values in the direction of applied motion were observed to be bracketed by the linear cases with and without cladding while they were found to be lower in directions other than the input direction. Peak interstory drift values for the different building faces are tabulated in Table 4.4-4 and peak story drift values are plotted in Figs. 4.4-13 and 4.4-14. Comparison of peak face drift values revealed

that hysteretic values were in between values for the linear clad and unclad cases in all instances but two and those two were not in the direction of applied ground motion. When hysteretic story drift values were compared to linear story drift values (Figs. 3.4-48 to 3.4-51), hysteretic case values were observed to follow linear clad case values closely.

The above response studies showed the hysteretic response behavior to be similar to the linear clad case for the allowable drift, Δ, and earthquake loadings chosen. The present model would become rather impractical with the use of a small Δ value since smaller timesteps would have to be employed due to the presence of the slip lines in the model (see Fig. 4.4-1 and Section 4.4.1). Further studies involving this hysteretic model and small Δ values were not performed based on the above comments. However, in the event that future experimental studies show this model to be a good representation of cladding behavior, a modification of the model such as moving the shear slip lines to a force level of zero would improve its practicality for computation. This modification results in fewer rules for the hysteresis model (see Section 4.4.1 for the current model) and also does not require the use of as small a time step since two relatively close shear slip lines are replaced by one.

4.5 Brake Pad Model

4.5.1 Description of Model

A cladding connection possessing elasto-plastic behavior and stable hysteretic response over several cycles would be beneficial to a structure during a strong motion earthquake because of its inherent energy dissipation capacity. The connection would be even more valuable if relatively large interstory displacements could be accommodated without any permanent

Table 4.4-1. Peak Roof Displacements, Degrading Hysteresis Case for the Eccentric Model, for the 1940 El Centro Record.

Ground Motion Input Direction (1)	Case (2)	Peak Roof Displacement Response		
		Rigid Direction (inches) (3)	Braced Direction (inches) (4)	Rotation (radians) (5)
Braced	Clad	2.7	15.2	7.8×10^{-3}
	Unclad	1.7	14.8	5.6×10^{-3}
	Hysteretic	2.9	14.9	7.5×10^{-3}
Rigid	Clad	15.0	1.9	5.2×10^{-3}
	Unclad	11.8	1.0	3.7×10^{-3}
	Hysteretic	14.1	1.9	5.7×10^{-3}

Note: 1 inch = 25.4 mm.

Table 4.4-2. Peak Interstory Drift, Degrading Hysteresis Case for the Eccentric Model, for the 1940 El Centro Record.

Ground Motion Input Direction (1)	Case (2)	Peak Relative Interstory Drift (inches) Face 1[a]	Face 2	Face 3	Face 4
Braced	Clad	1.1(16)	0.5(5)	1.0(16)	0.4(4)
	Unclad	1.0(21)	0.4(19)	1.3(18)	0.2(22)
	Hysteretic	1.1(16)	0.5(4)	1.1(16)	0.4(4)
Rigid	Clad	0.3(4)	1.0(19)	0.3(11)	1.3(19)
	Unclad	0.5(24)	1.3(24)	0.4(24)	1.2(24)
	Hysteretic	0.4(21)	1.0(19)	0.3(22)	1.4(19)

[a]Story at which peak drift occurred is shown in parentheses.

Note: 1 inch = 25.4 mm.

Table 4.4-3. Peak Roof Displacements, Degrading Hysteresis Case for the Eccentric Model, for the 1966 Parkfield Record.

Ground Motion Input Direction (1)	Case (2)	Peak Roof Response		
		Rigid Direction (inches) (3)	Braced Direction (inches) (4)	Rotation (radians) (5)
Braced	Clad	3.1	20.7	1.2×10^{-2}
	Unclad	2.8	23.9	1.1×10^{-2}
	Hysteretic	2.2	21.1	8.0×10^{-3}
Rigid	Clad	21.9	2.3	7.8×10^{-3}
	Unclad	25.2	1.6	1.2×10^{-2}
	Hysteretic	22.7	1.4	6.5×10^{-3}

Note: 1 inch = 25.4 mm.

Table 4.4-4. Peak Interstory Drift, Degrading Hysteresis Case for the Eccentric Model, for the 1966 Parkfield Record.

Ground Motion Input Direction (1)	Case (2)	Peak Relative Interstory Drift (inches) Face 1[a] (3)	Face 2 (4)	Face 3 (5)	Face 4 (6)
Braced	Clad	1.5(11)	0.7(7)	1.4(7)	0.4(4)
	Unclad	1.6(18)	0.7(22)	1.6(20)	0.5(22)
	Hysteretic	1.6(11)	0.5(16)	1.4(8)	0.4(5)
Rigid	Clad	0.4(16)	1.6(12)	0.4(4)	1.9(12)
	Unclad	1.1(22)	3.0(22)	1.0(22)	3.1(24)
	Hysteretic	0.4(19)	1.8(12)	0.3(20)	2.1(22)

[a]Story at which peak drift occurred is shown in parentheses.

Note: 1 inch = 25.4 mm.

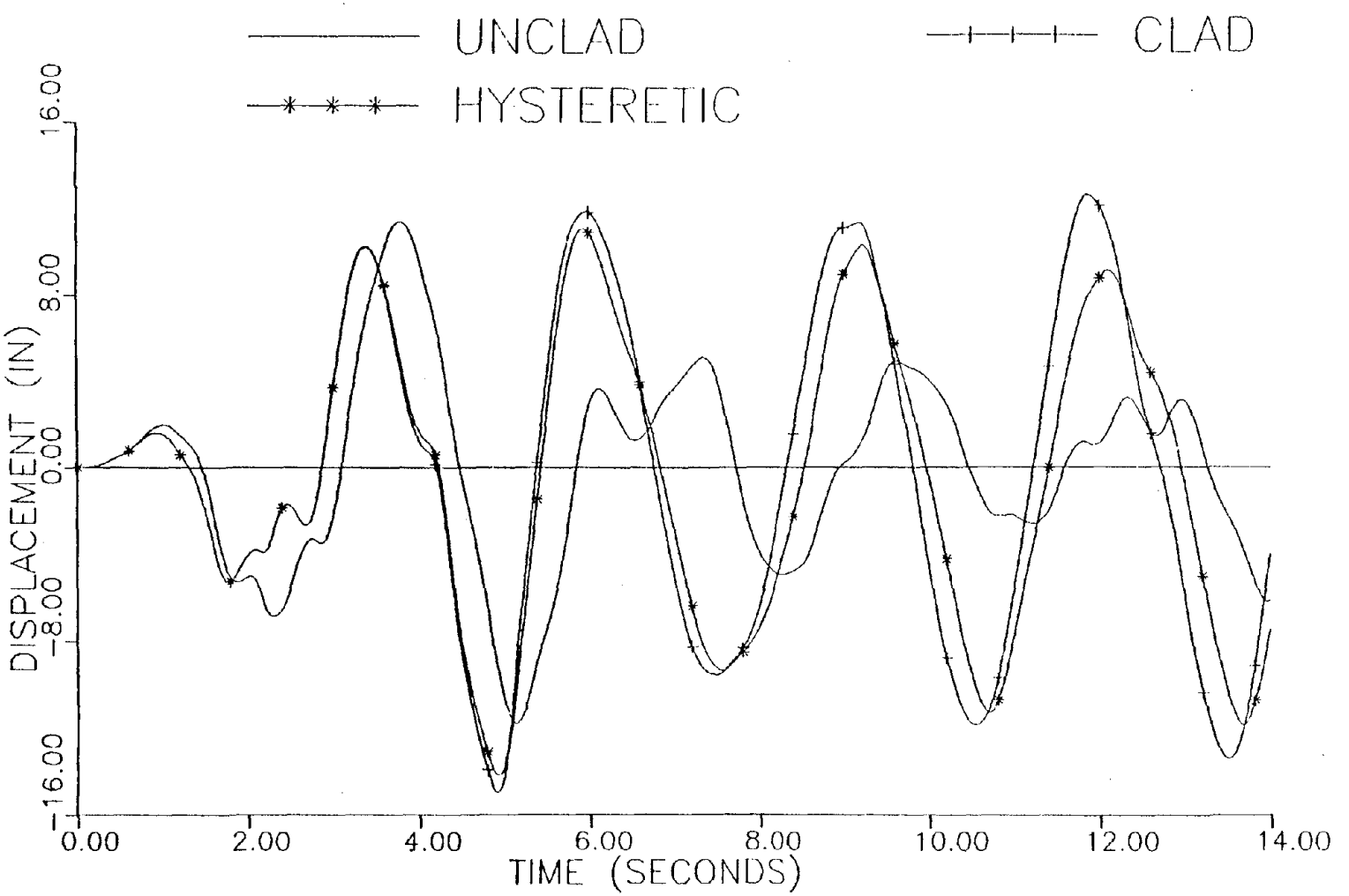

Figure 4.4-3. Roof Translational Response in Rigid Direction, Degrading Hysteresis Case for Eccentric Model, Compared to Linear Clad and Unclad Model Response for 1940 El Centro Record Acting in Rigid Direction.

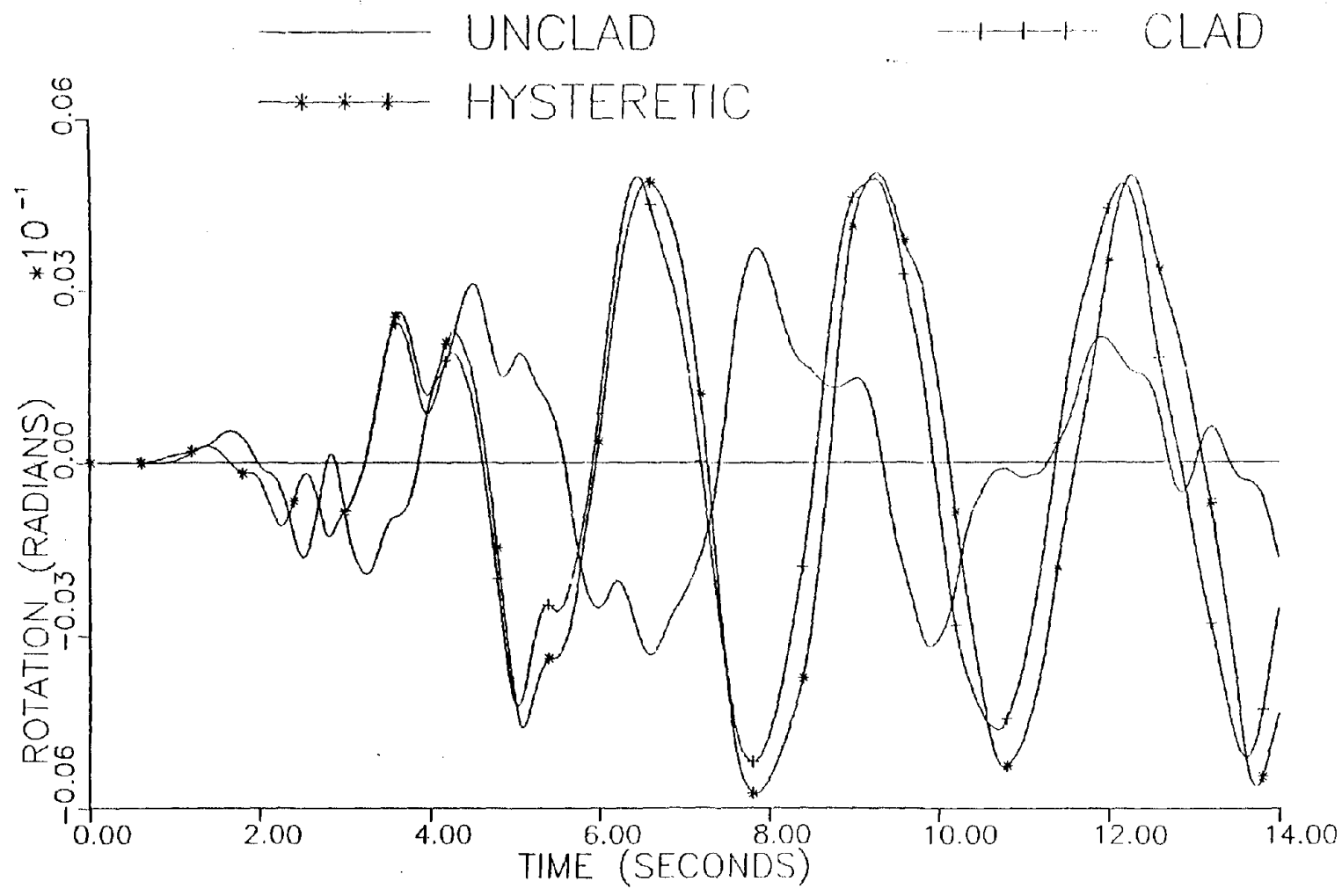

Figure 4.4-4. Roof Rotational Response, Degrading Hysteresis Case for Eccentric Model, Compared to Linear Clad and Unclad Model Responses, for 1940 El Centro Record Acting in Rigid Direction.

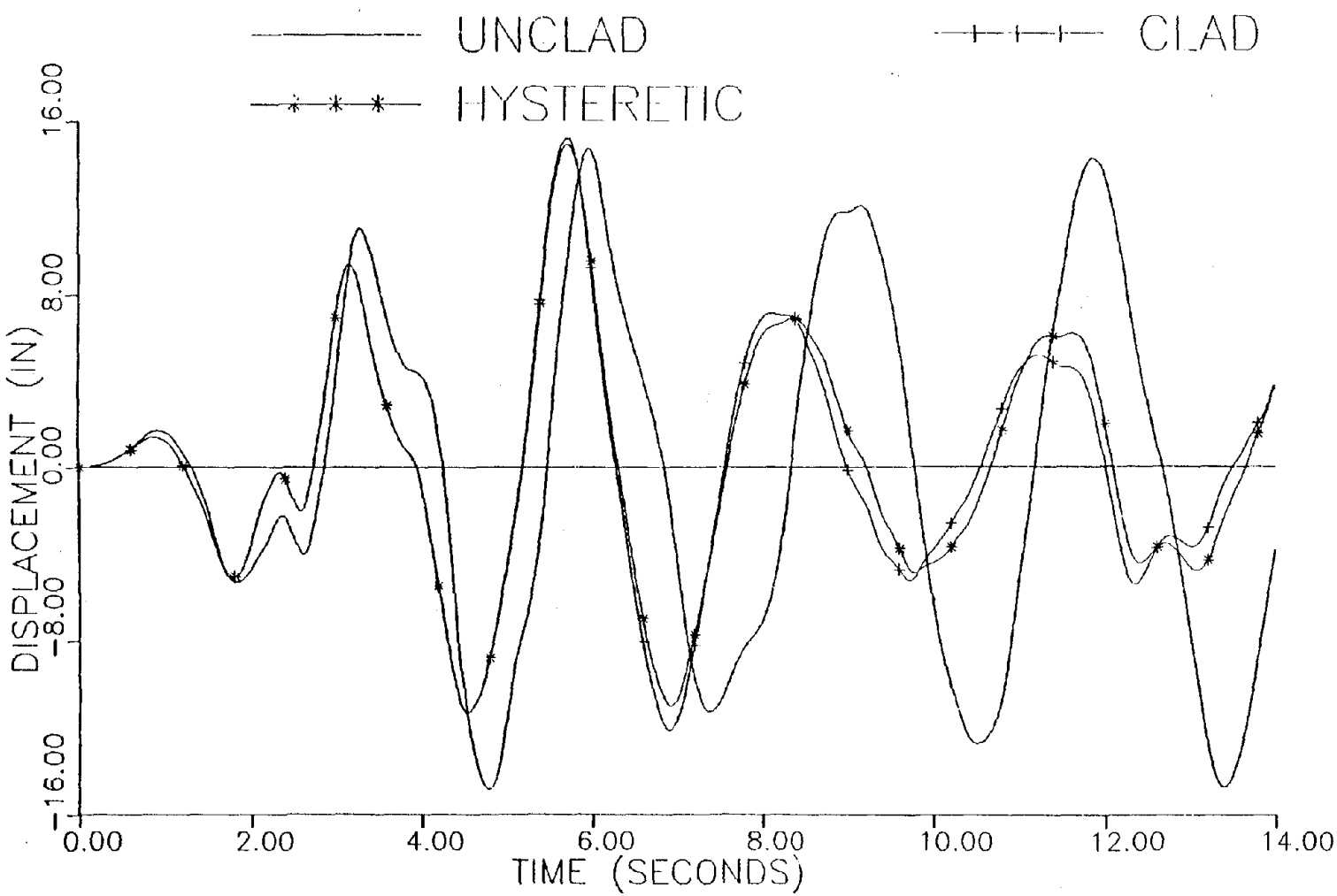

Figure 4.4-5. Roof Translational Response in Braced Direction, Degrading Hysteresis Case for Eccentric Model, Compared to Linear Clad and Unclad Model Responses for 1940 El Centro Record Acting in Braced Direction.

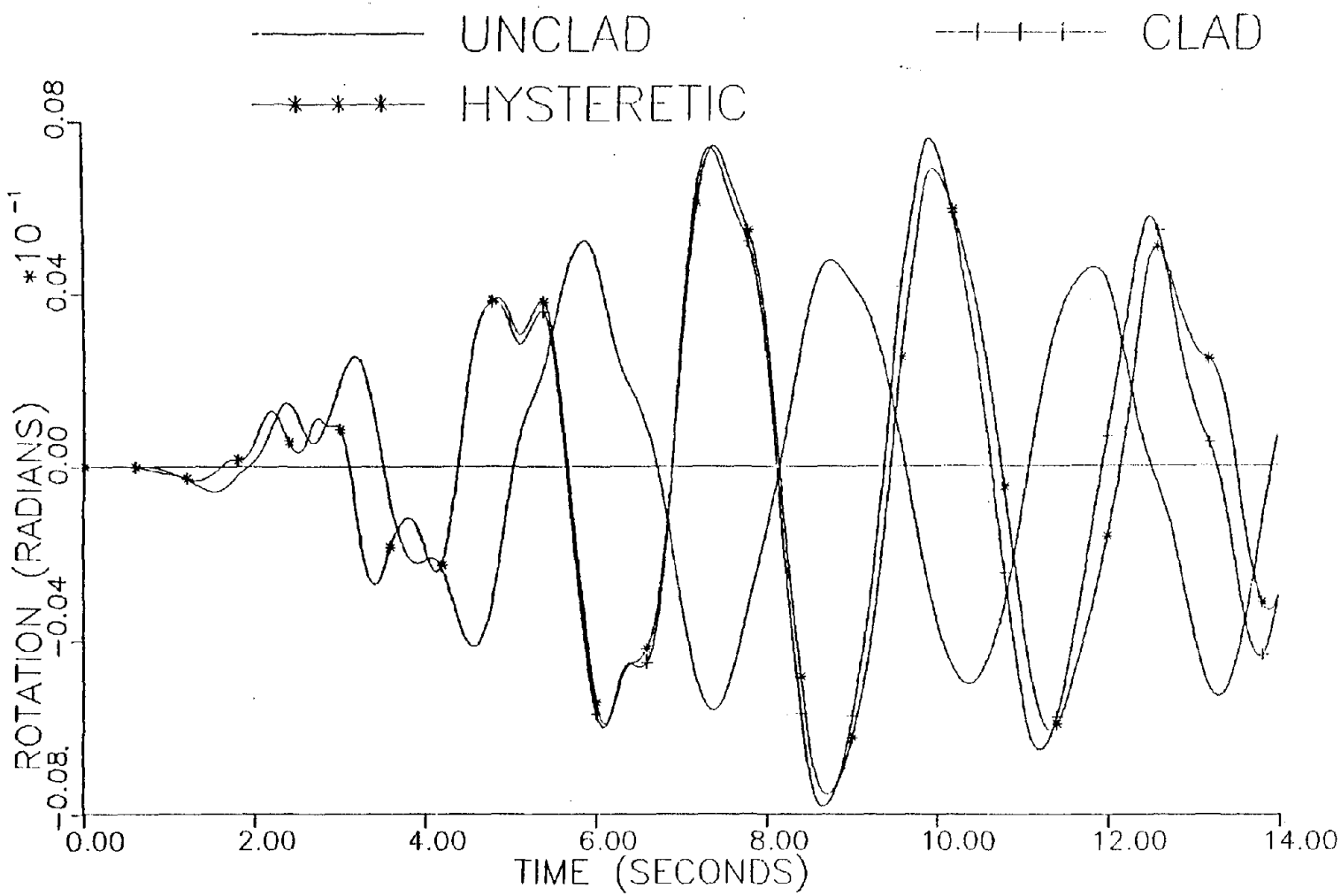

Figure 4.4-6. Roof Rotational Response, Degrading Hysteresis Case for Eccentric Model, Compared to Linear Clad and Unclad Model Responses for 1940 El Centro Record Acting in Braced Direction.

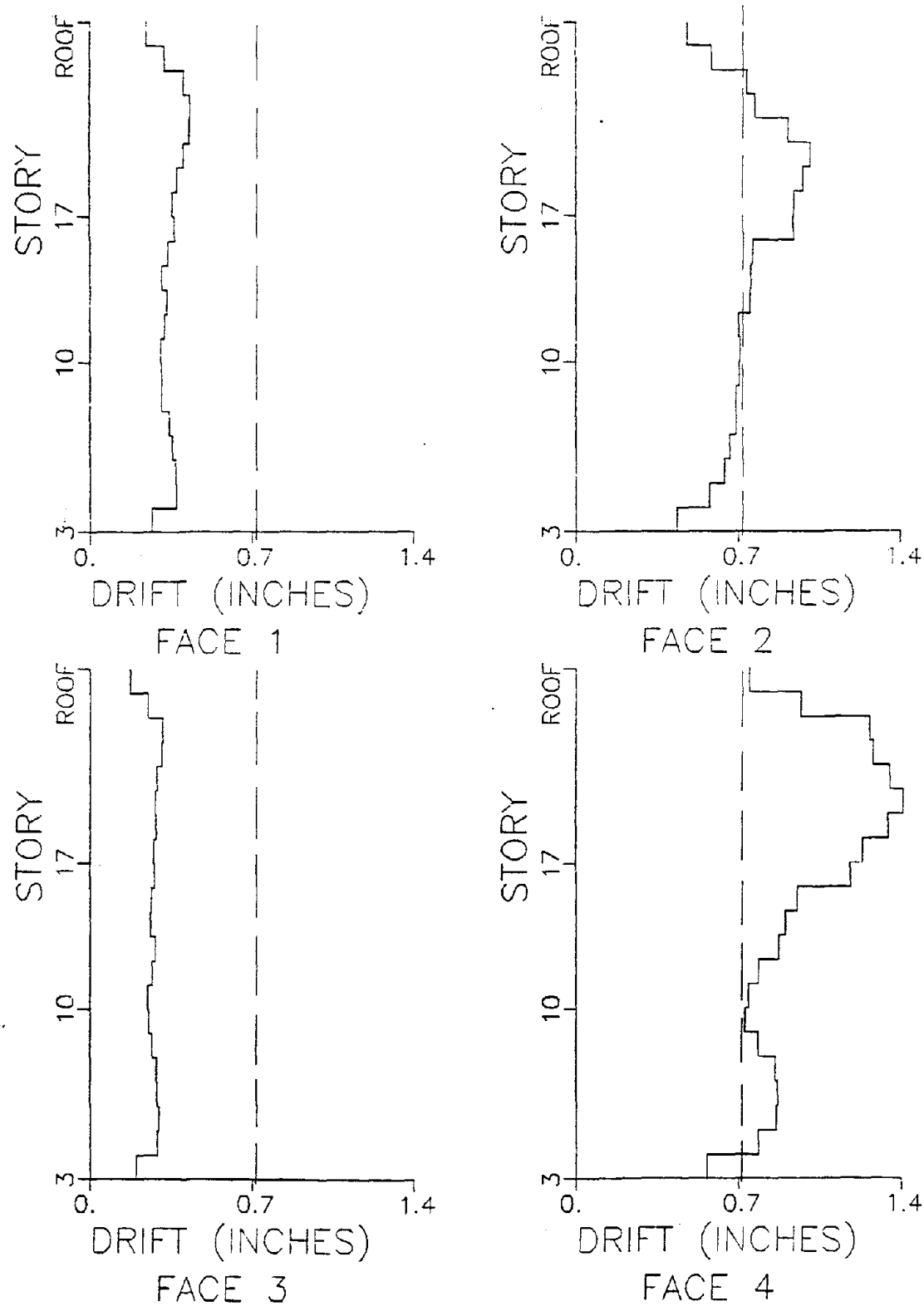

Figure 4.4-7. Peak Drift Values, Degrading Hysteresis Case with Δ set at 0.72 inches (1.8 cm), for 1940 El Centro Record Acting in Rigid Direction, Eccentric Model.

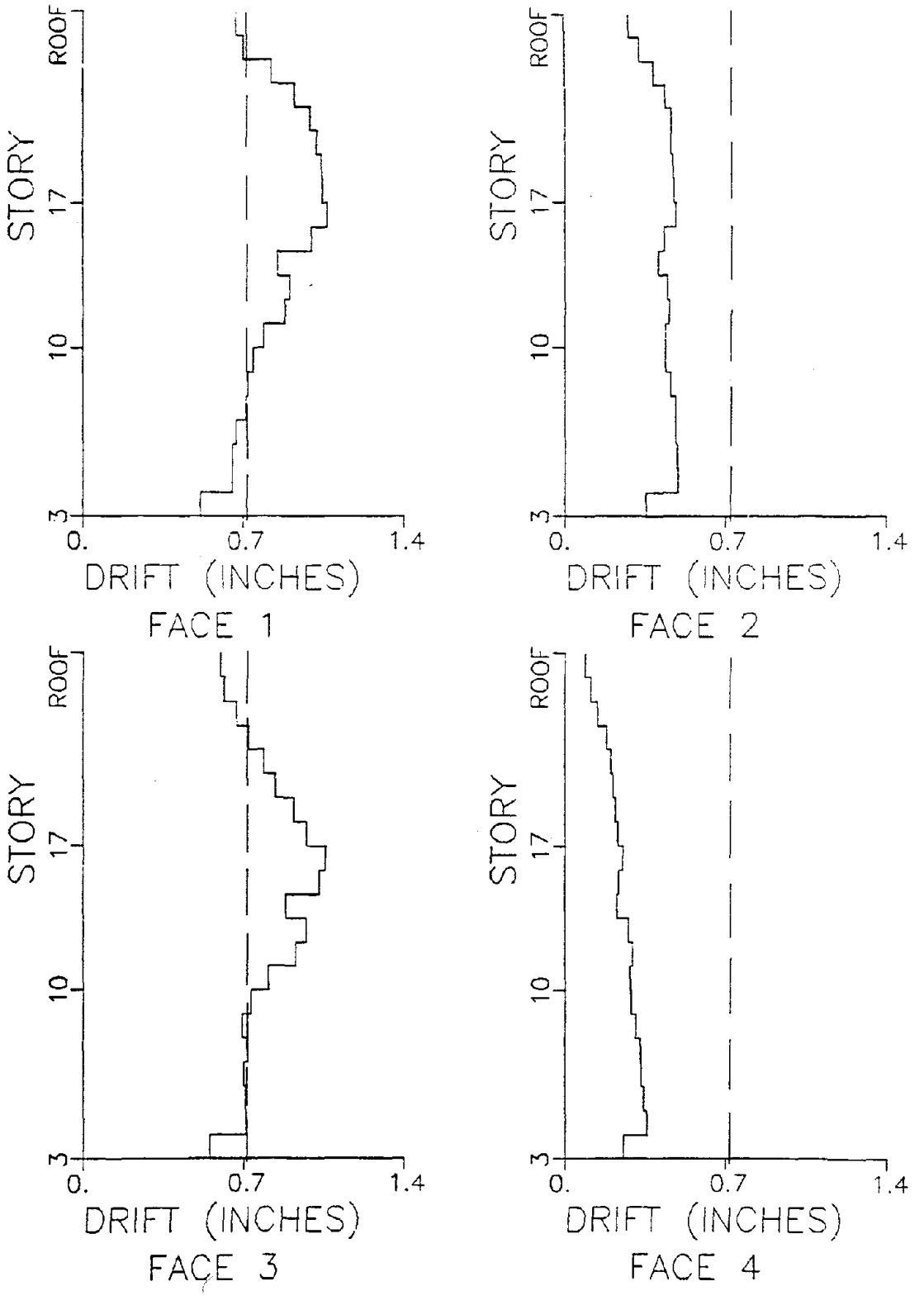

Figure 4.4-8. Peak Drift Values, Degrading Hysteresis Case with Δ set at 0.72 inches (1.8 cm), for 1940 El Centro Record Acting in Braced Direction, Eccentric Model.

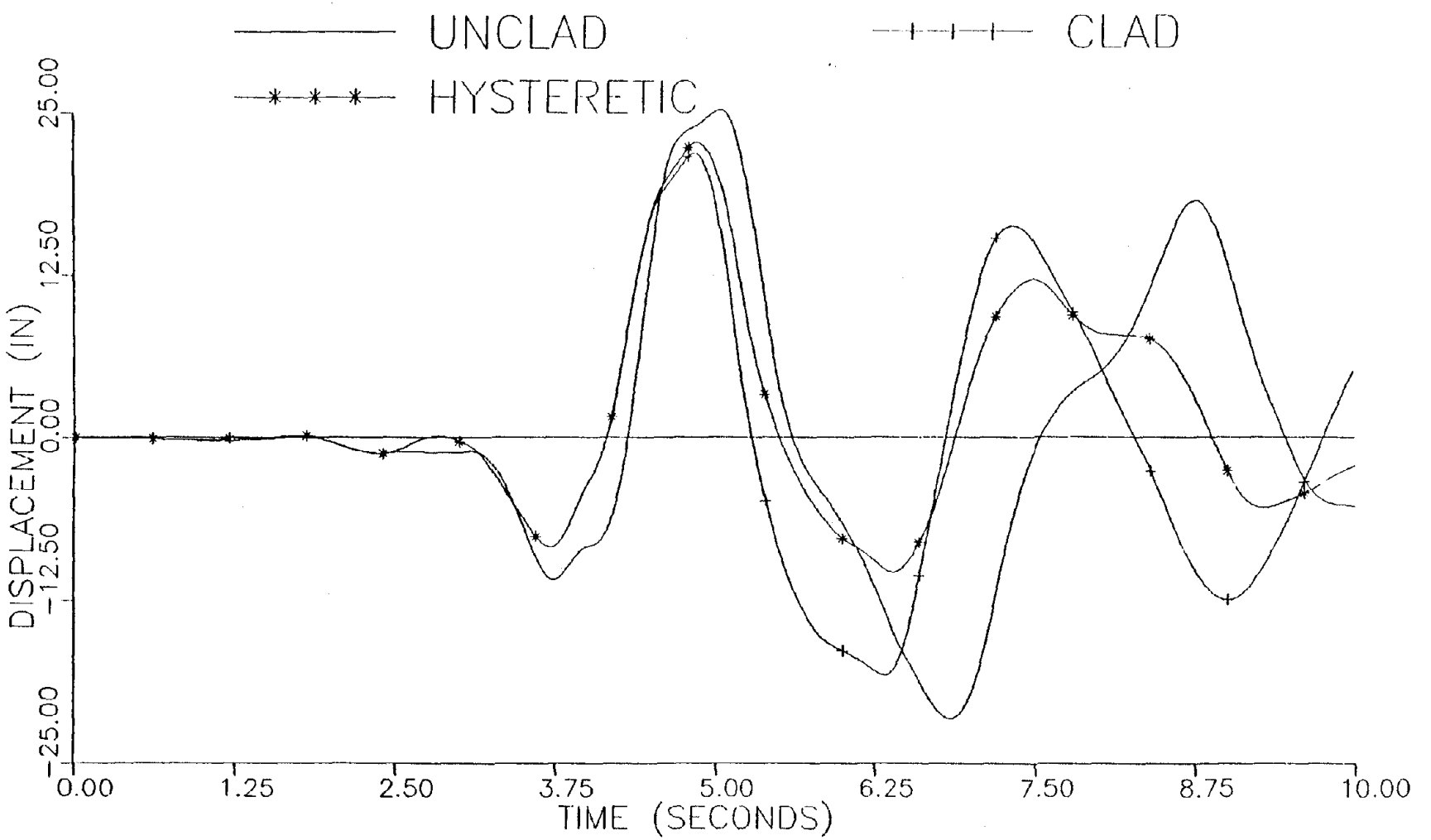

Figure 4.4-9. Roof Translational Response in Rigid Direction, Degrading Hysteresis Case for Eccentric Model, Compared to Linear Clad and Unclad Model Responses for 1966 Parkfield Record Acting in Rigid Direction.

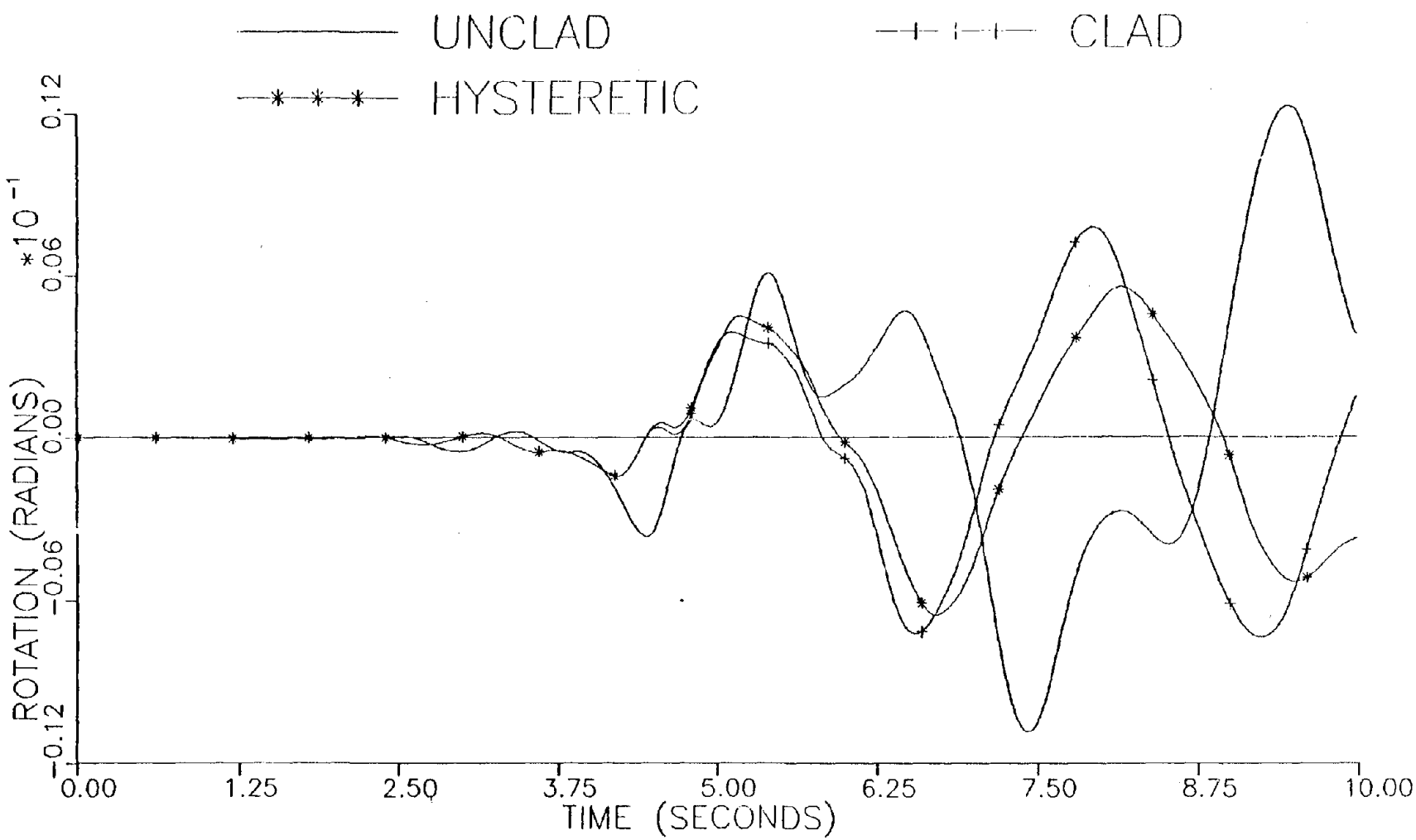

Figure 4.4-10. Roof Rotational Response, Degrading Hysteresis Case for Eccentric Model, Compared to Linear Clad and Unclad Model Responses for 1966 Parkfield Record Acting in Rigid Direction.

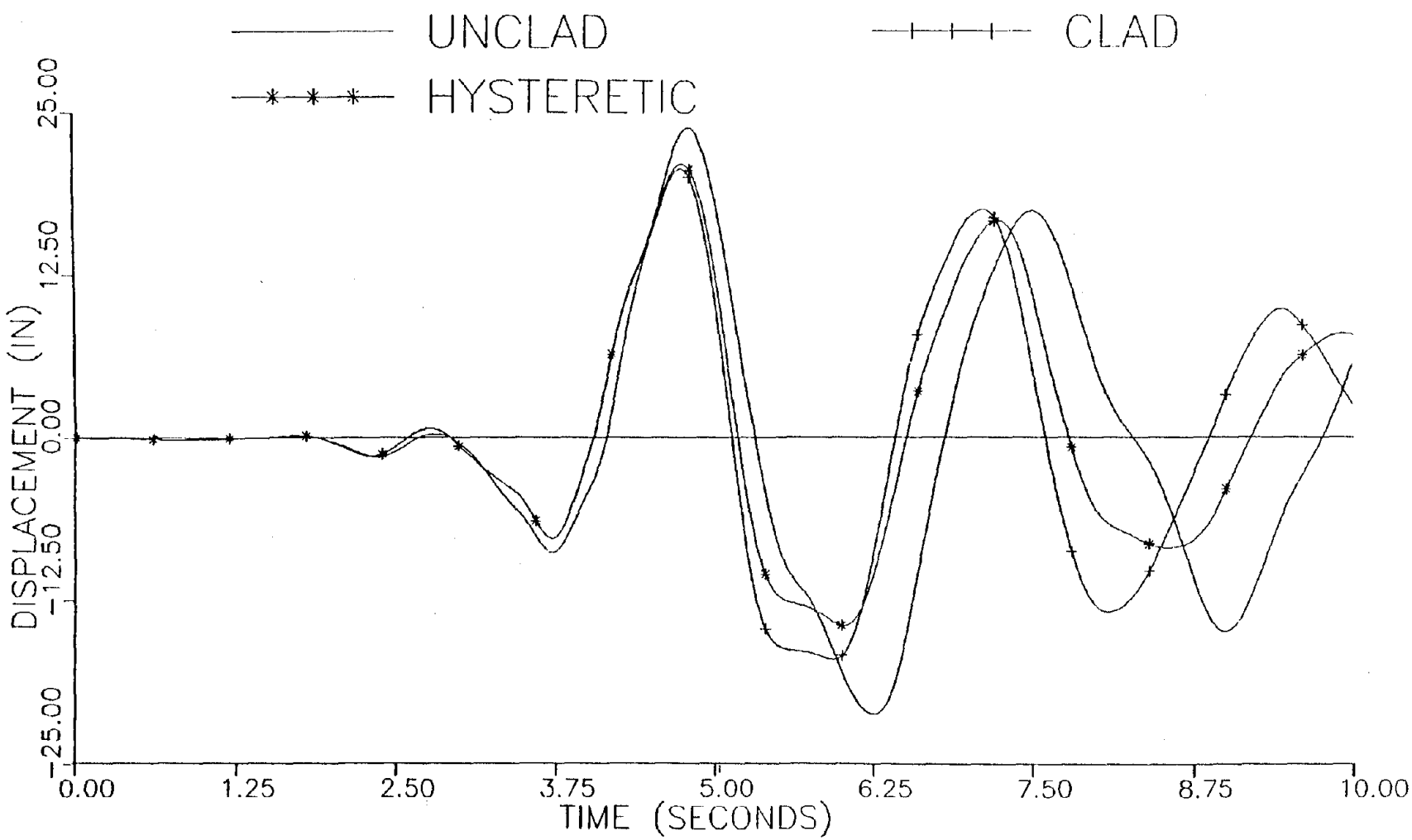

Figure 4.4-11. Roof Translational Response in Braced Direction, Degrading Hysteresis Case for Eccentricl Model, Compared to Linear Clad and Unclad Model Responses for 1966 Parkfield Record Acting in Braced Direction.

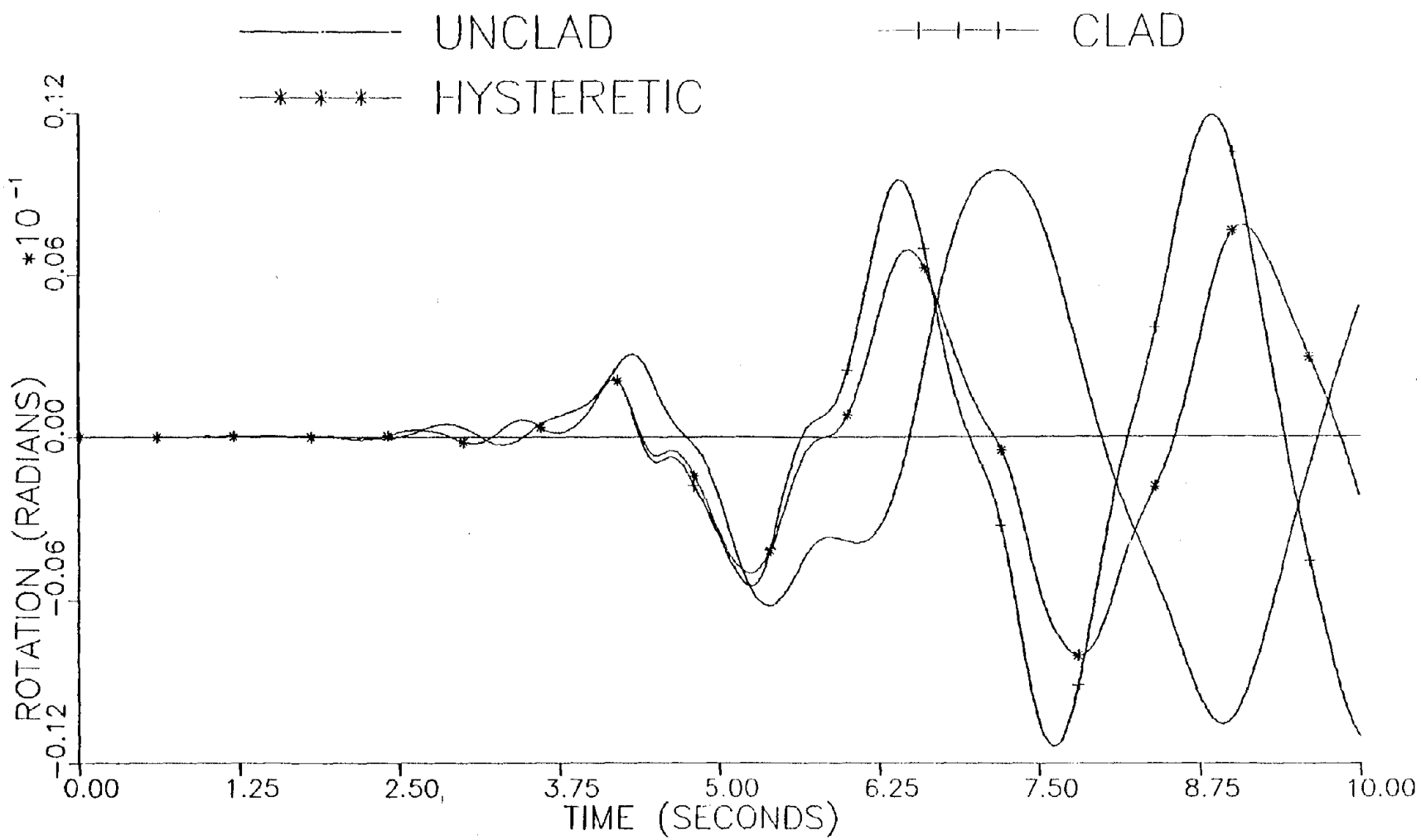

Figure 4.4-12. Roof Rotational Response, Degrading Hysteresis Case for Eccentric Model, Compared to Linear Clad and Unclad Model Responses for 1966 Parkfield Record Acting in Braced Direction.

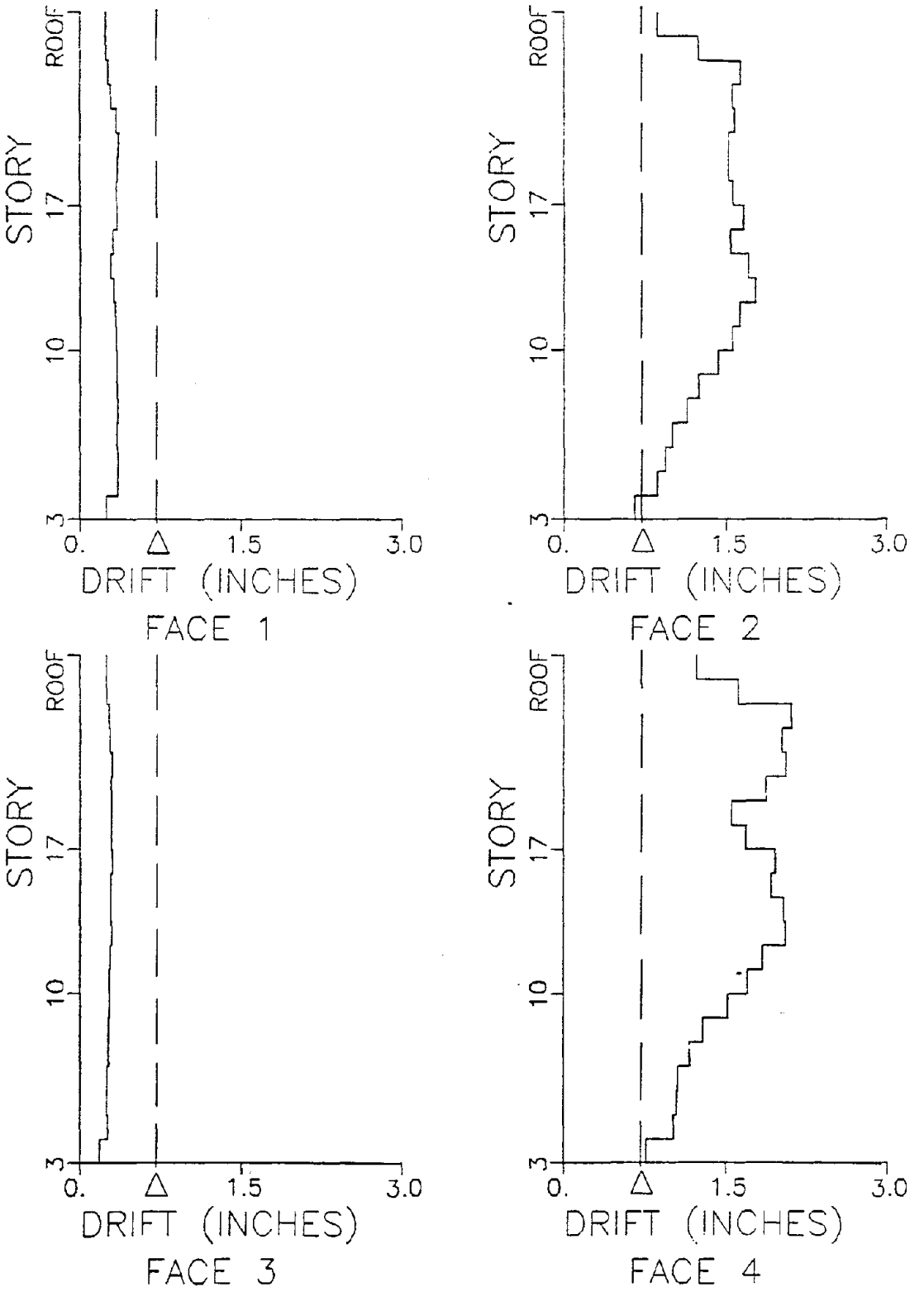

Figure 4.4-13. Peak Drift Values, Degrading Hysteresis Case with Δ set at 0.72 inches (1.8 cm), for 1966 Parkfield Record Acting in Rigid Direction, Eccentric Model.

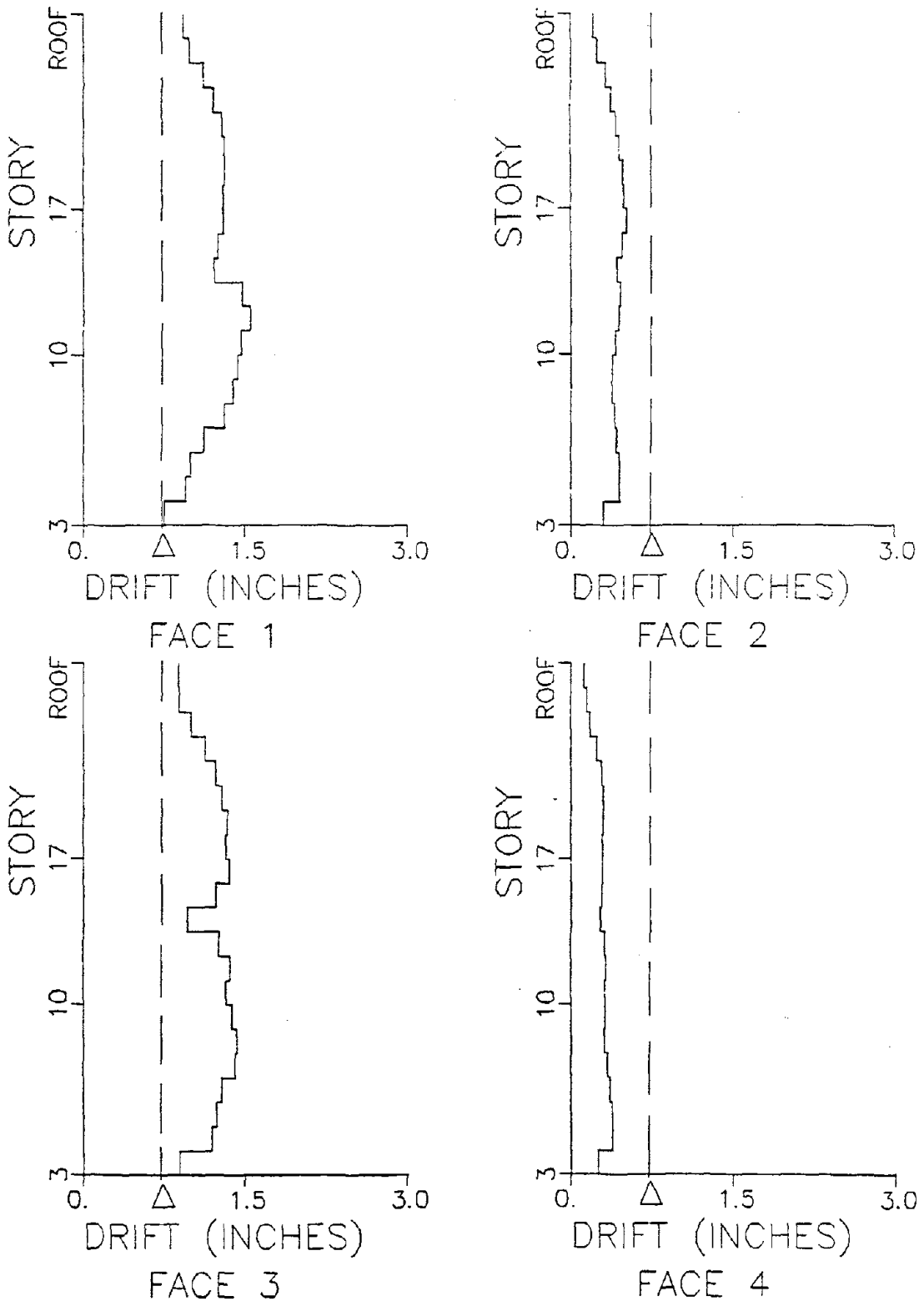

Figure 4.4-14. Peak Drift Values, Degrading Hysteresis Case with Δ set at 0.72 inches (1.8 cm), for 1966 Parkfield Record Acting in Braced Direction, Eccentric Model.

damage and with adequate safety against failure of the cladding. Most cladding connections used at present do not intentionally make use of any energy dissipation possibilities.

The connection shown in Fig. 4.5-1 was developed based on a connection proposed for use in precast concrete large panel construction [31]. This connection is intended for use at the top of the panel on one side only with the other top connection being an oversized hole similar to that recommended by PCI [35]. The proposed connection will allow vertical slip to take place in the panel insert without any resistance. Horizontal motion on the other hand is governed by a force displacement relationship which is idealized to be elasto-plastic as shown in Fig. 4.5-2. The slope of the loading and unloading lines in this idealized loop was taken to be 625 kips/inch (1.1×10^5 kN/m) based on the parameter studies in Section 2.4. The allowable drift value, Δ, which in this model is the drift at which slip starts, was varied in steps as discussed in the following section. The slot width of the clip angles in Fig. 4.5-1 were assumed to be large enough so that bolts would not come into bearing horizontally. However, if horizontal bearing were to be accounted for in the model, the hysteresis loop would have to be modified to look similar to the previous hysteresis model depicted in Fig. 4.4-1. The hysteretic behavior is achieved by inserting heavy duty brake lining pads between sliding steel plates. Experimental studies have shown that stable hysteresis is obtained with this plate-pad arrangement. It should be noted that the loading and unloading sections of the measured hysteresis loop are vertical [31].

It was recognized that the use of the proposed connection could have several disadvantages and problems in actual practice, such as:

(a) Possible high initial expense.

(b) Need for careful control and inspection during installation to insure proper tightening of bolts. (Otherwise, friction forces would vary leading to unreliable performance of connections.)

(c) Potential deterioration with time and need for maintenance.

(d) Cost of replacement.

(e) More complicated design.

In the analytical studies of the performance of cladding with brake pad connections, the equations of motion were integrated using the procedure described above in Section 4.4.2 to handle the nonlinearity introduced by the hysteretic behavior. Determination of current internal forces in step 5.b (see Section 4.4.2) became more simplified than for the degrading hysteresis model, but otherwise the procedure remained unchanged. Five percent simple modal damping based on the linear clad case was used in all response calculations in the absence of information about proper damping levels.

The following section contains results of structure dynamic response studies employing the idealized hysteresis loop for cladding shown in Fig. 4.5-2 and using the 1940 El Centro record and the 1966 Parkfield record as ground motion loadings.

4.5.2 Response Studies

The eccentric mass model defined in Section 3.4.1 was used in the response studies employing the brake pad model. Five different allowable interstory drift conditions (Δ) were considered as follows:

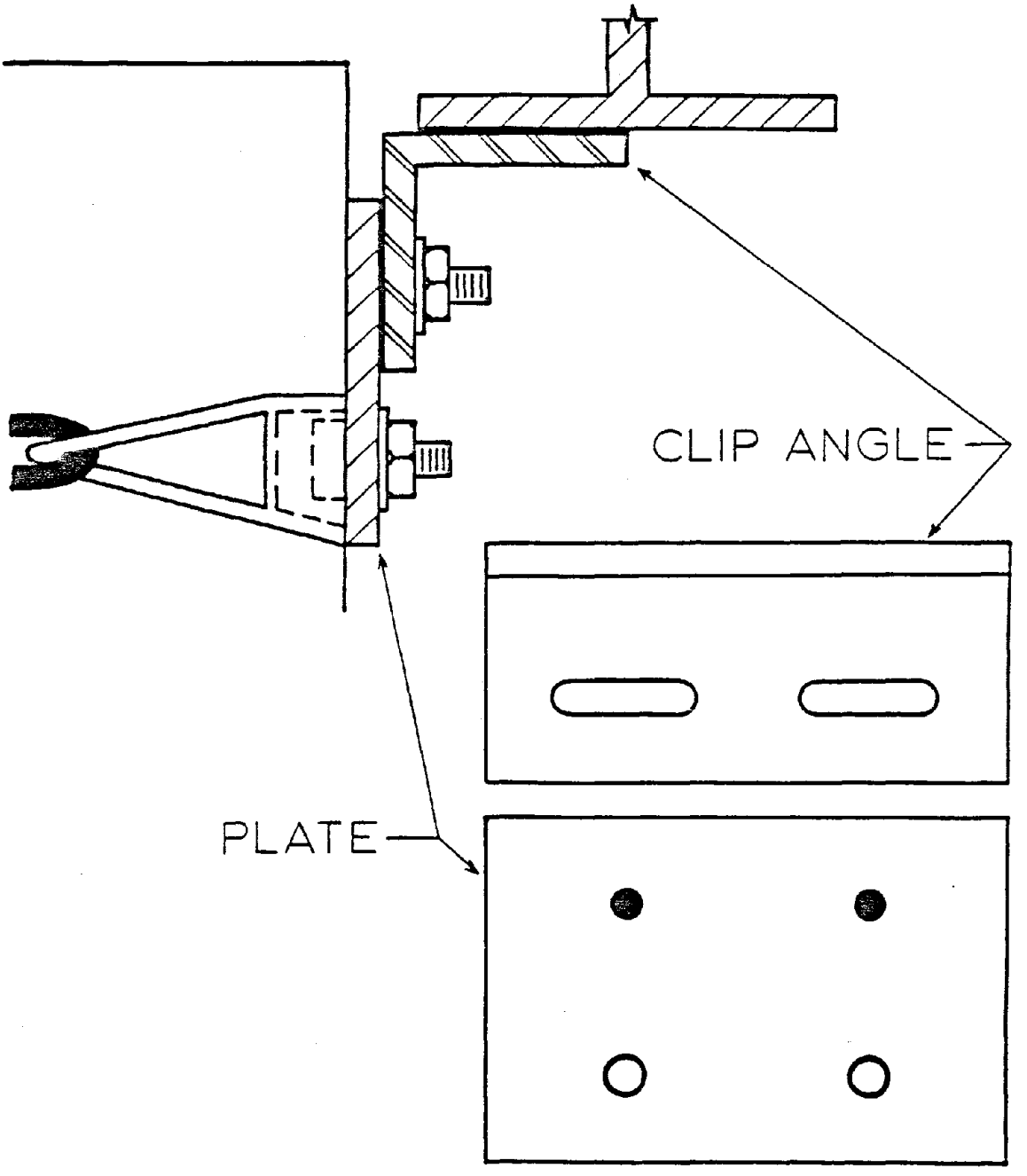

Figure 4.5-1. Cladding Panel Connection Employing Heavy Duty Brake Lining Pads Inserted Between the Clip Angle and the Plate.

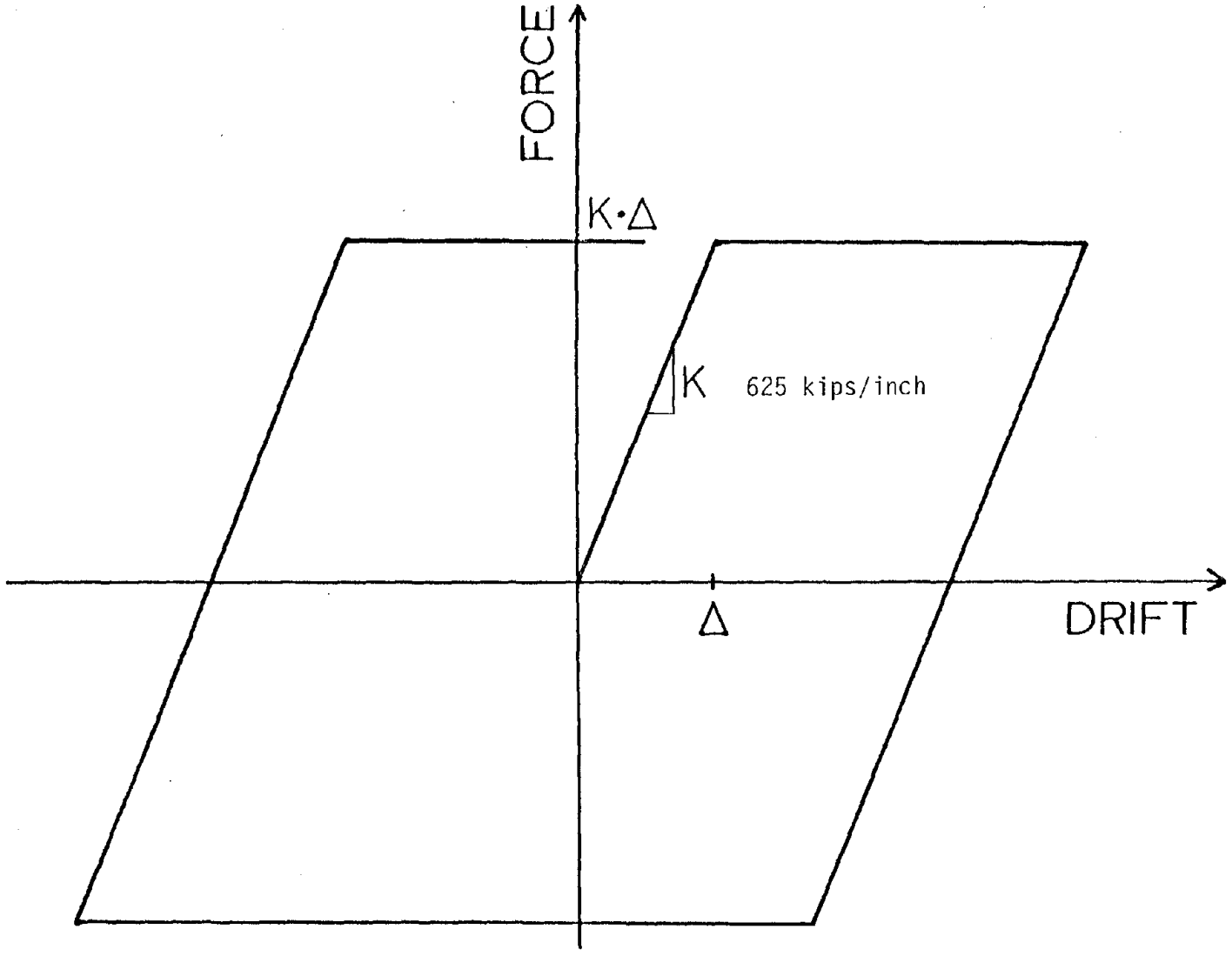

Figure 4.5-2. Idealized Hysteresis Loop for Cladding with Brake Pad Connections.

(1) Δ = 0 (i.e., cladding completely ineffective for the unclad case, V = 0).

(2) Δ = 0.00125 times an average story height of 12 feet (i.e., Δ = 0.18 inches or 0.5 cm).

(3) Δ = 0.0025 times an average story height of 12 feet (i.e., Δ = 0.36 inches or 0.9 cm).

(4) Δ = 0.005 times an average story height of 12 feet (i.e., Δ = 0.72 inches or 1.8 cm).

(5) Δ = infinity (i.e., the linear clad case, V = 625 kips/inch or 1.1×10^5 kN/m).

Conditions (1) and (5) correspond to the unclad and clad linear eccentric cases, respectively.

Peak roof displacement response values for the El Centro record are listed in Table 4.5-1 and roof translational and torsional time-histories are displayed in Figs. 4.5-3 to 4.5-6. Comparison of the different allowable drift cases showed that condition (2) with Δ set 0.18 inches (0.5 cm) was most effective in reducing peak response when compared to the linear cases in conditions (1) and (5). Braced direction response for input in the braced direction was lowered 24% by condition (2) over either linear case and rigid response for rigid direction input was reduced 11%. Response in directions other than the input directions was also observed to decrease such as rotational response by up to 24%.

Peak relative interstory drift values at the building faces for the El Centro record are tabulated in Table 4.5-2 and peak story drift values are presented in Figs. 4.5-7 to 4.5-12. Condition (2) was again more effective than conditions (3) and (4) in lowering response as compared

to conditions (1) and (5). Peak drift on faces in direction of applied motion was reduced up to 20% for braced direction input (face 1) and up to 30% for rigid direction input (face 2). Comparison of the story drift plots showed that not only peak face drift was reduced but overall building drift (see Figs. 3.4-40 to 3.4-43 for drift plots for conditions (1) and (5)).

Peak roof response values due to the Parkfield earthquake are tabulated in Table 4.5-3 and roof response time-histories are depicted in Fig. 4.5-13 to 4.5-16. Inspection of these data showed that peak roof response in the direction of applied ground motion decreased with increasing allowable drift, Δ. However, in directions other than the input direction, condition (2) was found to yield the lowest response values. For example, rotational response for condition (2) was reduced 45% when compared to the linear cases of conditions (1) and (5). While peak values in the direction of applied motion are not effectively reduced by the introduction of the brake pad model, the time-history plots revealed that displacement response was generally lowered by its introduction. When peak interstory drift values at the four structure faces listed in Table 4.5-4 and peak story drift values plotted in Figs. 4.5-17 to 4.5-22 were compared, a similar pattern as for the peak roof response values was observed. Peak drift on faces parallel to the input direction was bracketed by the linear clad and unclad cases (conditions (1) and (5)), but several instances of reduced peak drift were seen on faces orthogonal to the input direction.

The above studies showed the effects of employing the brake pad model on structure response. The additional contribution to damping

from hysteretic behavior of the brake pad cladding connection, expressed in percent of critical [44], was plotted versus interstory drift in Fig. 4.5-23. Hysteretic damping was assumed and the assumption was made that drift was of equal magnitude in both positive and negative directions when energy dissipation during each full cycle was determined. The following equation was used in the computation of the dimensionless equivalent viscous damping ratio [44]

$$\gamma_{eq} = \frac{\Delta U}{2\pi K X^2} \qquad (4.5\text{-}1)$$

where ΔU is the energy dissipated per cycle, K is the slope of the force-deflection curve and X the interstory drift (Fig. 4.5-23 shows γ_{eq} as a function of X). Additional damping levels for cladding of 5-15% of critical depending on the amount of interstory drift were observed in Fig. 4.5-23. In addition, the presence of additional damping at lower interstory drift levels for condition (2) (Δ = 0.18 inches or 0.5 cm) was observed as a possible explanation for its effectiveness in reducing overall response as reported above.

The question whether the potential advantages of the brake pad connection outweigh its disadvantages was not fully answered in this study. Relative costs, complications in design and construction, other loadings, and effects of slot length need to be addressed before conclusions can be reached.

When response values for the brake pad model were compared to response values for the three other cladding models presented in Sections 4.2, 4.3, and 4.4 above, it was evident that no other model was as effective as the brake pad model in reducing overall structure response for the

Table 4.5-1. Peak Roof Response, Brake Pad Case for the Eccentric Model, for the 1940 El Centro Record.

Ground Motion Input Direction (1)	Allowable Drift, Δ (inches) (2)	Peak Roof Displacement Response		
		Rigid Direction (inches) (3)	Braced Direction (inches) (4)	Rotation (radians) (5)
Braced	0.0[a]	1.7	14.8	5.6×10^{-3}
	0.18	1.3	11.3	4.3×10^{-3}
	0.36	1.6	12.3	4.6×10^{-3}
	0.72	2.4	14.9	7.4×10^{-3}
	∞[b]	2.7	15.2	7.8×10^{-3}
Rigid	0.0	11.8	1.0	3.7×10^{-3}
	0.18	10.5	0.7	2.8×10^{-3}
	0.36	11.3	1.2	4.1×10^{-3}
	0.72	14.1	1.8	5.1×10^{-3}
	∞	15.0	1.9	5.2×10^{-3}

[a]Clad case (V = 625 kips/inch).

[b]Unclad case (V = 0).

Note: one inch = 25.4 mm.

Table 4.5-2. Peak Interstory Drift, Brake Pad Case for the Eccentric Model, for the 1940 El Centro Record.

Ground Motion Input Direction (1)	Allowable Drift, Δ (inches) (2)	Peak Relative Interstory Drift (inches) Face 1[a] (3)	Face 2 (4)	Face 3 (5)	Face 4 (6)
Braced	0.0[b]	1.0(21)	0.4(19)	1.3(18)	0.2(22)
	0.18	0.8(16)	0.3(20)	0.9(16)	0.2(20)
	0.36	0.9(16)	0.4(20)	1.0(16)	0.2(4)
	0.72	1.1(16)	0.5(5)	1.1(16)	0.3(4)
	∞[c]	1.1(16)	0.5(5)	1.0(16)	0.4(4)
Rigid	0.0	0.5(24)	1.3(24)	0.4(24)	1.2(24)
	0.18	0.3(24)	0.7(19)	0.2(24)	1.0(24)
	0.36	0.3(24)	0.8(19)	0.2(24)	1.1(22)
	0.72	0.4(22)	1.0(19)	0.3(22)	1.4(19)
	∞	0.3(4)	1.0(19)	0.3(11)	1.3(19)

[a]Story at which peak drift occurred is shown in parentheses.

[b]Clad case (V = 625 kips/inch).

[c]Unclad case (V = 0).

Note: 1 inch = 25.4 mm.

Table 4.5-3. Peak Roof Response, Brake Pad Case for the Eccentric Model, for the 1966 Parkfield Record.

Ground Motion Input Direction (1)	Allowable Drift, Δ (inches) (2)	Peak Roof Displacement Response		
		Rigid Direction (inches) (3)	Braced Direction (inches) (4)	Rotation (radians) (5)
Braced	0.0[a]	2.8	23.9	1.1×10^{-2}
	0.18	1.0	22.4	6.1×10^{-3}
	0.36	1.6	21.7	6.5×10^{-3}
	0.72	2.2	21.1	8.2×10^{-3}
	∞[b]	3.1	20.7	1.2×10^{-2}
Rigid	0.0	25.2	1.6	1.2×10^{-2}
	0.18	23.7	0.8	4.6×10^{-3}
	0.36	23.0	1.1	5.5×10^{-3}
	0.72	22.7	1.7	6.4×10^{-3}
	∞	21.9	2.3	7.8×10^{-3}

[a]Clad case (V = 625 kips/inch).

[b]Unclad case (V = 0).

Note: one inch = 25.4 mm.

Table 4.5-4. Peak Interstory Drift, Brake Pad Case for the Eccentric Model, for the 1966 Parkfield Record.

Ground Motion Input Direction (1)	Allowable Drift, Δ (inches) (2)	Peak Relative Interstory Drift (inches) Face 1[a] (3)	Face 2 (4)	Face 3 (5)	Face 4 (6)
Braced	0.0[b]	1.6(18)	0.7(22)	1.6(20)	0.5(22)
	0.18	1.5(11)	0.4(19)	1.4(11)	0.3(5)
	0.36	1.5(11)	0.5(19)	1.4(11)	0.3(4)
	0.72	1.6(11)	0.5(18)	1.4(8)	0.3(12)
	∞[c]	1.5(11)	0.7(7)	1.4(7)	0.4(4)
Rigid	0.0	1.1(22)	3.0(22)	1.0(22)	3.1(24)
	0.18	0.4(24)	2.1(22)	0.4(24)	2.6(22)
	0.36	0.3(24)	1.9(22)	0.3(24)	2.4(22)
	0.72	0.4(19)	1.8(12)	0.3(12)	2.1(22)
	∞	0.4(16)	1.6(12)	0.4(4)	1.9(12)

[a]Story at which peak drift occurred is shown in parentheses.

[b]Clad case (V = 625 kips/inch).

[c]Unclad case (V = 0).

Note: 1 inch = 25.4 mm.

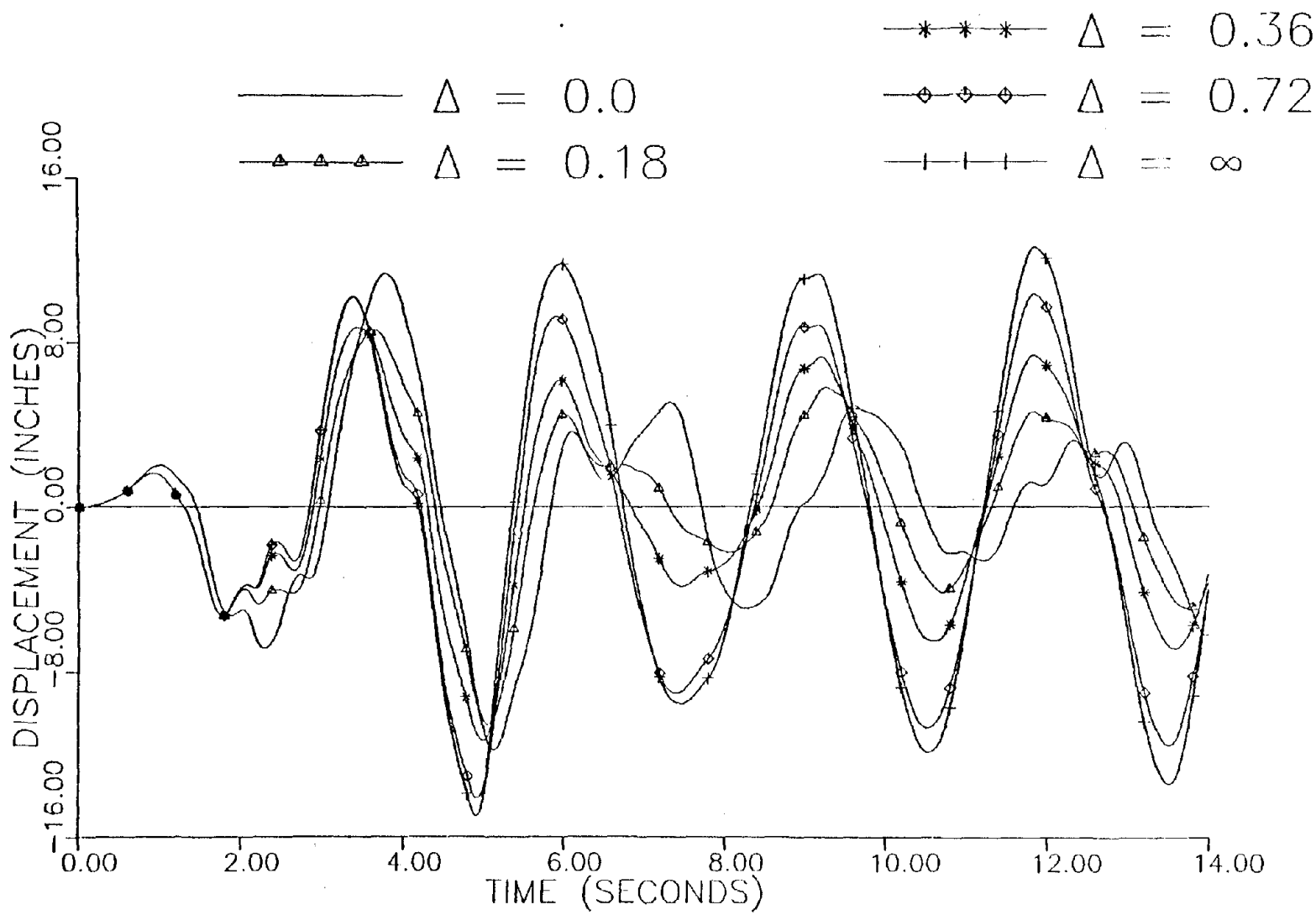

Figure 4.5-3. Roof Translational Response in Rigid Direction, Brake Pad Case for Eccentric Model, for 1940 El Centro Record Acting in Rigid Direction.

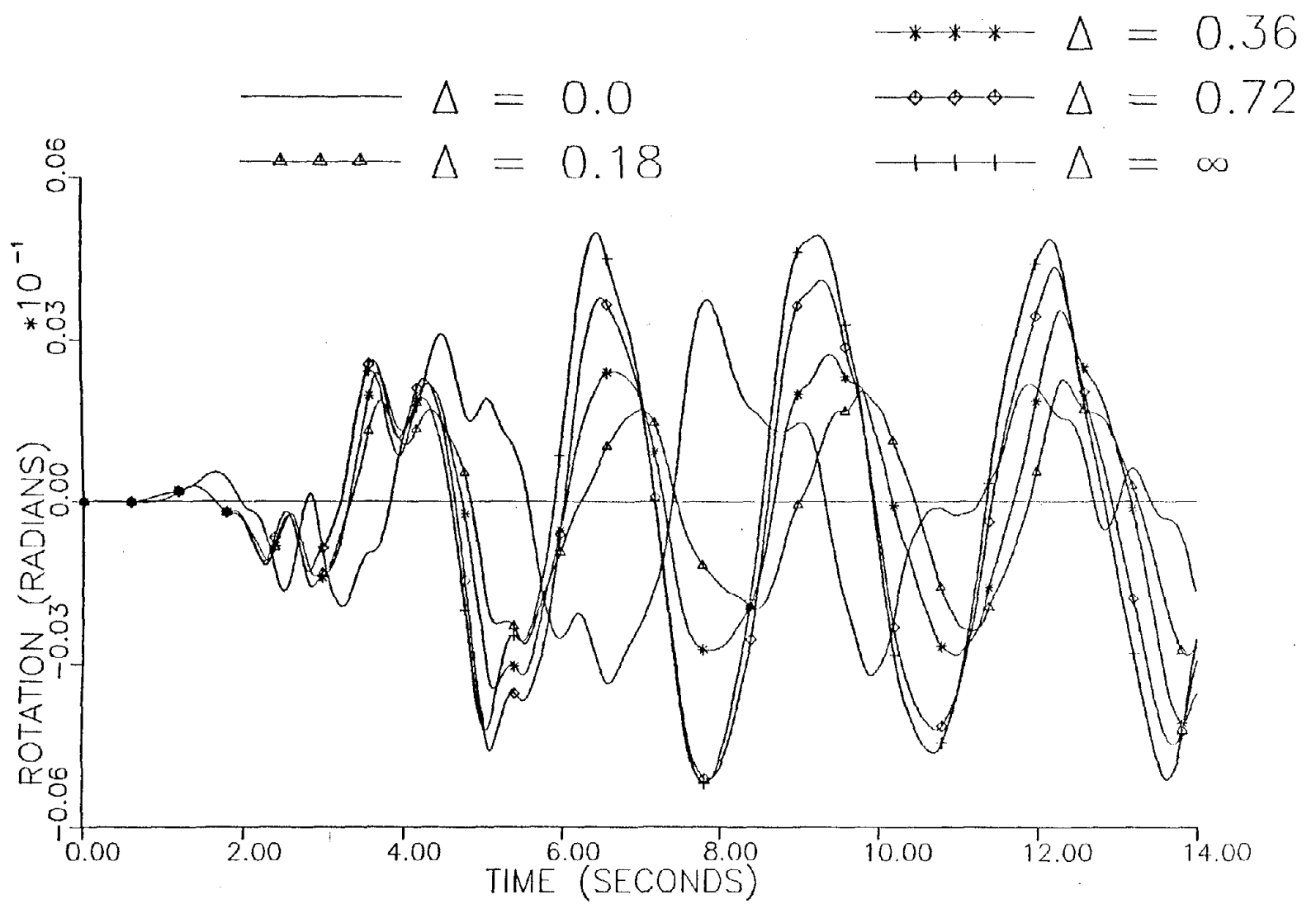

Figure 4.5-4. Roof Rotational Response, Brake Pad Case for Eccentric Model, for 1940 El Centro Record Acting in Rigid Direction.

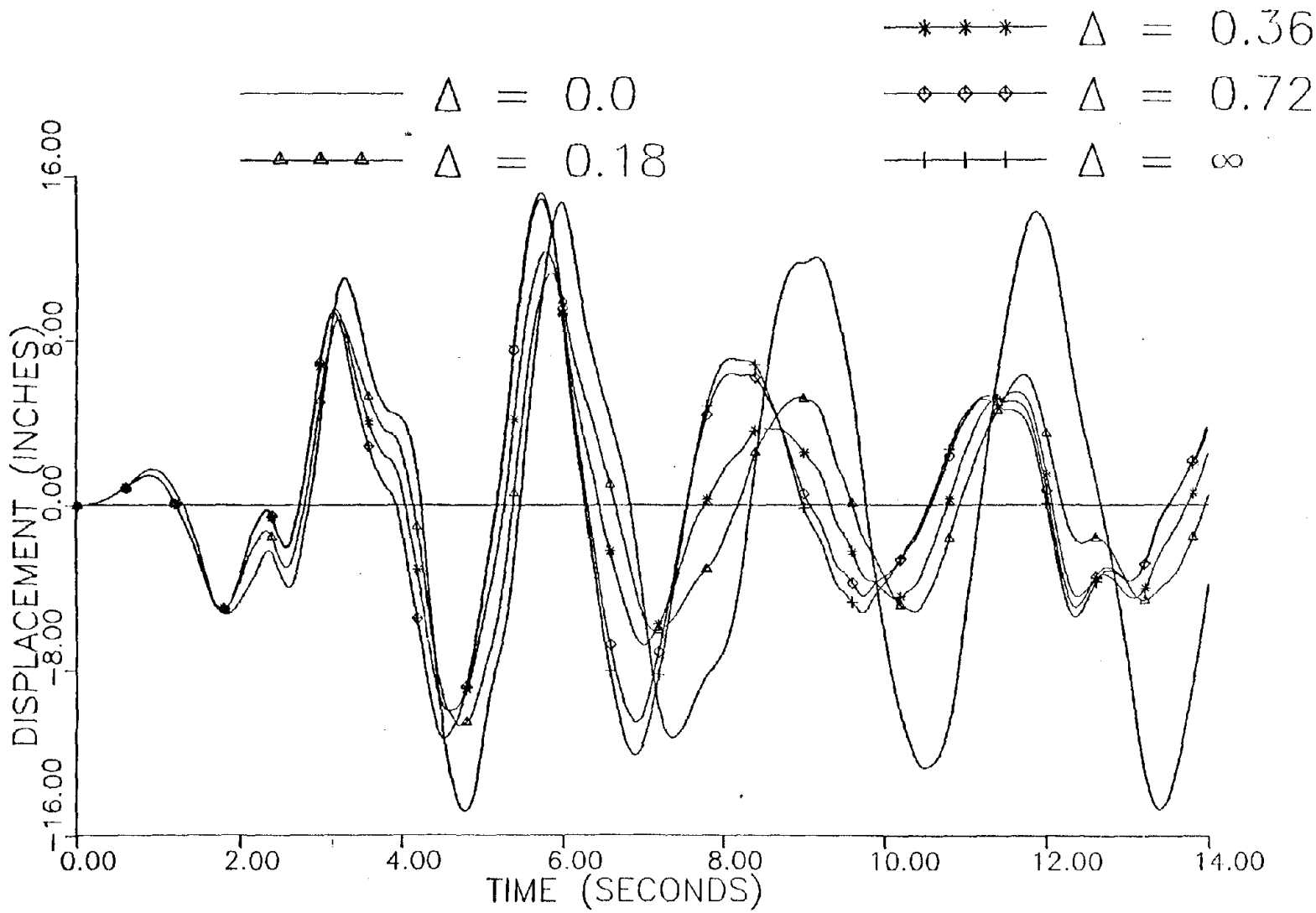

Figure 4.5-5. Roof Translational Response in Braced Direction, Brake Pad Case for Eccentric Model, for 1940 El Centro Record Acting in Braced Direction.

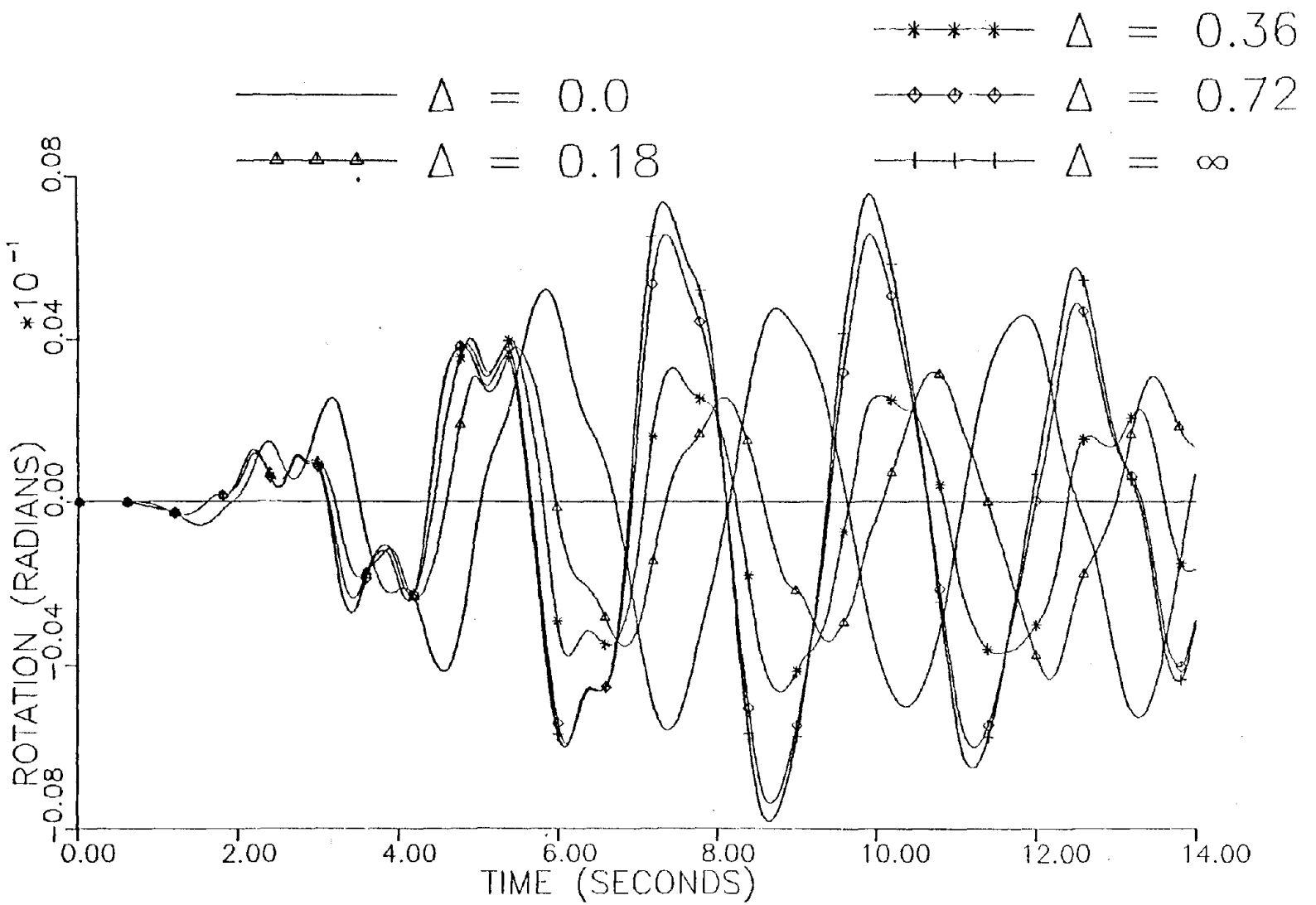

Figure 4.5-6. Roof Rotational Response, Brake Pad Case for Eccentric Model, for 1940 El Centro Record Acting in the Braced Direction.

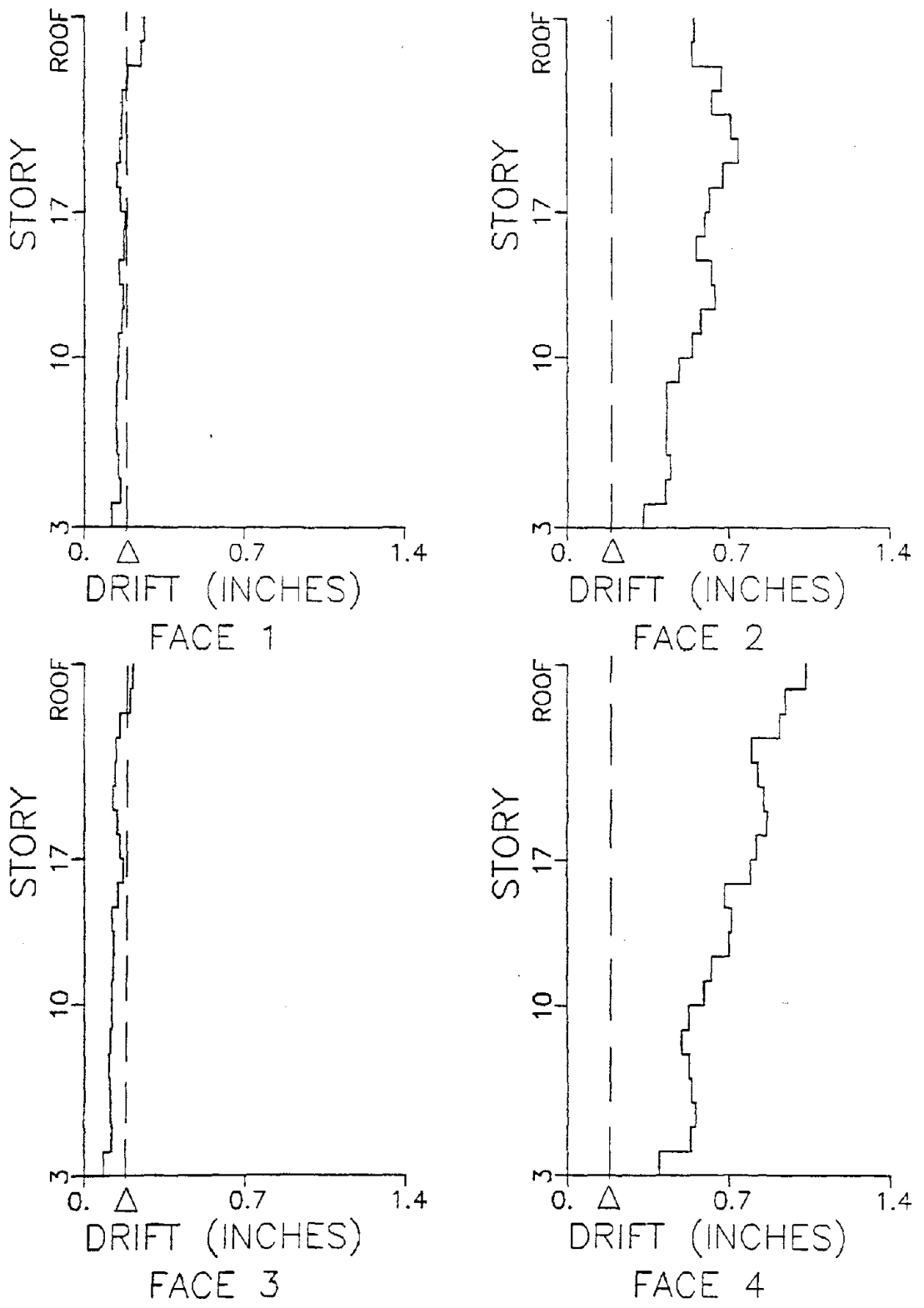

Figure 4.5-7. Peak Drift Values, Brake Pad Case with Δ set at 0.18 inches (0.5 cm), for 1940 El Centro Record Acting in Rigid Direction, Eccentric Model.

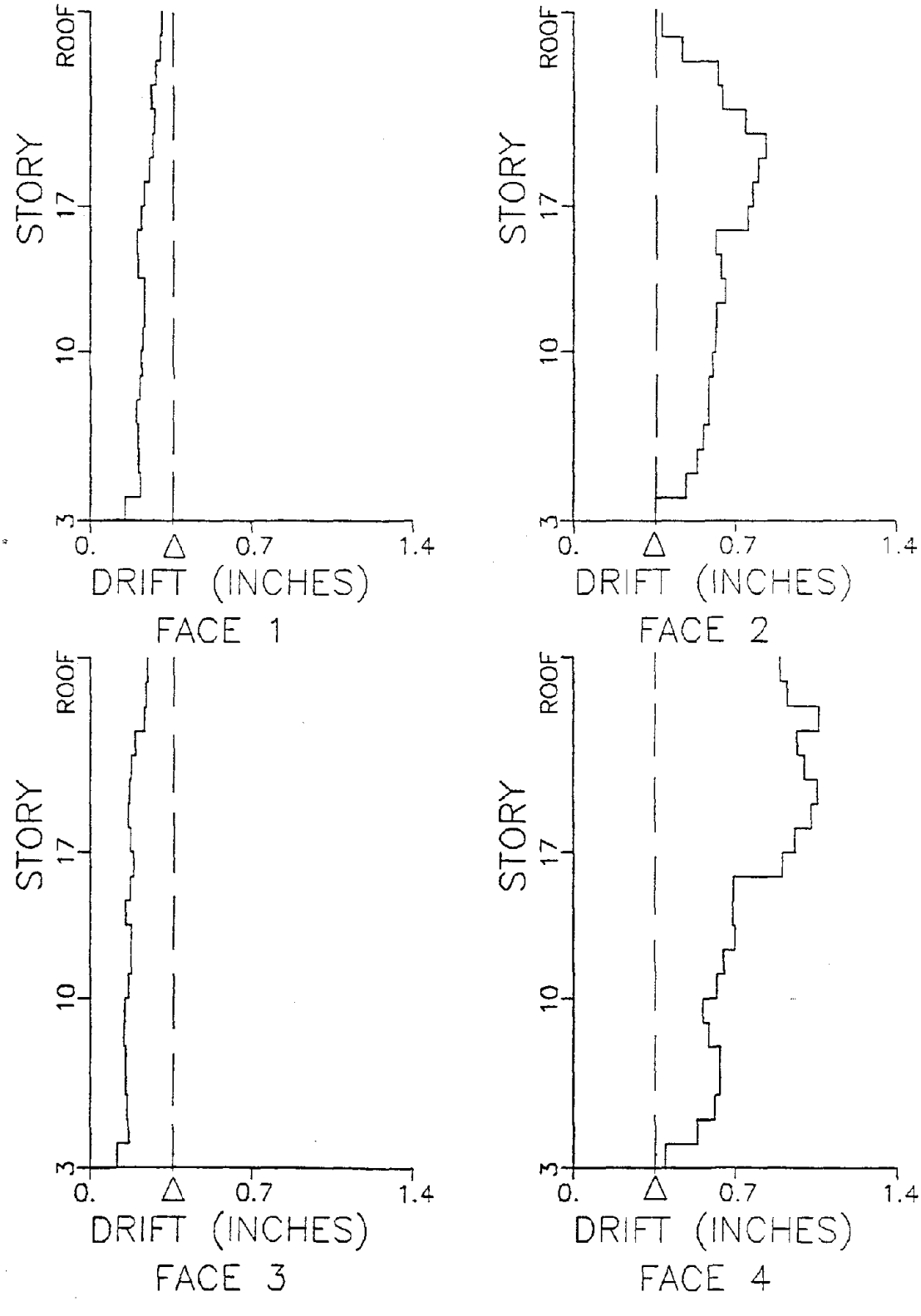

Figure 4.5-8. Peak Drift Values, Brake Pad Case with Δ set at 0.36 inches (0.9 cm), for 1940 El Centro Record Acting in Rigid Direction, Eccentric Model.

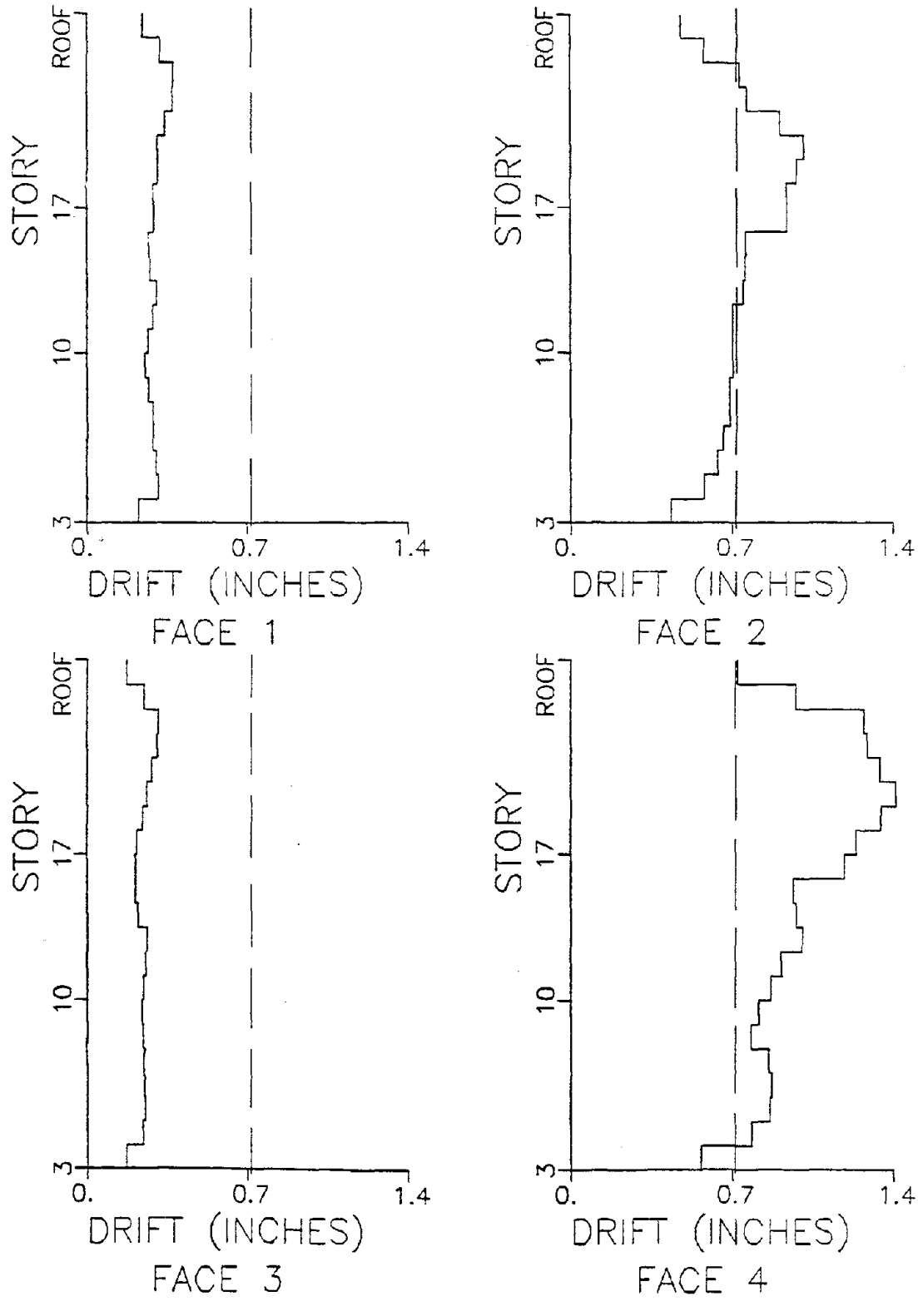

Figure 4.5-9. Peak Drift Values, Brake Pad Case with Δ set at 0.72 inches (1.8 cm), for 1940 El Centro Record Acting in Rigid Direction, Eccentric Model.

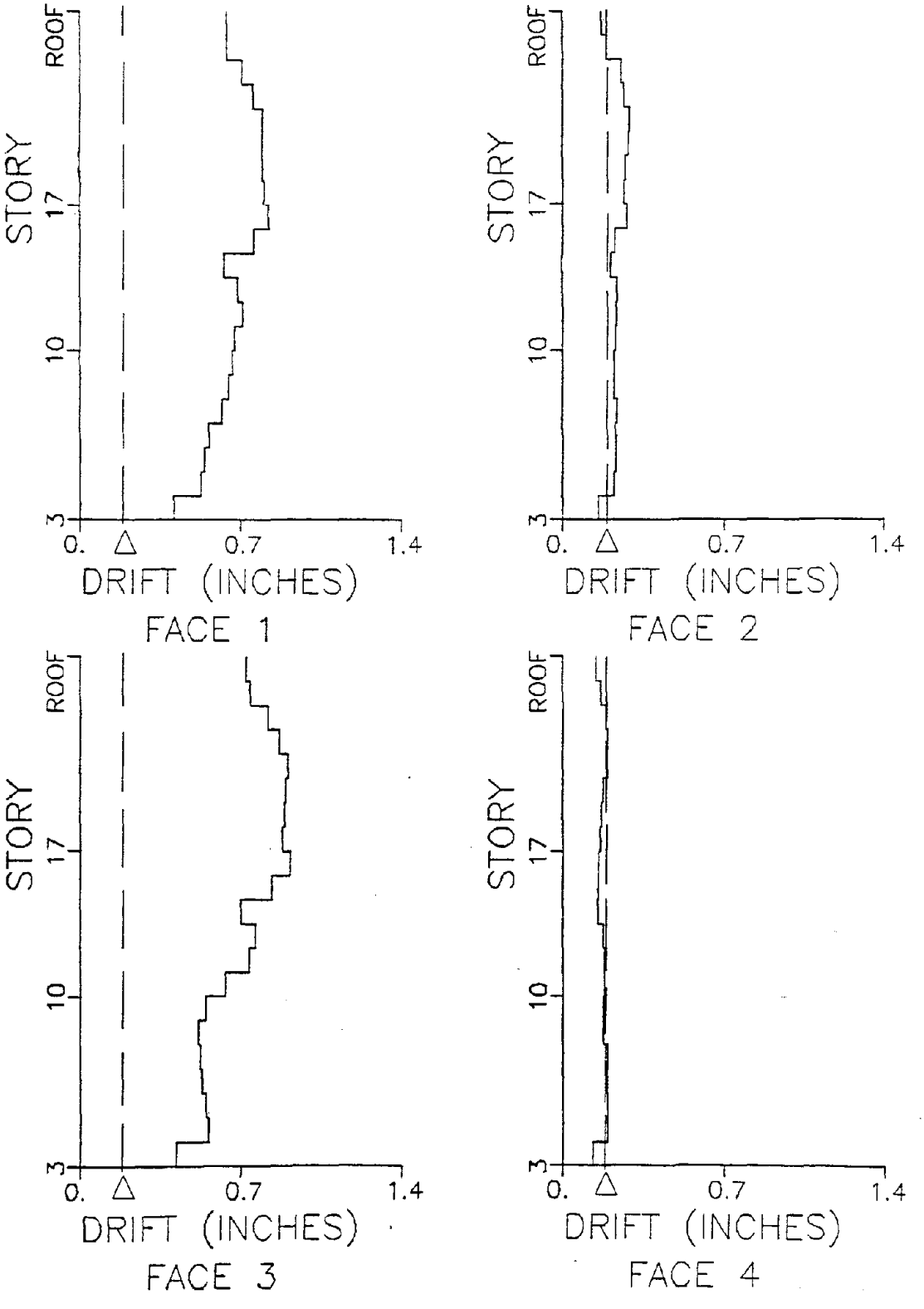

Figure 4.5-10. Peak Drift Values, Brake Pad Case with Δ set at 0.18 inches (0.5 cm), for 1940 El Centro Record Acting in Braced Direction, Eccentric Model.

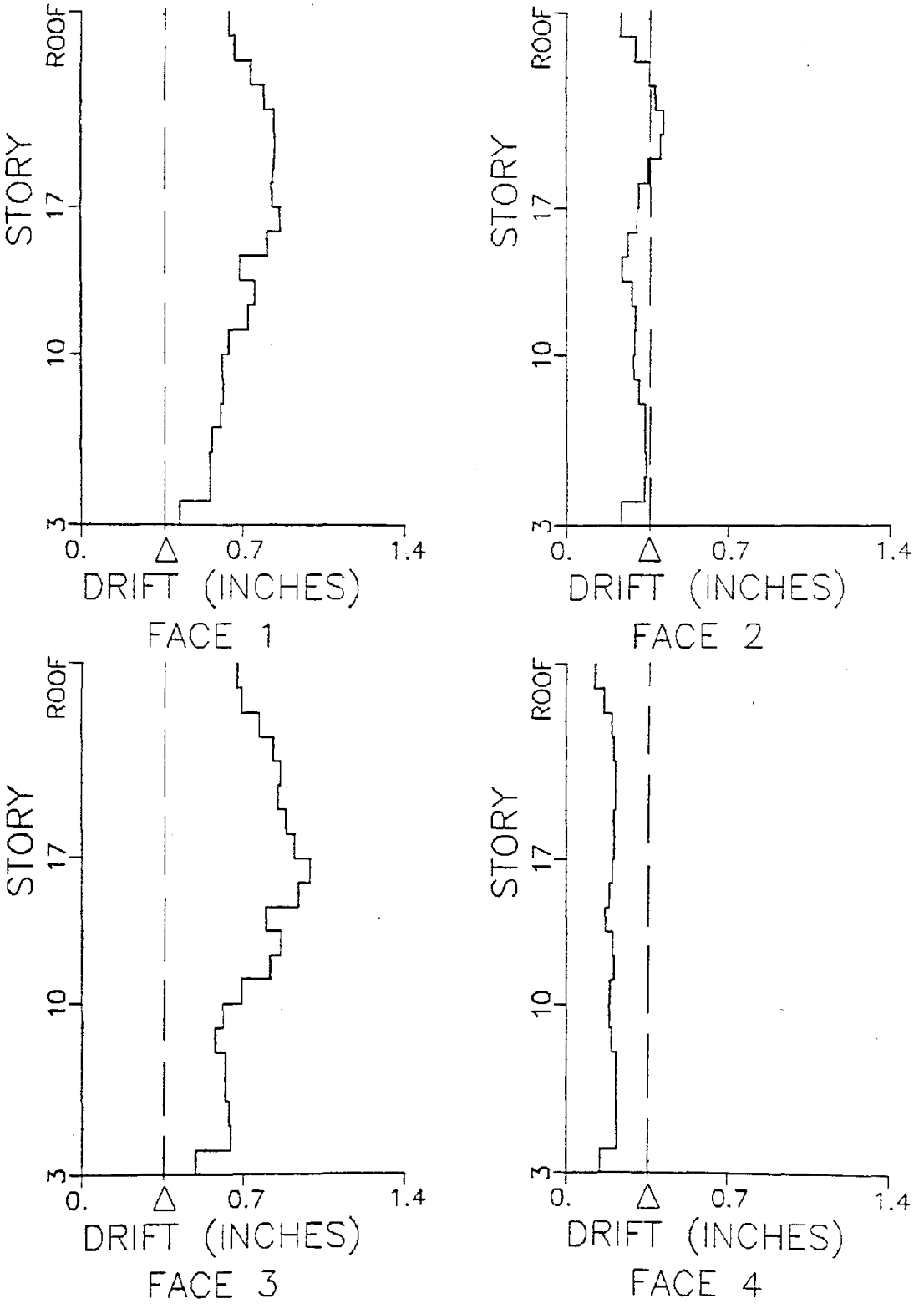

Figure 4.5-11. Peak Drift Values, Brake Pad Case with Δ set at 0.36 inches (0.9 cm), for 1940 El Centro Record Acting in Braced Direction, Eccentric Model.

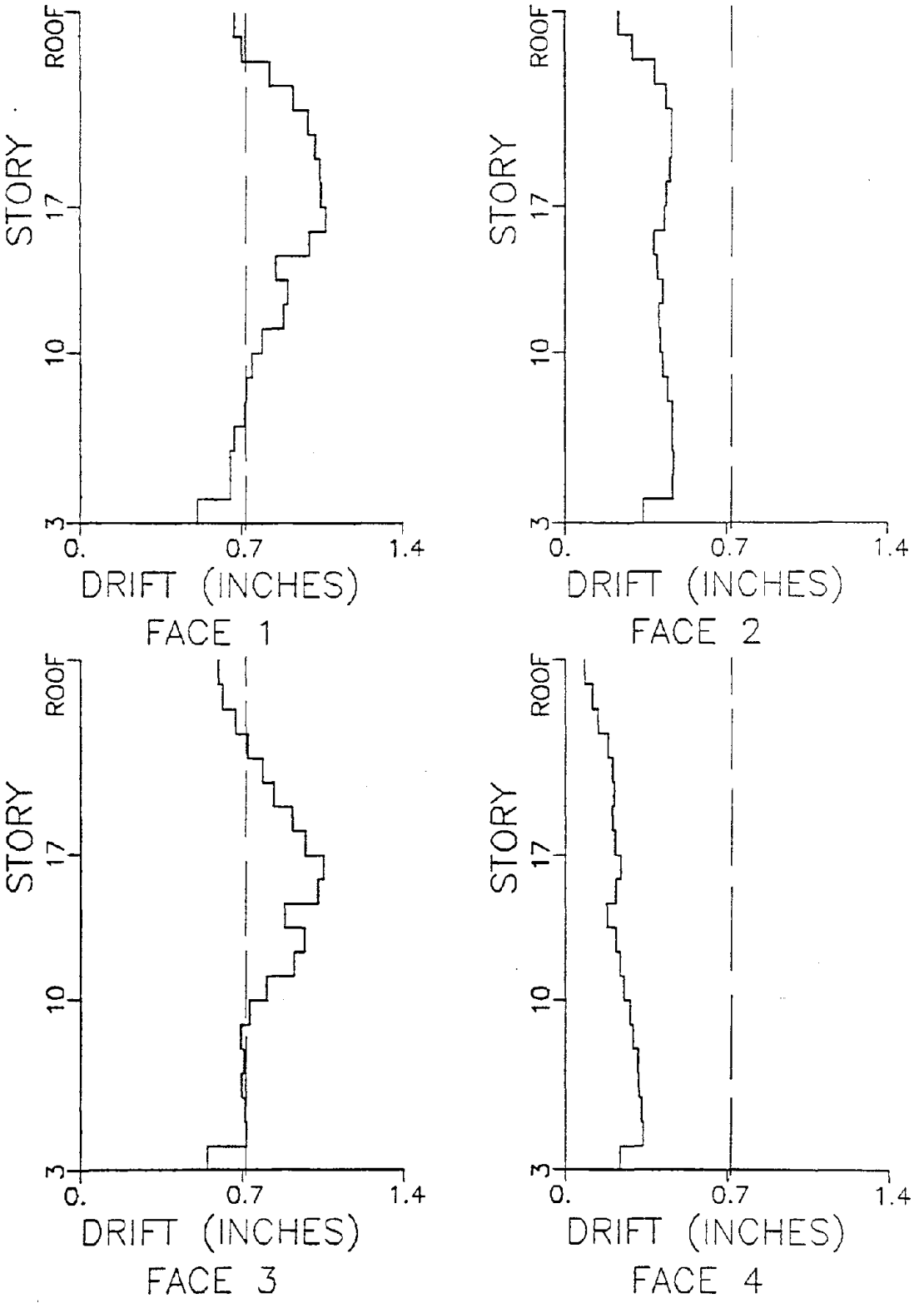

Figure 4.5-12. Peak Drift Values, Brake Pad Case with Δ set at 0.72 inches (1.8 cm), for 1940 El Centro Record Acting in Braced Direction, Eccentric Model.

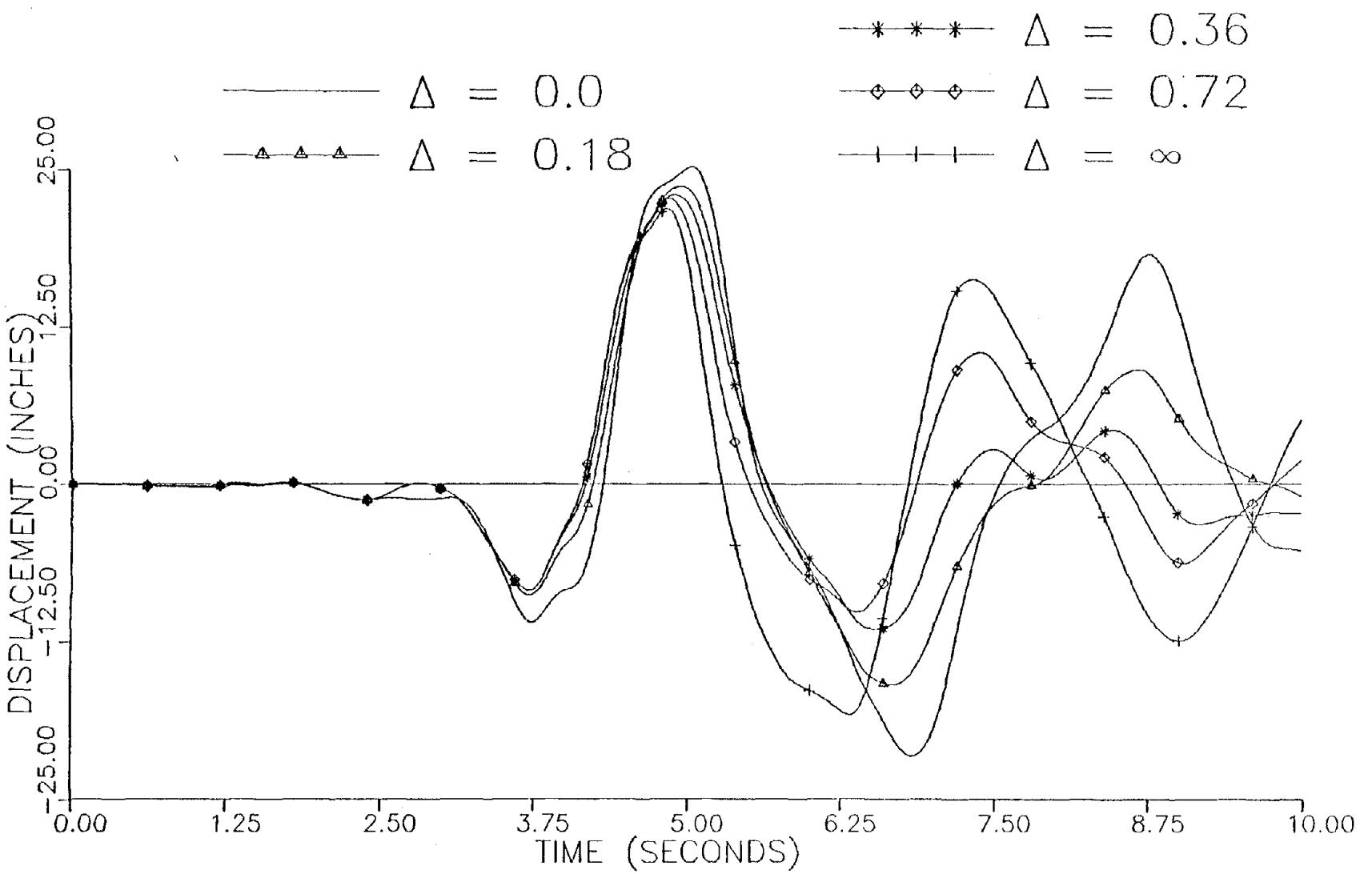

Figure 4.5-13. Roof Translational Response in Rigid Direction, Brake Pad Case for Eccentric Model, for 1966 Parkfield Record Acting in Rigid Direction.

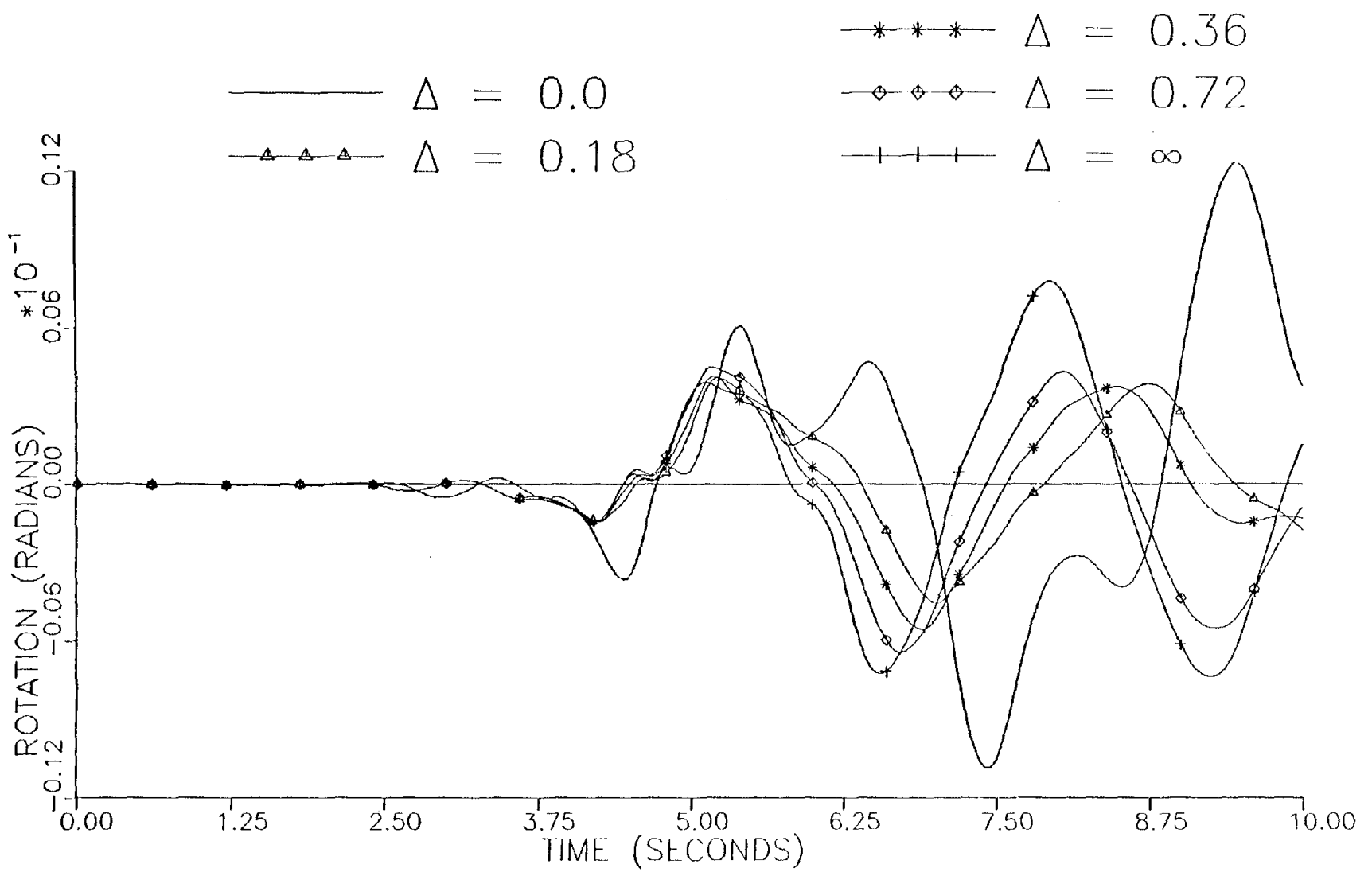

Figure 4.5-14. Roof Rotational Response, Brake Pad Case for Eccentric Model, for 1966 Parkfield Record Acting in Rigid Direction.

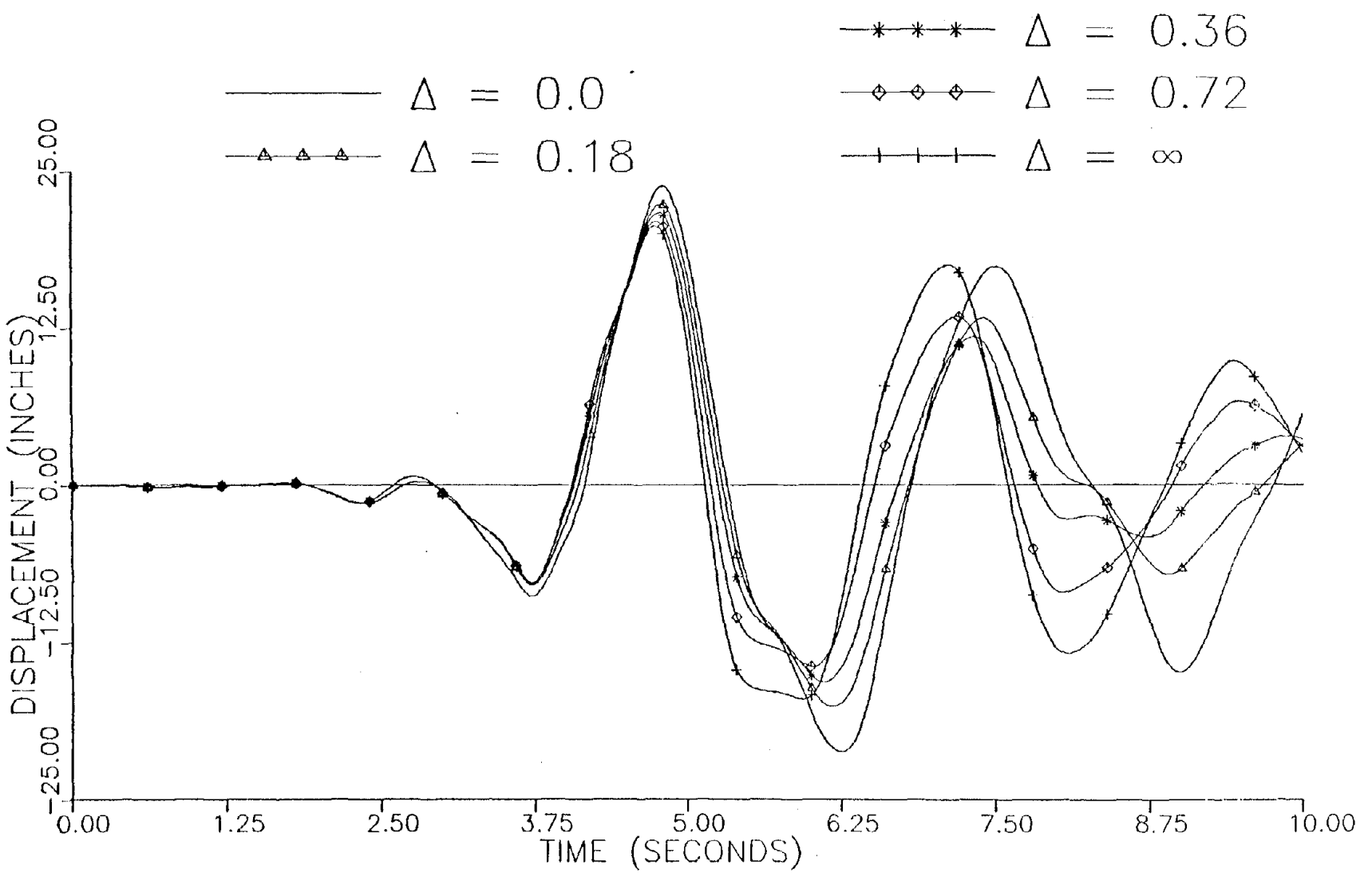

Figure 4.5-15. Roof Translational Response in Braced Direction, Brake Pad Case for Eccentric Model, for 1966 Parkfield Record Acting in Braced Direction.

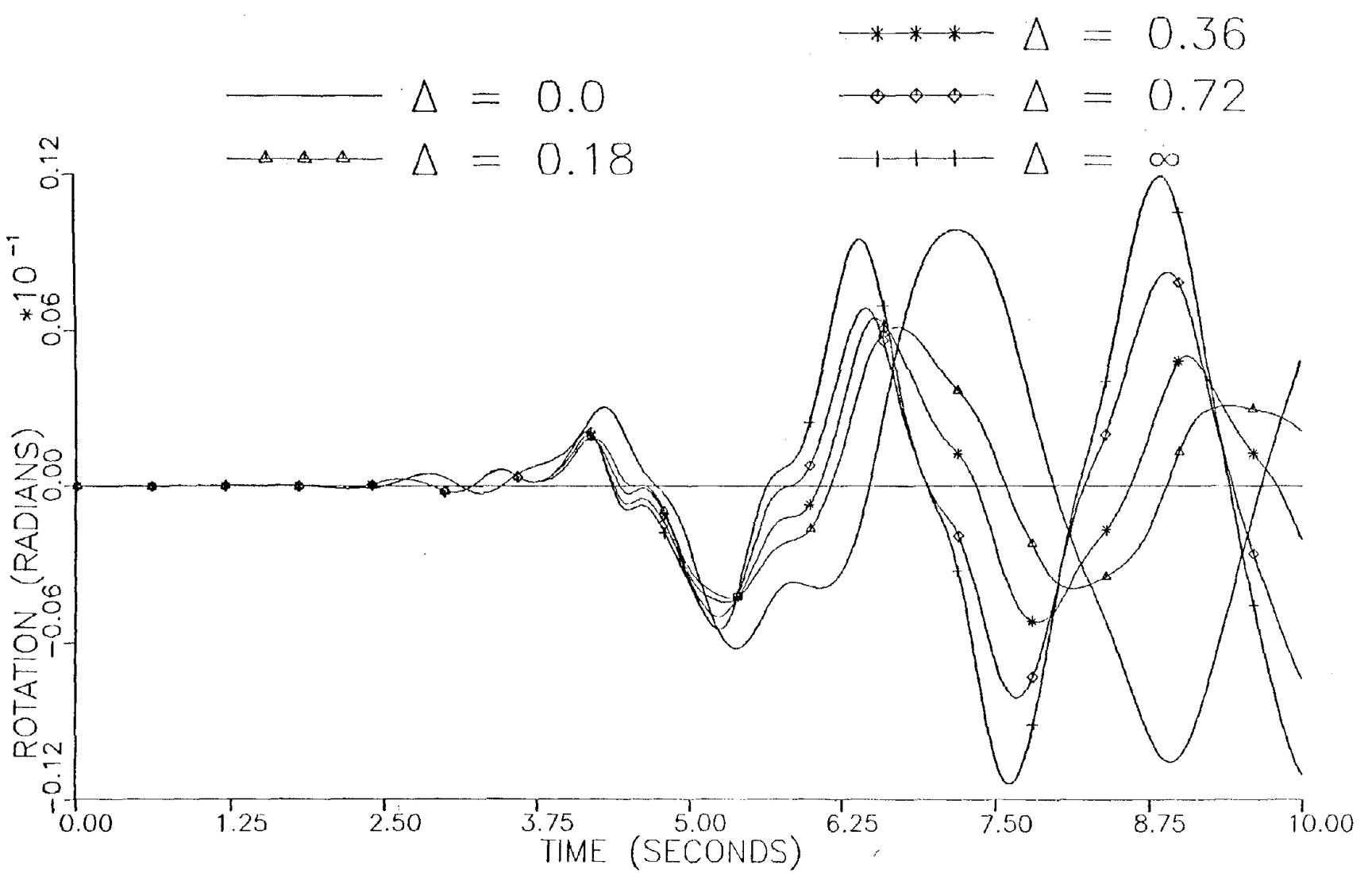

Figure 4.5-16. Roof Rotational Response, Brake Pad Case for Eccentric Model, for 1966 Parkfield Record Acting in Braced Direction.

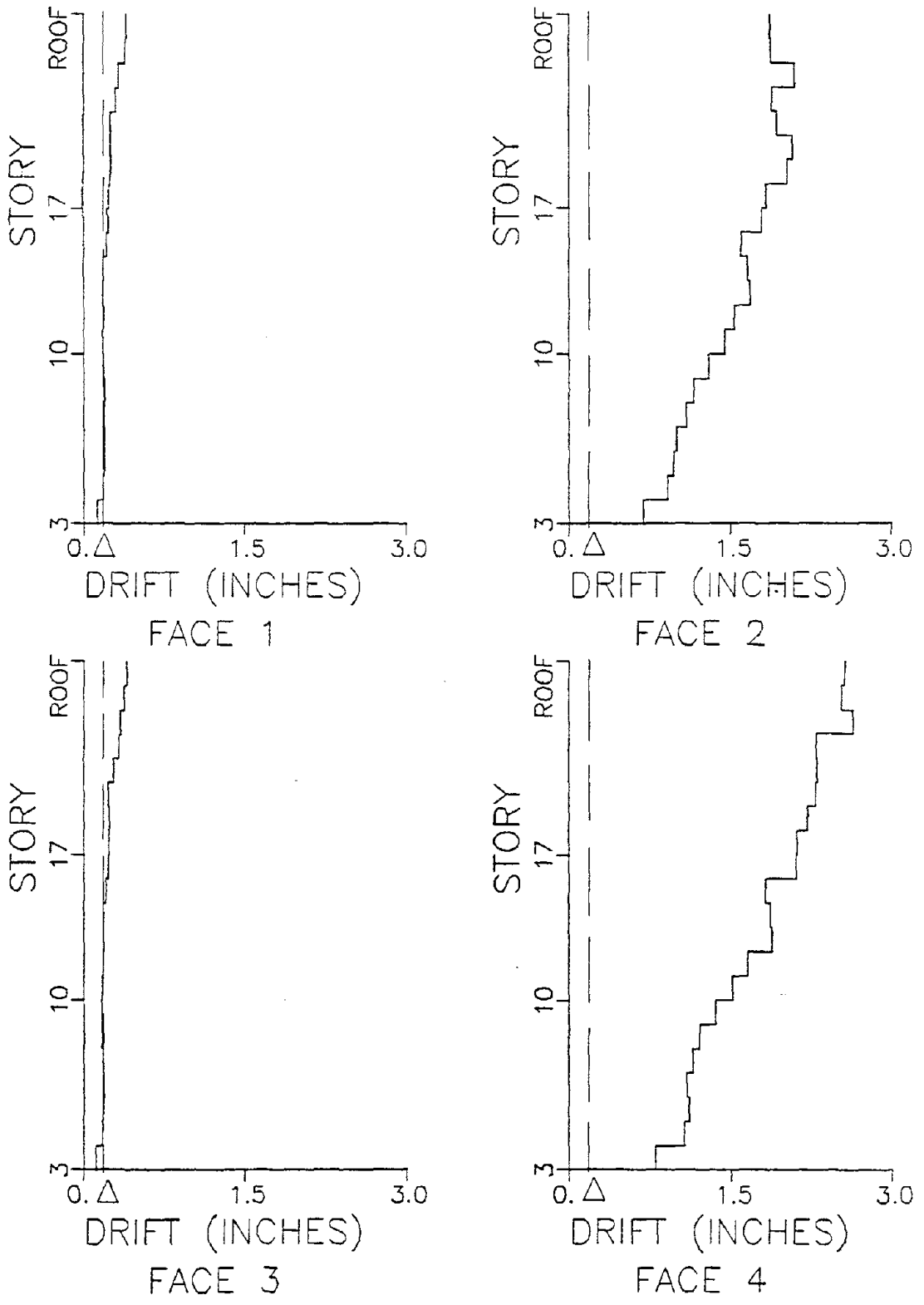

Figure 4.5-17. Peak Drift Values, Brake Pad Case with Δ set at 0.18 inches (0.5 cm), for 1966 Parkfield Record Acting in Rigid Direction, Eccentric Model.

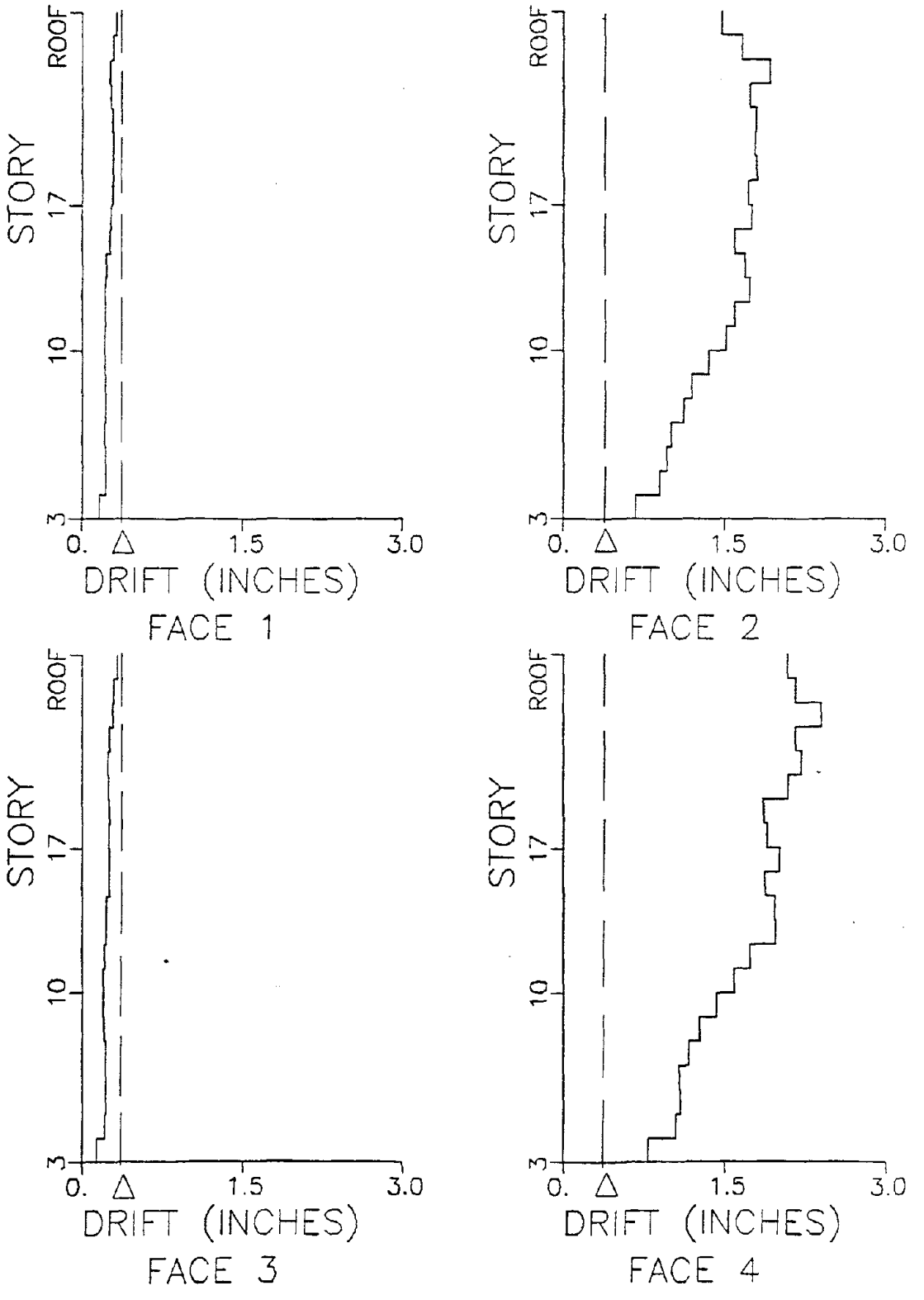

Figure 4.5-18. Peak Drift Values, Brake Pad Case with Δ set at 0.36 inches (0.9 cm), for 1966 Parkfield Record Acting in Rigid Direction, Eccentric Model.

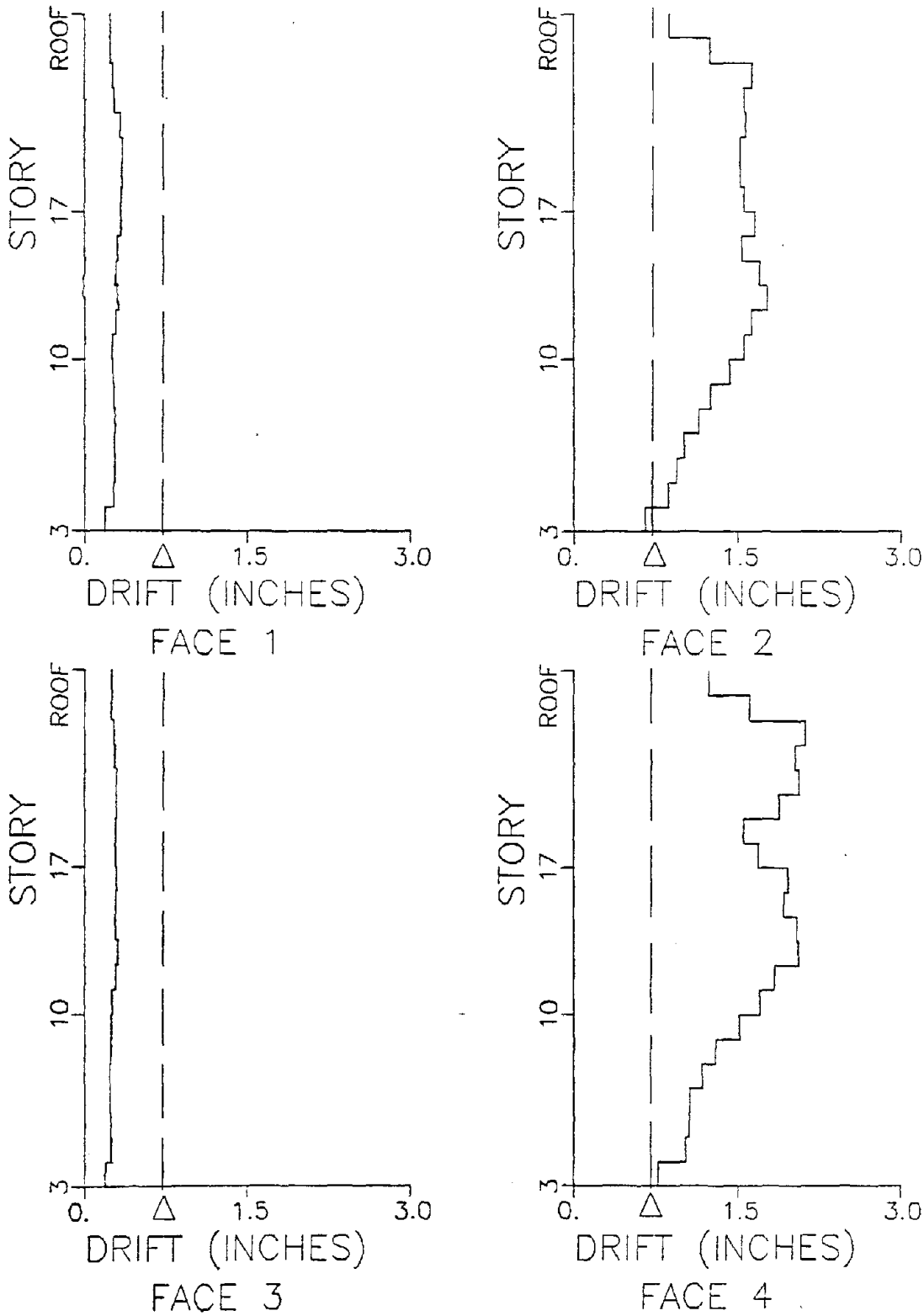

Figure 4.5-19. Peak Drift Values, Brake Pad Case with Δ set at 0.72 inches (1.8 cm), for 1966 Parkfield Record Acting in Rigid Direction, Eccentric Model.

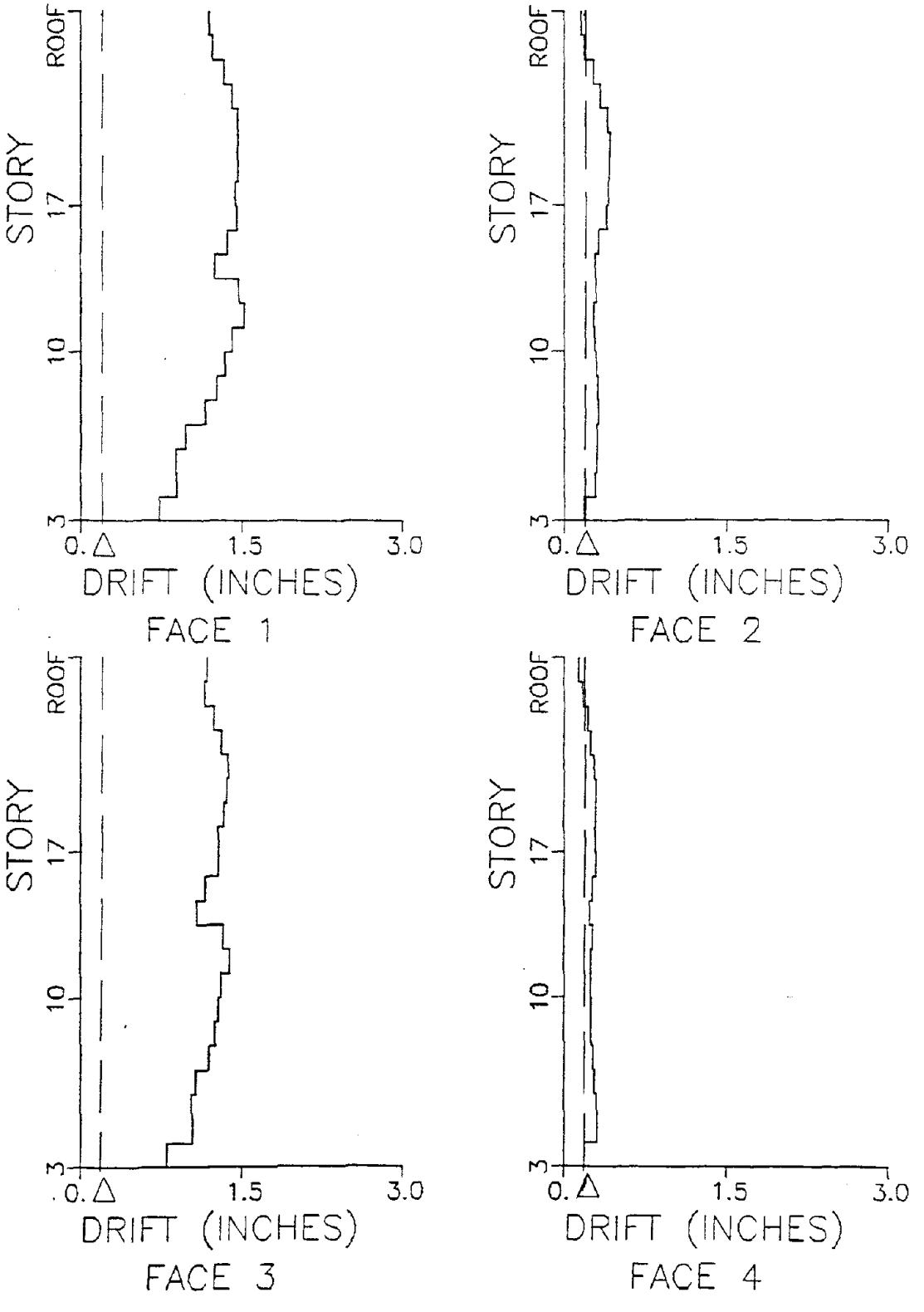

Figure 4.5-20. Peak Drift Values, Brake Pad Case with Δ set at 0.18 inches (0.5 cm), for 1966 Parkfield Record Acting in Braced Direction, Eccentric Model.

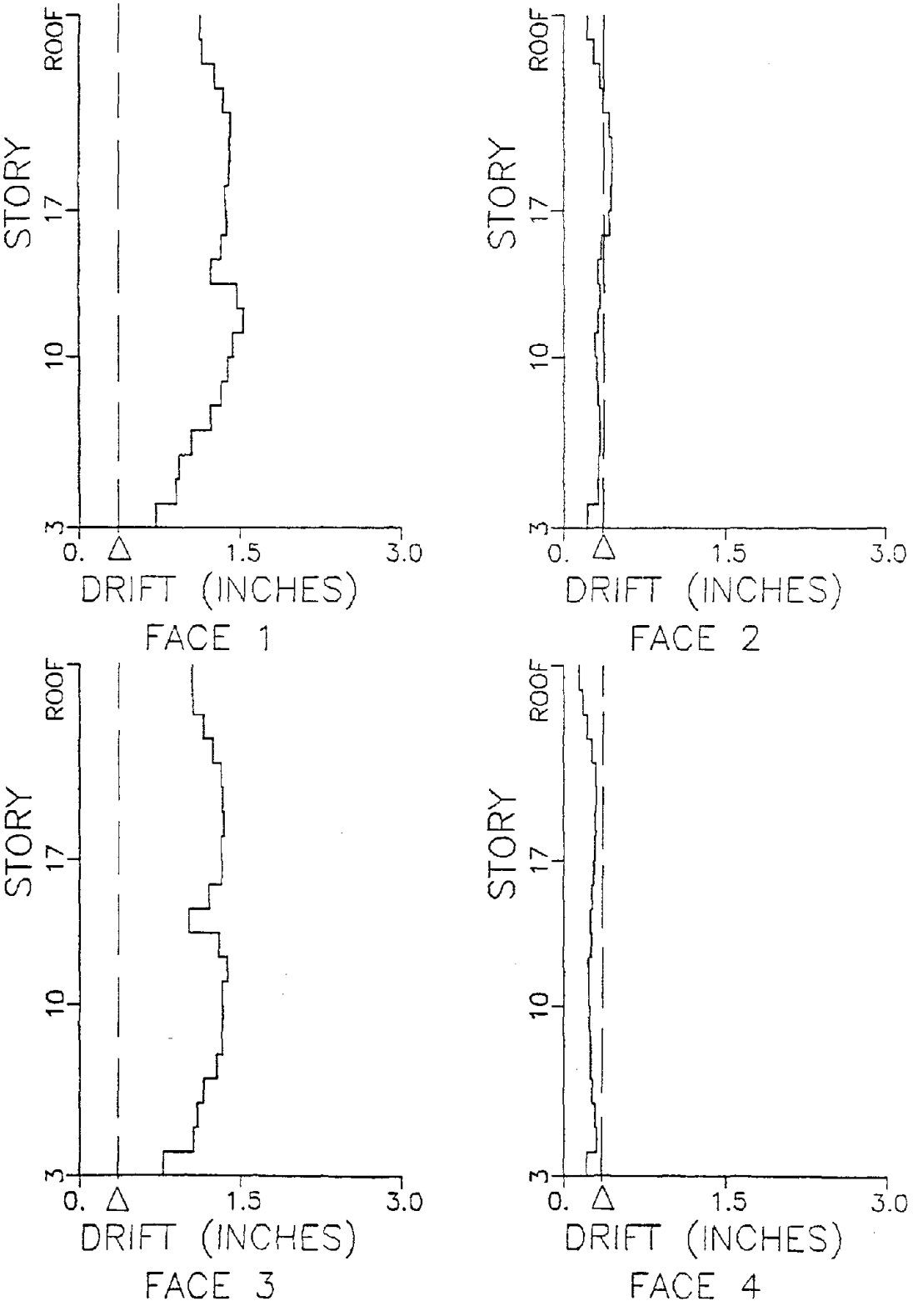

Figure 4.5-21. Peak Drift Values, Brake Pad Case with Δ set at 0.36 inches (0.9 cm), for 1966 Parkfield Record Acting in Braced Direction, Eccentric Model.

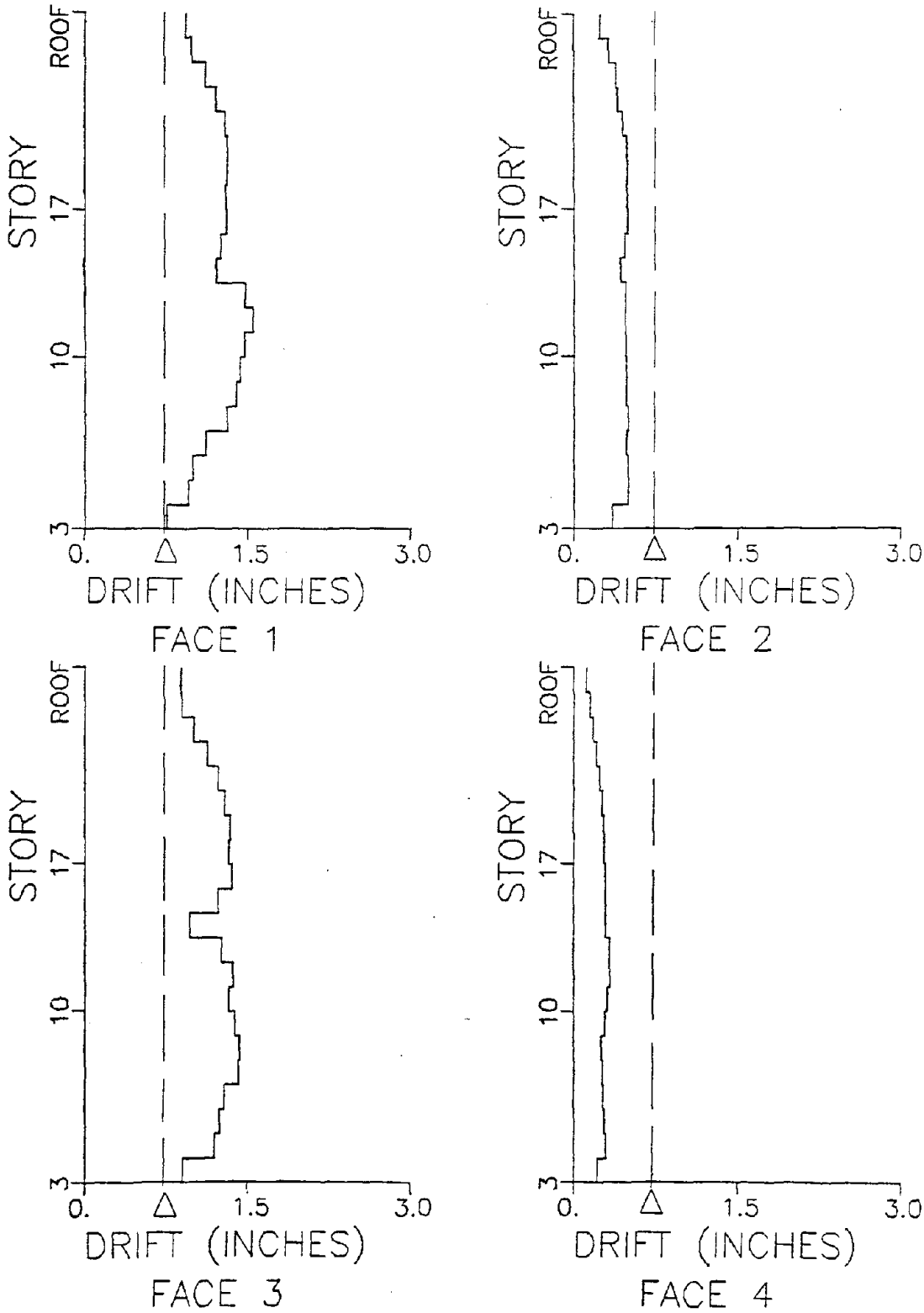

Figure 4.5-22. Peak Drift Values, Brake Pad Case with Δ set at 0.72 inches (1.8 cm), for 1966 Parkfield Record Acting in Braced Direction, Eccentric Model.

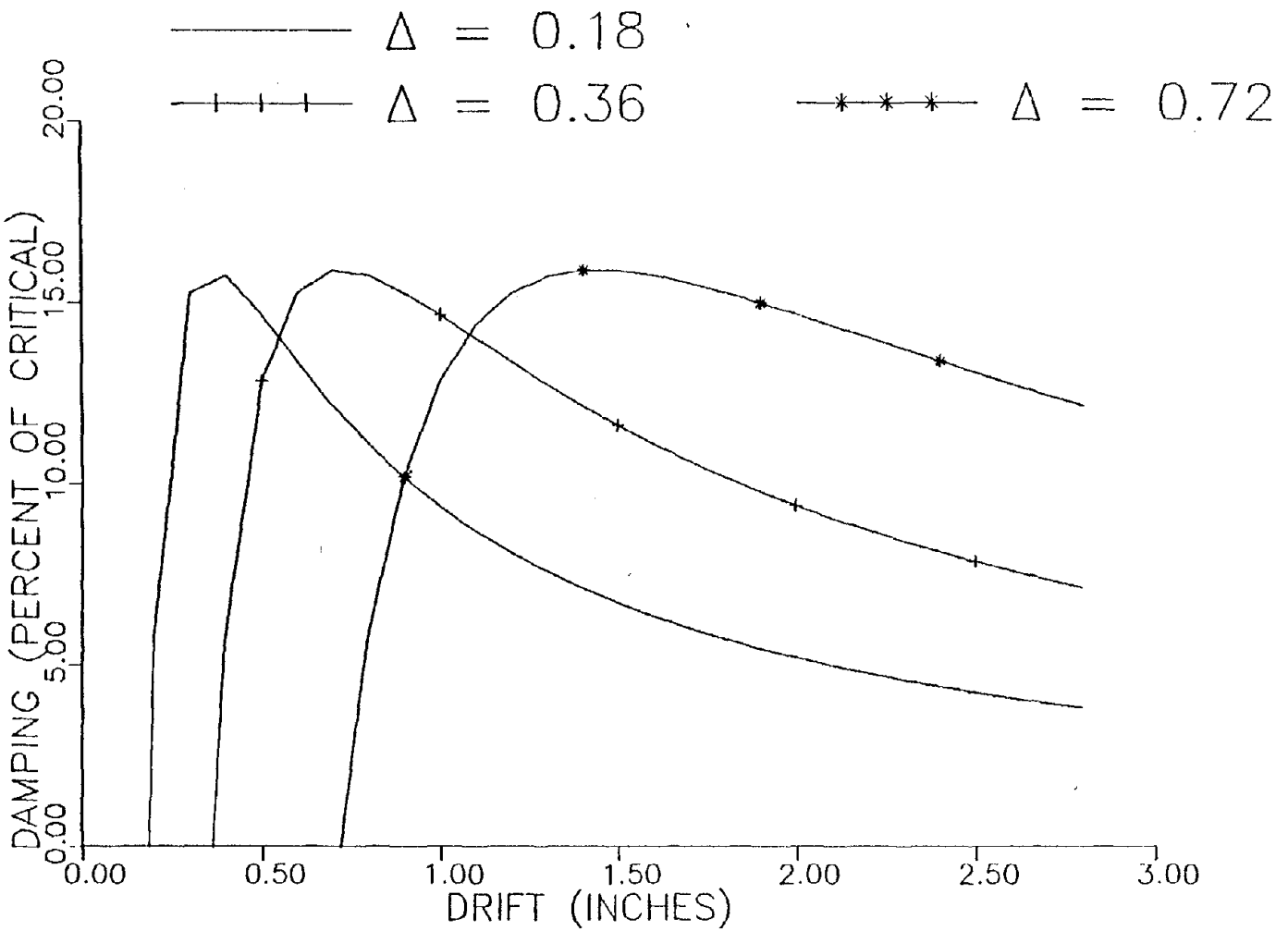

Figure 4.5-23. Additional Damping Due to Hysteretic Behavior of Cladding.

loadings considered in this study. This showed that energy dissipation in cladding connections can be used to an advantage in controlling response levels in modern tall buildings. However, further studies concerned with the feasibility of installing and maintaining the connections need to be performed before final comparisons can be made with other models. Other considerations, such as the influence of the connections on cladding failure, should be addressed in subsequent work.

4.6 Summary

In the four preceding sections, the influence of four different nonlinear force-deformation relationships for cladding on overall structure response were investigated and results compared to the linear cases of the clad and unclad structures. The principal results of these studies may be summarized as follows:

1. Incremental Failure Model. Peak roof response values for the Parkfield record decreased in the direction of applied ground motion in going from the unclad to the fully clad model. However, the reverse was true when the El Centro record was applied (see discussion on earthquake response spectra and altered dynamic properties of clad versus unclad structures in Section 3.4). Several instances of increased maximum drift were also found for the fully clad structure when compared to the partially-clad (i.e., cladding-failing) and the unclad structures. In addition, when partial cladding failure was imposed on the symmetric model as an initial state and response computed allowing the cladding to fail based on the incremental failure model, the rotational response was found to be greatly amplified over the clad and the unclad rotational responses.

2. Slotted Connection Model. Several occurrences of moderately increased peak roof displacement response were observed, but almost no instances of increased peak drift, when the slotted connection cases were compared to the linear cases (clad and unclad) for the loadings considered. Inspection of time-history plots revealed that changes in response were gradual with increasing allowable drift.

3. Degrading Hysteresis Model. Hysteretic response was observed to follow the response of the linear clad case closely for the allowable drift levels chosen. Smaller allowable drift values would not be practical since computation time steps would have to be reduced to handle the narrowing of the distance between the slip lines.

4. Brake Pad Model. The brake pad model was found to be effective in reducing overall structure response although peak roof displacement response values for the Parkfield record remained higher than for the linear clad case. However, the several drawbacks mentioned above in Section 4.5 may outweigh the potential benefits of the use of the proposed connection.

Considering current design and construction practice, it may be observed that use of the slotted connection model in conjunction with the linear clad and unclad models may be the most appropriate models to use at this time in cladding response studies to determine overall structure response for moderate earthquake loadings. Experimental measurements of cladding properties are, of course, needed to verify assumed behavioral models used above. Inspection of earthquake response spectra can be helpful in determining possible problems which may arise in earthquake response predictions for buildings when cladding stiffness is neglected.

If the response variation between the frequency values on the response spectrum for the clad and unclad states is relatively flat, as for the Parkfield record (see Section 3.4), cladding may not significantly alter response level predictions made on the basis of the bare frame (i.e., unclad) structure. However, when the spectral response is irregular, response differences between clad and unclad models may be more difficult to predict.

The principal results for the different cladding models have been summarized above. The assumptions made will also be summarized:

1. Mass. The mass of the cladding was included in all response computations, but no stiffness contribution was included in the case labeled as the unclad case. In addition, the eccentric mass model assumed that the center of mass was positioned in the same location on every floor. Torsional response could conceivable be amplified by varying the eccentric location of mass from floor to floor.

2. Damping. Simple modal damping set at five percent of critical was specified throughout these studies. It should be kept in mind that the amount of damping present in the model can affect displacement levels substantially. Furthermore, additional damping is introduced in the overall structure model by the nonlinear models for cladding which possess hysteretic behavior. This addition is also dependent on the prior displacement history of the structure.

3. Stiffness. In the response studies in this chapter, composite action of floor beams was considered in order to be more conservative in the estimation of cladding lateral stiffness. However, the response levels obtained clearly indicate that a noncomposite model would be more

appropriate. Additionally, the high response levels suggest that geometric effects might be important.

4. Loadings. Only the first 10 and 14 seconds of the 1966 Parkfield and 1940 El Centro records, respectively, were used on the basis of the response spectra presented in Section 3.4. However, the changes in overall structure stiffness with time based on the force-displacement relationship for cladding specified could require computing the response spectra from some point after the start of the record rather than from the beginning.

These studies reported above have been concerned only with displacement response levels and no investigation of forces generated in cladding and its connections as a result of interstory drift has been performed. The following chapter will be devoted to several case studies to determine connection force levels and the influence of cladding support conditions on the contribution of cladding to interstory shear stiffness.

5. LOCALIZED PANEL RESPONSE STUDIES

5.1 Introduction

A variety of cladding models were developed and described in Chapter 4 to represent the potential stiffness contribution of the precast cladding system and its influence on the dynamic response of the overall prototype structure. However, in this chapter a rigid panel model was employed to obtain information about the localized response of a typical bay of curtain wall for interstory drift motions. The objective of these studies was to determine the influence of panel support conditions on connection force levels and on the contribution of cladding to structure lateral stiffness in an actual curtain wall system subjected to lateral motions.

A linear static analysis was employed as described in Section 5.2 to study the influence of connection stiffnesses on connection force levels and interstory stiffness. Then the concepts of oversized holes, slots, and initial friction in connections were introduced in Section 5.3. Only static linear and nonlinear analyses were considered in these studies; dynamic analyses are recommended in the future as a logical extension of these studies.

5.2 Linear Static Analysis

5.2.1 Rigid Panel Model

Localized cladding response was investigated using the plane frame analytical model in Fig. 5.2-1 and making use of a computer program

written by another investigator [37]. The analytical model consists of steel framing and two heavyweight cladding panels connected to the spandrels with clip angle connections; this panel support arrangement is similar to that actually used in the prototype structure. Framing members were idealized as one-dimensional finite elements. Clip angles were represented by linear elastic spring elements with stiffnesses K_x, K_y and K_z (in these studies K_z was set at zero since connection rotational stiffness is mostly likely quite low), and the panels were assumed to be flat and perfectly rigid. All panel-to-panel contact was neglected. In addition, spandrel members with semi-rigid connections were included by means of elastic connection stiffnesses (K_z) at their ends. An intermediate rotational stiffness value of $K_z = 8 \times 10^4$ kips-inch/radian (9×10^3 kNm/radian) for AISC Type 2 connections was assumed for the present study [37]. Columns were specified to be W10 x 49 and spandrel members W18 x 35 steel shapes (A36 steel) to represent a typical exterior bay in the prototype structure. The investigation in this section (5.2) was limited to linear elastic, small displacement response studies involving heavyweight cladding only.

When the rigid panel model is compared to the cladding models employed in Chapter 4, the important differences in the models need to be kept in mind. While the present model is a one-story, one-bay model of cladding panels and exterior frame, the models of Chapter 4 approximated the force-deformation relationship of a row of cladding panels and their connections on one story and one side of the structure without including the effects of the exterior frame as part of the cladding. Rather, the exterior frame stiffness was handled as a separate contribution to overall structure stiffness. Because the rigid panel model included discrete

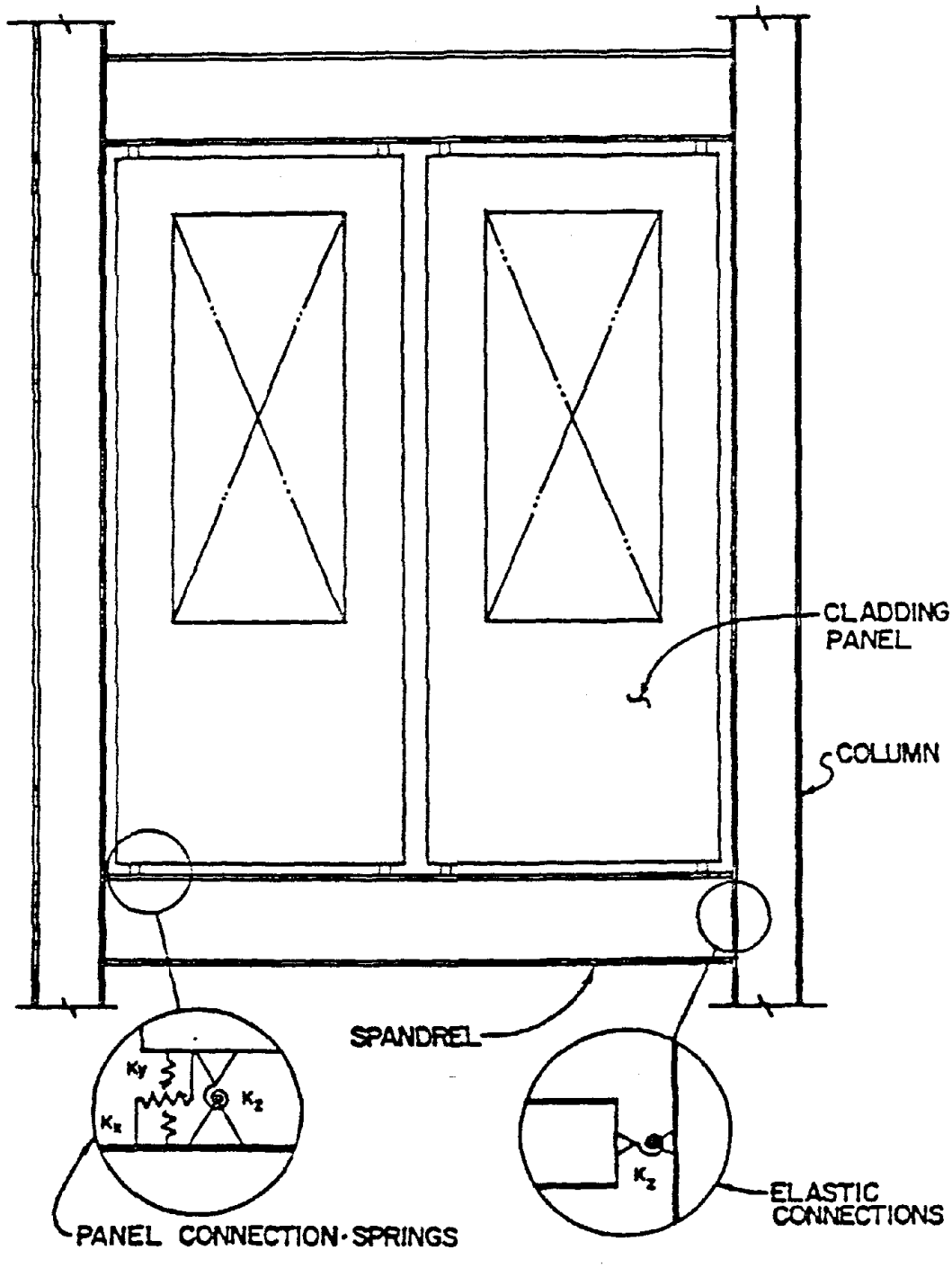

Figure 5.2-1. Analytical Model for Typical Portion of Cladding and Exterior Frame.

elements representing connections, panels and frame members, it was felt to be better suited for localized response studies.

Connection force levels resulting from applied interstory displacements as well as the increase in panel-frame system stiffness due to cladding were the results of principal interest in these investigations. Spandrel shears, column and spandrel moments, and system displacements were also studied and results for these quantities are reported below.

5.2.2 Uniform Spring Stiffness Case

The actual magnitudes of horizontal and vertical stiffnesses of the clip angle connections employed to attach the cladding panels to the exterior framing were not known. Analytical and experimental studies of similar connections show a wide range of stiffness values for the connections. Several variables affect the stiffness. For example, tightness of connection bolts, weld lengths connecting clip angles to spandrels, and interaction of spandrel flanges with the clip angles are all contributing factors. An additional unknown was the support condition state of the clip angles. Based on this lack of knowledge, the initial assumption was made that each of the four connection springs for both panels had equal, or uniform, stiffness in both the horizontal and vertical directions. This case is, therefore, referred to as the uniform stiffness case.

The lateral stiffness of the panel-frame system, defined as V, was computed by imposing lateral displacements at joints 7 and 12 in Fig. 5.2-2 and determining the required reaction forces at these joints. The interstory shear stiffness of the unclad frame (V = 11.53 kips/inch or 2.0×10^3 kN/m), determined in a separate analysis, was deducted from that of the clad frame to obtain the interstory shear stiffness contribution of cladding panels and connections only. The connection spring

stiffnesses were adjusted in steps and cladding lateral stiffness compared to the value of 625 kips/inch (1.1×10^5 kN/m) obtained for a row of panels on one face only in the parameter studies in Section 2.4. A row of panels on one face corresponds to 12 bays of cladding resulting in a cladding lateral stiffness value of 52.08 kips/inch (9121kN/m) per bay. A best match was obtained when connection stiffnesses were set at $K_x = K_y = 360$ kips/inch (6.3×10^4 kN/m) which yielded V = 63.69 - 11.53 = 52.16 kips/inch (9134 kN/m). Note that stiffness increments of 10 kips/inch (1751 kN/m) were used for K_x and K_y in the analysis. The uniform stiffness case properties and model dimensions are summarized in Fig. 5.2-2. Two more cases will be considered in the following section for later comparison with the uniform stiffness case.

5.2.3 Variable Spring Stiffness Cases

In the uniform spring stiffness case described in Section 5.2.2, all four connection springs were assumed to be equally stiff in in both the horizontal and vertical directions. In this section, two other cases with variable connection spring stiffnesses will be studied for comparison. Factors such as variable size of top and bottom connections and varying support conditions justify the consideration of additional cases.

The first case, labeled as the weaker top connection case, assumed that the two top connections of each panel were only two-twirds as stiff as the bottom connections in both the horizontal and vertical directions. This factor of two-thirds was arbitrarily chosen to reflect the fact that in many curtain wall systems, including that of the prototype structure, the top connections are smaller in size and hence presumably more flexible than the bottom connections. When the weaker top connection case was calibrated to match the value of 625 kips/inch (1.1×10^5 kN/m),

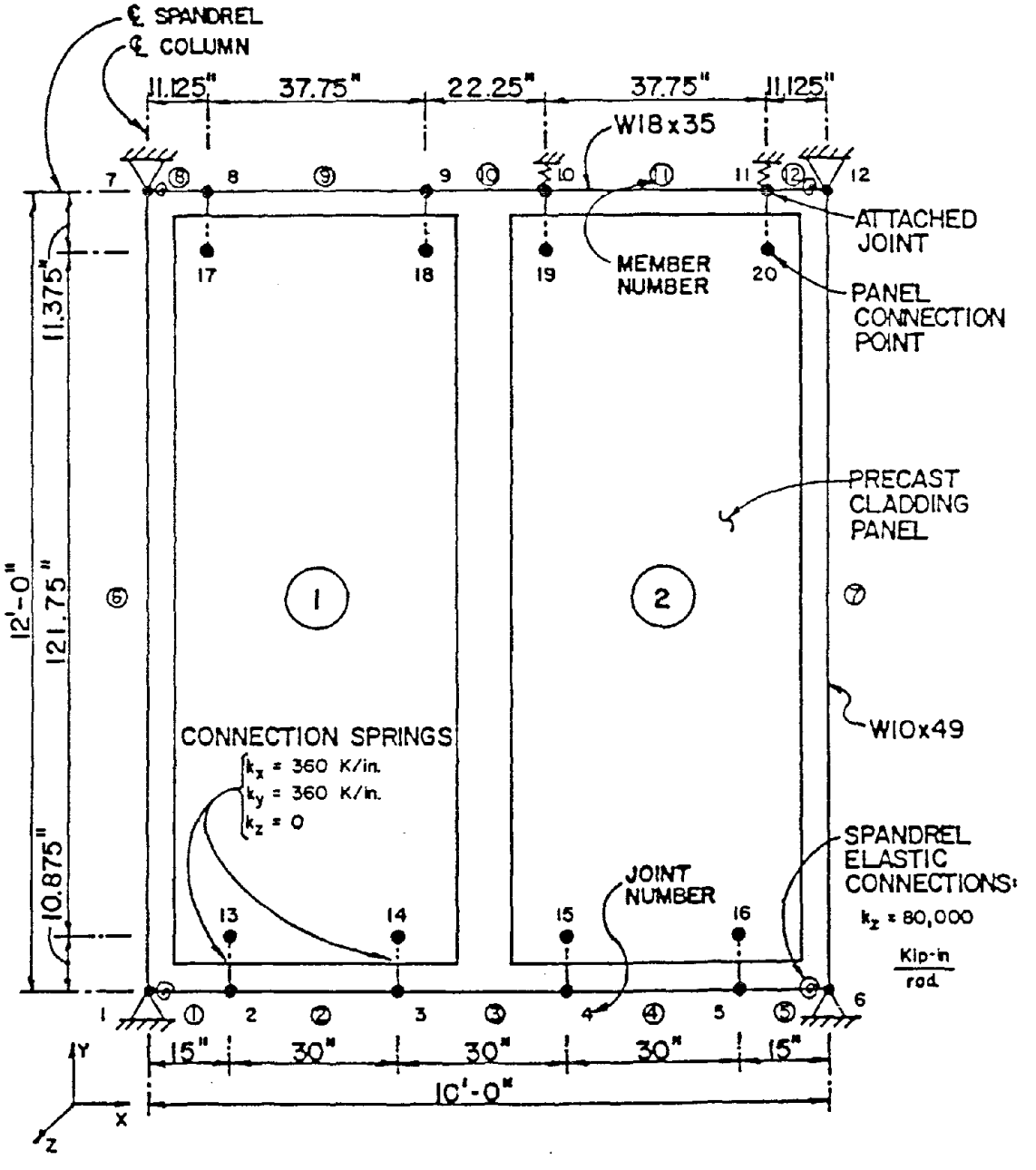

Figure 5.2-2. Uniform Spring Stiffness Case of Rigid Panel Model. (Note: 1 inch - 25.4 mm, 1 kip = 4.4482 kN).

as for the uniform spring stiffness case, the following results were obtained. The required stiffness for the top connections was computed to be $K_x = K_y = 300$ kips/inch (5.3×10^4 kN/m) and consequently, the bottom connections had a resulting stiffness of $K_x = K_y = 450$ kips/inch (7.9×10^4 kN/m).

The second case considered in this section approximated the support condition system recommended by PCI [35]. PCI recommends that the statically determinate support configuration shown in Fig. 5.2-3 be used for connections of non-load bearing, exterior cladding panels. The connections that were assumed free to slide as shown in Fig. 5.2-3 were actually given very low stiffness values in the analysis to simulate the ideal case. Even though the PCI support conditions were assumed to lead to a nonstructural cladding system, connection stiffness values (K_x, K_y) of 930 kips/inch (1.6×10^5 kN/m) for all connection directions not free to slide in Fig. 5.2-3 resulted in the familiar interstory shear stiffness value V of 625 kips/inch (1.1×10^5 kN/m). When a stiffness value (K_x, K_y) of 360 kips/inch (6.3×10^4 kN/m) was assigned to nonsliding connections directions in the PCI case (Fig. 5.2.3), the resulting interstory shear stiffness V was still as large as 248 kips/inch (4.3×10^4 kN/m) as compared to 625 kips/inch (1.1×10^5 kN/m) for the uniform stiffness case. Apparently, the lateral stiffness contribution of cladding is not totally negated by the support system of Fig. 5.2-3.

The following section contains a response comparison of the different panel-frame systems when subjected to imposed interstory displacements.

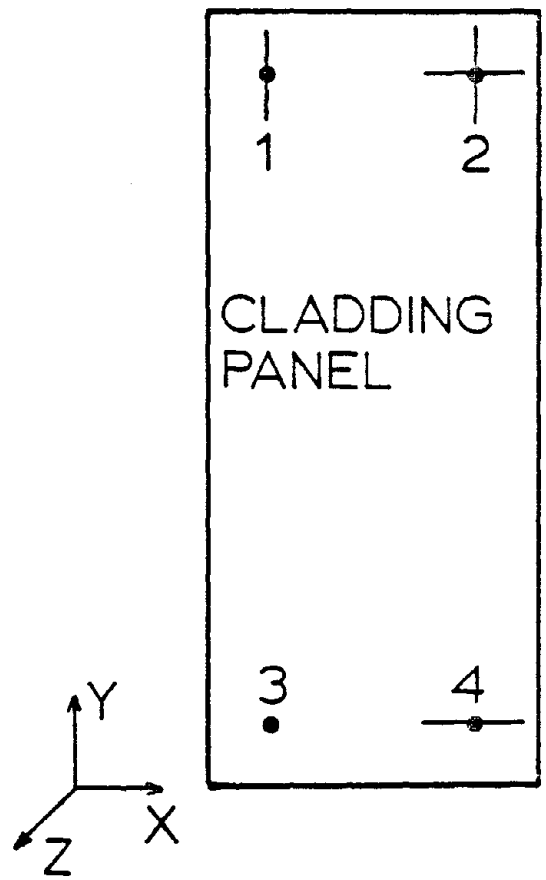

——— Connection free to slide in X-direction.

| Connection free to slide in Y-direction.

● Panel Connection.

Figure 5.2-3. Support Conidtions Recommended by PCI for Nonstructural Cladding Panels.

5.2.4 Response Studies

The different rigid panel models developed in the last two sections (i.e., the uniform stiffness case, the weaker top connection case and the PCI support condition case) will be employed in the response studies below to compare the effects of varying connection stiffnesses and panel support conditions on cladding system force levels. An interstory displacement of 0.72 inches (1.8 cm) was applied to the models by translating the two top supports of the panel-frame system (joints 7 and 12 in Fig. 5.2-2). This loading corresponds to the maximum allowable interstory drift of 0.005 times story height specified by the 1982 Uniform Building Code [49]. When this imposed drift was compared to response values obtained in the dynamic response studies of the overall prototype structure in Section 3.4, it was found that this amounted to 55% of the peak drift due to the 1940 El Centro record applied in either structure direction with or without cladding. In addition, 0.72 inches (1.8 cm) corresponded to 38% of the peak drift when the 1966 Parkfield earthquake was input in the rigid direction with cladding and 48% when applied in the braced direction with cladding. These response values and percentages are for the structure model with mass eccentricity.

Connection forces were computed as the product of connection spring stiffnesses (K_x, K_y) and associated nodal displacements in the model of Fig. 5.2-1. When system forces for the weaker top connection case were compared to the forces for the uniform spring stiffness case (see Table 5.2-1), changes in force levels were rather moderate. However, comparison of the PCI support condition case (V = 625 kips/inch = 1.1×10^5 kN/m) with the uniform spring stiffness case revealed increases

of 51% in maximum spandrel shear and 104% in maximum spandrel moment. In addition, the maximum horizontal force in the bottom connection was increased by 96%, maximum vertical force in the bottom connection by 157%, and maximum horizontal force in the top connection by 95% while maximum vertical force in the top connection dropped to almost zero (i.e., corresponding to a sliding connection). These increases in force levels can be explained by the much higher connection stiffnesses (930 kips/inch, 1.6×10^5 kN/m) present in the PCI support condition case. Finally, a PCI support condition case with connection stiffnesses of 360 kips/inch (6.3×10^4 kN/m) in the non-sliding directions resulting in an interstory shear stiffness of V = 248 kips/inch (4.3×10^4 kN/m) was considered. Note that the other three cases in Table 5.2-1 all have V = 625 kips/inch (1.1×10^5 kN/m). When this more flexible PCI case was compared to the uniform spring stiffness case, most values were comparable or slightly lower except in the case where sliding was permitted.

Computed moments and shears in the frame members were found to be well within their capacities, computed on the basis of AISC-specified allowable stresses, for the loading considered. Connection force levels, on the other hand, were observed in all instances to either approach or considerably exceed the ultimate capacity of 5 to 15 kips (22.2 to 66.7 kN) typical of cladding panel connections [1]. For example, the maximum vertical force in bottom connections for the uniform spring stiffness case is 29.44 kips (131 kN).

The presence of oversized holes, slots and initial friction in connections could affect force levels in connections considerably. However, this nonlinearity could not be handled by the present model. On that basis,

Table 5.2-1. Rigid Panel Model Response to Interstory Drift of 0.72 inches (1.8 cm) for Different Panel Support Conditions.

Case	Uniform Spring Stiffness Case	Weaker Top Connection Case	PCI Support Condition Cases	
			V = 625	V = 248
1. Interstory shear stiffness including frame	63.69	63.41	63.66	32.19
2. Maximum horizontal force in bottom connection	9.499	9.485	18.641	7.376
3. Maximum vertical force in bottom connection	29.440	36.676	75.596	29.886
4. Maximum horizontal force in top connection	9.539	9.454	18.641	7.376
5. Maximum vertical force in top connection	37.032	30.953	0.107	0.107
6. Maximum shear in spandrels	28.451	24.612	42.985	20.012
7. Maximum moment in spandrels	316.52	349.30	646.65	306.75
8. Maximum moment in columns	305.61	306.81	313.42	306.75
9. Maximum vertical deflections in spandrels	0.0038	0.0041	0.0058	0.0039

Note: Units kips and inches
1 kip = 4.4482 kN
1 inch = 2.54 cm

the linear static rigid panel model was modified to include piecewise-linear behavior of the connection springs as discussed in the following section.

5.3 Nonlinear Static Analysis

5.3.1 Introduction

The influence of oversized holes, slots and initial friction in cladding panel connections on connection force levels and cladding lateral stiffness was expected to be of importance in understanding panel-frame interaction. Based on the results of linear dynamic response studies performed by another investigator [37], the decision was made to conduct only static analyses in this investigation.

In order to study the influence of oversized holes, slots and initial friction, a piecewise-linear force-displacement relationship for the panel connection springs proved to be a convenient way to represent changes in connection stiffness as slots closed or friction was overcome. The piecewise-linear assumption required modification of the rigid panel model described in Section 5.2.1. However, only the force-displacement relationships for the panel connection springs were changed, while the remainder of the model remained the same. The panel-frame model was loaded by applying specified horizontal translational displacements at the two top supports (joints 7 and 12) shown in Fig. 5.2-2.

An incremental or stepwise procedure [7] was chosen for the solution process since information such as panel connection forces were sought at intermediate loading levels. The stepwise solution procedure approximates the nonlinearity as a series of linear problems. The nonlinear equilibrium equation for the model can be written as

$$\underset{\sim}{S}\ \underset{\sim}{D} = \underset{\sim}{Q} \tag{5.3-1}$$

where the nonlinearity is due to the stiffness matrix $\underset{\sim}{S}$ and where $\underset{\sim}{D}$ and $\underset{\sim}{Q}$ are vectors of displacements and loads, respectively. The equations employed in the incremental solution procedure of Eq. 5.3-1 can be written by defining the initial state of the model in terms of initial loads and displacements, $\underset{\sim}{Q}_o$ and $\underset{\sim}{D}_o$. Normally, the initial loads and displacements are all zero since the model is assumed to be undeformed initially. If the total load $\underset{\sim}{Q}$ is divided into M increments, then the total load can be written as

$$\underset{\sim}{Q} = \underset{\sim}{Q}_o + \sum_{j=1}^{m} \Delta\underset{\sim}{Q}_j \tag{5.3-2}$$

where $\Delta\underset{\sim}{Q}_j$ refers to the load applied in load increment j (the present analysis has all incremental loads equal). After the application of the i-th increment, the effective load at that point is given by

$$\underset{\sim}{Q}_i = \underset{\sim}{Q}_o + \sum_{j=1}^{i} \Delta\underset{\sim}{Q}_j \tag{5.3-3}$$

where, after M increments, i = M and $\underset{\sim}{Q}_M = \underset{\sim}{Q}$.

The increments of displacements $\Delta\underset{\sim}{D}_i$ are computed by using a constant value of stiffness $\underset{\sim}{S}_{i-1}$, which is evaluated at the end of the previous increment, using the equation

$$\underset{\sim}{S}_{i-1}\ \underset{\sim}{\Delta D}_i = \underset{\sim}{Q}_i \qquad (5.3\text{-}4)$$

for i = 1, 2, 3, . . . , M. The model displacements after the i-th step can then be written as

$$\underset{\sim}{D}_i = \underset{\sim}{D}_o + \sum_{j=1}^{i} \underset{\sim}{\Delta D}_j \qquad (5.3\text{-}5)$$

The incremental solution approach outlined above was incorporated into the linear static computer program used for studies reported in Section 5.2 above and trial runs were made to establish acceptable load increment levels. Iterative procedures were not used within each step. A listing of the computer program is contained in Appendix B.

The influence of oversized holes, slots and initial friction on panel connection forces and lateral stiffness is described in the following sections. Three different panel support conditions are employed in the parameter studies. First, a uniform spring stiffness case is considered in Section. 5.3.2. Then, a case representing the PCI recommended support conditions is studied in Section 5.3.3. Finally, a modification of the PCI case, such that both top connections are slotted in the horizontal direction, labeled as the slotted connection case is considered in Section 5.3.4.

5.3.2 Uniform Spring Stiffness Case

The effects of oversized holes and initial friction in connections on interstory shear stiffness and connection forces for the uniform spring stiffness case discussed in Section 5.2 are reported below. In this

study, all holes were assumed to be oversized except for the vertically aligned holes at the bottom load bearing connections to exclude panel rocking from the analysis.

First, the presence of oversized holes on the panel-frame model response was examined. The distance from the side of a centered bolt to the edge of an oversized hole was defined as the gap. All top connections were assigned a gap in both the vertical and horizontal directions resulting in the presence of two small slots perpendicular to each other. This was assumed to be an adequate representation of an oversized hole in the model. On the other hand, a gap was only assigned to the horizontal directions of the bottom connections to indicate the presence of a small horizontal slot at these locations. Four different gap sizes representing a typical range were considered:

1) No gap (linear case of frame with panels as in Section 5.2.2)
2) Gap of 0.03125 inches (0.08 cm)
3) Gap of 0.0625 inches (0.16 cm)
4) Gap of 0.125 inches (0.32 cm)

Normally, a hole is specified to be 0.0625 inches (0.16 cm) larger in diameter than the bolt diameter being used [35] resulting in a gap of 0.03125 inches (0.08 cm). However, gaps are present in both the clip angle and the panel insert thereby doubling the effective gap to 0.0625 inches (0.16 cm). The other cases (2, 4) were included to bracket the standard case, with case (2) being more conservative and case (4) representing the use of a larger than standard hole.

Figure 5.3-1 shows the interstory shear stiffness V for the frame-panel model as a function of interstory drift for the different gap sizes.

The interstory shear stiffness for one bay of the unclad frame model is shown for reference. Inspection of Fig. 5.3-1 showed that the initial interstory shear stiffness for the cases with gaps (i.e., cases 2, 3, and 4 above) was higher than for the unclad frame (13.4 kips/inch (2.3×10^3 kN/m) versus 11.53 kips/inch (2.0×10^3 kN/m)). This difference can be explained by the stiffening effects of the cladding panels on the bottom spandrel of the frame. When the drift-interstory shear stiffness relationship for the gap size of 0.0625 inches (0.16 cm) was followed in Fig. 5.3-1, the stiffness increased to 32.8 kips/inch (6.7×10^3 kN/m) at an interstory drift of 0.16 inches (0.41 cm) since all horizontal gaps were closed. Interstory stiffness later increased to 63.7 kips/inch (1.1×10^4 kN/m) at 0.56 inches (1.42 cm) when the vertical gaps of the top connections were also closed. When the limit of linear behavior for the frame was computed, values of 4.6 inches (11.7 cm) and 4.7 inches (11.9 cm) were obtained for the linear clad and unclad models, respectively.

Figures 5.3-2 to 5.3-5 show maximum connection forces versus drift in both horizontal and vertical directions for top and bottom connections. When the lines for the case with gap size of 0.0625 inches (0.16 cm) were followed in Figs. 5.3-2 and 5.3-3, two changes in slope were observed for maximum horizontal forces. The first slope change occurs at the point at which horizontal gaps were closed (point A) and the second slope change occurs at the point at which vertical gaps were also closed (point B). However, only one change in slope was observed for the maximum vertical forces (Figs. 5.3-4 and 5.3-5). In top connections this slope change occurred as vertical gaps closed. On the other hand, in bottom connections

the change in slope occurred at the point at which horizontal gaps closed.

Table 5.3-1 lists connection forces and framing member moments and shears for the different gap size cases when the specified interstory static displacement was set at 0.72 inches (1.8 cm). This displacement level corresponded to the maximum interstory drift allowed by UBC [49]. According to the PCI design handbook on precast and prestressed concrete [36], the ultimate vertical shear capacity of the bottom connections for the prototype structure was about 6.15 kips (27.4 kN). The capacity of the top connections, however, was approximately 4.1 kips (18.2 kN). PCI [36] uses the relation

$$V_u = (\phi t)^2 \frac{f_y b}{4 e_v} \qquad (5.3\text{-}1)$$

where ϕ is a capacity reduction factor taken as 0.90, t is the thickness of the angle, f_y the yield strength of the steel, b the length of angle and e_v the distance from surface of the panel to the point of support of the angle. When these ultimate values were compared to computed values in Table 5.3-1, vertical connection forces were found to be excessive in all cases except in top connections with a gap size of 0.125 inches (0.32 cm). Although values remained excessive in most cases, comparison of maximum connection forces showed a reduction with increasing gap size. When maximum moments in framing members were compared in Table 5.3-1, only a slight reduction was observed with increasing gap size, but the maximum spandrel shear was reduced considerably. The maximum spandrel shear occurred at the elastic framing connections for gap sizes

of 0.0625 inches (0.16 cm) and 0.125 inches (0.32 cm), while maximum shear was at the panel connection points in the middle of the top spandrel for the cases with no gap and a gap of 0.03125 inches (0.08 cm).

Initial friction in connections coupled with oversized holes or slotted connections could change connection forces and distribution of forces in connections significantly. In an experimental study involving both static and cyclic tests of bolted connections for panelized construction [30], the observation was made that the bolted connections were very stiff initially up to an applied load of 2 to 3 kips (8.9 to 13.3 kN). Both corner and in-line connections were considered. The study concluded that the 2 to 3 kips (8.9 to 13.3 kN) was the force needed to overcome the friction in the connection caused by preloading (pretensioning) of the bolts. After this initial friction was overcome, the connection was observed to slip a distance equal to the tolerance gap of the oversized hole followed by an increase in stiffness as deformation of the connection elements began. This initial high stiffness was observed only at the start of the test (cyclic tests were included in the study) and was not reached again during the test once the connection had slipped. Therefore, in the present study, it was assumed that the initial stiffness at the initiation of loading was equal to the stiffness of the connection after slipping when the bolt was bearing against the side of the hole.

Three different levels of initial friction were considered:

1) No initial friction which corresponded to the case with a gap size of 0.125 inches (0.32 cm) considered at the beginning of this section (Section 5.3-2)

2) Initial friction force of 2 kips (8.9 kN)

3) Initial friction force of 3 kips (13.3 kN)

All the cases had an oversized hole with a gap size of 0.125 inches (0.32 cm). The friction force levels chosen were based on values from the study of panelized construction [30] referenced above. While it is not clear whether or not this data also pertains to precast cladding panels and connections, the assumption was made that the data could be used in the present study; however, the validity of these friction values needs to be verified in future experimental investigations.

In Fig. 5.3-6 the interstory shear stiffness per bay including the frame is shown as a function of relative interstory drift for the different initial friction levels. Also shown for reference purposes are the interstory shear stiffness values for the clad (no gaps) and unclad frame models. Inspection of Fig. 5.3-6 showed that the initial interstory shear stiffness for both cases with initial friction was 63.7 kips/inch (1.1×10^4 kN/m). If, for example, the model behavior for the case with initial friction of 3 kips (13.3 kN) was followed, then the stiffness was first seen to drop to 32.8 kips/inch (5.7×10^3 kN/m) as friction was overcome in the vertical direction of the top connections at a drift of 0.08 inches (0.20 cm or 0.06% of the story height, point A). Later, the interstory shear stiffness dropped to 13.4 kips/inch (2.3×10^3 kN/m) when friction was overcome in the horizontal directions of both top and bottom connections at an interstory displacement of 0.52 inches (1.32 cm or 0.36% of the story height, point B). The stiffness remained at 13.4 kips/inch (2.3×10^3 kN/m) until gaps closed in the horizontal directions at a drift of 0.78 inches

(1.98 cm or 0.54% of the story height, point C) and then increased to 32.8 kips/inch (5.7 x 10^3 kN/m) beyond that point. Finally, the stiffness went up to 63.7 kips/inch (1.1 x 10^4 kN/m) when vertical gaps of top connections closed at an interstory displacement of 1.16 inches (2.95 cm or 0.81% of the story height, point D). The behavior of the case with an initial friction of 2 kips (8.9 kN) followed the same pattern but, due to the difference in initial friction values, changes in interstory shear stiffness occurred at lower drift levels. When the cases with initial friction were compared to the reference case having no initial friction, initial stiffness levels were observed to be much higher for the cases with initial friction. The reference case had an initial interstory shear stiffness of 13.4 kips/inch (2.3 x 10^3 kN/m) which increased to 32.8 kips/inch (5.7 x 10^3 kN/m) as gaps closed in the horizontal direction at 0.30 inches (0.76 cm or 0.21% of the story height). The interstory shear stiffness again increased at 1.10 inches (2.79 cm or 0.76% of the story height) to 63.7 kips/inch (1.1 x 10^4 kN/m) as vertical gaps closed. The increased initial stiffness levels for the cases with initial friction resulted in higher connection forces at low drift levels as will be shown in the force-drift plots presented below.

Figures 5.3-7 to 5.3-10 contain maximum horizontal and vertical connection force components as function of interstory drift for both top and bottom connections. Again the influence of initial friction is evident in these plots and, as expected, force levels for the cases with initial friction were much higher at low drift values than for the case with no initial friction.

The points of slope change in the force-drift plots (Figs. 5.3-7 to 5.3-10) corresponded to the points of change in stiffness levels in Fig. 5.3-6 which were at 0.08 inches, 0.52 inches, 0.78 inches and 1.16 inches (0.20 cm, 1.32 cm, 1.98 cm and 2.95 cm) for the case with an initial friction of 3 kips (13.3 kN). Once friction was overcome and all gaps were closed at a drift of 1.16 inches (2.95 cm), force levels equalled those of the case without initial friction, since at that stage all models were alike.

5.3.3 PCI Support Condition Case

The case considered in this section approximated the PCI [35] recommended support conditions shown in Fig. 5.2-3. The figure shows that both top connections are free to slide vertically, while only the top right connection and the bottom right connection are free to slide horizontally. Horizontal sliding was accomplished by the use of a clip angle with a slotted bolt hole. The size of horizontal slots was taken to be 1.5 inches (3.8 cm) in these studies based on an inspection of several top connections that were visible in the prototype structure. In addition, the assumption was made that the initial location of the three-quarter inch (1.9 cm) bolt was in the center of the slot resulting in an open horizontal slot dimension of 0.375 inches (0.95 cm) on each side of the bolt.

Vertical sliding, on the other hand, was due to the use of slotted panel inserts as recommended by PCI [35]. Based on information for a typical top connection insert device [1], the open slot dimension above and below the bolt was taken as 0.825 inches (2.10 cm) when the bolt was placed in the center of the slot. Very low stiffness values

Table 5.3-1. Rigid Panel Model Response to Static Interstory Drift of 0.72 inches (1.8 cm), for the Uniform Spring Stiffness Case with Varying Gap.

	Response/Case	No Gap	Gap = 0.03125 in.	Gap = 0.0625 in.	Gap = 0.125 in.
1.	Interstory shear stiffness including frame	63.7	63.7	63.7	32.8
2.	Maximum horizontal force in bottom connection	9.499	7.078	4.670	2.629
3.	Maximum vertical force in bottom connection	29.440	27.330	25.200	20.144
4.	Maximum horizontal force in top connection	9.539	7.108	4.689	2.640
5.	Maximum vertical force in top connection	37.032	23.259	9.500	0.072
6.	Maximum shear in spandrels	28.451	19.724	17.723	15.117
7.	Maximum moment in spandrels	316.52	304.82	304.02	302.70
8.	Maximum moment in columns	305.61	304.82	304.02	302.70
9.	Maximum vertical deflections in spandrels	0.0038	0.0037	0.0037	0.0035

Note: Units kips and inches; 1 kip = 4.4482 kN and 1 inch = 2.54 cm.

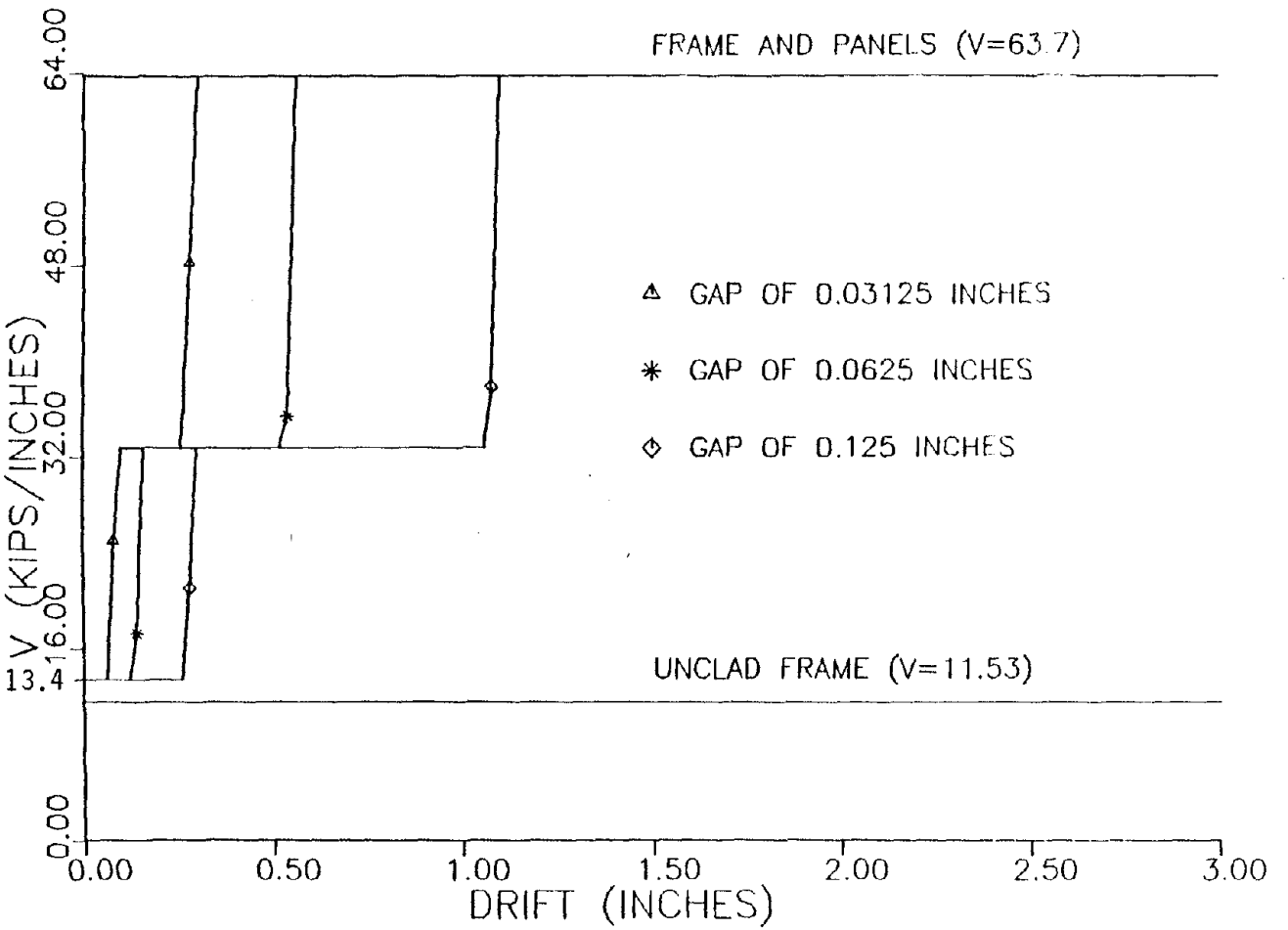

Figure 5.3-1. Interstory Shear Stiffness, V, Versus Interstory Drift for the Uniform Spring Stiffness Case with Oversize Holes.

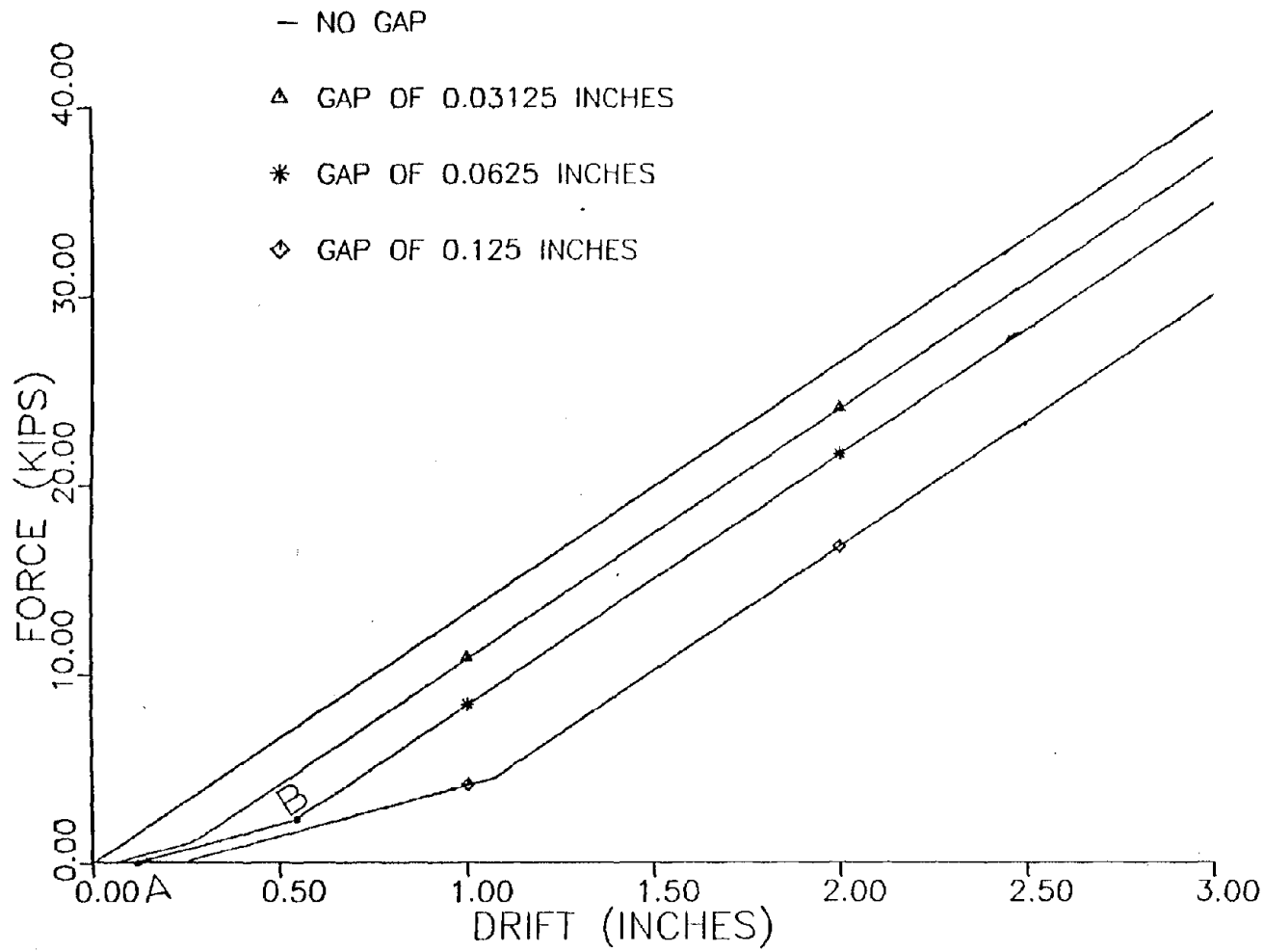

Figure 5.3-2. Maximum Horizontal Force in a Top Connection Versus Interstory Drift for the Uniform Spring Stiffness Case with Oversize Holes.

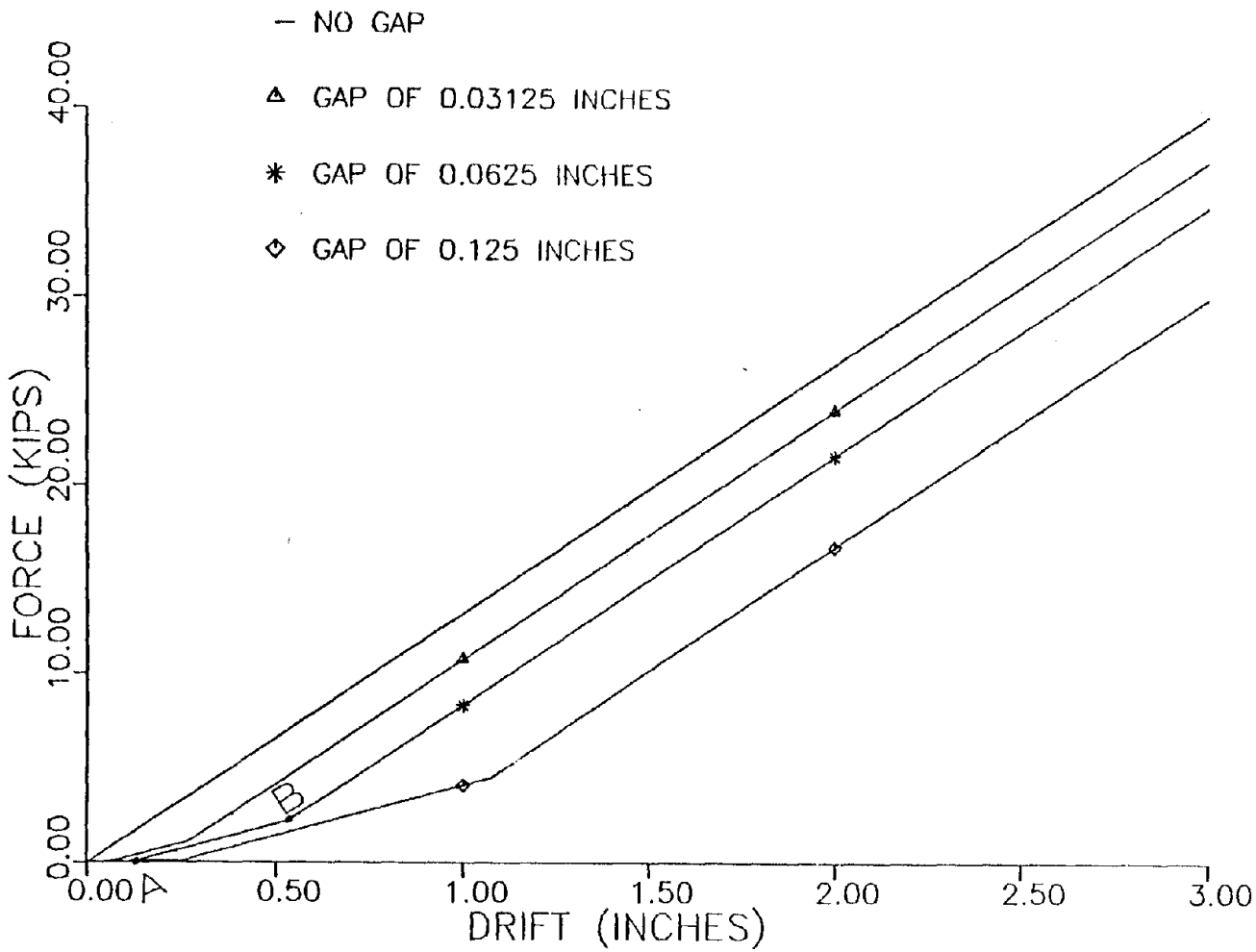

Figure 5.3-3. Maximum Horizontal Force in a Bottom Connection Versus Interstory Drift for the Uniform Spring Stiffness Case with Oversize Holes.

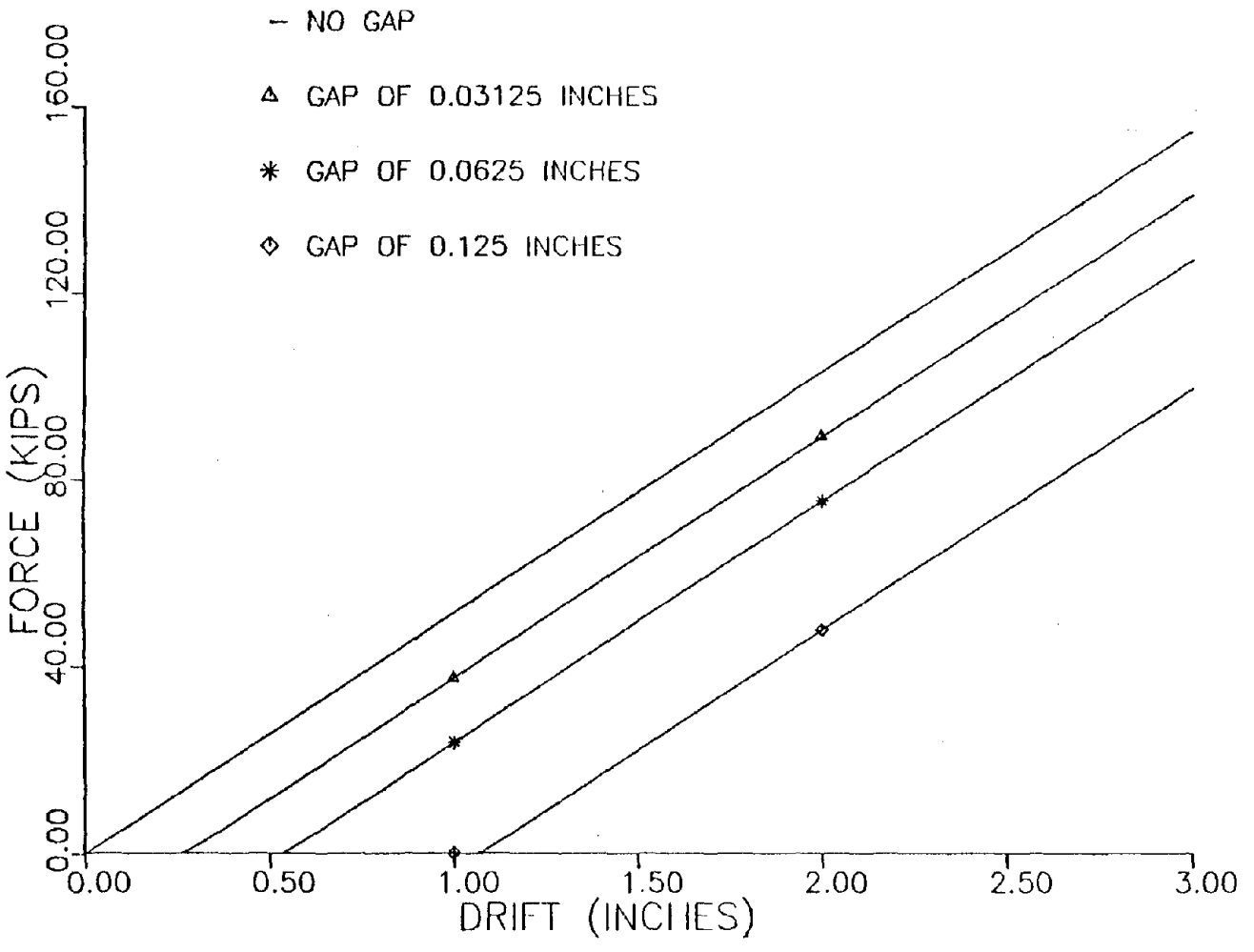

Figure 5.3-4. Maximum Vertical Force in a Top Connection Versus Interstory Drift for the Uniform Spring Stiffness Case with Oversize Holes.

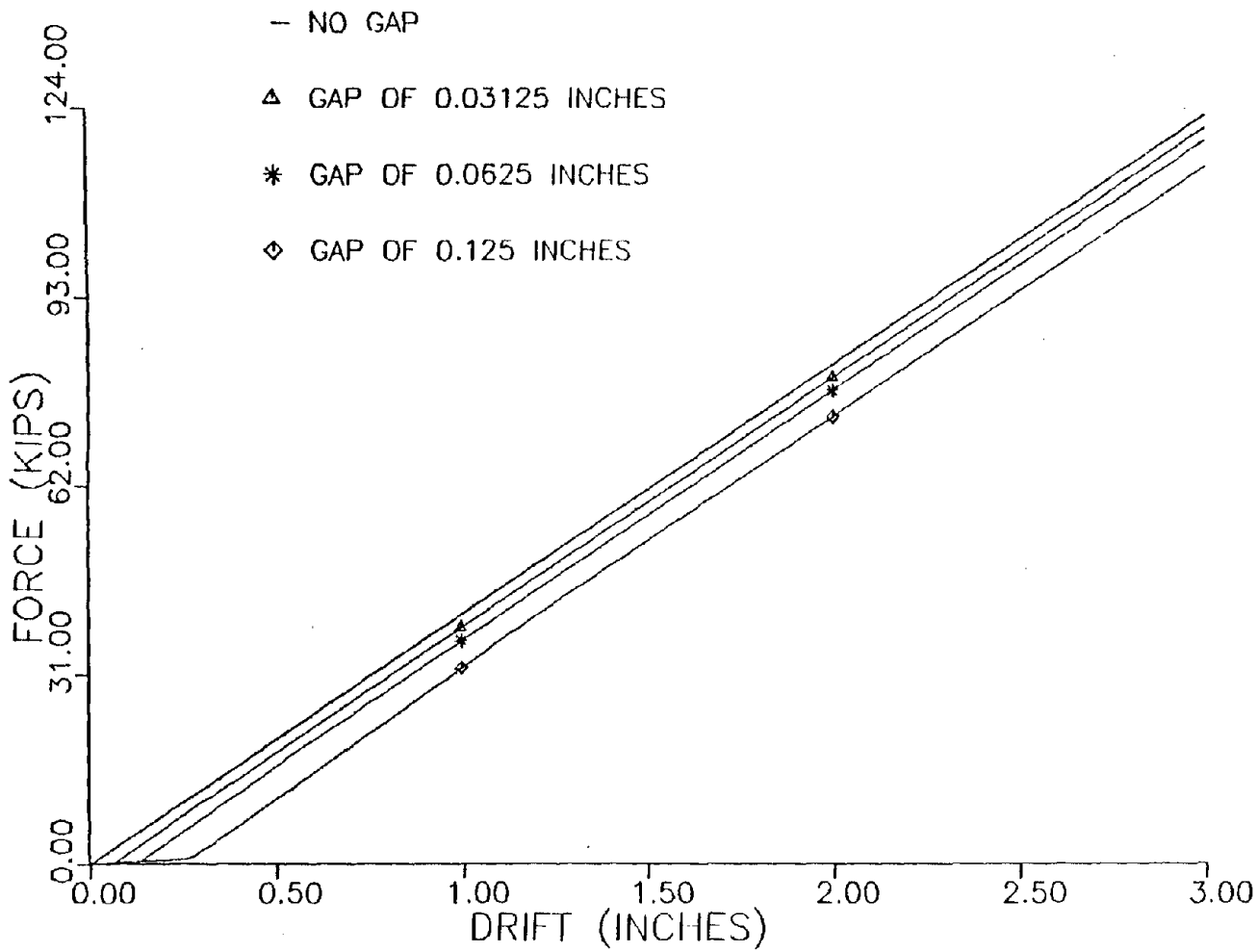

Figure 5.3-5. Maximum Vertical Force in a Bottom Connection Versus Interstory Drift for the Uniform Spring Stiffness Case with Oversize Holes.

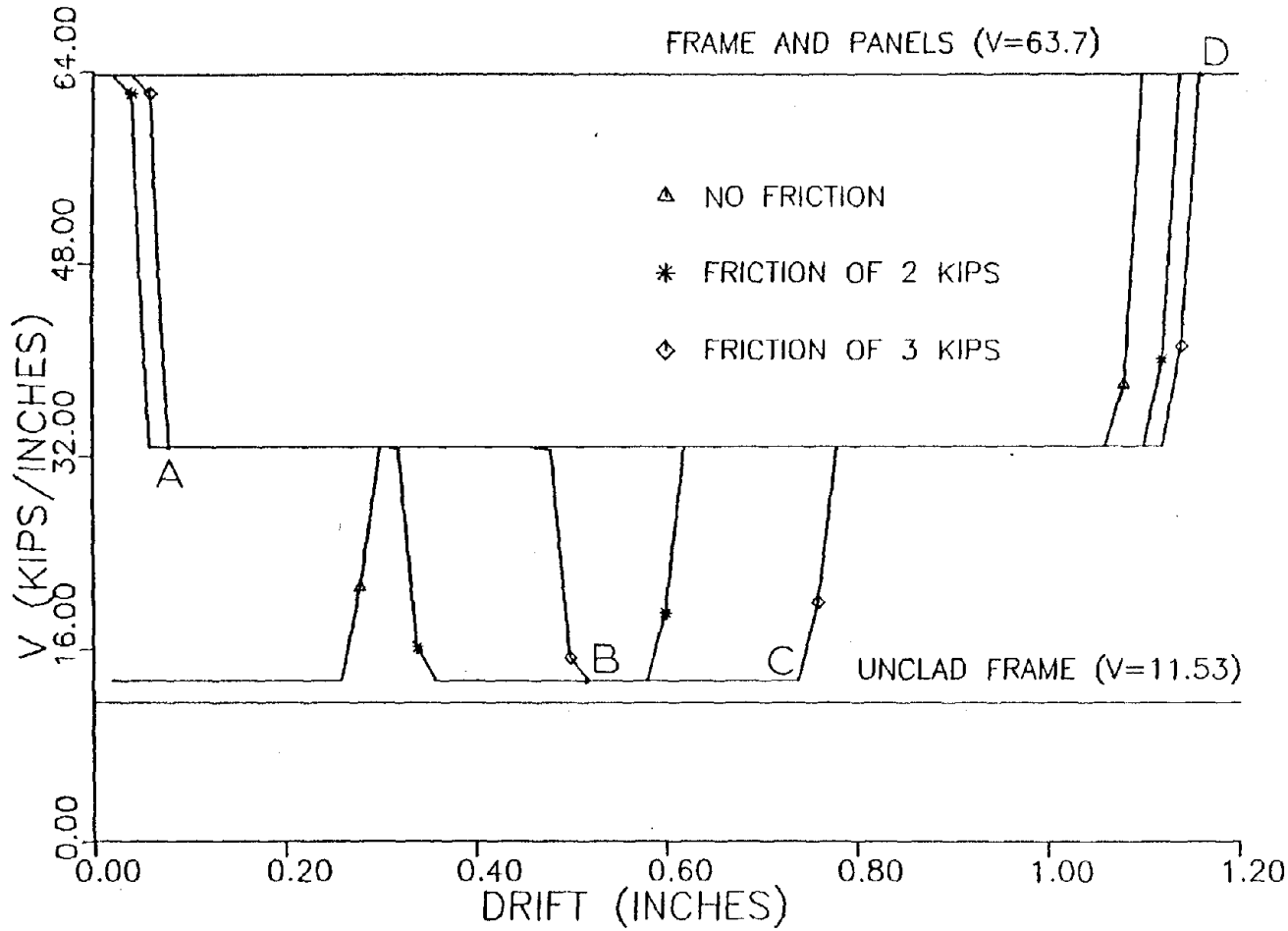

Figure 5.3-6. Interstory Shear Stiffness, V, Versus Interstory Drift for the Uniform Spring Stiffness Case with Initial Friction in Connections and Oversize Holes with a Gap Size of 0.125 inches (0.32 cm).

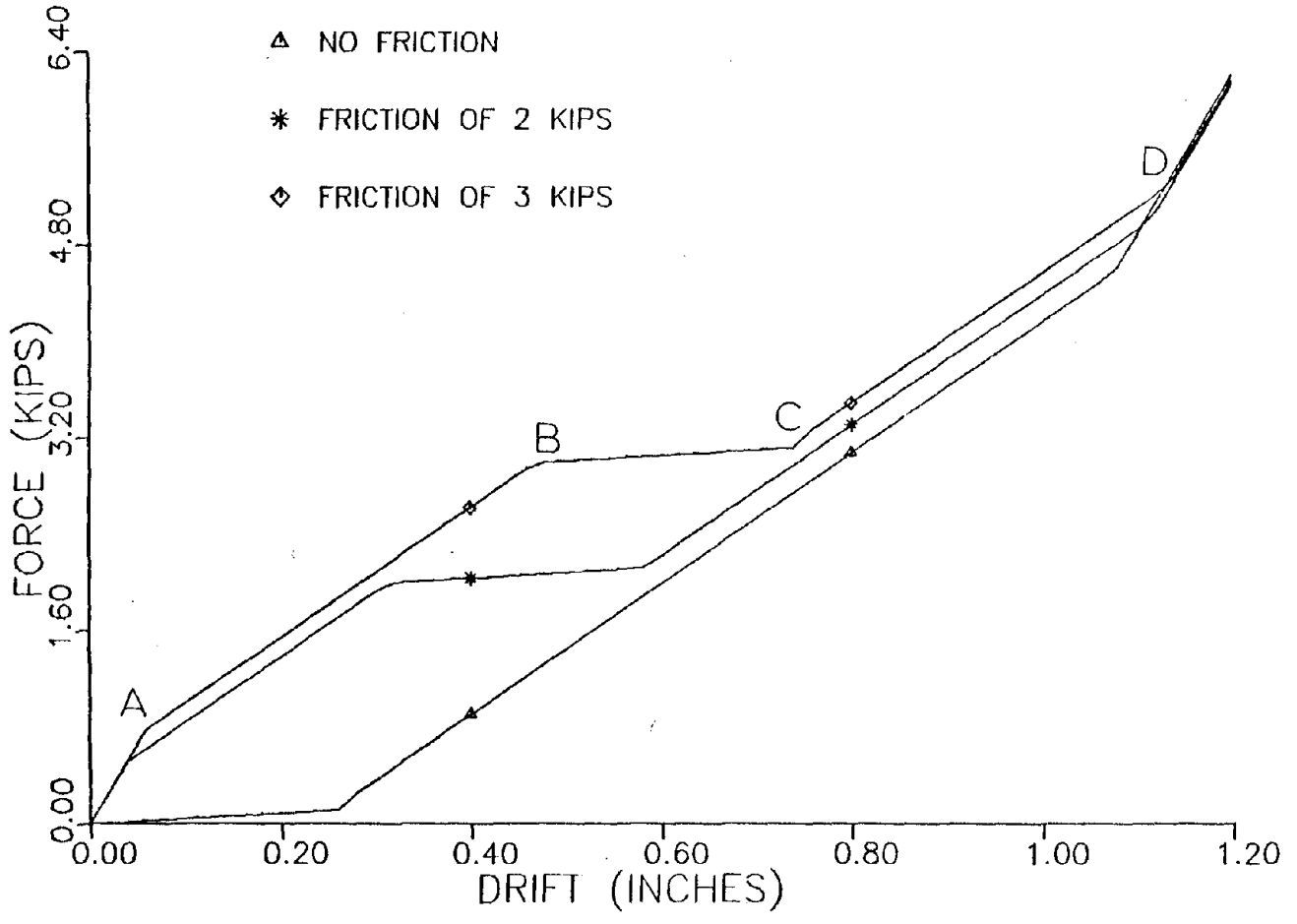

Figure 5.3-7. Maximum Horizontal Force in a Top Connection Versus Interstory Drift for the Uniform Spring Stiffness Case with Initial Friction in Connections and Oversize Holes with a Gap Size of 0.125 inches (0.32 cm).

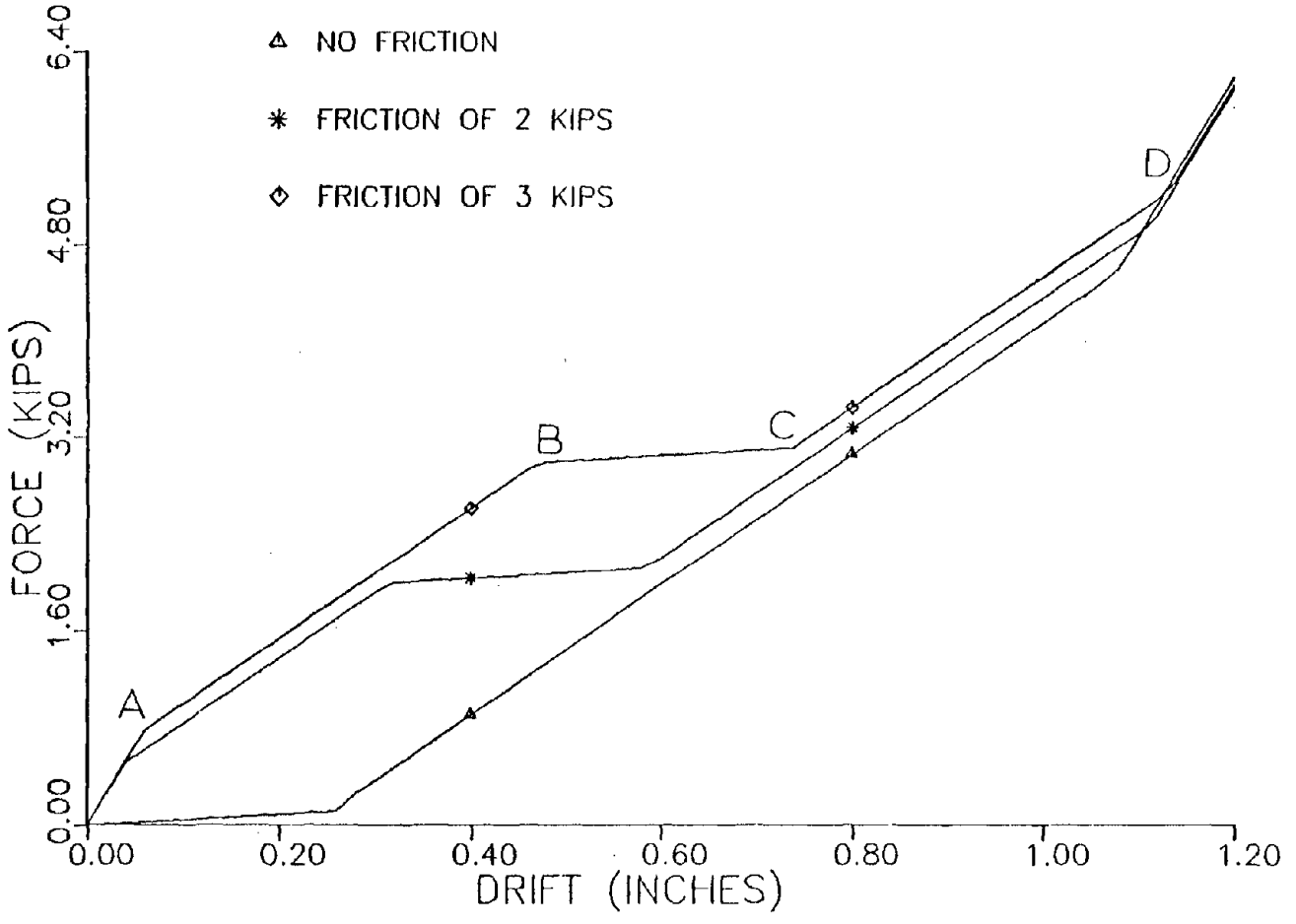

Figure 5.3-8. Maximum Horizontal Force in a Bottom Connection Versus Interstory Drift for the Uniform Spring Stiffness Case with Initial Friction in Connections and Oversize Holes with a Gap Size of 0.125 inches (0.32 cm).

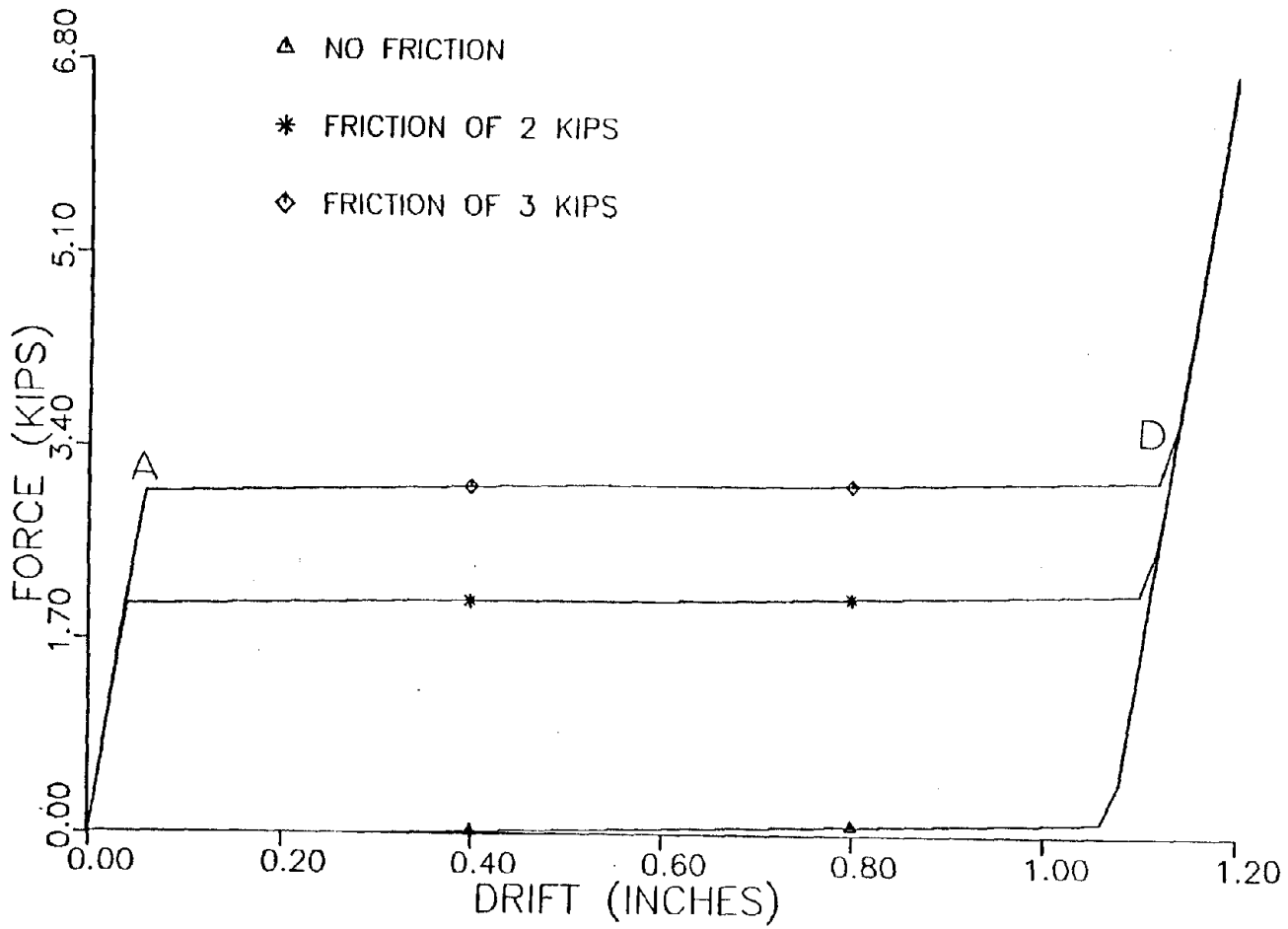

Figure 5.3-9. Maximum Vertical Force in a Top Connection Versus Interstory Drift for the Uniform Spring Stiffness Case with Initial Friction in Connections and Oversize Holes with a Gap Size of 0.125 inches (0.32 cm).

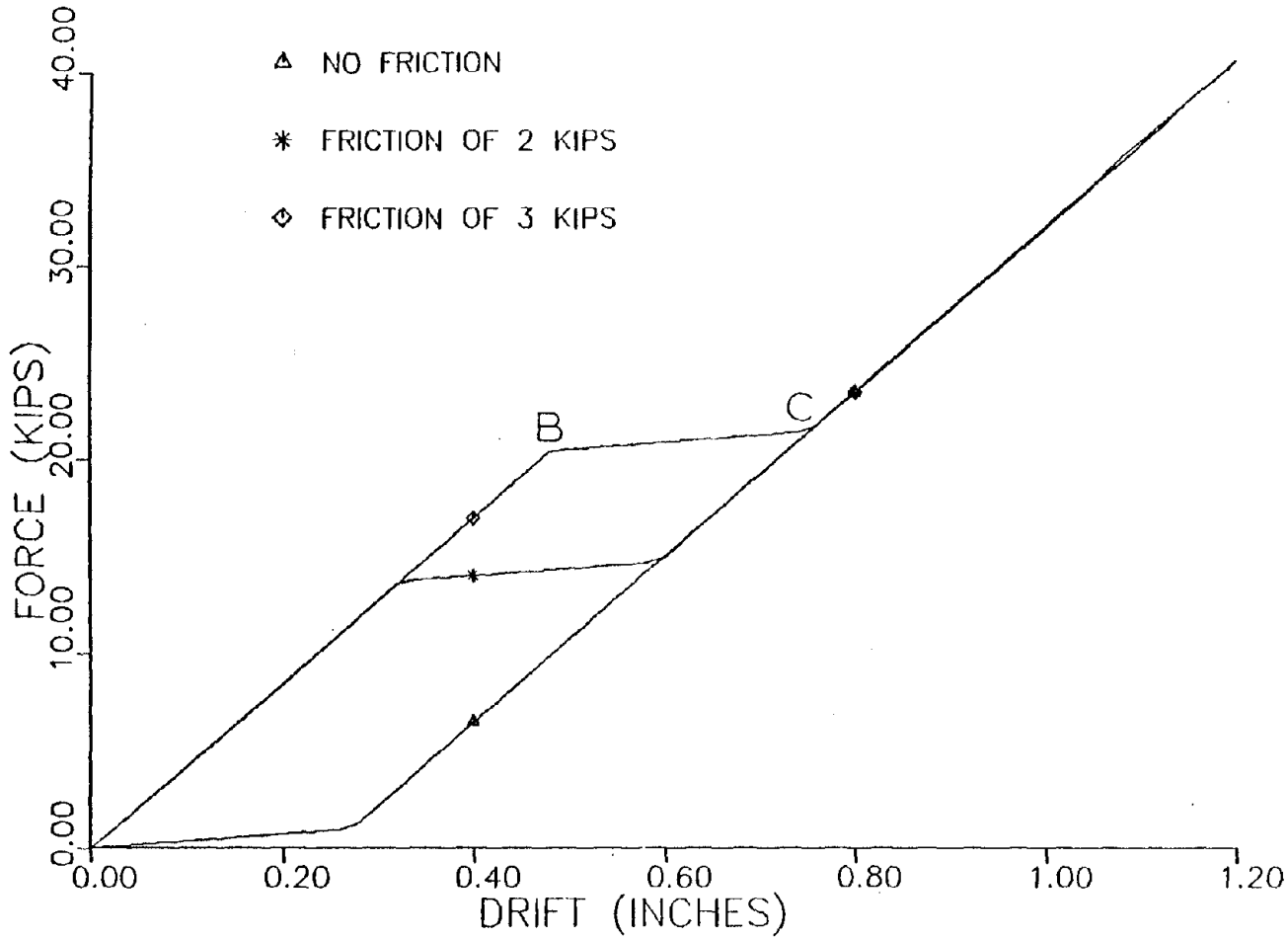

Figure 5.3-10. Maximum Vertical Force in a Bottom Connection Versus Interstory Drift for the Uniform Spring Stiffness Case with Initial Friction in Connections and Oversize Holes with a Gap of 0.125 inches (0.32 cm).

were assigned to the interval in which free sliding was assumed in the model to simulate the sliding behavior.

The investigation in this section examined the influence of oversized holes and initial friction in connections on interstory shear stiffness and connection forces for the PCI panel support case. The horizontal direction of the top left connection was not free to slide according to PCI recommendations and hence was not slotted. In this study, a comparison was made between the PCI case and a case which assumed the horizontal dimension of the top left vertically slotted hole to be larger than the diameter of the bolt or in other words, the hole was oversized in the horizontal direction. Recall that in Section 5.3.2 a gap was defined as the distance from the side of a centered bolt to the edge of the hole. Two gap sizes for the top left connection were considered:

1) No gap or the actual PCI case

2) Gap of 0.125 inches (0.32 cm)

In addition to studying the influence of placing a vertical slot, with oversized hole for horizontal movement, in the top left connection, the influence of initial friction in connections (i.e., in both PCI recommended slots and the oversized hole) was also considered. Two levels of initial friction were studied:

1) No initial friction in connections (i.e., actual PCI if no gap exists)

2) Initial friction of 3 kips (13.3 kN) based on the panelized construction connection study [30] discussed in Section 5.3.2

First, the above cases were compared by using connection spring stiffnesses of 930 kips/inch (1.6×10^5 kN/m) obtained for the PCI

case supported directions in the linear studies in Section 5.2.3. Recall that connection spring stiffnesses of 930 kips/inch (1.6×10^5 kN/m) were required to produce an overall interstory shear stiffness of 625 kips/inch (1.1×10^5 kN/m) for a row of all panels on one face of the building. The introduction of initial friction in connections increased the interstory shear stiffness at low drift levels before friction was overcome since higher stiffness was now present in connection directions which previously were free to slide in the linear case. However, in order to reduce the increase in interstory shear stiffness due to initial friction, the stiffness in directions of initial friction was set at 360 kips/inch (6.3×10^4 kN/m) as in the uniform spring stiffness case considered in Section 5.3.2 rather than 930 kips/inch (1.6×10^5 kN/m) as for the PCI case supported directions.

Figure 5.3-11 shows the influence of the oversized hole and initial friction on interstory shear stiffness. The line labeled as "frame and panels" corresponds to the case with no gap and no initial friction and hence is the actual PCI case. Inspection of the plots of Fig. 5.3-11 showed that the case with a gap but no initial friction began with an interstory shear stiffness of 15.3 kips/inch (2.7×10^3 kN/m). This value is higher than the stiffness of the unclad frame (i.e., V = 11.53 kips/inch, 2.0×10^3 kN/m) due to the stiffening effects of the panel on the bottom spandrel in the plane-frame model. The stiffness for the "gap, no friction" case increased to 63.7 kips/inches (1.1×10^4 kN/m) when the horizontal gap of the top left connection closed at a drift of 0.18 inches (0.46 cm, point A). When the cases with initial friction were considered, it was observed that both cases

had a stiffness in excess of 90 kips/inch (1.6×10^4 kN/m) initially. The stiffness for the "gap, friction" case decreased to 63.7 kips/inch (1.1×10^4 kN/m) as the friction was overcome in the vertical direction of top connections at 0.08 inches (0.20 cm, point B). The "gap, friction" case stiffness was then reduced further to 15.3 kips/inch (2.7×10^3 kN/m) at the point at which friction was overcome in the horizontal direction of both top connections at 0.22 inches (0.56 cm). The interstory shear stiffness for the "gap, friction" case increased to slightly over 63.7 kips/inch (1.1×10^4 kN/m) at 0.36 inches (0.91 cm, point D) as the gap of the horizontally oversized vertical slot in the upper left connection closed, but the stiffness decreased slightly to 63.7 kips/inch (1.1×10^4 kN/m) as friction was overcome in the horizontal direction of all top connections. When friction was overcome in the vertical direction of the top connection for the "no gap, friction" case, the stiffness decreased to 64.5 kips/inch (1.1×10^4 kN/m) and then later to 63.7 kips/inch (1.1×10^4 kN/m) as friction was overcome in the horizontal directions of the slotted connections. The limit of linear behavior for the frame in the case without a gap and without initial friction was found to be a lateral drift response of 2.3 inches (5.8 cm).

Figures 5.3-12 to 5.3-15 depict maximum connection forces as a function of relative interstory drift for both vertical and horizontal directions of top and bottom connections. Slope changes occurred at points where initial friction in connections was overcome and the gap in the top left connection closed. Inspection of vertical force levels in the bottom load bearing connections showed that at relatively low

interstory drift values the PCI determined ultimate shear capacity [36] of 6.15 kips (27.4 kN) discussed in Section 5.3.2 was exceeded.

The above study in this section used connection stiffness values which resulted in a variable peak interstory shear stiffness. The connection stiffnesses were adjusted in the following study such that the maximum interstory shear stiffness remained fixed. This was accomplished by using a connection stiffness of 360 kips/inch (6.3 x 10^4 kN/m) in the cases with initial friction, while the cases with no initial friction remained unchanged with connection stiffnesses of 930 kips/inch (1.6 x 10^5 kN/m) and were repeated for comparison. Again, the influence of the top left vertical slot being oversized in the horizontal direction (gap size of 0.125 inches, 0.32 cm) and initial friciton in connections (3 kips or 13.3 kN for both PCI recommended slots and the oversized slot) was studied.

Figure 5.3-16 shows the interstory shear stiffness versus relative interstory drift for the cases with and without initial friction, and with or without a gap. The initial stiffness for the "no gap, friction" case was 63.7 kips/inch (1.1 x 10^4 kN/m) but decreased to 32.8 kips/inch (5.7 x 10^3 kN/m) as friction was overcome in the vertical direction of top connections at a drift of 0.08 inches (0.20 cm, point A). This stiffness was reduced to 32.2 kips/inch (5.6 x 10^3 kN/m) when horizontal friction was overcome in horizontally slotted connections which occurred at an interstory displacement of 0.52 inches (1.32 cm, point B). When the case labeled as "gap, friction" was considered, it coincided with the "no gap, friction" case initially, but at a drift of 0.52 inches (0.20 cm, point C), the interstory shear stiffness of the frame-panel model was reduced to 14.9 kips/inch (2.6 x 10^3 kN/m). Once the gap

closed at 0.66 inches (1.68 cm, point D), the stiffness increased to 32.2 kips/inch (5.6×10^3 kN/m) and remained at that level for all remaining drift values considered.

Figures 5.3-17 to 5.3-20 display connection forces versus drift for both top and bottom connections. The reduction in connection forces was evident for the cases with initial friction, except in the vertical direction of top connections. This reduction in force levels can be explained by the lower connection stiffnesses used for cases with initial friction. The lower stiffnesses were specified to keep maximum interstory shear stiffnesses at 63.7 kips/inch (1.1×10^4 kips/inch). The lower forces were more appealing when ultimate vertical shear capacities for the connections were considered. In spite of the lower values, the critical load bearing bottom connections were observed to exceed their PCI determined ultimate capacities [36] discussed in Section 5.3.2 at relatively low drift levels.

Finally, it was noted that none of the slots recommended by PCI [35] were observed to close at the interstory displacement levels considered in this section. The fact that the slots remained open suggested that an alternate panel support scheme such as providing a horizontal slot in the top left connection would be beneficial in reducing excessive connection forces. This alternate scheme labeled as the slotted connection case will be considered in the following section.

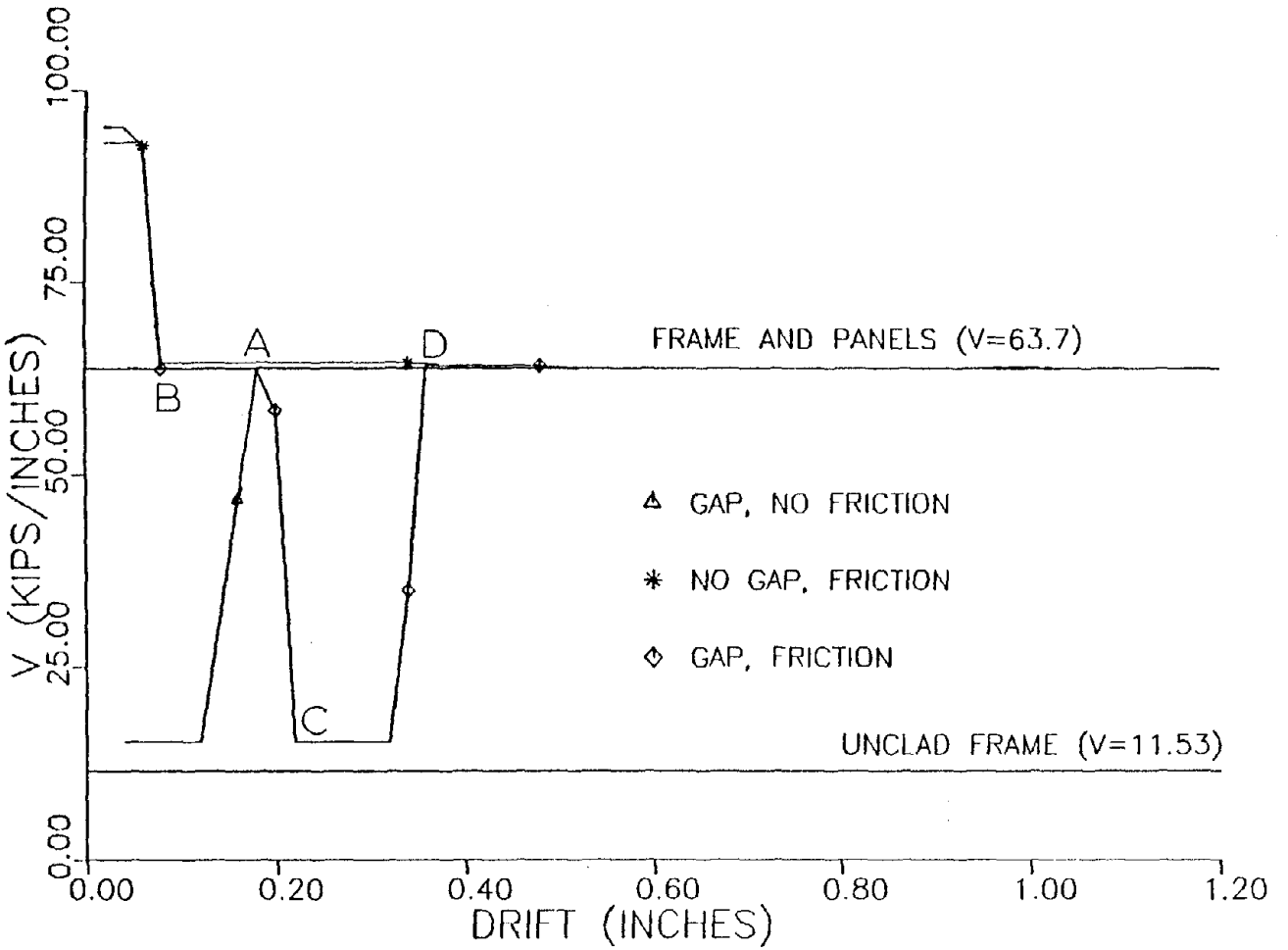

Figure 5.3-11. Interstory Shear Stiffness, V, Versus Interstory Drift for the PCI Support Condition Case, Considering Initial Friction in Connections and Oversize Holes with Stiffness for PCI Recommended Supports Remaining Fixed.

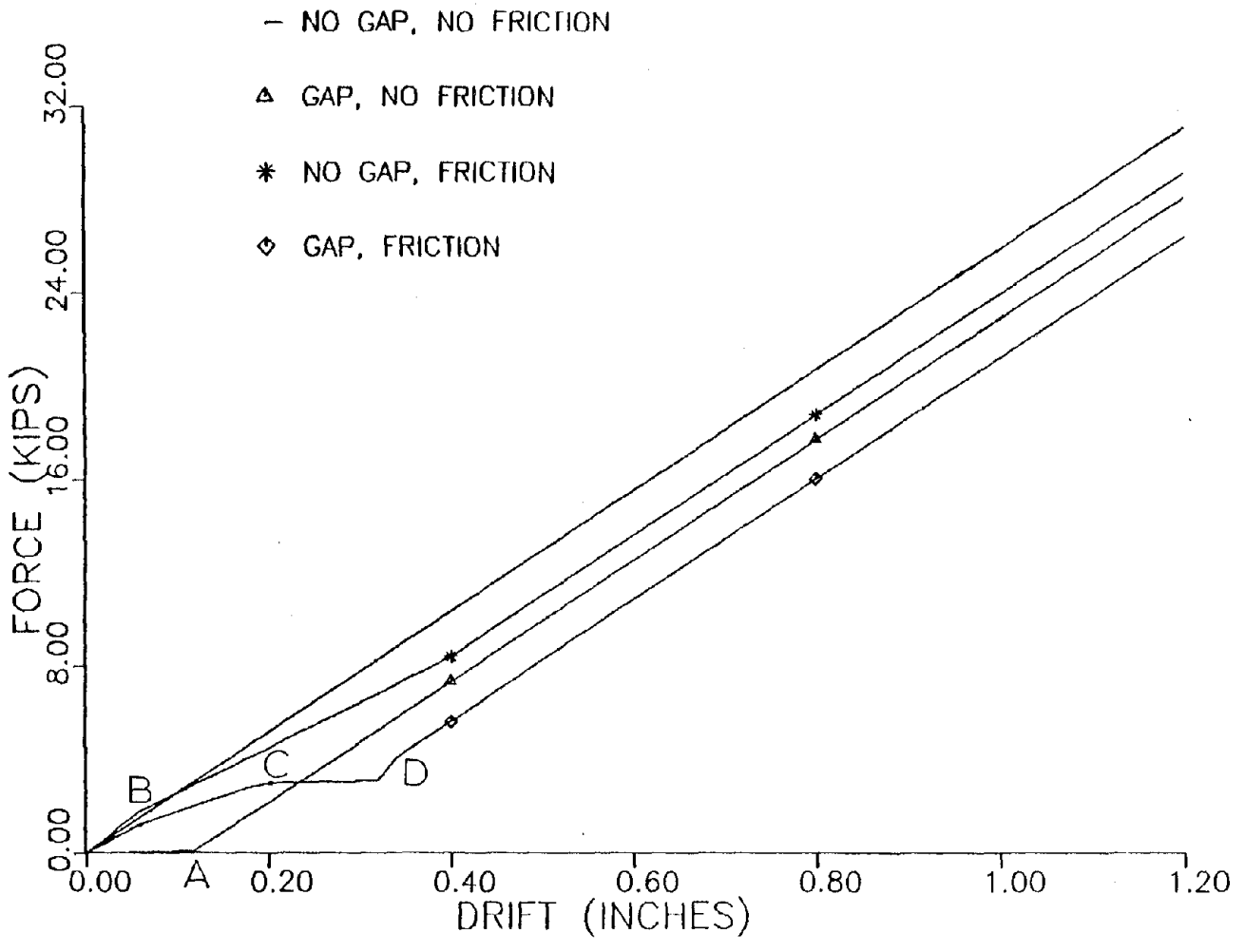

Figure 5.3-12. Maximum Horizontal Force in a Top Connection Versus Interstory Drift for the PCI Support Condition case, Considering Initial Friction in Connections and Oversize Holes with Stiffness for PCI Recommended Supports Remaining Fixed.

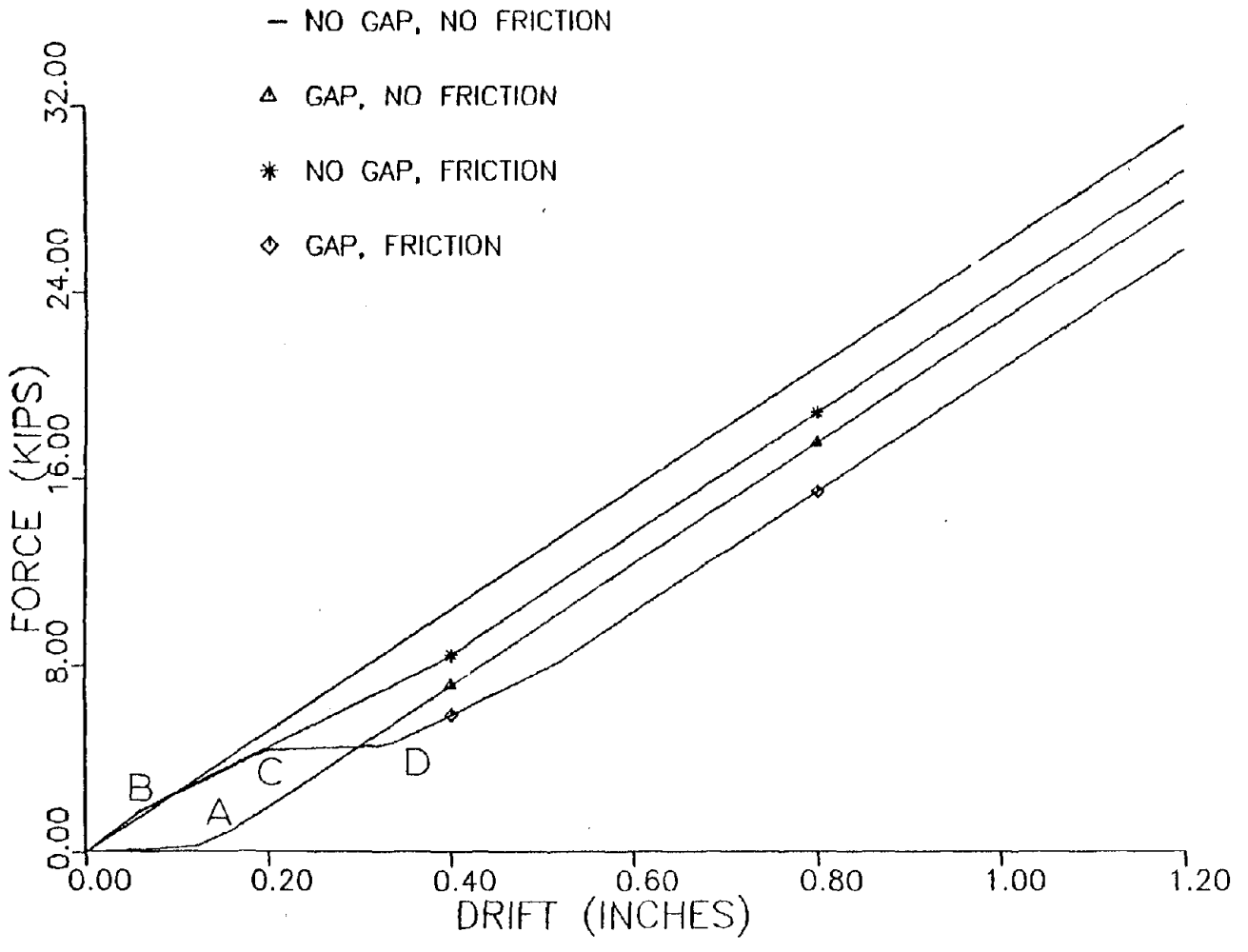

Figure 5.3-13. Maximum Horizontal Force in a Bottom Connection Versus Interstory Drift for the PCI Support Condition Case, Considering Initial Friction in Connections and Oversize Holes with Stiffness for PCI Recommended Supports Remaining Fixed.

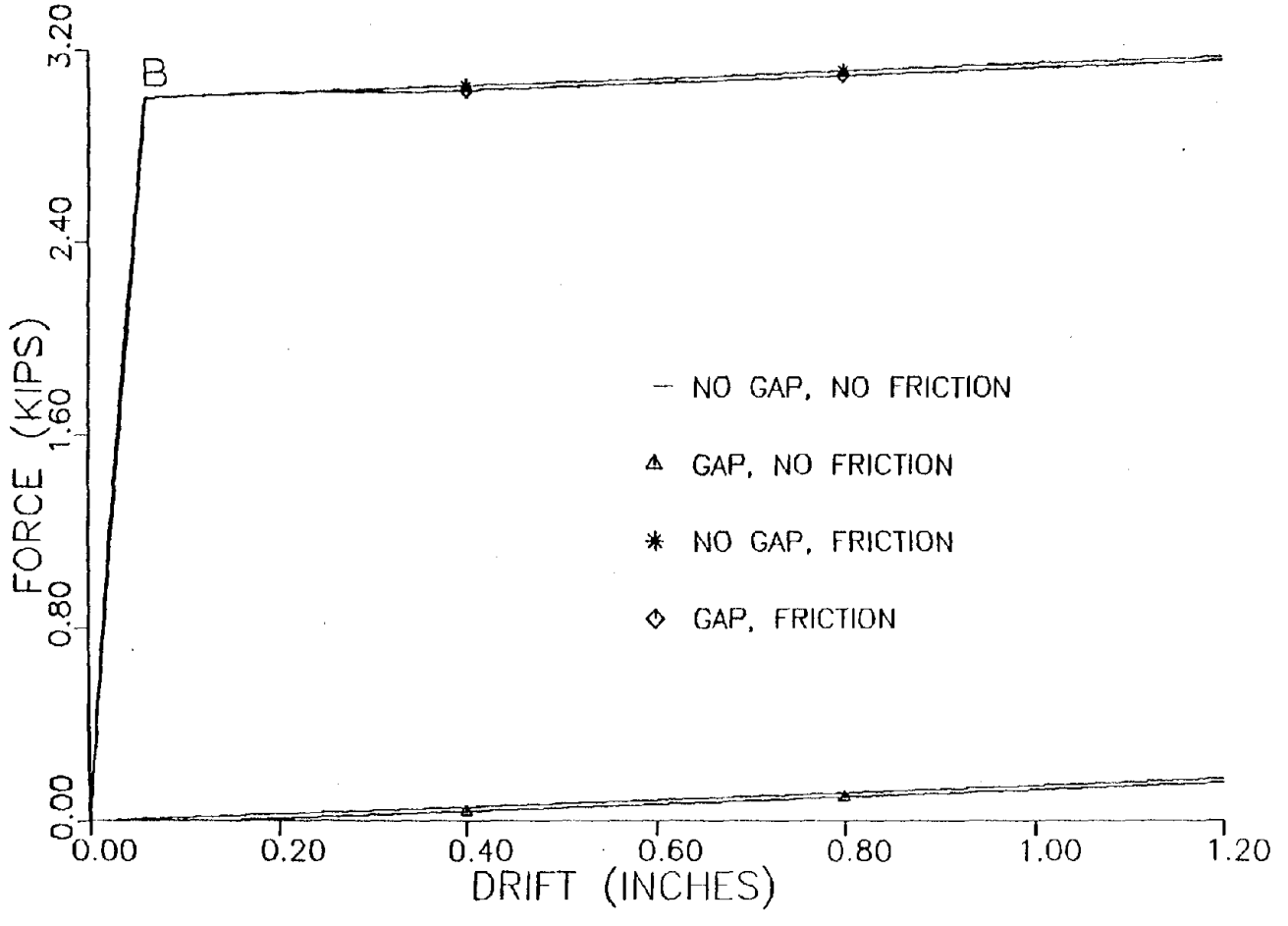

Figure 5.3-14. Maximum Vertical Force in a Top Connection Versus Interstory Drift for the PCI Support Condition Case, Considering Initial Friction in Connections and Oversize Holes with Stiffness for PCI Recommended Supports Remaining Fixed.

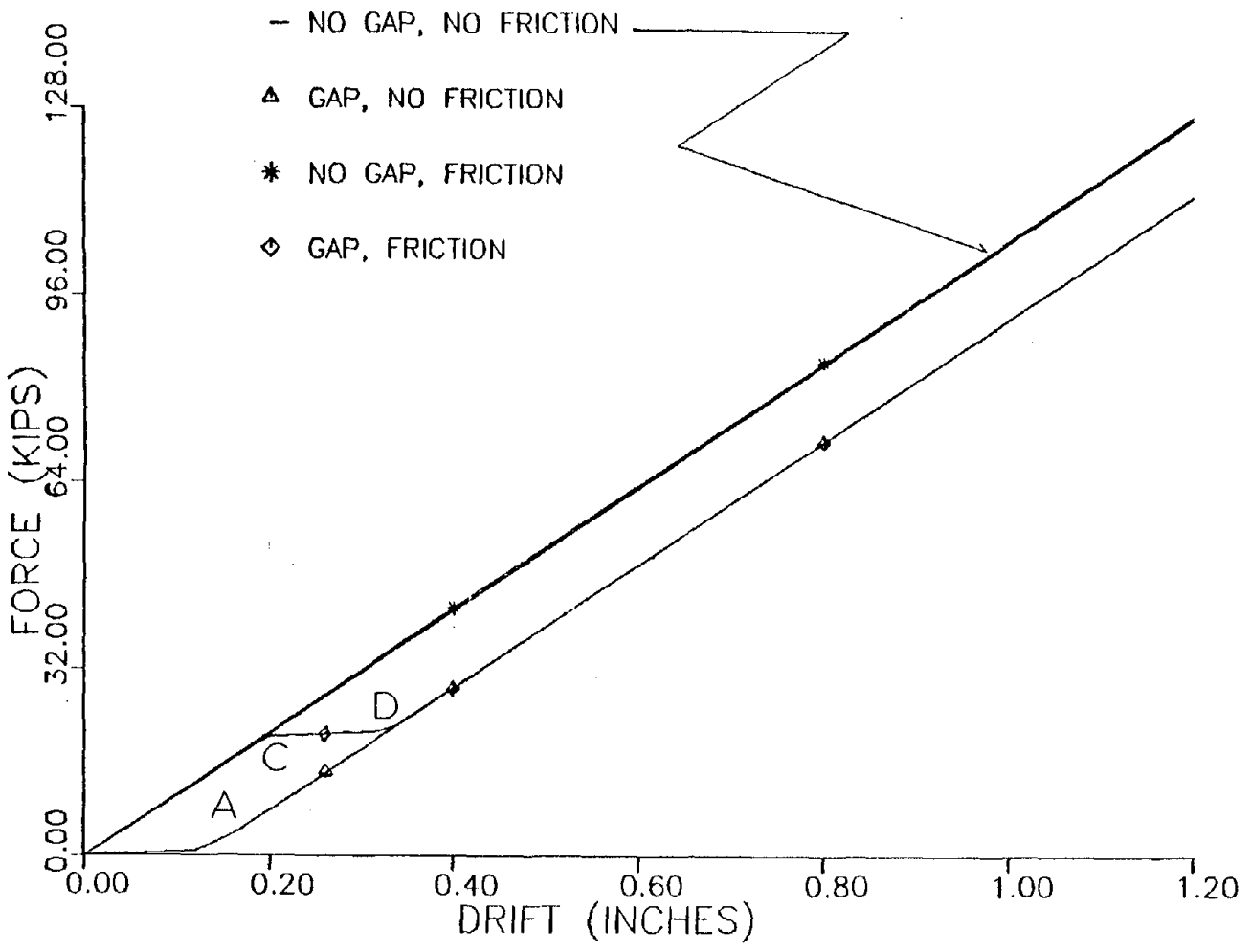

Figure 5.3-15. Maximum Vertical Force in a Bottom Connection Versus Interstory Drift for the PCI Support Condition Case, Considering Initial Friction in Connections and Oversize Holes with Stiffness for PCI Recommended Supports Remaining Fixed.

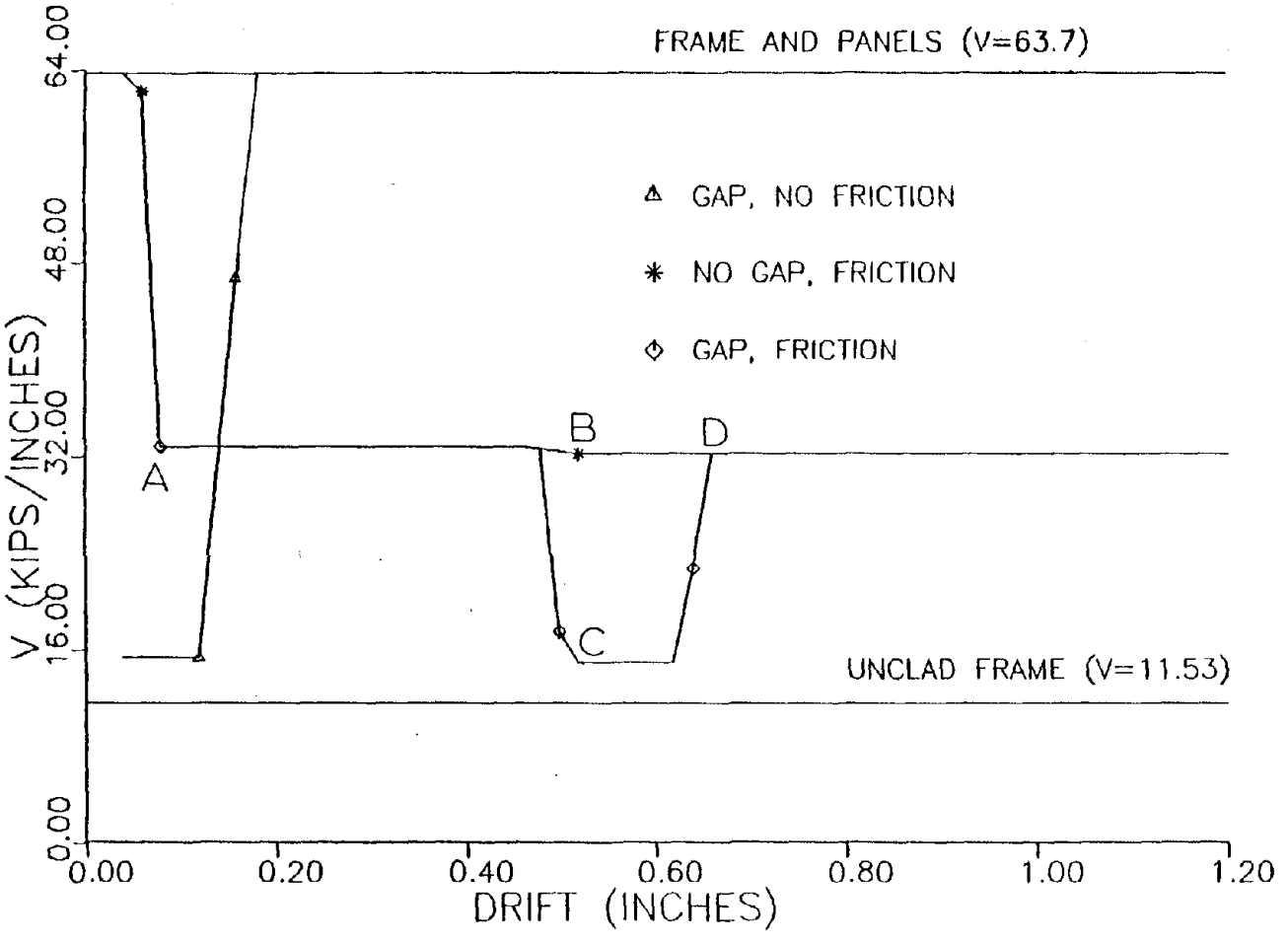

Figure 5.3-16. Interstory Shear Stiffness, V, Versus Interstory Drift for the PCI Support Condition Case, Considering Initial Friction in Connections and Oversize Holes with Stiffness Varied so that Maximum Interstory Shear Stiffness Remained Fixed.

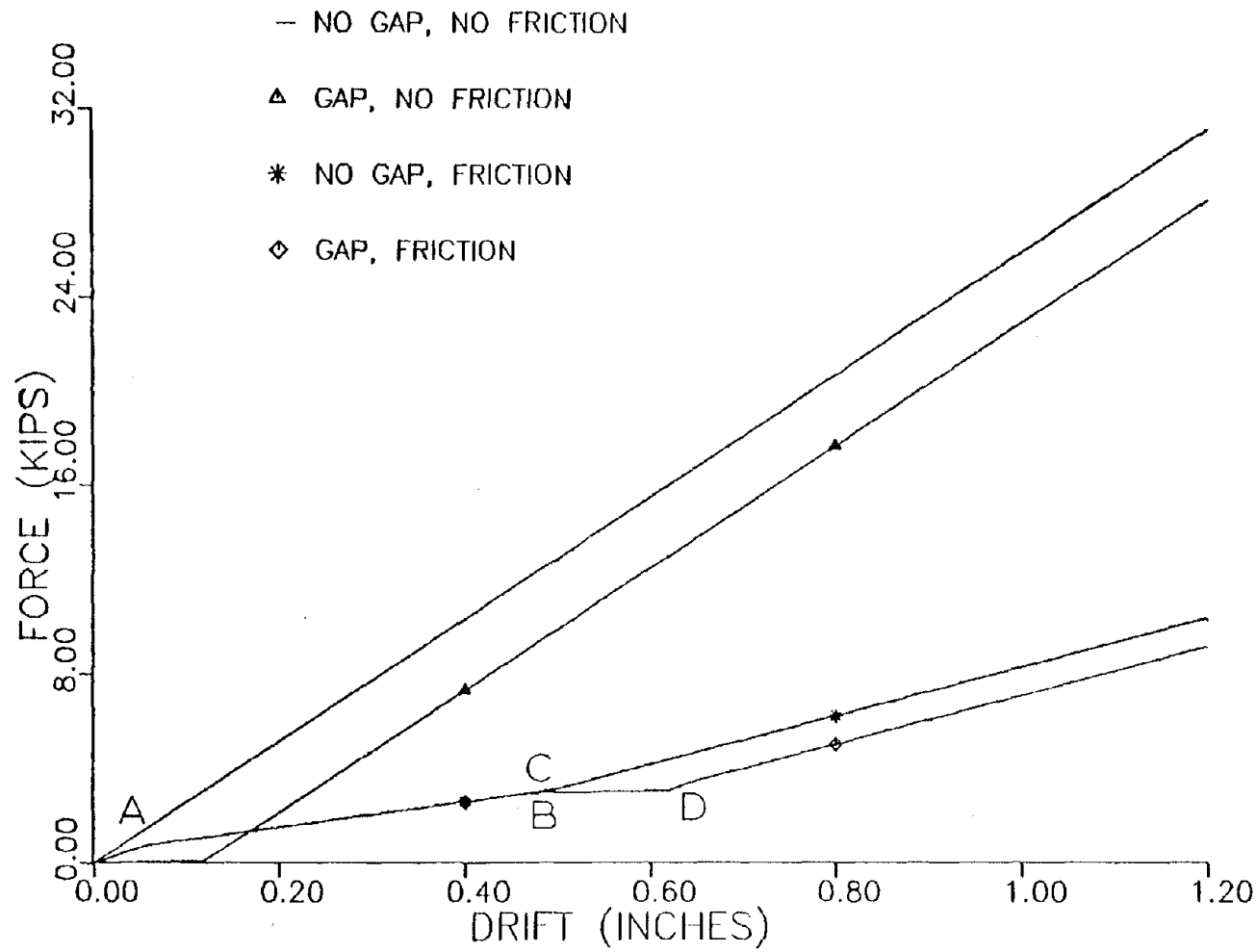

Figure 5.3-17. Maximum Horizontal Force in Top Connections Versus Interstory Drift for the PCI Support Condition Case, Considering Initial Friction in Connections and Oversize Holes with Stiffness Varied so that Maximum Interstory Shear Stiffness Remained Fixed.

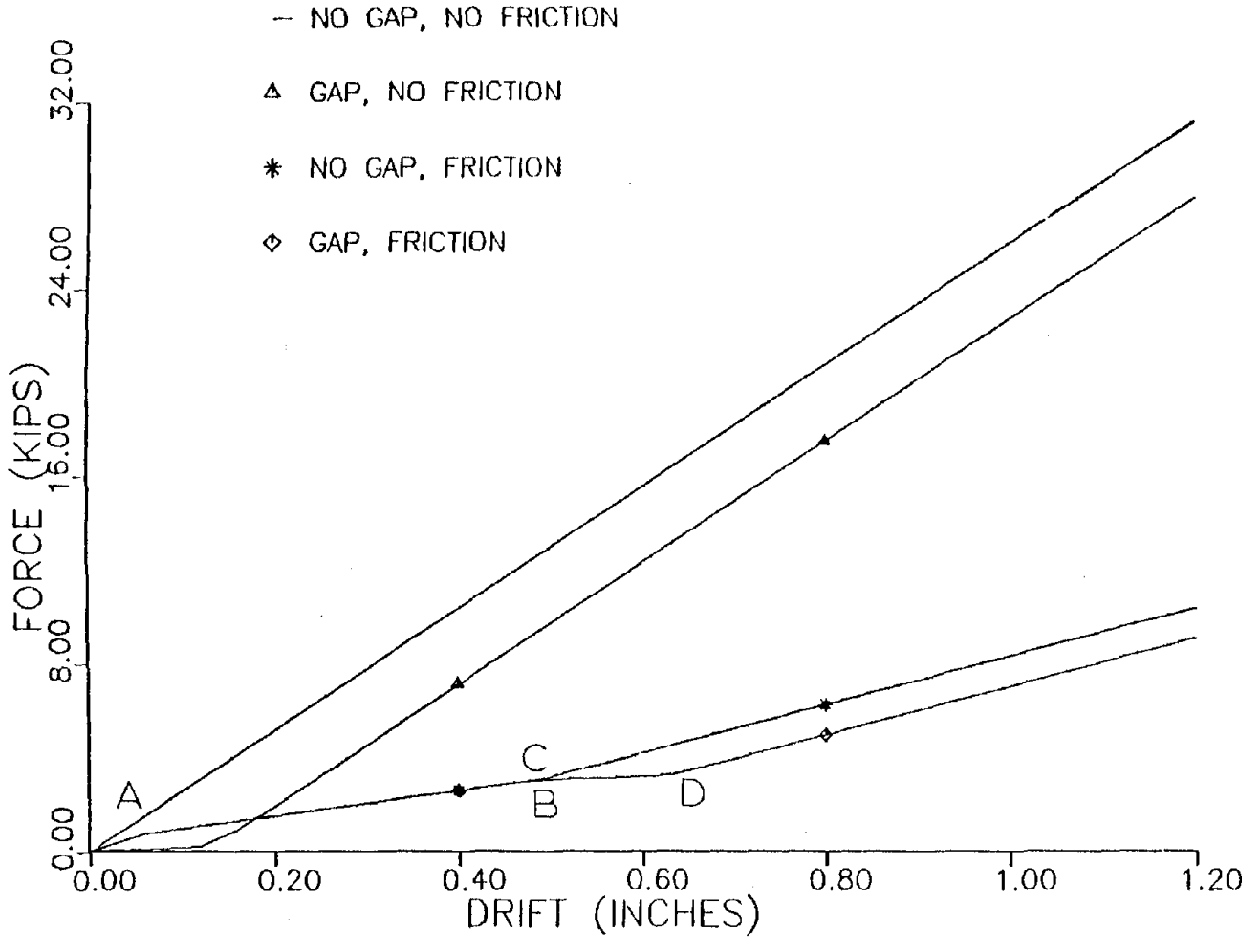

Figure 5.3-18. Maximum Horizontal Force in a Bottom Connection Versus Interstory Drift for the PCI Support Condition Case, Considering Initial Friction in Connections and Oversize Holes with Stiffness Varied so that Maximum Interstory Shear Stiffness Remained Fixed.

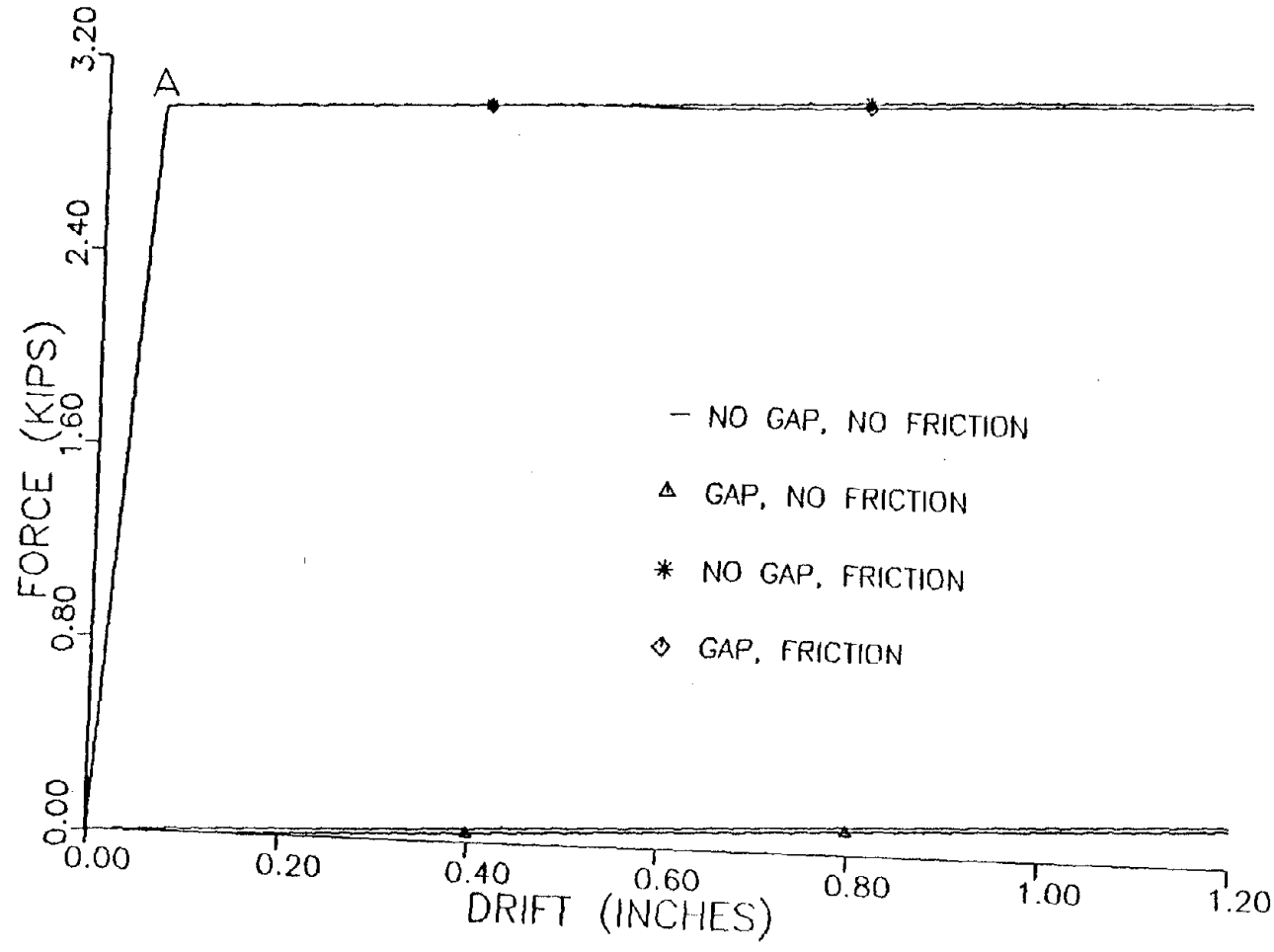

Figure 5.3-19. Maximum Vertical Force in a Top Connection Versus Interstory Drift for the PCI Support Condition Case, Considering Initial Friction in Connections and Oversize Holes with Stiffness Varied so that Maximum Interstory Shear Stiffness Remained Fixed.

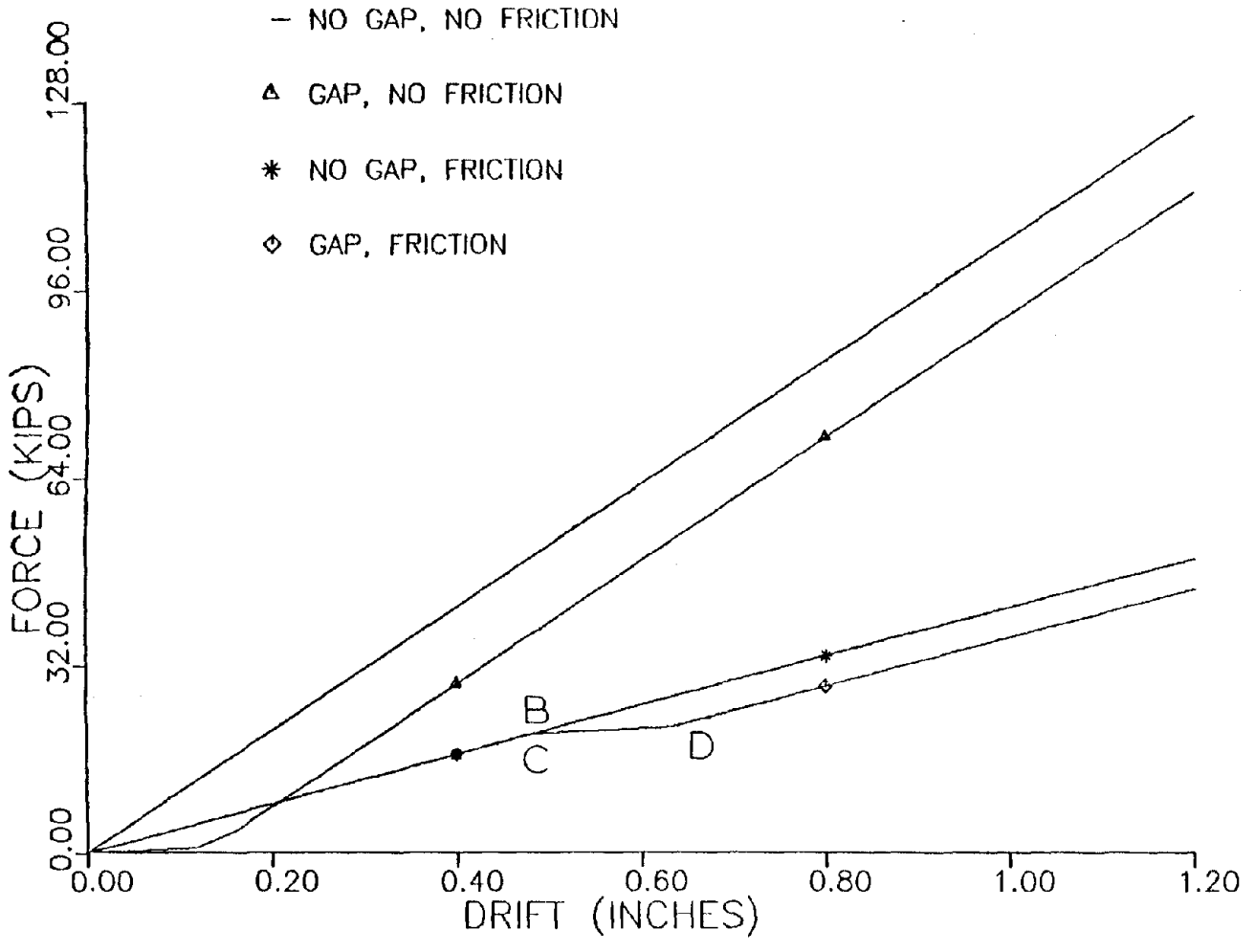

Figure 5.3-20. Maximum Vertical Force in a Bottom Connection Versus Interstory Drift for the PCI Support Condition Case, Considering Initial Friction in Connections and Oversize Holes with Stiffness Varied so that Maximum Interstory Shear Stiffness Remained Fixed.

5.3.4 Slotted Connection Case

The slotted connection case is a modification of the PCI recommended support conditions such that both top connections are free to slide both horizontally and vertically as described by Fig. 4.3.2 presented earlier. The slotted connection panel support system was considered because it was felt to be a more effective way to keep connection forces at moderate levels. Three levels of initial friction were considered when the effects of initial connection friction on both interstory shear stiffness and forces in connections were studied:

1) No initial friction in connections

2) Initial friction of 0.5 kips (2.2 kN)

3) Initial friction of 1.0 kip (4.4 kN)

The friction values above are lower than the values used in the previous two sections which were based on the panelized construction connection study [30]. However, preliminary parameter studies showed that these lower values permitted higher drift levels before ultimate shear capacities in connections were exceeded. Slot lengths were taken to be 0.375 inches (0.95 cm) for horizontal slots and 0.825 inches (2.10 cm) for vertical slots as used for the PCI support condition case and discussed above in Section 5.3.3. All connection spring stiffness values were set at 360 kips/inch (6.3×10^4 kN/m).

The results of these parameter studies are shown in Figs. 5.3-21 to 5.3-25. Inspection of Fig. 5.3-21 revealed that consideration of initial friction resulted in an interstory shear stiffness of 63.7 kips/inch (1.1×10^4 kN/m) initially, but that value decreased to 32.8 kips/inch (5.7×10^3 kN/m) at a drift level of 0.04 inches (0.10 cm,

point A) when initial friction in the vertical direction of top connections was overcome. The interstory shear stiffness of the frame-panel model was again reduced at interstory drifts of 0.12 inches (0.30 cm, point B) and 0.2 inches (0.51 cm, point C) to 14.9 kips/inch (2.6 x 10^3 kN/m) for the cases with an initial friction of 0.5 kips (2.2 kN) and 1 kip (4.4 kN), respectively, as friction was overcome in the horizontal directions of the slotted connections. The interstory shear stiffness was increased to 32.5 kips/inch (5.7 x 10^4 kN/m) when the horizontal slots of top connections closed at 0.56 inches (1.42 cm, point D) for the case with 0.5 kips (2.2 kN) friction and at 0.64 inches (1.63 cm, point E) for the case with 1 kip (4.4 kN) friction. Finally, the case with no initial friction had an initial stiffness of 14.9 kips/inch (2.6 x 10^3 kN/m) which increased to 32.5 kips/inch (5.7 x 10^3 kN/m) as horizontal slots of top connections closed at 0.48 inches (1.22 cm, point F).

Comparison of Figs. 5.3-22 to 5.3-25 with corresponding figures in Section 5.3.3 for the PCI case (see Figs. 5.3-17 to 5.3-20) showed that all connection forces were effectively reduced at a given interstory drift due to the presence of the horizontal slot provided in the top left connection in the present panel support system. However, when the vertical force in a bottom connection was compared with the PCI determined ultimate vertical shear capacity (see Section 5.3.2) of that critical load bearing connection, it was evident that the case of 1 kip (4.4 kN) initial friction limited the amount of drift possible to 0.14 inches (0.36 cm) for the prototype structure.

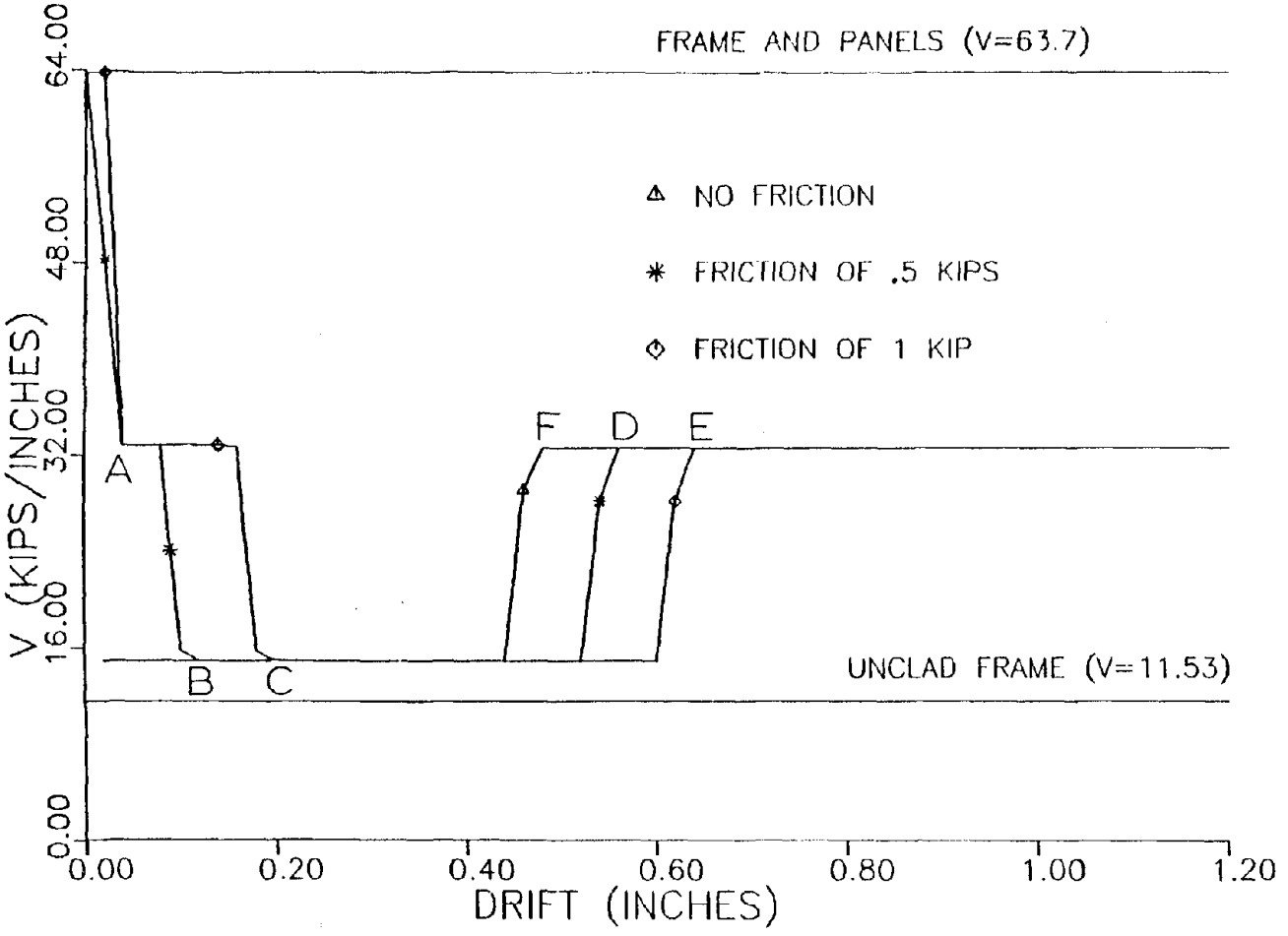

Figure 5.3-21. Interstory Shear Stiffness, V, Versus Interstory Drift for the Slotted Connection Case with Different Levels of Initial Friction in Connections.

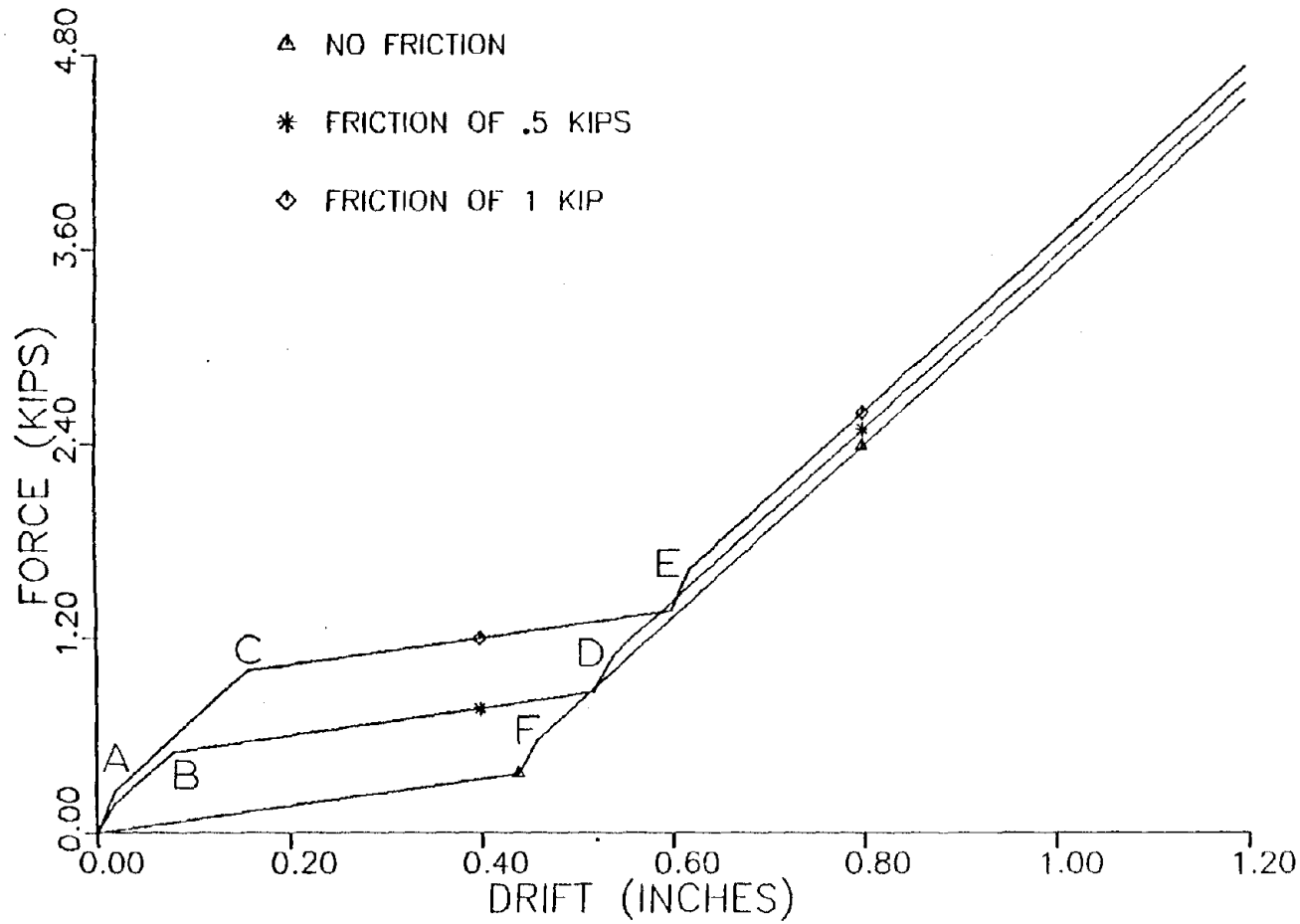

Figure 5.3-22. Maximum Horizontal Force in a Top Connection Versus Interstory Drift for the Slotted Connection Case with Different Levels of Initial Friction in Connections.

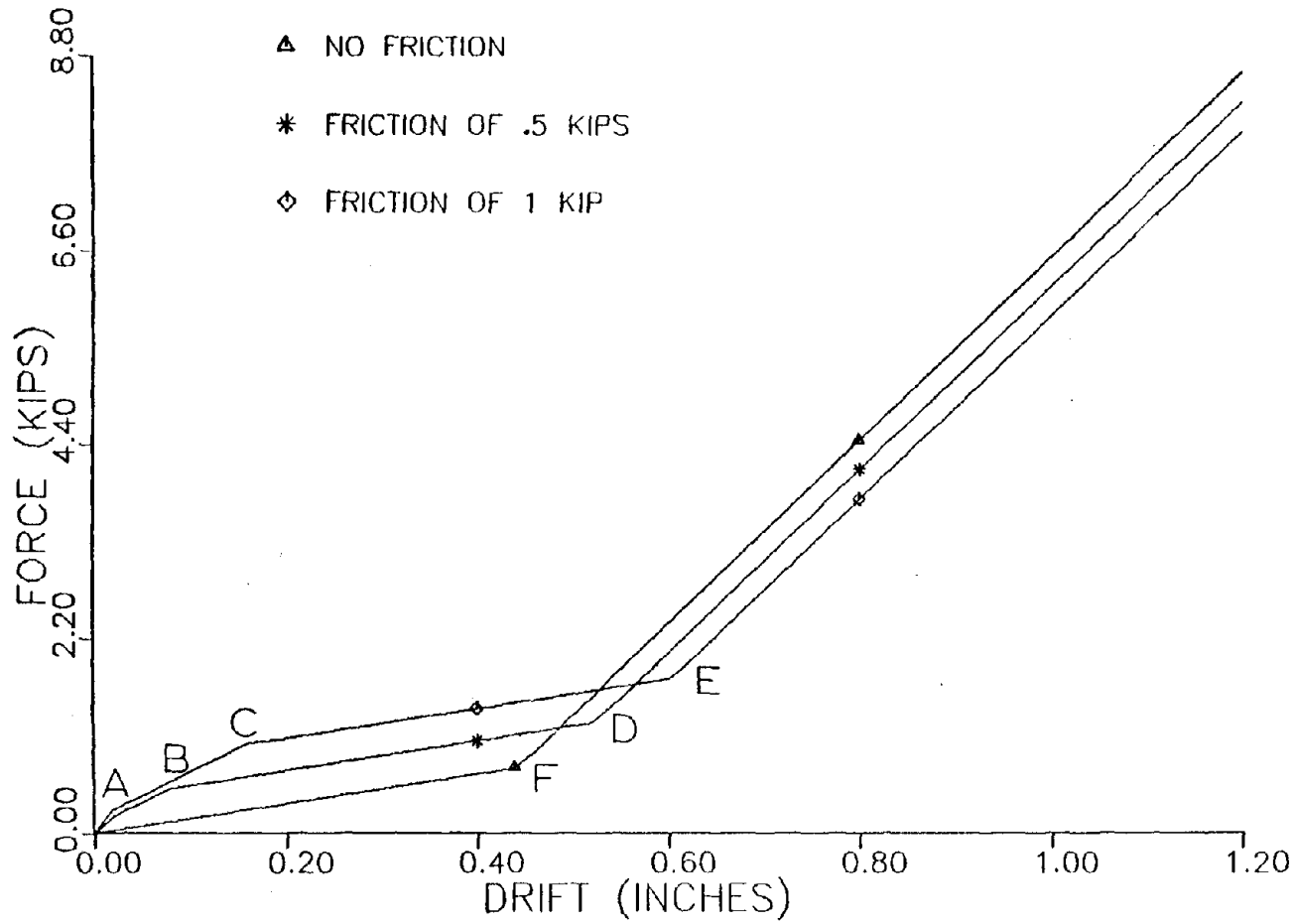

Figure 5.3-23. Maximum Horizontal Force in a Bottom Connection Versus Interstory Drift for the Slotted Connection Case with Different Levels of Initial Friction in Connections.

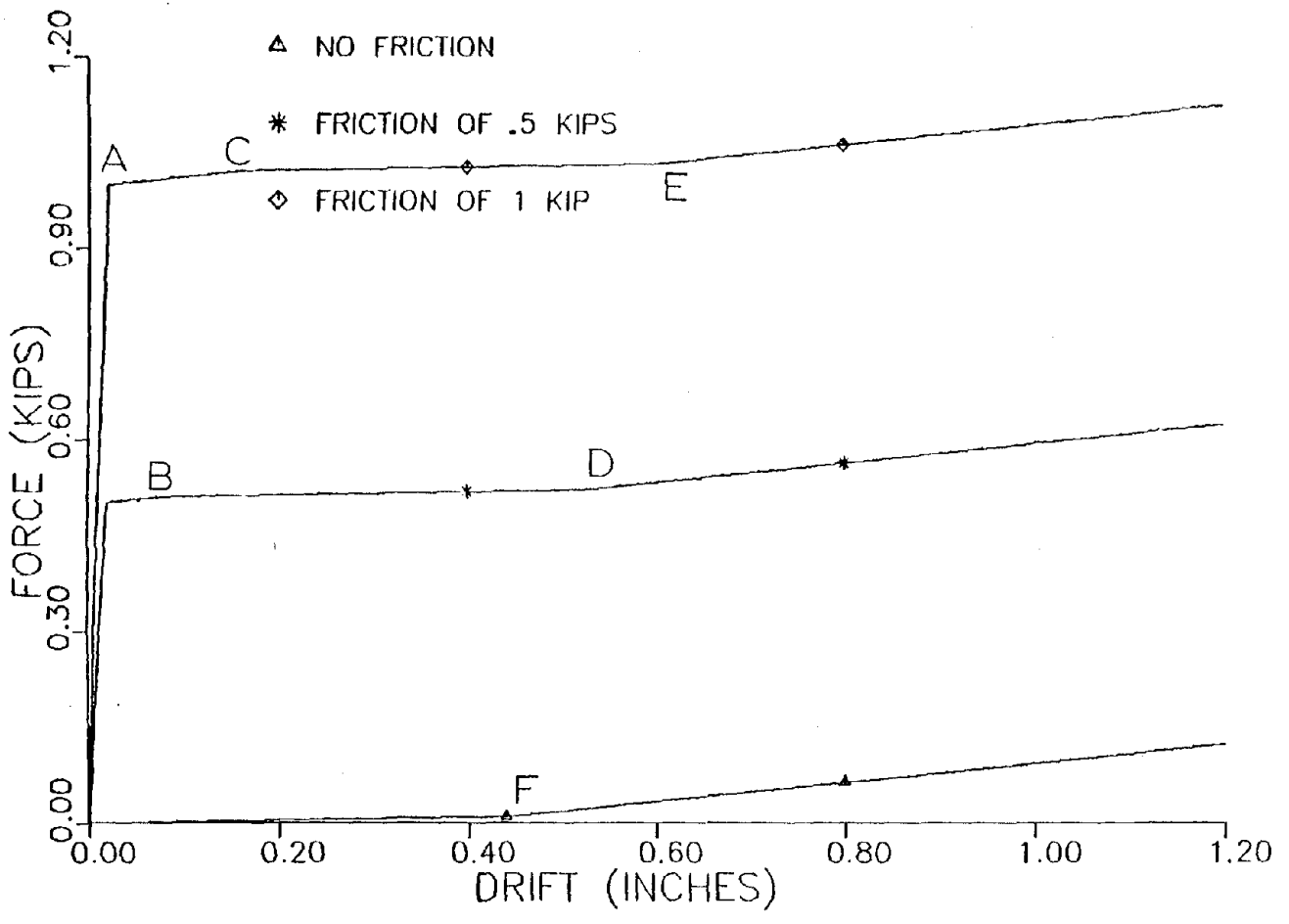

Figure 5.3.24. Maximum Vertical Force in a Top Connection Versus Interstory Drift for the Slotted Connection Case with Different Levels of Initial Friction in Connections.

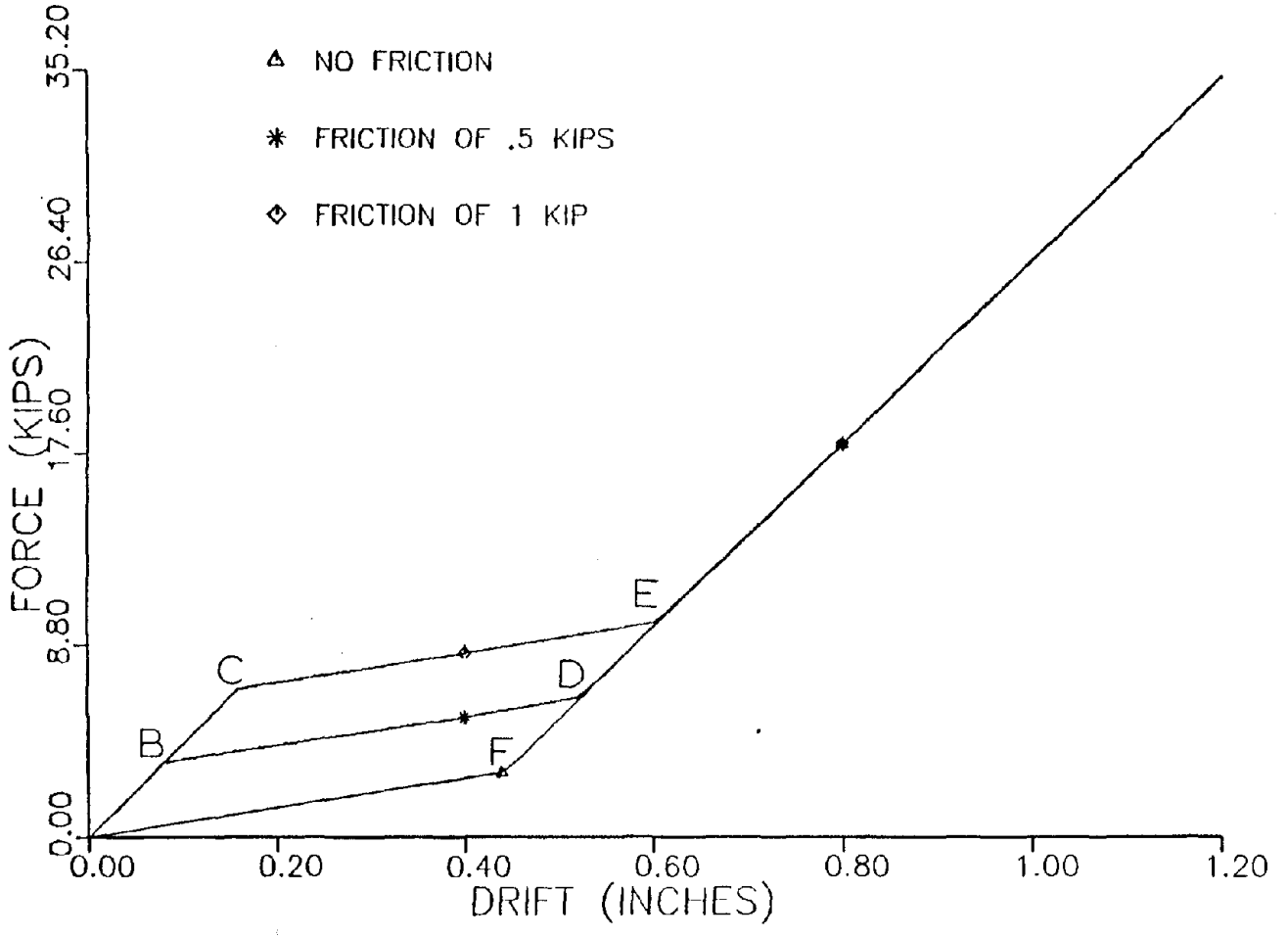

Figure 5.3-25. Maximum Vertical Force in a Bottom Connection Versus Interstory Drift for the Slotted Connection Case with Different Levels of Initial Friction in Connections.

The results of the above studies showed that the slotted connection model, and not the PCI recommended support conditions, was best suited for use when connection forces were to be kept at low levels for static interstory drift motions. Additionally, it was observed that the case with an initial friction of 0.5 kips (2.2 kN) performed better than the case of 1.0 kip (4.4 kN), since an interstory drift of 0.46 inches (1.17 cm) could be accommodated as compared to 0.14 inches (0.36 cm). Subsequently, it was concluded that low initial friction levels were desirable for the frame-panel system being considered.

5.4 Summary

Both linear and nonlinear static response studies were performed using a one-story, one-bay frame-rigid panel model for precast cladding subjected to static interstory displacement. Small displacement, linear elastic behavior was assumed except for the frame-panel connections which were assumed to have a piecewise-linear stiffness behavior. No contact between individual cladding panels was considered. The studies were performed to determine the effects of panel support conditions on the contribution of cladding to overall structure lateral stiffness and on connection force levels in a frame-panel system subjected to interstory displacements. The presence of oversized holes, slots and initial friction in connections was observed to impact both connection forces and interstory shear stiffness values substantially. In all cases, force levels exceeding the ultimate vertical shear capacity of the critical load bearing, bottom panel connections were attained at relatively low drift levels, except for the slotted connection case

discussed in Section 5.3.4. Finally, the PCI recommended support conditions did not protect the panels from forces resulting from inter-story drift motions as intended. The slotted connection case was more effective in limiting force levels than the PCI support case.

6. CONCLUSIONS AND RECOMMENDATIONS FOR FURTHER STUDY

6.1 Conclusions

This research effort focused on an investigation of the interaction between exterior precast concrete cladding and the primary structure of a typical medium highrise office building selected for in-depth study. The building chosen was a 25-story steel frame structure of core construction. A tier building model was employed to represent the primary core structure. The lateral stiffnesses of the exterior frames were developed separately and transformed to the center of rigidity of the floor at each level. Linear behavior of the core and exterior frames was assumed throughout the studies and both composite and noncomposite behavior of floor beams was considered. The unknown lateral stiffness contribution of cladding was defined by an assumed shear stiffness constant representing the interstory shear stiffness of a row of panels between story levels on each structure face. The assumed interstory shear constant was used to form a tridiagonal matrix representing cladding stiffness and the tridiagonal stiffness matrix was then transformed to the common reference point on each floor of the model. The potential stiffness contribution from other nonstructural elements such as interior partitions was not considered in the current study. The mass matrix was formed by lumping tributary mass at the center of mass of each floor. Structure frequencies were measured experimentally, using both ambient and forced vibration testing, and

compared to computed frequencies. The assumed interstory shear stiffness for cladding was adjusted in steps until a match in measured and computed frequencies was obtained. Values of 625 kips/inch (1.1×10^4 kN/m) and 800 kips/inch (1.4×10^4 kN/m) produced the best match for the composite model and the noncomposite model, respectively.

Dynamic response studies of the overall structure model were performed using a variety of different cladding models both linear and nonlinear. An enforced minimum mass eccentricity of 5% was specified in both structure directions as required for combined torsional and translational response studies and the resulting nondiagonal mass matrix was employed in the dynamic response studies.

The studies confirmed reports in the literature which suggest that the exterior facade is a participating structural element, in spite of design assumptions to the contrary. Building frequencies and dynamic responses predicted were found to be appreciably affected by cladding panel effects for the prototype structure. It was shown that translational frequencies were increased by as much as 33% and torsional frequencies by as much as 65% for the composite model. In addition, results showed that it may not always be conservative to neglect the additional stiffening contribution of heavyweight cladding-connection systems. Neglecting cladding effects may be unconservative because dynamic characteristics of the overall structure model can be altered to such a degree by the added stiffness that the sensitivity of the overall structure to certain earthquake loadings may be increased substantially. When results for cases employing the nonlinear cladding models were compared to results for the linear clad and unclad cases,

the linear models were generally found to bracket the nonlinear cases. However, several instances of increased nonlinear response as compared to linear response values were observed. For example, rotational response was found to be amplified more than twenty-fold, for the symmetric structure with initial partial cladding failure, in studies employing the incremental failure model. Either poor construction or prior motion of the building were taken as the reasons for the initial failure. The increase in rotational response was obtained even in the absence of enforced accidental mass eccentricity in the model. These results demonstrated clearly the potential effects of cladding on overall structure response.

In addition to the overall structure response studies, localized panel response studies were performed to examine panel connection force levels and the influence of connection stiffnesses on cladding lateral stiffness. A one-story, one-bay plane frame model with two attached cladding panels was subjected to static interstory displacements. The panels were assumed to be rigid and connections were represented by linear or piecewise-linear spring elements. Small displacement, linear-elastic behavior was assumed except for the cladding panel-to-frame spring connection elements. No panel-to-panel contact was considered in these studies.

Connection forces and interstory shear stiffness values for the local cladding model were found to be affected significantly by the presence of oversized bolt holes, slots in connection angles and initial friction in cladding connection attachments. However, the load bearing bottom connections were observed to exceed their ultimate vertical

shear capacity at relatively low interstory displacement levels in all cases except when both top panel connections were slotted horizontally. PCI recommended procedures for attaching precast concrete cladding panels to exterior building frame members for the purpose of isolating the brittle panels from potentially damaging interstory drift motions were found to be less than fully effective in accomplishing this objective.

6.2 Recommendations for Further Study

The results presented in Chapters 2 to 4 demonstrate the potential influence of cladding stiffness on structure dynamic properties and response to moderate earthquake ground motion. Due to increasing construction costs and the widespread use of heavyweight precast concrete facades for modern buildings, the potential stiffness contribution from the curtain wall needs further study. The influence of other nonstructural elements, such as interior partitions which were not considered in the present study, also needs to be investigated. In particular, laboratory tests should be performed to define the actual cyclic behavior of a full-scale cladding panel with a variety of connection details representative of those used in modern practice. The force-deformation relationships presented in Chapter 4 were felt to represent reasonable first approximations to the possible behavior of selected heavyweight cladding systems. However, measured test data together with updated and improved analytical models for the cladding need to be developed for follow-on studies. A desirable goal of such follow-on studies would be the exploration of the potential of cladding as a lateral stiffening element which could also provide an added source of damping in modern building construction.

The present studies considered only two earthquake loadings. Subsequent investigations should apply other earthquake records possessing a variety of different durations and spectral characteristics to study their effects on overall structure response. The difference in structure response characteristics for the two loadings considered in this study demonstrates the importance of considering other earthquake loadings in follow-on investigations.

Damping was specified to be 5% simple modal damping in the current studies. When the nonlinear cladding models were considered, the damping matrix was computed based on the stiffness of the linear clad case and was not updated as cladding stiffness levels changed during structure response. Future studies which investigate proper damping levels for cladding and its connections at different response levels are needed. Damping levels obtained from full-scale laboratory experiments of actual cladding elements would provide valuable data for use in subsequent response studies. It should be noted that a comparison of overall structure response levels for the undamped and 5% damped cases revealed that damping levels may have more effect than cladding effects on overall structural response; this comparison of the relative importance of damping and cladding stiffness must be substantiated by further investigation.

The current investigation was only concerned with displacement response in the dynamic response studies of the overall structure. Further studies should be conducted to investigate the effects of added cladding stiffness which could result in significant force level changes in primary structural framing members.

The rigid panel model employed in the localized panel response studies in Chapter 5 showed the importance of panel support conditions and panel connection stiffnesses on member and connection forces and response. Laboratory studies are needed to determine actual panel connection properties including possible ductile characteristics and/or ways of enhancing ductile behavior of cladding. The validity of the rigid panel assumption should also be studied in these experiments. Future studies should consider panel-to-panel contact in the model and also expand the one-story-, one-bay frame to include the possible interaction effects of adjacent bays and stories. Nonlinear dynamic analyses of the rigid panel model may also provide useful additional information.

Ultimately, investigations of cladding performance are expected to lead to increased knowledge of panel and connection forces for various levels of interstory motion and the potential lateral stiffening contribution of cladding. On this basis, improvements in design of cladding for wind and earthquake loadings will result, leading to greater safety and economy in modern building construction.

REFERENCES

1. "Accessories and Chemicals for Concrete Construction," Product Information Guide, Dayton Sure-Grip and Shore Company, Miamisburg, Ohio, 1978.

2. Adeli, H., "Solution Techniques for Linear and Nonlinear Dynamics of Structures Modeled by Finite Elements," Technical Report No. 23, The John A Blume Earthquake Engineering Center, Stanford University, Stanford, California, June 1976.

3. Anicic, D., Zamolo, M., and Soric, Z., "Experiments on Non-Structural Partition Walls Exposed to Seismic Forces," Proceedings, Seventh World Conference on Earthquake Engineering, Istanbul, Turkey, September 8-13, 1980, Vol. 6, pp. 144-150.

4. Becker, J. M., Llorente, C., and Mueller, P., "Seismic Response of Precast Concrete Walls," International Journal of Earthquake Engineering and Structural Dynamics, Vol. 8, No. 6, November-December 1980, pp. 545-564.

5. Bryson, J. O., and Gross, D., "Techniques for the Survey and Evaluation of Live Floor Loads and Fire Loads in Modern Office Buildings," NBS Building and Materials and Structures Report, 1971.

6. Clough, R. W., and Penzien, J., Dynamics of Structure, McGraw-Hill, 1975.

7. Desai, C. S., and Abel, J. F., Introduction to the Finite Element Method, Van Nostrand Reinhold, New York, 1972.

8. Dubas, P., "Interaction of Structural Elements with Cladding," Planning and Design of Tall Buildings, Proceedings of the 1972 ASCE-IABSE International Conference, Vol. 2, No. 17-5, ASCE, New York, pp. 675-686.

9. Eaton, K. J., "Cladding and the Wind," Journal of the Structural Division, ASCE, Vol. 102, No. ST5, Proc. Paper 12114, May 1976, pp. 1043-1058.

10. Emkin, L. Z., et al., GTSTRUDL User's Manual, Second Edition, GTICES Systems Laboratory, School of Civil Engineering, Georgia Institute of Technology, Atlanta, Georgia, August 1981.

11. "Facades: Errors Can Be Expensive," Engineering-News Record, Vol. 204, No. 5, January 24, 1980, pp. 30-34.

12. Gere, J. M., Moment Distribution, D. Van Nostrand, Princeton, New Jersey, 1963.

13. Gjelsvik, A., "Interaction Between Frames and Precast Panel Walls," Journal of the Structural Division, ASCE, Vol. 100, No. ST2, February 1973, pp. 405-426.

14. Glogau, O. A., "Damage Control in New Zealand Public Buildings Through Separation of Non-Structural Components," Proceedings, Sixth World Conference on Earthquake Engineering, Sarita Prakashan, Meerut, India, Vol. 5, 1977, pp. 43-48.

15. Goodno, B. J., Will, K. M., and Palsson, H., "Effect of Cladding on Building Response to Moderate Ground Motion," Proceedings, Seventh World Conference on Earthquake Engineering, Istanbul, Turkey, September 8-13, 1980, Vol. 7, pp. 449-456.

16. Goodno, B. J., and Palsson, H., "Torsional Response of Partially-Clad Structures," Proceedings, Conference on Earthquakes and Earthquake Engineering: The Eastern U. S., September 14-16, 1981, Knoxville, Tennessee, Vol. 2, pp. 859-877.

17. Gram, K. G., "The Shear Effects of Precast Cladding Panels on Multi-story Buildings," M.S.C.E. Special Problem Report, School of Civil Engineering, Georgia Institute of Technology, Atlanta, Georgia, June 1976.

18. Henry, R. M., "Cladding-Frame Interaction of a Reinforced Concrete Building," Ph.D. Thesis, Department of Civil and Urban Engineering, University of Pennsylvania, Pennsylvania, 1980.

19. Higgins, T. R., et al., Structural Design of Tall Buildings, Monography on Planning and Design of Tall Buildings, ASCE, 1979.

20. Kahn, L. F., and Hanson, R. D., "Infilled Walls for Earthquake Strengthening," Journal of the Structural Division, ASCE, Vol. 105, No. ST2, Proc. Paper 14364, February 1979, pp. 283-296.

21. Kulka, F., Lin, T. Y., and Yang, Y. C., "Prestressed Concrete Building Construction Using Precast Wall Panels," PCI Journal, Vol. 20, No. 1, January-February 1975, pp. 62-73.

22. LeBoeuf, P. M. S., "Dynamic Cladding-Structure Interaction in High-rise Buildings," M.S.C.E. Thesis, School of Civil Engineering, Georgia Institute of Technology, Atlanta, Georgia, September 1980.

23. "Market Frowns on Aluminum Faces," Engineering News-Record, Vol. 206, No. 9, February 26, 1981, p. 18.

24. Martin, L. D., and Korkosz, W. J., "Connections for Precast, Prestressed-Concrete Buildings," Technical Report, The Consulting Engineers Group Inc., Glenview, Illinois, 1981.

25. McCue, G. M., et al., "Building Enclosure and Finish Systems: Their Interaction with the Primary Structure During Seismic Action," Proceedings, U. S. National Conference on Earthquake Engineering, Ann Arbor, Michigan, June 18-20, 1975, pp. 235-244.

26. Meyyappa, M., Palsson, H., and Craig, J. I., "Modal Parameter Estimation for a Highrise Building Using Ambient Response Data Taken During Construction," Proceedings, Second Speciality Conference on Dynamic Response of Structures: Experimentation, Observation, Prediction, and Control, Atlanta, Georgia, January 15-16, 1981, pp. 141-151.

27. Meyyappa, M., "Identification of Cladding-Structure Interaction in Highrise Buildings Using Parameter Estimation Methods," Ph.D. Thesis, School of Aerospace Engineering, Georgia Institute of Technology, Atlanta, Georgia, 1982.

28. Mueller, P., and Becker, J. M., "Seismic Behavior of Precast Walls Coupled Through Vertical Connections," Proceedings, Seventh World Conference on Earthquake Engineering, Istanbul, Turkey, September 8-13, 1980, Vol. 7, pp. 23-30.

29. Oppenheim, I. J., "Dynamic Behavior of Tall Buildings with Cladding," Proceedings, Fifth World Conference on Earthquake Engineering, Rome, Italy, June 1973, pp. 2769-2773.

30. Osborn, A. E. N., Meinhert, D. F., and Hanson, J. M., "Cyclic and Monotonic Shear Tests on Connections Between Precast Concrete Panels," WJE No. 77578, Wiss, Janney, Elstner and Associates, Inc., Northbrook, Illinois, 1981, 133 pp.

31. Pall, A. S., and Marsh, C., "Optimum Seismic Resistance of Large Panel Structures Using Limited Slip Bolted Joints," Proceedings, Seventh World Conference on Earthquake Engineering, Istanbul, Turkey, September 8-13, 1980, Vol. 4, pp. 177-184.

32. Palsson, H., "Influence of Discrete Dampers on Seismic Response of a Free-Standing Tower," M.S.C.E. Special Problem Report, School of Civil Engineering, Georgia Institute of Technology, Atlanta, Georgia, December 1977.

33. Palsson, H., "Cladding-Structure Interaction Case Study for a High-rise Office Tower," Student Paper Competition, AIAA/ASCE/ASME/AHS Symposium, Dayton, Ohio, October 3, 1980.

34. Palsson, H., and Goodno, B. J., "A Degrading Stiffness Model for Precast Concrete Cladding," Proceedings, Seventh European Conference on Earthquake Engineering, Athens, Greece, September 20-25, 1982.

35. PCI Manual for Structural Design of Architectural Precast Concrete, PCI Publication No. MNL-121-77, Prestressed Concrete Institute, 20 North Wacker Drive, Chicago, Illinois, 1977.

36. "PCI Design Handbook, Precast and Prestressed Concrete," Prestressed Concrete Institute, Chicago, Illinois, First Edition, 1971.

37. Pless, D. G., "Static and Dynamic Response of Precast Cladding to Interstory Drift," M.S.C.E. Special Problem Report, School of Civil Engineering, Georgia Institute of Technology, Atlanta, Georgia, March 1982.

38. Powell, G., and Schricker, V., "Ductility Demands on Joints in Large Panel Structures," presented at the ASCE Fall Convention and Exhibit held in San Francisco, October 17-21, 1977 (Meeting Preprint No. 3022, 21 pp.).

39. Sack, R. L., et al., "Seismic Response of Precast Curtain Walls in Highrise Buildings," Final Project Report, NSF Award Number PFR-7720884, Department of Civil Engineering, University of Idaho, Moscow, Idaho, January 1981.

40. Saiidi, M., "Hysteresis Models for Reinforced Concrete," Journal of the Structural Division, ASCE, Vol. 108, No. ST5, Proc. Paper 17075, May 1982, pp. 1077-1087.

41. Sharpe, R. L., "Seismic Design of Nonstructural Elements," Proceedings of the International Conference on Planning and Design of Tall Buildings, ASCE-IABSE Joint Committee, Bethlehem, Pennsylvania, August 21-26, 1972, Vol. Ia-12, pp. 1143-1148.

42. Sherwood, G. C., "Effects of Precast Concrete Panels on the Stiffness of the 100 Colony Square Building," M.S.C.E. Special Problem Report, School of Civil Engineering, Georgia Institute of Technology, Atlanta, Georgia, August 1975.

43. Spencer, R. A., "The Earthquake Response of Prestressed Concrete Structures with Nonstructural Interfloor Elements," Proceedings, First Canadian Conference on Earthquake Engineering, Vancouver, British Columbia, May 1971, pp. 354-366.

44. Steidel, R. F., Jr., An Introduction to Mechanical Vibrations, First Edition, John Wiley and Sons, New York, 1971.

45. "Symposium Tags Ignorance as Root of Facade Problems," Engineering News Record, Vol. 204, No. 24, December 11, 1980, pp. 17-19.

46. Tentative Provisions for the Development of Seismic Regulations for Buildings, ATC Publication ATC 3-06, Applied Technology Council, Palo Alto, California, June 1978.

47. Timoshenko, S., Young, D. H., and Weaver, W., Jr., Vibration Problems in Engineering, Fourth Edition, John Wiley and Sons, New York, 1974.

48. Uchida, N., Aoygai, T., Kawamura, M., and Nakagawa, K., "Vibration Test of Steel Frame Having Precast Concrete Panels," Proceedings, Fifth World Conference on Earthquake Engineering, Rome, Italy, June 1973, pp. 1167-1176.

49. Uniform Building Code, International Conference of Building Officials, Whittier, California, 1982 Edition.

50. Weaver, W., Jr., and Nelson, M. F., "Three-Dimensional Analysis of Tier Buildings," Journal of the Structural Division, ASCE, Vol. 92, No. ST6, Proc. Paper 5019, December 1966, pp. 385-404.

51. Weaver, W. Jr., Nelson, M. F., and Manning, T. A., "Dynamics of Tier Buildings," Journal of the Engineering Mechanics Division, ASCE, Vol. 94, No. EM6, Proc. Paper 6293, December 1968, pp. 1455-1474.

52. Weidlinger, P., "Shear Field Panel Bracing," Journal of the Structural Division, ASCE, Vol. 99, No. ST7, Proc. Paper 9870, July 1973, pp. 1615-1631.

53. Will, K. M., Goodno, B. J., and Saurer, G. "Dynamic Analysis of Buildings with Precast Cladding," Proceedings, ASCE Seventh Conference on Electronic Computation, St. Louis, Missouri, August 6-8, 1979, pp. 251-264.

APPENDIX A

In the interest of computational and storage efficiency, a special purpose computer program was written for computation of dynamic response for each of the different cladding models rather than assembling one large program capable of handling all of the different cases. Table A-1 lists the names of the various cladding models used in the overall structure model together with the names of the computer programs employed to compute structure dynamic response for each case. Program "DLETR" is listed in reference [32]. Only program "HDLETR" is provided in this appendix due to space limitations. Program HDLETR is listed because it was felt to be representative of the other programs and of the level of programming effort involved.

(Pages 386 to 403, inclusive, consist of the listing of program HDLETR and are not reproduced in this report.)

Table A-1. Cladding Models Employed and Corresponding Computer Programs Used for Computation of Dynamic Response.

Cladding Model	Computer Program
Linear Model	DLETR
Incremental Failure Model	IDLETR
Slotted Connection Model	SDLETR
Degrading Hysteresis Model	HDLETR
Brake Pad Model	BDLETR

APPENDIX B

The computer program "SACLAD" listed in reference [37] was modified in this study to accommodate piecewise-linear behavior of panel-to-frame connections. This modified computer program called "NACLAD" is listed below.

(Pages 405 to 426, inclusive, consist of the listing of program SACLAD and are not reproduced in this report.)

Part II

IDENTIFICATION OF CLADDING-STRUCTURE INTERACTION IN HIGHRISE BUILDINGS USING PARAMETER ESTIMATION METHODS

TABLE OF CONTENTS

NOMENCLATURE

A, $\bar{A}$	-	Amplitude
A_i	-	Participation factor for mode i
$b[]$	-	Bias in an estimated quantity
$C_i(\tau)$	-	Autocorrelation function of a random process i
C_{ij}	-	Damping element in the system damping matrix
c_i	-	Damping factor for mode i
$E[]$	-	Expected value of []
e_i	-	Difference between the measured and the analytical values of the ith dependent variable
$F_i(\theta)$	-	Computed value of the ith dependent variable
f	-	Frequency in Hertz
f_o	-	Natural frequency of a single degree-of-freedom system
f_i	-	Natural frequency of mode i for a multidegree-of-freedom system
f_a	-	Lower frequency limit for a swept sine wave
f_b	-	Upper frequency limit for a swept sine wave
f_m	-	Maximum frequency of interest
f_N	-	Nyquist frequency
f_s	-	Sampling rate
$G_{ii}(f)$, $G_{ii}(\omega)$	-	Power spectral density function for a random process i
$G_{ij}(f)$, $G_{ij}(\omega)$	-	Cross-spectral density function between processes i and j
$\tilde{G}_{ii}$, $\tilde{G}_{ij}$	-	Raw estimates of power and cross-spectral density functions
$\hat{G}_{ii}$, $\hat{G}_{ij}$	-	Smoothed estimates of power and cross-spectral density functions

NOMENCLATURE Cont'd.

g_i	-	ith component of the gradient vector
$H(\omega)$, $H(f)$	-	Frequency response function
$\hat{H}(f)$	-	Estimate of frequency response function
J_{ij}	-	Element in the Jacobian matrix
K_{ij}	-	Stiffness element in the system stiffness matrix
k_i	-	Stiffness coefficient for mode i
$L(\theta)$	-	Likelihood function
M_{ij}	-	Mass element in the system mass matrix
M^i	-	ith spectral moment
m_i	-	Mass coefficient for mode i
N	-	Number of data points in a digitized record
n	-	Number of degrees of freedom
n_d	-	Number of nonoverlapping averages
P()	-	Probability density function
$P(Y/\theta)$	-	Conditional probability density function of the observations given the parameters
p	-	Number of parameters to be estimated
r	-	Sample size
S_{ij}	-	Element in the Hessian or the second derivative matrix
T	-	Record length or sweep time
t	-	Time in seconds
V_e	-	Covariance of the errors
V_F	-	Covariance of the analytical values
V_y	-	Covariance of the measured values

NOMENCLATURE Cont'd.

V_θ	-	Covariance of the parameters
$W(f)$	-	Fourier transform of the weighting function $w(t)$
$w(t)$	-	Window or weighting function in the time domain
$X(\omega)$, $X(f)$	-	Fourier transform of the input
$x(t)$	-	Input
$x_1(t)$, $x_2(t)$	-	Random processes
$Y(\omega)$, $Y(f)$	-	Fourier transform of the output
y, $y(t)$	-	Output
$y_1(t)$, $y_2(t)$	-	Random processes
$Z_i(\omega)$	-	Fourier transform of the ith modal response
$z_i(t)$	-	ith modal response
Δf	-	Frequency interval
Δf_o	-	Half-power bandwidth
Δt	-	Time or sampling interval
$\gamma^2_{ij}(f)$	-	Coherence function between random processes i and j
ε_b	-	Normalized bias error
ε_r	-	Normalized random error
$\varepsilon_1, \varepsilon_2, \varepsilon_3, \varepsilon_4, \varepsilon_5$	-	Small positive constants
θ_i	-	ith parameter to be estimated
$\bar{\theta}_i$, μ_i	-	mean of θ_i
λ_i	-	ith eigenvalue
μ	-	Marquardt parameter
ξ	-	Step size parameter

NOMENCLATURE Cont'd.

ρ	-	Damping ratio
ρ_i	-	Damping ratio for mode i of a multidegree-of-freedom system
$\sigma[]$	-	Standard deviation
τ	-	Time
$\tau_{\theta_i \theta_j}$	-	Correlation coefficient for parameters θ_i and θ_j
ϕ_{ij}	-	ith mode shape element of mode j
ψ	-	Objective or cost function
ω	-	Frequency in radians per second
ω_o	-	Natural frequency of a single degree-of-freedom system
ω_i	-	Natural frequency of mode i
ω_p	-	Peak frequency in the output power spectral density function
$\Delta\omega_o$	-	Half-power bandwidth

SUMMARY

The influence of cladding on the dynamic response of two high-rise buildings is investigated by studying its effect on the modal parameters. Ambient tests conducted in one of the buildings at different stages of construction during installation of cladding are described. The estimation of modal parameters from output data is carried out by curve fitting the analytical form of magnitude of the frequency response function to the measured response Fourier amplitude spectra, using the least squares criterion. An attempt is made to correlate the observed changes in the modal parameters with construction to the amount of clading that had been installed on various test dates. It is noted that the effect of cladding could be to increase the frequencies of the higher modes slightly.

The second building is used to evaluate the cladding performance analytically. First, transient forced vibration tests are carried out employing a rectilinear electrohydraulic shaker. The modal parameters are determined from transfer functions measured using swept sine waveforms as input. The experimental results are then utilized along with an a priori finite element model of the building to compute the cladding stiffness. The total stiffness matrix is assumed to be the sum of the stiffness matrices of different components including cladding, multiplied by certain stiffness correction parameters. These stiffness parameters are estimated using

a weighted least squares approach. Standard estimation procedures, namely ordinary least squares, maximum likelihood and Bayesian techniques, are also used and the results from different methods are compared.

II-1

1.0 INTRODUCTION

1.1 Background

The field of structural dynamics has attracted a considerable amount of interest and attention from researchers, engineers and others involved in structural design and construction. This is rightly so, since dynamic response often plays a critical role in the ultimate failure of a structural component or the structure itself. Its importance cannot be overemphasized in the case of aircraft components subject to unsteady aerodynamic loadings, machine tools and assemblies subject to mechanical vibrations and civil engineering structures such as buildings subject to environmental and seismic loadings. There are several additional factors in design, such as human comfort and vibration noise, that make it essential to take into accout the oscillatory reponse of structures. These considerations make imperative a thorough understanding of the dynamic behavior of structural systems before one embarks on their design and construction.

The first step in characterizing the behavior of dynamic systems usually involves approximating the physical system by a suitably chosen mathematical model. The process of determining an appropriate model for the system is known as system identification. For many systems, it is possible to construct an a priori analytical model. This model should in general incorporate

all the knowledge that the analyst has about the nature of the system. When the model is complete, it is employed to investigate the behavior of the system under prescribed input conditions. Experiments may then be conducted on the real system, if it exists, or a scale model to determine the actual behavior of the system, the results of which are used to estimate the accuracy of the analytical model.

For certain other systems, it is possible to take the reverse approach. Experiments are carried out first and the measured data is used to build the anlaytical model from scratch. This course may be desirable in such instances in which little, if any, prior knowledge of the physical properties of the system exists.

A third possible approach, which may especially prove useful in analyzing computer structures, combines both experimental and analytical techniques hand in hand to arrive at an acceptable mathematical model. The initial analytical model is recognized as being approximate which leaves room for improvement to be made on the basis of experimentally measured data. The ensuing advantages of this procedure are evident. It makes use of accounting for its true behavior in the modeling process.

System identification techniques, with or without use of prior knowledge, have found wide application in many different areas. In a great many cases, the form of the analytical model of the system is known or can be deduced from physical considerations. However, this model will generally contain some unknown parameters that remain

to be determined. Identification of such systems reduces to the estimation of these unknown parameters in the model. A general review of identification and estimation techniques can be found, for example, in References 1 and 2. Application of these techniques to problems in structural dynamics can be found in References 3 and 4. The present study is concerned with employing such techniques to estimate structural parameters for highrise building models.

With the construction of complex civil engineering structures becoming more prevalent, interest in more refined modeling and detailed response of these structures has surged in recent years. The type of structures referred to here include highrise buildings, offshore structures, bridges and nuclear reactors. In addition to helping evaluate the state of the art in modeling, studying such structures has wider ranging consequences. Their behavior during catastrophic events like earthquakes and tornadoes is of paramount importance. Periodic determination of their properties can be used as a tool for damage assessment. This is done by examining experimental results from tests conducted before and after a major destructive event. Any radical changes in their characteristics could be correlated to the extent and the type of damage suffered. Understanding the behavior of such structures could also lead to new and improved design in the future. These and several other reasons have caused a considerable amount of attention to be given such structures.

In the case of highrise buildings, one particular aspect that has long been neglected and has been considered only recently,

is the role played by nonstructural elements such as the interior partitions and fixtures and, more importantly because of their substantial cost, the cladding elements that make up the exterior curtain wall. The cladding elements, usually made of such materials as precast concrete or glass, are increasingly being used in unusual and innovative architectural designs. Besides providing a protective covering, they also serve as a visual attraction.

The response of the main structure is usually considered to be independent of the cladding elements. The influence of cladding, both as a member transferring loads to the main structure and as a lateral stiffening element by itself, has not been given sufficient consideration in the overall behavior of the structure. It has been stated that the facade elements do interact with the main structure (5, 6)†. It has also been suggested that they could be used as lateral stiffening elements (7, 8).

Recent analytical studies taking the cladding-structure interaction into account suggest that the dynamic response of the primary structure is significantly altered by the presence of cladding (9, 10). In these studies, it was found that the natural frequencies increased by a considerable amount when the contribution due to cladding was added and the peak displacement response actually increased for certain earthquake inputs. Additional investigations, analytical and experimental, are thus needed to ascertain the effects of the cladding elements. If they have a favorable influence on the response, they must be accounted for in the design to make it more cost-effective.

---

† See corresponding items in References.

The present research is specifically aimed toward this problem, namely the identification of the part played by the facade elements and the determination of their impact on the overall dynamic response of the building.

The performance of cladding in resisting lateral dynamic loads can be evaluated, among other ways, by assessing its effects on the modal parameters of the building. This is the approach adopted in this study. The principal subjects in the study are two highrise buildings in the Atlanta metropolitan area. For one building, the modal parameters are determined from tests conducted during the construction phase so that the effect of cladding on these parameters can be monitored. In the case of another highrise building, the experimentally determined values for these parameters are used to make changes in an a priori analytical model so that the improved model will duplicate the experimental results as closely as possible. The total stiffness matrix in the a priori model is expressed in terms of stiffness parameters that multiply the stiffness matrices of different components of the structure, including the cladding. These stiffness parameters are estimated using test data for the first few modes.

The lack of an a priori mathematical model prevented additional investigation of the first building in which tests were conducted during construction. The identification in this case would have to be carried out without utilizing an initial model of the structure. Since this is beyond the scope of the present research, the second building for which an a priori model was available was used in the analytical studies.

1.2 Objectives

With the preceding discussion in mind, the objectives of this study can now be summarized as follows.

(i) Determine the modal parameters from data obtained by carrying out tests on a 24-story, steel frame glass-clad building during its construction and trace the changes in modal parameters during the period when the cladding is being installed.

(ii) Obtain modal parameters for an existing 25-story steel frame concrete-clad building and use the results to determine a mathematical model that will produce the best match with experimental observations.

Techniques of parameter estimation to be discussed later are used in fulfilling the above objectives.

All estimation methods in general have a common underlying approach. Once the parameters to be estimated are identified, a cost or objective function is formed which is a measure of the deviation of the output of the assumed model from the experimental or the desired output. This function is then minimized to obtain the required estimates. This is the procedure followed here to obtain the modal and the stiffness parameters.

It is assumed throughout this study that the systems considered behave linearly and are time-invariant. It is also assumed that they are viscously damped. Since the parameters of interest are the modal parameters, rather than the physical parameters (the mass, damping and

stiffness coefficients that appear in the differential equations), the analysis is carried out in the frequency domain using auto and cross-spectral density and frequency response functions. Of course time domain techniques could be used to determine the same parameters, but the response of the structure is frequently better understood using the frequency domain functions. For example, the structural modes manifest themselves as peaks in the power spectral density function of the response and are thus readily identifiable.

1.3 Scope of Study

In Chapter II, the ambient tests carried out in the 24-story buildings at different stages of construction are detailed. The vibrational parameters are obtained from the response spectra using a nonlinear least squares multidegree-of-freedom curve fitting procedure. The analytical form of the magnitude of the frequency response function is fitted to the linear spectrum amplitude of the response. The Levenberg-Marquardt method is employed to minimize the sum of squares error function. The results obtained are discussed and the changes in the parameter estimates at different testing times are related to the changes in the amount of cladding present in the structure.

Chapter III describes the forced vibration tests conducted on the 25-story building. Unlike the previous investigations in this area which have predominantly used steady-state or harmonic testing methods, transient testing is employed here. Frequency response functions for the building are measured using rapid frequency sweeps utilizing a rectilinear electrohydraulic shaker. The results of the full scale

forced vibration tests are compared to those from ambient tests performed earlier in the building.

Chapter IV gives a detailed account of the procedures used to estimate the stiffness parameters for the 25-story building employing forced vibration test results. Along with the ordinary or unweighted least squares, maximum likelihood and Bayesian estimation techniques, a weighted least squares method is used in which the weighting matrix is computed from the experimental as well as the analytical covariance of the modal parameters. The objective function in all cases is minimized using the inverse rank one correction (IROC) method. The results obtained from the various methods are compared and the possible role of cladding is discussed.

Chapter V presents the conclusions drawn from different parts of this study described in the preceding chapters.

2.0 THE EVALUATION OF CLADDING PERFORMANCE DURING CONSTRUCTION

2.1 Introduction

This chapter describes the vibration tests performed on a glass-clad building at various stages of construction during the installation of cladding. The analytical procedures used to extract the modal parameters from the measurements are discussed in detail. Efforts were particularly directed toward detecting changes in the values of these parameters with construction and finding out the effect of cladding on these parameters from the observed changes.

One possible way to bring out the influence of a certain component on the overall behavior of the main structure is to conduct experiments before and after the integration of the component into the main structure. This means, in the present case, that tests are needed just prior to and after the installation of cladding. But conditions beyond the control of the experimentalist dictate that a different procedure be adopted here. There are numerous other items in addition to the facade that could appreciably alter the mass and stiffness properties of the structure during the time the cladding is installed. These include plumbing fixtures and partition walls which are gradually stockpiled, to be used later in construction. Subsequently it was decided to carry out vibration tests at different stages of construction, starting after the erection of steel frame and continuing

through the installation of cladding until it was completely in place.

The decision to conduct the tests during the construction phase imposed additional constraints on the type of testing that could be employed. Forced vibration tests demand a considerable amount of time and effort since they require the use of an exciter. Furthermore, the equipment would have to be set up everytime a test is carried out. It is not feasible to leave it in its place between tests because it may interfere with the ongoing construction activities. For this reason, ambient tests were judged to be the most appropriate under such conditions.

Ambient testing is the process of measuring the response of the structure subjected to random environmental loading and is applicable to a variety of civil engineering structures. Owing to the fact that no external excitation need be provided, these tests are relatively easy to conduct. But they are encumbered by serious shortcomings, some of which are:

(i) there is no control over the input level nor is there a way to measure or quantify it;

(ii) small levels of response caused by low excitation levels provided by the surroundings require more sensitive instruments for measurement; and

(iii) because of the low levels of response, a relatively large amount of data must be acquired to minimize statistical variance in the analytical functions computed from this data.

The nature of the input in ambient tests is such that it defies all

attempts to characterize its temporal or spatial behavior in general. However, because of the ease with which it can be carried out, ambient testing has been widely used to determine the modal properties of many structures. It has been applied to study the dynamic properties of highrise buildings (11-14), suspension bridges (15-18) and offshore structures (19). For highrise buildings, wind forces constitute a major part of ambient loading. Other sources include microtremors or minor ground movements and internal activities in the structure.

The basic principle involved in ambient testing is that the parameters of interest are estimated using the response alone. This leads to some rather restrictive assumptions which must be made in the analysis. The most important ones are the following:

(i) The response is stationary.

(ii) The input can be approximated by band limited white noise, at least in the region of structural modes in the output power spectral density function. Stated in another way, the input has a constant spectral density in the vicinity of each mode.

It should be noted that the assumption of stationarity is a general one and is not confined to ambient testing.

Several techniques have been used in the past to obtain modal parameter estimates from response data with the aforementioned assumption regarding the input. Some of these techniques are reviewed here, starting with techniques in the time domain.

Cherry and Brady (20) suggested that the output autocorrelation function can be used to determine the frequency and the damping ratio when the system is subjected to a constant spectral density excitation. If this constant power spectrum is denoted by $\bar{G}_{xx}$, then the autocorrelation of the response $C_y(\tau)$ is described by the cosinusoidal function (for a single degree-of-freedom system)

$$C_y(\tau) = \frac{\pi \bar{G}_{xx}}{2\rho \omega_0^3} e^{-\rho\omega_0\tau} \left(\cos \sqrt{1 - \rho^2}\, \omega_0\tau + \frac{\rho}{\sqrt{1 - \rho^2}} \sin \sqrt{1 - \rho^2}\, \omega_0\tau\right) \qquad (2.1)$$

where ω_0 is the natural frequency in radians per second and ρ is the viscous damping ratio. The natural frequency is obtained from the period and the damping ratio is estimated from the exponential decay of the above function. The logarithmic decrement method is employed in estimating the damping.

Another method to analyze the response due to random excitation is the random decrement analysis, developed by Cole (21, 22). This method involves the use of random decrement signature, which is similar to the free vibration decay of the structure subjected to an initial displacement or velocity. The step response or the response corresponding to an initial displacement is obtained by averaging a number of time segments of the response such that each is of the same duration and each starts at a fixed response level. If the segments averaged are such that each segment starts at zero response level with a positive

(or negative) slope, the signature obtained will be the impulse response or the response due to an initial velocity. Both this technique and the autocorrelation method require that the response be band-pass filtered to remove the effects of the other modes not of interest.

Gersche and others (23, 24) proposed evaluating the frequencies and the damping ratios of multidegree-of-freedom systems by employing maximum likelihood and least squares estimation procedures. This method uses the autoregressive moving average (ARMA) model representation of the response data. The ARMA model parameters are obtained first from which the modal parameters are determined.

Among the frequency domain techniques used to obtain the vibrational parameters from the output record, the most popular is the spectral density function method. The output power spectrum $G_{yy}(\omega)$ is related to the input spectrum $G_{xx}(\omega)$ by

$$G_{yy}(\omega) = |H(\omega)|^2 \, G_{xx}(\omega) \tag{2.2}$$

where $|H(\omega)|$ represents the magnitude of the frequency response function $H(\omega)$. For a single degree-of-freedom system excited by an input with constant spectral density $\bar{G}_{xx}$,

$$G_{yy}(\omega) = \left(\frac{\bar{G}_{xx}}{k^2}\right) \frac{1}{\left(1 - \frac{\omega^2}{\omega_0^2}\right)^2 + \left(2\rho \frac{\omega}{\omega_0}\right)^2} \tag{2.3}$$

where

$$|H(\omega)|^2 = \left(\frac{1}{k^2}\right) \frac{1}{\left(1 - \frac{\omega^2}{\omega_0^2}\right)^2 + \left(2\rho \frac{\omega}{\omega_0}\right)^2} \tag{2.3}$$

and k is the stiffness coefficient. It can be easily shown that the maximum value of Equation (2.3) occurs at a frequency ω_p, where

$$\omega_p = \omega_0 \sqrt{1 - 2\rho^2} \tag{2.5}$$

For systems with small damping ($\rho < 0.1$),

$$\omega_p \simeq \omega_0 \tag{2.6}$$

It can also be shown that the half-power bandwidth $\Delta\omega_0$, the difference between the frequencies at which $|H(\omega)|^2$ has fallen to 1/2 of the maximum value, is approximately given as

$$\Delta\omega_0 \simeq 2\rho\ \omega_0 \tag{2.7}$$

From the above relations it is clear that the natural frequencies of the structure can be taken as the frequencies at which $G_{yy}(\omega)$ peaks and the damping ratios can be determined from the half-power points using Equation (2.7). The mode shapes can be obtained from the peak amplitudes as follows.

$$\phi_{in} = \left[G_{ii}(\omega_n)\right]^{\frac{1}{2}} \tag{2.8}$$

where ϕ_{in} is the coefficient of the nth mode at point i and $G_{ii}(\omega_n)$ is the output spectrum at point i evaluated at the peak frequency corresponding to the nth mode.

Other frequency domain methods that employ the output spectrum are the spectral moments method of Vanmarcke (25, 26) and parametric curve fitting suggested by Schiff (27). In Vanmarcke's method which uses the moments of the spectral density function, the modal parameters are obtained by utilizing the first three moments of the output power spectrum. The spectral moments are defined as

$$M^i = \int_0^\infty \omega^i \, G(\omega) \, d\omega \tag{2.9}$$

where M^i is the ith spectral moment of a spectral density function $G(\omega)$. The natural frequency and the damping ratio can be expressed in terms of M^1, M^2 and M^3. In parametric curve fitting, an expression of the form given in Equation (2.3) is fitted to the region around each peak in the output spectrum to determine the required parameters for the different modes.

It is clear from the preceding discussion that all the frequency domain techniques considered above treat the response of the structure as that of a single degree-of-freedom system. Thus, their application in cases where there is a significant amount of modal overlapping in the response becomes difficult. Such modal overlapping is likely to occur when there are modes closely spaced in frequency.

The approach used here attempts to overcome this difficulty by employing a multidegree-of-freedom curve fitting procedure. The modal parameters are obtained by curve fitting the magnitude of the frequency response function to the response Fourier amplitude spectrum. The analytical form of $H(\omega)$ assumed is that for a multi-degree-of-freedom system. Since the Fourier amplitude spectrum, the magnitude of the Fourier transform, is the same as the square root of the power spectrum except for a scaling constant, the actual fitting process is carried out using $\left[G_{ii}(\omega)\right]^{\frac{1}{2}}$. The assumption made herein is that the input is broadband in character with a bandwith that spans all the modes taken into account in the curve fitting procedure.

2.2 Structure

The structure used in the experimental investigations is a 24-story steel frame highrise building, 350 feet high with lightweight partially opaque glass facade. The schematic diagram of this structure is shown in Figure 2-1. The building has a sloping south wall to increase shading and reduce energy costs and the sloped face is obtained by incrementally increasing the width of floors 3 to 23 by 15 inches so that an overhang is formed at each level. The end bay on the south wall is thus increased from 16.25 feet at the base to 43.5 feet at the roof. This causes the center of gravity to be slightly eccentric, but the resulting overturning effect was accounted for in the design of the structure and foundation system.

The building rests on 68 caissons whose diameters vary from 2.5 feet to 6 feet and whose average depth is about 65 feet. Caissons

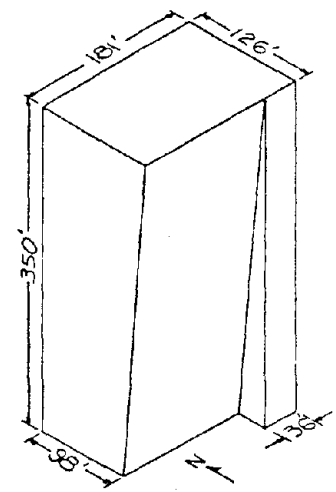

Figure 2.1. Building Geometry

which act as supporting columns in potential uplift are drilled 8 to 10 feet into rock and are heavily reinforced. Grade beams are used to tie the caissons together around the tower perimeter.

Steel stub-girder framing is used in the building floors in order to reduce the floor-to-floor height of each story. The slab is raised above the floor girders on short rolled stubs resting on and welded to the top flanges of the girders. Ductwork and other utilities pass between the stubs on top of the girders instead of below them. Shear connectors welded to the top of the stub girders make the slab composite with the steel structure.

2.3 Measurement

The testing process commenced after the steel frame was erected and the installation of cladding has just started. Table 2.1 gives the dates at which measurements were tkane and the corresponding cladding levels on different faces of the building. Cladding level is defined here as the floor up to which cladding is complete on any given face. A total of eight tests were conducted during the installation of cladding and one additional test was conducted on November 13 (1980), well after the process was completed. Table 2.1 also gives the percentage cladding levels which are the cladding levels expressed as percent of complete cladding for the face considered.

The measuring equipment used consisted of accelerometers, signal conditioner including amplifiers and filters, a tape-recorder and an oscilloscope. Five low level force-balance accelerometers (Kinetmatics FBA-1) were used so that response from up to five different floors could be measured simultaneously. The response signals were

Table 2.1. Cladding Levels on Different Test Data

Face / Date	East	West	North	South	Comments
1/16	4(17)[1]	2(8)	4(17)	0(0)	Floors, structural framing and overhang complete upto 22nd floor.
2/8	10(42)	6(25)[2]	10(42)	0(0)	Floors and structural framing complete. Overhang complete to 23rd floor.
2/15	12(50)	10(42)[2]	12(50)	7(29)	Overhang complete. Piping and mechanical equipment being installed.
2/22	13(54)	11(46)[2]	12(50)	9(38)	Piping installation complete. Mechanical equipment being installed.
3/7	16(67)	12(50)	12(50)	12(50)	Mechanical equipment being installed.
4/24	24(100)	19(79)	19(79)	20(83)	Elevator equipment and partitions being installed.
5/16	24(100)	23(96)	24(100)	23(96)	Elevator equipment and partitions being installed.
5/29	24(100)				—
11/13	24(100)				Elevator installation complete. Partitions complete to 20th floor.

1 Value in parentheses gives the cladding level as a percentage of complete cladding

2 Average cladding height

then passed through the signal conditioner which amplifies the usually low level signals and filters them to remove an unwanted dc component and the high frequency noise from the response. After amplification and filtering, the signals were recorded on magnetic tape using an 8 channel HP-3968 tape recorder. A recording speed of 5/16 inch per second was used. The oscilloscope (Tektronix 5440) was employed to monitor the signals being recorded.

To avoid interference with the ongoing construction activities, no permanent fixture was set up and the instrumentation was transported to the building site every time a set of measurements was taken. Each measurement lasted from 3 to 6 hours. The location and orientation for the accelerometers were chosen depending on the type of response desired. On the first occasion (January 16, 1980) three accelerometers were used on the 22nd floor to identify the bending and torsional frequencies (Figure 2.2). Accelerometer responses from locations 1 and 2 were used to detect the torsional and the North-South bending modes while the response at location 3 was used to detect the East-West bending modes. On all the other days except March 17, five accelerometers were placed on the 8th, 13th, 18th, 22nd and 24th floors. On one of these days (May 16), the 24th floor was inaccessible and the 20th floor was chosen instead. For three measurements the accelerometers were situated at location 3, twice in the North-South direction and once in the East-West direction. For the other measurements they were situated near the West face at location 1. It was decided to obtain data in both the bending directions on the last three days, so the accelerometers were rotated 90^{o} midway

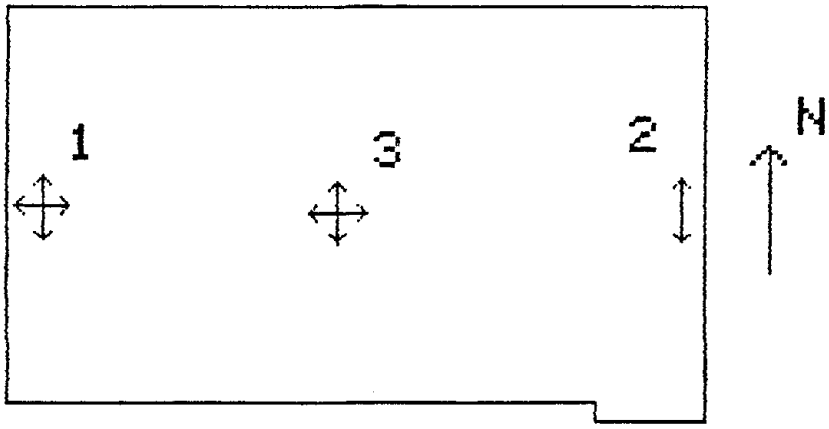

Figure 2.2. Accelerometer Layout

through the measurement process. About three hours of data were recorded in each direction on these days while the duration of the first six measurements was about six hours. Table 2.2 summarizes the locations and the orientations used on different test dates.

2.4 Estimation of Spectra

The use of frequency domain analysis necessitates the transformation of the time domain measurements into the frequency domain functions before one can proceed with the estimation of vibrational parameters. The functions to be determined in this case are the power and cross spectral densities of the response from different floors of the building. (The need for the cross spectral density will be discussed later.) The time domain measurements are first discretized by sampling at regular intervals. The sampled time series representation of a measurement signal is used to calculate its Discrete Fourier Transform (DFT) with the aid of Fast Fourier Transform (FFT) algorithms. The DFT thus obtained is utilized to compute estimates for the required spectral density functions.

There are several aspects that must be considered in spectral estimation using time series analysis. The important ones are the problems associated with processing of digitized data and the statistical aspects associated with the estimation procedure.

The need to sample the signal at discrete time intervals to convert it into digital form for subsequent use in the computations inherently places some restrictions on the analysis. For the DFT of the signal to be uniquely determined, the signal must be bandlimited, containing no frequency components higher than a certain frequency

Table 2.2. Locations and Orientations of the Accelerometers

Date	1/16		2/8	2/15	2/22	3/7		4/24	5/16		5/29		11/13	
Floor No.	22	22	8 13 18 22 24	8 13 18 22 24	8 13 18 22 24	13 24	24	8 13 18 22 24	8 13 18 20 22	8 13 18 20 22	8 13 18 22 24	8 13 18 22 24	8 13 18 22 24	8 13 18 22 24
Location No.	1 2	3	3	3	3	1 2	3	1	1	1	1	1	1	1
Orientation	N-S	E-W	N-S	N-S	E-W	N-S	E-W	N-S	N-S	E-W	N-S	E-W	N-S	E-W

f_N, referred to as the Nyquist frequency. This frequency is related to the sampling interval Δt by the following:

$$f_N = \frac{1}{2\Delta t} \tag{2.10}$$

The sampling frequency f_s is defined as the reciprocal of the sampling interval Δt. Therefore, from Equation (2.10), $f_s = 2f_N$.

The sampling rate f_s must be at least twice as high as the highest frequency present in the signal. Otherwise, the frequency components higher than f_N will appear as frequencies below f_N. This phenomenon is known as "aliasing" and is discussed in numerous books, for example Reference 28. The aliasing problem is minimized by low-pass filtering the signal to remove the frequencies higher than f_N. If f_m denotes the maximum frequency of interest, then a sampling rate of about 4-5 times f_m is recommended in practice with the cut-off frequency of the filter set slightly below the Nyquist frequency.

Since it is only possible to use finite length sequences in computations, the sampling of the signal is in general restricted to a finite duration. The resulting finite length record is equivalent to truncating the infinitely long signal by multiplying it with a rectangular window or weighting function of duration T, where T is the total time given by $T = N\Delta t$. N is the number of data points in the sampled record. The rectangular window, or the boxcar function as it is sometimes referred to, can be represented mathematically as

$$w_R(t) = 1 \qquad 0 \leq t \leq T$$

where $W_R(f)$ is the Fourier transform of the boxcar function. The Hanning window is capable of resolving frequencies that are at least $2\Delta f$ apart. Different types of windows generally employed in spectral analysis and estimation are treated in References 29 and 30 among others.

For two stationary signals $x_1(t)$ and $x_2(t)$ whose discrete Fourier transforms $X_1(k\Delta f)$ and $X_2(k\Delta f)$ are computed using filtered and properly weighted time samples, the auto and cross spectral density estimates can be calculated using the following relations.

$$\tilde{G}_{x_1x_1}(k\Delta f) = \frac{1}{T}\left|X_1(k\Delta f)\right|^2$$

$$\tilde{G}_{x_1x_2}(k\Delta f) = \frac{1}{T}\left(X_1^*(k\Delta f)X_2(k\Delta f)\right) \qquad (2.11)$$

where $\tilde{G}_{x_1x_1}$ is the autospectral estimate of $x_1(t)$, $\tilde{G}_{x_1x_2}$ is the cross spectral estimate between $x_1(t)$ and $x_2(t)$, k is an index that varies from zero to N/2 (N is assumed to be even) and * denotes conjugation of the complex quantity.

As will be pointed out below, the estimates determined using Equation (2.11) are subject to large variance errors. More acceptable estimates can be obtained by averaging over an ensemble. The available data are divided into smaller segments of equal time length and the relations given in Equation (2.11) are employed to compute estimates for each of these segments. The smoothed estimates $\hat{G}_{x_1x_1}$ and $\hat{G}_{x_1x_2}$ for the power and cross spectral density functions are computed by averaging the estimates for the individual segments.

$$\hat{G}_{x_1x_1}(k\ f) = \frac{1}{n_d} \sum_{i=1}^{n_d} \tilde{G}^i_{x_1x_1}(k\Delta f)$$

$$\hat{G}_{x_1x_2}(k\ f) = \frac{1}{n_d} \sum_{i=1}^{n_d} \tilde{G}_{x_1x_2}(k\Delta f) \qquad (2.12)$$

where n_d is the number of averages used. If a weighting function other than the rectangular window is used, it is necessary to divide the above estimates by a normalizing factor to obtain the actual magnitudes of the estimated functions. For the Hanning window, this factor is 3/8 (28).

Expressions for the mean and variance of the ensemble averaged spectal density estimates can be found in Reference 31. Let $b\left[\hat{G}_{x_1x_1}\right]$ denote the bias and $\sigma\left[\hat{G}_{x_1x_1}\right]$ the standard deviation of the estimate $\hat{G}_{x_1x_1}$. The normalized bias error $\varepsilon_b\left[\hat{G}_{x_1x_1}\right]$ and the normalized random error or the coefficient of variation $\varepsilon_r\left[\hat{G}_{x_1x_1}\right]$ are defined as

$$\varepsilon_b\left[\hat{G}_{x_1x_1}\right] = \frac{b\left[\hat{G}_{x_1x_1}\right]}{G_{x_1x_1}}$$

$$\varepsilon_r\left[\hat{G}_{x_1x_1}\right] = \frac{\sigma\left[\hat{G}_{x_1x_1}\right]}{G_{x_1x_1}} \qquad (2.13)$$

When disjoint or nonoverlapping averages are used to compute $\hat{G}_{x_1x_1}$, the approximate variance in the estimate is given by

$$\sigma^2\left[\hat{G}_{x_1x_1}\right] = \frac{\hat{G}^2_{x_1x_1}}{n_d}$$

from which

$$\varepsilon_r \left[\hat{G}_{x_1 x_1} \right] = \frac{1}{\sqrt{n_d}} \tag{2.14a}$$

The case where the individual segments used overlap with each other is treated in Reference 31. The variance for this case depends on the overlap ratio and will usually be smaller than the value given above.

It is clear from Equation (2.14a) that, if $n_d = 1$, the standard deviation of the quantity $\hat{G}_{x_1 x_1}$ is as large as the true value itself. It is for this reason that a sufficient number of averages are needed to ensure the quality of the estimates. For a fixed amount of data, the time length T of each segment must be chosen so as to give a large enough value of n_d that will produce acceptable variance in the estimates.

The bias in the autospectral estimate $\hat{G}_{x_1 x_1}$ depends mainly on the frequency resolution Δf which in turn depends on the time length T. An approximate expression that can be found in Reference 28 is

$$\varepsilon_b \left[\hat{G}_{yy}(f_0) \right] = -\frac{1}{3} \left(\frac{\Delta f}{\Delta f_0} \right)^2 \tag{2.14b}$$

where $\varepsilon_b \left[\hat{G}_{yy}(f_0) \right]$ is the normalized bias error at peak frequency f_0 in the output autospectrum of a single degree-of-freedom system subjected to white noise excitation and Δf_0 is the half-power bandwidth. While choosing a smaller value of T to increase the number of averages results in reduced variance, it also increases the bias in the estimates due to

a higher value of Δf. Thus the requirements for reducing the bias and the variance in spectral estimation conflict with each other. Therefore the parameter T must be chosen carefully so that the resulting estimates would possess bias and variance that are within tolerable limits.

The estimation of power and cross spectral densities for the building response data was carried out using digital signal analyzers such as the HP 5420A and HP 5423A. These analyzers employ a combination of analog and digital filtering techniques to bandlimit the input signals. The signals are first passed through analog anti-aliasing filters, with a cut off frequency of 300 Hz for the present case. In the second stage, the sampled version of the data is filtered using a digital filter to remove the frequency components higher than the analysis bandwidth. Ensemble averaging can be accomplished in the overlapping or the nonoverlapping mode by choosing appropriate triggering conditions. A user-selected window function, chosen as the Hanning window for the present application, is employed in the computation of the estimates.

To reduce the data processing time, the magnetic tape containing the response data was played back at a speed of 15 ips, 16 times faster than the recording speed. This resulted in an amplification factor of 16 for the frequency as used in the analyzer. The number of averages (overlapped) used ranged between 400 and 1500 depending on the amount of data available.

The autospectrum for the response from each accelerometer was computed in the above manner and stored for later use in modal

parameter estimation. Also computed were the cross-spectral density and coherence functions between a reference output, normally chosen as the response from the 24th floor, and the remaining outputs. The phase components of the cross-spectra were used to identify the torsional frequencies as well as the relative direction of motion of the different floors for bending modes. It is also possible to utilize the magnitude components in extracting the frequencies and the damping ratios. In fact, Bendat and Piersol (28) recommend that the half-power bandwidth method to determine the damping be applied to the cross-spectrum instead of the power spectral density functions.

The coherence function between two signals $y_1(t)$ and $y_2(t)$ is given by

$$\gamma^2_{y_1y_2} = \frac{|\hat{G}_{y_1y_2}|^2}{\hat{G}_{y_1y_1}\,\hat{G}_{y_2y_2}} \tag{2.15}$$

where $\gamma^2_{y_1y_2}$ is the coherence function. If the signals $y_1(t)$ and $y_2(t)$ are obtained from a common source by some linear filtering operations, the coherence between the two signals will be unity at all frequencies. For linear single-input multiple-output systems, values less than one for the coherence between two different outputs imply the presence of errors in the spectral estimates due to various sources such as poor signal-to-noise ratio in the measurements and resolution bias caused by insufficient frequency resolution. Hence the coherence function can be used to determine the quality of the spectral estimates especially

in the regions proximal to the structural modes. The mode shape estimates evaluated from the output records will be accurate only if the coherence between different outputs is close to one around the peak frequencies corresponding to the structural modes.

The identification of the different bending and torsional modes was accomplished by making use of the spectral estimates for the measurements taken on the first day (January 16, 1980). On this day, two accelerometers were placed on the 22nd floor at locations 1 and 2 (Figure 2.2) along the N-S direction and a third accelerometer was placed at location 3 along the E-W direction. The autospectra for measurements at locations 1 and 2 are shown in Figures 2.3 and 2.4 and contain both N-S bending and torsional modes. The E-W autospectrum at location 3 is given in Figure 2.5. Figure 2.6 shows the cross-spectrum between locations 1 and 2. These spectra were computed up to 8 Hz with a frequency resolution of 0.03125 Hz, using about 1500 averages obtained from approximately 6 hours of data.

From Figure 2.6 it is seen that the phase component of the cross-spectrum is near zero at frequencies corresponding to modes numbered 1, 3 and 6, which is indicative of N-S bending modes. On the other hand, the phase is close to 180° for modes 2 and 4, indicating that these are torsional modes. The mode that is numbered 5, where the phase is again close to 180°, is an unidentified mode which did not appear in later measurements. The modes 7 and 11 are possibly the 4th and 5th N-S bending modes while modes 8, 9, 10 and 12 are higher torsional and other unidentified modes.

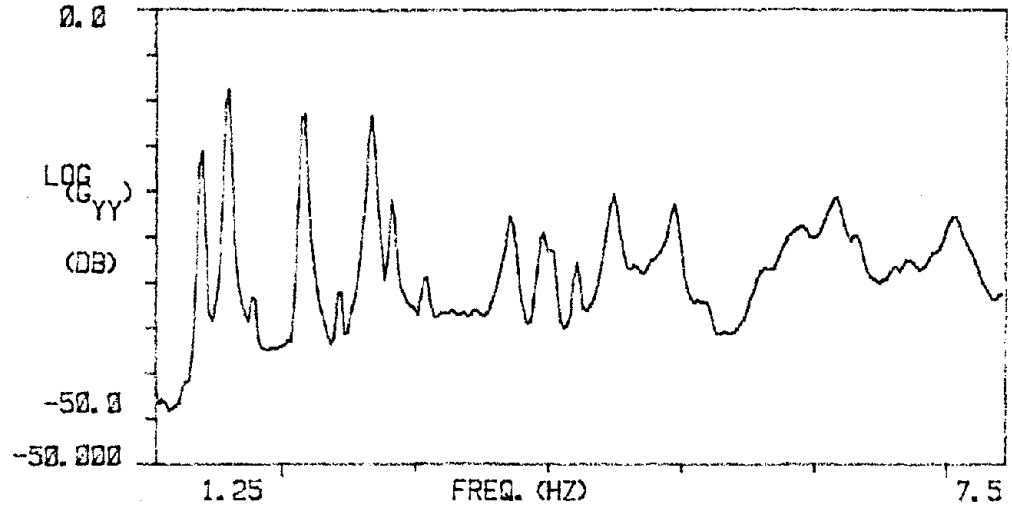

Figure 2.3. Autospectrum at Location 1

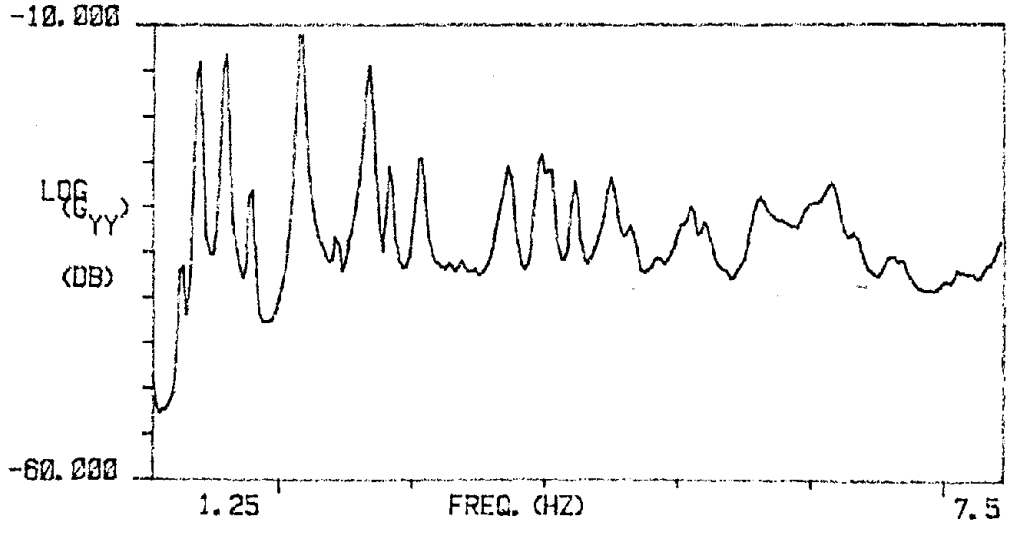

Figure 2.4. Autospectrum at Location 2

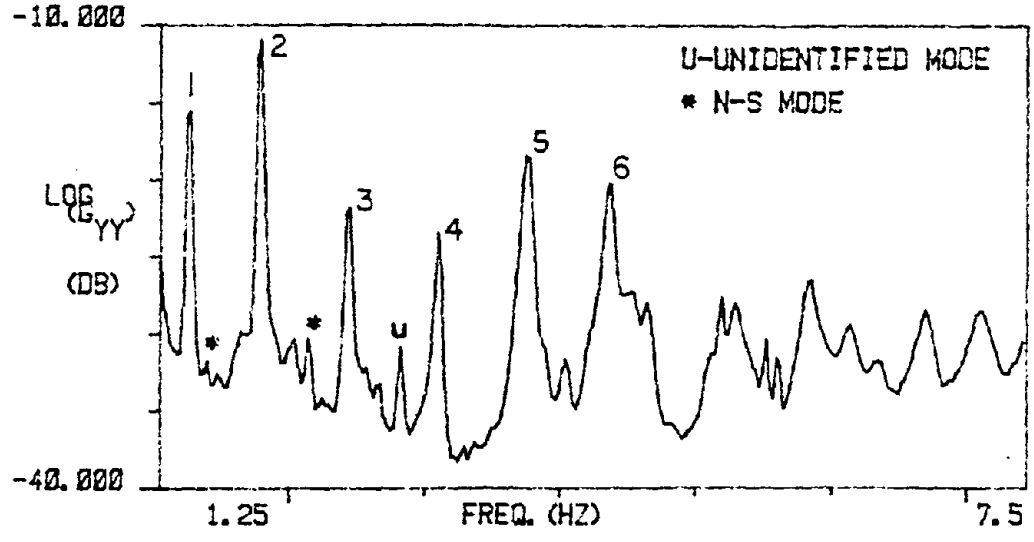

Figure 2.5. Autospectrum at Location 3

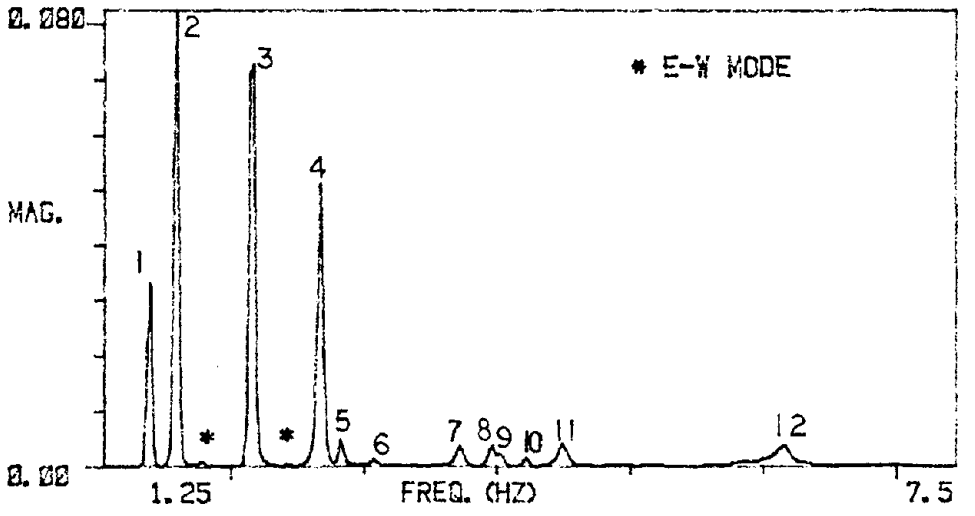

(a) Magnitude

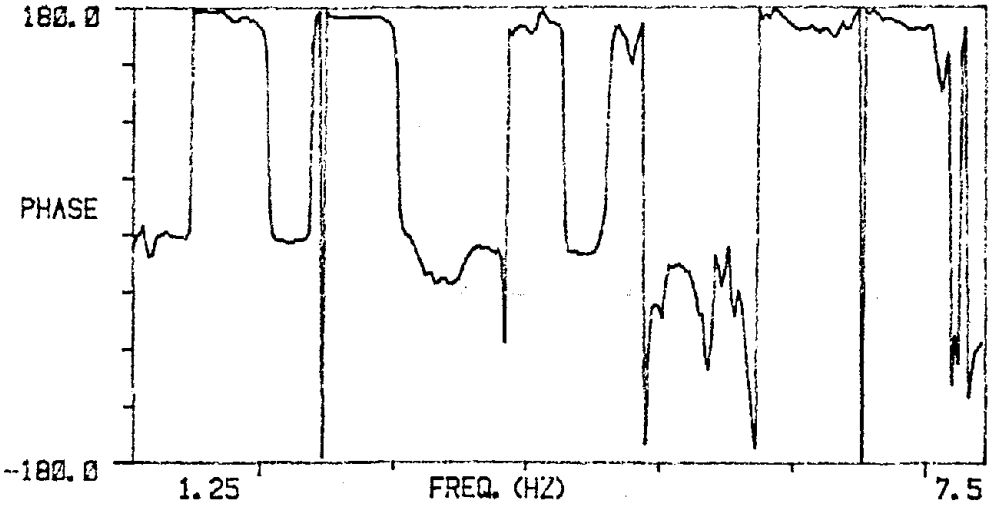

(b) Phase

Figure 2.6 Cross-Spectrum Between Location 1 and 2

In the E-W direction, modes 1 through 6 (Figure 2.5) are the possible bending modes. It is difficult to determine the order of the higher modes without further information from other floors. Some of these modes also appear in the N-S direction and these are denoted E-W in Figure 2.6. This could be due to some misalignment of the accelerometers oriented in the N-S direction. Similarly, Figure 2.5 contains N-S modal frequencies which could be due to misalignment of the accelerometer at location 3. Another possible cause is the presence of significant modal coupling for various modes so that the modes may have small components in directions other than their principal directions.

Figures 2.7 - 2.16 show the autospectra computed for the last set of measurements taken on November 13. The accelerometers in this case were placed at location 1 along the west edge, oriented first in the N-S direction and then turned around to point along the E-W direction. Since this location is away from the midpoint of the west edge, significant torsional response was picked up even in the latter case. The spectra containing the N-S and torsional modes are given in Figures 2.7 - 2.11 and those containing the E-W and torsional modes are given in Figures 2.12 - 2.16.

For floors other than the roof, the coherence with the roof is also shown. The values of coherence are upward of 0.9 in the vicinity of the first few natural frequencies except in cases where one autospectrum includes a mode that is absent in the other. The coherence function peaks at frequencies corresponding to the higher

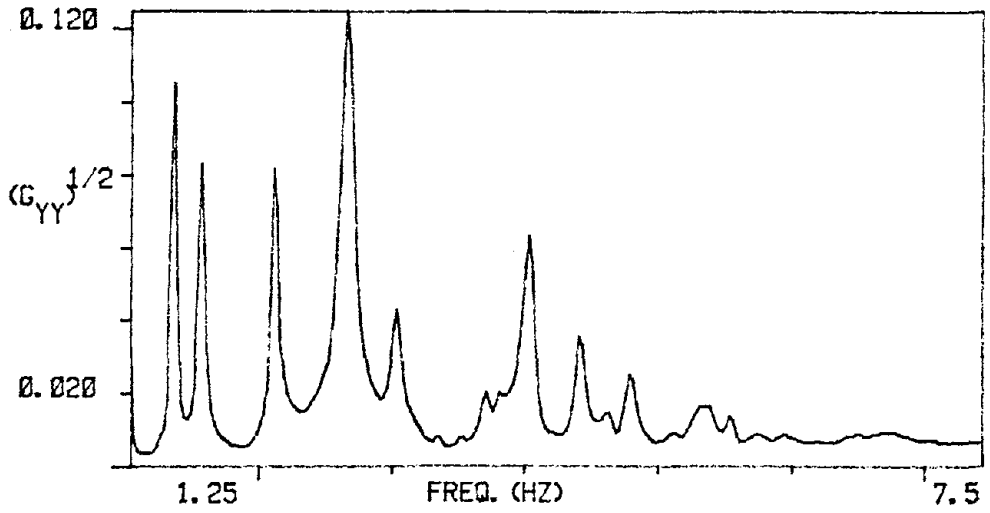

Figure 2.7. N-S Response on 24th Floor, Autospectrum

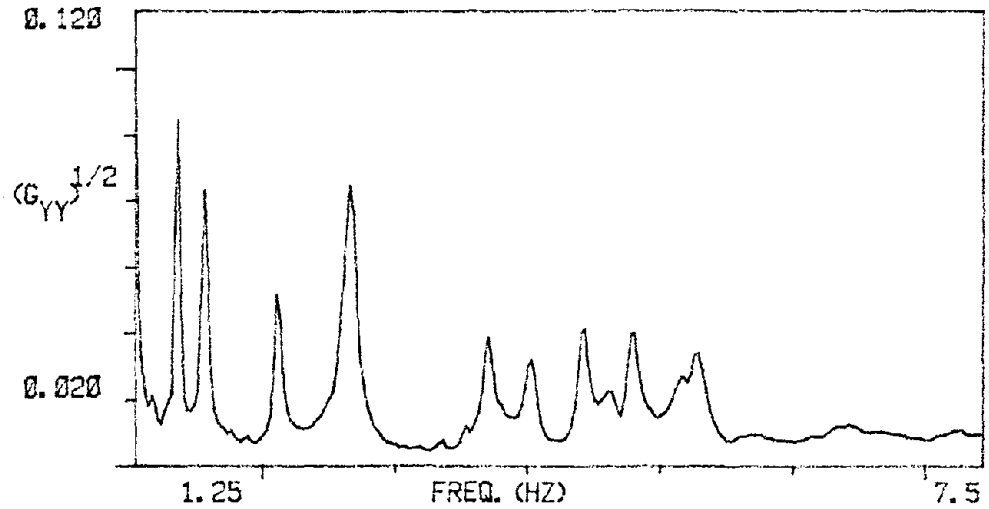

(a) Autospectrum

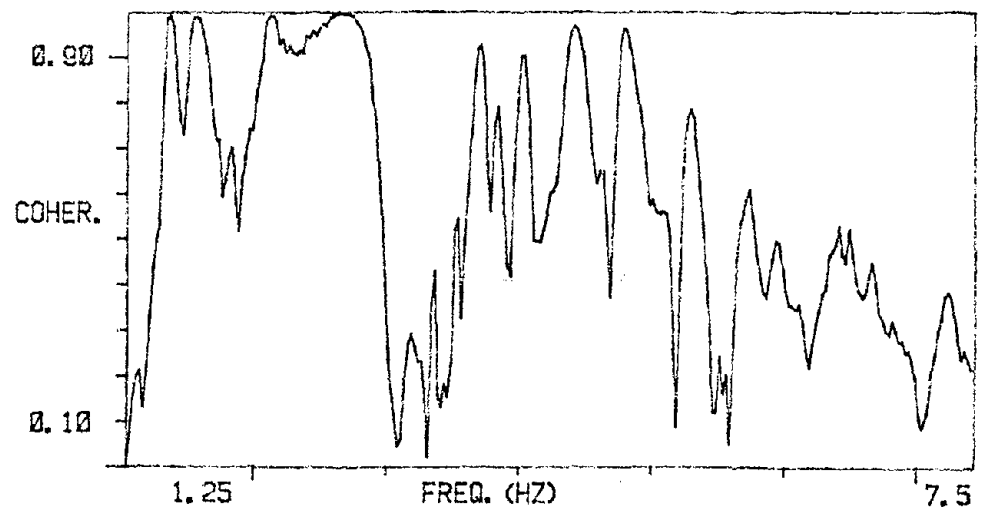

(b) Coherence

Figure 2.8. N-S Response on 22nd Floor

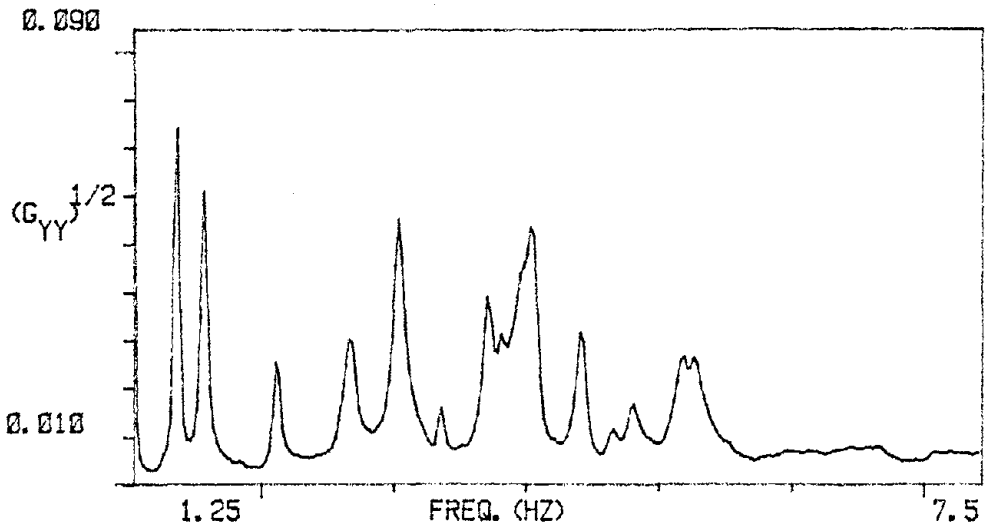

(a) Autospectrum

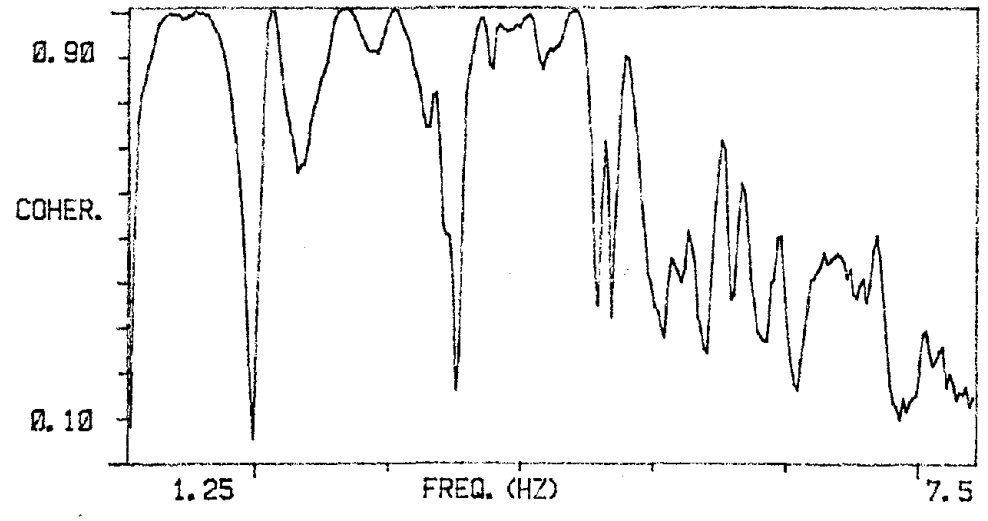

(b) Coherence

Figure 2.9. N-S Response on 18th Floor

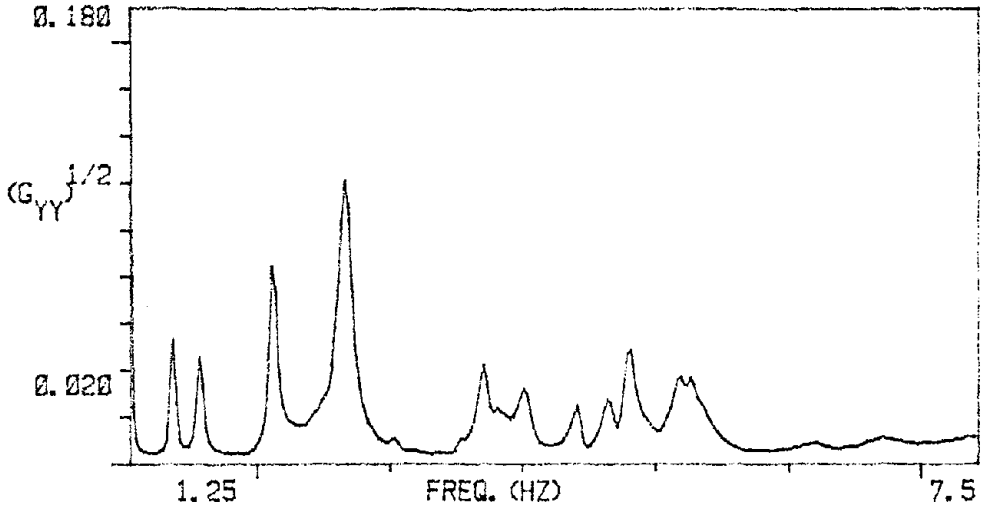

(a) Autospectrum

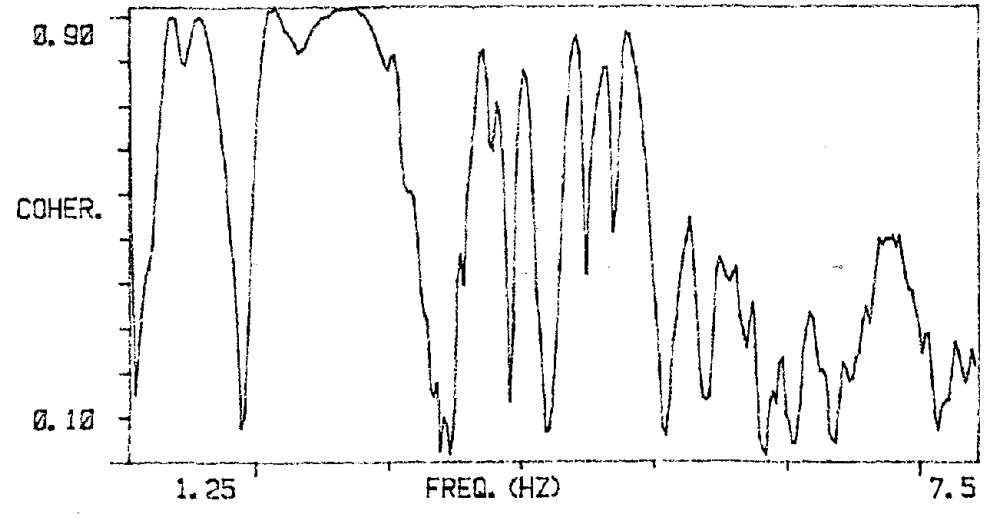

(b) Coherence

Figure 2.10. N-S Response on 13th Floor

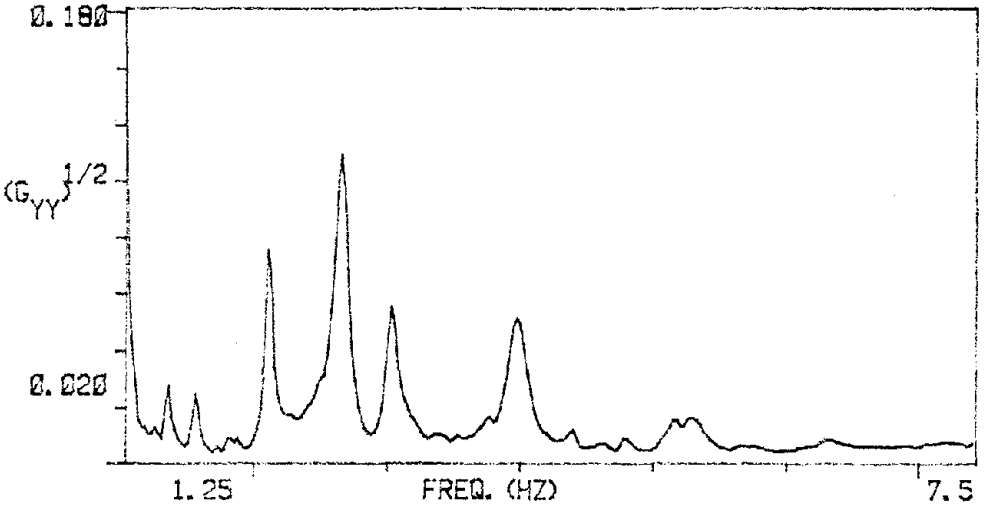

(a) Autospectrum

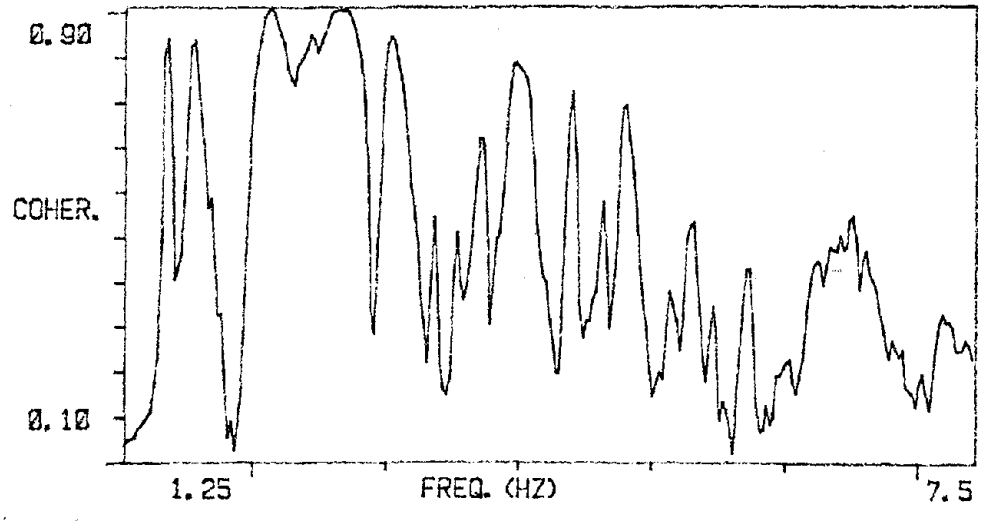

(b) Coherence

Figure 2.11. N-S Response on 8th Floor

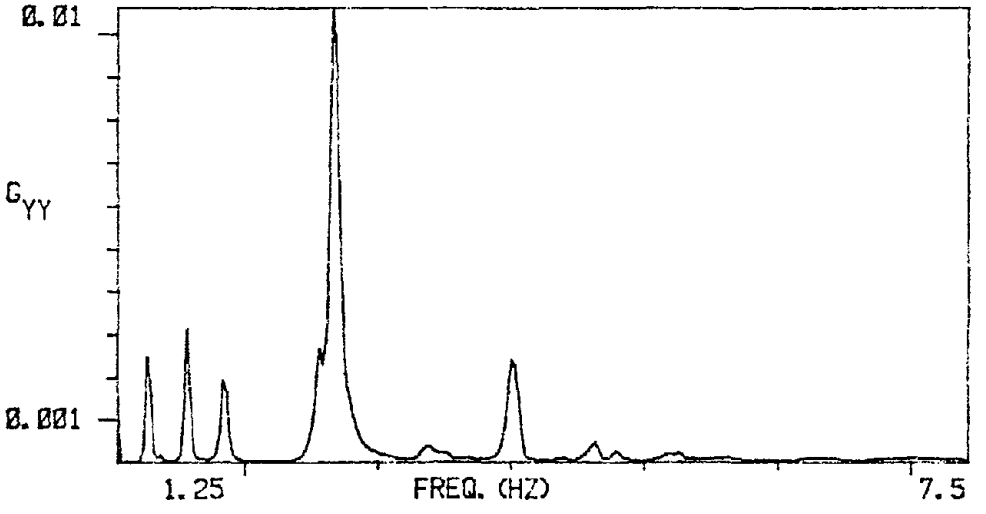

Figure 2.12. E-W Response on 24th Floor

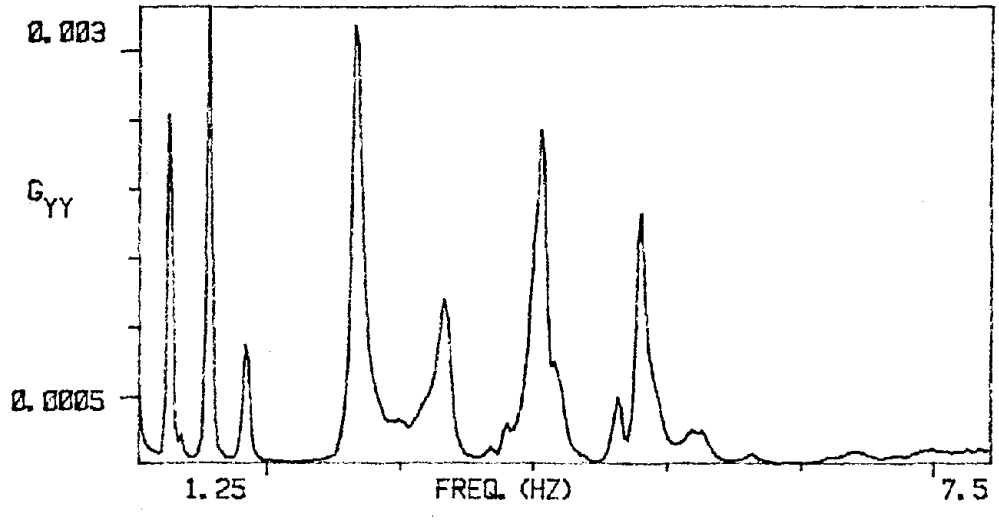

(a) Autospectrum

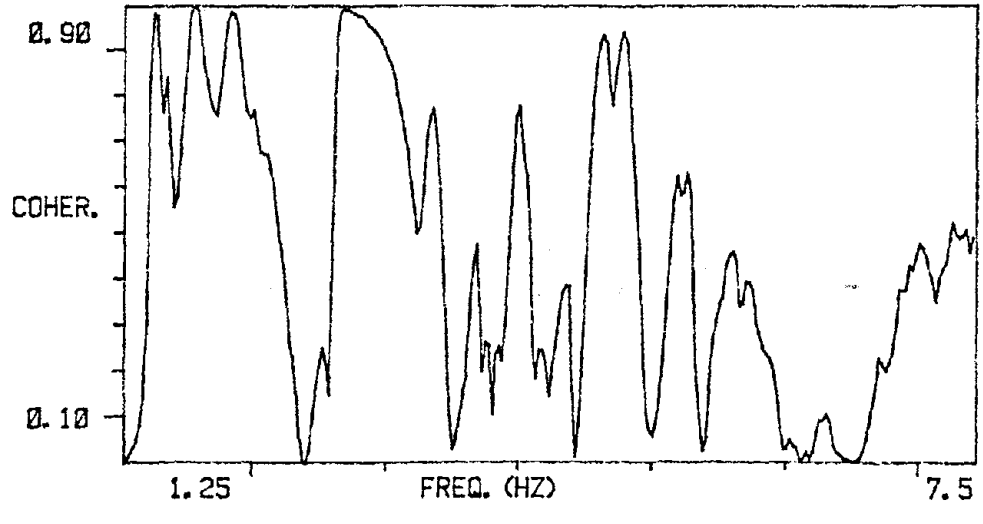

(b) Coherence

Figure 2.13 E-W Response on 22nd Floor

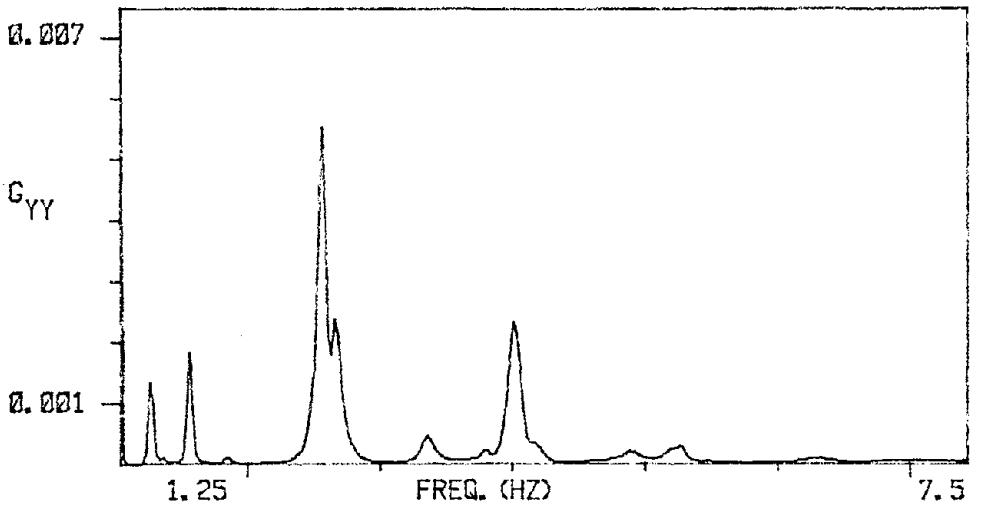

(a) Autospectrum

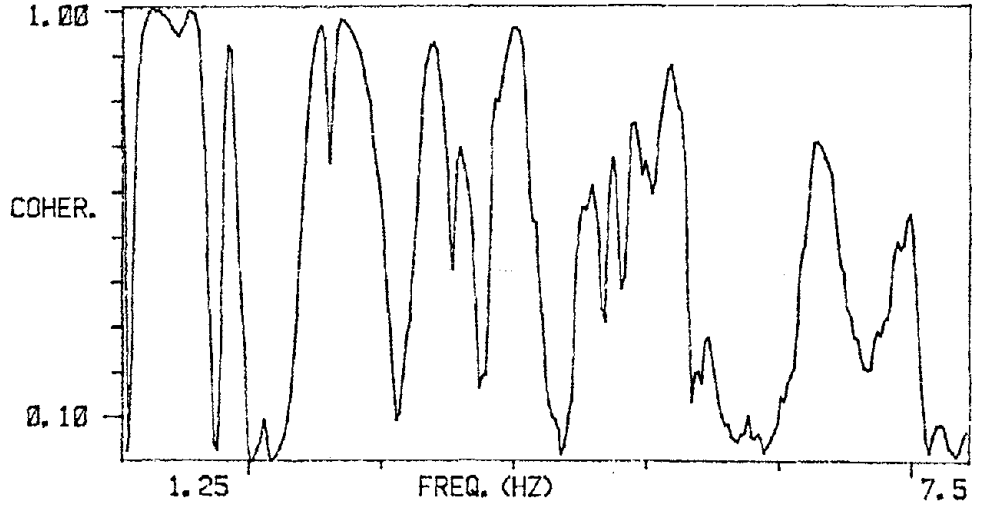

(b) Coherence

Figure 2.14. E-W Response on 18th Floor

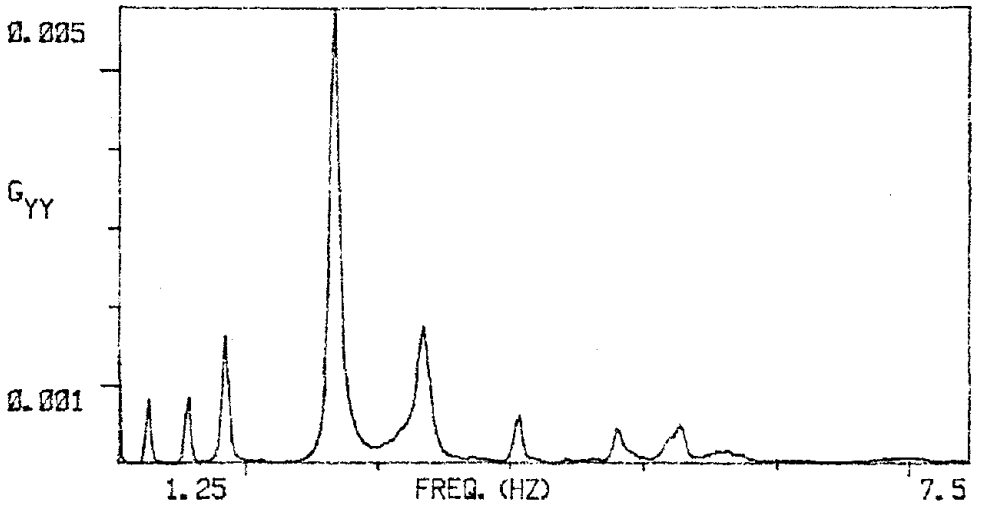

(a) Autospectrum

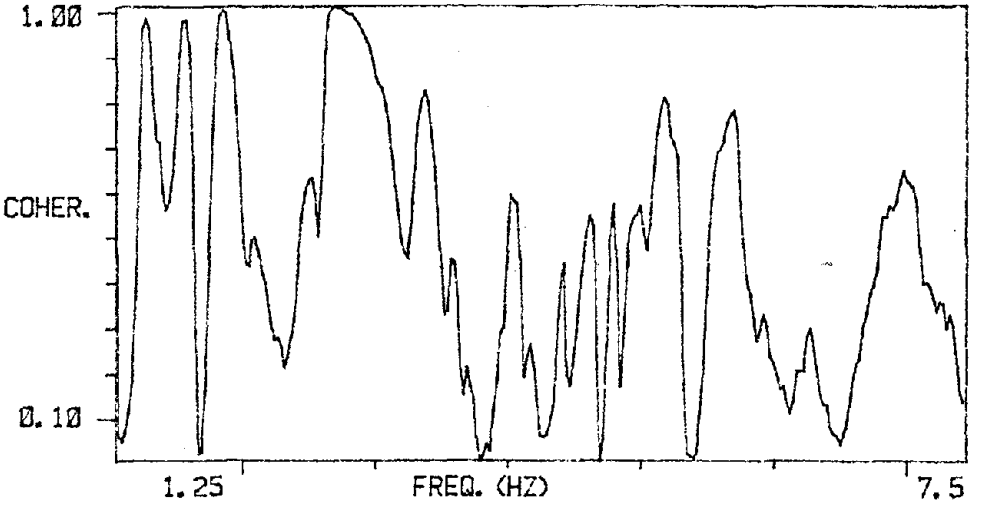

(b) Coherence

Figure 2.15. E-W Response on 13th Floor

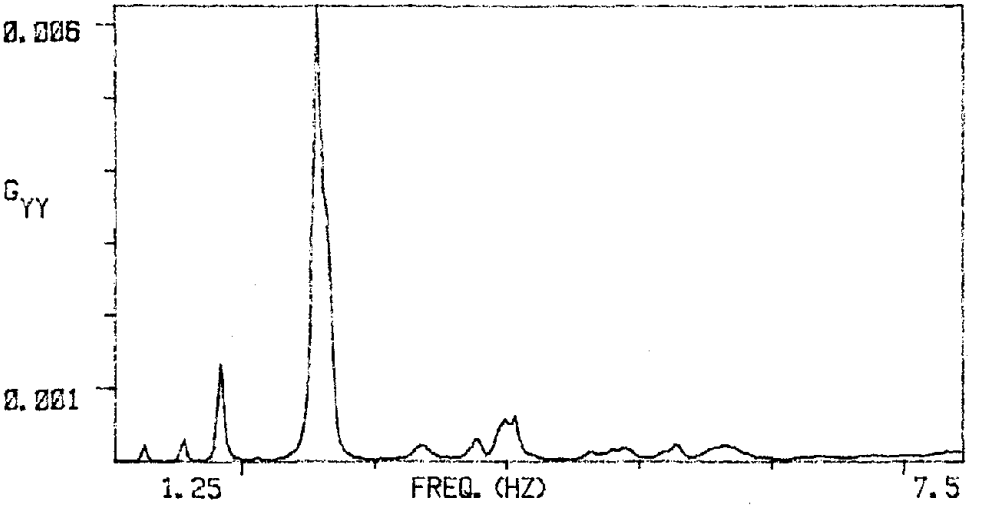

(a) Autospectrum

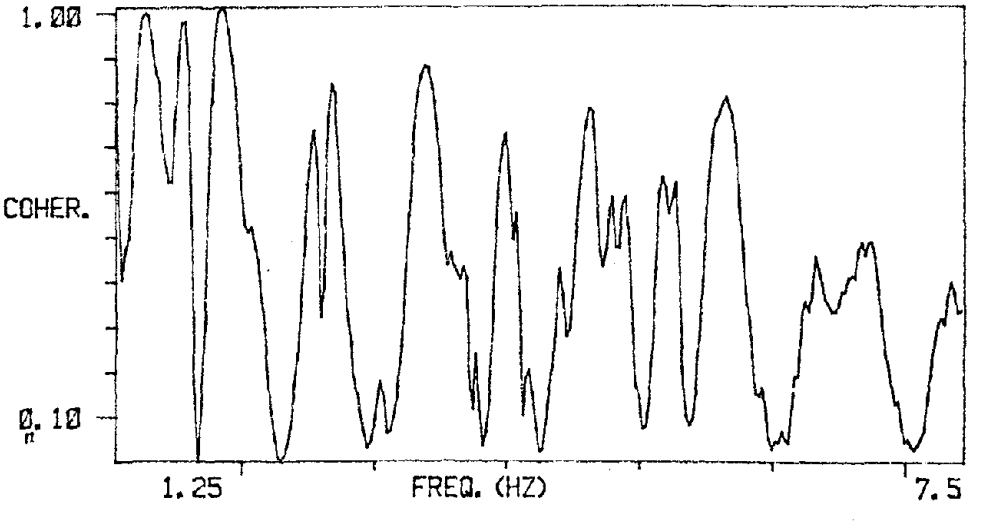

(b) Coherence

Figure 2.16. E-W Response on 8th Floor

modes but the values in these regions are generally less than those corresponding to the lower order modes. It is also observed from the autospectra that the higher order modes are rather difficult to distinguish without response data from additional floors.

In view of the above factors concerning the higher modes, it was decided to focus attention on the first few modes only. The autospectra to be used in curve fitting were computed up to 4 Hz with an increased frequency resolution of 0.05625 Hz so that the bias in the estimates would be reduced. The bias depends on the shape of the true spectra themselves and thus would be different in different regions of the spectra.

In the worst possible case when only 3 hours of data were employed, the approximate random error in the estimates can be determined as follows. The time length of each segment used in averaging is equal to 64 seconds. If nonoverlapping averages are employed, the number of averages that could be obtained with about 3 hours of data is given by $n_d \simeq 168$. Therefore, from Equation (2.14a), $\varepsilon_r \simeq 0.08$. Hence, in general, for all the power spectral density estimates calculated here, $\varepsilon_r < 0.08$ or less than 8 percent.

2.5 Analytical Formulation

The curve fitting procedure employed to determine the modal parameters consists of fitting the analytical form of $|H(f)|$ for a multidegree-of-freedom system subjected to a random loading at one of its coordinates to the square root of the autospectrum measured at different locations. The final parameter estimates are obtained by

averaging the individual estimates computed from various autospectra. In this section, the expression for $|H(f)|$ is derived first followed by a description of the Levenberg-Marquardt algorithm for the minimization of the sum of squares error function. The derivation of H(f) from which $|H(f)|$ is deduced is rather straightforward, but is carried out here nevertheless for the sake of completeness and consistency in notation.

Consider an n degree-of-freedom system governed by the following set of differential equations.

$$[M]\ \{\ddot{y}\} + [C]\{\dot{y}\} + [K]\ \{y\} = \{x(t)\} \tag{2.16}$$

where M = n x n mass matrix

K = n x n stiffness matrix

C = n x n viscous damping matrix

$\{x(t)\}$ = n x 1 forcing vector (input)

$\{y\}$ = n x 1 response vector (output)

and a dot denotes differentiation with respect to time, t. Equation (2.16) represents n coupled differential equations which can be uncoupled assuming proportional damping, by using the n x n modal matrix $[\phi]$.

$$[\phi] = \begin{bmatrix} \phi_{11} & \cdots & \phi_{1n} \\ \phi_{21} & & \vdots \\ \vdots & & \vdots \\ \phi_{n1} & & \phi_{nn} \end{bmatrix} = [\phi_1\ \phi_2\ \phi_3 \cdots \phi_n]$$

If $W_R(f)$ is the Fourier transform of $w'_R(t)$, then

$$W_R(f) = T \frac{\sin \pi fT}{\pi fT} e^{-j\pi fT}$$

where f is the frequency in Hertz. The Fourier transform of the truncated signal will be the convolution of the transform of the original signal and $W_R(f)$. Since the magnitude of $W_R(f)$ has large side lobe amplitudes, this may cause severe leakage of power at a single frequency into the neighboring frequencies. However, the rectangular window is capable of resolving frequencies that are at least Δf apart, where $\Delta f = \frac{1}{T}$ is the frequency resolution or interval at which the DFT samples are computed.

The leakage problem is reduced by using other types of window functions which possess diminished side lobe amplitudes. But this decrease in amplitude is accompanied by an increase in the main lobe width that causes a reduction in the frequency resolution possible. The window employed here is the commonly used Hanning window for which the time domain weighting function and its Fourier transform are described by the following equations.

$$w_H(t) = 0.5 \left(1 - \cos \frac{2\pi t}{T}\right) \qquad 0 \leq t \leq T$$

$$= 0 \qquad \text{otherwise}$$

and

$$W_H(f) = 0.5\, W_R(f) - 0.25\, W_R(f + \Delta f) - 0.25\, W_R(f - \Delta f)$$

where

$$\{\phi_i\} = \begin{Bmatrix} \phi_{1i} \\ \phi_{2i} \\ \vdots \\ \phi_{ni} \end{Bmatrix} \text{, the ith mode shape.}$$

Using the transformation

$$\{y\} = [\phi]\ \{z\} \tag{2.17}$$

Equation (2.16) can be rewritten in terms of the modal coordinates $\{z\}$ as

$$[\phi]^T [M][\phi]\{\ddot{z}\} + [\phi]^T [C][\phi]\{\dot{z}\} + [\phi]^T [K][\phi]\{z\} = [\phi]^T \{x\} \tag{2.18}$$

Assuming that the damping matrix can be decoupled by ϕ and using the orthogonality of the mode shapes, Equation (2.18) reduces to

$$[m]\ \{\ddot{z}\} + [c]\ \{z\} + [k]\ \{z\} = [\phi]^T x \tag{2.19}$$

where

$[m]$ = generalized diagonal mass matrix

$[c]$ = generalized diagonal damping matrix

and $[k]$ = generalized diagonal stiffness matrix

Equation (2.19) consists of n independent second order differential equations corresponding to the n degrees of freedom. The equation for

the ith degree of freedom is given by

$$m_i \ddot{z}_i + c_i \dot{z}_i + k_i z_i = \{\phi_i\}^T\{x\} \tag{2.20}$$

Equation (2.20) can be expressed in terms of the ith natural frequency ω_i and the ith damping ratio ρ_i.

$$\ddot{z}_i + 2\rho_i \omega_i \dot{z}_i + \omega_i^2 z_i = \{\phi_i\}^T\{x\}/m_i \tag{2.21}$$

where

$$\omega_i = \sqrt{k_i/m_i}$$

and

$$\rho_i = c_i/(2 m_i\omega_i)$$

If the input vector $\{x(t)\}$ consists of a load $x_k(t)$ applied at the kth coordinate, the right hand side of Equation (2.21) reduces to $\phi_{ki} x_k(t)/m_i$. The letter k, used to denote the generalized stiffness in Equations (2.19) and (2.20), is also used as an index here but should give rise to no confusion. Substituting for the right hand side in Equation (2.21) and taking the Fourier transform, with zero initial conditions,

$$Z_i(\omega) = H_i(\omega)\ X_k(\omega) \tag{2.22}$$

where $Z_i(\omega)$ is the Fourier transform of $z_i(t)$, $X_k(\omega)$ is the Fourier transform of $x_k(t)$ and $H_i(\omega)$ is defined as

$$H_i(\omega) = \frac{\phi_{ki}}{m_i \omega_i^2} \quad \frac{1}{(1 - \frac{\omega^2}{\omega_i^2}) + 2\, j\rho_i \frac{\omega}{\omega_i}} \tag{2.23}$$

where $j = \sqrt{-1}$. From Equation (2.17),

$$\{Y(\omega)\} = [\phi]\{Z(\omega)\}$$

and the Fourier transform of the response measured at location ℓ can be written as

$$Y_\ell(\omega) = \sum_{i=1}^{n} \phi_{\ell i}\, Z_i(\omega) \tag{2.24}$$

Substituting for $Z_i(\omega)$ from Equation (2.22),

$$Y_\ell(\omega) = X_k(\omega) \sum_{i=1}^{n} \phi_{\ell i}\, H_i(\omega) \tag{2.24a}$$

Using Equation (2.23) in the above equation,

$$Y_\ell(\omega) = X_k(\omega) \sum_{i=1}^{n} \frac{\phi_{ki}\phi_{\ell i}}{m_i \omega_i^2} \quad \frac{1}{(1 - \frac{\omega^2}{\omega_i^2}) + 2\, j\rho_i \frac{\omega}{\omega_i}} \tag{2.24b}$$

If the response measured at location ℓ is the acceleration $\ddot{y}_\ell(t)$, then the Fourier transform of the response can be expressed as

$$Y_{2\ell}(\omega) = -\omega^2\, Y_\ell(\omega) \tag{2.25}$$

where $Y_{2\ell}(\omega)$ is the Fourier transform of the acceleration response. Substituting the expression for $Y_{\ell}(\omega)$ in Equation (2.25), the frequency response function between acceleration at location ℓ due to a force at location k can be shown to be

$$H(f) = Y_{2\ell}(f)/X_k(f)$$

$$= -\sum_{i=1}^{n} \frac{\phi_{ki}\phi_{\ell i}}{m_i} \frac{\frac{f^2}{f^2}}{(1 - \frac{f^2}{f_i^2}) + 2\, j\rho_i \frac{f}{f_i}} \qquad (2.26)$$

where ω has been replaced by f, the frequency in Hz.

Defining the following quantities,

$$N_i = A_i(\frac{f}{f_i})^2 \quad , \quad D_i = \alpha_i^2 + \beta_i^2$$

where

$$A_i = \frac{\phi_{ki}\phi_{\ell i}}{m_i} \quad , \text{ the participation factor for the ith mode}$$

$$\alpha_i = 1 - (\frac{f}{f_i})^2$$

and $$\beta_i = 2\,\rho_i(\frac{f}{f_i})$$

Equation (2.26) becomes

$$H(f) = \mathrm{Re}[H(f)] + j\,\mathrm{Im}[H(f)] \tag{2.27}$$

where Re [] denotes the real part and Im[] denotes the imaginary part, given by

$$\mathrm{Re}[H(f)] = -\sum_{i=1}^{n} \frac{N_i \alpha_i}{D_i} \tag{2.28}$$

and

$$\mathrm{Im}[H(f)] = \sum_{i=1}^{n} \frac{N_i \beta_i}{D_i}$$

From the definition of the frequency response function H(f),

$$|Y_{2\ell}(f)| = |H(f)|\ |X_k(f)|$$

which is the same as

$$\sqrt{G_{yy}(f)} = |H(f)|\sqrt{G_{xx}(f)} \tag{2.29}$$

where $G_{yy}(f)$ is the power spectral density function of the acceleration output and $G_{xx}(f)$ is the power spectral density function of the force input. Noting that

$$|H(f)| = \{\mathrm{Re}^2[H(f)] + \mathrm{Im}^2[H(f)]\}^{\frac{1}{2}}$$

and using the identity

$$(a_1 + a_2 + a_3 + \ldots a_n)^2 = \sum_{p=1}^{n} a_p^2 + 2 \sum_{p=1}^{n-1} \sum_{q=p+1}^{n} a_p a_q$$

the equation for $|H(f)|$ is given by the following.

$$|H(f)| = \left[\sum_{p=1}^{n} \frac{N_p^2}{D_p} + 2 \sum_{p=1}^{n-1} \sum_{q=p+1}^{n} \frac{N_p N_q}{D_p D_q} (\alpha_p \alpha_q + \beta_p \beta_q) \right]^{\frac{1}{2}} \qquad (2.30)$$

In the above equation, the first term within the brackets is the contribution due to the n individual modes while the second term arises due to the interaction among various modes. When modal interference between the modes is small, the second term can be neglected without incurring much error. This situation occurs when all the modes have low damping and are well separated. If one of these two conditions is not satisfied, the cross-term may contribute a significant amount to $|H(f)|$ and therefore cannot be discarded.

It is assumed here that the output linear spectrum magnitude $|Y(f)|$ can be approximately represented by a function of the form given in Equation (2.30). This function is fitted to the measured values of $|Y(f)|$, which in this case are taken as $\sqrt{G_{yy}(f)}$. The modal frequencies f_i, the damping ratios ρ_i and the participation factors A_i for the first few modes are determined from the best possible fit. The least squares criterion is applied to arrive at the best fit to the data; that is, the sum of the squares of the errors between the measured and the analytical values is minimized to estimate the modal characteristics. This procedure is referred to as the unweighted or the ordinary least

squares method since no weights are used in the sum of squares function. When weights are assigned to the error terms, it is called the weighted least squares method.

The sum of squares cost function to be minimized is given by ψ, where

$$\psi = \sum_{i=1}^{r} \left[|Y(f)|_i - |H(f)|_i \right]^2 \tag{2.31}$$

where $|Y(f)|_i$ and $|H(f)|_i$ are the measured and the analytical values evaluated at the ith frequency point and r is the number of points in $|Y(f)|$ considered in curve fitting. Only those points which lie close to the natural frequencies and which are sufficient to define all the modes of interest are used.

Since the analytical function $|H(f)|$ is nonlinear in the modal parameters, the technique used to minimize the objective function ψ, as in almost all the nonlinear curve fitting problems, is iterative in nature. Some initial values are assumed for all the parameters to be estimated and these values are altered methodically until the desired convergence is attained. The minimization procedure employed in the present case is the Levenberg-Marquardt method, which is one of the many possible modifications of the Gauss-Newton method (32, 33). The development and application of this method are discussed next.

If $\{\Theta\}$ denotes the vector of parameters to be estimated by fitting a function $F(\Theta)$ to a vector of measured values $\{Y\}$, the least squares objective function ψ, which is dependent on the unknown

parameters, is defined as

$$\psi(\theta) = \sum_i [Y_i - F_i(\theta)]^2 = \sum_i e_i^2 \tag{2.32}$$

$$= \{e\}^T\{e\}$$

where $e_i = [Y_i - F_i(\theta)]$ and

$$\{e\} = \begin{Bmatrix} Y_1 - F_1(\theta) \\ Y_2 - F_2(\theta) \\ \vdots \end{Bmatrix}$$

Expanding $\psi(\theta)$ about some $\{\theta\} = \{\theta^k\}$ in a Taylor's series and retaining terms only up to the second order,

$$\psi(\theta) = \psi(\theta^k) + \{g^k\}^T\{\delta\theta\} + \tfrac{1}{2}\{\delta\theta\}^T[S^k]\{\delta\theta\} \tag{2.33}$$

where $\{g^k\}$ is the gradient of $\psi(\theta)$ evaluated at $\{\theta^k\}$ and $\{S^k\}$ is the Hessian or the second derivative matrix evaluated at $\{\theta^k\}$. $\{\delta\theta\}$ is defined as

$$\{\delta\theta\} = \{\theta\} - \{\theta^k\}$$

$\{g^k\}$ and $[S^k]$ are defined by

$$g_i^k = \frac{\partial \psi}{\partial \theta_i} \Big|_{\{\theta\} = \{\theta^k\}}$$

$$S_{ij}^k = \frac{\partial^2 \psi}{\partial \theta_i \partial \theta_j} \Big|_{\{\theta\} = \{\theta^k\}}$$

Differentiating Equation (2.33) with respect to $\{\theta\}$ and equating to zero,

$$\frac{\partial \psi(\theta)}{\partial \theta} = \{g^k\} + [S^k]\{\delta\theta\} = 0$$

from which

$$\{\delta\theta\} = - [S^k]^{-1} \{g^k\} \tag{2.34}$$

and

$$\{\theta\} = \{\theta^k\} - [S^k]^{-1} \{g^k\} \tag{2.35}$$

If $\psi(\theta)$ is quadratic in $\{\theta\}$ and $[S^k]$is positive definite, Equation (2.35) gives the parameter values at the minimum of $\psi(\theta)$. For functions that are not quadratic, $\{\theta\}$ given by Equation (2.35) is likely to be closer to the minimum than the original values $\{\theta^k\}$. This process would have to be repeated again for the next iteration and continued until the minimum is found. The above procedure in which the parameters are updated according to Equation (2.35) is known as the Newton method. It should be noted that Newton's method requires evaluation of the second derivative matrix.

Since in many practical problems the objective function is quite complicated, the task of obtaining the second derivatives may prove very difficult. It may be preferable to use a method that requires only the first derivatives or no derivatives at all. But the performance of the direct search methods, which do not use any derivatives, is usually poor in comparison with the gradient or descent methods that employ the first derivatives. So, for a wide class of problems, gradient methods are used to optimize the objective function.

The most widely employed gradient method is the Gauss-Newton method, which can be derived from Newton's method as follows (34). Using Equation (2.32), $\{g\}$ can be expressed as

$$\{g\} = -2[J]^T\{e\} \tag{2.36}$$

where

$[J_{ij}] = \left[\frac{\partial F_i(\theta)}{\partial \theta_j}\right]$, the Jacobian or the sensitivity matrix.

The Hessian is defined by

$$S_{k\ell} = -2 \sum [Y_i - F_i(\theta)] \frac{\partial^2 F_i(\theta)}{\partial \theta_k \partial \theta_\ell} + 2 \sum_i \frac{\partial F_i(\theta)}{\partial \theta_k} \frac{\partial F_i(\theta)}{\partial \theta_\ell} \tag{2.37}$$

The first term in the above equation contains the error, which will usually be small for adequate models that are capable of reproducing the experimental data fairly well. If this term is neglected as an approximation,

$$[S_{k\ell}] \simeq 2[J]^T[J] \tag{2.38}$$

Equations (2.36) and (2.38) in (2.35) give

$$\{\theta\} = \{\theta^k\} + ([J]^T[J])^{-1} [J]^T \{e^k\} \tag{2.39}$$

Equation (2.39) defines the Gauss-Newton method. As derived here, it is obtained from Newton's method by using an approximation for [S] in terms of [J]. But this method can also be derived by linearizing the nonlinear model and computing the necessary corrections for the parameters using the linear model. Expanding $F(\theta)$ in a Taylor's series about $\{\theta\} = \{\theta^k\}$,

$$\{Y\} = \{F(\theta^k)\} + [J] \{\delta\theta\}$$

or

$$\{e^k\} = [J] \{\delta\theta\} \tag{2.40}$$

The normal equations corresponding to the linearized form Equation (2.40) are given by

$$[J]^T[J]\{\delta\theta\} = [J]^T\{e^k\}$$

which is the same as Equation (2.39). Thus, the Gauss-Newton method is tantamount to solving a series of linearized problems in successive iterations. Vector $\{\theta\}$ determined using Equation (2.39) at the kth iteration is taken as the initial parameter vector for the $(k + 1)$th iteration.

For nonlinear problems, the direction of the correction vector computed using the Gauss-Newton method is usually acceptable but the size or length of this vector may not be appropriate. As a result, the parameters modified according to Equation (2.39) may eventually lead to noncovergence of the method (35). To prevent this occurrence, changes in the method that would improve its convergence properties are necessary.

A simple modification of the Gauss-Newton method consists of searching along the direction given by this method, to determine an acceptable step size. The parameter updating equation for this case can be written as

$$\{\theta\} = \{\theta^k\} + \xi\,([J]^T[J])^{-1}[J]^T\{e^k\} \qquad (2.41)$$

where ξ is the step size parameter. In one approach that requires the least effort, ξ is chosen such that the value of the objective function evaluated at $\{\theta\}$ is less than the value at $\{\theta^k\}$. When this condition is satisfied, $\{\theta\}$ is accepted as the improved estimate, to be used in the next iteration. A more sophisticated approach would involve finding the minimum of $\psi(\theta)$ as a function of the step size variable,

using some interpolation scheme (34, 36). The value of ξ that minimizes $\psi(\theta)$ along the Gauss-Newton direction is found by representing $\psi(\theta)$ as a quadratic in ξ. This value is employed in Equation (2.41) to compute $\{\theta\}$.

The modified Gauss-Newton method given by Equation (2.41) may still be unsatisfactory for many problems where $([J]^T[J])$ tends to be ill-conditioned. To account for such cases, Levenberg (32) and Marquardt (33) added some quantity to the diagonal elements of $([J]^T[J])$. Let

$$[B] = [J]^T[J]$$

Then

$$\{\theta\} = \{\theta^k\} + ([B] + \mu[D])^{-1}[J]^T\{e^k\} \tag{2.42}$$

where [D] is a diagonal matrix and μ is a scalar. The elements of [D] are normally chosen as the absolute values of the diagonal elements of [B]. As the parameter $\mu \to \infty$, the direction given by Equation (2.42) approaches that of the negative gradient used in the steepest descent method. As $\mu \to 0$, this direction approaches the direction given by the Gauss-Newton method. Thus the presence of the parameter μ has the effect of interpolating between the steepest descent and the Gauss-Newton directions.

The computational scheme employed here is based on Equation (2.42) and can be represented as

$$\{\theta^{k+1}\} = \{\theta^{k}\} + \xi^{k}\{\Delta\theta^{k}\} \tag{2.43a}$$

where

$$([B^{k}] + \mu^{k}[D^{k}])\ \{\Delta\theta^{k}\} = [J^{k}]^{T}\{e^{k}\} \tag{2.43b}$$

The corrections to the parameters in the kth iteration are calculated by first solving the simultaneous equations given by Equation (2.43b) and then determining a suitable step size. If the original problem is not scaled properly with respect to the different parameters, it may be desirable to use some scaling technique before proceeding with the solution of Equation (2.43b). The scaling used here is that employed by Marquardt, which reduces the diagonal elements of [B] to unity. If $[B^{*}]$ represents the scaled version of [B],

$$B^{*}_{ij} = \frac{B_{ij}}{(B_{ii}\ B_{jj})^{\frac{1}{2}}}$$

Equation (2.43b) is now transformed to

$$([B^{k*}] + \mu^{k}[I])\ \{\Delta\theta^{k*}\} = \{q^{k*}\} \tag{2.44}$$

where [I] is the identity matrix and

$$q^{*}_{i} = \frac{q_{i}}{(B_{ii})^{\frac{1}{2}}}$$

with

$$\{q\} = [J]^T\{e\}$$

The above procedure is equivalent to sealing the parameters $\{\theta\}$ so that

$$\theta_i^* = \theta_i (B_{ii})^{\frac{1}{2}}$$

$$= \theta_i \left(\sum_j \frac{\partial F_j(\theta)}{\partial \theta_i} \right)^{\frac{1}{2}}$$

Therefore, $\{\Delta\theta\}$ can be obtained from $\{\Delta\theta^*\}$ as

$$\Delta\theta_i = \frac{\Delta\theta_i^*}{(B_{ii})^{\frac{1}{2}}}$$

Since the foregoing scaling procedure makes use of the values of the parameters themselves, Equation (2.43b) must be rescaled every iteration.

The convergence of the Levenberg-Marquardt method depends, to a considerable extent, on the value of μ. This parameter is usually allowed to vary from iteration to iteration. If μ is not properly chosen, the method may prove to be highly inefficient. The procedure followed here is the original scheme of Marquardt with the modification suggested by Bard (34) and is described below.

(i) Set $\mu^1 = 0.01$ for the first iteration.

(ii) For the kth iteration (k=1,2,...), compute $\{\theta^{k+1}\}$ using Equation (2.43a) with $\xi^k = 1$. If $\psi(\theta^{k+1}) < \psi(\theta^k)$, accept $\{\theta^{k+1}\}$ as the new estimates. Set $\mu^{k+1} = \mu^k/10$. If $\mu^{k+1} < \varepsilon_1$, set $\mu^{k+1} = \varepsilon_1$ and go to the next iteration. Otherwise

(iii) Replace ξ^k by $\xi^k/2$. Compute $\{\theta^{k+1}\}$ and $\psi(\theta^{k+1})$. If $\psi(\theta^{k+1}) < \psi(\theta^k)$, accept $\{\theta^{k+1}\}$. Set $\mu^{k+1} = 10\mu^k$. If $\mu^{k+1} \geq M$, terminate the procedure. Otherwise go to the next iteration.

(iv) If $\psi(\theta^{k+1}) > \psi(\theta^k)$ and $\xi^k \leq \varepsilon_2$, stop. If $\xi^k > \varepsilon_2$, go to step (iii).

ε_1 and ε_2 appearing in this procedure are small positive constants and M is a large number. These constants were assigned values of 10^{-7}, 10^{-3} and 10^7 respectively.

Equations (2.43a) and (2.43b), along with the above procedure to choose μ, can effectively be used to progress toward the minimum. Once the minimum has been approximately located, the process must be stopped in accordance with one or more specified convergence criteria. Some of the regularly used termination criteria are the following.

(a) $$|\{\theta^{k+1}\} - \{\theta^k\}| < \{b\} \tag{2.45a}$$

(b) $$\left|\frac{\theta_i^{k+1} - \theta_i^k}{\theta_i}\right| < \varepsilon_3 \tag{2.45b}$$

(c) $$|\psi^{k+1} - \psi^k| < \varepsilon_4 \tag{2.45c}$$

$$\text{(d)} \qquad \left|\frac{\psi^{k+1} - \psi^{k}}{\psi^{k}}\right| < \varepsilon_5 \qquad (2.45d)$$

where $\psi^k = \psi(\theta^k)$, $\{b\}$ is a vector of small positive constants and ε_3, ε_4 and ε_5 are small positive scalars. Criterion (b) was employed here to terminate the algorithm, with $\varepsilon_3 = 0.0001$; i.e., the procedure is assumed to have converged if the relative change in the parameters in two successive iterations is less than 0.01 percent. Care must be exercised, however, to ensure that the procedure is not terminated prematurely at some intermediate stage due to a very small value for the step size in Equation (2.43a). This was accomplished in the present case by including a check to verify that no halving of the step size parameter was necessary for the final iteration.

The Levenberg-Marquardt procedure, like most of the other nonlinear optimization methods, converges to a point which may or may not be the global minimum. But for curve fitting problems in which appropriate analytical expressions are fitted to carefully measured experimental data, this point can be expected to be the global minimum. In practice, different starting values for $\{\theta\}$ can be used to check if the procedure converges to the same point. If this is found to be the case, the converged values will usually correspond to the global minimum.

2.6 Curve Fitting

The objective function for the modal parameter estimation problem treated here is defined by Equation (2.31). The parameter vector $\{\theta\}$ is chosen to consist of the frequencies, the damping ratios

and the participation factors for those modes included in estimation.

$$\{\theta\} = \begin{Bmatrix} f_1 \\ \rho_1 \\ A_1 \\ \vdots \\ f_n \\ \rho_n \\ A_n \end{Bmatrix}, \quad (3n \times 1) \text{ vector where n is the number of modes considered}$$

The derivatives of the function $|H(f)|$ with respect to the modal parameters are needed to evaluate the Jacobian [J]. It is possible to use finite-difference approximations for the derivatives but the overall convergence of the method can be greatly improved by using the exact values. The expressions for these derivatives, in terms of the α_i, β_i, N_i and D_i defined previously are the following.

$$2\,|H(f)|\,\frac{\partial|H(f)|}{\partial f_i} = -\frac{4}{f_i}\frac{N_i}{D_i^2}\left\{N_i\left(\alpha_i + \frac{\beta_i^2}{2}\right) + \sum_{\substack{j=1 \\ j\neq i}}^{n}\frac{N_j}{D_j}\left[\alpha_j\left(\alpha_i^2 - \beta_i^2\,\frac{f^2}{f_i^2}\right)\right.\right.$$

$$\left.\left. + \frac{\beta_i\beta_j}{2}\left(\beta_i^2 + 3\alpha_i + \alpha_i\,\frac{f^2}{f_i^2}\right)\right]\right\} \qquad (2.46a)$$

$$2\,|H(f)|\,\frac{\partial|H(f)|}{\partial \rho_i} = -\frac{8N_i}{D_i^2}\left(\frac{f}{f_i}\right)\left\{\frac{N_i\beta_i}{2} + \sum_{\substack{j=1 \\ j\neq i}}^{n}\frac{N_j}{D_j}\left[\alpha_j(\alpha_i\beta_i) - \frac{\beta_j}{2}(\alpha_i^2 - \beta_i^2\right.\right.$$

(2.46b)

$$2|H(f)|\frac{\partial|H(f)|}{\partial A_i} = \frac{2}{D_i}\left(\frac{f^2}{f_i^2}\right)\left\{N_i + \sum_{\substack{j=1 \\ j\neq i}}^{n} \frac{N_j}{D_j}\left[\alpha_i\alpha_j + \beta_i\beta_j\right]\right\} \qquad (2.46c)$$

To start the curve fitting procedure, initial estimates for all the frequencies, damping ratios and participation factors must be supplied. Starting values for frequencies pose no problem since these can be taken as the peak frequencies in the autospectra. Values for damping can be obtained by examining the width of the peaks. But choosing initial guesses for the participation factors needs some special care. The participation factor for a given mode can either be positive or negative depending upon the locations of the response and the applied input. While it is possible to estimate the magnitude of this factor from the peak amplitude, its sign cannot be determined except in some specific cases.

When the modal interaction between various modes is minimal, the contribution of the cross-product term in Equation (2.30) will be relatively small. In this case $|H(f)|$ would depend mostly on the sum of the individual modal responses given by the first term. Since this term contains only the squares of the participation factors, it remains unaffected by their signs. Consequently, the curve fitting procedure applied to such a case is not significantly influenced by the signs chosen for these factors and, in general, does not alter them. Specifically, the algorithm converged to a minimum point so that if the sign for a participation factor is initially chosen as positive (negative), it remains positive (negative). In order to obtain convergence to the correct values, it is therefore essential to start with correct signs for all the factors, which then must be determined beforehand.

A trial and error procedure is adopted here to find the signs of the participation factors in any given power spectral density funct The basis for this procedure is that if an incorrect combination of signs is used for various modes, the fit obtained would tend to be poorer than the fit that would result if the correct choice for the signs is employed. In other words, the minimum found using the estimation algorithm will be global with the lowest possible value for the objective function only if the proper combination of signs is used. With this assumption, attempts were made initially to determine the sign combination by taking two modes at a time. A two degree-of-freedom fit is carried out, using two modes including the most dominant mode, first with the same signs and then with opposing signs for the participation factors. The combination that gives a lesser value for ψ is taken to be the correct one. Next, one of these modes is dropped and another one added and the sign for this mode determined. This procedure is repeated until the signs for all the other modes with respect to the dominant one are found. Finally, a multidegree-of-freedom fit taking all the modes of interest into account is performed. If the fit is found to be unsatisfactory, the sign of one or more factors is changed so that a better fit with a lower cost function value is obtained.

Another procedure that worked more efficiently with analytical functions involves the use of 3 modes at once, but is otherwise similar to the one given above. A three degree-of-freedom fit is carried out for each of the four possible combinations of signs for the three modes considered initially. After the best fit is identified, one of these modes is dropped and another one added. This procedure yielded the

correct signs for many analytically created $|H(f)|$ provided that all the modes considered were quite prominent.

Determination of the signs of the modal participation factors is required only for the reference autospectrum with respect to which the cross-spectra are computed. The phase components of the cross-spectra together with the signs in the reference spectrum can be used to extract the signs for the other autospectra.

The curve fitting procedure described heretofore deals with the estimation of the vibrational parameters for a number of modes from the response power spectral density function. But for many applications, it is not enough to estimate the parameters alone; it is also desirable to determine some measure of the variability or reliability of the final parameter values. In most estimation procedures, this is accomplished by computing the approximate covariance matrix of the optimum estimates.

The ordinary least squares procedure employed here does not utilize any knowledge about the distribution of the errors. Yet, if one assumes normally distributed measurement errors with equal variance, it can be viewed as a maximum likelihood procedure since the objective function to be minimized is essentially the same in both cases under such conditions. If σ^2 denotes the variance of the errors, the approximate covariance matrix of the converged estimates $\{\theta^*\}$ is given by (34)

$$V_{\theta^*} = \sigma^2[B]^{-1} \tag{2.47}$$

If σ^2 is not known, it can be estimated as

$$\hat{\sigma}^2 = \frac{\psi(\theta^*)}{r - p} \tag{2.48}$$

where p is the number of parameters to be estimated, (r - p) is the number of degrees of freedom and $\psi(\theta^*)$ is the objective function value at the minimum.

In the current estimation procedure which uses $\sqrt{G_{yy}(f)}$, the errors are not distributed normally with equal variance. Nevertheless, it is assumed that this is true and the covariance matrix of the estimates is computed using Equations (2.47) and (2.48). When the covariance matrix is known, the coefficient of variation ε_r and the correlation coefficient τ can be calculated from

$$(\varepsilon_r)_{\theta_i} = \sqrt{(V_{\theta^*})_{ii}} / \theta_i^* \tag{2.49a}$$

$$\tau_{\theta_i\theta_j} = (V_{\theta^*})_{ij} / \sqrt{(V_{\theta^*})_{ii}(V_{\theta^*})_{jj}} \tag{2.49b}$$

where $(\varepsilon_r)_{\theta_i}$ is the coefficient of variation for parameter θ_i and $\tau_{\theta_i\theta_j}$ is the correlation coefficient for parameters θ_i and θ_j.

Finally, it is observed that a single degree-of-freedom fit can be carried out using the above estimation procedure. To handle this special case, only the first terms in Equations (2.30) and (2.46) are retained. The rest of the procedure is the same except for the determination of the signs of the participation factors, which does not arise here. Single degree-of-freedom fits are likely to give good

results for modes that are well separated from the others.

Before closing this section, two aspects that were ignored in the present estimation scheme will be discussed briefly.

(1) No attempts were made to consider the effects of the frequencies that lie outside the bandwidth of interest. Approximate terms, which are functions of the frequency variable f and additional unknown constants, can be added to $|H(f)|$ to include the effects of those modes that fall below or above the frequency range being considered. The additional unknown constants can be estimated along with the modal parameters themselves. The expressions for these terms can be derived from the analytical form of $|H(f)|$. The inclusion of such terms will probably improve the quality of the fits obtained.

(2) No constraints were imposed on the parameters. In general, the frequencies and the damping ratios must be prevented from assuming negative values at any stage in the estimation procedure. Hence, the estimation of the modal parameters must be treated as a constrained problem. But experience with the experimental data from the building indicates that no constraints are necessary. It was found that only in those cases where unreasonable initial values are used and/or highly insignificant modes with very small peaks are taken into account, the estimates could assume negative values. But in the case of single degree-of-freedom fits, the estimates for damping could become negative more frequently since $|H(f)|$ now depends on ρ^2. Even in these cases, starting from slightly different initial estimates usually helped prevent this from occurring.

2.7 Results

The application of the curve fitting procedure described in the preceding sections will now be discussed. The estimation algorithm was implemented in an HP 1000 minicomputer. The autospectra determined from the ambient data were transferred from the signal analyzers employed in their calculation to the computer using an HP 9825A programmable calculator.

The computer program utilized in estimation was developed for interactive use since this would enable greater operator control over the curve fitting process. Plotting routines were used to check the quality of the fits obtained. In almost all the cases, the program converged to the final values in about 6-10 iterations.

The number of modes considered varied for different spectra. Since attention was directed at the first few modes only, the higher modes were not included except for those spectra in which they appeared to influence the lower modes. In particular, the first three bending modes in either direction and the first two torsional modes were taken into account, with the fourth bending mode being included only when it is one of the dominant modes overlapping with the other modes of interest. The modes above 3 Hz were not considered at all.

The number of points around each mode used in curve fitting varied from peak to peak. While too few points can result in poor estimates, too many points away from the peaks can slow down the convergence considerably and in some cases can even cause nonconvergence. This is because the output power spectral density function is only a

dubious approximation of $|H(f)|^2$ in the regions away from the peaks. A number of points just sufficient to completely define each modal peak must be used and this number, in the present procedure, ranged from about 7 for the sharpest peak encountered to about 15 for the broader ones. For closely spaced modes, all the points in between the modes were included.

As has already been mentioned, the intial estimates for the frequencies were taken as the peak frequencies in the autospectra. Although the half-power bandwidth method could have been used to estimate the initial values for damping, these values were taken as 0.01 for all the modes and the algorithm seemed to converge just as well. Likewise, no efforts were made to choose the participation factors from the peak amplitudes. The factors for all the modes were set equal to a constant that depended on the maximum value of $G_{yy}(f)$. The trial and error procedure to determine the signs of the participation factors was applied to the reference spectrum. The cross-spectra were used to fix the signs in the remaining autospectra.

Before discussing the results of the estimation procedure obtained using the building data, the results obtained using an analytical function to evaluate the performance of the procedure are presented. The values of the modal parameters assumed to create the function $|H(f)|$ with 5 degrees-of-freedom are listed in Table 2.3. The initial estimates assumed and the converged values are listed in Table 2.4. It is seen that the procedure has converged to the exact values. Next, the initial guesses for all the participation factors were assumed

Table 2.3. Modal Properties for the Test Case

Mode No.	Frequency (Hz)	Damping Ratio (%)	Participation Factor
1	10.0	1.5	1.50
2	20.0	2.0	-1.75
3	30.0	2.5	2.00
4	40.0	3.0	-2.25
5	50.0	3.5	2.50

Table 2.4. Initial and Converged Values for the Test Case - Case (i)

Mode No.	Frequency (Hz)		Damping Ratio (%)		Participation Factor	
	Initial	Final	Initial	Final	Initial	Final
1	9.9	10.0	1.00	1.50	1.00	1.50
2	19.9	20.0	1.00	2.00	-1.00	-1.75
3	29.9	30.0	1.00	2.50	1.00	2.00
4	39.9	40.0	1.00	3.00	-1.00	-2.25
5	49.9	50.0	1.00	3.50	1.00	2.50

$\psi = 0.192 \times 10^{-5}$

Table 2.5. Initial and Converged Values for the Test Case - Case (ii)

Mode No.	Frequency (Hz)		Damping Ratio (%)		Participation Factor	
	Initial	Final	Initial	Final	Initial	Final
1	9.9	10.03	1.00	1.46	1.00	1.48
2	19.9	20.01	1.00	2.10	1.00	1.81
3	29.9	29.98	1.00	2.78	1.00	2.14
4	39.9	39.80	1.00	3.84	1.00	2.57
5	49.9	48.85	1.00	4.17	1.00	2.23

$\psi = 39.292$

positive. Table 2.5 shows the initial and the converged values for this case. The value of the sum of squares error function is 39.29 as opposed to a value of 0.19×10^{-5} when the correct signs are assumed. The converged values of the parameters are closer to the true values for the lower modes than for the higher modes, which suggests more modal overlapping at higher frequencies. The analytical function and the fit for the latter case are given in Figure 2.17.

Samples of fits obtained using data taken on the last test date (November 13, 1980) are shown in Figures 2.18 - 2.27. Figures 2.18 - 2.22 give the measured and the estimated functions in the magnitude squared form $G_{yy}(f)$ and Figures 2.23 - 2.27 give the same in the magnitude form $\sqrt{G_{yy}(f)}$. The values of the frequencies and damping ratios corresponding to these fits are tabulated in Tables 2.6 and 2.7. All the modes are well separated in the autospectra measured in the N-S direction (Figures 2.23 - 2.27), but the E-W response contains two closely spaced modes, the third bending and the second torsion (Figures 2.18 - 2.22). It is in such cases that the multiple degree-of-freedom curve fitting procedures are extremely useful.

The fits for all the spectra are satisfactory around all the modal peaks of interest. Greatest deviation of the fit from the measured function occurs at frequencies around the third bending mode in the N-S direction and the parameters for this mode show the greatest variation (Table 2.6). Values for the torsional modes determined from the response in two directions agree closely with each other. Frequencies and damping ratios for the second torsional mode show

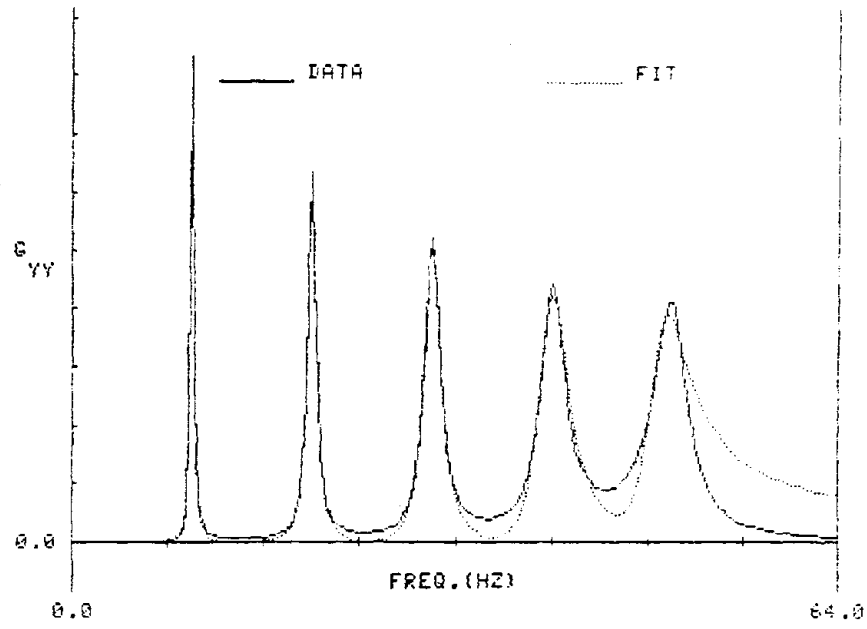

Figure 2.17. Analytical Magnitude Squared Function and its Best Fit with all Participation Factors Positive

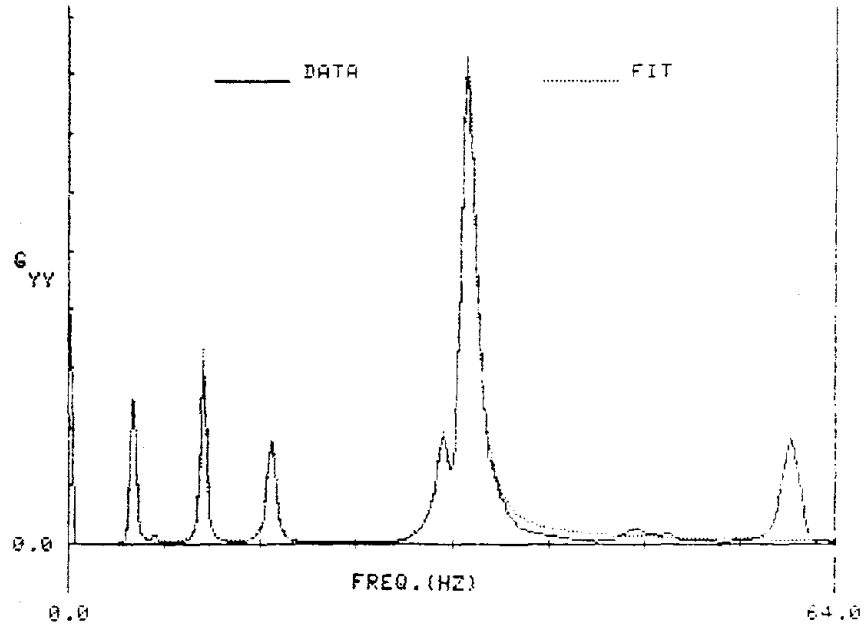

Figure 2.18. E-W Autospectrum on 24th Floor and its Best Fit

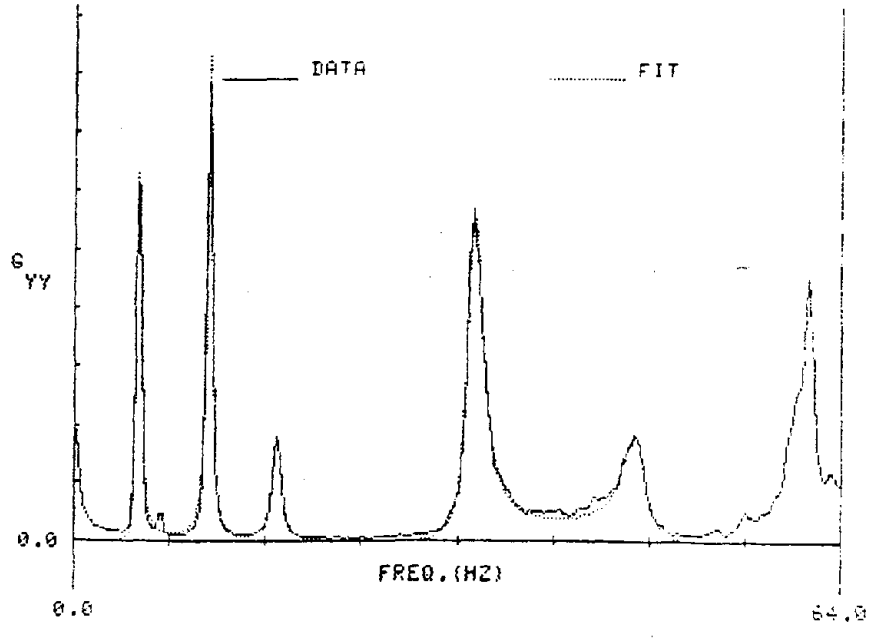

Figure 2.19. E-W Autospectrum on 22nd Floor and its Best Fit

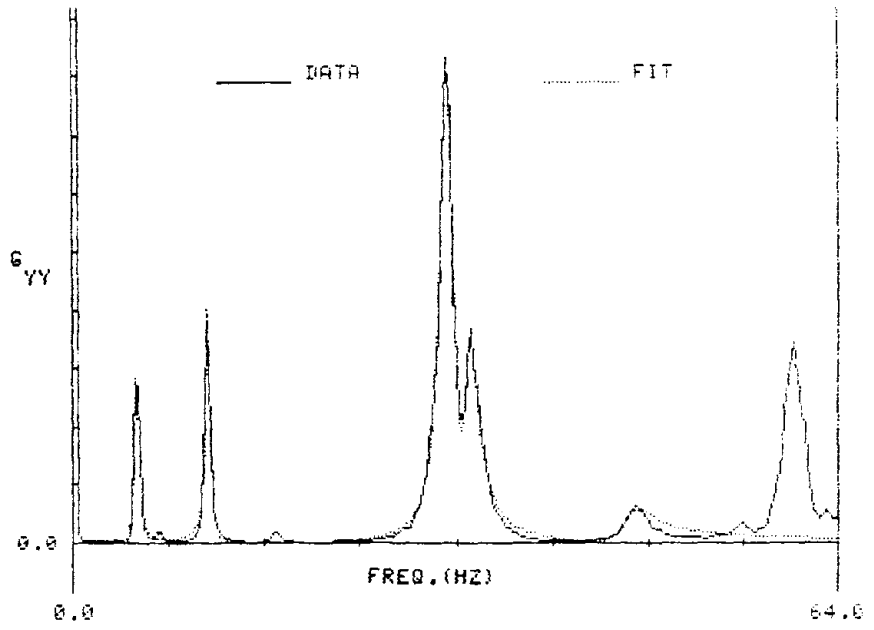

Figure 2.20. E-W Autospectrum on 18th Floor and its Best Fit

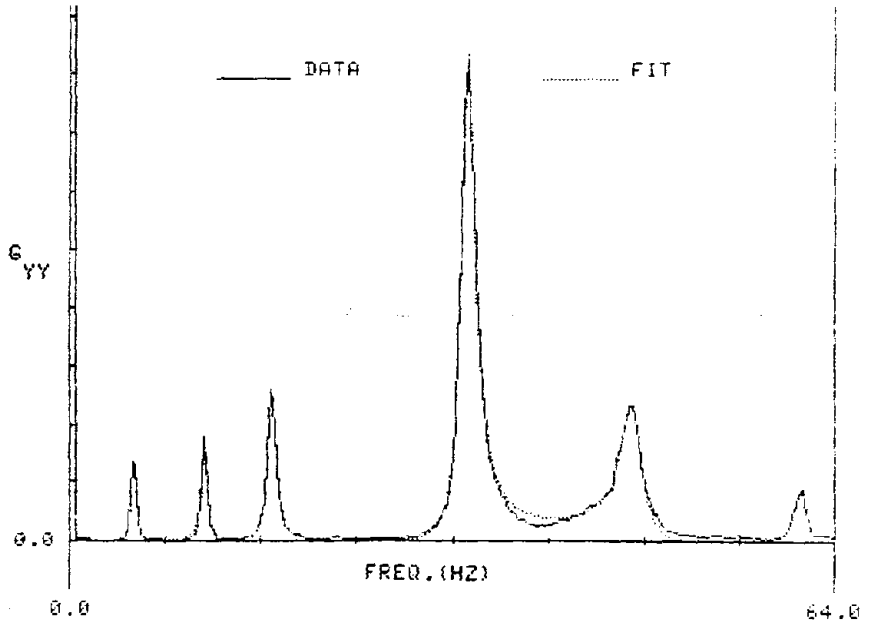

Figure 2.21. E-W Autospectrum on 13th Floor and its Best Fit

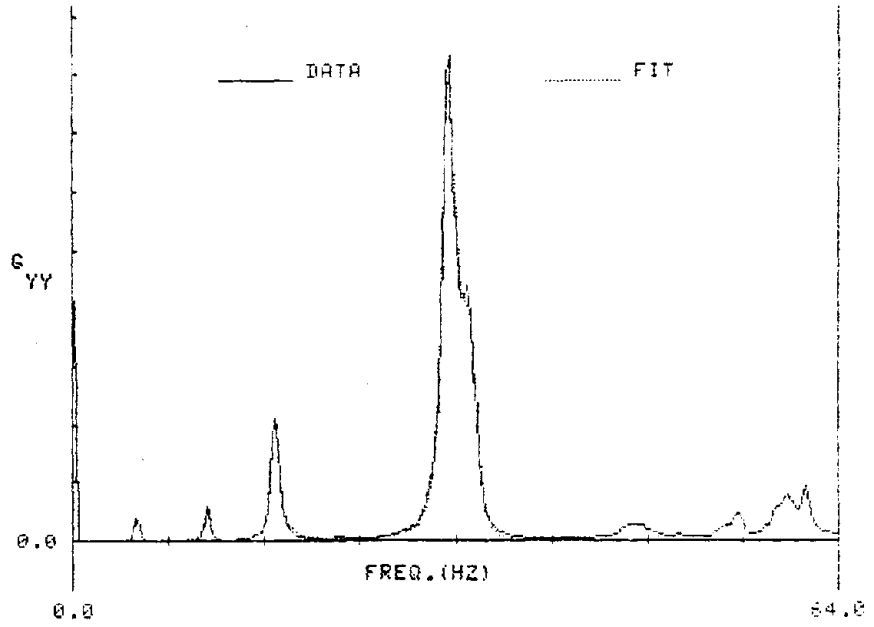

Figure 2.22. E-W Autospectrum on 8th Floor and its Best Fit

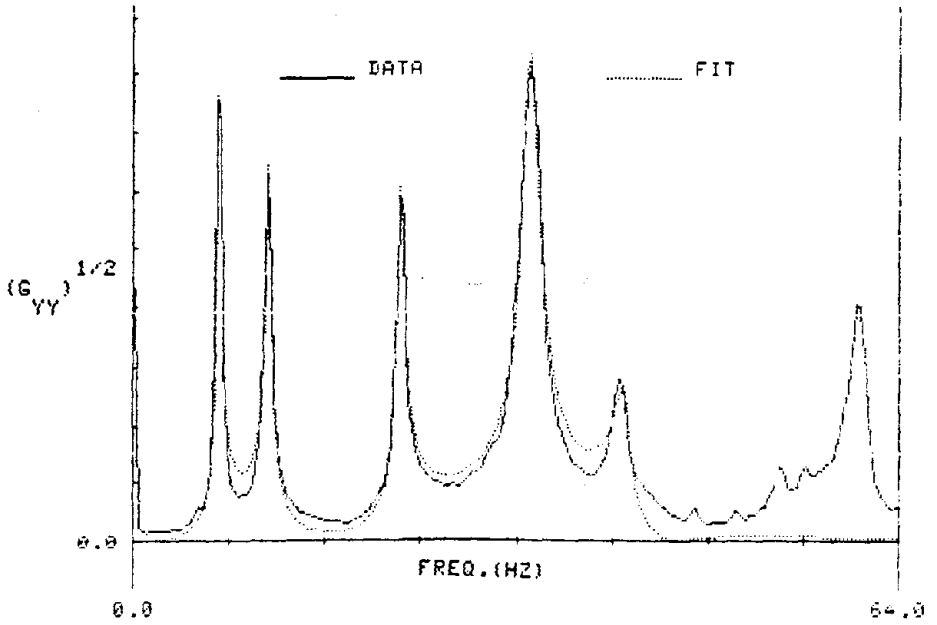

Figure 2.23. N-S Autospectrum on 24th Floor and its Best Fit

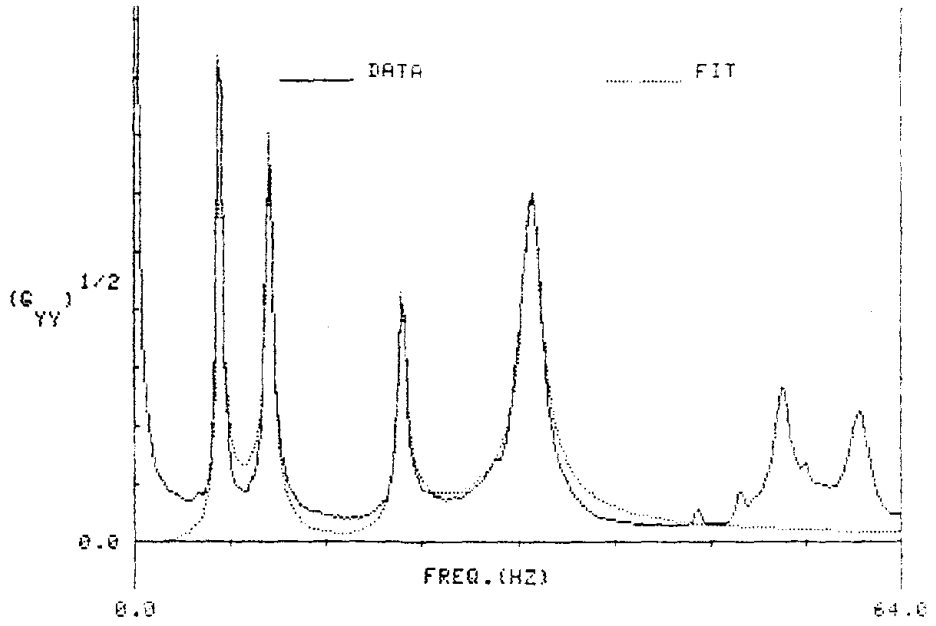

Figure 2.24. N-S Autospectrum on 22nd Floor and its Best Fit

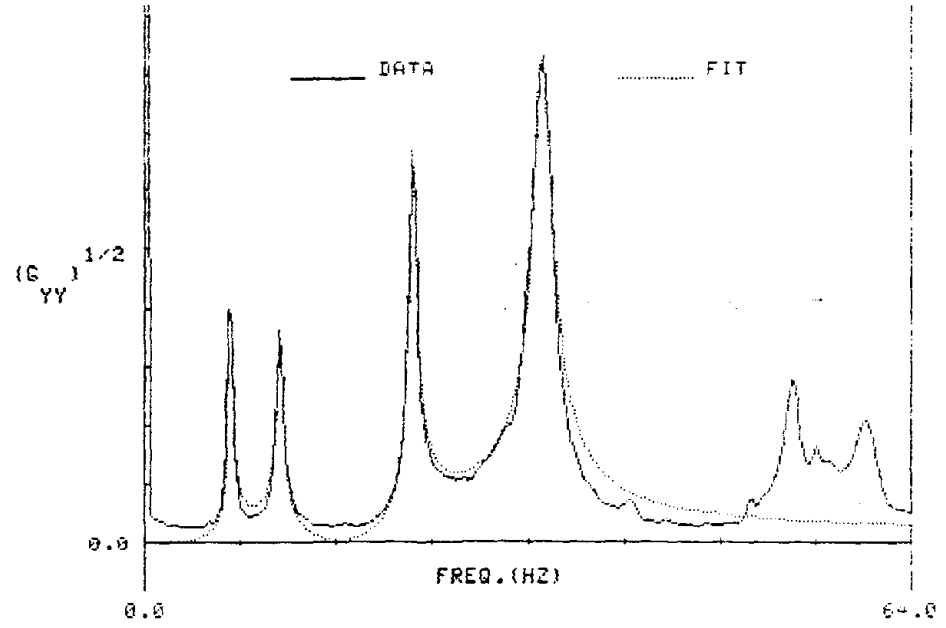

Figure 2.25. N-S Autospectrum on 18th Floor and its Best Fit

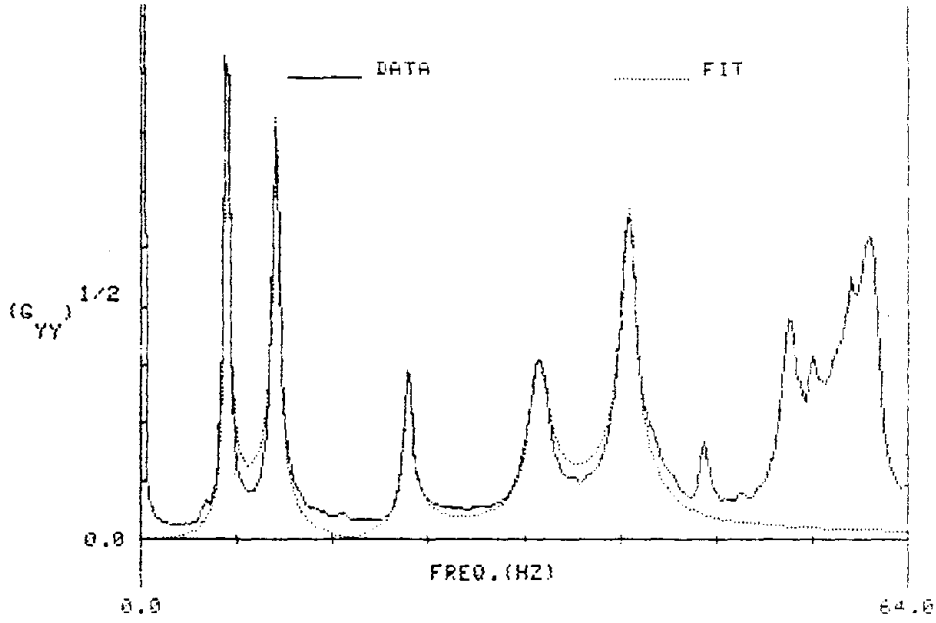

Figure 2.26. N-S Autospectrum on 13th Floor and its Best Fit

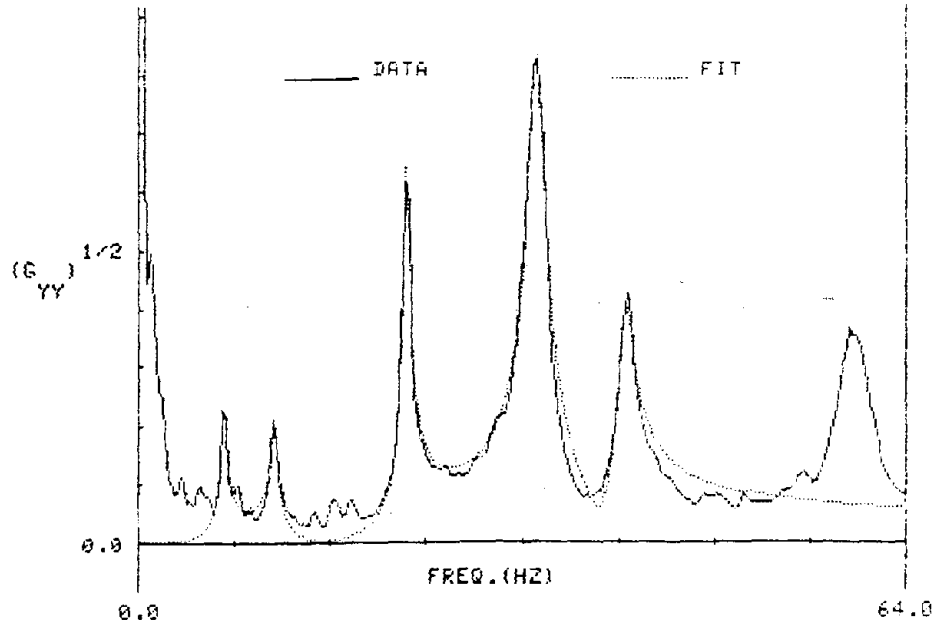

Figure 2.27. N-S Autospectrum on 8th Floor and its Best Fit

Table 2.6. Estimates for the N-S Directional Response

Mode No. (Type)	Floor No.	8	13	18	22	24
1 (Bending)	Freq.(Hz)	0.443	0.444	0.444	0.444	0.444
	Damp. (%)	2.42	1.05	0.97	1.24	1.07
2 (Torsion)	Freq.(Hz)	0.709	0.706	0.706	0.707	0.706
	Damp. (%)	2.19	1.90	1.88	1.88	1.76
3 (Bending)	Freq.(Hz)	1.393	1.393	1.394	1.392	1.394
	Damp. (%)	1.28	1.24	1.31	1.30	1.29
4 (Torsion)	Freq.(Hz)	2.073	2.073	2.070	2.074	2.075
	Damp. (%)	2.08	2.09	2.16	2.10	2.01
5 (Bending)	Freq.(Hz)	2.530	-	2.545	-	2.556
	Damp. (%)	1.67	-	1.41	-	1.58

Table 2.7. Estimates for the E-W Directional Response

Mode No. (Type)	Floor No.	8	13	18	22	24
1 (Bending)	Freq.(Hz)	0.335	0.335	0.335	0.335	0.335
	Damp. (%)	1.62	1.89	2.32	2.44	1.90
2 (Torsion)	Freq.(Hz)	0.707	0.707	0.705	0.704	0.702
	Damp. (%)	2.02	2.00	1.92	1.96	1.89
3 (Bending)	Freq.(Hz)	1.051	1.053	-	1.055	1.056
	Damp. (%)	2.20	2.18	-	2.42	2.07
4 (Bending)	Freq.(Hz)	1.952	-	1.955	-	1.957
	Damp. (%)	2.09	-	2.06	-	1.81
5 (Torsion)	Freq.(Hz)	2.092	2.077	2.068	2.081	2.077
	Damp. (%)	2.45	2.17	1.90	2.24	2.08

greater variation in the E-W response (Table 2.7). This is attributable to the fact that this mode appears as one of the two closely spaced modes and, except in the 24th floor response, is not the dominant of the two. In fact, this mode is barely discernible in the 8th floor response. The estimates obtained from this response are considerably different from estimates for other floors (Figure 2.18 and Table 2.7). Damping values for the fundamental N-S bending and torsional modes are somewhat high for the 8th floor response because their modal peaks are relatively insignificant in this response (Figures 2.23 and Table 2.6).

Typical values computed for the approximate coefficients of variation and the correlation coefficients will be given next. Table 2.8 lists the values of ε_r calculated from the diagonal elements of the parameter covariance matrix V_θ* for the E-W response from the 24th floor. The correlation coefficients computed from the off-diagonal elements are shown in Table 2.9. As would normally be anticipated, the values of ε_r are the least for the parameters of the dominant mode, which in this case is the second torsional mode. Relatively high values of ε_r for the 3rd bending mode are mostly due to this mode being the lesser pronounced of the two closely spaced modes. But the highest ε_r corresponds to the damping ratio of the lowest mode. This trend was observed in almost all the estimated spectra. The probable cause is the resolution bias error which is higher for the lower modal frequencies since, for the same value of ρ, a lower frequency mode is defined by fewer points than a higher frequency mode. The above trend is also confirmed by Table 2.7, in which the

Table 2.8. Approximate Coefficients of Variation for the Modal Parameters from the E-W Directional Roof Response

Mode No.	Frequency (Hz)		Damping Ratio (%)		Participation Factor	
	Estimate	Coeff. Var.	Estimate	Coeff. Var.	Estimate (1)	Coeff. Var.
1	0.335	0.0009	1.90	0.133	1.789	0.046
2	0.702	0.0011	1.89	0.050	-1.326	0.034
3	1.056	0.0011	2.07	0.065	1.107	0.043
4	1.957	0.0010	1.81	0.099	0.604	0.096
5	2.077	0.0004	2.08	0.028	2.184	0.025

(1) Not the actual or true values. The actual values are obtained using a multiplication factor that depends on the maximum magnitude of the spectrum and the gain of the amplifier.

Table 2.9. Correlation Coefficients for the Modal Parameters from the E-W Directional Roof Response

	f_1	ρ_1	A_1	f_2	ρ_2	A_2	f_3	ρ_3	A_3	f_4	ρ_4	A_4	f_5	ρ_5	A_5
f_1	1	-.21	-.16	-.03	-.02	.02	.02	-.00001	-.001	.009	-.02	-.03	.03	.01	.02
ρ_1		1	.89	.18	.009	-.005	-.16	.05	.06	-.06	.11	.17	-.21	-.09	-.14
A_1			1	.20	.009	-.002	-.18	-.06	.07	-.07	.12	.19	-.24	-.10	-.16
f_2				1	.06	-.007	-.02	-.06	-.06	-.006	.01	.02	-.03	-.02	-.02
ρ_2					1	-.84	.14	-.06	-.07	.04	-.06	-.10	.12	.05	.08
A_2						1	-.16	.06	.07	-.04	.08	.11	-.15	-.06	-.10
f_3							1	-.009	-.04	.01	-.02	-.04	.07	.03	.05
ρ_3								1	.09	-.05	.09	.14	-.17	-.08	-.12
A_3									1	-.06	.10	.16	-.20	-.09	-.14
f_4										1	.02	.006	.20	-.18	-.18
ρ_4											1	.89	-.04	-.49	-.68
A_4												1	-.10	-.64	-.82
f_5													1	.08	.14
ρ_5														1	.90
A_5															1

damping values for the lowest mode show the greatest variation.

Table 2.9 shows moderate values of τ for the parameters of the 4th and the 5th modes and high values between the damping ratio and the participation factor for each mode. The correlation values for the closely spaced modes are to be expected, whereas the high values between ρ_i and A_i are due mainly to the following reason. Considering the case of a single degree-of-freedom system, the value of $|H(f)|$ at the peak frequency, using Equation (2.30), is given by

$$|H(f)|_{f = f_i} = \frac{A_i}{2\rho_i}$$

Thus, including only those points that lie close to the peak will lead to significant correlation between A_i and ρ_i. The high values of τ could possibly be reduced by using a weighted least squares approach in which the weights are chosen inversely proportional to the measured $\sqrt{G_{yy}(f)}$. This problem was not pursued further in this study.

The frequency and damping estimates found using three different methods for the N-S response from the 24th floor will now be compared. The methods employed here are the following:

1. Multidegree-of-freedom curve fitting
2. Single degree-of-freedom curve fitting for each mode
3. Direct method in which the peak frequencies are taken as the natural frequencies and the damping ratios are computed using the half-power points.

The 24th floor N-S response was chosen for comparison since it does not contain any closely spaced modes and the direct as well as the single

degree-of-freedom curve fitting methods can be applied to all the modes.

It has already been pointed out that the spectral estimates in the vicinity of the lower modes suffer from insufficient resolution. The damping ratios computed using the half-power bandwidth method will be acceptable only if the frequency resolution is such that there are at least 4 points between the half-power points (28). This condition was not satisfied for the first 3 modes in the spectrum given in Figure 2.23. So, the time domain data was processed again with twice the frequency resolution as before (Δf = 0.0078125 Hz) to obtain the parameters for the third mode and with four times the frequency resolution (Δf = 0.00390625 Hz) to obtain the parameters for the first 2 modes. Figures 2.28 and 2.29 show the resulting high resolution autospectra. Owing to the smaller number of averages used in their computation, these spectra are subject to higher variance.

The second modal peak in the high resolution spectrum of Figure 2.29 exhibits behavior that is characteristic of nonlinear modes. At this point, it is not clearly understood what causes such behavior. Possible reasons other than nonlinearities include nonstationary response and peculiarities in the input spectrum. The half-power bandwidth method could not be applied to determine the damping ratio for this mode. In any event, the modal parameters obtained by applying the single and multidegree-of-freedom curve fitting procedures to the low resolution spectrum would be those for an equivalent linear system.

The estimates for the remaining parameters calculated using the three methods are given in Table 2.10. All the three methods give

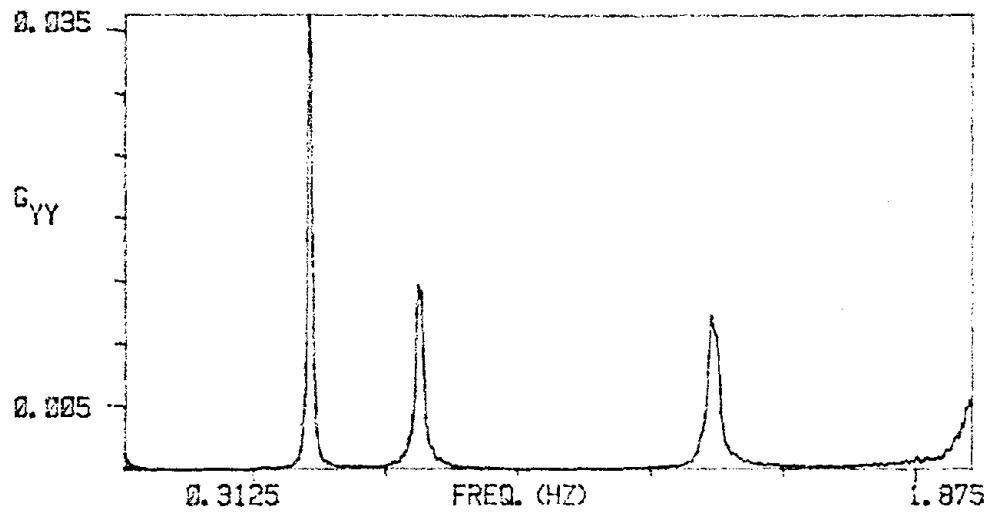

Figure 2.28. High Resolution Autospectrum with Δf = 0.0078125 Hz

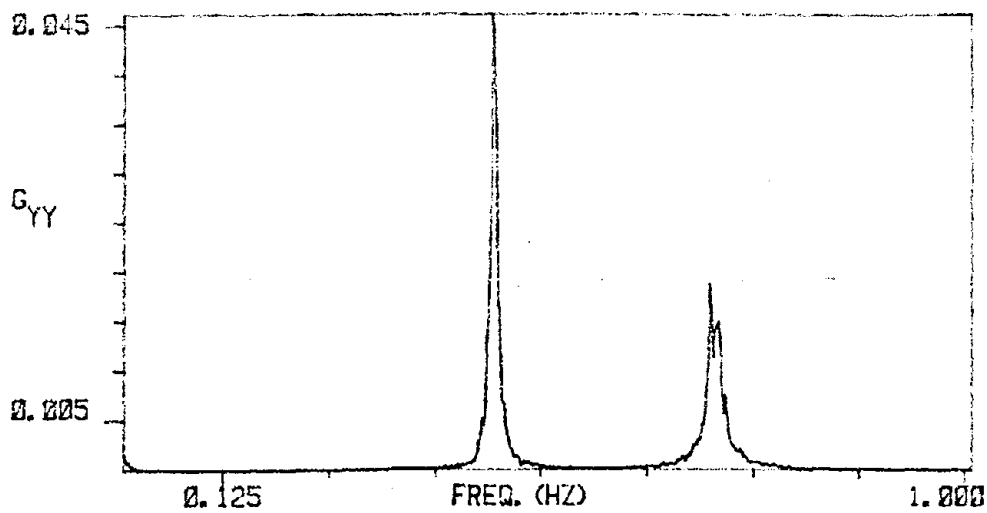

Figure 2.29. High Resolution Autospectrum with Δf = 0.003906 Hz

Table 2.10. Comparison of Modal Parameter Estimates from SDOF Fit, MDOF Fit and the Direct Method

Mode No.	Frequency (Hz)			Damping Ratio (%)		
	Direct	SDOF	MDOF	Direct	SDOF	MDOF
1	0.443	0.445	0.444	0.91	1.05	1.07
2	0.701	0.702	0.706	-	1.97	1.76
3	1.393	1.396	1.394	1.10	1.21	1.29
4	2.075	2.073	2.075	2.31	2.16	2.01
5	2.544	2.533	2.556	1.57	1.59	1.58

about the same values for the frequencies. The damping estimates for the second mode are considerably different for the single and multidegree-of-freedom curve fitting methods, which could be due to the underlying abnormal modal behavior. The values are comparable for all the other modes. The estimates for the fifth mode show excellent agreement. This could be the result of the fact that the spectral estimates in this region are subject to comparatively low bias errors.

The estimates of damping from the different procedures given above suggest the use of the following technique to obtain reasonable damping values from a given autospectrum with minimum effort.

(i) To start with, the half-power bandwidth method could be used.

(ii) If the frequency resolution is not high enough so that there is an insufficient number of points between the half-power points, a single degree-of-freedom fit could be carried out.

(iii) If the mode is not well separated from the neighboring modes, a multiple degree-of-freedom curve fitting procedure including all the modes in the neighborhood could be used.

2.8 Effect of Cladding

The discussion that follows, on the influence of cladding on the modal parameters, is restricted to frequencies and damping only. Mode shapes are not considered because not enough measurements could be made for sufficient characterization of each mode. Because of the long periods of time required for each measurement, the five available

accelerometers could not be moved around to measure the response from additional floors. Hence the response data could not be obtained for more than five floors on any given day. Also, the locations used for placing the accelerometers were different on different days and not the same five floors could be used on all days due to the inaccessibility of certain floors.

Attempts were made to keep track of the mass in the building on different test dates but were unsuccessful. Quantification of the amount of mass on various days would enable easier correlation of the changes in the modal parameters to structural modifications with construction, but was found infeasible. Nonetheless some important activities and events on the test dates were taken note of and these are included in Table 2.1. Despite the lack of estimates of mass in the structure, it can be assumed with reasonable confidence that, once the steel frame is erected and the floor slabs are in place, further construction activities would tend to increase the total mass of the structure due to the accumulation of materials for later use in construction.

Variations of frequencies and damping ratios with construction, for the period when the installation of cladding was completed, are given in Tables 2.11 and 2.12. It is evident from these tables that all the frequencies show a decreasing trend initially. This can be ascribed to an increase in the mass of the building. The largest drop, as seen in the values of the E-W bending frequencies, occurs between February 22 and March 7, indicating a large influx of mass into the building during this period. However, after March 7, the frequencies

Table 2.11. Variation of Frequencies with Construction

Direction	Mode No. \ Date	1/16	2/8	2/15	2/22	3/7	4/24	5/16	5/29
N-S	1	0.479	0.475	0.469	-	0.458	0.446	0.444	0.444
	2	1.444	1.424	1.412	-	1.367	1.365	1.368	1.375
	3	2.604	2.587	2.581	-	2.473	2.511	2.526	2.545
E-W	1	0.321	-	-	0.320	0.306	-	0.317	0.319
	2	0.977	-	-	0.955	0.908	-	0.962	0.980
	3	1.785	-	-	1.789	1.707	-	1.798	1.823
Torsion	1	0.732	-	-	-	0.702	0.694	0.692	0.692
	2	2.083	-	-	-	1.960	2.008	2.024	2.030

Table 2.12. Variation of Damping With Construction

Direction	Mode No. \ Date	1/16	2/8	2/15	2/22	3/7	4/24	5/16	5/29
N-S	1	0.91	0.61	1.92	-	1.02	0.88	0.82	0.71
	2	0.47	0.67	0.62	-	0.62	1.04	1.54	1.32
	3	-	0.66	0.92	-	1.10	1.56	1.30	1.23
E-W	1	0.44	-	-	0.56	0.53	-	3.15	2.32
	2	0.97	-	-	0.97	1.04	-	1.72	1.78
	3	1.03	-	-	0.87	0.62	-	1.76	1.49
Torsion	1	1.15	-	-	-	1.32	1.33	1.56	1.56
	2	0.71	-	-	-	0.79	1.11	1.56	1.47

of all the modes except the fundametnal bending and tosional modes show an increasing trend in contrast to the decreasing trend that would generally be expected throughout.

Comparison of Tables 2.1 and 2.11 brings out an interesting feature. From Table 2.1, which lists the cladding levels on different days, it is observed that there is a considerable change in the levels on all four faces before and after March 7. This leads to the possible inference that the increase in frequencies after this date could be attributed, at least in part, to the continuing installation of exterior cladding. The frequencies of the fundamental modes in N-S bending and torsion remain relatively unaffected. This again is in conformity with the expected behavior of cladding, which could influence the higher modes more since they involve greater curvatures. The cladding levels and frequencies are plotted against time in days in Figures 2.30 and 2.31 respectively.

Although there are definite trends in the frequency variations, the magnitudes of the variations themselves are quite small. But one must realize that the building considered here is only a glass-clad structure, which, due to the lightweight nature of glass, perhaps is not the best candidate for studying cladding effects (This particular building was employed because it was the only one available at the time of the study.) On the other hand, it is also possible that the observed variations in the modal parameters were caused by other effects or components such as the interior partitions.

Table 2.12 shows increasing values for the damping of torsional modes in general. Except the 2nd mode in the E-W direction, the bending

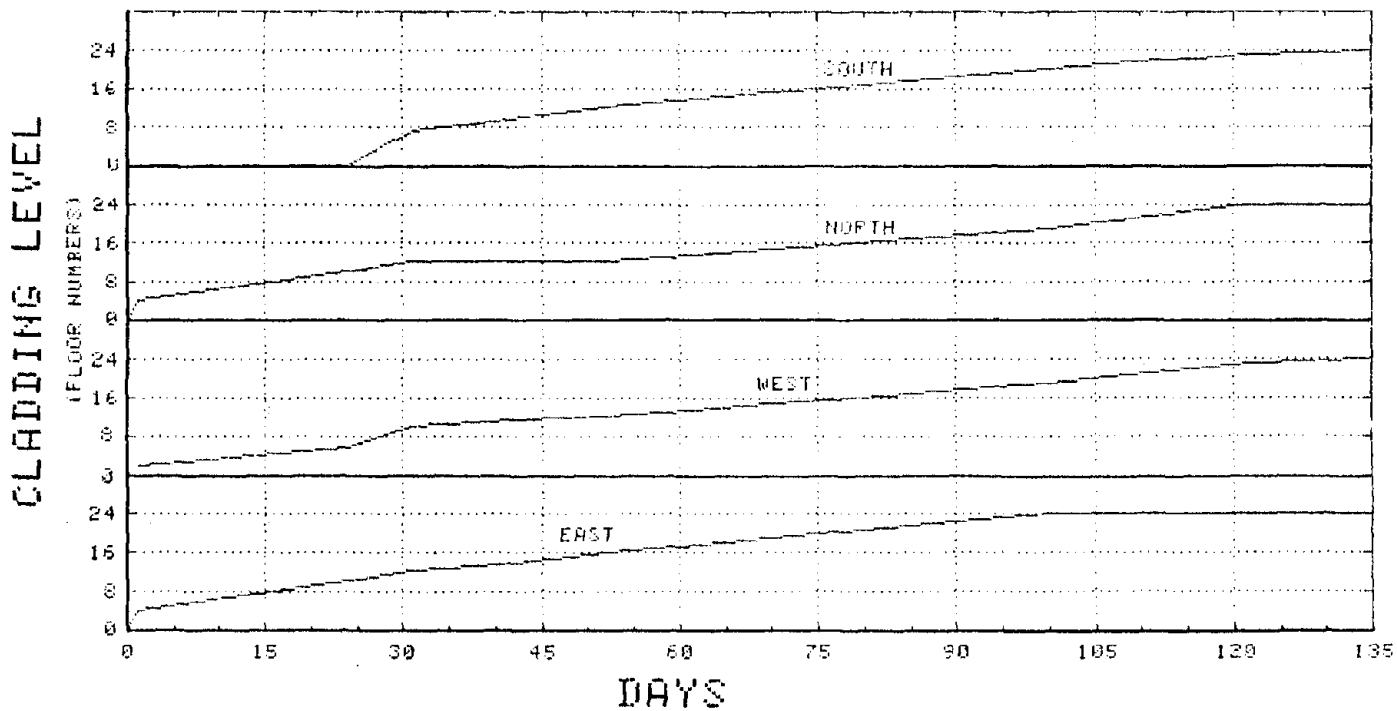

Figure 2.30. Variation of Cladding Levels with Construction

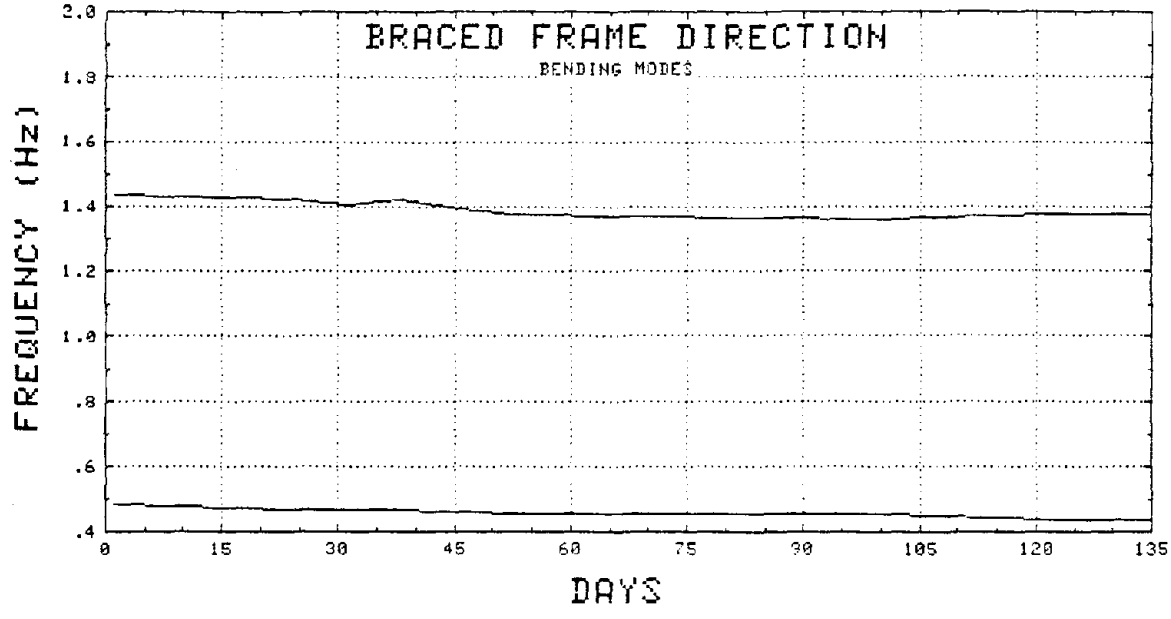

(a) N-S Direction

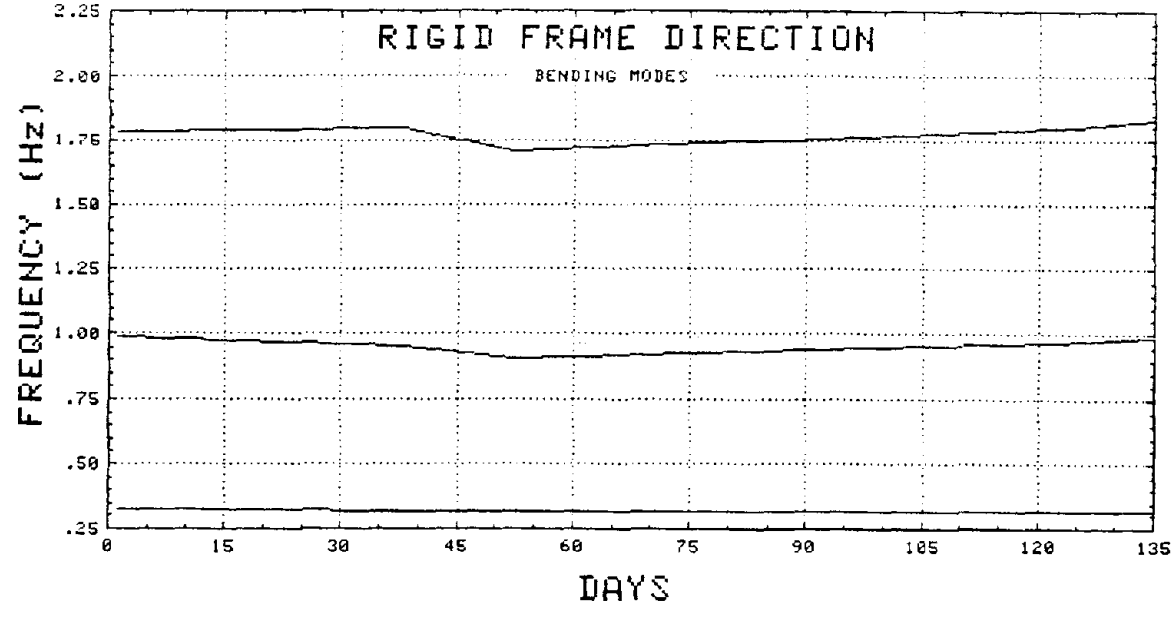

(b) E-W Direction

Figure 2.31. Variation of Frequencies with Construction

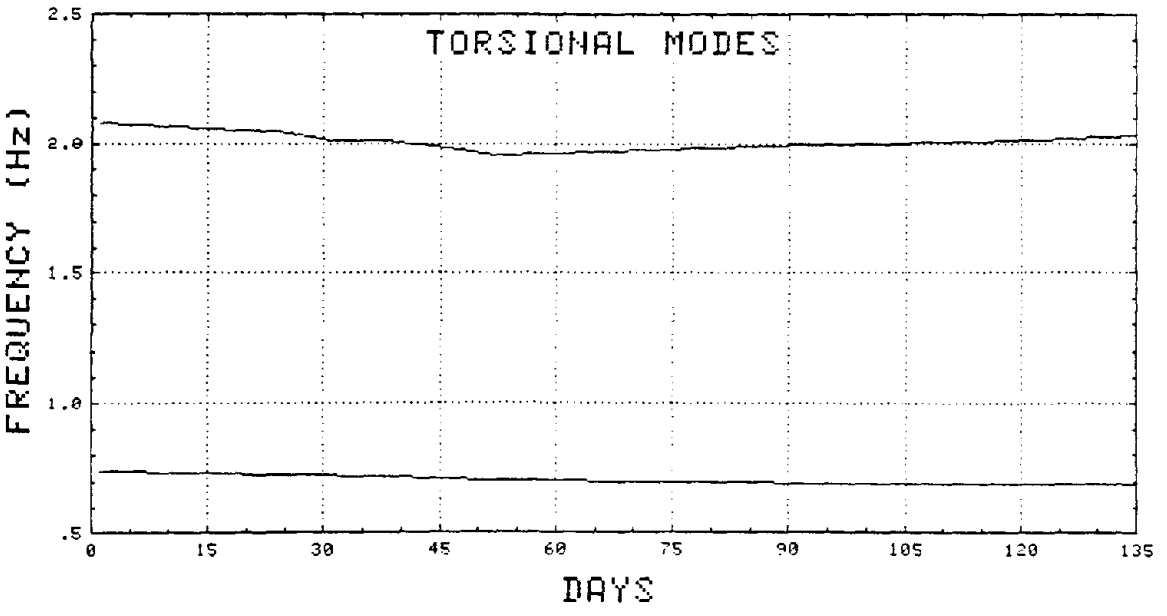

(c) Torsional Frequencies

Figure 2.31 (Cont'd.). Variation of Frequencies with Construction

modes do not exhibit a definite trend. But the values of damping for all the modes tend to be high after March 7, when most of the cladding was in place.

The average modal parameters computed from the data taken on November 13, well after the cladding installation was complete, are given in Table 2.13. All the frequencies in E-W bending and torsion shown increases of considerable amounts but only the 2nd frequency in N-S bending exhibits an increase. The observed changes in this case are mostly due to other nonstructural elements such as the interior partition walls.

In conclusion, it can be stated that the possible influence of cladding on the modal parameters, based on the findings here, is to increase the frequencies of the higher modes slightly and, to a lesser degree, increase the damping in general.

Table 2.13. Frequency and Damping Estimates from Data Taken on 11/13/80

Mode No.	N-S Direction		E-W Direction		Torsion	
	Freq. (Hz)	Damp. (%)	Freq. (Hz)	Damp. (%)	Freq. (Hz)	Damp. (%)
1	0.444	1.12	0.335	2.21	0.706	1.86
2	1.393	1.28	1.054	2.21	2.073	2.07
3	2.543	1.49	1.954	2.03	-	-

3.0 FORCED VIBRATION TESTING

3.1 Introduction

Forced vibration testing is the most widely employed technique in the experimental determination of the dynamic characteristics of structures. While, under certain conditions, it is possible to resort to special techniques like ambient testing that obviate the need for a prescribed external input, the measurement of the dynamic properties of a general structure requires one or more excitation sources. Force generating devices or shakers that provide well-defined controllable and measurable force input are usually employed as the excitation sources. Even for structures like highrise buildings where ambient testing is applicable, the use of prescribed external excitation eliminates the uncertainty regarding the input and thus improves the credibility of the results obtained. A survey of full scale testing techniques can be found in Reference 37.

There are many different ways in which a structure can be excited with a shaker. In the conventional method known as harmonic testing, the steady-state response of the structure at different frequencies is obtained by incrementally increasing the exciter frequency. The natural frequencies are taken as those corresponding to the peaks in the gain versus frequency plot. The damping ratio for each mode is computed by applying the half-power bandwidth method to

the modal peaks or the logarithimic decrement method to the decaying response acquired by turning the power off to the shaker at resonance. The mode shapes are determined from the values of the gain at modal frequencies, measured at various locations. Other analysis tools such as the vector or Nyquist plot method can also be used to extract the vibrational parameters (38). In this method, the parameters are derived from a curve obtained by plottting the in-phase response against the out-of-phase response.

A more accurate but laborious testing procedure would require using multiple shakers (3). The structure is made to response in one particular mode by controlling the forces provided by the shakers, which are distributed throughout the structure. This process is referred to as "modal tuning". It may not always be possible to apply this technique because, due to the inaccessibility of certain locations in the structure, it may be impracticable to position all the shakers in optimum spots to tune a specific mode.

When the modal properties for several modes are needed, the process of acquiring the steady-state response around each mode becomes lengthy and tedious. In such cases, it may be easier to make use of techniques that impart energy to the structure over the entire frequency range of interest in a short interval of time, and compute the frequency response function from the input-output measurements. Such techniques simplify the testing procedure at the cost of increased calculations in the post-test analysis of the data. With the rapid development and deployment of computers, these are increasingly being used in dynamic testing of many types of structures. However, the

methods that have been employed to date in vibration tests on buildings are almost exclusively of the harmonic type (40-45). This can mostly be traced to the unavailability of an exciter that fills the needs for full scale testing of structures like buildings.

The three most commonly employed types of shakers are the electrodynamic, electrohydraulic and mechanical (rotating eccentric mass) models. The electrodynamic shakers produce force directly whereas the others produce motion. All types of shakers must possess certain desirable performance characteristics for their effective use. In addition to delivering the required force levels, they must have good frequency response over the frequency range of interest. This implies that for testing buildings whose natural frequencies vary from a fraction of a Hertz to several Hertz, the shakers employed must be capable of low frequency operation.

The mechanical exciters can usually generate only steady harmonic motion which renders them useless when an arbitrary waveform is desired for the forcing function. On the other hand, the electrodynamic exciters often have performance limitations owing to their size and construction. The force levels generated by practical-sized models are inadequate for testing civil engineering structurs such as buildings. Besides, they suffer from poor low frequency response due to the inherent restrictions on the components used in their construction. As a consequence, these models have found little use in dynamic tests on buildings.

An electrohydraulic sharker that circumvents the above problems has recently been developed for use in full scale testing (46). This chapter describes the forced vibration tests conducted on a 25 story steel frame building employing this shaker. The results of these tests are compared to the ambient test results obtained by measuring the ambient response of the building. The forced vibration test results are also used in the estimation of stiffness parameters in the analytical model of the building, to be dealt with in the next chapter. Detailed discussions on the design, construction and operation of the shaker are given in Reference 46. A brief outline of some of its important aspects will now follow.

3.2 The Shaker

The electrohydraulic force generator in its basic form consists of a seismic mass that moves in a rectilinear manner under the action of a hydraulic actuator. The seismic mass is made-up of lead "bricks" (4" x 4" x 8") that weigh approximately 55 lbs. each. This mass is placed on a weight table which is supported on 4 trackless air bearings (Figure 3.1). The hydraulic actuator produces horizontal to-and-fro motion of the weight table. Supporting the table on air bearings enables easy and quick reorientation of the table so that the axis of the actuator can be aligned in any desired direction.

The maximum force generated by the shaker at low frequencies ($f < 1$ Hz) is limited by the maximum stroke of the actuator. In the intermediate frequency range ($1 < f < 3.5$ Hz), the constraining

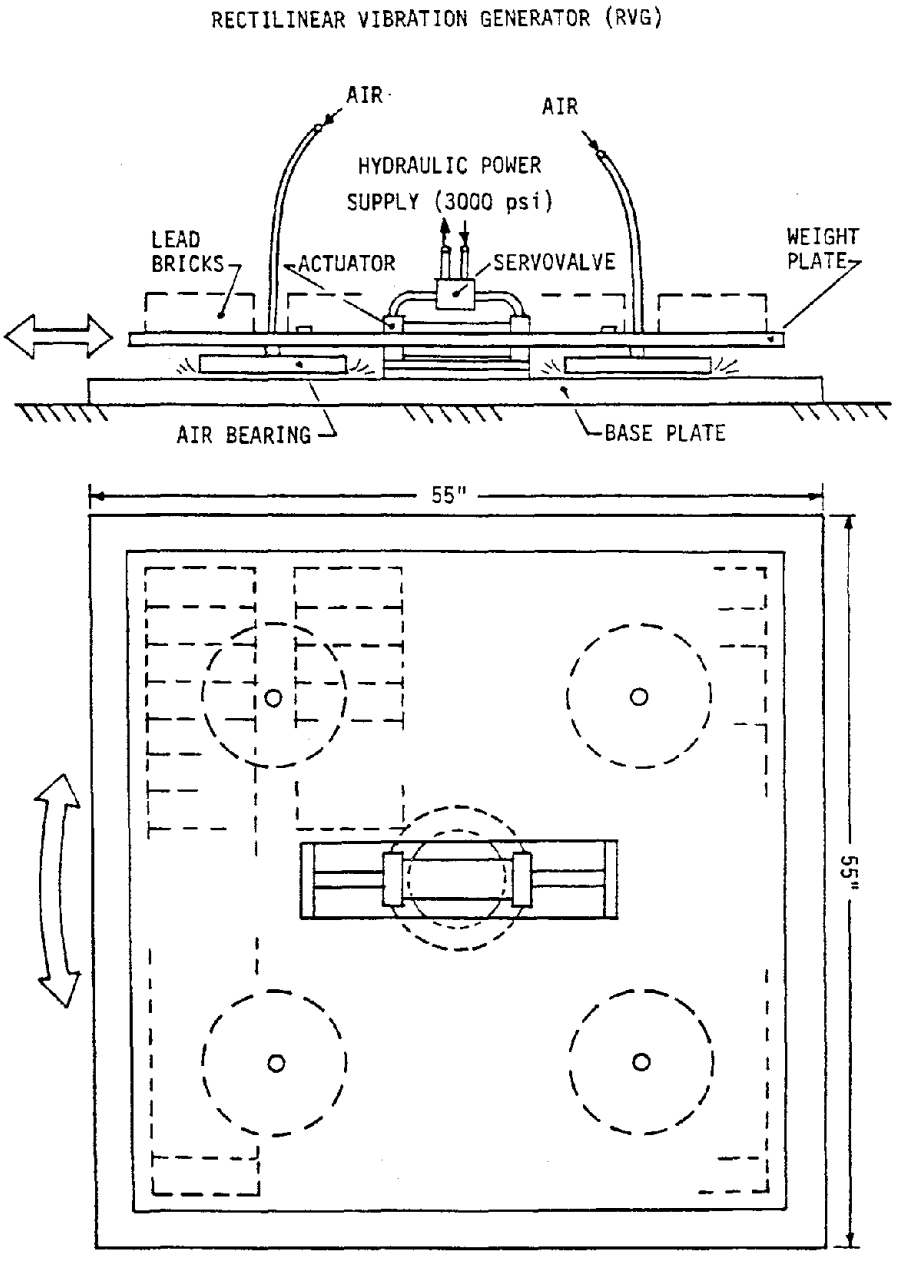

Figure 3.1. Rectilinear Electrohydraulic Shaker

factor is the hydraulic flow rate and at high frequencies (f > 3.5 Hz), the performance is restricted by the maximum permissible hydraulic pressure and the actuator piston area. For a given seismic mass, the force produced is thus proportional to the square of the frequency up to 1 Hz and to the frequency itself from 1 to 3.5 Hz. Above 3.5 Hz, the force remains a constant. The performance curve for the shaker is reproduced from Reference 46 in Figure 3.2.

The most important advantage in using this shaker is its ability to produce motion of the weight table according to any arbitrary prescribed waveform. In the present study, the approach adopted was to compute the desired waveform at discrete time intervals in a desktop computer and transform the resulting digital signal to the analog form by means of a digital-to-analog converter (DAC). The output waveform from the DAC is lowpass filtered to remove the jaggedness in the signal caused by the "sample and hold" mode of operation of the DAC. The final analog waveform is fed to the servocontroller unit which controls the actuator to generate corresponding table motion. The block diagram in Figure 3.3 illustrates this procedure.

3.3 The Forcing Function

The types of waveforms that permit the excitation of the structure over a range of frequencies can be grouped into the following three categories (47):

(a) Bandlimited white noise or random input

(b) Swept-sine input

(c) Impact or impulse input

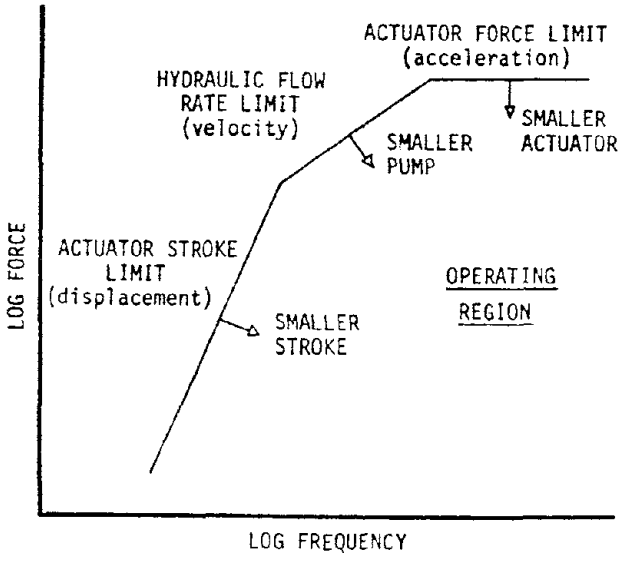

Figure 3.2 Performance Curve of the Shaker

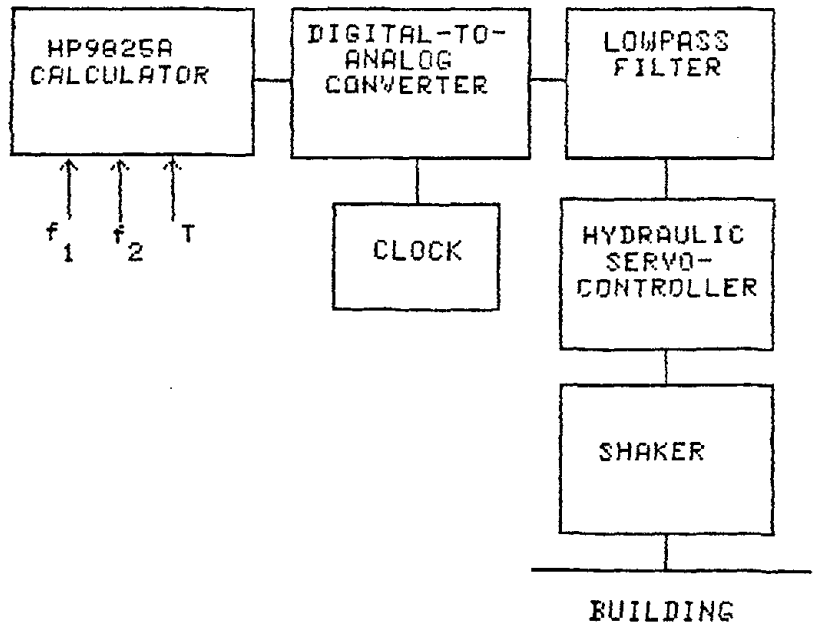

Figure 3.3. Block Diagram for the Shaker Input

All of the above inputs give rise to time waveforms that possess approximately flat spectral density functions. Since impact techniques are not suitable for use in buildings, they will not be considered here. White noise input involves synthesizing the time waveform by inverse Fourier transforming the desired linear spectrum in the frequency domain. A comparatively easy method of generating a time function that has approximately uniform distribution of power between two frequency limits is to use a sinusoid whose frequency is varied between these limits in a predetermined manner. This technique of varying the frequency between the lower and upper limits is known as "sweeping" and the input thus generated is usually referred to as "swept-sine wave" or "chirp".

For the case where the frequency is varied linearly, the swept-sine wave is defined by

$$x(t) = \sin\left[\frac{\pi(f_b - f_a)t^2}{T} + 2\pi f_a t\right] \qquad (3.1)$$

where $x(t)$ = swept-sine input

f_a = lower frequency limit

f_b = upper frequency limit

T = sweep time

The function $x(t)$ has a linear spectrum whose magnitude between f_a and f_b is a constant with a ripple superimposed on it (48). Figures 3.4a and b show a typical linearly swept sine wave and its spectrum. All the forcing functions employed here are swept-sine waves computed on the basis of Equation (3.1).

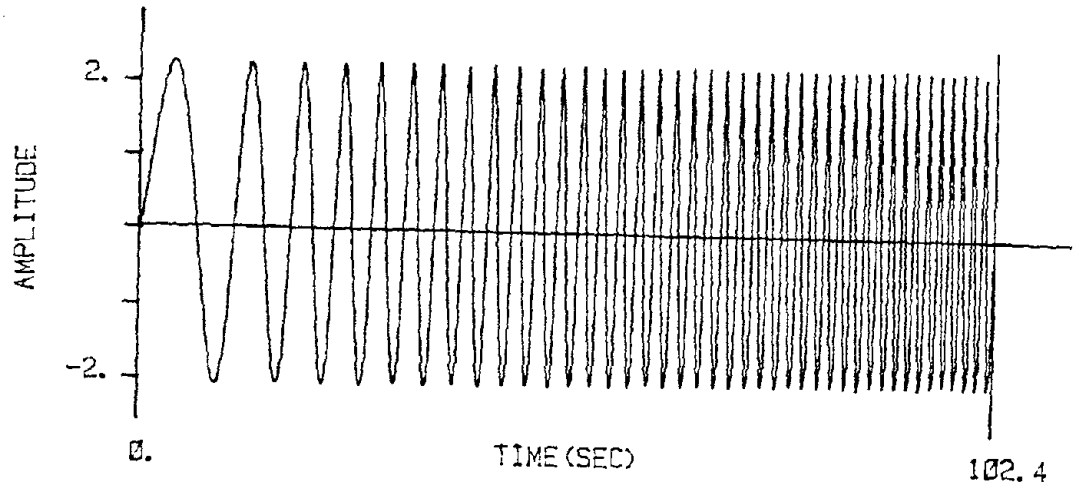

(a) Time Waveform

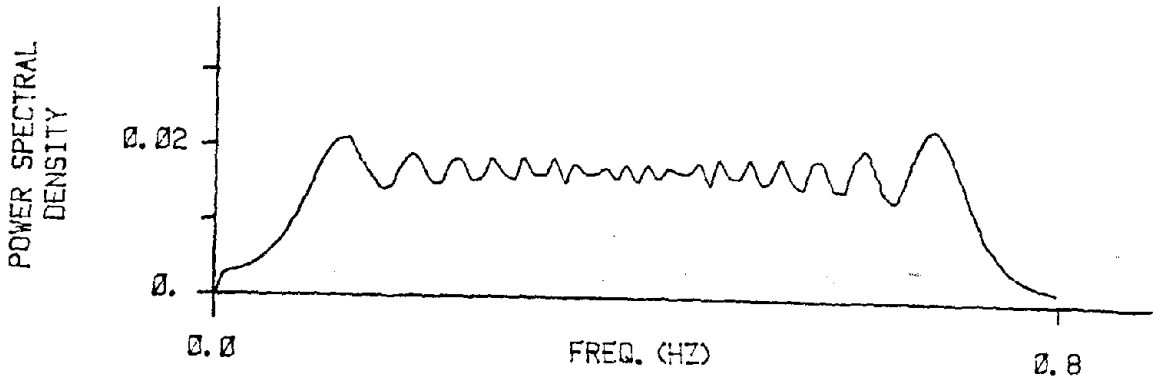

(b) Power Spectral Density

Figure 3.4. Linearly Swept Sine Wave; f_1 = 0.05 Hz, f_2 = 0.75 Hz, T = 102.4 sec

In creating waveforms to drive the shaker, some pertinent aspects of its performance must be taken into account. Equation (3.1) can be assumed to be the force produced from which the required displacement signal to control the shaker can be derived. However, since higher force levels can be obtained with increasing frequencies for a given stroke, the shaker can be operated more efficiently by using Equation (3.1) for displacement rather than force. But, due to the physical limitations of the exciter, the displacement signal must be tapered in such a fashion that the amplitude of the generated force follows a curve similar to the operating curve given in Figure 3.2. Specifically, it must be attenuated so that the force varies linearly between 1 and 3.5 Hz and remains constant thereafter. To provide some safety margin, the tapering of all the signals utilized here was started at frequencies 10 percent below these values (0.9 and 3.15 Hz). The complete waveform is determined using

$$x(t) = \bar{A} \sin \left[\frac{\pi(f_b - f_a)t^2}{T} + 2\pi f_a t \right] \tag{3.2}$$

where
$$\bar{A} = A, \qquad f \leq 0.9$$
$$= \left(\frac{0.9}{f}\right)A, \qquad 0.9 < f \leq 3.15$$
$$= \left(\frac{0.9}{f}\right)\left(\frac{3.15}{f}\right)A, \qquad f > 3.15$$
$$f = \frac{(f_b - f_a)t}{T} + f_a, \text{ the instantaneous frequency}$$

and A is the amplitude initially at $f = f_a$. Figures 3.5a and b show a tapered waveform and its spectrum.

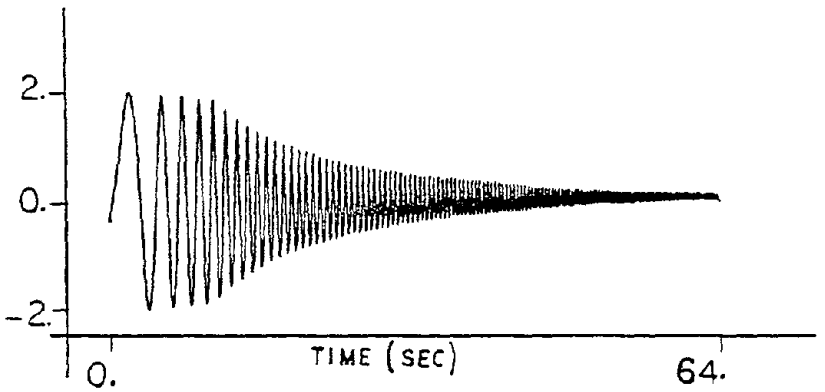

(a) Time Waveform

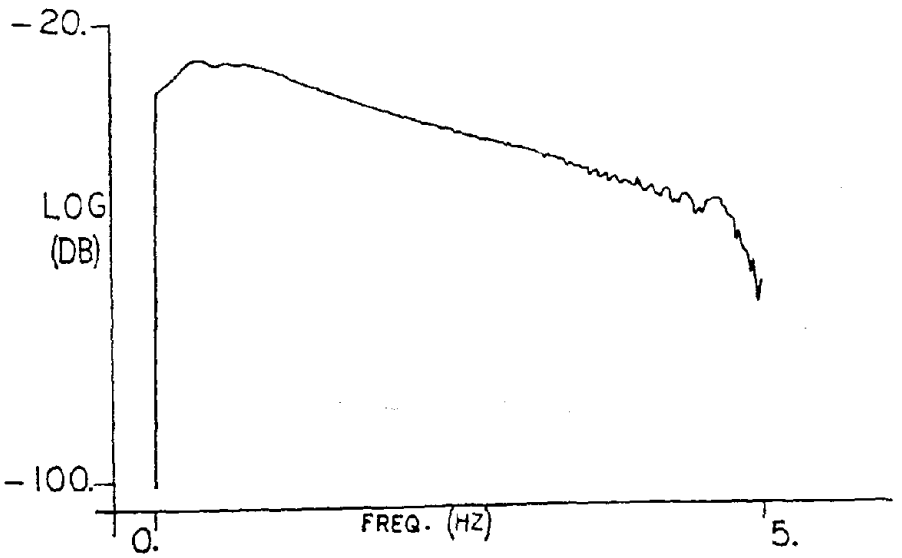

(b) Power Spectral Density

Figure 3.5. A Tapered Sine Wave Input; f_1 = 0.1 Hz, f_2 = 4.9 Hz, T = 51.2 sec

3.4 Structure

The structure chosen for forced vibration and optimum stiffness estimation studies is a 25-story steel frame office tower. It consists of a central steel core surrounded by a lightweight exterior steel frame which supports a highly contoured precast concrete panel curtain wall. The building core is constructed with braced framing in one direction and rigid framing in the other (Figure 3.6). The exterior frame is supported by a reinforced concrete, rigid frame pedestal. Further aspects of the construction of this building can be found in Reference 49.

3.5 Measurement

3.5.1 Ambient Tests

Prior to conducting full scale forced vibration tests, the ambient response of the structure was measured on November 20 (1980). The objectives of this measurement were first to determine the modal frequencies for later use in forced vibration tests, and second to provide a basis from which to make comparisons of the ambient and forced vibration testing methods. The equipment used was the same as that employed in the ambient tests described in the previous chapter. Five accelerometers were placed on the 2nd, 9th, 17th and 21st floors and the roof. The accelerometers were situated near the center of the building and about 3 hours of data were recorded in each of the two bending directions. No torsional response was measured.

3.5.2 Forced Vibration Tests

Full scale dynamic tests using the shaker were carried out

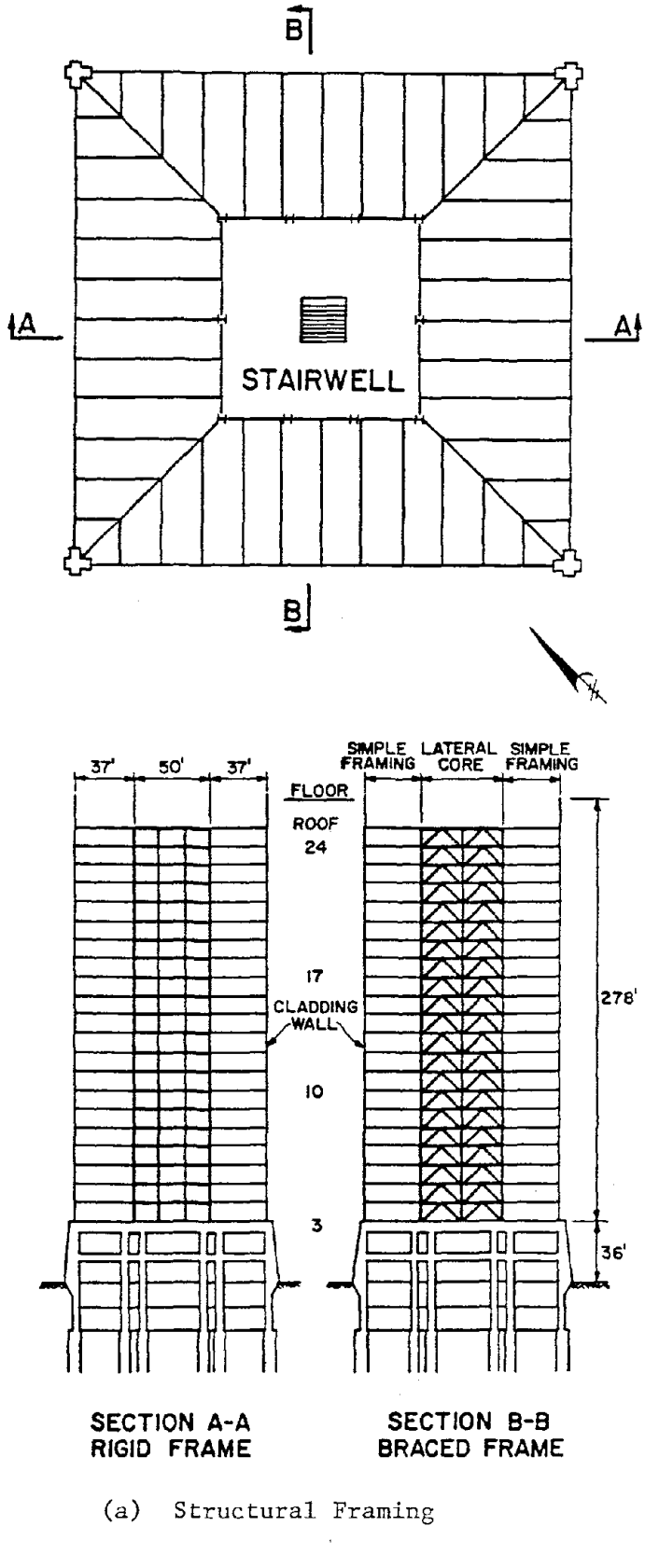

(a) Structural Framing

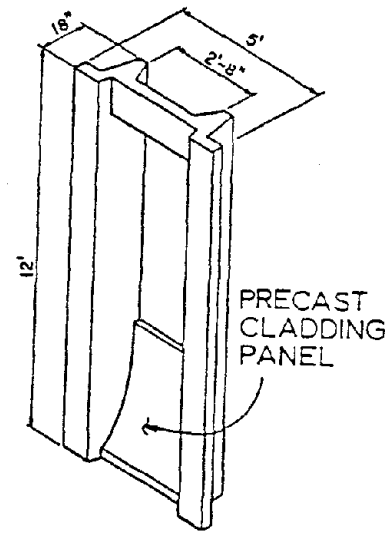

(b) Cladding Panel

Figure 3.6. Structure Used in Forced Vibration Tests

starting June 26 (1981). The instrumentation used consisted of the response measuring equipment utilized in ambient measurements and the shaker along with its peripheral devices. The latter included a hydraulic pump to provide the hydraulic power for the actuator, an air compressor to provide the air supply for the bearings and a specially constructed vibration control system. The control system was based around an HP 9825A calculator which was used to generate the desired waveforms and to synchronize the operation with other equipment. The control system also included a DAC to convert the digital waveforms to analog form and an MTS 406 servocontroller to control the hydraulic valve.

Ideally, it would be desirable to locate the shaker near the building top so as to avoid placing it near the node points for any of the modes of interest. This was not possible because adequate floor space and power connections were not available in this area. Rather, the shaker was mounted on the 15th floor, which is the mechanical floor in the building. The shaker assembly was left in place between tests and was dismantled only after all tests were completed. The rest of the equipment was set up and removed when required.

Since only five accelerometers were employed to measure the response, the testing process was carried out in several stages to get sufficient definition of the mode shapes. The accelerometers were first placed on the roof and four lower floors and a set of measurements was made. Next, the accelerometers on the lower floors were moved to four different floors and the measurements were repeated. The response from the roof was used as the reference in computing the mode shapes,

which were thus defined by a total of nine coordinate points. Along with the roof, the 23rd, 21st, 19th, 17th, 15th, 12th, 9th and 6th floors were chosen for response measurement. The accelerometers were located in a stairwell close to the center of the building for measuring the bending response and near the edges of the building for torsional response. The shaker was located at the midpoint of the north edge on the 15th floor. Since access to the four sides of the building was limited, torsional measurements were made only on the roof, 15th and 10th floors. Consequently, proper definition of the torsional mode shapes could not be obtained.

The orientation of the accelerometers and the line-of-action of the shaker were selected depending upon the type of response desired. For measuring bending response in either the braced or the rigid frame direction, the shaker and the accelerometers were aligned in the braced or rigid directions respectively. Torsional data was obtained by locating the accelerometers along the east and west edges oriented in the rigid frame direction, with the shaker aligned in the braced frame direction (Figure 3.7).

The HP 9825A calculator employed to synthesize the waveforms was programmed so that, for given values of f_a, f_b and T, a swept-sine data block containing 2048 points is calculated according to Equation (3.2). To avoid large inertial forces that might occur if the shaker is started or stopped abruptly, two additional harmonic waveforms, one with frequency f_a and the other with frequency f_b, were synthesized and used together with the swept-sine waveform. The calculator was instructed to repeatedly output the lower harmonic

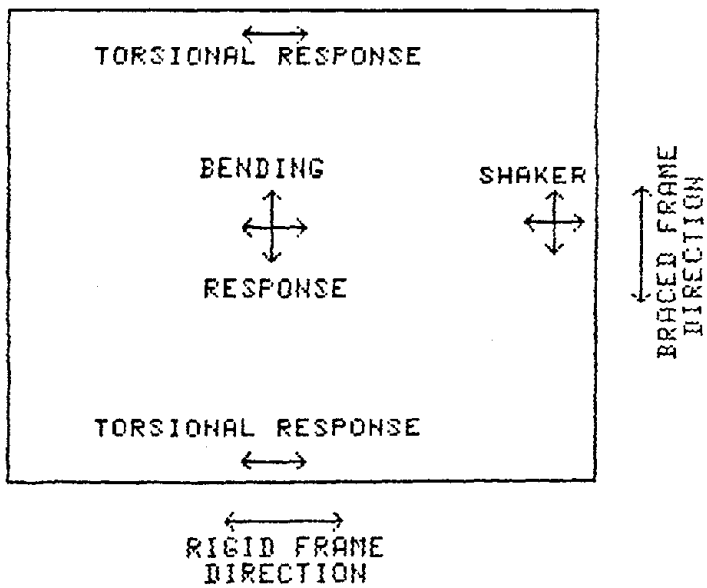

Figure 3.7. Accelerometer and Shaker Layout

cycle initially and the upper harmonic cycle after every sweep. The actual testing procedure consists of the following steps.

(i) With the calculator transmitting the lower harmonic cycle, increase the stroke of the shaker from zero to the required level.

(ii) Issue a command to the calculator to start the sweep.

(iii) After the sweep is over, the stroke of the shaker, which is now being driven by a harmonic signal of frequency f_b, is reduced to zero.

(iv) Issue a second command to the calculator to switch to the lower harmonic signal.

(v) Go to step (i) and repeat as many times as needed.

All data blocks were computed with a constant time interval Δt between two successive points, given by

$$\Delta t = T/2048$$

An external clock, which is a part of the integral DAC unit, was used to pace the transmission of data points from the calculator to the DAC at Δt intervals.

The input measurement consisted of a displacement signal from an LVDT attached to the actuator. This signal is proportional to the displacement of the weight table. The table acceleration can be computed from this signal if necessary, and used as a measure of the force produced.

To facilitate post-processing of the measurements using signal analyzers, a trigger signal was created in DAC with the aid of the calculator and recorded. This signal was such that it assumed a constant dc value for the duration of the sweep and zero otherwise. By employing this signal to control the triggering, the start of data acquisition in the analyzer can be synchronized with the start of the recorded sweep.

The seismic mass used on the weight table comprised 32 lead bricks for a combined mass of about 1760 lbs. The stroke length was adjusted for a maximum displacement of about 8 inches in the low frequency range.

Different ranges of sweeps were used by choosing different values for f_a and f_b. All the modal parameters for the higher modes were estimated from sweep data with f_a = 0.1 Hz and f_b = 4.9 Hz. Although this range includes the frequencies of the fundamental modes, the force generated at low frequencies ($f < 0.5$ Hz) is so small that the estimates of the frequency response function in this range are very poor. For this reason, a separate sweep with f_a = 0.05 Hz and f_b = 0.85 Hz was employed for measuring the fundamental mode response. The sweep time T was selected as 51.2 seconds for the 0.1 - 4.9 Hz sweep and 102.4 seconds for the 0.05 - 0.85 Hz sweep. These figures were chosen to comply with the time taken for a block of data to be accumulated in the signal analyzer employed to compute H(f).

Each sweep was repeated 5 to 10 times and the data recorded each time so that ensemble averaging could be used to estimate the spectral density functions from which the frequency response function is obtained.

3.6 Frequency Response and Spectral Estimation

Procedures similar to those given in the previous chapter were used to compute the autospectra and the cross-spectra from the ambient data. The autospectra measured on the roof in the braced and rigid frame directions are shown in Figures 3.8 and 3.9 respectively.

In the case of forced vibration test data, the frequency response functions are estimated as

$$\hat{H}(f) = \hat{G}_{xy}(f)/\hat{G}_{xx}(f) \tag{3.3}$$

where $\hat{H}(f)$ is the estimate of $H(f)$, $\hat{G}_{xx}(f)$ is the estimate of the input power spectral density and $\hat{G}_{xy}(f)$ is the estimate of the cross-spectral density between the input and the output. The coherence function between the input and the output, computed according to Equation (2.15), can be utilized as a measure of the accuracy of the estimate $\hat{H}(f)$.

The bias and variance errors involved in estimating the frequency response function are discussed in Reference 28. The variance of the estimate decreases as the coherence approaches unity. The variance is also reduced by increasing the number of averages used to calculate $H(f)$. The bias in the estimate depends on many factors. An important fact worth noting here is that the presence of other sources of excitation does not cause any bias in $H(f)$ if the input due to these sources is not correlated with the externally applied input. Therefore, the modal parameter estimates will not be influenced by these sources. In contrast, the harmonic or steady-state testing method employs the response directly to

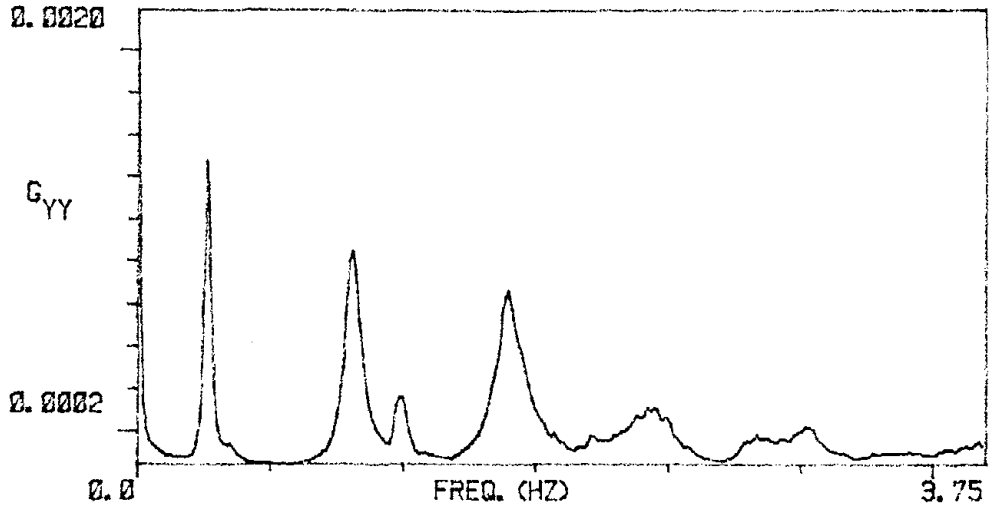

Figure 3.8. Ambient Results; Autospectrum on Roof in the Rigid Frame Direction

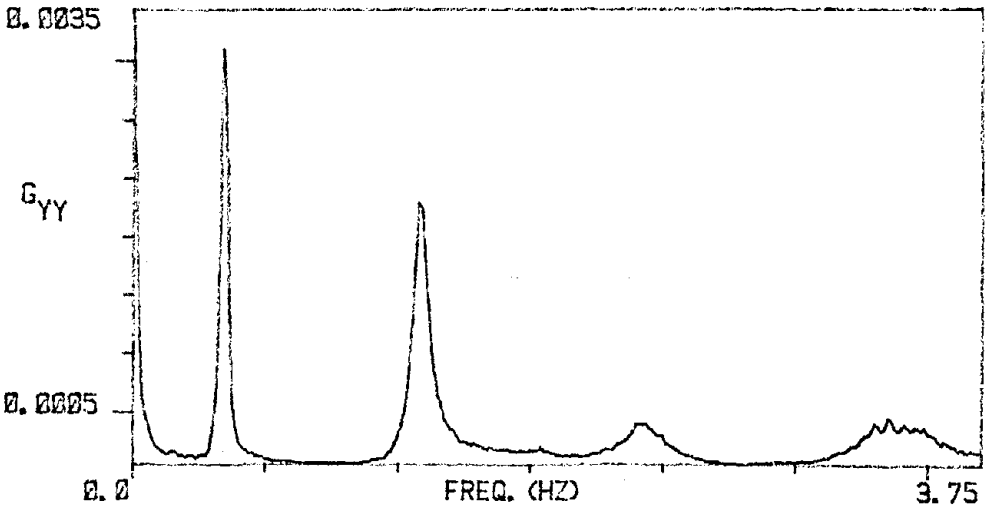

Figure 3.9. Ambient Results; Autospectrum on Roof in the Braced Frame Direction

determine the modal properties. Thus, if the external input is not large enough so that other inputs can be considered negligibly small, the parameter estimates will be significantly affected. This is an added advantage in using the frequency response function to determine the modal parameters.

The computation of H(f) was carried out in an HP 5451B mini-computer based Fourier analyzer. The Hanning window was employed to reduce leakage and smooth the spectra. The trigger signal was used to identify the start of each sweep and trigger the analog-to-digital conversion of the recorded shaker input and the response at each point. Time records of 1024 points were employed to compute 512-point frequency domain functions. Number of averages used range from 5 to 10 depending on the number of measurements made. Values of the coherence function estimates were close to one near all the modal frequencies except the fundamental modes. Since the force levels near the fundamental frequencies were quite low, the values of coherence in this region were only about 0.5 - 0.6.

Figures 3.10 - 3.18 show the frequency response functions computed using 0.1 - 4.9 Hz sweep data in the braced frame direction. The torsional frequency response functions measured on the roof are given in Figures 3.19 - 3.20. It can be seen from Figures 3.19 and 3.20 that the H(f) measured along the east and the west sides show a 180^{o} phase shift, confirming that the response measured in either of these locations was indeed predominatnly torsion. A typical coherence function obtained is given in Figure 3.21. A frequency response function measured in the 0.05 - 0.85 Hz range and its associated coherence are illustrated in Figures 3.22a and b.

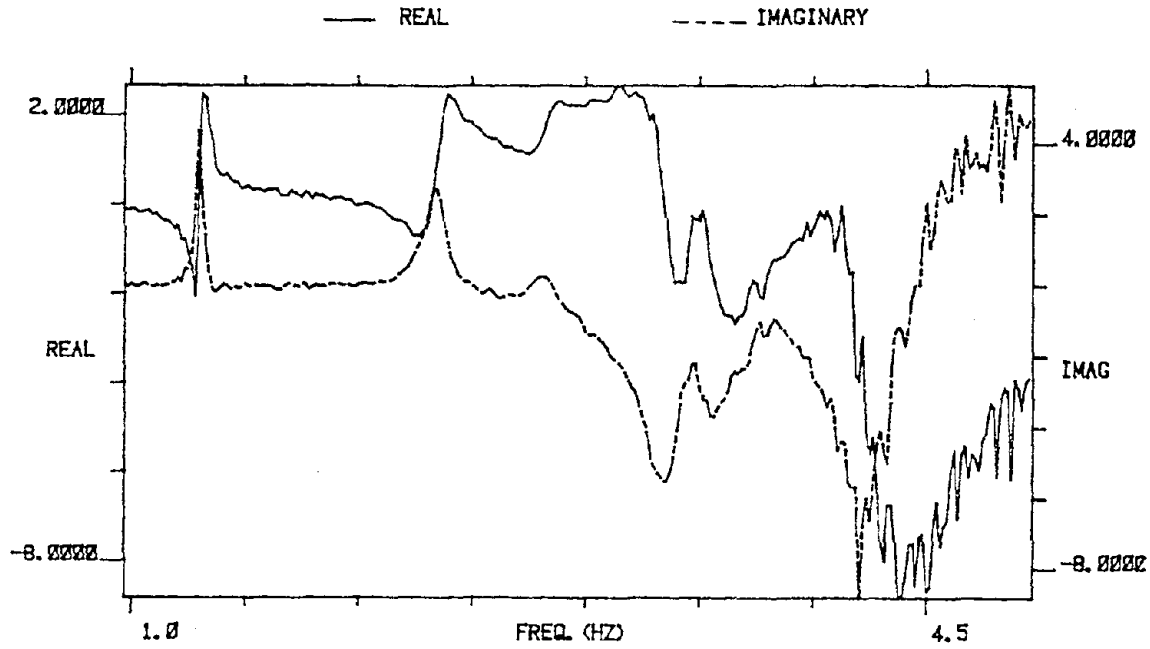

Figure 3.10. Transfer Function Measured on the Roof

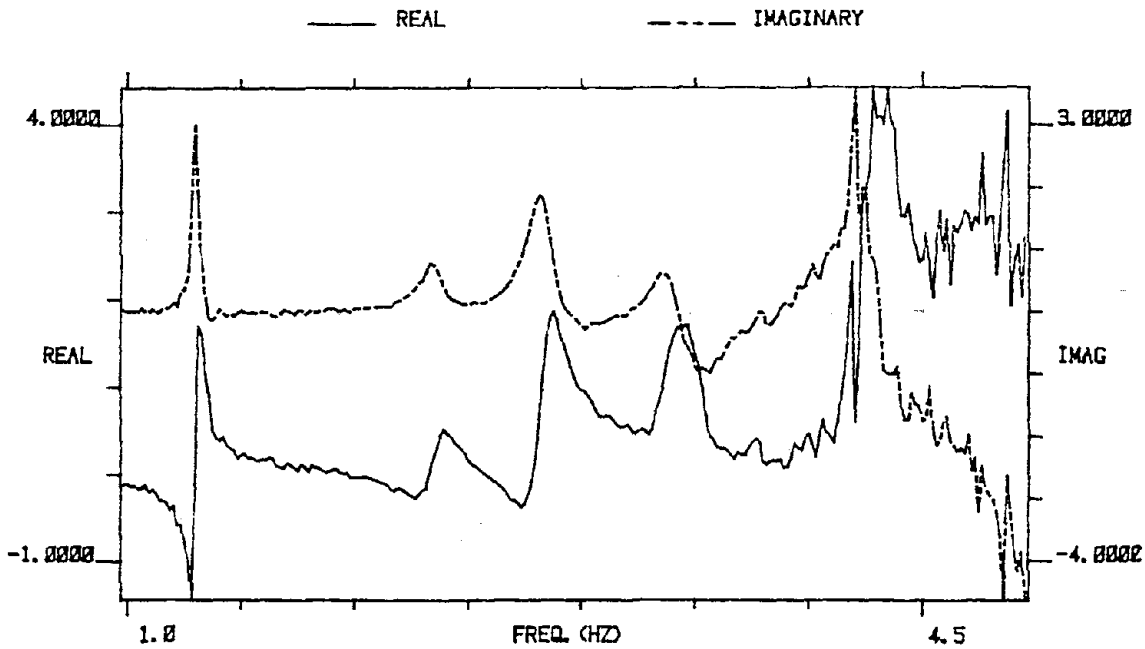

Figure 3.11. Transfer Function Measured on the 23rd Floor

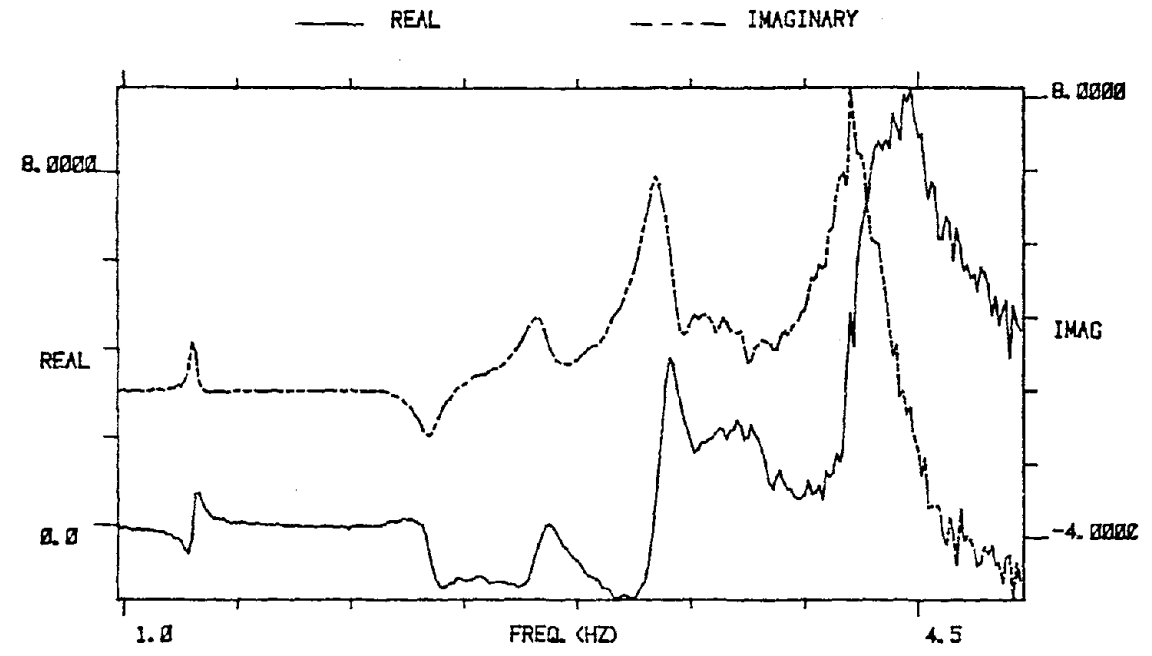

Figure 3.12. Transfer Function Measured on the 21st Floor

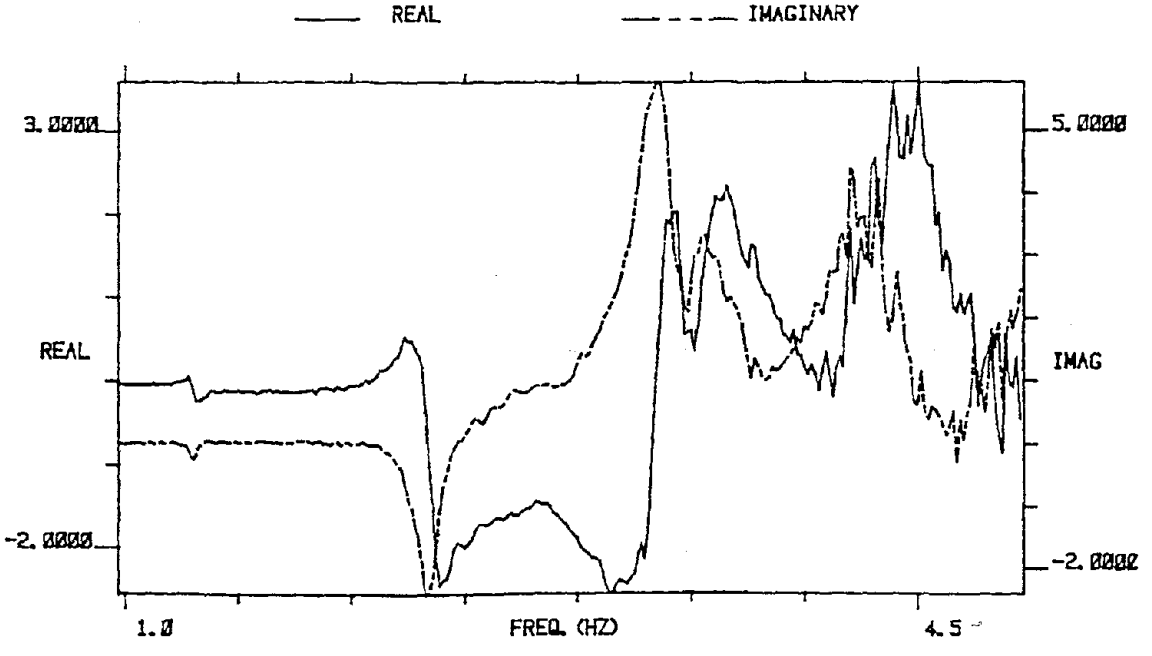

Figure 3.13. Transfer Function Measured on the 19th Floor

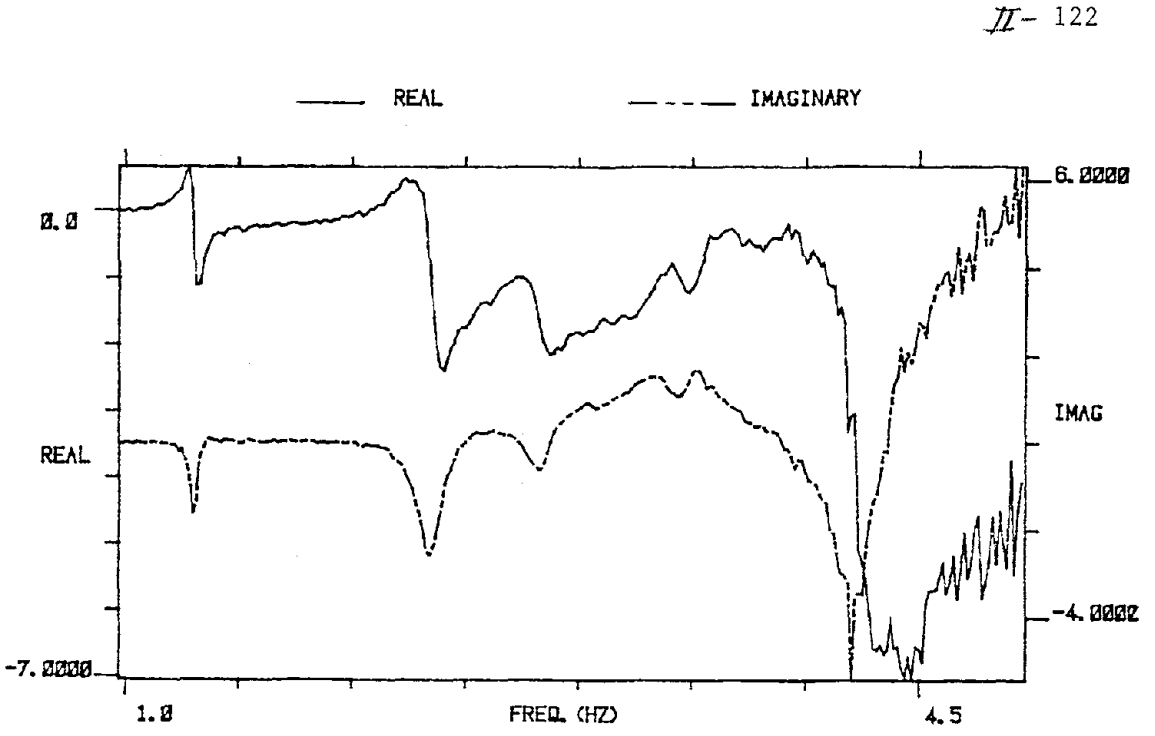

Figure 3.14. Transfer Function Measured on the 17th Floor

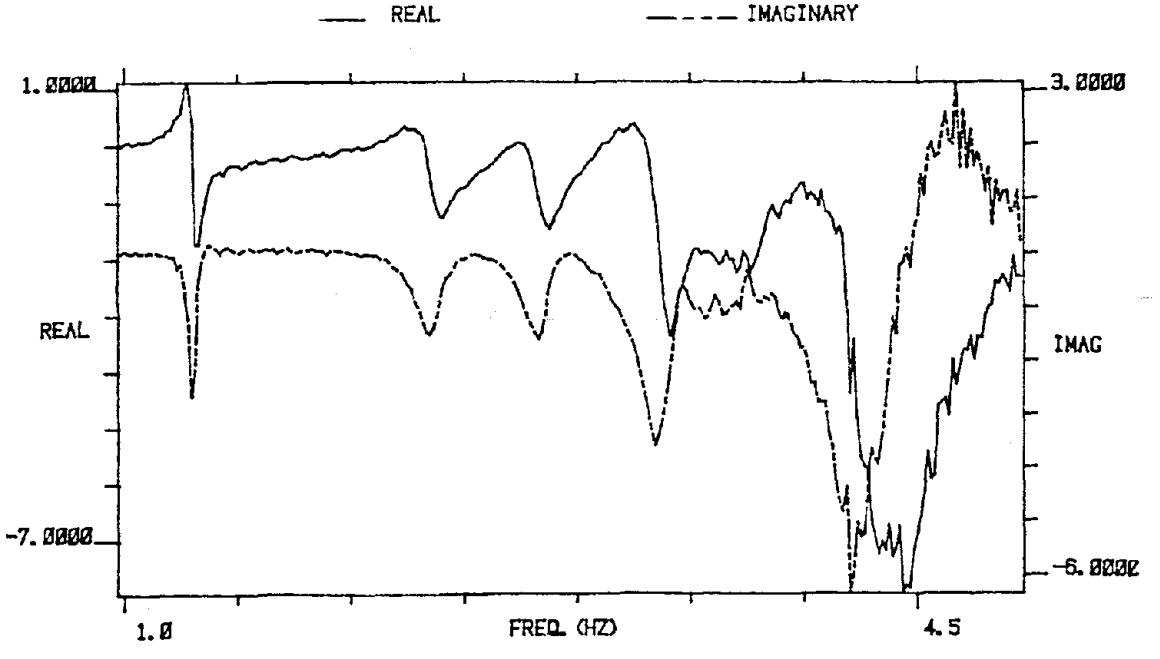

Figure 3.15. Transfer Function Measured on the 15th Floor

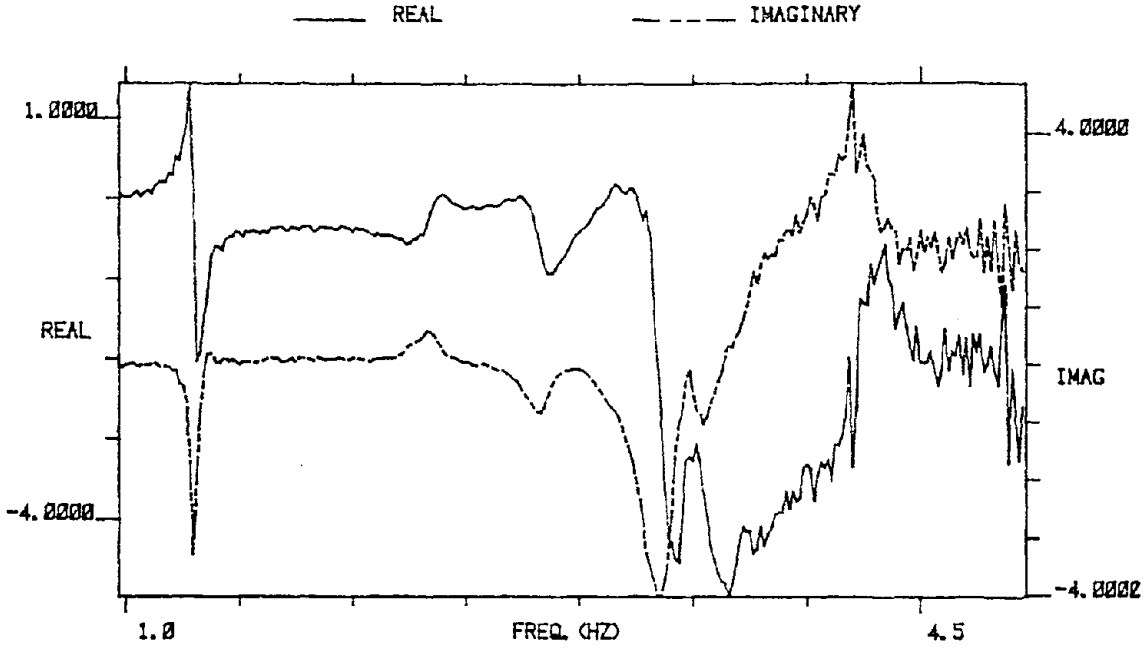

Figure 3.16. Transfer Function Measured on the 12th Floor

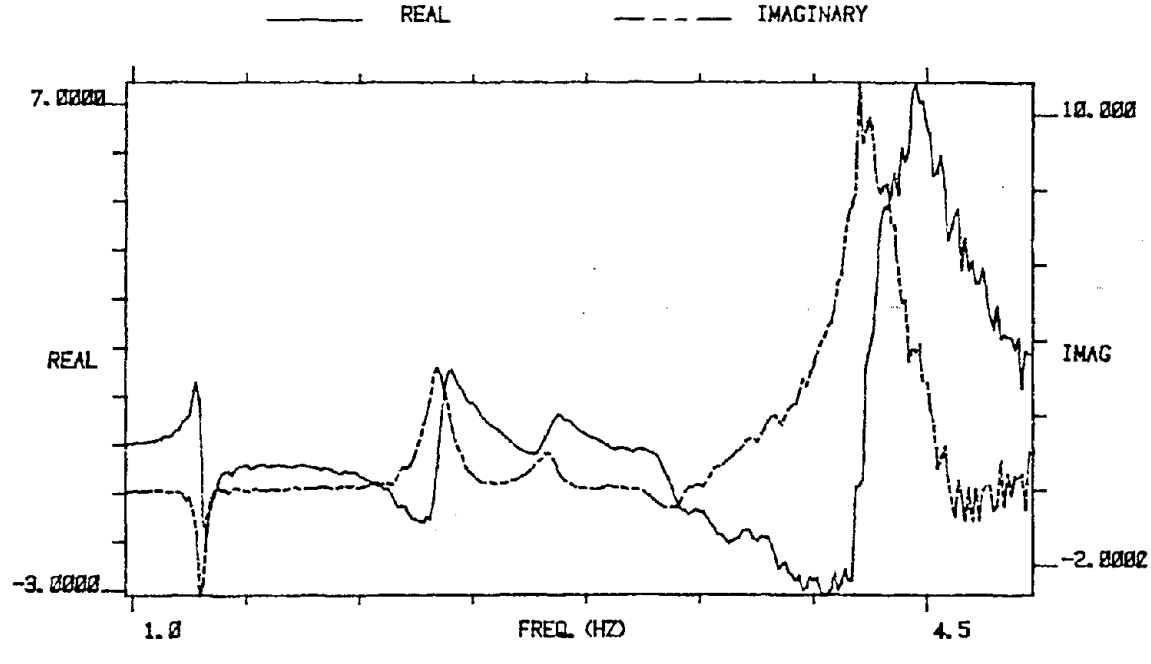

Figure 3.17. Transfer Function Measured on the 9th Floor

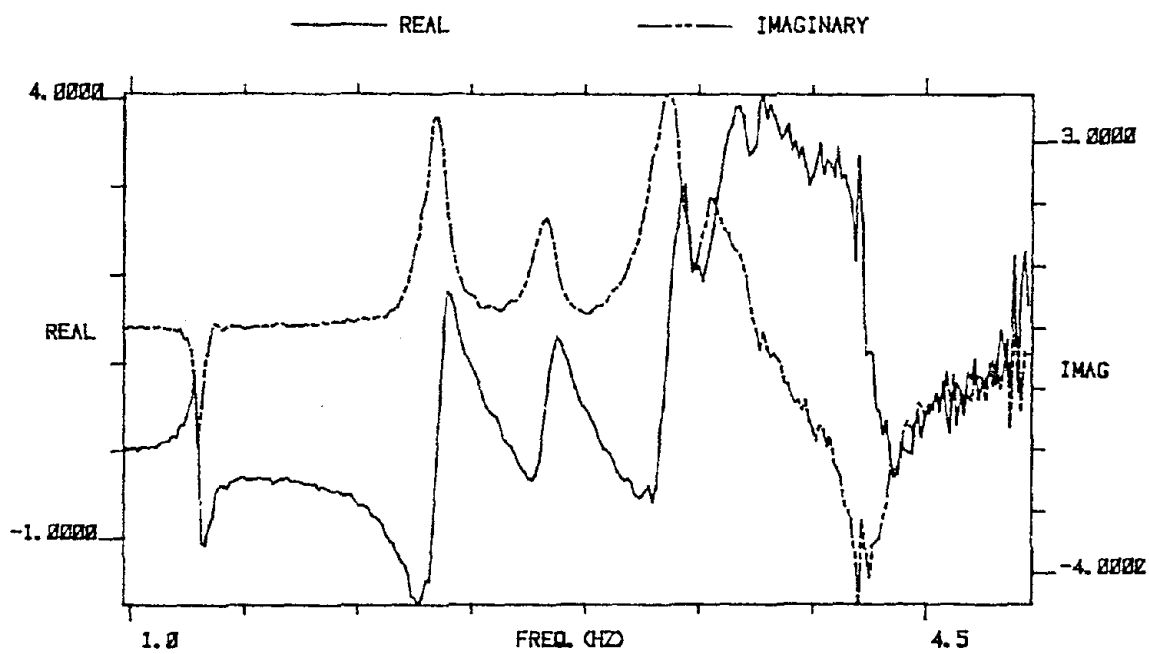

Figure 3.18. Transfer Function Measured on the 6th Floor

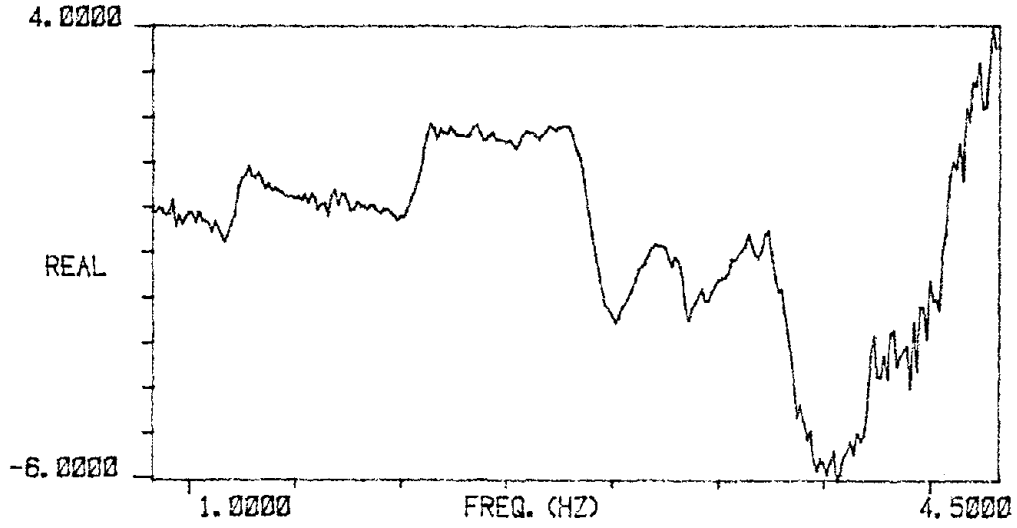

(a) Real

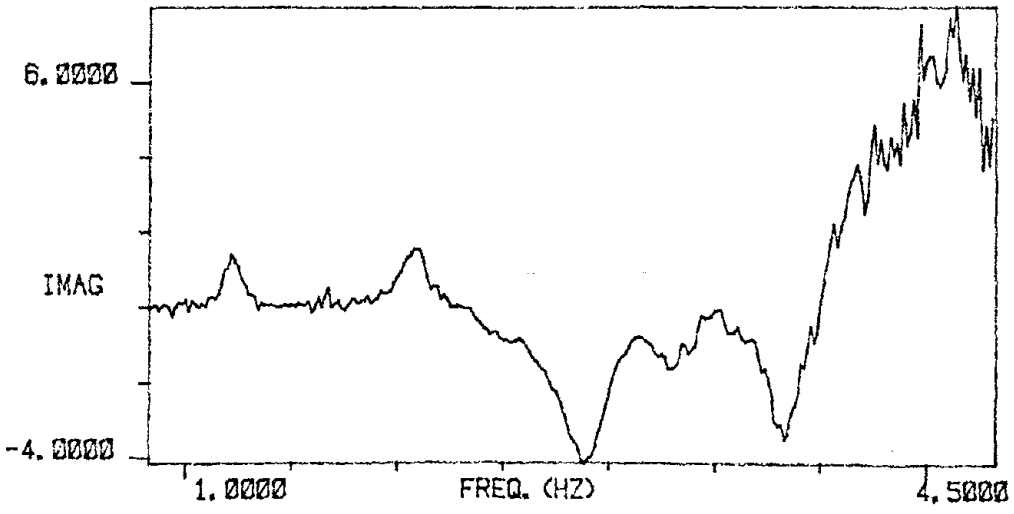

(b) Imaginary

Figure 3.19. Transfer Function For Torsional Response (North)

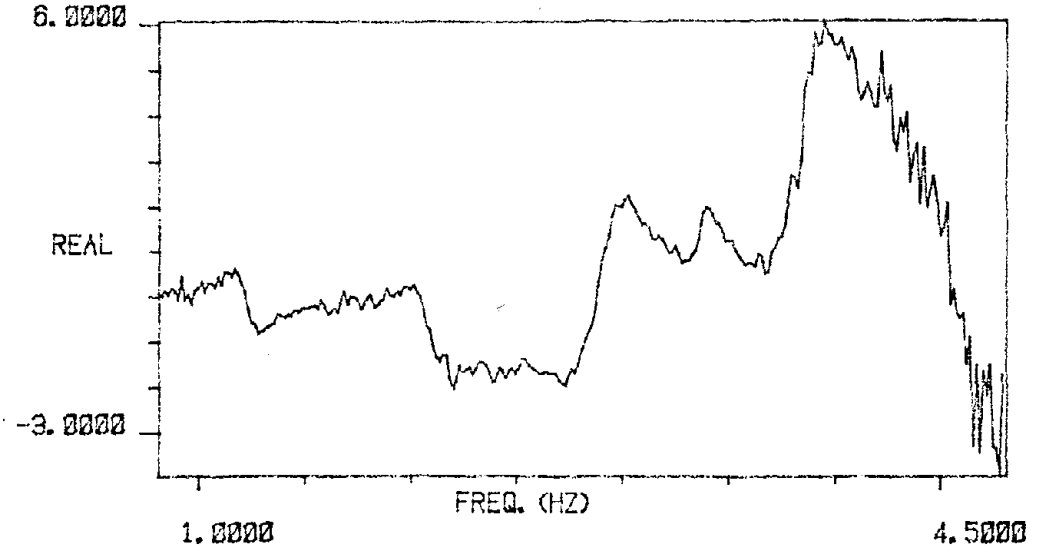

(a) Real

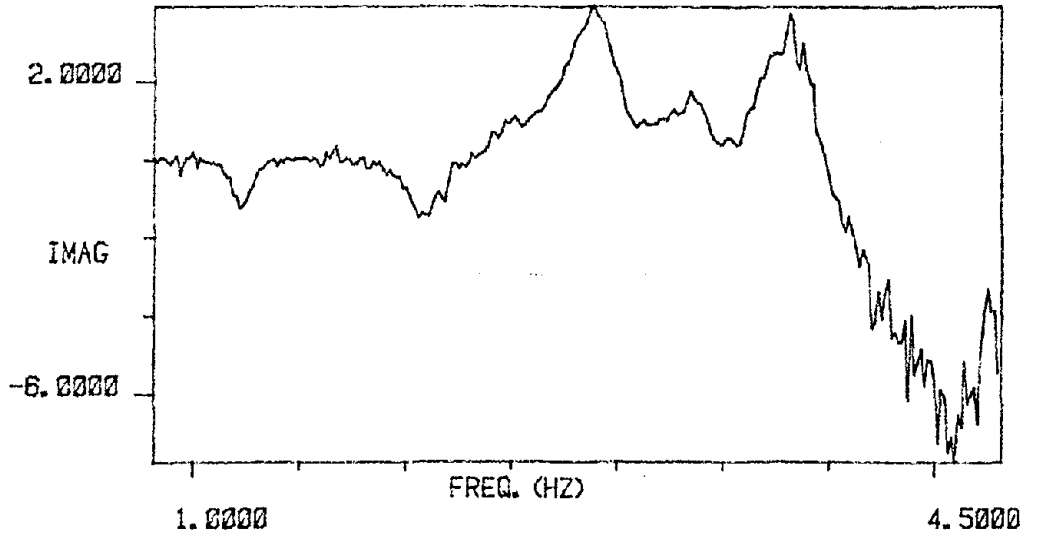

(b) Imaginary

Figure 3.20. Transfer Function for Torsional Response (South)

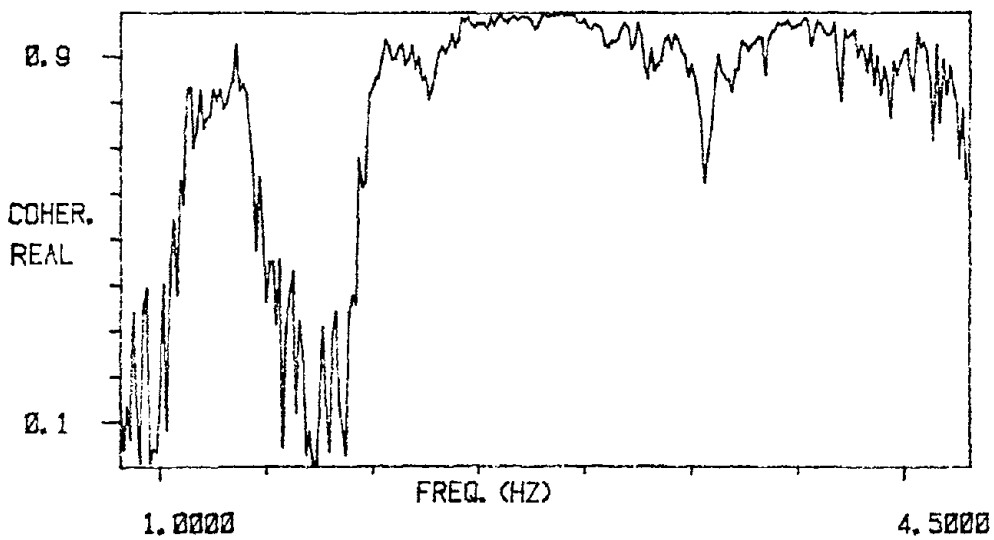

Figure 3.21. A Typical Coherence Function

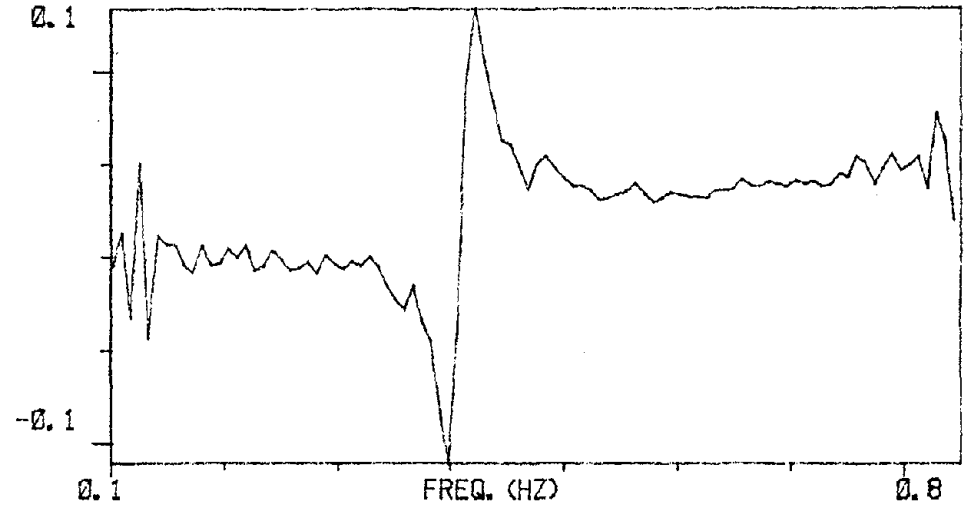

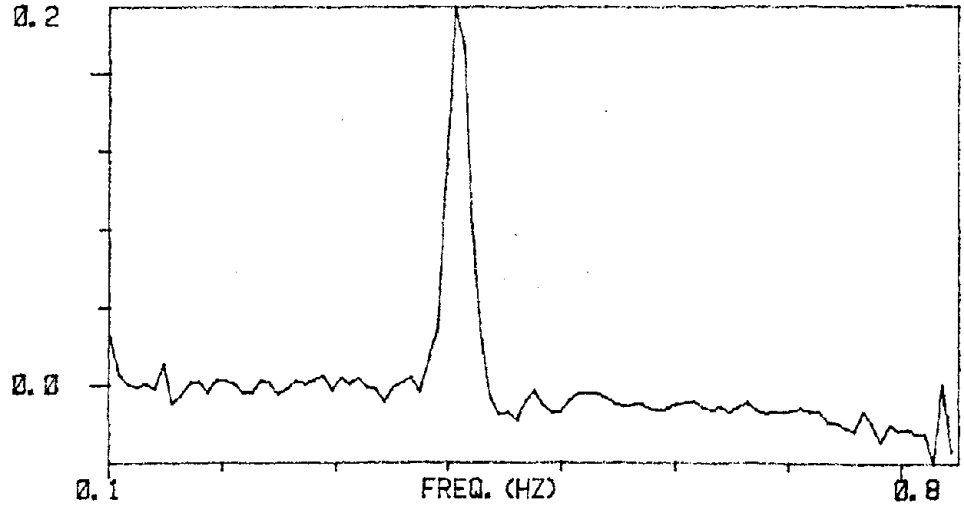

Figure 3.22. A Transfer Fuction in the Low Frequency Range (0.05 - 0.85 Hz); Real and Imaginary Parts

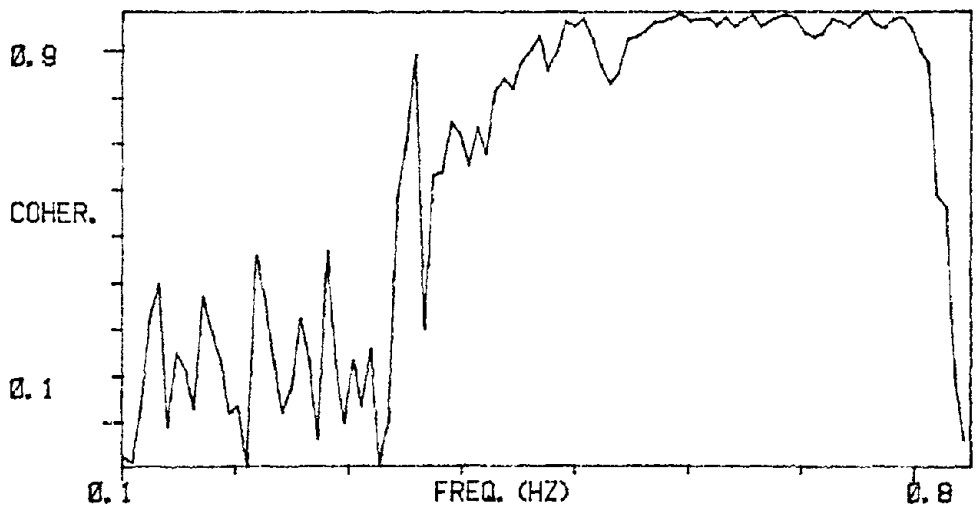

(b) Coherence

Figure 3.22 (Cont'd.)

3.7 Modal Parameter Estimation

The autospectra from the ambient data were curve fitted by the procedure detailed in the preceding chapter. The average values of frequencies and damping ratios for the first three bending modes in the braced and rigid frame directions are tabulated in Table 3.1.

The frequency respone functions from the forced vibration tests were curve fitted using a commercially available software system, the HP Modal Analysis Package (50). This system fits a transfer function model to the measured H(f) for the estimation of frequencies, damping and complex mode shapes. The complex mode shapes, which are characterized by a magnitude and phase for each mode shape coefficient, will be obtained if the damping matrix [C] cannot be uncoupled using the modal matrix [ϕ] (51). When this occurs, all the points in the structure do not move exactly in or out of phase with each other and no normal modes exist. For the present application, the real parts of the complex modes were extracted and normalized to obtain the approximate natural modes.

Careful examination of all the frequency response functions revealed that only the lowest four modes in bending and torsion could be identified. High modal density in the upper frequency region, which included modes other than the primary bending and torsional modes, and a lack of sufficient number of response measurements complicated the identification of the higher modes with any degree of certainty. The parameters for the first four modes were obtained using a combination of single and multidegree-of-

Table 3.1. Ambient Test Results

Mode No.	Braced Frame Direction		Rigid Frame Direction		Torsion	
	Freq. (Hz)	Damp. (%)	Freq. (Hz)	Damp. (%)	Freq. (Hz)	Damp. (%)
1	0.43	3.8	0.33	5.5	-	-
2	1.34	3.4	1.01	4.9	-	-
3	2.41	4.8	1.73	4.8	-	-

Table 3.2. Forced Vibration Test Results

Mode No.	Braced Frame Direction		Rigid Frame Direction		Torsion	
	Freq. (Hz)	Damp. (%)	Freq. (Hz)	Damp. (%)	Freq. (Hz)	Damp. (%)
1	0.41	2.7	0.32	4.2	0.41	4.3
2	1.30	1.4	0.96	2.4	1.23	3.5
3	2.35	3.0	1.66	3.3	2.09	5.5
4	3.37	2.3	2.32	4.7	2.92	4.9

freedom curve fitting procedures. Single degree-of-freedom fits were used for all the fundamental modes and the fourth bending mode in the braced frame direction. All the other modes were fitted using multidegree-of-freedom functions. An example of the type of fit obtained using the software system is given in Figure 3.23 for a frequency response function measured on the roof.

The final estimates for the frequencies and the damping ratios obtained by curve fitting are listed in Table 3.2 . The mode shapes for bending modes are plotted in Figures 3.24 and 3.25. Torsional mode shapes are omitted here since only 3 floors were used for torsional response measurement.

Comparison of Tables 3.1 and 3.2 shows that the ambient test frequencies are higher than the forced vibration test frequencies. This is in agreement with the findings of previous investigations on highrise buildings (14, 52). The damping values in the ambient results are also consistently higher. But in this case, the signal-to-noise ratio in the ambient measurements used to compute the autospectra was rather low. Therefore, no definite conclusions can be drawn from the above results. Only the modal parameter values from the forced vibration tests were employed in the identification of an optimum stiffness matrix for the analytical model of the building. This identification procedure, carried out to determine the possible contribution of the exterior curtain wall to the total stiffness, is described in the next chapter.

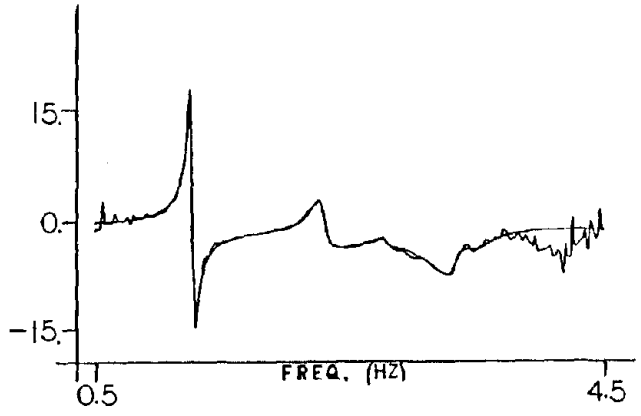

(a) Real

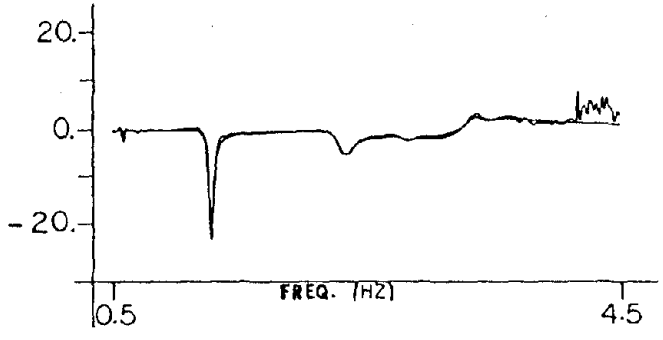

(b) Imaginary

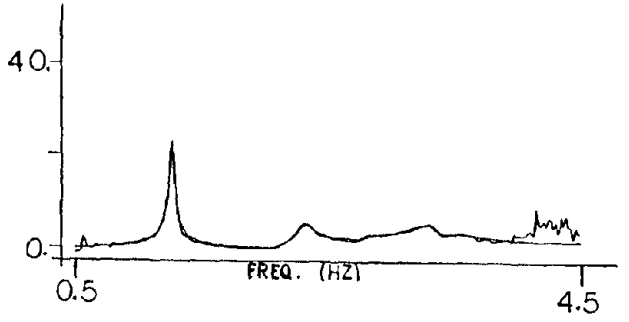

(c) Magnitude

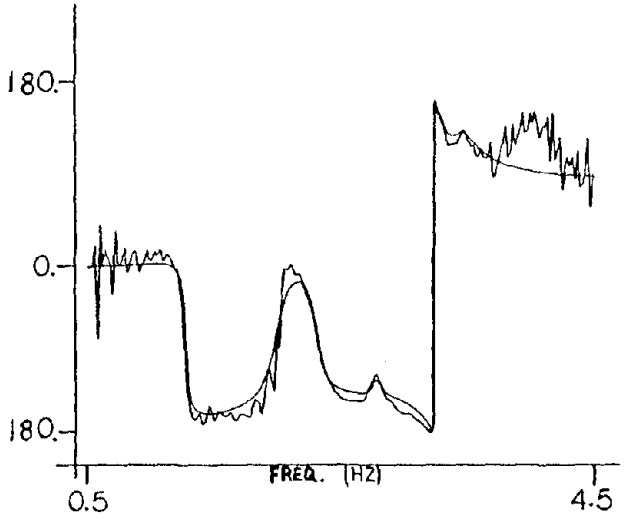

(d) Phase

Figure 3.23. A Transfer Function and its Fit

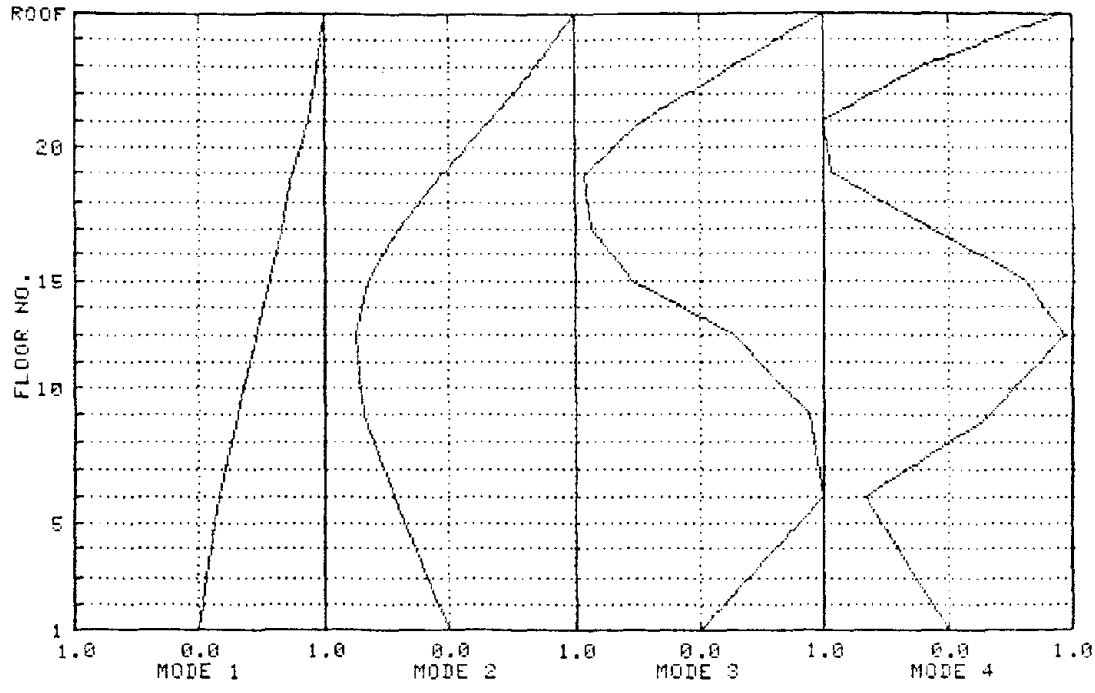

Figure 3.24. Braced Frame Bending Mode Shapes

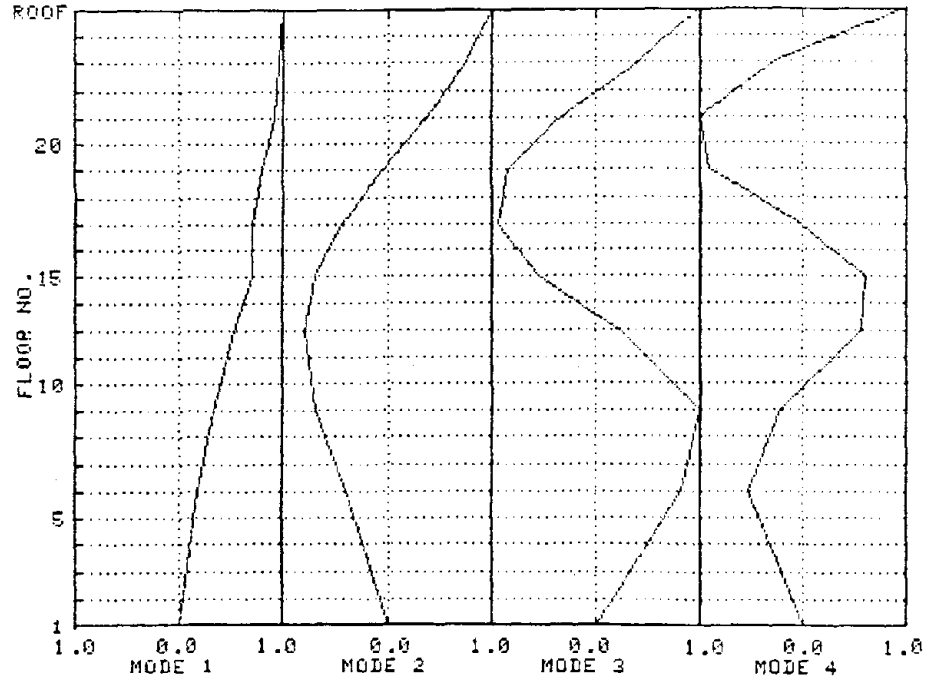

Figure 3.25. Rigid Frame Bending Mode Shapes

4.0 ESTIMATION OF STIFFNESS

4.1 Introduction

One of the primary reasons for structural dynamic testing is to validate, modify, update or construct the analytical or finite-element model of the structure. In most cases an a priori model of the structure exists. This model, for many complex structures, usually consists of a set of second order linear differential equations in terms of the mass, stiffness and damping parameters (Equation 2.16). But the dynamic behavior of the structure is often better interpreted in terms of the modal parameters. However, for several applications such as the direct integration of the equations of motion, the system matrices containing the mass, stiffness and damping constants are required to be known explicitly.

A number of procedures have been employed in the past to construct or alter the system matrices utilizing experimental data. The fundamental motivation for such procedures has been the need for an analytical model that is capable of simulating the experimentally observed behavior as closely as possible. Some of these procedures use the modal parameters while others employ the time domain response directly.

Flannelly and others (53) and Thoren (54) describe schemes to construct the system matrices from measured modal data without

making use of an a priori theoretical model. These are applicable only when the model is restricted to have as many degrees of freedom as the number of measured modes, which in turn must be equal to the number of measurement points. Their usefulness is thus limited for structures such as highrise buildings whose analytical models are generally required to possess many more degrees of freedom than the number of measured modes. Berman and Flannelly (55) used a procedure that overcomes this problem to some extent. In this procedure, the analytical model is derived from data for fewer modes than the number of measurement points, using an initial estimate of the mass matrix. The resulting "incomplete" model simulates the structural response in a specific frequency range when all the modes within this range are included in model construction.

Baruch and others (56, 57) developed a method to determine an optimum stiffness matrix when the mass matrix is known. This method requires that the measured mode shapes satisfy the orthogonality conditions. Caravani and Thomson (58) considered the estimation of damping assuming that the mass and stiffness matrices are known. This problem was pursued further by Thomson and others (59). Beliveau (60) describes a procedure to obtain the mass, stiffness and damping matrices using the Bayesian estimation technique. Experimentally measured frequencies, damping and complex mode shapes are used in the estimation scheme. Ross (61) applied the least squares method to find an optimum mass matrix.

Collins and others (62) discuss an estimation procedure to alter the mass and stiffness matrices. Ibanez (63) outlines a perturbation method to compute the necessary changes in the mass and stiffness matrices. Torkamani and Hart (64) split the total stiffness of the structure into those due to different components.

$$[K] = \sum_{i=1}^{NC} \theta_i [K_i] \tag{4.1}$$

where $[K_i]$ is the stiffness due to the ith component, θ_i is a scalar parameter and NC is the number of components. The values of θ_i (which are all equal to one in the a priori model) are adjusted to produce the best possible match with experimental results. Recently, Chen and Garba (65) proposed another method to identify the mass and stiffness matrix coefficients.

Numerous other investigators have studied the dynamic behavior of structural systems under various conditions by applying system identification and parameter estimation techniques. An extensive survey of the work done in this area can be found in the articles by Young and On (66), Collins and others (67), Hart and Yao (68) and Ibanez (69).

The purpose of the present chapter is to describe the procedures employed to estimate the stiffness due to the exterior cladding for the 25-story building with heavyweight cladding which was used in forced vibration tests. An a priori finite-element model of this

building has recently been developed and used in analytical cladding-structure interaction studies (10, 49). It was found in these studies that the analytical frequencies increased by substantial amounts, particularly for torsional modes, when the cladding stiffness was added. The influence of cladding is explored further here by utilizing both the a priori model and the experimental results from forced vibration tests. Starting from the initial model, an improved model is arrived at so that the modal parameters of the improved model are closer to the experimental values than the parameters of the original model. The contribution of cladding to the total stiffness is determined in the process.

Since the major objective was to investigate the stiffness effects of cladding as a lateral force resisting system, the procedures described below do not make any attempt to alter the mass matrix of the original model. Furthermore, the damping effects are not considered. Only the frequencies and the normal mode shapes measured in experiments are employed to modify the a priori stiffness matrix.

The process of revising the stiffness matrix, to make the model conform with the experimental results, can be carried out using any of the several techniques discussed in the references given above. For highrise building models with many degrees of freedom, methods that alter the individual elements of the stiffness matrix directly may involve large, and at times prohibitive, amount of computational effort. The technique that may be preferable in such cases is to decompose the structural stiffness matrix into

components due to various structural subsystems. A structural or stiffness parameter is associated with each of the component stiffness matrices. The total stiffness is obtained using Equation (4.1). This particular approach of manipulating the stiffness matrix by decomposition and the subsequent estimation of the stiffness parameters offers the advantage of being able to handle large systems with relative ease. However, this technique is less powerful than others that modify the coefficients of the stiffness matrix directly, which, for this very reason, can be expected to give better results and produce closer matches.

In the current study, the above technique has a distinct advantage since the role of cladding can be determined by estimating the parameter θ_i associated with the approximate cladding stiffness matrix developed in the a priori model. Therefore, this technique is adopted and the stiffness matrix is decomposed to explicitly represent the effects of various components including the curtain wall.

4.2 The A Priori Model

The construction details and features of the prior analytical model for the building employed are given in Reference 49. The mass of the structure was lumped at each floor level giving rise to a diagonal mass matrix. The stiffness matrix was assembled from independently developed stiffnesses for three different parts, namely the primary core, the exterior frame that supports the cladding panels and the cladding. The model consists of three degrees of freedom per floor (bending in the braced and rigid frame

directions and torsion). The cladding stiffness matrix was developed in terms of an interstory shear stiffness parameter that quantifies the stiffness effects of cladding and its connection elements on each face between floors. The initial value for this parameter was determined by the least squares method on a trial and error basis, employing preliminary ambient test results. This value was found to be 625 Kips/inch.

4.3 The Estimation Methods

The stiffness parameters for the three components, viz. the core, the frame and the cladding, are estimated using a weighted least squares approach. The weighting matrix is selected by considering the uncertainties in the measurements as well as the prior values of the parameters. The estimates are also obtained by the usual ordinary least squares, maximum likelihood and maximum posterior density methods. The results from these three procedures, are compared with the results of the weighted least squares method. A concise review of the three standard estimation procedures will now be presented followed by a description of the weighted least squares method used.

4.3.1 Ordinary Least Squares (OLS) Estimation

The cost function for the OLS method is given by Equation (2.32). Experimental values $\{Y_i\}$ correspond to the measured frequencies and mode shape coefficients and $\{F_i(\theta)\}$ correspond to the analytical eigenparameters obtained by solving the eigenvalue problem for given

values of the parameters $\{\theta\}$. The summation index i in this case refers to the different dependent variables rather than different experiments as for the single equation least squares problem. The OLS procedure does not take into account any information regarding the distribution of the data or the confidence in the prior values of $\{\theta\}$; the measurement and the modeling errors are completely ignored.

4.3.2 Maximum Likelihood (ML) Estimation

The ML estimates are obtained by maximizing the likelihood function $L(\theta)$. If $P(Y/\theta)$ denotes the probability density function of the observations for given $\{\theta\}$,

$$L(\theta) = P(Y/\theta) \tag{4.2}$$

where $\{\theta\}$ is considered variable. When the errors in the measurement are normally distributed with zero mean and a covariance matrix $[V_y]$, the logarithm of the likelihood function can be expressed as (34)

$$\ell n[L(\theta)] = -\frac{1}{2} r\ [\ell n(2\pi)] - \frac{1}{2} \ell n[|V_y|]$$

$$-\frac{1}{2} \{e\}^T [V_y]^{-1} \{e\} \tag{4.3}$$

where r is the number of dependent variables, $|V_y|$ is the determinant of $[V_y]$ and $\{e\}$ is the r x 1 error vector. Maximizing $L(\theta)$ reduces to minimizing ψ, where

$$\psi = \{e\}^T [V_y]^{-1} \{e\} \tag{4.4}$$

when $[V_y]$ is completely known. Thus, the maximum likelihood method with the above assumptions is equivalent to weighted least squares estimation where the weighting matrix is taken as the inverse of the covariance matrix. If $[V_y]$ is not completely known, an objective function that is different from Equation (4.4) can be used. The form of this function will depend on the amount of knowledge of the covariance (34); that is, it depends on the degree to which $[V_y]$ is known.

The ML procedure considers the measurement errors in estimation but does not treat the parameters to be estimated as random variables. Although the ML estimates do not possess optimal statistical properties, they are usually satisfactory.

4.3.3 Maximum Posterior Density (MPD) or Bayesian Estimation

If a prior density function $P_b(\theta)$ can be assigned to the parameters, the posterior density function $P_a(\theta/Y)$ can be written, using Bayes' theorem, as

$$P_a(\theta/Y) = \frac{P(Y/\theta)\ P_b(\theta)}{P(Y)} = \frac{L(\theta)\ P_b(\theta)}{P(Y)} \tag{4.5}$$

where

$$P(Y) = \int P(Y/\theta)\ P_b(\theta)\ d\theta$$

The process in which the parameters are estimated by maximizing the posterior density function is known as the maximum posterior density method. If both $P(Y/\theta)$ and $P_b(\theta)$ are normally distributed, maximizing $P_a(\theta/Y)$ is the same as minimizing the following function (34):

$$\psi = \{e\}^T [V_y]^{-1}\{e\} + \{\theta - \mu\}^T[V_\theta]^{-1} \{\theta - \mu\} \tag{4.6}$$

where $\{\mu\}$ and $[V_\theta]$ are the mean and covariance of the prior distribution of $\{\theta\}$.

The MPD method includes the effects of uncertainty in the data and the model. It is even applicable to some cases where it is not feasible to use least squares or maximum likelihood method.

4.3.4 Weighted Least Squares (WLS) Estimation

In WLS estimation, the objective function ψ takes the form

$$\psi = \{e\}^T[W]\{e\} \tag{4.7}$$

where [W] is the weighting matrix. The OLS method is a special case of the WLS procedure with [W]equal to the identity matrix. Also, ML estimation with normally distributed errors and known covariance is equivalent to assuming $[W] = [V_y]^{-1}$. But these are by no means the only types of weighting possible. In the present study, the weighting matrix is taken as the inverse of the error covariance $[V_e]$ computed by treating both $\{Y\}$ and $\{F(\theta)\}$ as random. Under the assumption that the experimental values Y_i and the analytical values

$F_i(\theta)$ are uncorrelated, it is easy to show that

$$\text{cov}\,[e_i e_j] = \text{cov}[Y_i Y_j] + \text{cov}\,[F_i(\theta)\ F_j(\theta)] \qquad (4.8)$$

in which cov $[x_i x_j]$ denotes the covariance of two random variables x_i and x_j. In matrix form,

$$[V_e] = [V_y] + [V_F] \qquad (4.9)$$

where

$$[V_e] = \begin{bmatrix} \text{Var}\ (e_1) & \text{Cov}[e_1 e_2] & \cdots & \text{cov}[e_1 e_r] \\ \text{cov}[e_2 e_1] & \text{Var}(e_2) & \cdots & \vdots \\ \vdots & & & \\ \text{cov}[e_r e_1] & \cdots & & \text{Var}(e_r) \end{bmatrix}$$

and

$$[V_F] = \begin{bmatrix} \text{Var}(F_1(\theta)) & \text{Cov}[F_1(\theta)F_2(\theta)] & \cdots & \text{Cov}[F_1(\theta)F_r(\theta)] \\ \text{Cov}[F_2(\theta)F_1(\theta)] & \text{Var}(F_2(\theta)) & \cdots & \vdots \\ \vdots & & & \\ \text{Cov}[F_r(\theta)F_1(\theta)] & \cdots & & \text{Var}(F_r(\theta)) \end{bmatrix}$$

The matrix $[V_F]$ is evaluated using the prior covariance matrix of the parameters $[V_\theta]$.

$$[V_\theta] = \begin{bmatrix} \mathrm{Var}(\theta_1) & \mathrm{Cov}[\theta_1\theta_2] \ldots & \mathrm{Cov}[\theta_1\theta_p] \\ \vdots & & \vdots \\ \mathrm{Cov}[\theta_p\theta_1] \ldots & & \mathrm{Var}(\theta_p) \end{bmatrix}$$

The procedures for computing the elements $\mathrm{cov}[F_i(\theta)F_j(\theta)]$ using $[V_\theta]$ are well established (70-72). These procedures are based on the small perturbation assumption that the analytical values can be expressed as

$$F_i(\theta) = F_i(\bar{\theta}) + \sum_{k=1}^{p} \left.\frac{\partial F_i(\theta)}{\partial \theta_k}\right|_{\{\theta\}=\{\bar{\theta}\}} (\theta_k - \bar{\theta}_k) \qquad (4.10)$$

where $\{\bar{\theta}\}$ is the mean of the distribution of $\{\theta\}$. From the above equation,

$$E[F_i(\theta)] = F_i(\bar{\theta})$$

and

$$\mathrm{Cov}\,[F_i(\theta)\ F_j(\theta)] = \sum_{k=1}^{p}\sum_{\ell=1}^{p} \left.\frac{\partial F_i(\theta)}{\partial\theta_k}\ \frac{\partial F_j(\theta)}{\partial\theta_\ell}\right|_{\{\theta\}=\{\bar{\theta}\}} \mathrm{Cov}(\theta_k\theta_\ell)$$

where E[ ] denotes expectation. Cast in the matrix form,

$$\{E\ [F(\theta)]\} = \{\bar{F}(\theta)\} = \{F(\bar{\theta})\} \qquad (4.11a)$$

and

$$[V_F] = \left[\frac{\partial F}{\partial\theta}\right]^T [V_\theta] \left[\frac{\partial F}{\partial\theta}\right] \qquad (4.11b)$$

where

$$\left[\frac{\partial F}{\partial \theta}\right] = \begin{bmatrix} \frac{\partial F_1}{\partial \theta_1} & \frac{\partial F_2}{\partial \theta_1} & \cdots & \frac{\partial F_r}{\partial \theta_1} \\ \vdots & & & \vdots \\ \frac{\partial F_1}{\partial \theta_p} & \cdots & & \frac{\partial F_r}{\partial \theta_p} \end{bmatrix}$$

in which the dependence on $\{\theta\}$ is omitted for convenience.

The matrix $\left[\frac{\partial F}{\partial \theta}\right]$ consists of the derivatives of the modal parameters with respect to the stiffness parameters. In the case of frequencies, the derivative $\frac{\partial f_i}{\partial \theta_j}$ is given by

$$\frac{\partial f_i}{\partial \theta_j} = \left(\frac{d f_i}{d \lambda_i}\right)\left(\frac{\partial \lambda_i}{\partial \theta_j}\right) = \frac{1}{4\pi\sqrt{\lambda_i}}\left(\frac{\partial \lambda_i}{\partial \theta_j}\right) \tag{4.12}$$

where λ_i is the analytical eigenvalue, expressed as

$$\lambda_i = \omega_i^2 = (2\pi f_i)^2$$

Therefore, in order to compute $\left[\frac{\partial F}{\partial \theta}\right]$, the eigenvalue derivative $\frac{\partial \lambda_i}{\partial \theta_j}$ and the eigenvector derivatives $\{\frac{\partial \phi_i}{\partial \theta_j}\}$ must be evaluated. Several investigators have dealt with the problem of obtaining the eigenparameter derivatives (72-76). These derivatives are acquired as follows.

The eigenvalue problem to be solved can be written as

$$[K]\{\phi_i\} = \lambda_i [M]\{\phi_i\} \tag{4.13}$$

Differentiating Equation (4.13) with respect to θ_j,

$$[K_{,j}]\{\phi_i\} + [K]\{\phi_{i,j}\} = \lambda_{i,j}[M]\{\phi_i\} + \lambda_i[M_{,j}]\{\phi_i\}$$

$$+ \lambda_i[M]\{\phi_{i,j}\} \qquad (4.14)$$

where $[K_{,j}]$ represents the matrix of the derivatives of the stiffness elements with respect to θ_j and so on. Multiplying Equation (4.14) by $\{\phi_i\}^T$ and recognizing that [M] and [K] are symmetric, the above equation reduces to

$$\{\phi_i\}^T[K_{,j}]\{\phi_i\} = \lambda_{i,j}\{\phi_i\}^T[M]\{\phi_i\} + \lambda_i\{\phi_i\}^T[M_{,j}]\{\phi_i\}$$

where Equation (4.13) has been used. Therefore

$$\lambda_{i,j} = \frac{\{\phi_i\}^T\left[[K_{,j}] - \lambda_i[M_{,j}]\right]\{\phi_i\}}{\{\phi_i\}^T[M]\{\phi_i\}} \qquad (4.15)$$

Rearranging Equation (4.14)

$$\left[[K] - \lambda_i[M]\right]\{\phi_{i,j}\} = \left[\lambda_{i,j}[M] + \lambda_i[M_{,j}] - [K_{,j}]\right]\{\phi_i\} \qquad (4.16)$$

Since the matrix $\left[[K] - \lambda_i[M]\right]$ is of rank (n-1), Equation (4.16) cannot be directly solved for $\{\phi_{i,j}\}$. If one of the elements of $\{\phi_{i,j}\}$ is fixed, the other elements can be determined by deleting the corresponding equation from Equation (4.16). It is obvious from

Equations (4.15) and (4.16) that to evaluate the derivatives of an eigenpair, only that pair is needed and Equation (4.13) need not be solved completely for all the eigenvalues and eigenvectors.

Another method to determine the eigenvector derivatives utilizes the representation of $\{\phi_{i,j}\}$ as a linear combination of the n independent eigenvectors which span the n-dimensional space. This method requires all the eigenvectors though it is possible to truncate the sum of the eigenvector contributions in some cases and obtain an approximation for $\{\phi_{i,j}\}$. However, it does not involve the solution of a set of simultaneous equations. Details of this procedure can be found in the references cited above. In the current procedure, Equations (4.15) and (4.16) are employed to obtain the required derivatives.

Once the eigenparameter derivatives are known, $[V_F]$ can be evaluated using Equation (4.11). The weighting matrix [W] is computed as

$$[W] = [V_e]^{-1} = [V_y + V_F]^{-1} \tag{4.17}$$

The amount of computational effort involved can be greatly reduced if the off-diagonal terms in [W] are neglected. For this case,

$$[W] = \begin{bmatrix} \ddots & & \\ & \frac{1}{\mathrm{Var}(Y_i) + \mathrm{Var}(F_i)} & \\ & & \ddots \end{bmatrix} \tag{4.18}$$

Equation (4.18) defines the weighting matrix used here. This

procedure can be viewed as one in which the weights are chosen based on the confidence in the measured as well as the analytical values of the dependent variables.

4.4 The Minimization Algorithm

The objective functions in all four estimation procedures described in the previous section were minimized by the inverse rank one correction (IROC) method. This method involves replacing the Hessian [S] with an approximation that is updated every iteration. A discussion of this method and a derivation are given in Appendix A. The improved estimates for the parameters $\{\theta^{k+1}\}$ are calculated from the old values $\{\theta^{k}\}$ using Equation (A.11) in the Appendix. The approximation $[A^{k}]$ to the Hessian is updated by adding a correction $[\Delta A^{k}]$ computed according to Equation (A.10). The series of matrices $[A^{k}]$ thus generated converges to the Hessian evaluated at the minimum as $\{\theta\}$ converges to $\{\theta^{*}\}$. The Hessian at the minimum is therefore generated along with the minimum itself.

Each iteration in the algorithm involves solving an eigenvalue problem of order n. Only the first few eigenvalues and eigenvectors corresponding to the experimentally measured frequencies and mode shapes are needed to evaluate the objective function and its derivatives with respect to $\{\theta\}$. In addition, the computation of the eigenvector derivative employing Equation (4.16) requires the solution of a set of simultaneous equations which, if it is assumed that one of the equations has been deleted, is of order (n-1). In the present case,

the eigenvectors and the measured mode shapes were normalized so that the coefficient of the degree of freedom corresponding to the roof was set equal to one. Hence, the mode shape derivatives were calculated with respect to the roof response by excluding the equation for the roof coordinate. The actual solution was carried out by replacing the off-diagonal elements of the row and the column corresponding to the roof with zeros and solving the system of n equations.

The weighted least squares method requires the evaluation of the analytical covariance $[V_F]$. But for this additional computation in WLS estimation, all four methods require approximately the same amount of computations with a major part of the effort being spent on the function and the gradient evaluations. Therefore, in the discussion to follow, these methods will be compared on the basis of the number of function and gradient evaluations necessary for convergence and not the number of iterations.

The termination criterion adopted to stop the algorithm after the minimum has been approximately located is that given in Equation (2.45d). The computations were terminated if the values of the objective function in two successive iterations differed by less than 0.5 percent by choosing $\varepsilon_5 = 0.005$.

4.5 Application and Results

The prior analytical model of the subject highrise building consists of a coupled 63 x 63 stiffness matrix assembled using independent component stiffness matrices belonging to the core, the

exterior frame and the cladding. The stiffness matrix for each of these components is assembled, in turn, using three stiffness matrices corresponding to the respone in the three directions, namely bending in braced and rigid frame directions and torsion.

In the following procedure, it is assumed that the response of the structure in any direction is independent of the response in the other directions and the coupling effects in the stiffness matrix are ignored. Uncoupling the stiffness matrix allows decomposition of the original problem into three smaller problems, one for each of the three directions. The order of the system to be solved is now reduced from 63 to 21, but the complete solution is obtained by solving three 21 x 21 systems (The 21 coordinates correspond to the topmost 21 floors. The lower floors were considered laterally supported at the floor levels due to the stiff concrete pedestal at the base of the building.) Dealing with the reduced systems instead of the original coupled system offers the following advantages.

(i) The treatment of three 21 x 21 systems is more economical in terms of computer time and storage than the treatment of the coupled 63 x 63 system.

(ii) By introducing three parameters for the core, the frame, and the cladding in each direction, a total of nine parameters can be estimated. The match between the experimental and the anlaytical frequencies and mode shapes using these 9 parameters is likely to be better

than the match that would be obtained with only 3 parameters associated with the coupled component stiffness matrices.

Whereas the frame and the cladding have the same stiffness in both the bending directions, the core does not. This is due to the fact that the core is not symmetric and consists of both rigid and braced frame components.

The uncoupled stiffness matrices in the three directions can be written as

$$[\bar{K}_i] = \sum_{j=1}^{3} \theta_{ij}[K]_{ij} \quad , \; i=1,2,3 \tag{4.19}$$

where $j = 1$ corresponds to the core

$j = 2$ corresponds to the exterior frame

$j = 3$ corresponds to the cladding

$i = 1$ corresponds to bending in braced frame direction

$i = 2$ corresponds to bending in rigid frame direction

$i = 3$ corresponds to torsion

$[\bar{K}_i]$ = total stiffness in the ith direction

$[K_{ij}]$ = stiffness of the jth component in the ith direction

and θ_{ij} = parameter associated with $[K]_{ij}$

The equations of motion to be solved are

$$[\bar{M}]_i\{\ddot{x}\}_i + [\bar{K}]_i\{x\}_i = 0, \quad i=1,2,3 \tag{4.20}$$

where $\{x\}_i$ = the response vector in the ith direction and $[\bar{M}]_i$ = the diagonal 21 x 21 mass matrix for the ith directional response.

For estimating the parameters in the two bending directions, the first four frequencies and the first three mode shapes measured in forced vibration tests were considered. The fourth bending mode shapes were not deemed accurate enough to be included here because the convergence of the curve fitting program employed to fit the measured transfer functions was relatively poor in this region. In torsion, only the first four frequencies were used and no mode shapes were considered due to the lack of a sufficient number of response locations to define these adequately.

The analytical values for the modal parameters as predicted by the uncoupled a priori model, which were virtually the same as those predicted by the original coupled model, are compared with the experimental values in Tables 4.1 and 4.2. The a priori model is the one in which all θ_{ij} equal unity. Table 4.1 lists the computed and the measured frequencies. The mode shape coefficients are tabulated in Table 4.2 and the analytical shapes are compared with the experimental mode shapes in Figures 4.1 and 4.2. Also listed in Tables 4.1 and 4.2 are the values of the sum of the squares of the errors (SSQ), which is a measure of the deviation of the predicted values from the observed values and which forms the objective function in OLS estimation.

From Table 4.1 it is observed that the frequencies in the braced frame direction are the closest to the experimental values (SSQ = 0.0108) while the frequencies in torsion show the greatest deviation (SSQ = 0.0322). The analytical frequencies in braced frame

Table 4.1. Comparison of Experimental and A Priori Analytical Frequencies

Dir. / Mode No.	Braced Frame		Rigid Frame		Torsion	
	Exp.	Anal.	Exp.	Anal.	Exp.	Anal.
1	0.41	0.402	0.32	0.345	0.41	0.408
2	1.30	1.263	0.96	0.995	1.23	1.174
3	2.35	2.349	1.66	1.778	2.09	2.000
4	3.37	3.273	2.32	2.366	2.92	2.776
SSQ	0.108×10^{-1}		0.179×10^{-1}		0.322×10^{-1}	

Table 4.2. Comparison of Experimental and A Priori Analytical Mode Shapes

Floor No.	Braced Frame Direction Mode No.						Rigid Frame Direction Mode No.					
	1		2		3		1		2		3	
	Exp.	Anal.	Exp.	Anal.	Exp.	Anal.	Exp.	Anal.	Exp.	Anal.	Exp.	Anal.
Roof	1.00	1.00	1.00	1.00	1.00	1.00	1.00	1.00	1.00	1.00	1.00	1.00
23	0.94	0.93	0.68	0.69	0.27	0.30	0.96	0.95	0.75	0.69	0.42	0.15
21	0.87	0.85	0.33	0.30	-0.46	-0.47	0.91	0.87	0.39	0.27	-0.34	-0.67
19	0.75	0.76	-0.06	-0.11	-0.92	-0.97	0.80	0.78	-0.04	-0.17	-0.86	-1.00
17	0.66	0.67	-0.41	-0.47	-0.87	-0.98	0.70	0.67	-0.43	-0.52	-0.96	-0.76
15	-	0.56	-0.65	-0.73	-0.54	-0.46	0.70	0.56	-0.69	-0.72	-0.57	-0.17
12	-	0.45	-0.75	-0.80	0.28	0.34	0.53	0.45	-0.80	-0.74	0.24	0.52
9	0.31	0.28	-0.68	-0.69	0.89	1.26	0.33	0.28	-0.69	-0.59	1.03	1.04
6	0.16	0.13	-0.45	-0.37	1.01	1.02	0.17	0.13	-0.40	-0.31	0.84	0.72
SSQ (4 Freq. +3 Mode Shapes)	0.197						0.590					

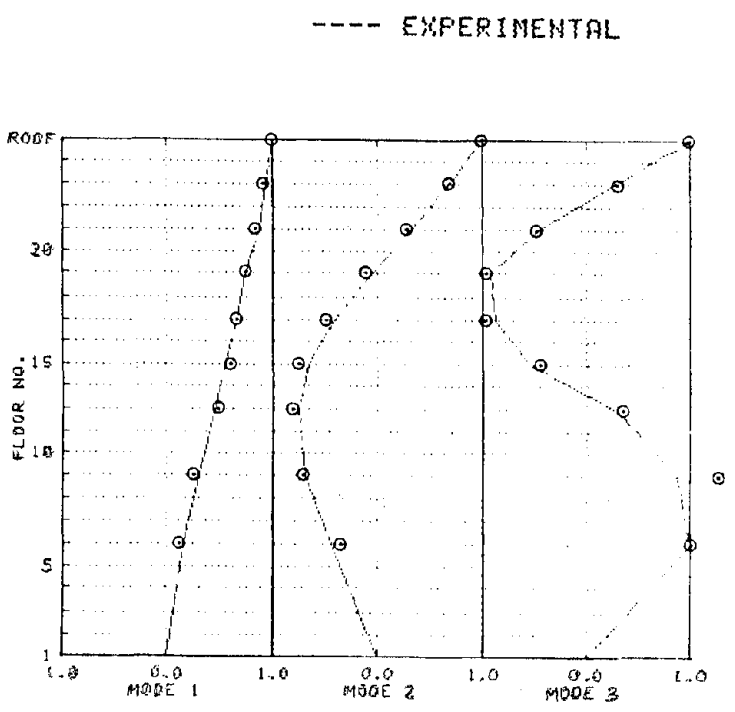

Figure 4.1. Comparison of Experimental and Analytical Mode Shapes; Braced Frame Direction

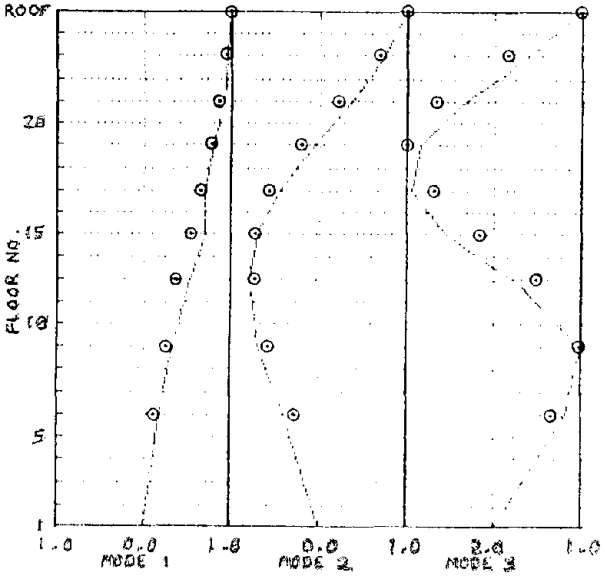

Figure 4.2. Comparison of Experimental and Analytical Mode Shapes; Rigid Frame Direction

bending and torsion are lower than the measured values. On the other hand, the analytical rigid frame bending frequencies are higher than the experimental frequencies. When the mode shapes are included, it is again seen that the parameters in the braced frame direction are closer (SSQ = 0.197) than in the rigid frame direction (SSQ = 0.590). In both the directions, the deflections in the experimentally determined fundamental mode shape are higher than in the analytical shape in general. For higher modes, the measured shapes possess nodal points that are closer to the base.

In most cases, the experimental frequencies are much more accurate than the experimental mode shapes. Accordingly, the coefficients of variation for all the frequencies were taken as 0.002 (0.2% standard deviation) while the values for the mode shapes were taken as 0.05, 0.10 and 0.15 for the first, second and third modes respectively (5, 10 and 15% standard deviation). These values were chosen after examining the modal parameter estimates from different response locations in the building. The diagonal measurement covariance matrix $[V_y]$ was constructed using the above values of standard deviation for the modal parameters.

The matrix $[V_F]$ employed in WLS estimation will be a true representation of the analytical covariance of the modal parameters only for small values of standard deviations for θ_{ij}. This is due to the first order approximations of the eigenparameters employed in deriving expressions for the covariance. The values assumed here in both WLS and MPD estimation are the following:

$\sigma(\theta_{i1})$, the standard deviation for the core parameter = 0.03

$\sigma(\theta_{i2})$, the standard deviation for the exterior frame parameter = 0.05

$\sigma(\theta_{i3})$, the standard deviation for the cladding parameter = 0.05

The diagonal prior covariance $[V_\theta]$ was computed using these values.

The approximate posterior covariance $[V_{\theta^*}]$ for the optimum parameters $\{\theta^*\}$ can be computed by making use of the general expression given in Reference 34.

$$[V_{\theta^*}] \simeq [S^*]^{-1} \left[\frac{\partial^2 \psi}{\partial \theta \, \partial Y}\right] [V_y] \left[\frac{\partial^2 \psi}{\partial \theta \, \partial Y}\right]^T [S^*]^{-1} \tag{4.21}$$

where

$$\left(\frac{\partial^2 \psi}{\partial \theta \, \partial Y}\right)_{ij} = \frac{\partial^2 \psi}{\partial \theta_i \, \partial Y_j}$$

and $[S^*]$ is the Hessian evaluated at the optimum estimate $\{\theta^*\}$. For objective functions of the form considered here,

$$\left[\frac{\partial^2 \psi}{\partial \theta \, \partial Y}\right] = -2\left[\frac{\partial F}{\partial \theta}\right] [W]$$

In OLS estimation, $[W] = [I]$, the identity matrix and

$$[V_{\theta^*}] \simeq 4 [S^*]^{-1} \left[\left(\frac{\partial F}{\partial \theta}\right)^*\right] [V_y] \left[\left(\frac{\partial F}{\partial \theta}\right)^*\right]^T [S^*]^{-1} \tag{4.22}$$

For ML estimation, $[W] = [V_y]^{-1}$ and Equation (4.21) reduces to

$$[V_{\theta^*}] \simeq 4[S^*]^{-1}\left[\left(\frac{\partial F}{\partial \theta}\right)^*\right][V_y]^{-1}\left[\left(\frac{\partial F}{\partial \theta}\right)^*\right]^T[S^*]^{-1} \quad (4.23)$$

If the errors are assumed to be small, it can be shown that (34)

$$[V_{\theta^*}] \simeq 2[S^*]^{-1} \quad (4.24)$$

Equation (4.23) also holds good for MPD estimation. For the WLS procedure, $[W] = [V_e]^{-1}$ and

$$[V_{\theta^*}] \simeq 4[S^*]^{-1}\left[\left(\frac{\partial F}{\partial \theta}\right)^*\right][V_e]^{-1}[V_y][V_e]^{-1}\left[\left(\frac{\partial F}{\partial \theta}\right)^*\right]^T[S^*]^{-1} \quad (4.25)$$

Equations (4.22), (4.23), (4.24) and (4.25) can be used to compute the covariance in the four different procedures. When the IROC method is employed to minimize the objective function, the final updated matrix $[A^*]$, which is an approximation to the Hessian at $\{\theta^*\}$ can be substituted for $[S^*]$ in the above equations. However, in this study, no attempts are made to evaluate the performance of the methods using the posterior covariance. Consequently, the values of $[V_{\theta^*}]$ are excluded from the results reported below.

The IROC minimization algorithm was first applied to a simulated case in which the measured modal parameters were taken as the values corresponding to $\theta_{11} = 0.85$, $\theta_{12} = 0.95$ and $\theta_{13} = 0.90$. The parameters for this test case were then estimated using the

OLS procedure with initial values of (1, 1, 1). The results obtained are summarized in Table 4.3. When only the first four frequencies are used, the estimates are (0.846, 0.960, 0.916). The inclusion of the first three mode shapes results in (0.845, 0.959, 0.916), which is very close to the values obtained with only the frequencies. The two sets of estimates are close because the mode shapes corresponding to the initial estimates are very close to the exact mode shapes. This is evident from the values of SSQ, which increases from 0.9103×10^{-1} when only the frequencies are considered to 0.9111×10^{-1} when the mode shapes are also included.

In several other test cases it was observed that the farther the "true" values were from the initial estimates (1, 1, 1), the better the estimates became when mode shapes were included. This is due to larger differences between the exact and the intial mode shapes. In some cases the final estimates were considerably different from the true values when only the frequencies were considered. This is a direct consequence of the fact that, when the total stiffness of the structure is modeled as in Equation 4.1, the frequencies are much more sensitive than the mode shapes to changes in $\{\theta\}$ and several combinations of the parameters could produce approximately the same frequencies. Thus the estimates obtained are not unique. Even when the mode shapes are included, the final estimates depend on the starting values to some extent. But if the minimum is sufficiently close to the starting values, the final estimate is a good approximation of the minimum. This implies that if the measured mode shapes are

Table 4.3. Results for the Test Case with $\theta_{11} = 0.85$, $\theta_{12} = 0.95$, $\theta_{13} = 0.90$

	Parameters			SSQ		No. of Function and Gradient Evaluations
	Core	Frame	Cladding	Initial	Final	
4 Freq. Only	0.846	0.960	0.916	0.9103×10^{-1}	0.708×10^{-6}	10
4 Freq. +3 Mode Shapes	0.845	0.959	0.919	0.9111×10^{-1}	0.198×10^{-4}	10

sufficiently close to the initial mode shapes corresponding to the initial estimates, good approximations to the minimum will be obtained.

In the rest of this chapter, the estimates of stiffness parameters for different components in different directions determined using various estimation schemes are examined. In all cases, no constraints were imposed on the parameters.

4.5.1 Braced Frame Direction

Table 4.4 lists the results of OLS estimation employed to determine the parameters for bending in the braced frame direction. The value of SSQ decreases from 0.108×10^{-1} at the initial estimate (1, 1, 1) to 0.33×10^{-2} at the final estimate, for a reduction of about 69%, when the frequencies alone are considered. Inclusion of mode shapes causes SSQ to decrease from 0.197 to 0.191, a reduction of only 3%. Examination of the measured and the initial mode shapes reveals that the initial estimate (1, 1, 1) yields mode shapes that are quite close to the experimental values and, as a result, no significant improvement is achieved by including the mode shapes. It is also observed from this table that the third natural frequency, which was approximately equal to the experimental value initially (2.35 Hz), has undergone considerable change after estimation and is no longer a good approximation of the experimental value. This makes it clear that the improvement in the match between the measured and the model values due to the parameter estimation procedures is only in an overall sense and not for any specific parameter.

Table 4.4. OLS Estimates for Bending in Braced Frame Direction

		Freq. Only (Hz)	4 Freq.+ 3 Mode Shapes								
			Freq. (Hz)	Mode Shapes Floor No.							
				Roof	23	21	19	17	15	12	9	6
Mode No.	1	0.411	0.414	1.00	0.93	0.85	0.76	0.67	0.56	0.45	0.28	0.13
	2	1.291	1.301	1.00	0.69	0.30	-0.11	-0.47	-0.73	-0.80	-0.69	-0.38
	3	2.402	2.419	1.00	0.30	-0.47	-0.97	-0.98	-0.46	0.34	1.26	1.02
	4	3.347	3.371									
Parameters	Core	1.051	1.061									
	Frame	0.995	1.041									
	Cladding	1.034	1.061									
SSQ		0.330×10^{-2}	0.191									
No.of Funct. and Grad. Evaluations		9	6									

The estimates from the ML, MPD and WLS procedures are tabulated in Tables 4.5 - 4.7. Except for the exterior frame stiffness parameter, the results are almost identical for the three procedures when only the frequencies are used. Taking the mode shapes into account does not appreciably alter the parameters in ML and MPD estimation methods. The WLS procedure produces slightly different values, however. The value of SSQ is the same in all three procedures (0.189). The core stiffness parameter assumes approximately the same value in all three procedures with or without the mode shapes included.

4.5.2 Rigid Frame Direction

Estimation of the stiffness parameters in the rigid frame direction yields the results given in Tables 4.8 - 4.11. With only the frequencies included, SSQ is reduced from an initial value of 0.179×10^{-1} to 0.472×10^{-2} in OLS, 0.537×10^{-2} in WLS, 0.553×10^{-2} in ML and 0.662×10^{-2} in MPD estimation, for reductions of 74, 70, 69 and 63 percent respectively. As in the braced frame direction, the ML and MPD estimates remain relatively unaffected compared to the OLS and WLS estimates when the first three mode shapes are included. The ordinary and weighted least squares procedures produce about 70 percent change in the parameters from the initial values of (1, 1, 1). For this reason, the match obtained in these procedures is far better than that obtained in ML or MPD estimation. The reduction in SSQ is about 82 - 83% (from 0.590 to 0.102 in OLS and 0.106 in WLS) for the least squares procedures as opposed to a reduction of only 3% (from 0.59 to 0.57) in ML and MPD estimation. Among the two least squares methods, the WLS procedure converges after 15 function

Table 4.5. ML Estimates for Bending in Braced Frame Direction

		Freq. Only (Hz)	4 Freq.+ 3 Mode Shapes								
			Freq. (Hz)	Mode Shapes Floor No.							
				Roof	23	21	19	17	15	12	9	6
Mode No.	1	0.409	0.409	1.00	0.93	0.85	0.76	0.66	0.56	0.45	0.28	0.13
	2	1.285	1.285	1.00	0.69	0.30	-0.11	-0.47	-0.73	-0.80	-0.69	-0.38
	3	2.390	2.391	1.00	0.30	-0.47	-0.97	-0.97	-0.45	0.34	1.26	1.02
	4	3.332	3.332									
Parameters	Core	1.042	1.042									
	Frame	0.959	0.957									
	Cladding	1.022	1.023									
SSQ		0.334 -2 X10	0.189									
No.of Funct. and Grad. Evaluations		10	10									

Table 4.6. MPD Estimates for Bending in Braced Frame Direction

		Freq. Only (Hz)	4 Freq.+ 3 Mode Shapes								
			Freq. (Hz)	Mode Shapes Floor No.							
				Roof	23	21	19	17	15	12	9	6
Mode No.	1	0.409	0.409	1.00	0.93	0.85	0.76	0.66	0.56	0.45	0.28	0.13
	2	1.285	1.285	1.00	0.69	0.30	-0.11	-0.47	-0.73	-0.80	-0.69	-0.38
	3	2.391	2.391	1.00	0.30	-0.47	-0.97	-0.97	-0.45	0.34	1.26	1.02
	4	3.332	3.332									
Parameters	Core	1.043	1.043									
	Frame	0.949	0.948									
	Cladding	1.023	1.024									
SSQ		0.334 -2 X10	0.189									
No.of Funct. and Grad. Evaluations		10	10									

Table 4.7. WLS Estimates for Bending in Braced Frame Direction

		Freq. Only (Hz)	4 Freq.+ 3 Mode Shapes								
			Freq. (Hz)	Mode Shapes Floor No.							
				Roof	23	21	19	17	15	12	9	6
Mode No.	1	0.409	0.411	1.00	0.93	0.85	0.76	0.67	0.56	0.45	0.28	0.13
	2	1.285	1.290	1.00	0.69	0.30	-0.11	-0.47	-0.73	-0.80	-0.69	-0.38
	3	2.392	2.399	1.00	0.30	-0.47	-0.97	-0.98	-0.46	0.33	1.26	1.02
	4	3.333	3.343									
Parameters	Core	1.043	1.043									
	Frame	0.963	0.940									
	Cladding	1.023	1.059									
SSQ		0.332×10^{-2}	0.189									
No.of Funct. and Grad. Evaluations		10	9									

Table 4.8. OLS Estimates for Bending in Rigid Frame Direction

		Freq. Only (Hz)	4 Freq.+ 3 Mode Shapes								
			Freq. (Hz)	Mode Shapes Floor No.							
				Roof	23	21	19	17	15	12	9	6
Mode No.	1	0.333	0.331	1.00	0.97	0.92	0.85	0.76	0.66	0.54	0.35	0.16
	2	0.963	0.975	1.00	0.77	0.41	-0.01	-0.42	-0.71	-0.81	-0.71	-0.39
	3	1.720	1.665	1.00	0.39	-0.39	-0.95	-1.02	-0.53	0.35	1.24	0.97
	4	2.290	2.306									
Parameters	Core	0.923	0.338									
	Frame	1.026	1.777									
	Cladding	0.944	1.759									
SSQ		0.472 $^{-2}$ X10	0.102									
No. of Funct. and Grad. Evaluations		9	7									

Table 4.9. ML Estimates for Bending in Rigid Frame Direction

		Freq. Only (Hz)	4 Freq.+ 3 Mode Shapes								
			Freq. (Hz)	Mode Shapes Floor No.							
				Roof	23	21	19	17	15	12	9	6
Mode No.	1	0.329	0.327	1.00	0.95	0.87	0.78	0.67	0.56	0.45	0.28	0.13
	2	0.949	0.944	1.00	0.69	0.27	-0.16	-0.52	-0.72	-0.75	-0.60	-0.31
	3	1.695	1.687	1.00	0.16	-0.67	-1.00	-0.77	-0.18	0.52	1.04	0.72
	4	2.256	2.245									
Parameters	Core	0.902	0.894									
	Frame	0.948	0.929									
	Cladding	0.914	0.905									
SSQ		0.553 -2 X10	0.570									
No.of Funct. and Grad. Evaluations		9	8									

Table 4.10. MPD Estimates for Bending in Rigid Frame Direction

		Freq. Only (Hz)	4 Freq.+ 3 Mode Shapes								
			Freq. (Hz)	Mode Shapes Floor No.							
				Roof	23	21	19	17	15	12	9	6
Mode No.	1	0.327	0.327	1.00	0.95	0.87	0.78	0.67	0.56	0.45	0.28	0.13
	2	0.944	0.945	1.00	0.69	0.27	-0.16	-0.52	-0.72	-0.75	-0.60	-0.31
	3	1.687	1.687	1.00	0.16	-0.67	-1.00	-0.77	-0.18	0.52	1.04	0.72
	4	2.245	2.246									
Parameters	Core	0.895	0.894									
	Frame	0.938	0.939									
	Cladding	0.903	0.905									
SSQ		0.662 $X10^{-2}$	0.569									
No. of Funct. and Grad. Evaluations		8	9									

Table 4.11. WLS Estimates for Bending in Rigid Frame Direction

		Freq. Only (Hz)	4 Freq.+ 3 Mode Shapes								
			Freq. (Hz)	Mode Shapes Floor No.							
				Roof	23	21	19	17	15	12	9	6
Mode No.	1	0.329	0.327	1.00	0.97	0.92	0.85	0.76	0.66	0.55	0.36	0.17
	2	0.950	0.965	1.00	0.78	0.42	0.00	-0.41	-0.70	-0.81	-0.72	-0.40
	3	1.697	1.640	1.00	0.40	-0.37	-0.94	-1.02	-0.56	0.33	1.24	1.00
	4	2.258	2.277									
Param-eters	Core	0.904	0.323									
	Frame	0.952	0.890									
	Clad-ding	0.916	1.850									
SSQ		0.537 -2 X10	0.106									
No. of Funct. and Grad. Evaluations		9	15									

and gradient evaluations which is more than twice the number required for the OLS method.

4.5.3 Torsion

The results of the various estimation techniques for the torsional response of the building are listed in Tables 4.12 - 4.15. The decrease in SSQ is the highest for the OLS method, from 0.322×10^{-1} to 0.468×10^{-3} or about 99%, which indicates an excellent match. The reduction in the other methods is about 87 - 88%.

4.5.4 Comparison

It is seen from Tables 4.4 - 4.15 that, in most cases, the OLS method requires the lowest number of function and gradient evaluations and also procudes the best match by yielding the lowest value for SSQ. The different estimation methods do not yield significantly different values in the braced frame direction as in the rigid frame direction when mode shapes are included. This is mainly due to the remarkable agreement between the experimental and the prior analytical braced frame mode shapes. All four methods converge to values that do not differ much from the initial estimates (less than 7 percent change in all θ_{ij}).

The large changes for the parameters given by the OLS and WLS methods in the rigid frame direction would normally be considered unacceptable. These changes are mainly attributable to the considerable difference between the measured and the prior analytical rigid frame mode shapes. Due to the relative insensitivity of the mode shapes to changes in $\{\theta\}$, the measured and the analytical mode shapes can be reconciled only by producing large changes in the parameters. This is easily accomplished in the OLS procedure since it does not impose

Table 4.12. OLS Estimates for Torsional Response

	Parameters			Frequencies(Hz)			
	Core	Frame	Cladding	Mode No.			
				1	2	3	4
	1.091	1.079	1.102	0.427	1.230	2.093	2.907
SSQ	0.468×10^{-3}						
No. of Funct. and Grad. Evaluations	9						

Table 4.13. ML Estimates for Torsional Response

	Parameters			Frequencies(Hz)			
	Core	Frame	Cladding	Mode No.			
				1	2	3	4
	1.051	1.022	1.081	0.421	1.213	2.063	2.966
SSQ	0.401×10^{-2}						
No. of Funct. and Grad. Evaluations	9						

Table 4.14. MPD Estimates for Torsional Response

	Parameters			Frequencies(Hz)			
	Core	Frame	Cladding	Mode No.			
				1	2	3	4
	1.049	1.015	1.081	0.421	1.212	2.063	2.865
SSQ	0.416×10^{-2}						
No.of Funct. and Grad. Evaluations	9						

Table 4.15. WLS Estimates for Torsional Response

	Parameters			Frequencies(Hz)			
	Core	Frame	Cladding	Mode No.			
				1	2	3	4
	1.051	1.023	1.081	0.421	1.213	2.064	2.867
SSQ	0.395×10^{-2}						
No.of Funct. and Grad. Evaluations	9						

any constraints on the parameters nor does it make use of a weighting matrix by which the frequencies are given more importance than the mode shapes. Therefore, the OLS method generates final estimates that differ by large amounts from (1, 1, 1).

In maximum likelihood estimation, the mode shape terms contribute a relatively small amount to the objective function on account of the relatively high values of variance assumed for the mode shapes. As a result, the match between the analytical and the experimental mode shapes is given much less consideration than the match in the frequencies. Hence, this procedure yields estimates reasonably close to the prior values so that the improved analytical model reproduces the experimental frequencies with a greater degree of accuracy than it does for the mode shapes.

The same is also true of Bayesian estimation in which, in addition to the smaller weights used for the mode shapes, the parameters are also constrained by the inclusion of the prior distribution term in ψ. The effect of this term is such that the objective function increases as the parameters deviate more from their prior mean values, which in this case are all equal to one. Consequently, this procedure also produces estimates that lie near the initial values. However, the WLS method converges to values that differ as much from the initial values as the OLS estimates. This could be ascribed to the following. Since the mode shapes are much less sensitive to $\{\theta\}$ than the frequencies, they also possess much smaller variance for a given parameter covariance $[V_\theta]$. When these values are added to the

experimental covariance $[V_y]$, they tend to reduce the differences between the low values of variance for the frequencies and the high values for the mode shapes. The weights generated by the inverse of $[V_e]$ may then be such that the frequencies and the mode shapes are given about the same weightage. It may even be true in some cases that some of the mode shape coefficients are given more weight than any of the frequencies. The weighted least squares method will, in this case, function like the ordinary least squares method and the estimates will tend to differ by large amounts as in the OLS method.

Comparison of the two methods that utilize the prior covariance of the parameters, namely the WLS and the MPD procedures, shows that in all cases the WLS method gives a better match with lower values of SSQ. The effect of changing $[V_\theta]$ in these two methods was examined by using various values for $\sigma(\theta_{ij})$. In addition to the 3, 4 and 5% standard deviations for the core, frame and cladding parameters, two cases with 3, 5 and 10 and 5, 10 and 15% standard deviations were considered. The results obtained are summarized in Table 4.16 for bending in the rigid frame direction considering the frequencies alone. This table suggests that the value of SSQ is higher for increasing variance of the parameters in both of the methods. The core and the cladding parameters remain relatively unaltered for the different cases.

The final parameter estimates for the four procedures taken from Tables 4.4 - 4.15 are summarized in Table 4.17. Though the OLS

Table 4.16. Comparison of Estimates from MPD and WLS Methods

Method	Maximum Posterior Density				Weighted Least Squares			
Std.dev. (Core,Frame, Cladding)	Core	Frame	Clad-ding	SSQ	Core	Frame	Clad-ding	SSQ
3,4,5 %	0.895	0.938	0.903	0.662×10^{-2}	0.904	0.952	0.916	0.537×10^{-2}
3,5,10 %	0.895	0.935	0.903	0.666×10^{-2}	0.903	0.949	0.915	0.547×10^{-2}
5,10,15 %	0.895	0.930	0.903	0.672×10^{-2}	0.903	0.950	0.915	0.548×10^{-2}

Table 4.17. Comparison of Estimates from Different Methods

		Freq. Only			Freq.+ Mode Shapes		
	Method	Core	Frame	Cladding	Core	Frame	Cladding
Braced Frame Bending	OLS	1.051	0.995	1.034	1.061	1.041	1.061
	ML	1.042	0.959	1.022	1.042	0.957	1.023
	MPD	1.043	0.949	1.023	1.043	0.948	1.024
	WLS	1.043	0.963	1.023	1.043	0.940	1.059
Rigid Frame Bending	OLS	0.923	1.026	0.944	0.338	1.777	1.759
	ML	0.902	0.948	0.914	0.894	0.929	0.905
	MPD	0.895	0.938	0.903	0.894	0.939	0.905
	WLS	0.904	0.952	0.916	0.323	0.890	1.850
Torsion	OLS	1.091	1.079	1.102	-	-	-
	ML	1.051	1.022	1.081	-	-	-
	MPD	1.049	1.015	1.081	-	-	-
	WLS	1.051	1.023	1.081	-	-	-

procedure understandably yields the least error in most cases, the estimates obtained may be highly unreliable. The other three methods produce values that are approximately equal when only the frequencies are included. The estimates obtained with the mode shapes taken into account are not to be relied upon since the form of the stiffness model used is such that large changes in $\{\theta\}$ are called for to cause considerable changes in the mode shapes. Furthermore, as discussed earlier, the OLS and ML estimates are not unique, especially when the mode shapes are excluded. The question of uniqueness does not arise in MPD and WLS estimation since a prior distribution is assigned to the parameters in each case.

Taking the above factors into account, the estimates obtained from the WLS method without the mode shapes are considered acceptable here. These values, for core, frame and cladding respectively, are 0.904, 0.952 and 0.916 in the rigid frame direction, 1.043, 0.963 and 1.023 in the braced frame direction and 1.051, 1.023 and 1.081 in torsion. The ML and MPD estimates also exhibit the same trend as the above values.

The parameter estimates for the cladding stiffness suggest that the insterstory shear stiffness is greater than the assumed value of 625 Kips/inch in the braced frame direction and torsion and less in the rigid frame direction. All the estimates are not too far from one which implies that the initial value is a good approximation in all three directions. The final estimate in torsion is the highest

(about 8 percent more than the assumed value), which could mean that the cladding affects the torsional response of the structure slightly more than the bending response, or the contribution to stiffness is greater in torsion. This is consistent with the analytical finite element model studies of Reference 10, which show that the torsional frequencies are most altered by cladding effects. However, the above values are too close to make any decisive conclusions at this point and further investigations are needed to consolidate these findings.

5.0 SUMMARY AND CONCLUSIONS

Two highrise buildings were studied in an effort to investigate the effects of the exterior cladding on the dynamic behavior of the main structure. The role of cladding was studied experimentally by conducting vibration tests and employing parameter estimation techniques to determine the dynamic properties from test data. Parameter estimation techniques were also employed to evaluate certain parameters in the structural stiffness matrix which included the effects of cladding as an added interstory shear stiffness.

The first building was studied during its construction as the cladding was installed in order to directly assess its effects on the dynamic response. Ambient tests were carried out over a period of several months at different stages of construction, starting after the erection of the steel frame and the commencement of the installation of cladding and continuing at regular intervals until the building was completely clad. The time domain measurements were used to compute the spectral density functions. The modal parameters were obtained using nonlinear least squares curve fitting techniques. The analytical form of the magnitude of the frequency response function was fitted to the magnitude of each of the computed linear spectra. The Levenberg-Marquardt method was applied to minimize the sum of squares objective function. The modal parameters

were determined from the best possible fit. It was found that the frequencies (a) show an initial decreasing trend and, except for the fundamental frequencies in braced frame bending and torsion, (b) show a subsequent increasing trend throughout the construction phase.

The initial decrease in all the frequencies was attributed to the overall increase in the mass of the structure, which could more than offset any possible increase in the stiffness due to the cladding or other elements. The subsequent increase in the frequencies was ascribed to the stiffness effects being more predominant than the mass effects during this period. Comparing the amount of cladding that had been installed on different test dates with the frequencies, it was observed that the cladding levels had gone up considerably in the same period, suggesting that the cladding could play a significant role in altering the total stiffness of the structure. The fact that only the upper frequencies show an increasing trend is also in accordance with the anticipated behavior of cladding, which can be expected to interact with the higher modes to a greater degree than the lower modes, due to more curvature associated with the higher modes. The above considerations indicate that at least part of the increase in the frequencies could be ascribed to the exterior curtain wall. It should be noted that some of this increase could also be due to other effects or elements such as the interior partitions.

The second building was employed to evaluate the cladding performance from an analytical viewpoint, making use of dynamic test results. Full scale forced vibration tests were carried out with the aid of an electrohydraulic shaker. The ability of this shaker to

produce arbitrary waveforms for the input function was utilized and rapid sine sweep techniques were employed, resulting in a testing time that is only a fraction of the time required for steady-state testing methods. Transfer functions were computed and fitted to determine the modal parameter estimates for the building. These estimates were also compared with the ambient test results obtained earlier. The frequencies and the damping ratios from the ambient tests were found to be higher than the corresponding values from the forced vibration tests.

The forced vibration test results were used to modify an a priori stiffness matrix model of the building so that the match between the analytical and the experimental modal parameters as improved and also a measure of the cladding stiffness was obtained. A weighted least squares method was employed to estimate the stiffness parameters associated with the stiffness matrices for the core, the exterior frame and the cladding in each of the three directions, namely bending in the braced and rigid frame directions and torsion. The parameters were also determined using the ordinary least squares, maximum likelihood and maximum posterior density (Bayesian) estimation procedures and the results from the various methods were compared.

With only the frequencies taken into account in estimation, all the methods yielded reasonable parameter values that were close to unity. But when the mode shapes were also included, it was found that if the initial mode shapes were not sufficiently close to the experimental values, large and unacceptable changes in the parameters were necessary to significantly improve the mode shapes predicted by

the analytical model. The final parameter values were chosen as those that gave an acceptable match for the frequencies alone. The interstory shear stiffness parameter utilized in constructing the cladding stiffness matrix was found to be somewhat higher in torsion than in either of the two bending directions. This could imply that, for the highrise building considered, the stiffness effects of the curtain wall are slightly more in torsion, which is consistent with the results of Reference 10.

The preliminary findings reported in this research work are only a first step in understanding the role of cladding as it affects the dynamic response of the main structure. More investigations, both experimental and analytical, are needed to bring out fully the cladding influence and the cladding-structure interaction effects. Experimental studies during the construction of a building with heavyweight cladding are necessary to determine the role of cladding more effectively. In addition, further studies, in which the experimental results are used with analytical models for each of the different stages of construction with different levels of cladding, would be valuable in evaluating the cladding performance. Analytical studies are also needed in which the parametric model used is such that the inclusion of the mode shapes would not cause excessive and unacceptable changes in the prior values of the structural parameters. This would make it possible to include the mode shapes in choosing the final values for the parameters.

APPENDIX A

THE IROC METHOD

The inverse rank one correction (IROC) method belongs to the class of methods known as variable metric or quasi-Newton methods. These methods are applicable to any general objective function as opposed to the Gauss-Newton and the Levenberg-Marquardt methods which are applicable to sum of squares type functions only. In all these methods, the inverse to the Hessian $[S^k]$ appearing in Equation (2.35), or the Hessian itself as in the IROC method, is approximated initially by a symmetric matrix which is then updated in the subsequent iterations. The various variable metric methods differ in the updating formula used. The sequence of matrices generated is expected to converge to the Hessian or the inverse of the Hessian as the minimum is approached. If the objective function is quadratic, this takes place in p iterations where p is the number of unknown parameters.

In the well known Davidon-Fletcher-Powell (DFP) method (77, 78), the approximation to the inverse of the Hessian is updated by adding a matrix of rank two in each iteration. This method and its other modifications require a unidirectional search along the descent directions generated to locate the optimum value for the step size ξ; that is, ψ is minimized with respect to ξ in every iteration. Rewriting Equation (2.35) with the step size parameter ξ,

$$\{\theta^{k+1}\} = \{\theta^{k}\} - \xi\, [S^{k}]^{-1} \{g^{k}\} \tag{A.1}$$

from which

$$\{\theta^{k+1}\} = \{\theta^{k}\} - \xi^{*}\, [B^{k}] \{g^{k}\} \tag{A.2}$$

where $[B^{k}]$ is the current approximation to $[S^{k}]^{-1}$ and ξ^{*} is the value of ξ such that $\psi(\xi^{*})$ is a minimum as a function of ξ.

Bard, in his survey (79), found that another group of methods that use correction matrices of rank one and that do not require unidirectional minimization performed considerably better than the DFP methods. The IROC method belongs to this group, but the matrix that is approximated is the Hessian itself (34, 79). The development of the IROC method is as follows.

Since $[S^{k}]$ is the matrix of the second derivatives, it can be approximated as

$$[S^{k}] = \left[\frac{\Delta g}{\Delta \theta}\right] \tag{A.3}$$

where

$$\{\Delta g\} = \{g^{k+1}\} - \{g^{k}\}$$

and

$$\{\Delta \theta\} = \{\theta^{k+1}\} - \{\theta^{k}\}$$

Let $[A^{k}]$ denote the approximation to $[S^{k}]$ in the kth iteration and let $[A^{k+1}]$ be the updated version of $[A^{k}]$ such that

$$[A^{k+1}] = [A^{k}] + [\Delta A^{k}] \tag{A.4}$$

where $[\Delta A^k]$ is the correction matrix added to $[A^k]$. Substituting $[A^{k+1}]$ for $[S^k]$ in Equation (A.3)

$$[\Delta A^k]\ \{\Delta\theta\} = \{\Delta g\} - [A^k]\ \{\Delta\theta\} \tag{A.5}$$

Let $[\Delta A^k]$ be of rank one. Therefore it can be represented as

$$[\Delta A^k] = \{b^k\}\{b^k\}^T \tag{A.6}$$

where $\{b^k\}$ is an arbitrary vector. Equation (A.6) in (A.5) gives

$$\{b^k\}\ \{b^k\}^T\ \{\Delta\theta\} = \{a^k\} \tag{A.7}$$

in which $\{a^k\}$ is defined as the right hand side of Equation (A.5). From Equation (A.7)

$$\{b^k\} = \{a^k\}/\{b^k\}^T\ \{\Delta\theta\} \tag{A.8}$$

Substituting Equation (A.8) into (A.7), it can be shown that

$$\{b^k\}^T\ \{\Delta\theta\} = [\{a^k\}^T\ \{\Delta\theta\}]^{\frac{1}{2}} \tag{A.9}$$

Equation (A.6) now becomes, in view of Equation (A.8) and (A.9),

$$[\Delta A^k] = \{a^k\}\ \{a^k\}^T/\{a^k\}^T\ \{\Delta\theta\} \tag{A.10}$$

which is the required correction matrix. To make certain that all the matrices generated remain positive definite, Marquardt type corrections can be added to the diagonal elements of $[A^k]$. The parameters $\{\theta\}$ are calculated using

$$\{\theta^{k+1}\} = \{\theta^k\} - \xi \left[[A^k] + \mu^k [I] \right]^{-1} \{g^k\} \qquad (A.11)$$

where μ^k is the Marquardt parameter. The procedure for choosing μ^k was discussed in detail in Chapter II. The value of ξ is chosen so that $\psi^{k+1} < \psi^k$. It is not necessary to determine the optimum ξ as for the DFP methods.

The initial approximation $[A^1]$ for the first iteration can be computed following the recommendations given in Reference 34. The diagonal elements of $[A^1]$ are taken as

$$A^1_{ii} = - \frac{g^1_i}{\theta^1_i} \qquad (A.12)$$

and the off-diagonal elements are all set equal to zero. When the iterative procedure is terminated after locating the approximate minimum $\{\theta^*\}$, the matrix $[A^*]$ will be the approximate Hessian evaluated at $\{\theta^*\}$.

REFERENCES

1. Bekey, G.A., "System Identification - An Introduction and a Survey," Simulation, Vol. 15, October 1970, pp. 151-166.

2. Eykhoff, P., System Identification - Parameter and State Estimation, John Wiley and Sons, Inc., New York, 1974.

3. Pilkey, W.D. and Cohen, R., (eds.), System Identification of Vibrating Structures: Mathematical Models from Test Data, ASME, New York, 1972.

4. Proceedings, ASCE/EMD Specialty Conference on Dynamic Response of Structures: Instrumentation, Testing Methods and System Identification, held at University of California, Los Angeles, March 30-36, 1976.

5. Eaton, K.J., "Cladding and the Wind," Journal of the Structural Division, ASCE, Vol. 102, May 1976, pp. 1043 - 1058.

6. "Facades: Errors Can be Expensive", Engineering News Record, Vol. 204, January 1980, pp. 30-34.

7. Gjelsvik, A., "Interaction Between Frames and Precast Panel Walls," Journal of the Structural Division, ASCE, Vol. 100, February 1973, pp. 405-426.

8. Oppenheim, I., "Dynamic Behavior of Tall Buildings with Cladding," Proceedings, 5th World Conference on Earthquake Engineering held at Rome, Italy, June 25-29, 1973, pp. 2769-2773.

9. Will, K.M., Goodno, B.J. and Saurer, G., "Dynamic Analysis of Buildings with Precast Cladding," Proceedings, ASCE 7th Conference on Electronic Computation Held at St. Louis, Missouri, August 6-8, 1979, pp. 251-264.

10. Goodno, B.J., Will, K.M. and Palsson, H., "Effect of Cladding on Building Response to Moderate Ground Motion," Proceedings, 7th World Conference on Earthquake Engineering held at Istanbul, Turkey, September 1980, pp. 449-456.

11. Ward, H.S. and Crawford, R., "Wind Induced Vibrations and Building Modes," Bulletin of the Seismological Society of America, Vol. 56, August 1966, pp. 763-813.

12. Crawford, R. and Ward, H.S., "Determination of the Natural Periods of Buildings," Bulletin of the Seismological Society of America, Vol. 54, December 1964, pp. 1743-1756.

13. Udwadia, F.E. and Trifunac, M.D., "Time and Amplitude Dependent Response of Structures," International Journal of Earthquake Engineering and Structural Dynamics, Vol. 2, 1974, pp. 359-378.

14. Trifunac, M.D., "Comparison Between Ambient and Forced Vibration Experiments," International Journal of Earthquake Engineering and Structural Dynamics, Vol. 1, 1973, pp. 133-150.

15. McLamore, V.R., et al., "Ambient Vibration of Two Suspension Bridges," Journal of the Structural Division, ASCE, Vol. 97, October 1971, pp. 2567-2582.

16. Abdel-Ghaffer, A.M. and Housner, G.W., "Ambient Vibration Tests of Suspension Bridge," Journal of the Engineering Mechanics Division, ASCE, Vol. 104, October 1978, pp. 983-999.

17. Abdel-Ghaffer, A.M., "Vibration Studies and Tests of a Suspension Bridge," International Journal of Earthquake Engineering and Structural Dynamics, Vol. 6, 1978, pp. 473-496.

18. Buckland, P.G., et al., "Suspension Bridge Vibrations: Computed and Measured," Journal of the Structural Division, ASCE, Vol. 105, May 1979, pp. 859-874.

19. Rubin, S., "Ambient Vibration Survey of Offshore Platforms," Journal of the Engineering Mechanics Division, ASCE, Vol. 106, June 1980, pp. 425-441.

20. Cherry, S. and Brady, A.G., "Determination of Structural Dynamics Properties by Statistical Analysis of Random Vibrations," Proceedings, 3rd World Conference on Earthquake Engineering held at Wellington, New Zealand, January 22-Feb. 1, 1965.

21. Cole, H.A., "On-the-line Analysis of Random Vibrations," AIAA Paper No. 68-288, AIAA/ASME 9th Structures, Structural Dynamics and Materials Conference held at Palm Springs, California, April 1-3, 1968.

22. Cole, H.A., "On-the-line Failure Detection and Damping Measurements of Aerospace Structures by Random Decrement Signature," NASA-CR-2205, 1973.

23. Gersch, W., et al., "Maximum Likelihood Estimation of Structural Parameters from Random Vibration Data," Journal of Sound and Vibration, Vol. 31, 1973, pp. 295-308.

24. Gersch, W. and Foutch, D.A., "Least Squares Estimation of Structural System Parameters Using Covariance Function Data," IEEE Transactions on Automatic Control, Vol. AC-19, 1974, pp. 898-903.

25. Vanmarcke, E.H., "Properties of Spectral Moments with Applications to Random Vibrations," Journal of the Engineering Mechanics Division, ASCE, Vol. 98, April 1972, pp. 425-446.

26. Vanmarcke, E.H., "Method of Spectral Moments to Estimate Structural Damping," In Stochastic Problems in Dynamics, B.L. Clarkson (ed.), Pitman Press, London, 1977.

27. Schiff, A.J., "Identification of Large Structures Using Data from Ambient and Low Level Excitations," in System Identification of Vibration Structures, Loc. Cit. Ref. 3.

28. Bendat, J.S. and Piersol, A.G., Engineering Applications of Correlation and Spectral Analysis, John Wiley and Sons, Inc., New York, 1980.

29. Otnes, R.K. and Enochson, L.D., Applied Time Series Analysis, Wiley-Interscience, New York, 1978.

30. Jenkins, G.M. and Watts, D.G., Spectral Analysis and Its Application, Holden Day, San Francisco, 1969.

31. Welch, P.D., "The Use of Fast Fourier Transform for the Estimation of Power Spectra," IEEE Transactions on Audio and Electroacoustics, Vol. AU-15, June 1967, pp. 70-73.

32. Levenberg, K., "A Method for the Solution of Certain Nonlinear Problems in Least Squares," Quarterly of Applied Mathematics, Vol. 2, 1944, pp. 164-168.

33. Marquardt, D.W., "An Algorithm for Least Squares Estimation of Nonlinear Parameters," SIAM Journal, Vol. 11, 1963, pp. 431-441.

34. Bard, Y., Nonlinear Parameter Estimation, Academic Press, New York, 1974.

35. Kowalik, J. and Osborne, M.R., Methods for Unconstrained Optimization Problems, American Elsevier, New York, 1968.

36. Beck, J.V. and Arnold, K.J., Parameter Estimation in Engineering and Science, John Wiley and Sons, Inc., New York, 1977.

37. Hudson, D.E., "Dynamic Tests of Full Scale Structures," Journal of the Engineering Mechanics Division, ASCE, Vol. 103, December 1977, pp. 1141-1157.

38. Kennedy, C.D. and Pancu, C.D.P., " Use of Vectors in Vibration Measurements and Analysis," Journal of the Aeronautical Sciences, Vol. 14, 1947, pp. 603-623.

39. Lewis, R.C. and Wrisley, D.L., "A System for the Excitation of Pure Natural Modes of Complex Structures," Journal of the Aeronautical Sciences, Vol. 17, 1950, pp. 705-722.

40. Jennings, P.C., et al., "Forced Vibration of a Tall Steel Frame Building," International Journal of Earthquake Engineering and Structural Dynamics, Vol. 1, 1972, pp. 107-132.

41. Jennings, P.C. and Kuroiwa, J.H., "Vibration and Soil0Structure Interaction Tests of a 9-Story Reinforced Concrete Building," Bulletin of the Seismological Society of America, Vol. 58, 1968, pp. 891-915.

42. Nielsen, N.N., "Vibration Tests of a 9-Story Steel Frame Building," Journal of the Engineering Mechanics Division, ASCE, Vol. 92, 1966, pp. 81-110.

43. Foutch, D.A., "The Vibrational Characteristics of a 12-Story Steel Frame Building," International Journal of Earthquake Engineering and Structural Dynamics, Vol. 6, 1978, pp. 265-294.

44. Englekirk, R.E. and Matthiesen, R.B., "Forced Vibration of an 8-Story Reinforced Concrete Building," Bulletin of the Seismological Society of America, Vol. 57, 1967, pp. 421-436.

45. Bouwkamp, J.G. and Blohm, J.K., "Dynamic Response of a 2-Story Steel Frame Structure," Bulletin of the Seismological Society of America, Vol. 56, 1966, pp. 1289-1303.

46. Craig, J.I. and Lewis, F.D., "A Rectilinear Force Generator for Full Scale Vibration Testing," Proceedings, 2nd ASCE/EMD Specialty Conference on Dynamic Response of Structures: Experimentation, Observation, Prediction and Control held at Atlanta, Georgia, January 15-16, 1981.

47. Ramsey, K.A., "Effective Measurements for Structural Dynamic Testing (Part II)", Sound and Vibration, April, 1976, pp. 18-31.

48. White, R.G., "Evaluation of the Dynamic Characteristics of Structures By Transient Testing," Journal of Sound and Vibration, Vol. 15, 1971, pp. 147-161.

49. Goodno, B.J. and Palsson, H., "Torsional Response of Partially-Clad Structures," Proceedings, Conference on Earthquakes and Earthquake Engineering: The Eastern U.S. held at Knoxville, Tennessee, September 14-17, 1981.

50. "Modal Analysis Opearing and Service Manual (Optien 402)", Hewlett-Packard, January 1976.

51. Meirovitch, L., Analytical Methods in Vibration, Macmillan, New York, 1967.

52. Foutch, D.A., "A Study of the Vibrational Characteristics of Two Multistory Buildings, EERL 76-03, Cal Tech, Pasadena, California.

53. Flannelly, W.G., et al., "A Theory of Identification of the Parameters in the Equations of Motion of a Structure Through Dynamic Testing," Paper No. C.1, Symposium on Structural Dynamics held at Laughborough, England, March 23-25, 1970.

54. Thorem, A.R., "Derivation of Mass and Stiffness Matrices from Dynamic Test Data," AIAA Paper No. 72-346, AIAA/ASME/SAE 13th Structures, Structural Dynamics and Materials Conference held at San Antonio, Texas, April 10-12, 1972.

55. Berman, A. and Flannelly, W.G., "Theory of Incomplete Models of Dynamic Structures," AIAA Journal, Vol. 9, August 1971, pp. 1481-1487.

56. Baruch, M., "Optimization Procedure to Correct Stiffness and Flexibility Matrices Using Vibration Tests," AIAA Journal, Vol. 16, November 1978, pp. 1208-1210.

57. Fu-Shang Wei, "Stiffness Matrix Correction from Incomplete Test Data," AIAA Journal, Vol. 18, October 1980, pp. 1274-1275.

58. Caravani, P. and Thomson, W.T., "Identification of Damping Coefficients in Multidimensional Linear Systems," Journal of Applied Mechanics, Vol. 41, 1974, pp. 379-382.

59. Thomson, W.T., et al., "A Numerical Study of Damping," International Journal of Earthquake Engineering and Structural Dynamics, Vol. 3, 1974, pp. 97-103.

60. Beliveau, J.G., "Identification of Viscous Damping in Structures from Modal Information," Journal of Applied Mechanics, Vol. 43, 1976, pp. 335-339.

61. Ross, R.G., "Synthesis of Stiffness and Mass Matrices from Experimental Vibration Modes," SAE Paper No. 710787, SAE Transaction, Vol. 80, 1971, pp. 2627-2635.

62. Collins, J.D., et al., "Statistical Identification of Structures," AIAA Journal, Vol. 12, February 1974, pp. 185-190.

63. Ibanez, P., "Methods for the Indentification of Dynamic Parameters of Mathematical Structural Models from Experimental Data," Nuclear Engineering and Design, Vol. 27, 1974, pp. 209-219.

64. Torkamani, M.A.M. and Hart, G.C., "Earthquake Engineering: Parameter Identification," Preprint No. 2499, ASCE National Structural Engineering Convention held at New Orleans, Louisiana, April 14-18, 1975.

65. Chen, J.C. and Garba, J.A., "Analytical Model Improvement Using Perturbation Techniques," AIAA Journal, Vol. 18, June, 1980, pp. 684-690.

66. Young, J.P. and Cu, F.J., "Mathematical Modeling via Direct Use of Vibration Data," SAE Paper No. 690615.

67. Collins, J.D., et al., "Methods and Applications of System Identification in Shock and Vibration," in System Identification of Vibrating Structures, Loc. Cit. Ref. 3.

68. Hart, G.C. and Yao, T.P., "System Identification in Structural Dynamics," Journal of the Engineering Mechanics Division, ASCE, Vol. 103, December 1977, pp. 1089-1104.

69. Ibanez, P., "Review of Analytical and Experimental Techniques for Improving Structural Dynamic Models," Welding Research Council Bulletin No. 249, June 1979.

70. Hart, G.C., "Eigenvalue Uncertainty in Stressed Structures," Journal of the Engineering Mechanics Division, ASCE, Vol. 99, June 1973, pp. 481-494.

71. Hart, G.C. and Collins, J.D., "The Treatment of Randomness in Finite Element Modeling," Transactions of the SAE, Vol. 81, 1970, pp. 2408-2416.

72. Collins, J.D. and Thomson, W.T., "The Eigenvalue Problem for Structural Systems with Statistical Properties," AIAA Journal, Vol. 7, April 1969, pp. 642-648.

73. Kiefling, L.A., "Comment on the Eigenvalue Problem for Structural Systems with Statistical Properties," AIAA Journal, Vol. 8, July 1970, pp. 1371-1372.

74. Fox, R.L. and Kapoor, M.P., "Rates of Change of Eigenvalues and Eigenvectors," AIAA Journal, Vol. 6, December 1968, pp. 2426-2429.

75. Nelson, R.B., "Simplified Calculation of Eigenvector Derivatives," AIAA Journal, Vol. 14, September 1976, pp. 1201-1205.

76. Vanhonacker, P., "Differential and Difference Sensitivities of Natural Frequencies and Mode Shapes of Mechanical Systems," AIAA Journal, Vol. 18, December 1980, pp. 1511-1514.

77. Fletcher, R. and Powell, M.J.D., "A Rapidly Convergent Descent Method for Minimization," Computer Journal, Vol. 6, 1963, pp. 163-168.

78. Fiacco, A.V. and McCormick, G.P., Nonlinear Programming: Sequential Unconstrained Minimization Techniques, John Wiley and Sons, Inc., New York, 1968.

79. Bard, Y., "Comparison of Gradient Methods for the Solution of Nonlinear Parameter Estimation Problems," SIAM Journal of Numerical Analysis, Vol. 7, 1970, pp. 157-186.